Investigations into New Functionalised Thiosemicarbazones and Related Carbon Nanohybrids for the Imaging of Prostate Cancer

Cortezon Tamarit, Fernando

Award date:
2017

Awarding institution:
University of Bath

Investigations into New Functionalised Thiosemicarbazones and Related Carbon Nanohybrids for the Imaging of Prostate Cancer

Fernando Carlos Cortezón Tamarit

A thesis submitted for the degree of Doctor of Philosophy

University of Bath

Department of Chemistry

November 2016

Table of Contents

Acknowledgements

First, I would like to thank my supervisor Prof Sofia Pascu for giving me the opportunity of carrying out the work in this PhD. Her support has been essential throughout the duration of this work, giving timely advice, suggesting exciting ideas and also giving me the freedom to explore these and other ideas.

I also would like to thank Dr Pedro Estrela for his superb work in coordinating PROSENSE, successfully putting together people of so many countries and backgrounds. I tried to attract him to the Chemistry side and he introduced me into the world of sensing.
I also thank Prof Rex Tyrrel for all the helpful insight into the biological part of this work.

A special thanks to Prof Jon Dilworth for his attention and the good mood over the numerous meetings we had over Oxford and Bath. Those meetings always finished with some answers and, generally, enough suggestions to start another PhD. He always helped me to keep the feet on the ground with the final goal always in mind.

I want to thank all the Prosensian fellows for making all our meetings during the PROSENSE project so much fun despite all the posters and early morning presentations.

All the members of the SIP group contributed to create an enjoyable environment throughout my stay in Bath. I want to thank Dr Haobo Ge for the help with cell culturing and the biological aspects in general and Dr Vincenzo Mirabello for his help, as the absolute expert in fluorescence, with the microscopy aspects presented in this thesis. I also would like to thank Dr David Gonzalez Calatayud for his help with TEM, his ability to fix any possible device and the scientific and non-scientific conversations.

Special thanks to Boyang Mao for all the time we shared in the office. He provided some insights into the Chinese culture over the conversations we had despite the apparent incompatibility of the Spanish and Chinese accents. You owe me a guided visit to China!

Giles Prentice was always supportive, close and willing to join all our group activities.

My desk neighbour, Alex Coxon was also a great support as a great chemist and an expert in international politics and cricket. His assistance in the improvement of my English with the “word of the day” or slang terms was priceless. He was always up for a pint and a chat and helped me to appreciate and understand this country a bit better.

The group of Spanish people in Bath, especially Patricia, Silvia and David (a.k.a. Bataman), made these years real fun with many hours spent in the pub or big events like Halloween film nights, Guy Fawke's fireworks, cocktail parties or Christmas dinners (most of them surprisingly held in Silvia's place…).

The group of chemists (Javi, Alex, Miguel) and Sara I met somewhere around 2006 deserve a special mention as their long-lasting friendship has been fundamental in all this time and more importantly since I left Madrid four years ago. Alex, Sara and Miguel made me appreciate the hidden beauty of Birmingham and were always welcoming and willing to listen when I felt down.

I would like to thank particularly my parents for all the support throughout the years. You have made a real effort and showed real passion for Science and Chemistry and have helped me to get where I stand today. You got used to the Madrid-Bristol flight and planned every visit with lots of excitement, even practising your English in advance.

Lastly, I want to thank Patri for being the biggest support of all. You have always been there and your ability to look for the bright side of everything helped me through the bad times. The time we spent living here and all your visits were unforgettable and constituted a motivation for many months in advance. Te quiero!

Abstract

This work describes investigations into novel fluorescent nanohybrids based on carbon nanomaterials for the optical imaging of prostate cancer cells. The synthesis and characterisation of the different components of the nanoprobes are described within each chapter. The cellular response of as-prepared fluorophores, peptide conjugate and nanoprobes was evaluated in PC-3 cells by optical microscopy techniques for the first time. The new fluorescent conjugate synthesised showed targeted behaviour towards prostate cancer cells and the functional hybrids showed promising characteristics as synthetic scaffolds for future imaging nanomaterials.

Chapter 1 describes the context of this work, including different imaging modalities applied to the diagnosis, staging and follow-up of prostate cancer. The use of bombesin as a targeting peptide for prostate cancer, and its incorporation in different imaging probes from current state-of the-art is discussed. The use of specific imaging probes as thiosemicarbazonato-based species is described, due to their current importance in tumour hypoxia detection and multimodality imaging potential. Finally, the use of single walled carbon nanotubes as biomedical scaffolds with a special interest in imaging applications is reviewed.

Chapter 2 describes synthetic approaches towards novel functional unsymmetrical thiosemicarbazonato metal complexes. The synthesis of functional novel thiosemicarbazides and the formation of the thiosemicarbazone ligands is reported hereby. Several aromatic dicarbonylic starting materials (other than the known acenaphthenequinone) were explored and a panel of new zinc thiosemicarbazonato complexes were obtained and characterised spectroscopically.

Chapter 3 contains the synthesis of bifunctional BODIPY derivatives which incorporate a protected amino acid residue. The synthetic approach towards new derivatives with fluorescence emission in the near-infrared region of the spectra is also reported.

Chapter 4 describes the methodology towards the incorporation of the new carbon nanomaterial scaffold. The functionalisation of pristine single walled carbon nanotubes and graphene oxide to incorporate linkers in the structure, and the characterisation of the functionalised materials, are given hereby.

Chapter 5 contains the synthesis and purification of the targeting peptide and the BODIPY-peptide conjugate involved as key components for the novel nanohybrids. Other nanohybrids containing the BODIPY or gallium thiosemicarbazonato species are also reported. The behaviour of these compounds

in living PC-3 cells was evaluated and the cytotoxicity of a selection of compounds determined, for the first time.

Chapter 6 provides a summary of the work carried out during this thesis and some proposals for future work arising from the research findings described herein.

Chapter 7 contains detailed experimental details and characterisation data for the compounds described.

The Appendices provide supporting spectroscopic evidence and X-ray diffraction data for the new compounds synthesised.

List of publications and conference proceedings resulting from this PhD

- J. A. Tyson, F. Cortezon, F. Marken, P. Estrela and S. I. Pascu, Labelling carbon nanomaterials as biocomposites with organic molecules as fluorescent tags: towards non-invasive biosensing of prostate cancer cells, *J. Labelled Comp. Radiopharm.*, 2014, **57**, 187-188.

- I. S. Alam[‡], R. L. Arrowsmith[‡], F. Cortezon-Tamarit[‡], F. Twyman, G. Kociok-Kohn, S. W. Botchway, J. R. Dilworth, L. Carroll, E. O. Aboagye and S. I. Pascu, Microwave gallium-68 radiochemistry for kinetically stable bis(thiosemicarbazone) complexes: structural investigations and cellular uptake under hypoxia, *Dalton Trans.*, 2016, **45**, 144-155.

- F. Cortezon-Tamarit, S. Sarpaki, D. G. Calatayud, V. Mirabello and S. I. Pascu, Applications of "Hot" and "Cold" Bis(thiosemicarbazonato) Metal Complexes in Multimodal Imaging, *Chem. Rec.*, 2016, **16**, 1380-1397.

- F. Cortezon-Tamarit, H. Ge, V. Mirabello, M.B.M. Theobald, D.G. Calatayud and S. I. Pascu, Carbon Nanotubes and Related Nanohybrids Incorporating Inorganic Transition Metal Compounds and Radioactive Species as Synthetic Scaffolds for Nanomedicine Design, in *Inorganic and Organometallic Transition Metal Complexes with Biological Molecules and Living Cells*, Academic Press, 2017, pp. 245-327.

List of conference presentations resulting from this PhD

- Carbon nanomaterials with potential multimodality imaging applications of prostate cancer. PROSENSE meeting on Microfluidics and point of care devices, Lisbon, Portugal, July 2015.

- Fluorescent SWNT nanoprobes for imaging of prostate cancer cells. PROSENSE Conference on Prostate Cancer Diagnosis, Bath, UK, September 2016.

List of abbreviations

APCI	Atmospheric-pressure chemical ionisation
ATSM	Diacetyl-bis(N4-methylthiosemicarbazone)
BBN	Bombesin
Boc	N-tertbutoxycarbonyl
BODIPY	Boron-dipyrromethene
BPH	Benign prostatic hyperplasia
BTSC	Bis(thiosemicarbazone)
CNT	Carbon nanotube
COSY	Correlation spectroscopy
CT	Computed tomography
DIPEA	N,N-Diisopropylethylamine
DMF	Dimethylformamide
DOTA	1,4,7,10-tetraazacyclododecane-1,4,7,10-tetraacetic acid
DRE	Digital rectal examination
DTPA	Diethylenetriaminepentaacetic acid
EDC	N-(3-Dimethylaminopropyl)-N′-ethylcarbodiimide
ESI	Electrospray ionisation
FITC	Fluorescein isothiocyanate
FLIM	Fluorescence lifetime imaging
Fmoc	Fluorenylmethyloxycarbonyl
FTIR	Fourier transform infrared spectroscopy
GO	Graphene oxide
GPCR	G protein-coupled receptors
GRP	Gastrin-releasing peptide
GRPR	Gastrin-releasing-peptide receptor
HATU	1-[Bis(dimethylamino)methylene]-1H-1,2,3-triazolo[4,5-b]pyridinium-3-oxide hexafluorophosphate
HMBC	Heteronuclear multiple bond correlation spectroscopy
HOBt	1-Hydroxybenzotriazole
HPLC	High Performance Liquid Chromatography
HSQC	Heteronuclear single quantum coherence spectroscopy
MRI	Magnetic resonance imaging
MRSI	Magnetic resonance spectroscopy imaging
MS	Mass spectrometry
MTT	3-(4,5-dimethylthiazol-2-yl)-2,5-diphenyltetrazolium bromide

MWNT	Multi walled carbon nanotubes
NIR	Near infrared
NMR	Nuclear Magnetic Resonance
PBS	Phosphate Buffered Saline
PCa	Prostate cancer
PCR	Polymerase chain reaction
PET	Positron emission tomography
PSA	Prostate specific antigen
pyBOP	(Benzotriazol-1-yloxy)tripyrrolidinophosphonium hexafluorophosphate
RBM	Radial breathing mode
RPMI	Roswell Park Memorial Institute medium
Rt	Retention time
SAED	Selected area electron diffraction
SIM	Structured illumination microscopy
SPS	Solvent purification system
SWNT	Single-walled carbon nanotubes
TCSPC	Time-correlated single photon counting
TEM	Transmission electron microscopy
TFA	Trifluoroacetic acid
TGA	Thermogravimetric analysis
TIPS	Triisopropylsilane
TOCSY	Total Correlated Spectroscopy
TRUS	Transrectal ultrasound

List of compounds

Chapter 2

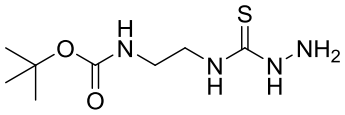

7

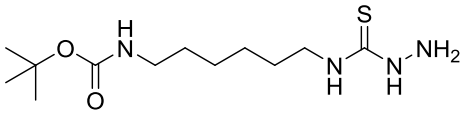

8

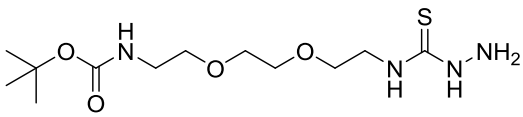

9

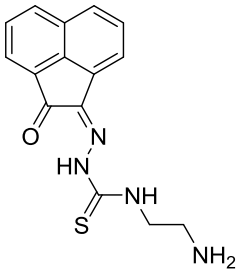

10

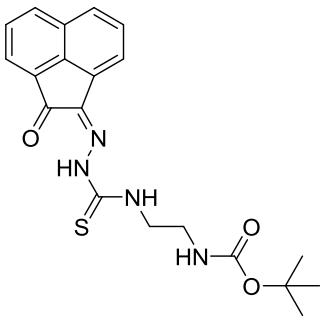

11

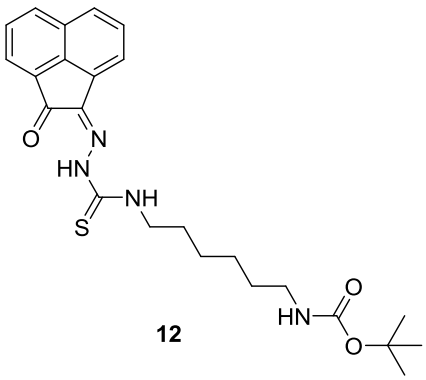

12

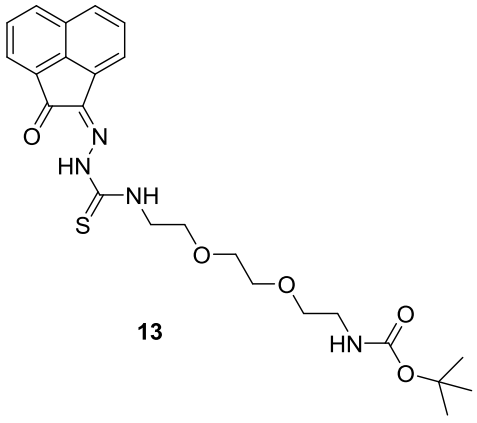

13

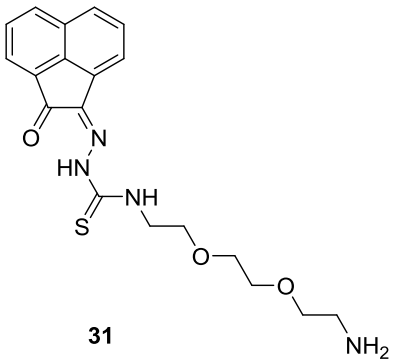

31

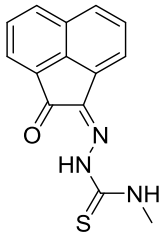

14

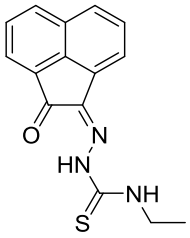

15

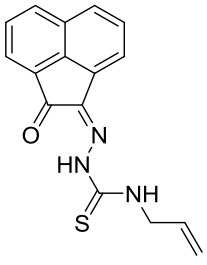

16

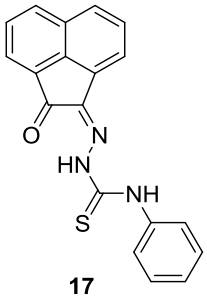

17

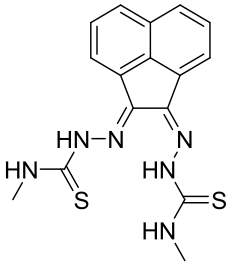

18

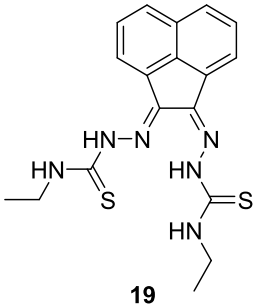

19

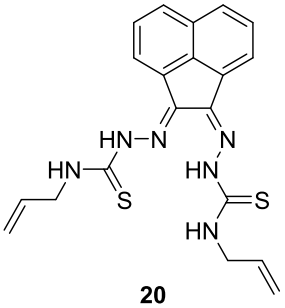

20

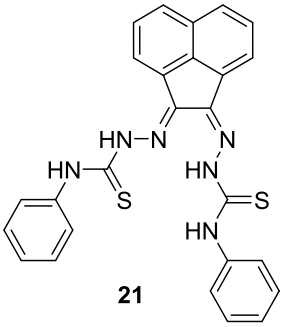

21

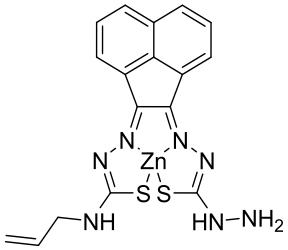

22

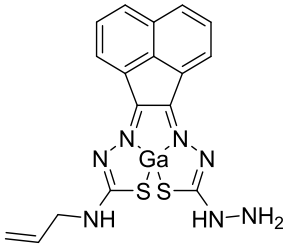

23

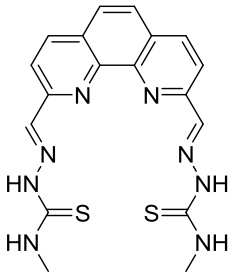

26

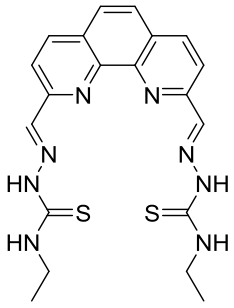

27

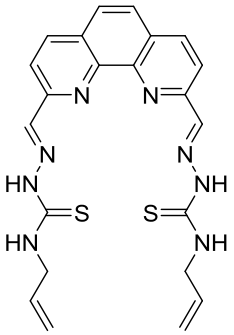

28

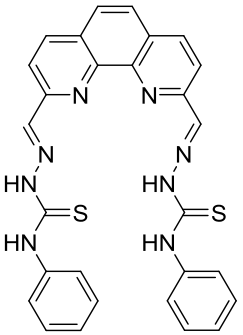

29

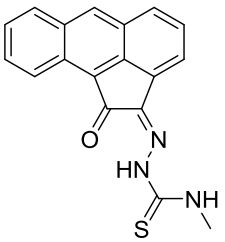

32

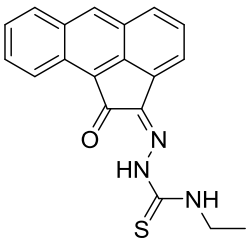

33

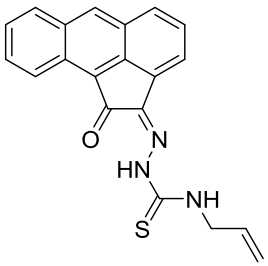

34

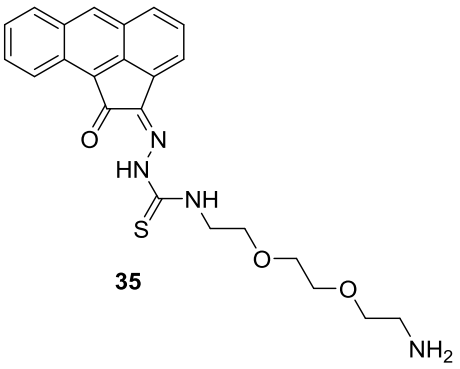

35

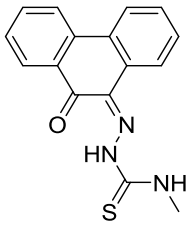

36

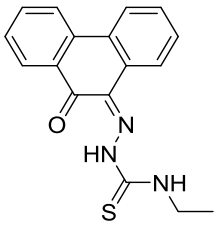

37

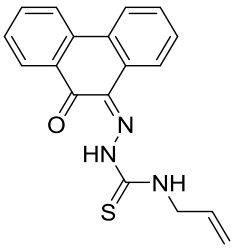

38

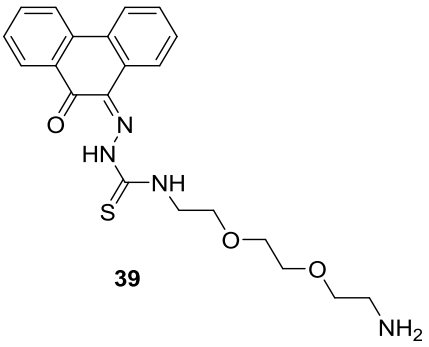

39

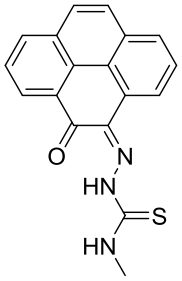

40

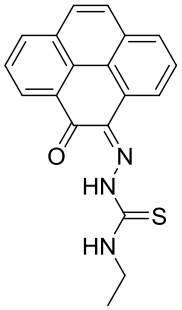

41

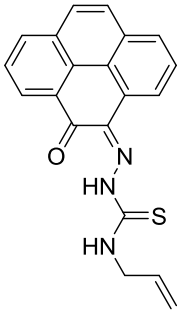

42

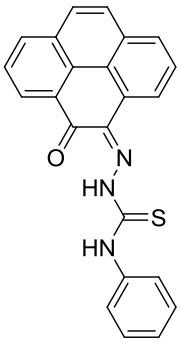

43

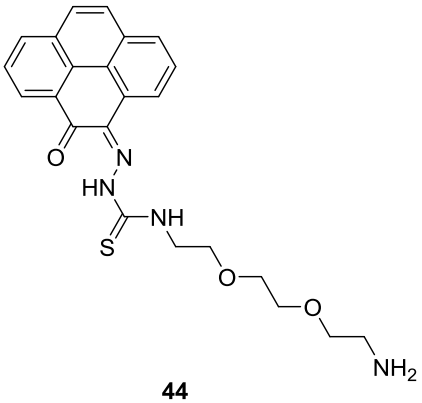

44

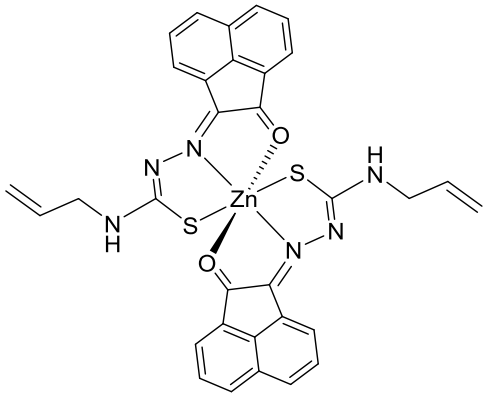

45

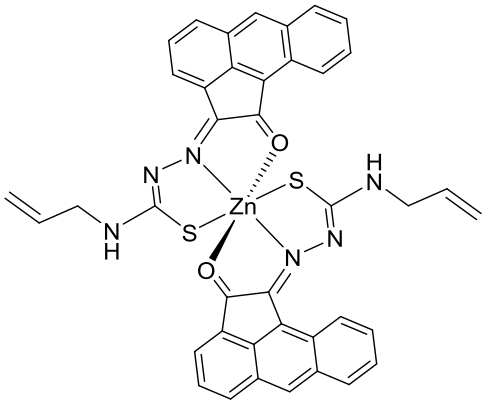

46

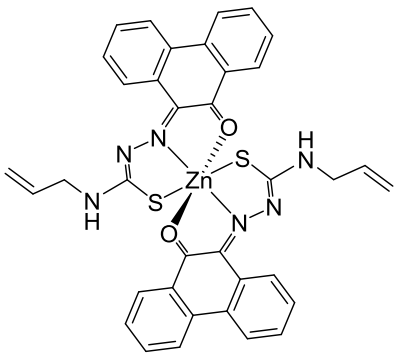

47

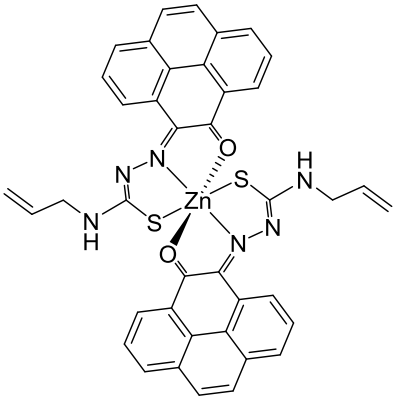

48

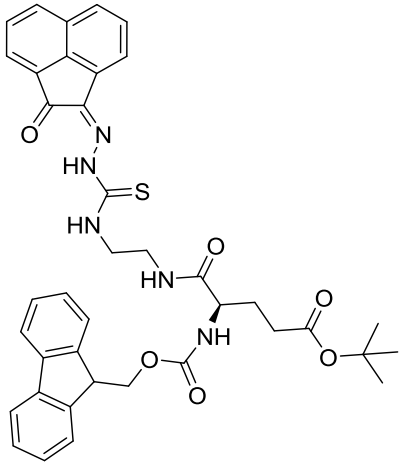

49

Chapter 3

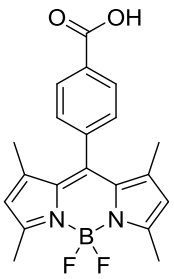

50

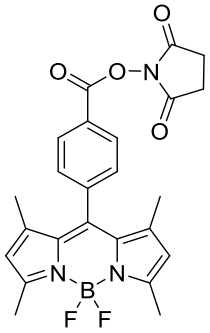

52

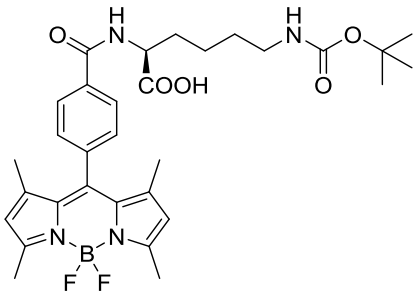

53

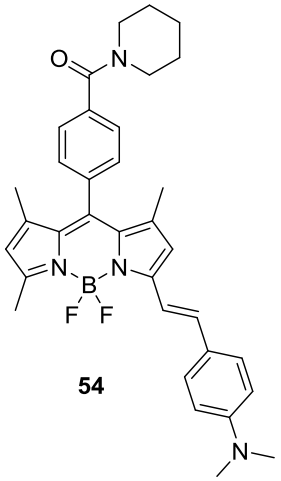

54

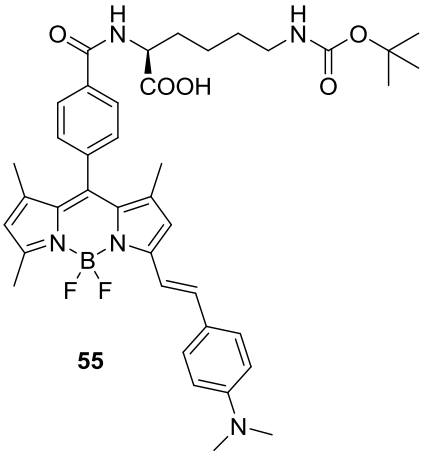

55

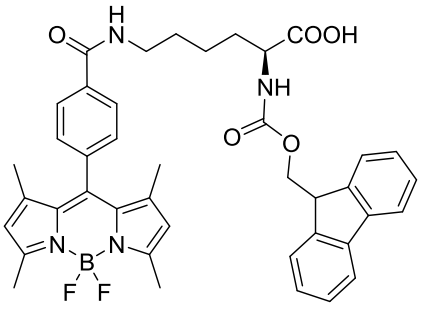

57

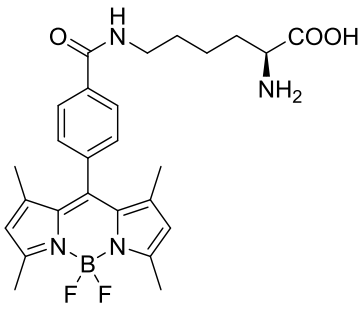

58

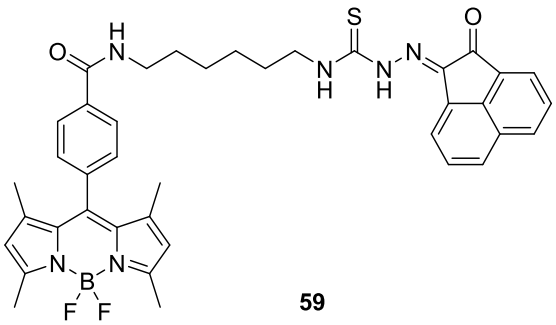

59

Chapter 4

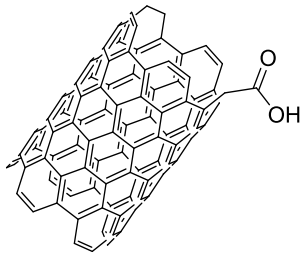

60

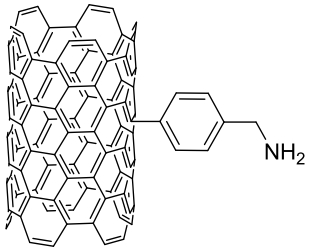

63

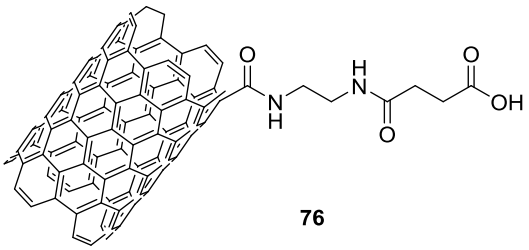

76

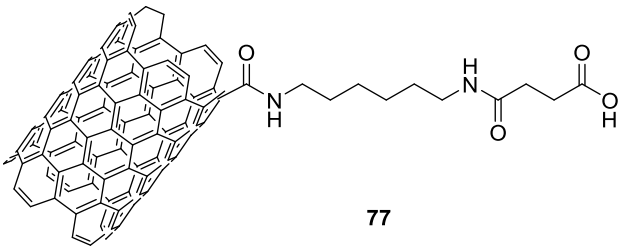

77

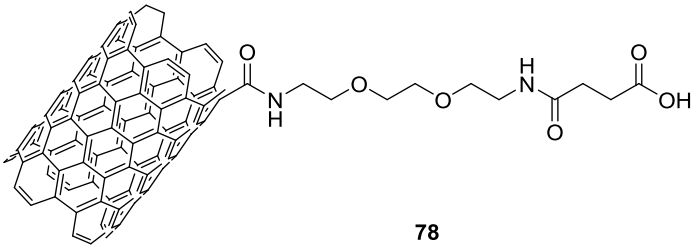

78

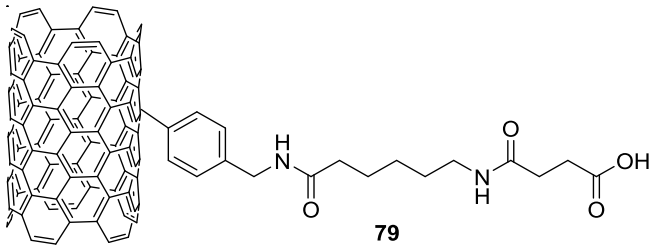

79

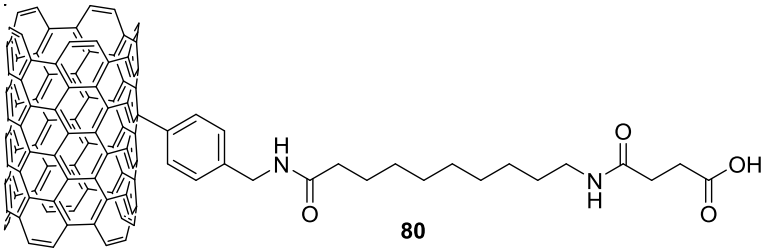

80

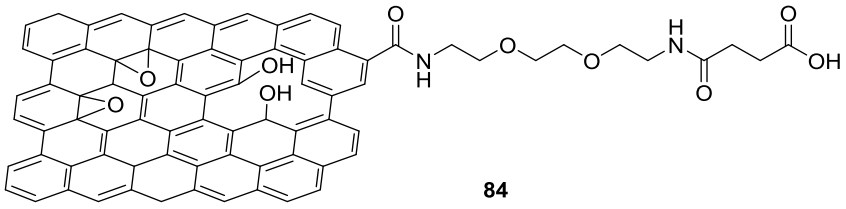

84

Chapter 5

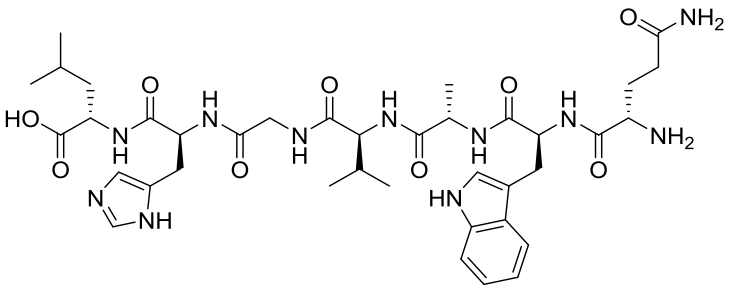

85

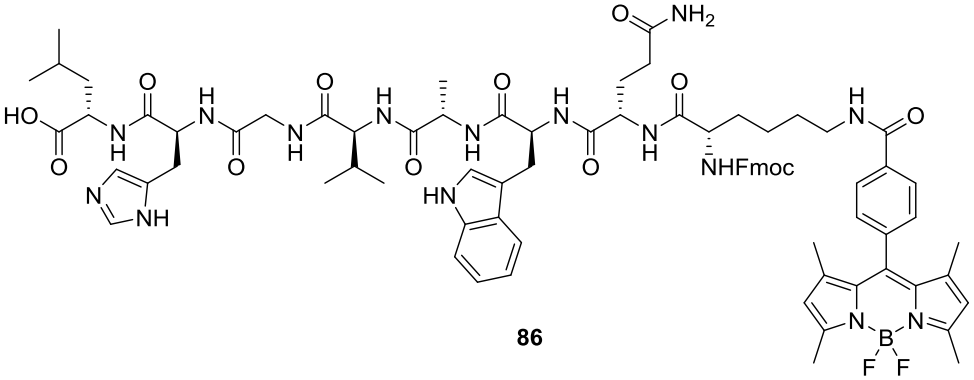

86

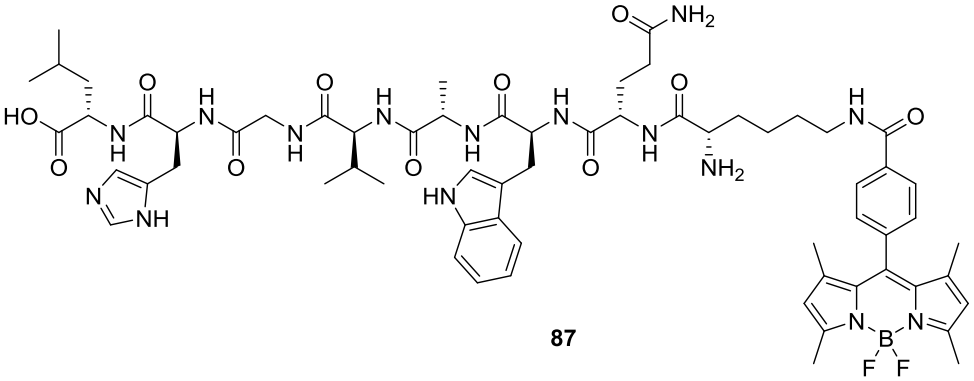

87

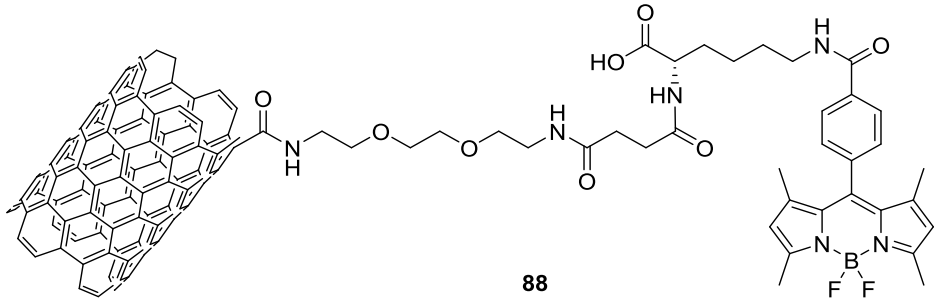

88

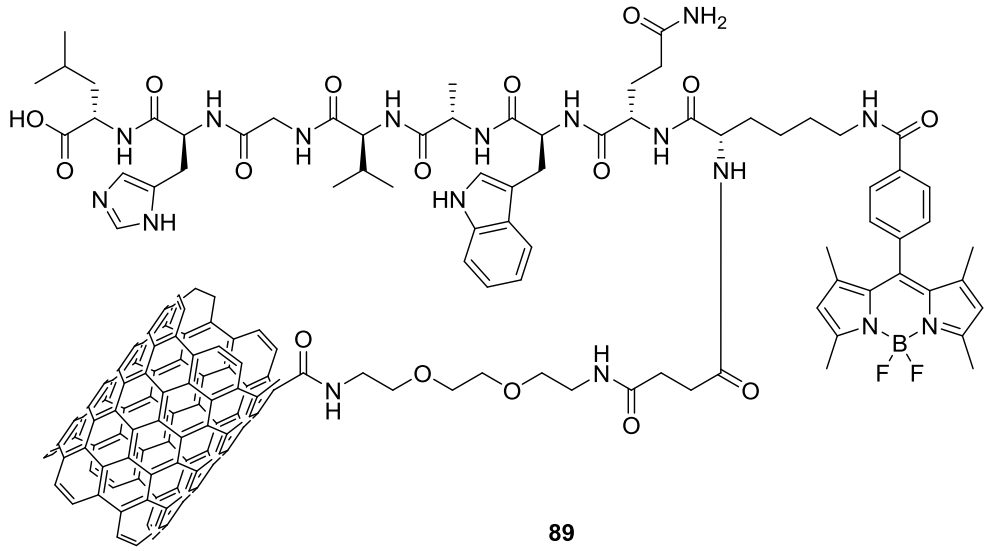

89

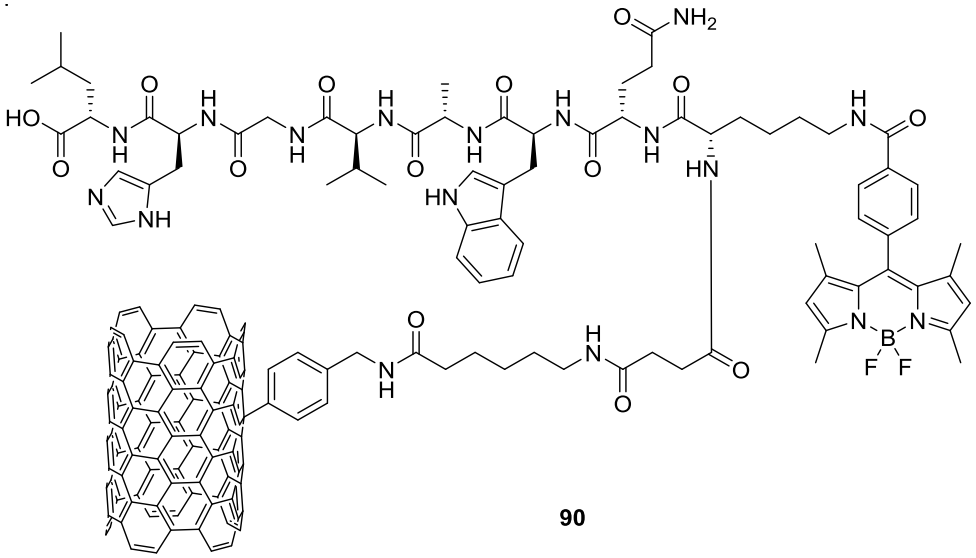

90

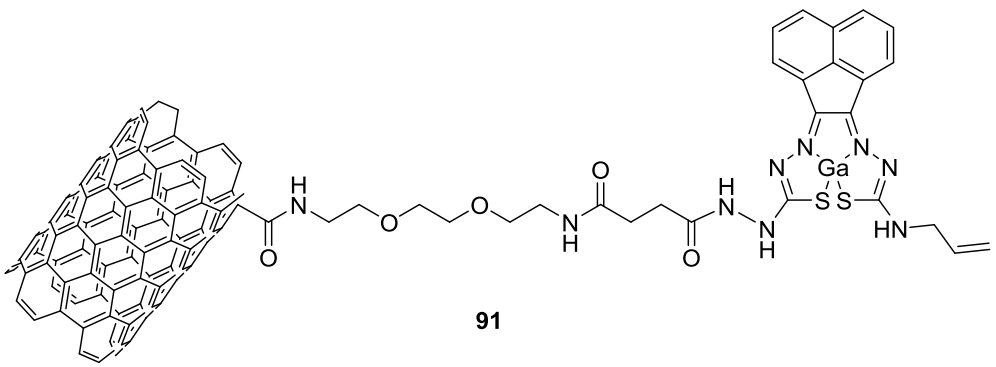

91

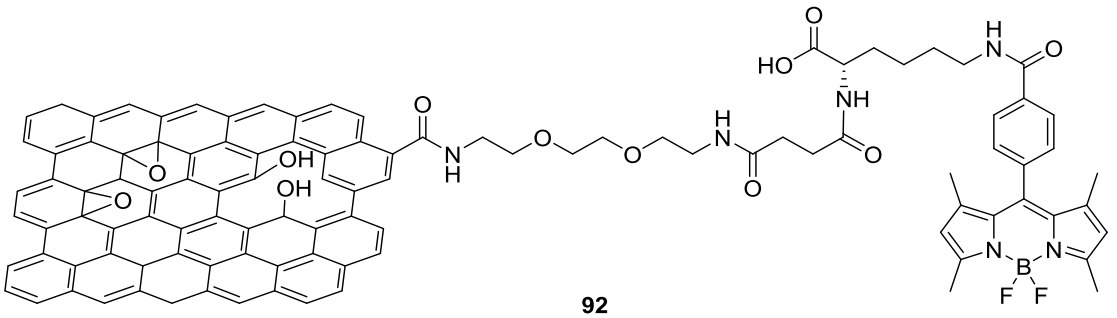

92

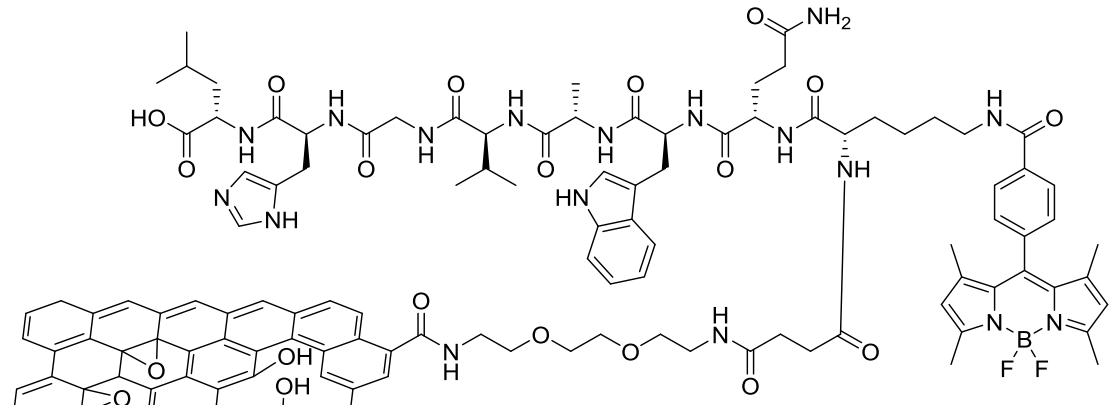

93

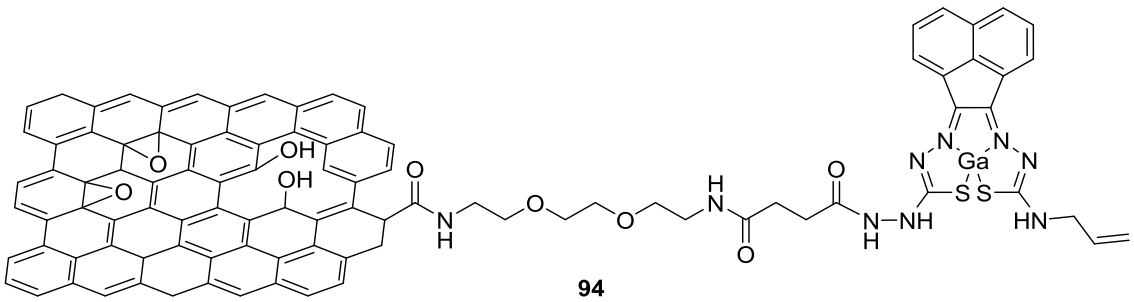

94

Chapter 1 : Introduction

1.1 Overview of molecular imaging techniques applied to prostate cancer

1.1.1 General considerations of prostate cancer diagnosis

Prostate cancer (PCa) is the most common type of cancer diagnosed in men, second to lung cancer with more than 47,000 new cases in the UK last year, accounting for 13% of all cases.[1] The numbers in other industrialised countries are similar to the aforementioned with PCa representing 15% of all cancers globally although in the US and the EU the percentage increases to 26% and 22% respectively with prostate cancer being the second cancer diagnosed among men.[2-4] It has been highlighted that ca. 70% of the cases of prostate cancer cases worldwide are diagnosed in more developed regions.[3] The number of cases have significantly increased since the 1990s mainly due to prostate specific antigen (PSA) screenings to the population. Considering age groups, prostate cancer is strongly age-dependent with more than 50% of the cases diagnosed in men of 70 or over.[1] Despite the improvement in diagnosis techniques and treatment, prostate cancer still is one of the leading causes of mortality in cancer. This disease accounts for 13% of the deaths, being the second cause of death among men and the third overall in the UK with more than 10,000 cases per year.[1] The death rate predicted in the US is comparable and it will be in second place after lung cancer with 9% of all cancer cases.[4]

The prostate is a complex organ with glandular and non-glandular parts surrounding the urethra and located between the bladder and the pelvic diaphragm and anterior to the rectum (Figure 1.1).[5] The prostate is generally described to be the size of a walnut but its size can increase with age due to benign prostatic hyperplasia (BPH).[6] The prostate physiological function is to generate an alkaline fluid containing ions (calcium, citrate, phosphate) and a clotting enzyme, among other constituents, that are part of semen. The prostatic fluid accounts for 30% of the composition of the semen. It is hypothesised that the basic pH of the prostatic fluid has an important role in obtaining the optimal conditions for the mobility of sperm.[7]

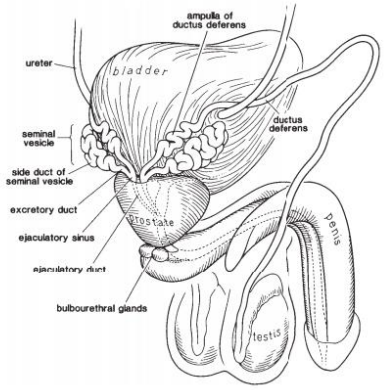

Figure 1.1: Representation of the male urogenital system. Figure reproduced from ref. 5 with permission from the publisher.

The denomination of prostate cancer generally refers to prostate adenocarcinoma while other types of cancers as sarcomas, small cell carcinomas, neuroendocrine tumours or transitional cell carcinomas are rare.[8-10] In addition, most cases of PCa are multifocal diseases, meaning that multicentric lesions are present in the prostate. Furthermore, the different carcinomas can have different grades and be genetically different adding complexity to the identification and treatment of the disease.[9, 11]

The most common diagnostic methods for prostate cancer are all invasive (i.e. digital rectal examination (DRE), trans-rectal ultrasound (TRU), PSA blood tests and needle biopsy). The former can reveal an enlargement of the prostate gland and the presence of abnormalities in the prostate anatomy, and patients with other conditions as BPH or prostatitis can lead to false positive results. Meanwhile, the use of TRU has been relegated to guidance during needle biopsies as the probability of finding the tumour just with ultrasound is low.[10] After a biopsy of the prostate is conducted, the aggressiveness of a prostate tumour may be classified depending on the arrangement of the cells in the prostatic tissue according to the Gleason system. This contemplates grades from 1 to 5. In grade 1, the tumorous cells are small, distinguishable and with minimal changes while in grade 5, the tumour tissue is composed of planes of non-differentiated cells (Figure 1.2). As mentioned above, prostate tumours can be heterogeneous so in order to take into account the different zones of the tumour, the grades of the two most representative zones are added constituting the Gleason score. The probability of progression of the tumour increases with the Gleason score.[10]

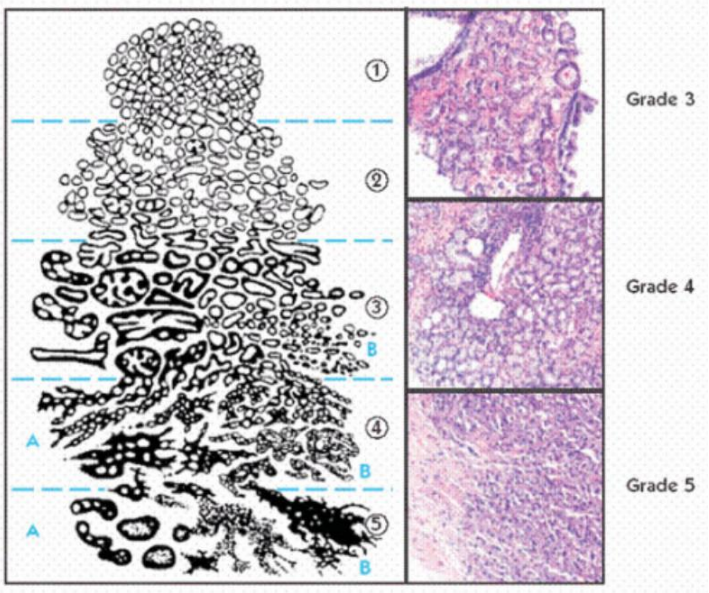

Figure 1.2: Representation of the arrangement of cells in a prostate tumour with the Gleason score (left) and actual tumour samples (right). Figure reproduced from ref. 12 with permission from the publisher.

The routine diagnostic tool for PCa in the last two decades has been the PSA test. The prostate-specific antigen is a protein synthesised in healthy prostate, zones with BPH and prostate cancer. It is believed to have a role in the viscosity of the semen liquefying specific gel proteins. It is present in the semen in concentrations up to 3 ng/mL and in healthy subjects the concentration in blood is negligible. The presence of prostate cancer produces an increase in the level of PSA in blood which is the basis of its use as a diagnostic tool. Therapeutic measures are generally adopted when a total PSA value of 4.0 ng/mL in blood is detected although the concentration of PSA tends to increase with age and due to other conditions as BPH or prostatitis.[13] Despite its wide application, there is a strong controversy on massive PSA screening of the men population due to the risk of overdiagnosis. The number of men overdiagnosed and overtreated because of early PSA screening has been calculated to be as high as 40-50% in population where the test was performed.[14, 15] The statistics show that the mortality in men aged 65 or over is generally not caused due to the presence of localised prostate cancer.[16] Men diagnosed with PCa who undergo treatment are under risk of suffering serious side effects when the disease could not have shown symptoms for years.[17] Based on these findings, European and American health agencies recommend against the massive screening of the population or the application of the test below the age of 60.[18, 19]

These results have stimulated the research in novel biomarkers to diagnose and target prostate cancers early and in a non-invasive way.

1.1.2 Imaging methods of relevance for prostate cancer diagnosis

Despite the increase of diagnosed prostate cancer cases there has been a significant decrease in the use of imaging techniques with diagnostic purposes.[20] The adequacy of the use of imaging is under debate in the clinical world as early diagnosed cancers have only a low risk to become metastatic hence imaging would be redundant. On the other hand, it has been observed that imaging tests have been underused or misused according to health agency guidelines.[21-24] Therefore, imaging techniques are being applied to patients with more advanced diseases. Thanks to other tests and early diagnosis, imaging techniques can be applied to other relevant aspects as a preoperative tool to guide the surgery, localising metastases, helping plan, deliver and verify radiation treatments, detail staging or following-up after treatment. New imaging methods are also shifting to find out the aggressiveness of the cancer which can be determined nowadays only histologically after a biopsy.[25]

Transrectal ultrasound is based on the emission of sound waves that produce different echoes or reflections when crossing different tissues. The detection of tumours is achieved because tumorous areas are generally anechoic or hypoechoic with relationship to the surrounding tissue.[26] Transrectal ultrasound was widely used in the past as the first method of choice to image the prostate because it could detect abnormal zones that could not be identified by DRE with a high level of accuracy. However,

as early diagnostic tests progressed, that accuracy decreased dramatically in asymptomatic cases since TRU fails to see the smallest tumours that can be present in the early stages of the disease and other conditions can lead to false positives.[27] This technique is still widely used as it can provide relevant information to measure the volume of the prostate and relate it to PSA levels and also to guide transrectal needle biopsies.

X-ray computed tomography (CT) is an imaging technique where X-rays are used to image the subject with detectors moving at different angles. The images can be visualised as 2D slices or reconstructed to generate a three-dimensional image.[28] CT can be used with high spatial and temporal resolution at a relatively low cost and it is quantifiable so it can be employed to correct other imaging techniques as PET. CT is optimal for bone scanning due to the different contrast between the bones and the surrounding tissues. However, it has low sensitivity and a reduced soft-tissue contrast so the use of contrast agents becomes a condition to image soft tissue.[29] For this reason, CT has limited applicability to the diagnosis or staging of prostate cancer and its use is only recommended in patients in the advanced stage of the disease.[25] Due to the advantages of the technique it could be utilised to detect bone metastases although other techniques as bone scanning or magnetic resonance imaging (MRI) have demonstrated superior properties.[30, 31]

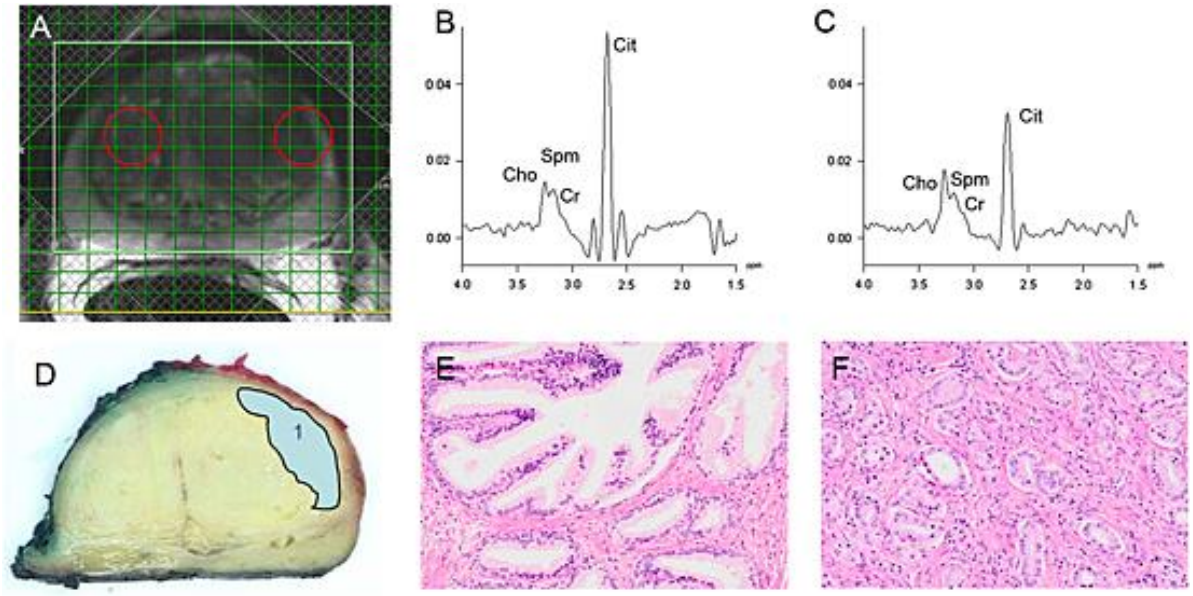

Figure 1.3: Example of the use of MRSI for the diagnosis of PCa. A) T2-weighted image of a patient with PCa. Normal tissue is marked by the red circle on the left while tumorous tissue corresponds to the red circle on the right. B) Spectrum corresponding to normal tissue. C) Spectrum corresponding to PCa tissue. D) Slice of the prostate indicating the tumorous tissue. E) Stained sample of normal tissue and F) tumorous tissue. Figure reproduced from ref. 37 with permission from the publisher.

MRI is characterised by a great spatial resolution but low specificity.[32] The basis of the technique in imaging is equivalent to its application in spectroscopy, consisting in the measurement of the relaxation of active nuclei after a radiofrequency pulse in a strong magnetic field, but constructing a three-dimensional image. This is achieved by the application of magnetic field gradients in the three dimensions of space.[33] MRI modalities are often classified depending on the relaxation mechanism as T1- and T2- weighted imaging. T1 refers to the spin-lattice relaxation that accounts for the relaxation of the nuclei by interactions with the environment surrounding the nuclei while T2 refers to the spin-spin relaxation which is based on the redistribution of energy among the nuclei in a spin system.[33]

MRI has not been generally used as a screening tool due to the high costs and low specificity as mentioned above.[32] Its use in determining the stage of prostate cancer has been studied in more detail and technological improvements as the introduction of endorectal MRI probes have been proposed.[34, 35] However, there is still no total agreement about the general applicability of the technique to the screening or staging of prostate cancer.[35] T2-weighted imaging is generally used in prostate cancer as it can provide an excellent resolution when observing the prostate anatomy and where the tumours appear dark.[27] Recently, the application of magnetic resonance spectroscopy (MRS) along with the imaging experiments has been explored as a way to identify key metabolites (e.g. citrate, creatine, choline) and their concentration to improve the specificity of MRI (Figure 1.3).[36, 37] The resonance of citrate at 2.6 ppm is known to be reduced in PCa while the resonance of choline at 3.2 ppm increases. The ratio of choline to citrate constitutes a promising indicator for the presence of prostate cancer tumorous tissue.

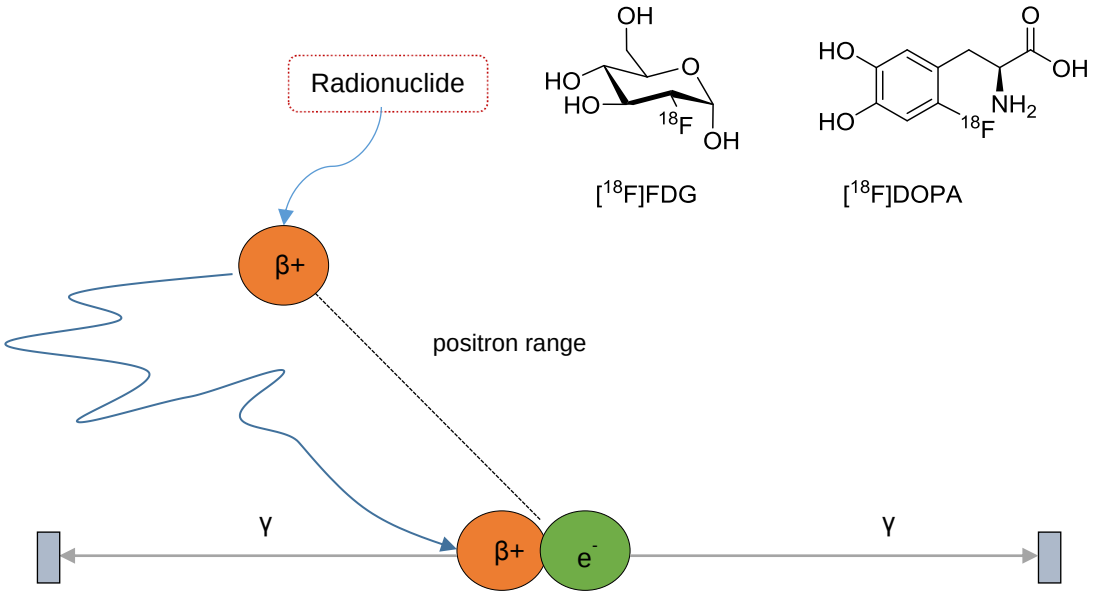

Figure 1.4: Basic principle of PET imaging and structure of two of the most used radionuclides ([^{18}F]FDG and [^{18}F]DOPA). An emitted positron during the radionuclide decay is annihilated with an electron emitting a pair of gamma rays that are detected by scintillation crystals (grey rectangles).

Furthermore, contrast agents have also been evaluated to improve the imaging quality of the prostate in MRI. Compounds of gadolinium(III) have generally been used in the acquisition of magnetic resonance images as T1 contrast agents due to its high magnetic moment generated by its unpaired electrons. The research interest in T2 contrast agents is focused in compounds as superparamagnetic iron oxide nanoparticles (SPION) or other iron particles.[38] Much interest has been attracted by targeted derivatives and the application of peptides in this role and they will be discussed in detail in the following section.

Differently, the generation of images by PET is achieved by the detection of a couple of gamma rays emitted in opposite directions. The gamma rays are generated by the annihilation of a positron (emitted by a radionuclide) and an electron of the surrounding tissue (Figure 1.4). A circular detector measures the pair of gamma rays at different positions and angles, allowing to construct a three-dimensional image.[39]

Some of the most common radionuclides used in PET imaging are shown in Table 1.1. Carbon-11, nitrogen-13 or oxygen-15 offer the possibility to perform isotopic substitutions in biological metabolites hence not altering their structure, biological functions or pharmacokinetics.[40] Their short lifetimes, however, increase the difficulty towards their application as any synthetic steps must be kept to a minimum, nevertheless ^{11}C has been applied to the imaging to the identification of bone metastases as ^{11}C-acetate or tumours as ^{11}C-choline.[41] Fluorine-18 is the radionuclide routinely utilised by substitution of hydrogen atoms in biological compounds as in the case of 2-[^{18}F]-fluoro-deoxy-D-glucose ([^{18}F]-FDG) to study glucose metabolism or 6-[^{18}F]-fluoro-3,4-dihydroxyphenylalanine ([^{18}F]-6-Fluoro-L-DOPA) to study cerebral dopamine metabolism.[42] The comparatively long life-time of fluorine-18 allows longer synthetic procedures to be performed and the transport from the production site to the clinical centre which favours the use of [^{18}F]-FDG, performed routinely in most imaging centres.[43]

Table 1.1: Properties of selected positron-emitting radionuclides.[44]

Nuclide	Half-life (min)	Max. energy (MeV)	Mode of decay	Max. positron range (mm)
^{18}F	110	0.64	β+ (97%), EC (3%)	2.1
^{11}C	20.3	0.97	β+ (99%)	-
^{13}N	10	1.20	β+ (100%)	-
^{15}O	2	1.74	β+ (100%)	-
^{76}Br	972	4.0	β+ (57%), EC (43%)	-
^{124}I	60192	2.14	β+ (25%), EC (75%)	-
^{68}Ga	68.1	1.90	β+ (89%), EC (11%)	8.4
^{64}Cu	762	0.655	β+ (41%), EC (3%)	2.2
^{89}Zr	4704	0.90	β+ (23%), EC (%)	3.4

However, the incorporation of ^{18}F into biomolecules still presents a challenge due to its short lifetime in the timescale of a chemical synthesis. For this reason, late stage fluorination is attracting much research interest.[45] In addition, the production of [^{18}F] is still carried out in a cyclotron, a facility that is not readily available in all hospitals and research facilities. The use of [^{18}F]-FDG in the imaging of prostate cancer has demonstrated little applicability as it has little sensitivity for tumour detection, it cannot distinguish prostate tumours from BPH and it gives a strong signal in the bladder when excreted.[25, 35, 46]

For this reason, the research into the chemistry and biomedical applications of radiometals have attracted much attention in recent years. The use of radiometals like [^{64}Cu] or [^{89}Zr], although produced equally in a synchrotron, offers a prolonged lifetime compared to fluorine-18 which permits for an easier handling and allows the study slower metabolic processes in detail. The use of [^{68}Ga] presents an additional advantage that is the production in a generator from the decay of [^{68}Ge] facilitating the use of the radionuclide in research and clinical environments. The functionalisation of biomolecules with highly selective chelators for Ga(III) has also paved the way to targeted imaging where the radiolabelling is generally an efficient final step.[47] The use of macrocyclic compounds (DOTA, NOTA) in nuclear imaging as chelators for ^{64}Cu or ^{68}Ga has been widely applied.[48] However, new species with a higher selectivity have been proposed for ^{64}Cu as cyclam derivatives or sarcophagine compounds as well as for ^{68}Ga as TRAP and NOPO.[49] The structures of common chelators can be observed in Figure 1.5.

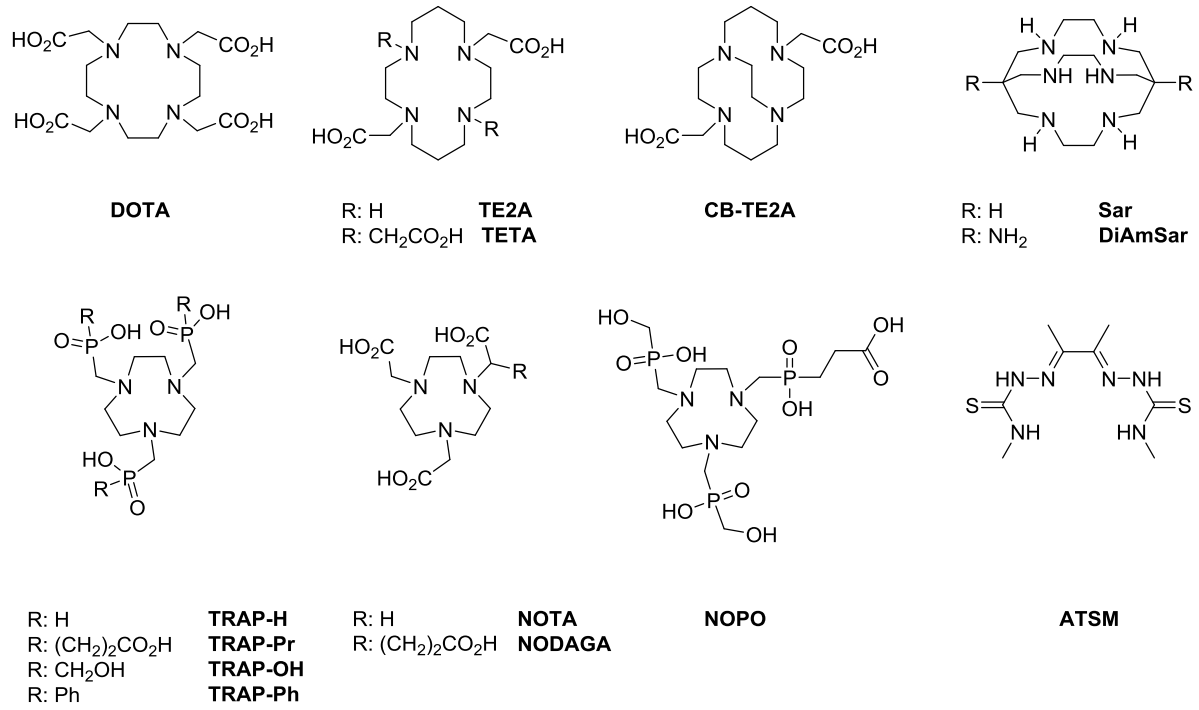

Figure 1.5: Structural representations of common chelators used with ^{64}Cu and ^{68}Ga. Figure adapted from ref. 49.

PET imaging agents including PCa targeting groups are being developed. The prostate-specific membrane antigen (PSMA) is a membrane protein found in a higher concentration in PCa tumours, especially in advanced stage and metastatic.[50] The compounds to target PSMA are specific antibodies, ureas and phosphoramidates that can be radiolabelled with a range of nuclei as ^{64}Cu, ^{89}Zr or ^{68}Ga.[46, 51] The gastrin-releasing peptide receptor is another well studied target of prostate cancer. Several examples of imaging agents using bombesin as a targeting group are discussed in the following section.

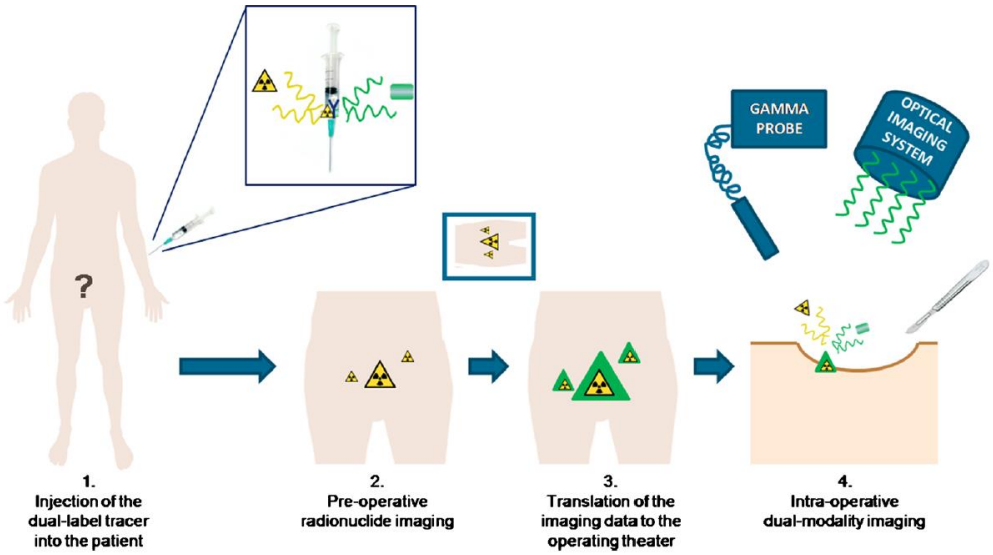

Figure 1.6: Use of a multimodal PET-optical multimodal probe to perform pre-operative imaging and assisted surgery. Figure reproduced from ref. 54 with permission from the publisher.

The use of various techniques in multimodality imaging aspires to combine their characteristics to obtain the advantages of the combined methods. The interest in multimodal probes with an optical component has increased in the recent past as a way to enhance the functionality of an imaging probe and reduce the number of tests for the patient. PET/CT and SPECT/CT are being applied together routinely in the clinic as a result of the development of scanners incorporating both imaging detector systems.[52] More recent has been the application of MRI/PET, as a consistent way to get high spatial resolution and sensitivity, or MRI/optical combined for the preoperative assessment and surgery guidance.[52] PET/optical probes allow for imaging *in vitro*, *in vivo* and *ex vivo* of the disease.[29, 53]

Ideally, a multimodal probe would allow to reveal the regions where the tumour is present in a preliminary imaging stage and help the surgeon during the surgery to delimitate the tumour removing all affected tissue differentiating it effectively from the healthy tissue (Figure 1.6).[54] For this reason, the research into probes combining nuclear imaging techniques or MRI with optical techniques is receiving increasing attention.[53]

The structure of PET/optical probes must contain specific groups for the two modalities. This implies the presence of a radioisotope, a chelator group and a fluorophore emitting in the visible or NIR. In a few cases, such as acenaphthenequinone bis(thiosemicarbazonato) complexes or BODIPYs, both groups can be present in the same molecule.[55-57]

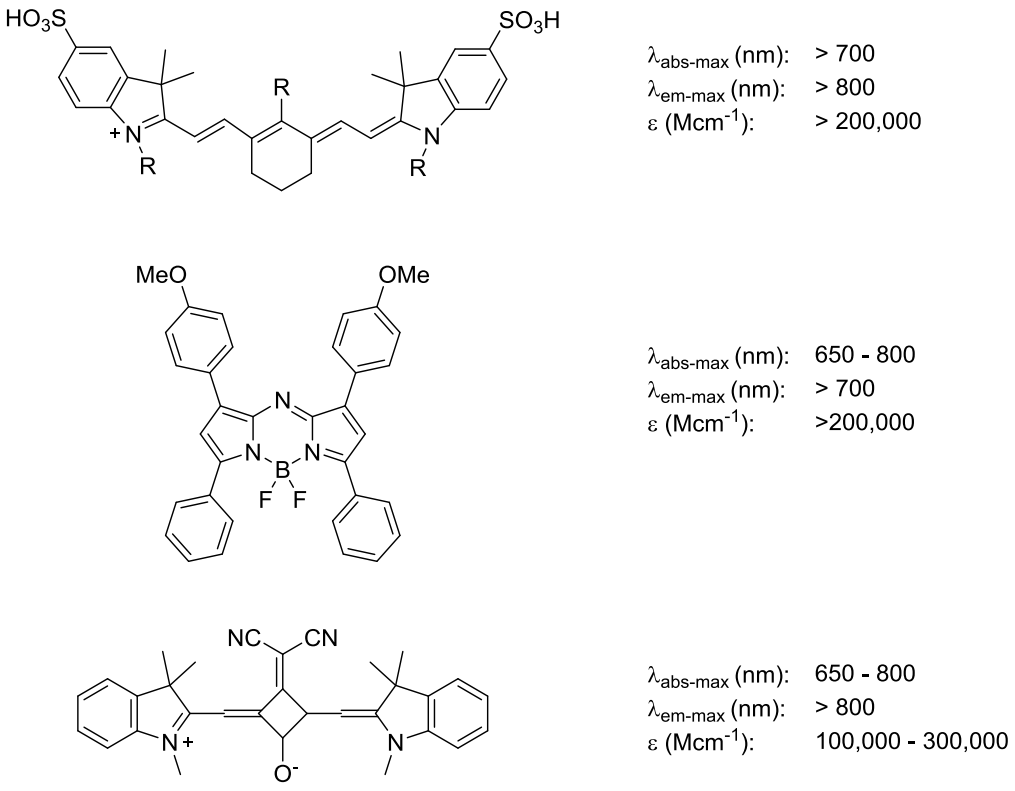

Figure 1.7: Structural representations of some commonly used NIR dyes: cyanine compounds (top), BODIPY compounds (middle) and squaraine derivatives (bottom) and their general photophysical properties.

The application of red and near infrared (NIR) fluorescent dyes in multimodal probes attracts special interest due to the advantageous characteristics of this region of the electromagnetic spectrum for bioimaging. NIR radiation has deeper penetration abilities in the tissue. Moreover, in the 700 – 1000 nm window, the autofluorescence of the tissue is reduced and the absorption of the light, produced because of haemoblobin, deoxyhaemoglobin and water, is not that intense.[58] The observation of tumours with fluorescence imaging agents has been described, especially with NIR dyes.[59] Furthermore, the use of fluorescence or multimodal imaging agents during surgery has been applied to localise and remove lymph nodes suspicious of containing metastatic tissue.[60, 61]

The structures of commonly used NIR dyes in cancer imaging is depicted in Figure 1.7.

1.2 Bombesin as a targeting biomolecule for prostate cancer

The G protein-coupled receptors are a large family of surface protein receptors that convert extracellular stimuli into intracellular responses. G protein coupled-receptors share a common structure formed by a heptahelical transmembrane unit with three intracellular and three extracellular domains.[62] Recently, GPCR have attracted increasing attention as pharmacological targets due to their involvement in a number of diseases, especially cancer growth, angiogenesis and metastasis being many of them overexpressed in tumorous cells.[63-65]

Bombesin is part of a family of neuropeptides that are agonists of the gastrin releasing peptide receptors (GRPR). Bombesin is a tetradecapeptide found in the skin of two frogs of the Alytidae or Discoglossidae family (Figure 1.8).[66] Its mammalian equivalent, that was isolated from porcine tissue, is the 27 amino acids gastrin releasing peptide (GRP).[67] Since the identification of bombesin in the 1970s, it arose much interest within the scientific community as early studies demonstrated its activity in tissues of smooth muscle during animal studies.[66,68]

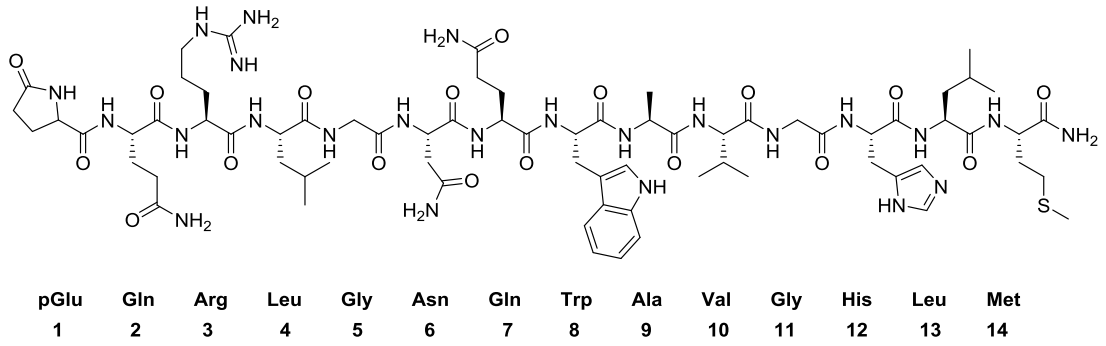

Figure 1.8: Structural representation of bombesin.

Early activity studies demonstrated that the minimum length of the peptide chain showing biological response in tissue corresponded to the heptapeptide from the C-terminal. Furthermore, the tryptophan and histidine residues proved to be essential to maintain the activity.[68-70]

The presence of differentiated receptors for bombesin-like peptides was reported by von Schrenk in 1989. In this pioneering work, the presence of at least two receptors was established by comparing the binding affinities of bombesin/GRP and Neuromedin B in rat oesophagus tissue.[71] Later, it was found that bombesin/GRP and Neuromedin B presented specific receptors. The receptors for bombesin/GRP peptides were cloned and characterised in Swiss 3T3 rodent cells.[72,73,74] The same group also characterised the Neuromedin B receptor shortly after.[75] An additional receptor that did not show great affinity for GRP or Neuromedin B was also identified.[76,77]

All bombesin-like receptors form part of this group of G protein-coupled receptors and the nomenclature varies depending on the source but it can be summarised for the three receptors found in mammals as follows, BB1 or Neuromedin B receptor, BB2 bombesin receptor or GRPR and BB3 or orphan receptor.[78] Bombesin binds with similar affinity to BB1 and BB2 while the affinity of Neuromedin B for the BB2 receptor is significantly lower (2 orders of magnitude difference in the nM range).[71] Both bombesin and Neuromedin B bind with low affinity to BB3. All three are heptahelical transmembrane GPCR in the 40-60 kDa range. BB1 and BB2 share 55% of the amino acids in the peptide sequence[79] whereas BB3 shares approximately 50% with the first two.[76] Despite the presence of BB1 and BB2 receptors in many tissues, the ability of bombesin/GRP to bind to both with comparable affinities made difficult the differentiation. For this reason, the expression, structure, role in disease and binding considerations will be commented for the specific bombesin receptor BB2 or GRPR. The GRP receptor in humans is a 384 amino acids protein with a heptahelical transmembrane GPCR structure.[79] The calculated molecular weight for human GRPR is ca. 60 kDa when the protein is glycosylated.[80,81] A schematic representation of the amino acid sequence of a rodent GRPR receptor can be seen in Figure 1.9.

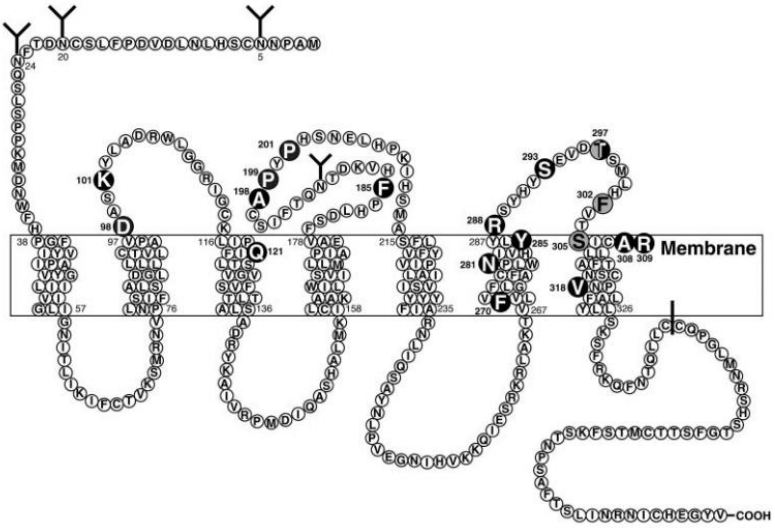

Figure 1.9: Amino acid sequence of the mice transmembrane gastrin releasing peptide receptor. Key amino acids for signalling are represented in black circles. Figure reproduced from ref. 78 with permission from the publisher.

The presence of GRPR was widely detected by binding studies over the brain, digestive tract, colon and urogenital smooth muscle.[82-84] Moreover, the GRP and GRPR have a variety of functions in the urological system.[67] The numerous expression and roles in healthy tissue of both in the male urogenital system are summarised in Figure 1.10. Interestingly, the presence of GRP in the prostate is very limited and GRP receptors has been identified but their function is not known.[84, 85]

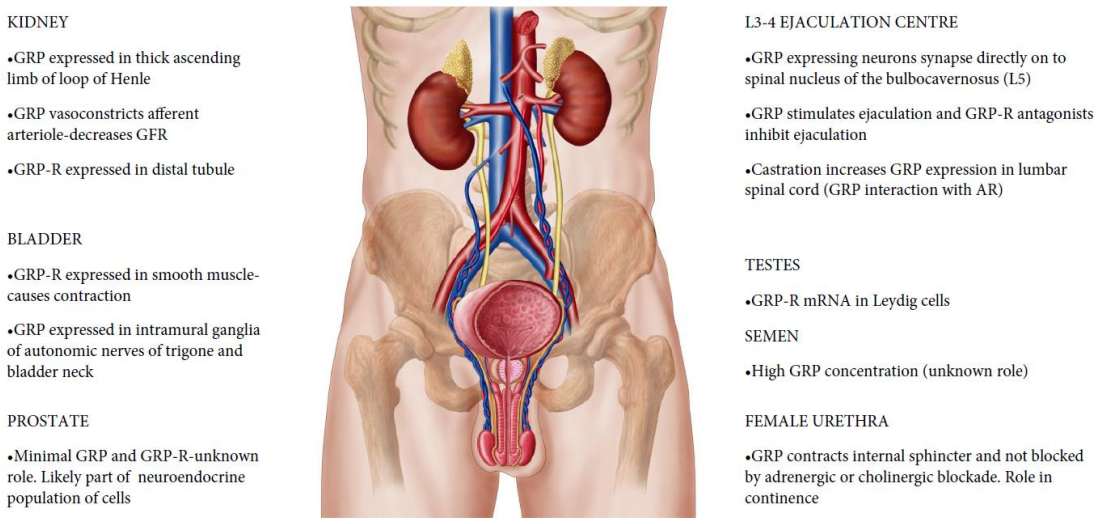

Figure 1.10: Normal functions and presence of GRP and GRPR in the male urological system. Figure reproduced from ref. 85 with permission from the publisher.

Besides the numerous physiological functions of bombesin-like peptides and BB2 receptors, their presence and overexpression in neoplastic tissues has strongly stimulated the interest in their use as targets for theranostics. The research in the roles of GRP and GRPR in cancer cells has evolved along with the understanding of the receptor and their agonists. The first examples go back to 1985 where bombesin-like peptides were identified to act as autocrine growth factors in small-cell lung cancer (i.e. the cell produces the peptide that is secreted and has a function in autoproliferation).[86] This hypothesis has been extended to other diseases as squamous cell carcinoma of head and neck, neuroblastomas or renal cancers.[84, 85, 87, 88] In addition, GRP receptors have been found to be overexpressed in a big percentage of breast, lung, renal and colorectal cancers and to a lower extent in gastric and pancreatic cancers.[84, 85] The overexpression of GRPR in prostate neoplastic tissues is significant and has been largely demonstrated in the literature by binding assays, polymerase chain reaction (PCR) or immunohistochemistry.[89-91] The percentage of cases varies with the source and technique applied but it always comprehends a significant value. Using PCR expression of the mRNA associated to GRP receptors, 63% of prostate carcinomas were found to express the receptor.[92] The expression of GRP receptors in normal tissue or benign prostatic hyperplasia showed weak or no staining in 90% of the cases by immunohistochemistry.[90] The expression of GRP receptors at the cellular level was studied by real-time reverse transcription PCR in different human cell lines including prostate cancer (LNCap, PC-3, 22rv1), human embryonic kidney (HEK), cervical cancer (HeLa), BPH, glioma (SNB19, U373) or human osteosarcoma cells (U2OS).

The results showed that the expression was noticeably higher in prostate cancer cell lines (i.e. LNCaP (lymph node carcinoma of the prostate) and PC-3 cells) than in any other of the cell lines tested (Figure 1.11). The expression on a third PCa cell line (22rv1) was considerably lower. The difference between the first two PCa cell lines and the last is that 22rv1 is androgen-dependent so the authors hypothesised that the presence of testosterone in the cell medium could be the cause of low GRPR expression.[93]

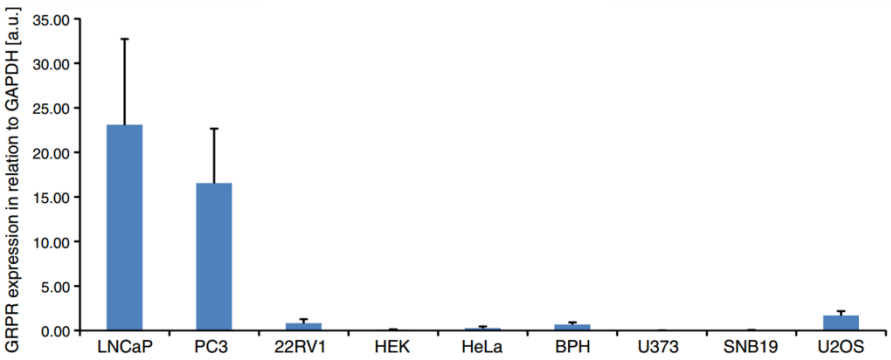

Figure 1.11: Relative GRPR expression of different cell lines measured by real-time transcriptase chain reaction in different cell lines. Figure reproduced from ref. 94 with permission from the publisher.

Additionally, GRP receptors were also overexpressed in advanced stages of prostate cancer as metastatic tissue or castration resistant tumours.[94, 95] As a result of the latter studies, the detection of the presence of this receptor as an indicator of the progression of the disease has been proposed[85, 94] showing a good correlation with other diagnostic markers as the Gleason score but inconclusive with PSA levels.[89] All the above characteristics in neoplastic tissues, especially in prostate cancer, converts GRPR and their agonists and antagonists as ideal candidates for the diagnostic imaging and potential treatment of these diseases. Bombesin constitutes an optimal agonist for GRPR as it is formed by an accessible sequence and the affinity for the receptors is maintained when shorter versions of the peptide are used. The [6-14] fragment has been extensively radiolabelled with ^{125}I Tyr as the imaging agent that helped to unveil the biochemical nature of bombesin-like receptors by binding studies or immuno-radiochemistry in different tissues.[96, 97] Equally, the [7-14] fragment has been profusely applied to the preparation of drugs and imaging agents.[98] Other fragments, like the des-Met [7-13] still maintain the biological activity towards GRP receptors and have been used as well in the study of anticancer drugs and imaging probes.[99, 100]

Over the years, a number of examples and radioisotopes have been applied to clinical imaging using bombesin-like peptides as targeting agents. All imaging agents can be classified by their modality, namely radiolabelled analogues, fluorescent analogues, or multimodal analogues (Table 1.2).

The use of bombesin or its fragments for imaging has been extensively studied in the literature, focusing especially in the preparation of radioimaging probes for PET or SPECT.[101] A selection of examples of functionalised bombesin peptides for imaging reported in the literature over the past decade are discussed below. During the early study of bombesin effects and specifity *in vivo*, the preferred radiolabelled analogue was ^{125}I-TyrBBN. However, iodinated versions of bombesin presented the disadvantage of being rapidly decomposed liberating radiotyrosine and defying the selective diagnostic purpose depending on the timescale of the imaging experiment.[99, 102] Therefore, other radioisotopes have been studied and radioanalogues of bombesin obtained (*vide infra*) although ^{125}I-TyrBBN remained as gold standard to evaluate the binding of novel imaging probes.

Table 1.2: Imaging agents including diverse bombesin fragments classified by imaging modality.

Entry	Analogue	Peptide sequence	Radioisotope / dye	Linker	Ref.
		PET			
1	RP527	Gln-Trp-Ala-Val-Gly-His-Leu-Met-NH_2	^{99m}Tc	Gly-5ava	103
2	Pesin	Gln-Trp-Ala-Val-Gly-His-Leu-Met-NH_2	$^{69/67/68}$Ga, ^{177}Lu	PEG	104
3	ATSM-BBN	Gln-Trp-Ala-Val-Gly-His-Cha-NLe-NH_2	$^{64/67}$Cu	Asp-$(Ala)_2$	105
		OPTICAL			
4	Alexa	Gln-Trp-Ala-Val-Gly-His-Leu-Met-NH_2	Alexa fluor 680	$(Gly)_3$	106
5	FITC	Gln-Trp-Ala-Val-Gly-His-Leu-Met-NH_2	FITC	-	107
		MULTIMODAL			
6		Gln-Trp-Ala-Val-Gly-His-Leu-Met-NH_2	DOTA / FITC	Lys	107
7	^{18}F-BD-BBN	Gln-Trp-Ala-Val-Gly-His-Sta-Leu	^{18}F / BODIPY	alkyne	108
8		Gln-Trp-Ala-Val-Gly-His-Leu-Met-NH_2	^{18}F / BODIPY	PEG	109

Other derivatives for PET imaging of GRPR positive tumours using ^{18}F have also appeared in the literature.[110, 111] The entire sequence and the shortened [7-14] version of bombesin have been compared, with ^{18}F as a label in a phenyl group at the end of an aminocaproic acid molecule used as a linker. The whole sequence showed higher affinity for GRP receptors but was more unstable *in vivo* that the shorter analogue.[112] Becaud *et al.* reported the preparation of a BBN[7-14] derivative that included an aromatic group in which ^{18}F was incorporated in moderate radiochemical yields by nucleophilic aromatic substitution with a trimethylammonium moiety as the leaving group.[113] The same group explored the ^{18}F labelling strategy in mice bearing prostate GRPR positive tumours with positive targeting to the tumour.[114]

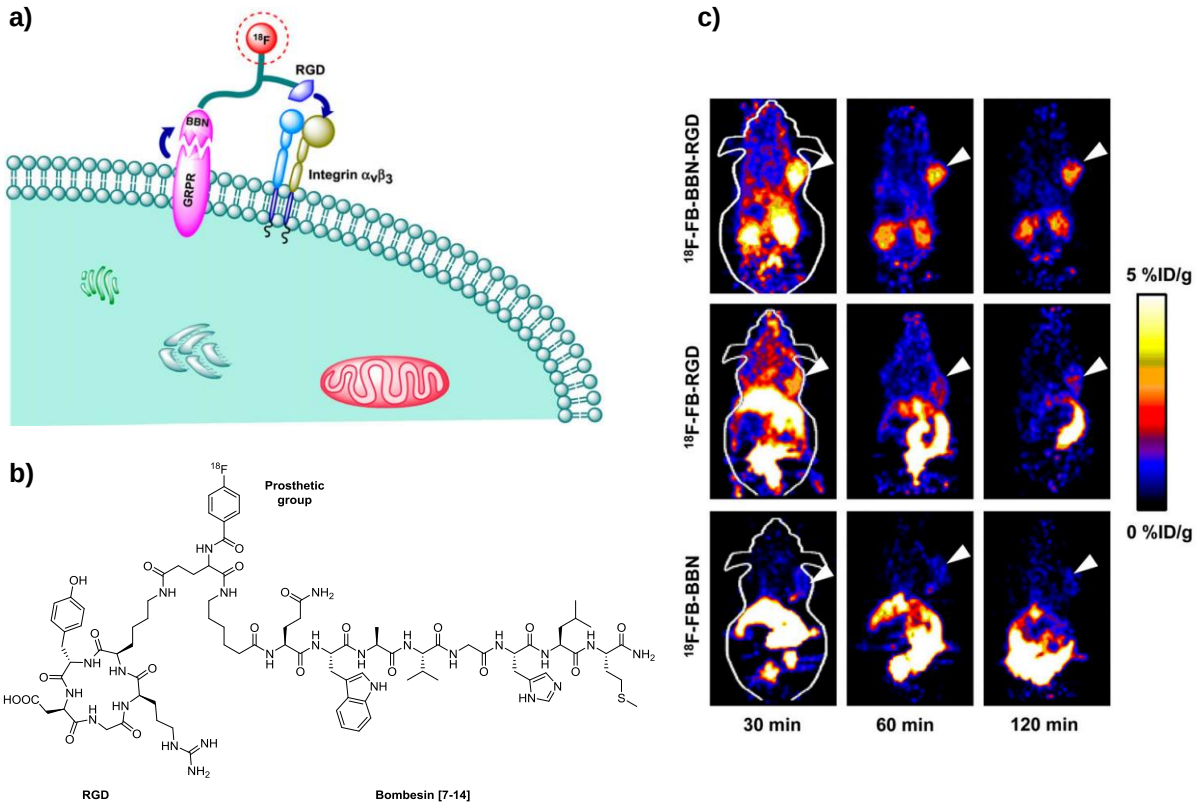

Figure 1.12: Heterodimeric imaging agent to target GRP receptors and integrin receptors in prostate cancer. a) Representation of the binding of the imaging agent to the receptors in the membrane. b) Structure of the imaging agent. c) Micro PET images in mice at 30, 60 and 120 min where the monomer and heterodimer compounds are compared. Tumours are marked by the white arrow. This research was originally published in JNM. Z. B. Li, Z. Wu, K. Chen, E. K. Ryu and X. Chen. ^{18}F-Labeled BBN-RGD Heterodimer for Prostate Cancer Imaging. J Nucl Med. 2008; 49, 453-461. © by the Society of Nuclear Medicine and Molecular Imaging, Inc.

Modifications of the [7-14] fragment of bombesin have been reported[110, 111] and include several linkers to improve uptake[115, 116], the formation of heterodimers with RGD[117, 118, 119] to expand the targeting abilities in prostate tumours (Figure 1.12) or the substitution of the fluorine-18 prosthetic group to favour the metabolic processing through the kidneys.[120] In most of these examples fluorine-18 was incorporated by nucleophilic aromatic substitution but other radiolabelling strategies such as the use of NOTA or similar macrocyclic chelators for Al^{18}F[110, 121], trimethylamonium fluoride salts or the functionalisation with ^{18}F-FDG have been described. The effect of agonists versus antagonists in GRPR bearing tumours have been compared and the agonist analogues provided better results in terms of internalisation for ^{18}F labelling, opposite to the case of radioactive metals (^{99m}Tc or ^{111}In).[116]

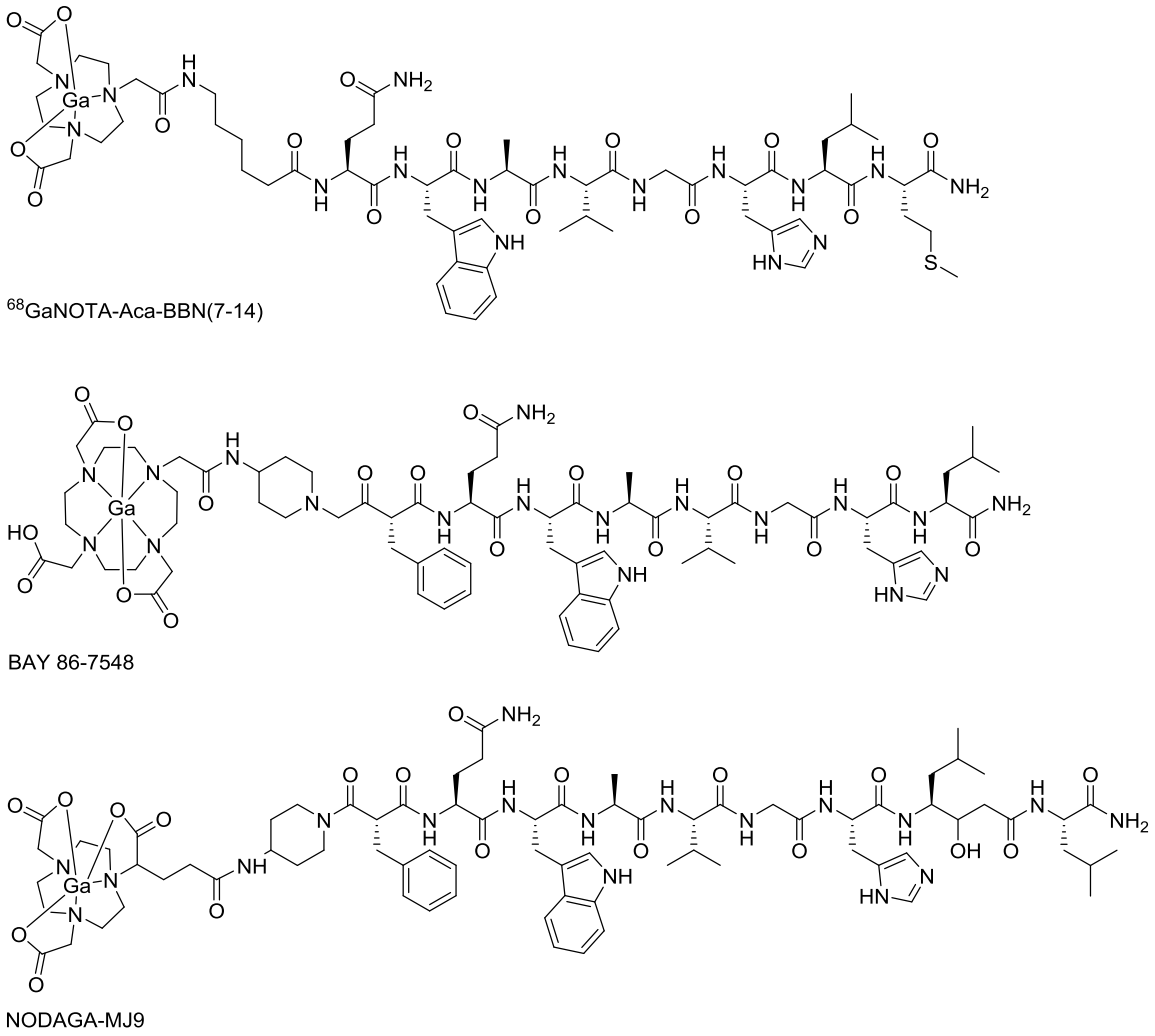

Figure 1.13: Structure of ^{68}Ga-bombesin probes being evaluated in ongoing clinical trials.[122, 123]

Despite the current interest in the application of nuclides as ^{99m}Tc or ^{18}F, as well as the search of other elements like transition metals as ^{64}Cu, some new and intense research effort has been recently dedicated to the preparation and optimisation of radioprobes based on ^{68}Ga. This is motivated due to its promise of generator availability. The chelation of the radiometal is generally achieved by a macrocylic chelator as DOTA or NOTA. However, other examples as bis(thiosemicarbazones), TRAP, NOPO, etc. have been described because of their higher selectivity or potential hypoxia detection (Figure 1.5).[105, 124] The possibilities of radiolabelling one derivative with more than one nuclei are possible thanks to the versatility of the chelators. Maecke *et al.* described a [7-14] fragment of bombesin functionalised with a PEG linker and a DOTA chelator that was radiolabelled with ^{67}Ga and ^{177}Lu for SPECT imaging and ^{68}Ga for PET. The derivative presented a promising tumour uptake although experiments *in vivo* showed an increased uptake in the kidneys and pancreas.[104] The dual functionalisation with two targeting groups to aim for more than one target has also been explored. The GRP and integrin receptors were targeted by the preparation of a bombesin-RGD heterodimer radiolabelled with ^{68}Ga (Figure 1.12). The binding

affinities were comparable to that of the monomers and the specificity was promising as demonstrated by blocking studies.[125] A PSMA inhibitor was also incorporated in a heterodimer with a modified version of bombesin to bind to the two targets and chelate ^{68}Ga. The different parts of the probe were assembled by using click chemistry and the products evaluated *in vitro* and *in vivo*, showing good binding to the two targets and reduced uptake in the rest of the organs *in vivo* when compared to the monomers.[126] Furthermore, at the moment of writing this document, at least 10 clinical trials involving bombesin derivatives for imaging purposes in prostate cancer were active over Europe and USA.[122, 123] The vast majority of the ongoing clinical trials involved the use of different bombesin-like peptides, functionalised with a variety of chelators and ^{68}Ga as a radioisotope, demonstrating the current interest in the application of this radioisotope in clinical imaging. [127-129] A selection of these compounds can be observed in Figure 1.13.

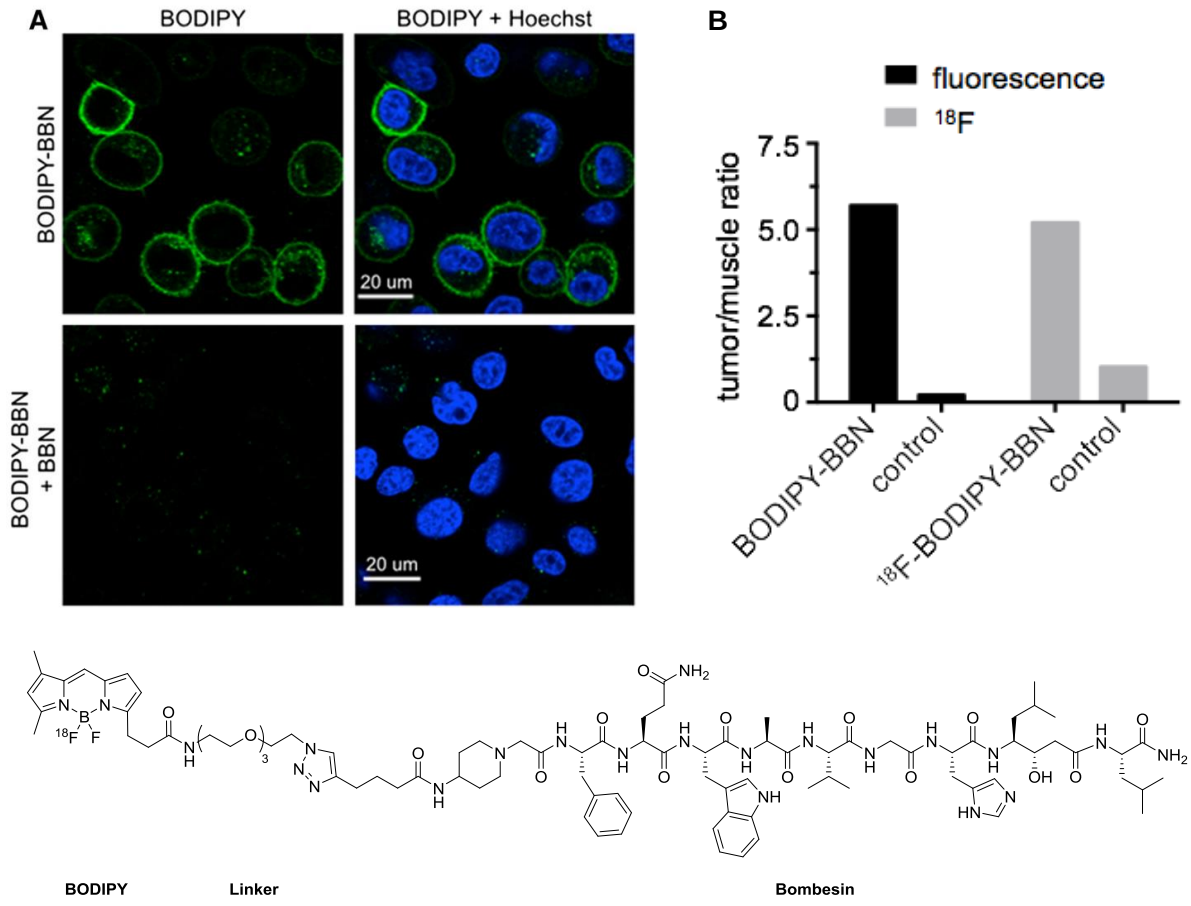

Figure 1.14: *In vitro* evaluation of a bimodal bombesin-based imaging probe (entry 8 in Table 1.2). A) Confocal imaging of BD-BBN in PC-3 cells (top) along with blocking experiments in which bombesin was added in a 100-fold excess (bottom). Hoechst co-localisation experiments are shown in the right column. B) Quantification of tumour uptake by fluorescence and gamma counting. Figure reproduced from ref. 108 with permission from the publisher.

The development of fluorescent probes is receiving increasing attention to characterise imaging probes *in vitro* prior to animal experiments and as part of bimodal/multimodal imaging probes. In addition, the inclusion of nanomaterials in biomedical research, requires fluorescence experiments to study the materials *in vitro* before their translation to animal models.

The study of the behaviour of a bombesin derivative conjugated with a rhodamine dye was investigated by Heckl *et al.* The uptake of the conjugate was studied in human cancerous and healthy cell lines by flow cytometry, confocal microscopy and it proved to be receptor-mediated evolving from membrane bound to localised in the cytoplasm over time. The presence of GRP receptors in different cell lines was also evaluated comparing the fluorescence intensities of the confocal images.[93] Near-infrared dyes are another area of great interest as tissue auto-fluorescence is considerably reduced in this area of the spectrum (Figure 1.7). Commercial dyes, as AlexaFluor 680, have been studied *in vitro* in breast cancer cells but also for the detection of metastases in mice.[106, 130] The commercial derivative IR800 or MPA has been coupled to bombesin [7-14] through different linkers and the imaging probes studied *in vitro* and *in vivo*. In both cases, all prepared derivatives showed uptake in PC-3 cells and PC-3 containing tumours but the first highlighted the importance of the nature of the linker as it impacts in the efficiency of the binding.[131, 132] In addition, the design of multimodal probes is attracting much attention as explained in section 1.1. Examples of multimodal probes to target prostate cancer including bombesin have been described in the literature.[133] Optical / PET derivatives are formed by the functionalisation of bombesin with a fluorophore and a chelating group. Fluorescein isothiocyanate (FITC) was conjugated to two different chelators (DTPA and DOTA) and to a 7-14 residue through a lysine linker. The position of the chelating agent directly to the N-terminus or to the lysine linker affected greatly the binding affinity. In this case, no nuclear imaging experiments were reported.[107]

Another bombesin-based derivative conjugated to a BODIPY took advantage of the fluorine atoms in BODIPY dyes that can be exchanged for ^{18}F (Figure 1.14). The preparation of different multimodal probes based on BODIPY dyes was reported by Goze *et al.* including NIR derivatives. The linkage to the peptide was conducted by click chemistry and a competitive binding study proved that the final product binding efficiency was not affected by the incorporation of the fluorophore.[109] Another study described the preparation of a similar multimodal probe assembled through click chemistry, *in vitro* imaging in PC-3 cells and *in vivo* imaging in PC-3 tumour bearing mice. The results proved promising although the tumour uptake was low with a high bone uptake that was attributed to free ^{18}F according to the authors' hypothesis.

1.3 Bis(thiosemicarbazonato) complexes in molecular imaging applications

The thiosemicarbazone moiety (Scheme 1.1) has been known for over a century. The first reports date from the early 1900s where the study of these compounds was motivated as a way to identify ketones.[134] The primitive interest in thiosemicarbazones was triggered by the varied biological properties presented by this family of compounds (e.g. antiviral, antifugal or antibacterial).[135-138] However, the interest in bis(thiosemicarbazonato) complexes for medical imaging goes back to the late 1990s when the first aliphatic complexes were applied to the imaging of cardiac hypoxia by Fujibayashi.[139] This interest has been sustained over recent times with some derivatives reaching clinical trials for imaging of lung, cervical or rectal cancers.[140-142] Despite the good results obtained in patients, the use of aliphatic thiosemicarbazonato complexes for hypoxia imaging should be considered with caution as the fate of the complex *in vivo* is not totally understood. The latest results suggesting a prompt decomplexation of the radioactive copper are discussed below.

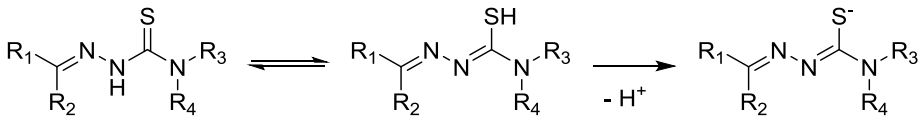

Scheme 1.1: Thione – thiol equilibrium in thiosemicarbazones.

In the past decade, bis(thiosemicarbazonato) complexes for imaging are gaining attention as multimodal probes since the introduction of acenaphthenequinone for the preparation of ligands and complexes by Pascu *et al.*[143] The acenaphthene aromatic backbone provides an inherently fluorescent group (weak in the ligands and stronger in the complexes where ligand to metal charge transfers (LMCT) and metal to ligand charge transfers (MLCT) are possible).[144] This yields a versatile chelator able to form complexes that can act as multimodal imaging probes. The preparation of acenaphthenequinone mono(thiosemicarbazone) ligands and complexes had been reported before in the literature but acting as tridentate ligands toward the metal and not applied as imaging agents.[136] The chemistry of thiosemicarbazones has been extensively reviewed over the past decades with the earliest example in 1974 in the framework of a compendium of ligands containing nitrogen and sulphur.[145] Later, other reviews focused exclusively in thiosemicarbazones and the corresponding metal complexes covering their coordination chemistry comprehensively.[146-149] The role of thiosemicarbazones and their complexes in imaging[150] and pharmaceuticals[151, 152] have also been covered.

The preferred way to obtain thiosemicarbazones usually involves the reaction of carbonyl-based compounds with thiosemicarbazides in ethanolic solutions, using acids as catalysts.[153] Other methods as using hydrazones, oximes, dithiocarbazides or isothiocyanates have been described.[153, 154] The carbonylic compounds for the synthesis of bis(thiosemicarbazones) are generally 1,2-disubstituted although 1,3-, 1,4- and 1,5-dicarbonylic compounds have been explored.[155-157] The synthesis of

symmetrical bis(thiosemicarbazones) is usually straightforward and the products are obtained in good yields although side reactions are known to take place (cyclisations or dimerisations). Therefore, the reaction conditions have to be cautiously monitored in order to avoid side reactions or the formation of mixture of products difficult to separate.[158] Despite being more challenging, the synthesis of unsymmetrical derivatives has been reported, being the stepwise condensation of the thiosemicarbazides to the dicarbonylic compounds the most successful method. The synthesis of aliphatic bis(thiosemicarbazones) for imaging applications was reviewed by Dilworth *et al.*[154]

The wide range of metals that thiosemicarbazones are able to chelate (Table 1.3) makes them outstandingly flexible ligands which broadens their chemistry and applications. The synthesis of the corresponding complexes generally varies with the thiosemicarbazones and the metallic species but generally involves heating the thiosemicarbazone with the metal precursor in the form of halide, acetate, etc.[149]

Table 1.3: Examples of metals forming thiosemicarbazonato complexes.[149]

Group	**5**	**6**	**7**	**8**	**9**	**10**	**11**	**12**	**13**	**14**	**15**
									Al		
	V	Cr	Mn	Fe	Co	Ni	Cu	Zn	Ga		
Element		Mo	Tc	Ru	Rh	Pd	Ag	Cd	In	Sn	
		W	Re			Pt	Au	Hg	Tl	Pb	Bi
	U										

Mono(thiosemicarbazones) have different coordination modes to the metal: bidentate, through the N and S atoms or tridentate, involving any other donor atoms in the thiosemicarbazone structure (Figure 1.15, A and B). The most common coordination mode in bis(thiosemicarbazones) is tetradentate through the N and S atoms of both arms (Figure 1.15, C).

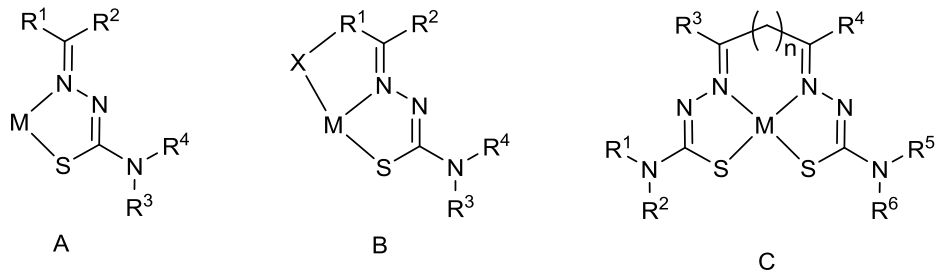

Figure 1.15: Selected coordination modes of mono(thiosemicarbazones) (A, B) and bis(thiosemicarbazones) (C) to a metal atom.

The aliphatic family of complexes has been extensively explored for their use in PET imaging, chelating mainly ^{64}Cu for the detection of hypoxia in tumours and cardiac ischaemia.[159, 160] The hypoxic selectivity was related to the lipophilicity and redox potential of the bis(thiosemicarbazonato) complexes so the structures were modified by changing the backbone (using 2,3-butanedione, glyoxal or pyruvaldehyde as starting materials) and substituents in an effort to adjust these two parameters.[161] Experimental data such as UV-vis spectra, cyclic voltammetry or pKa values were explored for a series of derivatives (Figure 1.16) resulting Cu(II)ATSM the most promising species. Furthermore, other parameters as HOMO and LUMO levels or energies of protonated and reduced species were obtained by DFT calculations.[162]

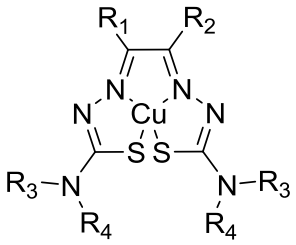

	R_1	R_2	R_3	R_4	$E_{1/2}$ Cu(II/I)	logP
GTS	H	H	H	H	-0.43	0.45
GTSM	H	H	CH_3	H	-0.43	0.84
PTS	CH_3	H	H	H	-0.50	0.53
PTSM	CH_3	H	CH_3	H	-0.51	1.45
$PTSM_2$	CH_3	H	CH_3	CH_3	-0.53	2.35
PTSE	CH_3	H	C_2H_5	H	-0.52	1.96
PTSP	CH_3	H	C_6H_5	H	-0.31	1.96
ATS	CH_3	CH_3	H	H	-0.59	0.65
ATSM	CH_3	CH_3	CH_3	H	-0.59	1.48
CTS	C_2H_5	CH_3	H	H	-0.59	2.34
CTSM	C_2H_5	CH_3	CH_3	H	-0.58	2.69
DTS	C_2H_5	C_2H_5	H	H	-0.59	1.69
DTSM	C_2H_5	C_2H_5	CH_3	H	-0.58	2.34

Figure 1.16: Aliphatic family of Cu(II) bis(thiosemicarbazonato) complexes with their standard reduction potentials and lipophilicity. $E_{1/2}$ values expressed in volts vs. Ag/AgCl. $E_{1/2}$ and log P values obained from ref. 163.

However, the insights underlying the behaviour of these complexes and their hypoxia selectivity remain under debate. The established mechanism for Cu(II)ATSM hypoxia selectivity agreed over the years involved the presence of an equilibrium in the cellular environment between the Cu(II) and Cu(I) species. The trigger of hypoxia selectivity was related to the reduction of the Cu(II) complex to the negatively charged Cu(I). The latter could not cross the cellular membrane so it protonates and dissociates resulting in an accumulation of copper into hypoxic cells or tissues. In normoxic tissues, the Cu(II) species was free to cross the cellular membrane and exit the cell.

The preparation of bis(thiosemicarbazonato) complexes from an aromatic precursor as acenaphthenequinone provides a number of advantages when compared to the aliphatic counterparts as higher stability in biological media, a greater versatility in the formation of complexes (with other metals as Ga(III), Ni(II) or In(III)) and the possibility to function as multimodal probes that can be used either *in vitro* thanks to its fluorescence or *in vivo* when transmetallated with a radioisotope. Furthermore, the fluorescence of these metal complexes provided a new dimension in the study of thiosemicarbazones and their complexes *in vitro* by optical techniques.

Only a few examples of bis(thiosemicarbazonato) metal complexes could be studied optically *in vitro* prior to the appearance of these complexes. Dilworth *et al.* reported an inherently fluorescent Zn(II) derivative, with the exception of this case, all other examples implied the attachment of a dye molecule with the risk of changing the intrinsic properties of the compound. Different groups have been used as dyes attached to thiosemicarbazonato complexes as pyrene, BODIPY or stilbene (although in this case, the stilbene group worked as a targeting molecule towards beta amyloid plaques in the brain).[164]

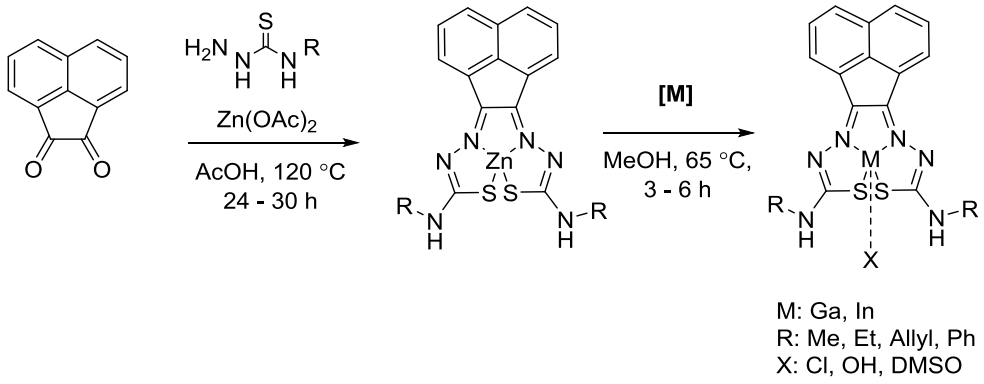

Scheme 1.2: General synthesis of acenaphthenequinone bis(thiosemicarbazonato) metal complexes.

The general synthesis of acenaphthenequinone bis(thiosemicarbazonato) complexes is depicted in Scheme 1.2. The mono and bis(substituted) ligands can be obtained by heating the diketone and thiosemicarbazide in the presence of an acid. The zinc complex can be obtained in a one-pot templated process from acenaphthenequinone and an excess of thiosemicarbazide and zinc acetate heating in acetic acid for 24 – 30 h. It was found that complexes of other metals could be obtained but optimal conditions resulted by transmetallation from the Zn analogue rather than from the ligands or from acenaphthenequinone.[57, 165]

Unsymmetrical acenaphthenequinone derivatives have been prepared from the mono(substituted) ligand and thiocarbohydrazide in similar conditions as in the formation of symmetrical Zn(II) complexes (Scheme 1.3). Unfortunately, the strategy for the conjugation to a targeting peptide proved unsuccessful.[166]

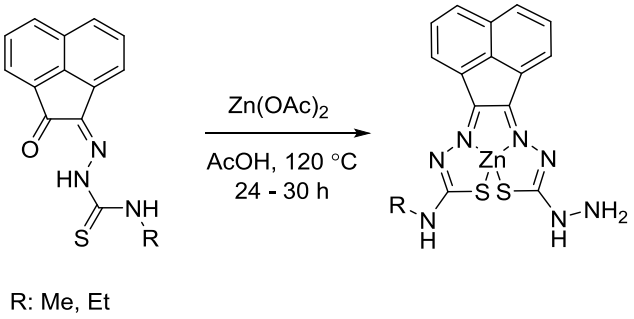

R: Me, Et

Scheme 1.3: Synthesis of unsymmetrical bis(thiosemicarbazonato) acenaphthenequinone complexes from the corresponding mono(substituted ligand).

The transmetallation of this family of compounds with ^{68}Ga has been described for a small number of derivatives so far but appears to constitute a significant advantage towards the application of these complexes in imaging.[167] Much research effort is being done in the optimisation of efficient gallium chelators as ^{68}Ga has a number of advantages compared to other radionuclides as mentioned earlier.

Furthermore, some of the gallium derivatives (R: allyl) have proved to be hypoxia selective under specific conditions in a range of cells.[168] In this case, the proposed mechanism of hypoxia selectivity proposed for Cu(II)ATSM would not be applicable as Ga(III) cannot be reduced under biological conditions. One hypothesis is that the complex gets involved in the iron metabolism pathways that are known to change under hypoxia.[169, 170] This could be explained due to the capability of gallium of mimicking iron metabolism and compete in the binding to enzymes or proteins. The reason why biomolecules and living systems cannot distinguish between Fe(III) and Ga(III) is based on their physicochemical similarities, as ionic radii (55 pm vs. 62 pm), oxidation states or coordination chemistry.[171]

1.4 Application of carbon nanomaterials to biomedical imaging: towards nanotheranostics design and testing

Carbon nanomaterials are allotropes of carbon where at least one dimension is measured on the nanoscale (<100 nm). The main types of carbon nanomaterials are nanotubes, first described by Iijima *et al.*[172, 173] and graphene, a more recent material with the single layer derivative reported in 2004.[174] Other nanoallotropes of carbon are the well-studied fullerenes although several other, nano-dimensional members of this family such as carbon dots, nanohorns, nanoonions or nanodiamonds have emerged.[175] In this work we focused on the functionalisation of carbon nanotubes with small molecules and biomolecules of relevance to PCa targeting.

Carbon nanotubes can be described as a wrapped graphene sheet with ca. 1 nm diameter and lengths in the scale of the hundreds of nm to μm. They can be classified according to the number of carbon concentric layers as single walled (SWNT) and multi walled (MWNT). The simplest MWNT are double-walled nanotubes but the number of layers can be higher with the diameter going up to tens of nm. The structure of nanotubes can be described by three parameters: the chiral angle (θ) and two vectors (n,m). The variation of the two vectors produces three types of tubes: when the vectors are (n,0) a zigzag nanotube is obtained; if the vectors are n = m (n,n) an armchair nanotubes is obtained while if n and m are different (n,m) a chiral nanotube is obtained. The construction of a chiral (6,3) nanotube from a graphene sheet is depicted in Figure 1.17.

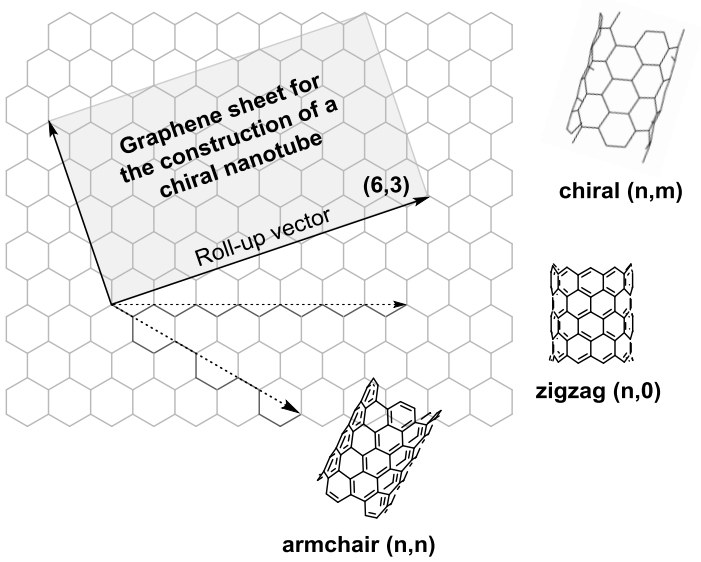

Figure 1.17: Diagram showing the construction of SWNT from a graphene sheet.

The chirality of the nanotube is determinant for its electrical properties as armchair nanotubes are metallic, zigzag are metallic if n is a multiple of 3 and chiral tubes can indistinctively be metallic or semiconducting.[176] The synthesis of nanotubes with specific chirality has been explored and methods exist to obtain a desired chirality.[177] SWNT present certain properties that make them unique materials as a high surface area, excellent electrical conductivity or high mechanical resistance. For these reasons, carbon nanotubes have been applied to composite materials, electronic devices, biosensors, drug delivery, cancer treatment or imaging.[178] The last part of this section will focus on the applications and challenges of SWNT in the bioimaging field although toxicity concerns can be generalised to the biomedical field.

The applications of carbon nanomaterials in biological applications leads to concerns about their toxicity. A great number of studies have been published examining the toxicity of these materials *in vitro* and *in vivo*. The results are occasionally controversial but there are certain widely accepted aspects like the strong dependence of the toxicity with a number of factors as dose, shape, impurities, surface functionalisation or exposure route of the nanomaterial.[179] The modification of the mentioned factors can lead to the reduction of the toxicity making possible the use of carbon nanomaterials in biomedical applications.

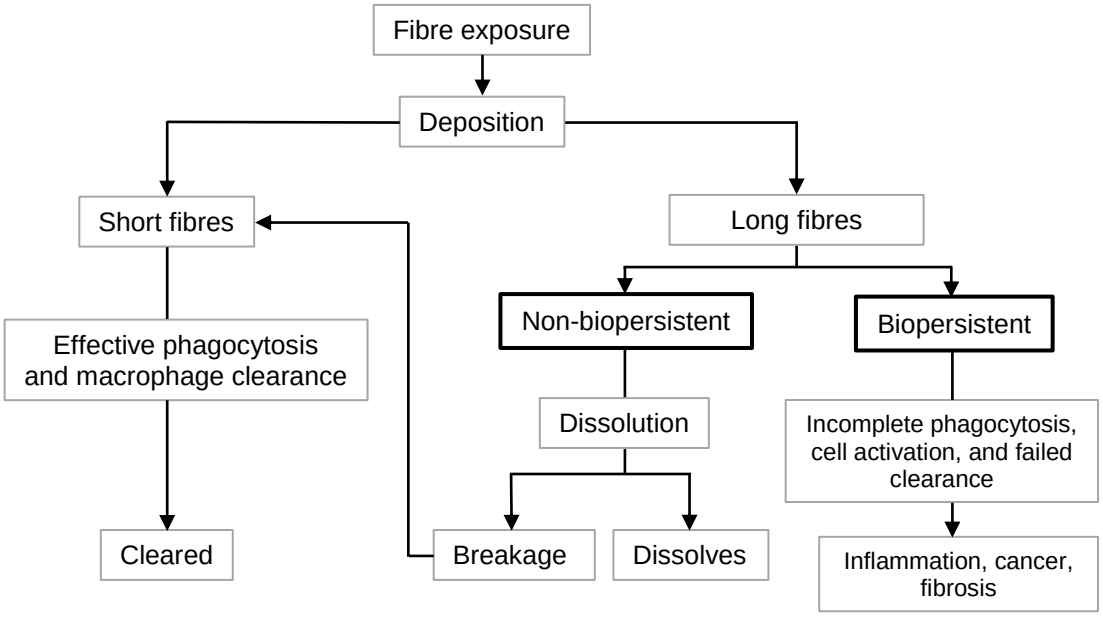

Figure 1.18: Summary of the possible outcomes to fibre exposure based on length and biopersistence. Figure adapted from ref. 169.

Exposure to carbon nanotubes through inhalation is the main cause of concern towards the use of carbon nanotubes in industrial or biomedical environments. Carbon nanotubes can be considered fibres due to the large aspect ratio so they could present similar toxicity as asbestos-like materials. According to this

route, inhaled carbon nanotubes of a certain length, diameter and biopersistence can be accumulated in the lungs and pleura causing oxidative stress, inflammation, genotoxicity and in the end neoplasia (Figure 1.18).[180, 181] Different *in vitro* and *in vivo* studies have confirmed the biopersistence of pristine carbon nanotubes and the described behaviour in pleural tissue.[182] However, this response is dependent on the form of the carbon nanotubes as fibres and many nanotubes are present in tangles that can be regarded as particles so would not present this toxicity. The functionalisation type and degree is another important factor, as some functionalisation strategies tend to shorten the carbon nanotubes while others enhance the dispersibility making the nanotubes able to be excreted through different routes. In addition, the presence of metallic contaminants and defects in the tubes originated during the synthetic process can trigger inflammatory responses and must be considered.[183] Other routes of exposure like dermal absorption or ingestion had been less explored although there is evidence that SWNT can present toxic effects as reviewed recently by Ong *et al.* The authors concluded, however, that more research was needed along with the production of standard SWNT samples for the sake of comparison with new materials.[184]

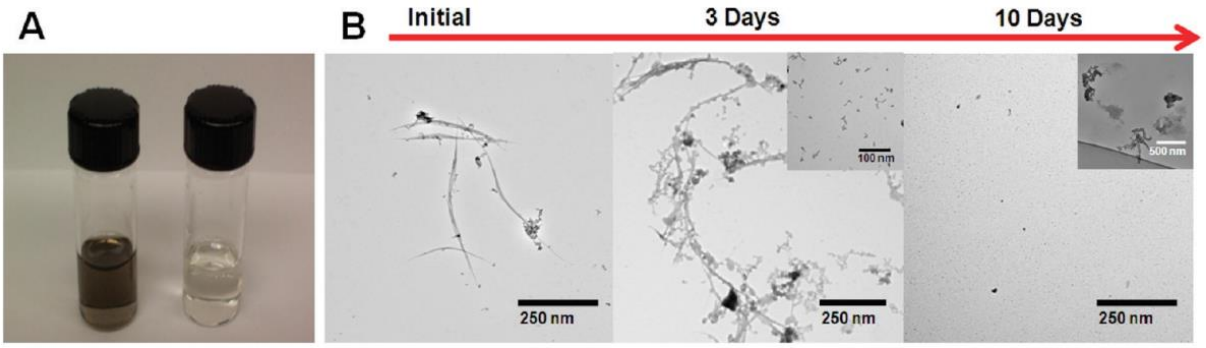

Figure 1.19: Enzymatic degradation experiments of carboxylated SWNT. A) Photograph of initial carboxylated SWNT dispersion and after 10 days of incubation with HRP and H_2O_2. B) TEM micrographs before the incubation and after 3 or 10 days (left to right). Adapted with permission from B. L. Allen, G. P. Kotchey, Y. Chen, N. V. K. Yanamala, J. Klein-Seetharaman, V. E. Kagan and A. Star, J. Am. Chem. Soc., 2009, **131**, 17194-17205. © 2009 American Chemical Society.

Nagai *et al.* compiled a series of *in vitro* studies evaluating the uptake properties and toxicity of SWNT and MWNT according to their functionalisation, length and diameter. Observing this compilation, it can be concluded that pristine single walled carbon nanotubes with small dimensions (< 1 µm length and 1-5 nm diameter) showed little toxicity in a range of cell types such as cervical cancer cells (HeLa), leukemic T-cells (Jurkat) or breast cancer cells (Michigan Cancer Foundation-7, MCF-7). The covalent or non-covalent functionalisation helped to the internalisation of the nanotubes that was produced by endocytosis or diffusion.[185] Regarding the *in vivo* biodistribution and toxicokinetics of nanotubes, the

response depended on the properties and functionalisation of the material and the accumulation in an organ could be controlled to a certain degree. Elimination in urine was observed to be the main excretion route for functionalised CNT while pristine samples have a tendency to accumulate in organs like the liver, the spleen or the lungs.[186]

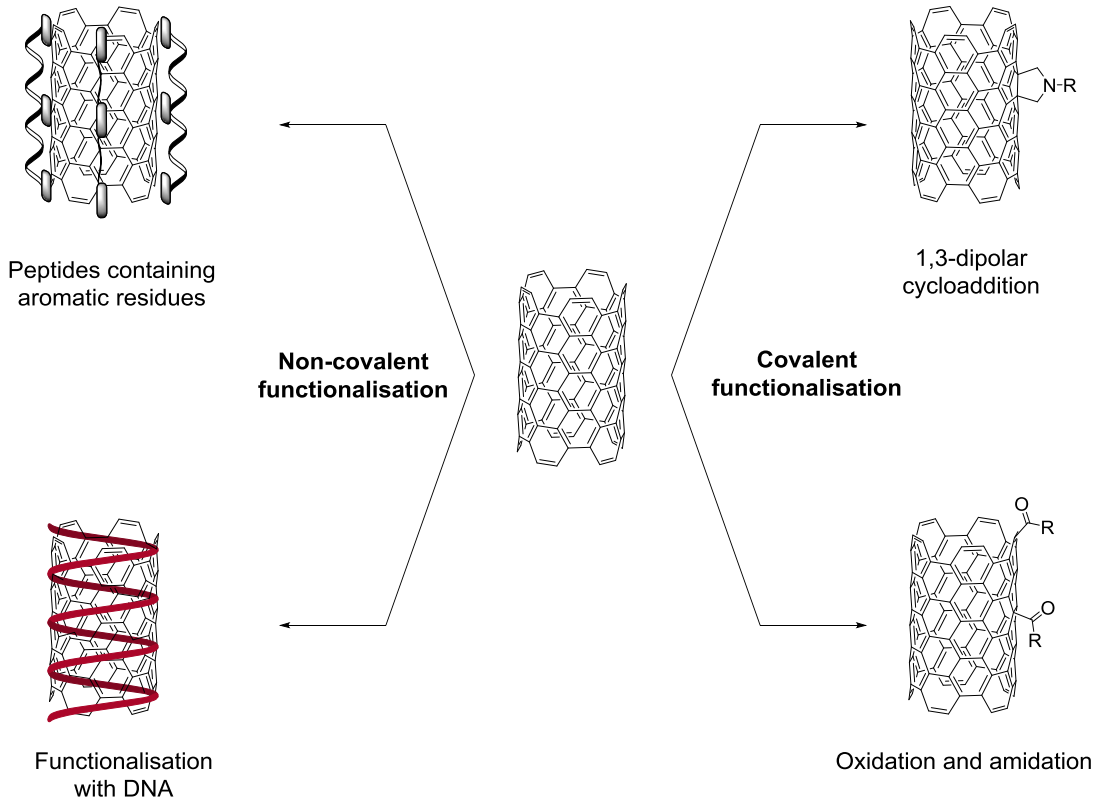

Scheme 1.4: Functionalisation strategies of pristine SWNT to allow their biomedical application.

Interestingly, oxidised SWNT have been reported to be biodegraded through an enzymatic pathway. Several different oxidised SWNT dispersions were incubated in the presence of the horseradish peroxidase enzyme (HRP) and hydrogen peroxide. After several weeks, the nanotubes were strongly degraded as observed by Raman spectroscopy or TEM (Figure 1.19).[187, 188] The fate of the nanotubes *in vitro* and *in vivo* was also followed, finding indications of biodegradation that can be rationalised based on this oxidative mechanism that renders the prospect of using carbon nanotubes as delivery agents able to be easily excreted or biodegraded after performing their function.[189] In a recent study, the production of reactive oxygen species in macrophages was found to be of paramount importance in the biodegradability of MWNT.[190] In summary, the toxicity of carbon nanotubes depends on the exposure route, physicochemical properties as fibre-like shape, length or insolubility in biological media.

The properties of pristine carbon nanotubes of a certain length make them impossible to eliminate by phagocytosis so they accumulate in the tissues triggering inflammation responses. However, the

physicochemical properties of pristine nanotubes can be dramatically modified by different functionalisation methods so the nanomaterial can be physiologically processed and excreted so it does not pose a toxicological risk, paving the way to the biomedical applications.

Despite the described potential adverse effects of carbon nanotubes, much research effort has been applied to enhance their biocompatibility by covalent or non-covalent functionalisation (Scheme 1.4).[191] SWNT conjugates with biologically active molecules as peptides or antibodies have been used in drug delivery, imaging or therapy.[192] The applications of SWNT in biomedical imaging is broad and examples of functionalised imaging probes with fluorophores and chelators have appeared in the literature applied with a variety of imaging techniques as optical, Raman or nuclear imaging (Figure 1.20, Figure 1.21 and Figure 1.22).

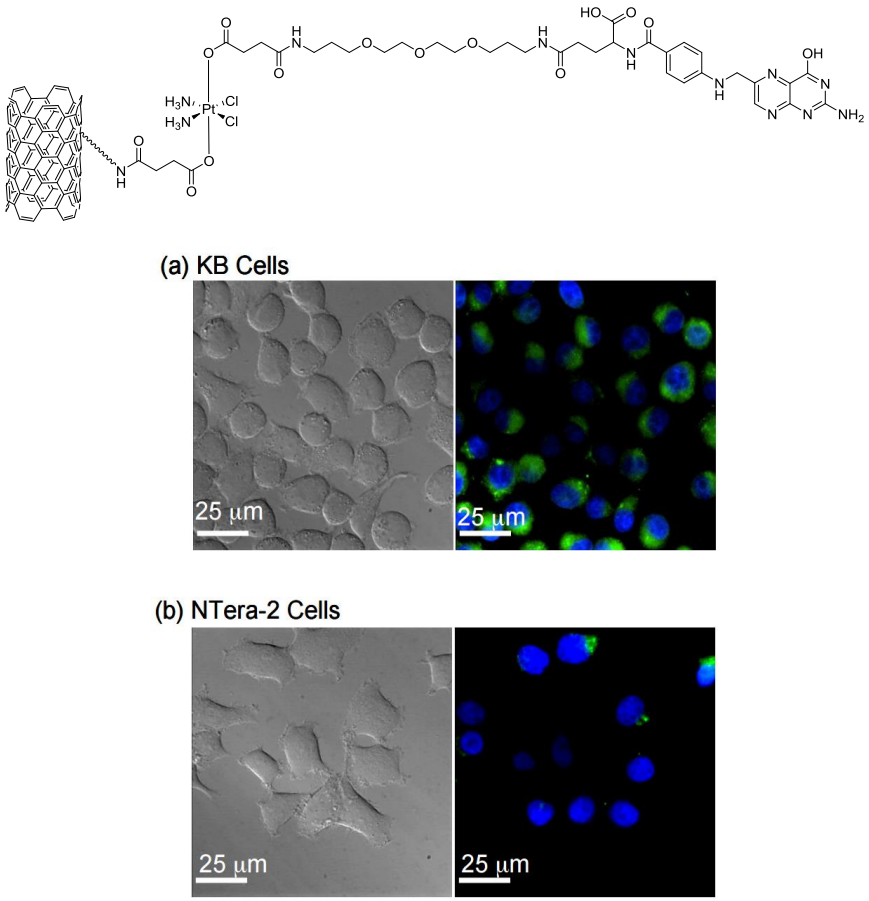

Figure 1.20: Structure of SWNT-Pt(IV)-FL probe and fluorescence microscopy images after 2.5 h incubation in a) human nasopharyngeal epidemoid carcinoma cells (KB) and b) human testicular cancer (Ntera-2) cells. Adapted with permission from S. Dhar, Z. Liu, J. Thomale, H. Dai and S. J. Lippard, J. Am. Chem. Soc., 2008, 130, 11467-11476. © 2008 American Chemical Society.

The use of carbon nanomaterials for biomedical purposes has been recently covered in several reviews. Dai *et al.* covered the use of carbon nanotubes, evaluating functionalisation strategies for their application in sensing, imaging and drug delivery.[193] Prato *et al.* covered the application of delivery probes based on nanotubes for imaging and therapeutics that had reached animal experimentation and summarised the concerns over the use of these materials.[194] The use of carbon nanomaterials in imaging has also been reviewed looking at their applications in fluorescence and Raman imaging[195, 196] with a comprehensive review by Dai *et al.* on imaging, focusing especially in NIR, sensing and therapy of carbon nanomaterials.[197]

Due to the nature of this project our interest lies in the use of SWNT for a probe applied to the imaging of prostate cancer cells by optical imaging in the visible range with an interest in the NIR-I region of the spectra and the potential application of the probes as PET/optical multimodal agents.

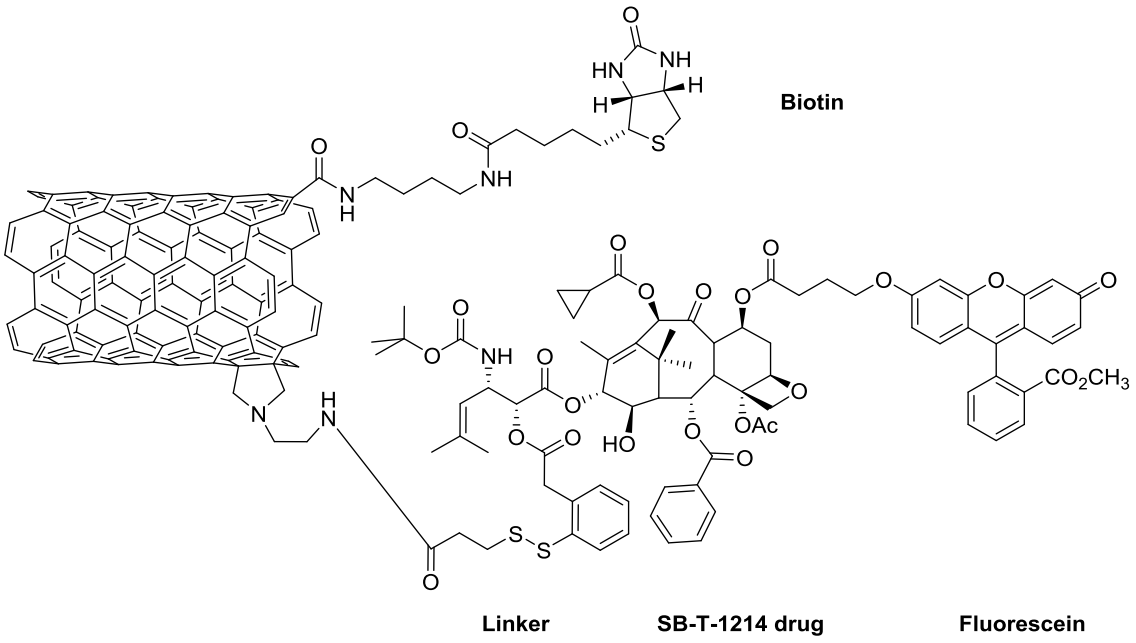

Figure 1.21: Schematic representation of SWNT nanoprobe incorporating a taxoid drug.[198]

The covalent functionalisation of SWNT with chelator groups or its filling with radionuclides has attracted interest since the beginning of the exploration of carbon materials as biomedical probes. Nuclear imaging allows us to follow the fate of the material *in vivo* and to evaluate its clearance from the body. Several radionuclides as ^{86}Y and ^{111}In have been attached covalently to functionalised SWNT using DOTA or DTPA chelator.[199] Other probes used in targeted approaches including antibodies with DOTA chelated ^{225}Ac for treatment and ^{89}Zr for imaging have been reported.[200, 201]

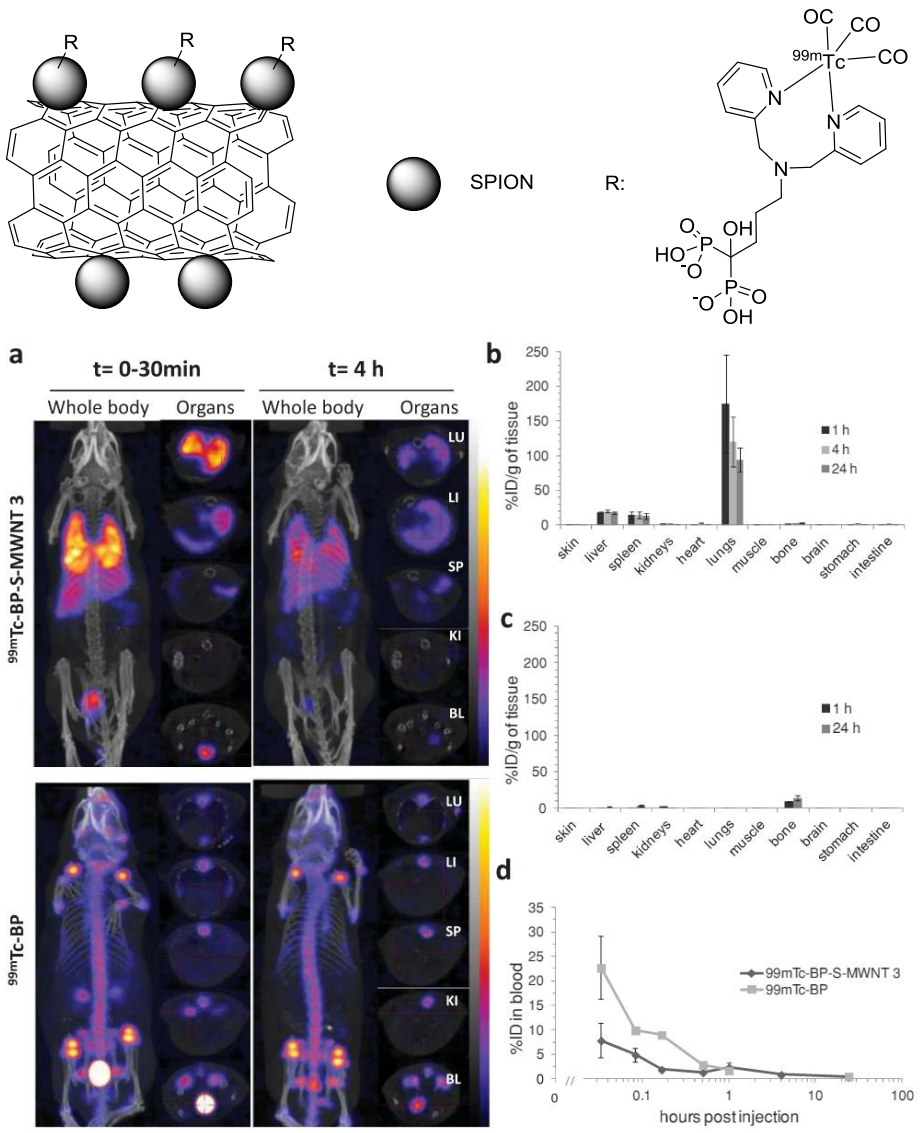

Figure 1.22: Structure of a carbon nanotube multimodal probe for MRI/SPECT imaging decorated with SPION and incorporating ^{99m}Tc as radionuclide. a) *In vivo* imaging comparing the biodistribution of the nanoprobe and the ^{99m}Tc chelated agent in mice. b) Biodistribution of the nanoprobe and c) the ^{99m}Tc chelated agent. d) Blood clearance profile of the radioprobe and nanoprobe. Figure reproduced from ref. 202 with permission from the publisher.

The covalent functionalisation of carbon nanotubes with fluorophores that allows to follow the nanomaterial *in vitro* by optical microscopy have been profusely reported in the literature. Specifically for SWNT, the attachment of different fluorophores to study the cellular uptake has been described. Fluorescein isocyanate have been employed as a commercially available dye and linked to SWNT functionalised through 1,3-dipolar cycloadditions.[203, 204] In other case, functionalised SWNT with fluorescein were used to evaluate the *in vitro* inflammatory response.[205] However, in most cases, the preparation of the imaging probe was conducted attempting to introduce an additional moiety acting as

a target or drug. Lippard *et al.* described the preparation of a targeted anticancer drug system anchored to SWNT. The nanoprobe incorporated a folate receptor to target KB tumour cells, a fluorescein fluorophore and a Pt(IV) compound based on cis-platin. The anticancer drug improved its efficacy supported on the SWNT.[206] The structure of the probe and the corresponding *in vitro* imaging can be observed in Figure 1.20.

In a similar manner, Ojima *et al.* combined a biotin targeting molecule, a taxoid drug and a fluorescein group through a double functionalisation route (oxidation and 1,3-dipolar cycloaddition) into a SWNT based nanoprobe (Figure 1.21). The conjugate showed promising cytotoxicity and selectivity for cancer cell lines.[198] The multiple functionalisation of SWNT can be further extended and triple functionalised derivatives have been achieved by combining covalent and non-covalent functionalisation.[207] In this way, oxidised SWNT were modified covalently to attach fluorescein and a targeting antibody while the drug doxorubicin was adsorbed onto the surface.[208]

The description of multiple functionalisation strategies and the development of nanoparticles as contrast agents has facilitated the development of multimodal imaging probes. In this way, nanotubes can be functionalised with magnetic particles for MRI, radionuclides for nuclear imaging and fluorophores for optical or photoacoustic imaging and different imaging modalities like MRI/SPECT (Figure 1.22)[202], Raman/photoacoustic/MRI[209], or SPECT/optical[210] can be achieved.

1.5 Objectives

The aim of this thesis is to obtain a probe able to be used in the imaging of prostate cancer with attention to possible multimodal applications by functionalisation of carbon nanomaterials.
The design elements envisage that a new nanoprobe can be devised, which can be composed of a carbon nanomaterial, a linker molecule, a fluorophore and a prostate cancer targeting molecule as depicted in Figure 1.23.

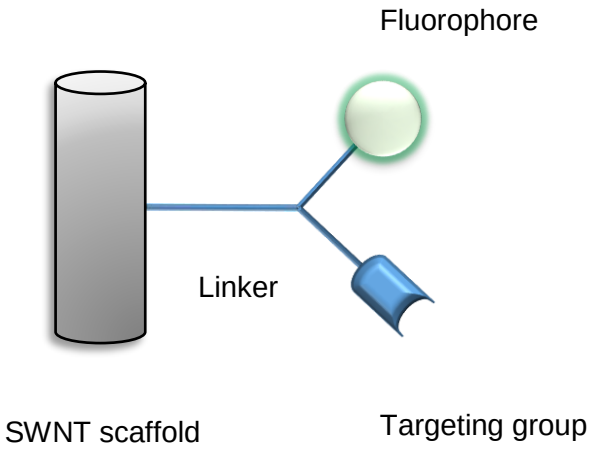

Figure 1.23: Representation of a potential imaging probe based on carbon nanotubes.

The Objectives are:

- Synthesis of a functional fluorophore capable to be coupled with the targeting molecule and/or nanomaterial. The chemistry of acenaphthenequinone bis(thiosemicarbazonato) metal complexes will be especially considered due to their multimodal properties and potential hypoxia selectivity.

- Covalent functionalisation of carbon nanomaterials, with emphasis in SWNT, and introduction of linker groups to allow the coupling with the fluorophore and targeting molecule moieties.

- Synthesis of a fragment of the peptide bombesin to act as targeting molecule toward prostate cancer cells.

- Coupling of the different parts of the nanoprobe and *in vitro* evaluation in prostate cancer cells.

1.6 References

1. Cancer Research UK, http://www.cancerresearchuk.org/health-professional/cancer-statistics/statistics-by-cancer-type/prostate-cancer#heading-Zero, Accessed 25/05/2016.
2. J. Ferlay, D. M. Parkin and E. Steliarova-Foucher, *Eur. J. Cancer*, **46**, 765-781.
3. World Health Organization GLOBOCAN 2012: Estimated Cancer Incidence, Mortaliy and Prevalence Worldwide 2012, http://globocan.iarc.fr/Pages/fact_sheets_cancer.aspx, Accessed 25/05/2016.
4. R. L. Siegel, K. D. Miller and A. Jemal, *CA. Cancer J. Clin.*, 2015, **65**, 5-29.
5. S. W. Fine and K. K. McKenney, in *Histology for pathologists*, Wolters Kluwer, Lippincott Williams et Wilkins, Philadelphia [u.a.], 2012, pp. 987-1002.
6. J. L. H. R. Bosch, K. Tilling, A. M. Bohnen, C. H. Bangma and J. L. Donovan, *The Prostate*, 2007, **67**, 1816-1824.
7. J. E. Hall and A. C. Guyton, *Guyton and Hall textbook of medical physiology*, 2011.
8. P. T. Scardino, *Trans. Am. Clin. Climatol. Assoc.*, 2000, **111**, 201-241.
9. G. J. Miller and K. C. Torkko, *Epidemiol. Rev.*, 2001, **23**, 14-18.
10. R. S. Kirby, *Fast facts prostate cancer*, Health Press, Oxford, UK, 2012.
11. E. D. Crawford, *Urology*, 2009, **73**, S4-S10.
12. R. W. Veltri, C. Marlow, M. A. Khan, M. C. Miller, J. I. Epstein and A. W. Partin, *The Prostate*, 2007, **67**, 1202-1210.
13. P. Sindhwani and C. M. Wilson, *Curr. Prostate Rep.*, 2005, **3**, 81-86.
14. H. G. Welch and P. C. Albertsen, *J. Natl. Cancer Inst.*, 2009, **101**, 1325-1329.
15. F. H. Schröder, J. Hugosson, M. J. Roobol, T. L. J. Tammela, S. Ciatto, V. Nelen, M. Kwiatkowski, M. Lujan, H. Lilja, M. Zappa, L. J. Denis, F. Recker, A. Berenguer, L. Määttänen, C. H. Bangma, G. Aus, A. Villers, X. Rebillard, T. van der Kwast, B. G. Blijenberg, S. M. Moss, H. J. de Koning and A. Auvinen, *New Engl. J. Med.*, 2009, **360**, 1320-1328.
16. P. C. Albertsen, D. F. Moore, W. Shih, Y. Lin, H. Li and G. L. Lu-Yao, *J. Clin. Oncol.*, 2011, **29**, 1335-1341.
17. E. A. M. Heijnsdijk, E. M. Wever, A. Auvinen, J. Hugosson, S. Ciatto, V. Nelen, M. Kwiatkowski, A. Villers, A. Páez, S. M. Moss, M. Zappa, T. L. J. Tammela, T. Mäkinen, S. Carlsson, I. J. Korfage, M. L. Essink-Bot, S. J. Otto, G. Draisma, C. H. Bangma, M. J. Roobol, F. H. Schröder and H. J. de Koning, *New Engl. J. Med.*, 2012, **367**, 595-605.
18. NHS, http://www.nhs.uk/Conditions/cancer-of-the-prostate/Pages/prevention.aspx, Accessed 11/07/2016.
19. AUA, http://www.nhs.uk/Conditions/cancer-of-the-prostate/Pages/prevention.aspx, Accessed 11/07/2016.
20. D. V. Makarov, S. Loeb, D. Ulmert, L. Drevin, M. Lambe and P. Stattin, *J. Natl. Cancer Inst.*, 2013, **105**, 1306-1313.

21. R. Palvolgyi, T. J. Daskivich, K. Chamie, L. Kwan and M. S. Litwin, *Urology*, 2011, **77**, 1330-1336.
22. A. D. Falchook, L. H. Hendrix and R. C. Chen, *J. Oncol. Pract.*, 2015, **11**, e239-e246.
23. A. D. Falchook, R. G. Salloum, L. H. Hendrix and R. C. Chen, *Int. J. Radiat. Oncol. Biol. Phys.*, 2014, **89**, 243-248.
24. S. P. Porten, A. Smith, A. Y. Odisho, M. S. Litwin, C. S. Saigal, P. R. Carroll, M. R. Cooperberg and P. the Urologic Disease of America, *Prostate Cancer Prostatic Dis.*, 2014, **17**, 246-251.
25. H. Hricak, P. L. Choyke, S. C. Eberhardt, S. A. Leibel and P. T. Scardino, *Radiology*, 2007, **243**, 28-53.
26. S. Ghai and A. Toi, *Radiol. Clin. North Am.*, 2012, **50**, 1061-1073.
27. S. S. Taneja, *Reviews in Urology*, 2004, **6**, 101-113.
28. J. R. Ashton, J. L. West and C. T. Badea, *Front. Pharmacol.*, 2015, **6**, 256.
29. M. F. Kircher and J. K. Willmann, *Radiology*, 2012, **263**, 633-643.
30. S. M. Abtahi, Y. Mao, D. Prapruttam, A. Elmi and S. S. Hedgire, *Magn. Reson. Imaging Clin. N. Am.*, 2014, **22**, 201-215.
31. A. W. J. M. Glaudemans and A. Signore, in *Bone Metastases: A translational and Clinical Approach*, eds. V. Vassiliou, E. Chow and D. Kardamakis, Springer Netherlands, Dordrecht, 2014, pp. 71-94.
32. A. P. S. Kirkham, M. Emberton and C. Allen, *Eur. Urol.*, 2006, **50**, 1163-1175.
33. V. P. B. Grover, J. M. Tognarelli, M. M. E. Crossey, I. J. Cox, S. D. Taylor-Robinson and M. J. W. McPhail, *J. Clin. Exp. Hepatol.*, 2015, **5**, 246-255.
34. J. Nakashima, A. Tanimoto, Y. Imai, M. Mukai, Y. Horiguchi, K. Nakagawa, M. Oya, T. Ohigashi, K. Marumo and M. Murai, *Urology*, 2004, **64**, 101-105.
35. A. H. Hou, D. Swanson and A. B. Barqawi, *Adv. Urol.*, 2009, **2009**.
36. K. L. Zakian, W. Hatfield, O. Aras, K. Cao, D. Yakar, D. A. Goldman, C. S. Moskowitz, A. Shukla-Dave, Y. M. Tehrani, S. Fine, J. Eastham and H. Hricak, *Magn. Reson. Imaging*, 2016, **34**, 674-681.
37. T. Kobus, A. J. Wright, T. W. J. Scheenen and A. Heerschap, *NMR Biomed.*, 2014, **27**, 39-52.
38. M. K. Yu, D. Kim, I.-H. Lee, J.-S. So, Y. Y. Jeong and S. Jon, *Small*, 2011, **7**, 2241-2249.
39. D. W. Townsend, *Ann. Acad. Med. Singapore*, 2004, **33**, 133-145.
40. I. Castiglioni, F. Gallivanone and M. C. Gilardi, in *PET-CT and PET-MRI in Neurology: SWOT Analysis Applied to Hybrid Imaging*, eds. A. Ciarmiello and L. Mansi, Springer International Publishing, Cham, 2016, pp. 23-30.
41. H. Jadvar, *J. Nucl. Med.*, 2011, **52**, 81-89.
42. S. M. Ametamey, M. Honer and P. A. Schubiger, *Chem. Rev.*, 2008, **108**, 1501-1516.
43. P. W. Miller, N. J. Long, R. Vilar and A. D. Gee, *Angew. Chem. Int. Ed.*, 2008, **47**, 8998-9033.
44. D. Brasse and A. Nonat, *Dalton Trans.*, 2015, **44**, 4845-4858.
45. M. G. Campbell and T. Ritter, *Org. Process Res. Dev.*, 2014, **18**, 474-480.

46. N. Ibrahim and S. Y. Cho, *Reports in Medical Imaging*, 2015, **8**, 51-62.
47. I. Velikyan, *J. Labelled Compd. Radiopharm.*, 2015, **58**, 99-121.
48. G. J. Stasiuk and N. J. Long, *Chem. Commun.*, 2013, **49**, 2732-2746.
49. J. Simecek, H.-J. Wester and J. Notni, *Dalton Trans.*, 2012, **41**, 13803-13806.
50. S. Lutje, S. Heskamp, A. S. Cornelissen, T. D. Poeppel, S. A. van den Broek, S. Rosenbaum-Krumme, A. Bockisch, M. Gotthardt, M. Rijpkema and O. C. Boerman, *Theranostics*, 2015, **5**, 1388-1401.
51. J. R. Osborne, N. H. Akhtar, S. Vallabhajosula, A. Anand, K. Deh and S. T. Tagawa, *Urol. Oncol.*, 2013, **31**, 144-154.
52. L. Martí-Bonmatí, R. Sopena, P. Bartumeus and P. Sopena, *Contrast Media Mol. Imaging*, 2010, **5**, 180-189.
53. L. E. Jennings and N. J. Long, *Chem. Commun.*, 2009, 3511-3524.
54. S. Lütje, M. Rijpkema, W. Helfrich, W. J. G. Oyen and O. C. Boerman, *Mol. Imag. Biol.*, 2014, **16**, 747-755.
55. Z. Li, *Chem Comunn*, 2011, **47**.
56. J. A. Hendricks, E. J. Keliher, D. Wan, S. A. Hilderbrand, R. Weissleder and R. Mazitschek, *Angew. Chem. Int. Ed. Engl.*, 2012, **51**.
57. S. I. Pascu, P. A. Waghorn, B. W. C. Kennedy, R. L. Arrowsmith, S. R. Bayly, J. R. Dilworth, M. Christlieb, R. M. Tyrrell, J. Zhong, R. M. Kowalczyk, D. Collison, P. K. Aley, G. C. Churchill and F. I. Aigbirhio, *Chem. Asian J.*, 2010, **5**, 506-519.
58. A. M. Smith, M. C. Mancini and S. Nie, *Nat. Nanotech.*, 2009, **4**, 710-711.
59. S. Luo, E. Zhang, Y. Su, T. Cheng and C. Shi, *Biomaterials*, 2011, **32**, 7127-7138.
60. F. W. B. van Leeuwen, J. C. H. Hardwick and A. R. van Erkel, *Radiology*, 2015, **276**, 12-29.
61. G. H. KleinJan, N. S. van den Berg, J. de Jong, E. M. Wit, H. Thygessen, E. Vegt, H. G. van der Poel and F. W. B. van Leeuwen, *Eur. J. Nucl. Med. Mol. Imag.*, 2016, **43**, 1278-1287.
62. K. L. Pierce, R. T. Premont and R. J. Lefkowitz, *Nat. Rev. Mol. Cell Biol.*, 2002, **3**, 639-650.
63. R. T. Dorsam and J. S. Gutkind, *Nat. Rev. Cancer*, 2007, **7**, 79-94.
64. R. Lappano and M. Maggiolini, *Nat. Rev. Drug Discov.*, 2011, **10**, 47-60.
65. Y. Liu, S. An, R. Ward, Y. Yang, X.-X. Guo, W. Li and T.-R. Xu, *Cancer Lett.*, 2016, **376**, 226-239.
66. V. Erspamer, G. Falconieri Erspamer, M. Inselvini and L. Negri, *Br. J. Pharmacol.*, 1972, **45**, 333-348.
67. T. J. McDonald, H. Jörnvall, G. Nilsson, M. Vagne, M. Ghatei, S. R. Bloom and V. Mutt, *Biochem. Biophys. Res. Commun.*, 1979, **90**, 227-233.
68. M. Broccardo, G. Falconieri Erspamer, P. Melchiorri, L. Negri and R. de Castiglione, *Br. J. Pharmacol.*, 1975, **55**, 221-227.
69. J. E. Rivier and M. R. Brown, *Biochemistry*, 1978, **17**, 1766-1771.
70. W. Marki, M. Brown and J. E. Rivier, *Peptides*, 1981, **2**, 169-177.

71. T. Von Schrenck, P. Heinzerian, T. Moran, S. A. Mantey, J. D. Gardner and R. T. Jensen, *Am. J. Physiol.*, 1989, **256**, G747-G758.
72. J. F. Battey, J. M. Way, M. H. Corjay, H. Shapira, K. Kusano, R. Harkins, J. M. Wu, T. Slattery, E. Mann and R. I. Feldman, *Proc. Natl. Acad. Sci. U. S. A.*, 1991, **88**, 395-399.
73. E. R. Spindel, E. Giladi, P. Brehm, R. H. Goodman and T. P. Segerson, *Mol. Endocrinol.*, 1990, **4**, 1956-1963.
74. E. R. Spindel, E. Giladi, T. P. Segerson and S. Nagalla, in *Recent Prog. Horm. Res.*, ed. C. W. Bardin, Academic Press, Inc., 1250 Sixth Ave., San Diego, California 92101, USA; Academic Press Ltd., 14 Belgrave Square, 24-28 Oval Road, London NW1 70X, England, UK, 1993, vol. 48, pp. 365-391.
75. E. Wada, J. Way, H. Shapira, K. Kusano, A. M. Lebacq-Verheyden, D. Coy, R. Jensen and J. Battey, *Neuron*, 1991, **6**, 421-430.
76. V. Gorbulev, A. Akhundova, H. Büchner and F. Fahrenholz, *Eur. J. Biochem.*, 1992, **208**, 405-410.
77. Z. Fathi, M. H. Corjay, H. Shapira, E. Wada, R. Benya, R. Jensen, J. Viallet, E. A. Sausville and J. F. Battey, *J. Biol. Chem.*, 1993, **268**, 5979-5984.
78. R. T. Jensen, J. F. Battey, E. R. Spindel and R. V. Benya, *Pharmacol. Rev.*, 2008, **60**, 1-42.
79. M. H. Corjay, D. J. Dobrzanski, J. M. Way, J. Viallet, H. Shapira, P. Worland, E. A. Sausville and J. F. Battey, *J. Biol. Chem.*, 1991, **266**, 18771-18779.
80. B. Y. Williams and A. Schonbrunn, *Cancer Res.*, 1994, **54**, 818-824.
81. T. Kusui, R. V. Benya, J. F. Battey and R. T. Jensen, *Biochemistry*, 1994, **33**, 12968-12980.
82. W. P. ter Beek, E. S. M. Muller, R. A. van Hogezand, I. Biemond and C. B. H. W. Lamers, *J. Clin. Pathol.*, 2004, **57**, 1047-1051.
83. A. Fleischmann, B. Waser, J.-O. Gebbers and J. C. Reubi, *J. Clin. Endocrinol. Metab.*, 2005, **90**, 4722-4729.
84. O. Patel, A. Shulkes and G. S. Baldwin, *Biochim. Biophys. Acta*, 2006, **1766**, 23-41.
85. J. Ischia, O. Patel, D. Bolton, A. Shulkes and G. S. Baldwin, *BJU Int.*, 2014, **113**, 40-47.
86. F. Cuttitta, D. N. Carney, J. Mulshine, T. W. Moody, J. Fedorko, A. Fischler and J. D. Minna, *Nature*, 1985, **316**, 823-826.
87. M. N. Lango, K. F. Dyer, V. W. Y. Lui, W. E. Gooding, C. Gubish, J. M. Siegfried and J. R. Grandis, *J. Natl. Cancer Inst.*, 2002, **94**, 375-383.
88. A. L. Abujamra, V. R. Almeida, A. L. Brunetto, G. Schwartsmann and R. Roesler, *Cell Biol. Int.*, 2009, **33**, 899-903.
89. S. Nagasaki, Y. Nakamura, T. Maekawa, J. Akahira, Y. Mikii, T. Suzuki, S. Ishidoya, Y. Arai and H. Sasano, *Neoplasma*, 2012, **59**, 224-232.
90. M. Beer, M. Montani, J. Gerhardt, P. J. Wild, T. F. Hany, T. Hermanns, M. Müntener and G. Kristiansen, *The Prostate*, 2012, **72**, 318-325.
91. R. Markwalder and J. C. Reubi, *Cancer Res.*, 1999, **59**, 1152-1159.

92. B. Sun, G. Halmos, A. V. Schally, X. Wang and M. Martinez, *The Prostate*, 2000, **42**, 295-303.
93. A. Sturzu, S. Sheikh, H. Echner, T. Nägele, M. Deeg, B. Amin, C. Schwentner, M. Horger, U. Ernemann and S. Heckl, *Invest. New Drugs*, 2013, **32**, 37-46.
94. C. Constantinides, A. C. Lazaris, K. N. Haritopoulos, D. Pantazopoulos, M. Chrisofos and A. Giannopoulos, *World J. Urol.*, 2003, **21**, 183-187.
95. H. J. K. Ananias, M. C. van den Heuvel, W. Helfrich and I. J. de Jong, *The Prostate*, 2009, **69**, 1101-1108.
96. R. T. Jensen, T. Moody, C. Pert, J. E. Rivier and J. D. Gardner, *Proc. Natl. Acad. Sci. U. S. A.*, 1978, **75**, 6139-6143.
97. E. E. Ladenheim, R. T. Jensen, S. A. Mantey, P. R. McHugh and T. H. Moran, *Brain Res.*, 1990, **537**, 233-240.
98. I. E. Valverde, S. Vomstein and T. L. Mindt, *J. Med. Chem.*, 2016, **59**, 3867-3877.
99. B. E. Rogers, M. E. Rosenfeld, M. B. Khazaeli, G. Mikheeva, M. A. Stackhouse, T. Liu, D. T. Curiel and D. J. Buchsbaum, *J. Nucl. Med.*, 1997, **38**, 1221-1229.
100. A. Safavy, K. P. Raisch, M. B. Khazaeli, D. J. Buchsbaum and J. A. Bonner, *J. Med. Chem.*, 1999, **42**, 4919-4924.
101. R. P. J. Schroeder, W. M. v. Weerden, C. Bangma, E. P. Krenning and M. d. Jong, *Methods*, 2009, **48**, 200-204.
102. W. A. P. Breeman, L. J. Hofland, M. de Jong, B. F. Bernard, A. Sinivasan, D. J. Kwekkeboom, T. J. Visser and E. P. Krenning, *Int. J. Cancer*, 1999, **81**, 658-665.
103. C. Van de Wiele, F. Dumont, R. Vanden Broecke, W. Oosterlinck, V. Cocquyt, R. Serreyn, S. Peers, J. Thornback, G. Slegers and A. R. Dierckx, *Eur. J. Nucl. Med.*, 2000, **27**, 1694-1699.
104. H. Zhang, J. Schuhmacher, B. Waser, D. Wild, M. Eisenhut, J. C. Reubi and H. R. Maecke, *Eur. J. Nucl. Med. Mol. Imag.*, 2007, **34**, 1198-1208.
105. R. Hueting, M. Christlieb, J. R. Dilworth, E. G. Garayoa, V. Gouverneur, M. W. Jones, V. Maes, R. Schibli, X. Sun and D. A. Tourwe, *Dalton Trans.*, 2010, **39**, 3620-3632.
106. L. X. Ma, P. Yu, B. Veerendra, T. L. Rold, L. Retzloff, A. Prasanphanich, G. Sieckman, T. J. Hoffman, W. A. Volkert and C. J. Smith, *Mol. Imaging*, 2007, **6**, 171-180.
107. S. Achilefu, H. N. Jimenez, R. B. Dorshow, J. E. Bugaj, E. G. Webb, R. R. Wilhelm, R. Rajagopalan, J. Johler and J. L. Erion, *J. Med. Chem.*, 2002, **45**, 2003-2015.
108. A. Paulus, P. Desai, B. Carney, G. Carlucci, T. Reiner, C. Brand and W. A. Weber, *EJNMMI Research*, 2015, **5**, 1-9.
109. B. Brizet, V. Goncalves, C. Bernhard, P. D. Harvey, F. Denat and C. Goze, *Chem. Eur. J.*, 2014, **20**, 12933-12944.
110. G. Carlucci, A. Kuipers, H. J. K. Ananias, D. de Paula Faria, R. A. J. O. Dierckx, W. Helfrich, R. Rink, G. N. Moll, I. J. de Jong and P. H. Elsinga, *Peptides*, 2015, **67**, 45-54.
111. M. Pourghiasian, Z. Liu, J. Pan, Z. Zhang, N. Colpo, K.-S. Lin, D. M. Perrin and F. Bénard, *Biorg. Med. Chem.*, 2015, **23**, 1500-1506.

112. X. Zhang, W. Cai, F. Cao, E. Schreibmann, Y. Wu, J. C. Wu, L. Xing and X. Chen, *J. Nucl. Med.*, 2006, **47**, 492-501.
113. J. Becaud, L. Mu, M. Karramkam, P. A. Schubiger, S. M. Ametamey, K. Graham, T. Stellfeld, L. Lehmann, S. Borkowski, D. Berndorff, L. Dinkelborg, A. Srinivasan, R. Smits and B. Koksch, *Bioconjugate Chem.*, 2009, **20**, 2254-2261.
114. L. Mu, M. Honer, J. Becaud, M. Martic, P. A. Schubiger, S. M. Ametamey, T. Stellfeld, K. Graham, S. Borkowski, L. Lehmann, L. Dinkelborg and A. Srinivasan, *Bioconjugate Chem.*, 2010, **21**, 1864-1871.
115. M. Honer, L. Mu, T. Stellfeld, K. Graham, M. Martic, C. R. Fischer, L. Lehmann, P. A. Schubiger, S. M. Ametamey, L. Dinkelborg, A. Srinivasan and S. Borkowski, *J. Nucl. Med.*, 2011, **52**, 270-278.
116. M. Yang, H. K. Gao, Y. R. Zhou, Y. Ma, Q. M. Quan, L. X. Lang, K. Chen, G. Niu, Y. J. Yan and X. Y. Chen, *Theranostics*, 2011, **1**, 220-229.
117. Z.-B. Li, Z. Wu, K. Chen, E. K. Ryu and X. Chen, *J. Nucl. Med.*, 2008, **49**, 453-461.
118. Y. Yan, K. Chen, M. Yang, X. Sun, S. Liu and X. Chen, *Amino Acids*, 2011, **41**, 439-447.
119. Z. Liu, Y. Yan, F. T. Chin, F. Wang and X. Chen, *J. Med. Chem.*, 2009, **52**, 425-432.
120. S. Richter, M. Wuest, C. N. Bergman, J. D. Way, S. Krieger, B. E. Rogers and F. Wuest, *Bioconjugate Chem.*, 2015, **26**, 201-212.
121. F. Chen, B. Zhu, D. Pan, Y. Xu, X. Lin, R. Yang, L. Wang and M. Yang, *J. Radioanal. Nucl. Chem.*, 2016, **308**, 905-911.
122. Prostate disease - Clinical trials, http://www.nhs.uk/Conditions/Prostate-disease/Pages/Clinical-trial.aspx?CT=0&Rec=0&Condition=Prostate+disease~bombesin, Accessed 02/05/2016.
123. https://clinicaltrials.gov/ct2/results?term=bombesin&Search=Search, Accessed 02/05/2016.
124. B. M. Paterson, J. A. Karas, D. B. Scanlon, J. M. White and P. S. Donnelly, *Inorg. Chem.*, 2010, **49**, 1884-1893.
125. Z. Liu, G. Niu, F. Wang and X. Chen, *Eur. J. Nucl. Med. Mol. Imag.*, 2009, **36**, 1483-1494.
126. C. Liolios, M. Schäfer, U. Haberkorn, M. Eder and K. Kopka, *Bioconjugate Chem.*, 2016, **27**, 737-751.
127. E. Gourni, R. Mansi, M. Jamous, B. Waser, C. Smerling, A. Burian, F. Buchegger, J. C. Reubi and H. R. Maecke, *J. Nucl. Med.*, 2014, **55**, 1719-1725.
128. R. Minamimoto, S. Hancock, B. Schneider, F. T. Chin, M. Jamali, A. Loening, S. Vasanawala, S. S. Gambhir and A. Iagaru, *J. Nucl. Med.*, 2016, **57**, 557-562.
129. E. Kähkönen, I. Jambor, J. Kemppainen, K. Lehtiö, T. J. Grönroos, A. Kuisma, P. Luoto, H. J. Sipilä, T. Tolvanen, K. Alanen, J. Silén, M. Kallajoki, A. Roivainen, N. Schäfer, R. Schibli, M. Dragic, A. Johayem, R. Valencia, S. Borkowski and H. Minn, *Clin. Cancer. Res.*, 2013, **19**, 5434-5443.

130. Q.-Y. Cai, P. Yu, C. Besch-Williford, C. J. Smith, G. L. Sieckman, T. J. Hoffman and L. Ma, *The Prostate*, 2013, **73**, 842-854.
131. A. Shrivastava, H. Ding, S. Kothandaraman, S.-H. Wang, L. Gong, M. Williams, K. Milum, S. Zhang and M. F. Tweedle, *Mol. Imag. Biol.*, 2014, **16**, 661-669.
132. H. Chen, S. Wan, F. Zhu, C. Wang, S. Cui, C. Du, Y. Ma and Y. Gu, *Contrast Media Mol. Imaging*, 2014, **9**, 122-134.
133. J. Kuil, A. H. Velders and F. W. B. van Leeuwen, *Bioconjugate Chem.*, 2010, **21**, 1709-1719.
134. C. Neuberg and W. Neimann, *Ber. Dtsch. Chem. Ges.*, 1902, **35**, 2049-2056.
135. İ. Kizilcikli, Y. D. Kurt, B. Akkurt, A. Y. Genel, S. Birteksöz, G. Ötük and B. Ülküseven, *Folia Microbiol.*, 2007, **52**, 15-25.
136. M. C. Rodriguez-Argüelles, M. B. Ferrari, G. G. Fava, C. Pelizzi, G. Pelosi, R. Albertini, A. Bonati, P. P. Dall'Aglio, P. Lunghi and S. Pinelli, *J. Inorg. Biochem.*, 1997, **66**, 7-17.
137. D. X. West, J. S. Ives, J. Krejci, M. M. Salberg, T. L. Zumbahlen, G. A. Bain, A. E. Liberta, J. Valdes-Martinez, S. Hernandez-Ortiz and R. A. Toscano, *Polyhedron*, 1995, **14**, 2189-2200.
138. F. A. French, B. L. Freedlander, A. Hoskino and J. French, *Cancer Res.*, 1958, **18**, 1290-1300.
139. Y. Fujibayashi, H. Taniuchi, Y. Yonekura, H. Ohtani, J. Konishi and A. Yokoyama, *J. Nucl. Med.*, 1997, **38**, 1155-1160.
140. N. Takahashi, Y. Fujibayashi, Y. Yonekura, M. Welch, A. Waki, T. Tsuchida, N. Sadato, K. Sugimoto and H. Itoh, *Ann. Nucl. Med.*, 2000, **14**, 323-328.
141. F. Dehdashti, M. Mintun, J. Lewis, J. Bradley, R. Govindan, R. Laforest, M. Welch and B. Siegel, *Eur. J. Nucl. Med. Mol. Imag.*, 2003, **30**, 844-850.
142. D. W. Dietz, F. Dehdashti, P. W. Grigsby, R. S. Malyapa, R. J. Myerson, J. Picus, J. Ritter, J. S. Lewis, M. J. Welch and B. A. Siegel, *Dis. Colon Rectum*, 2008, **51**, 1641-1648.
143. S. I. Pascu, P. A. Waghorn, T. D. Conry, H. M. Betts, J. R. Dilworth, G. C. Churchill, T. Pokrovska, M. Christlieb, F. I. Aigbirhio and J. E. Warren, *Dalton Trans.*, 2007, 4988-4997.
144. P. Papanikolaou, P. D. Akrivos, A. Czapik, B. Wicher, M. Gdaniec and N. Tkachenko, *Eur. J. Inorg. Chem.*, 2013, **2013**, 2418-2431.
145. M. Akbar Ali and S. E. Livingstone, *Coord. Chem. Rev.*, 1974, **13**, 101-132.
146. M. J. M. Campbell, *Coord. Chem. Rev.*, 1975, **15**, 279-319.
147. S. Padhyé and G. B. Kauffman, *Coord. Chem. Rev.*, 1985, **63**, 127-160.
148. J. S. Casas, M. S. García-Tasende and J. Sordo, *Coord. Chem. Rev.*, 2000, **209**, 197-261.
149. T. S. Lobana, R. Sharma, G. Bawa and S. Khanna, *Coord. Chem. Rev.*, 2009, **253**, 977-1055.
150. J. R. Dilworth and R. Hueting, *Inorg. Chim. Acta*, 2012, **389**, 3-15.
151. D. X. West, A. E. Liberta, S. B. Padhye, R. C. Chikate, P. B. Sonawane, A. S. Kumbhar and R. G. Yerande, *Coord. Chem. Rev.*, 1993, **123**, 49-71.
152. B. M. Paterson and P. S. Donnelly, *Chem. Soc. Rev.*, 2011, **40**, 3005-3018.
153. D. L. Klayman, J. F. Bartosevich, T. S. Griffin, C. J. Mason and J. P. Scovill, *J. Med. Chem.*, 1979, **22**, 855-862.

154. M. Christlieb and J. R. Dilworth, *Chem. Eur. J.*, 2006, **12**, 6194-6206.
155. B. A. Gingras, T. Suprunchuk and C. H. Bayley, *Can. J. Chem.*, 1962, **40**, 1053-1059.
156. N. A. Bailey, S. E. Hull, C. J. Jones and J. A. McCleverty, *J. Chem. Soc. D.*, 1970, 124-126.
157. M. C. Rodriguez-Argüelles, M. B. Ferrari, G. G. Fava, C. Pelizzi, P. Tarasconi, R. Albertini, P. P. Dall'Aglio, P. Lunghi and S. Pinelli, *J. Inorg. Biochem.*, 1995, **58**, 157-175.
158. L. Alsop, A. R. Cowley, J. R. Dilworth, P. S. Donnelly, J. M. Peach and J. T. Rider, *Inorg. Chim. Acta*, 2005, **358**, 2770-2780.
159. M. G. Handley, R. A. Medina, E. Nagel, P. J. Blower and R. Southworth, *J. Mol. Cell. Cardiol.*, 2011, **51**, 640-650.
160. K. A. Krohn, J. M. Link and R. P. Mason, *J. Nucl. Med.*, 2008, **49**, 129S-148S.
161. J. L. J. Dearling and P. J. Blower, *Chem. Commun.*, 1998, 2531-2532.
162. J. P. Holland, J. C. Green and J. R. Dilworth, *Dalton Trans.*, 2006, 783-794.
163. J. L. Dearling, J. S. Lewis, G. E. Mullen, M. J. Welch and P. J. Blower, *J. Biol. Inorg. Chem.*, 2002, **7**, 249-259.
164. S. Lim, B. M. Paterson, M. T. Fodero-Tavoletti, G. J. O'Keefe, R. Cappai, K. J. Barnham, V. L. Villemagne and P. S. Donnelly, *Chem. Commun.*, 2010, **46**, 5437-5439.
165. R. L. Arrowsmith, P. A. Waghorn, M. W. Jones, A. Bauman, S. K. Brayshaw, Z. Hu, G. Kociok-Kohn, T. L. Mindt, R. M. Tyrrell, S. W. Botchway, J. R. Dilworth and S. I. Pascu, *Dalton Trans.*, 2011, **40**, 6238-6252.
166. R. L. Arrowsmith, PhD thesis, University of Bath, 2012.
167. F. Cortezon-Tamarit, S. Sarpaki, D. G. Calatayud, V. Mirabello and S. I. Pascu, *Chem. Rec.*, 2016, **16**, 1380-1397.
168. I. S. Alam, R. L. Arrowsmith, F. Cortezon-Tamarit, F. Twyman, G. Kociok-Kohn, S. W. Botchway, J. R. Dilworth, L. Carroll, E. O. Aboagye and S. I. Pascu, *Dalton Trans.*, 2016, **45**, 144-155.
169. C. Peyssonnaux, V. Nizet and R. S. Johnson, *Cell Cycle*, 2008, **7**, 28-32.
170. S. V. Torti and F. M. Torti, *Nat. Rev. Cancer*, 2013, **13**, 342-355.
171. C. R. Chitambar and W. E. Antholine, *Antiox. Redox Signal.*, 2012, **18**, 956-972.
172. S. Iijima, *Nature*, 1991, **354**, 56-58.
173. S. Iijima and T. Ichihashi, *Nature*, 1993, **363**, 603-605.
174. K. S. Novoselov, A. K. Geim, S. V. Morozov, D. Jiang, Y. Zhang, S. V. Dubonos, I. V. Grigorieva and A. A. Firsov, *Science*, 2004, **306**, 666-669.
175. V. Georgakilas, J. A. Perman, J. Tucek and R. Zboril, *Chem. Rev.*, 2015, **115**, 4744-4822.
176. T. W. Odom, J.-L. Huang, P. Kim and C. M. Lieber, *Nature*, 1998, **391**, 62-64.
177. F. Yang, X. Wang, M. Li, X. Liu, X. Zhao, D. Zhang, Y. Zhang, J. Yang and Y. Li, *Acc. Chem. Res.*, 2016, **49**, 606-615.
178. M. F. L. De Volder, S. H. Tawfick, R. H. Baughman and A. J. Hart, *Science*, 2013, **339**, 535-539.

179. S. Lanone, P. Andujar, A. Kermanizadeh and J. Boczkowski, *Adv. Drug Del. Rev.*, 2013, **65**, 2063-2069.
180. C. A. Poland, R. Duffin, I. Kinloch, A. Maynard, W. A. H. Wallace, A. Seaton, V. Stone, S. Brown, W. MacNee and K. Donaldson, *Nat. Nanotech.*, 2008, **3**, 423-428.
181. F. A. Murphy, C. A. Poland, R. Duffin, K. T. Al-Jamal, H. Ali-Boucetta, A. Nunes, F. Byrne, A. Prina-Mello, Y. Volkov, S. Li, S. J. Mather, A. Bianco, M. Prato, W. MacNee, W. A. Wallace, K. Kostarelos and K. Donaldson, *Am. J. Pathol.*, 2011, **178**, 2587-2600.
182. K. Donaldson, C. A. Poland, F. A. Murphy, M. MacFarlane, T. Chernova and A. Schinwald, *Adv. Drug Del. Rev.*, 2013, **65**, 2078-2086.
183. J. Muller, F. Huaux, A. Fonseca, J. B. Nagy, N. Moreau, M. Delos, E. Raymundo-Piñero, F. Béguin, M. Kirsch-Volders, I. Fenoglio, B. Fubini and D. Lison, *Chem. Res. Toxicol.*, 2008, **21**, 1698-1705.
184. L.-C. Ong, F. F.-L. Chung, Y.-F. Tan and C.-O. Leong, *Arch. Toxicol.*, 2016, **90**, 103-118.
185. H. Nagai and S. Toyokuni, *Cancer Sci.*, 2012, **103**, 1378-1390.
186. H. Ali-Boucetta and K. Kostarelos, *Adv. Drug Del. Rev.*, 2013, **65**, 2111-2119.
187. B. L. Allen, G. P. Kotchey, Y. Chen, N. V. K. Yanamala, J. Klein-Seetharaman, V. E. Kagan and A. Star, *J. Am. Chem. Soc.*, 2009, **131**, 17194-17205.
188. J. Russier, C. Menard-Moyon, E. Venturelli, E. Gravel, G. Marcolongo, M. Meneghetti, E. Doris and A. Bianco, *Nanoscale*, 2011, **3**, 893-896.
189. G. P. Kotchey, Y. Zhao, V. E. Kagan and A. Star, *Adv. Drug Del. Rev.*, 2013, **65**, 1921-1932.
190. D. Elgrabli, W. Dachraoui, C. Ménard-Moyon, X. J. Liu, D. Bégin, S. Bégin-Colin, A. Bianco, F. Gazeau and D. Alloyeau, *ACS Nano*, 2015, **9**, 10113-10124.
191. A. Battigelli, C. Ménard-Moyon, T. Da Ros, M. Prato and A. Bianco, *Adv. Drug Del. Rev.*, 2013, **65**, 1899-1920.
192. R. Singh and S. V. Torti, *Adv. Drug Del. Rev.*, 2013, **65**, 2045-2060.
193. Z. Liu, S. Tabakman, K. Welsher and H. Dai, *Nano Research*, 2009, **2**, 85-120.
194. K. Kostarelos, A. Bianco and M. Prato, *Nat. Nanotech.*, 2009, **4**, 627-633.
195. J. Wen, Y. Xu, H. Li, A. Lu and S. Sun, *Chem. Commun.*, 2015, **51**, 11346-11358.
196. J. Bartelmess, S. J. Quinn and S. Giordani, *Chem. Soc. Rev.*, 2015, **44**, 4672-4698.
197. G. Hong, S. Diao, A. L. Antaris and H. Dai, *Chem. Rev.*, 2015, **115**, 10816-10906.
198. J. Chen, S. Chen, X. Zhao, L. V. Kuznetsova, S. S. Wong and I. Ojima, *J. Am. Chem. Soc.*, 2008, **130**, 16778-16785.
199. R. Singh, D. Pantarotto, L. Lacerda, G. Pastorin, C. Klumpp, M. Prato, A. Bianco and K. Kostarelos, *Proc. Natl. Acad. Sci. U. S. A.*, 2006, **103**, 3357-3362.
200. A. Ruggiero, C. H. Villa, J. P. Holland, S. R. Sprinkle, C. May, J. S. Lewis, D. A. Scheinberg and M. R. McDevitt, *Int. J. Nanomed.*, 2010, **5**, 783-802.
201. J. J. Mulvey, C. H. Villa, M. R. McDevitt, F. E. Escorcia, E. Casey and D. A. Scheinberg, *Nat. Nanotech.*, 2013, **8**, 763-771.

202. J. T.-W. Wang, L. Cabana, M. Bourgognon, H. Kafa, A. Protti, K. Venner, A. M. Shah, J. K. Sosabowski, S. J. Mather, A. Roig, X. Ke, G. Van Tendeloo, R. T. M. de Rosales, G. Tobias and K. T. Al-Jamal, *Adv. Funct. Mater.*, 2014, **24**, 1880-1894.

203. D. Pantarotto, J.-P. Briand, M. Prato and A. Bianco, *Chem. Commun.*, 2004, 16-17.

204. K. Kostarelos, L. Lacerda, G. Pastorin, W. Wu, WieckowskiSebastien, J. Luangsivilay, S. Godefroy, D. Pantarotto, J.-P. Briand, S. Muller, M. Prato and A. Bianco, *Nat. Nanotech.*, 2007, **2**, 108-113.

205. M. Yang, K. Flavin, I. Kopf, G. Radics, C. H. A. Hearnden, G. J. McManus, B. Moran, A. Villalta-Cerdas, L. A. Echegoyen, S. Giordani and E. C. Lavelle, *Small*, 2013, **9**, 4194-4206.

206. S. Dhar, Z. Liu, J. Thomale, H. Dai and S. J. Lippard, *J. Am. Chem. Soc.*, 2008, **130**, 11467-11476.

207. G. Lamanna, A. Battigelli, C. Ménard-Moyon and A. Bianco, *Nanotechnol. Rev.*, 2012, **1**, 17-29.

208. E. Heister, V. Neves, C. Tîlmaciu, K. Lipert, V. S. Beltrán, H. M. Coley, S. R. P. Silva and J. McFadden, *Carbon*, 2009, **47**, 2152-2160.

209. C. Wang, X. Ma, S. Ye, L. Cheng, K. Yang, L. Guo, C. Li, Y. Li and Z. Liu, *Adv. Funct. Mater.*, 2012, **22**, 2363-2375.

210. C. H. Villa, M. R. McDevitt, F. E. Escorcia, D. A. Rey, M. Bergkvist, C. A. Batt and D. A. Scheinberg, *Nano Lett.*, 2008, **8**, 4221-4228.

Chapter 2 : Synthesis of functionalised thiosemicarbazonato metal complexes

2.1 Overview

The chemistry of bis(thiosemicarbazonato) complexes has been under investigation over the past decades, mainly with a focus on the alkylic family that yielded the agent Cu(II) diacetyl-bis(N4-methylthiosemicarbazone) (CuATSM).[1, 2] CuATSM has demonstrated to be an important probe for the detection of tumour hypoxia and has been evaluated in several clinical studies, especially applied to lung cancer.[3-5] However, the weak or lack of fluorescence of the alkylic family implied the attachment a fluorophore to the bis(thiosemicarbazonato) core in order to visualise their response *in vitro* thus modifying considerably the structure and pharmacokinetics of the original complexes. Acenaphthenequinone-based ligands offer an aromatic backbone inherently fluorescent that presents a fluorescence intensity increase when the metal is chelated to form the complex.

The chemistry and biological properties of acenaphthenequinone bis(thiosemicarbazonato) complexes have been explored by the Pascu and Dilworth groups over the last 10 years to develop multimodal imaging agents with interesting properties for the potential diagnosis of cancerous diseases.[6] Furthermore, the finding of hypoxia selectivity in Ga(III) acenaphthenequinone bis(thiosemicarbazonato) complexes under certain *in vitro* conditions, certainly maintains the interest in these derivatives. The compounds in this family would provide a readily available hypoxia-focused imaging probe able to function *in vitro* and *in vivo* when radiolabelled.

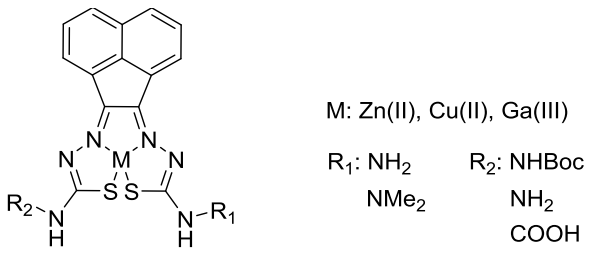

Figure 2.1: Proposed structure for an unsymmetrical metal complex with orthogonal functional groups.

While a variety of thiosemicarbazone substituents (alkyl, allyl, aryl) and metallic species (Zn(II), Ni(II), Cu(II), Ga(III)) have been explored for acenaphthenequinone-based compounds, their chemistry has been limited to symmetrical bis(substituted) derivatives, and the introduction of functional groups has been subjected to little exploration. The introduction of functional groups to obtain unsymmetrical

derivatives is challenging in the chemistry of acenaphthenequinone bis(thiosemicarbazones) as the rigidity and planarity of the system does not allow for free rotation around the CO-CO bond, permitted when 2,3-butanedione, glyoxal or pyruvaldehyde are used as starting materials, making the preparation of unsymmetrical ligands relatively easy in the case of the aliphatic family.

The aim of the work presented in this chapter was to develop unsymmetrical acenaphthenequinone bis(thiosemicarbazonato) metal complexes able to be introduced in the desired nanoprobe (see Figure 1.23). The design showed in Figure 1.23 implies the existence of two orthogonal functional groups able to react with the nanomaterial and the targeting molecule (Figure 2.1).

2.2 Synthesis of functional thiosemicarbazides and mono(thiosemicarbazone) ligands

The first step towards the synthesis of functional unsymmetrical bis(thiosemicarbazonato) metal complexes was the preparation of the corresponding functional thiosemicarbazides in order to obtain the ligands. As depicted in Figure 2.1, the introduction of protected amines in the design plan is a reasonable starting point as the use of similar derivatives has been previously described in thiosemicarbazone chemistry found in the literature.[7, 8] The synthesis of an aliphatic bis(thiosemicarbazone) ligand containing a Boc-protected amino group has been described following two strategies. In the work by Donnelly *et al.*, the Boc-protected ethylenediamino group was introduced by transamination of a reactive dimethyl thiosemicarbazone (denoted A in Scheme 2.1). The corresponding Cu(II) complex was formed from the protected derivative and deprotected with TFA.[7] Differently, Dilworth *et al.* prepared a thiosemicarbazide species containing the terminal Boc-protected amino group. The thiosemicarbazide was condensed with a mono(substituted) derivative based on the 2,3-butanedione backbone under reflux in an acidic ethanolic solution (B in Scheme 2.1).[8]

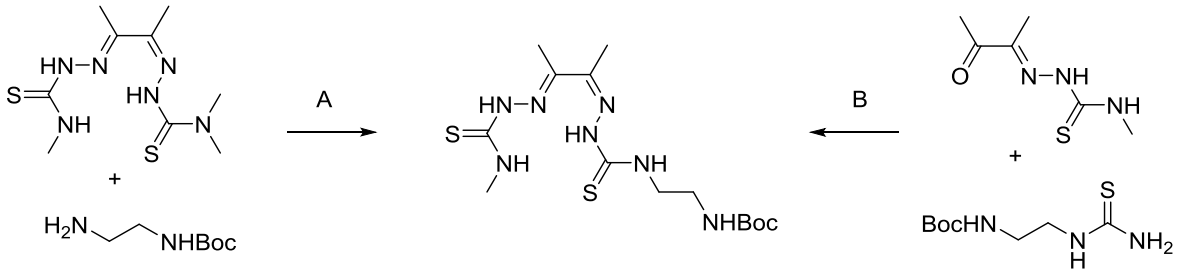

Scheme 2.1: Different synthetic strategies to a bis(thiosemicarbazone) ligand including a protected amino group.

Consequently, three different thiosemicarbazides containing a terminal NHBoc group were prepared following the procedure described by Dilworth *et al.* from protected diamines. The only example

described in the literature was the one prepared from ethylenediamine but the procedure was successfully generalised to the novel derivatives **8** and **9**.

The synthesis started with the corresponding protected diamines **1** – **3** and followed the same strategy (Scheme 2.2). The reaction proceeded through the condensation of the amine with carbon disulphide in a basic ethanolic medium. The addition of methyl iodide to the reaction mixture formed the thiocarbamate intermediates (**4** – **6**) that were isolated.

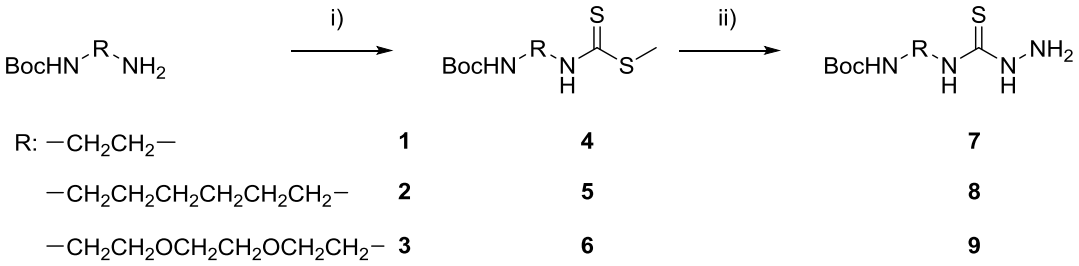

Scheme 2.2: Synthetic route for the preparation of protected thiosemicarbazides. i) Et_3N, CS_2, CH_3I, EtOH, 25 ºC, 3 h; ii) H_2NNH_2, EtOH, 78 ºC, 3 h.

The reaction continued with the hydrazinolysis of the intermediate by reflux in ethanol to obtain the corresponding thiosemicarbazides (**7** – **9**) in moderate yields. The preparation of 4,4-dimethyl-3-thiosemicarbazide was also attempted to explore the alternative route to prepare functional thiosemicarbazones by transamination. The methyl dithiocarbamate intermediate could be isolated in high yield as a crystalline solid. However, the hydrazinolysis step did not proceed as expected and the product was obtained as a complex mixture, likely due to known cyclisation issues which were encountered and reported before for other thiosemicarbazone derivatives, that could not be purified hereby. Therefore, 4,4-dimethyl-3-thiosemicarbazide was obtained from a commercial source.

The synthesis of acenaphthenequinone bis(thiosemicarbazonato) metal complexes has been reported by heating the metal, generally $Zn(OAc)_2$, with the bis(substituted) ligand[9], the mono(substituted) ligand and an excess of thiosemicarbazide[10] or acenaphthenequinone and an excess of thiosemicarbazide[6]. However, all these reported examples corresponded to symmetrical complexes. In this work, two synthetic strategies were attempted: forming the zinc(II) metal complex from the mono(substituted) ligand with an excess of the second thiosemicarbazide in a one-pot reaction (Scheme 2.3, dashed line) and preparing the complex from the unsymmetrical bis(substituted) ligand (Scheme 2.3). The route involving the preparation of the unsymmetrical bis(thiosemicarbazone) ligand is envisaged to offer more control over the entire process as the complexation is a separate step and its conditions can be optimised independently hence this route would be preferred.

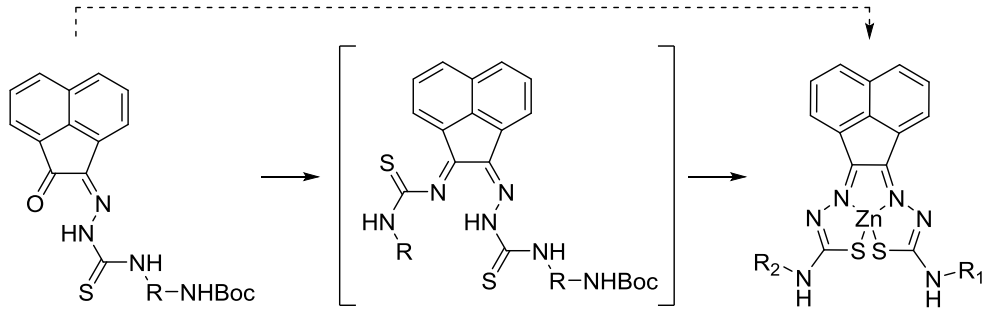

Scheme 2.3: Possible synthetic routes attempted to form an unsymmetrical Zn(II) acenaphthenequinone bis(thiosemicarbazonato) complex.

Nevertheless, different mono(thiosemicarbazone) acenaphthenequinone ligands were prepared with commercial thiosemicarbazides, namely 4-methyl, ethyl, allyl or phenyl thiosemicarbazides, in order to explore the possible alternative route through a templated process from the alkylic or arylic mono(thiosemicarbazones). Furthermore, these mono(thiosemicarbazone) derivatives were used to evaluate the reaction conditions in the preparation of unsymmetrical ligands. The synthesis of mono(thiosemicarbazone) ligands from acenaphthenequinone was conducted by heating an equimolar amount of the diketone and thiosemicarbazide in an acidic ethanolic solution as previously described by our group.[11]

The synthesis of the unsymmetrical ligand from the alkylic derivative mono(4-ethyl-3-thiosemicarbazone) acenaphthenequinone and compound **7** was attempted but proved unsuccessful in an acidic solution of ethanol by refluxing 3.5 or 7 h although a small proportion of the product (ca. 3% as calculated by ^{1}H NMR integration) was observed in the second case. In the same way, the formation of the unsymmetrical complex in a one-pot templated process was attempted from the same ethyl-substituted acenaphthenequinone derivative, compound **7** and $Zn(OAc)_2$ but led to a mixture of products. Different solvents (ethanol, toluene or acetic acid) and times were tested hereby but in all cases a complex mixture of products was obtained.

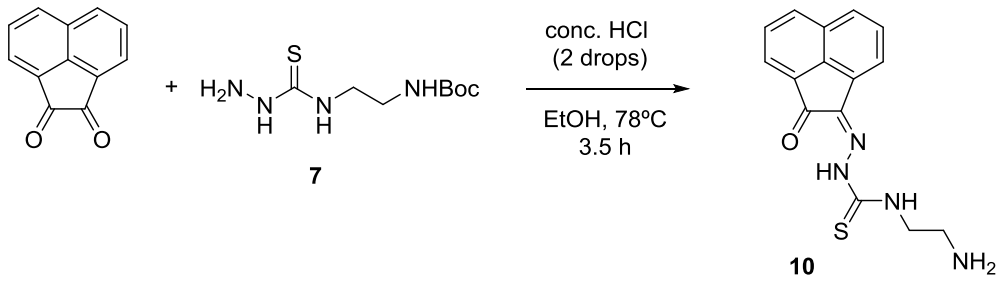

7 **10**

Scheme 2.4: Reaction conditions for the preparation of a mono(thiosemicarbazone) ligand with a 2-aminoethyl group.

Therefore, the preparation of the mono(thiosemicarbazone) ligands with thiosemicarbazides **4** – **6** followed. However, the optimisation of the conditions was necessary to obtain the desired product. The formation of thiosemicarbazones from carbonylic compounds is an example of the formation of an imine from a carbonylic compound and an amine. This reaction is generally performed via acid catalysis that results in the elimination of water. Despite the Boc protecting group being sensitive to acidic conditions, the small amount of HCl used in the formation of acenaphthenequinone thiosemicarbazones (1 – 2 drops of conc. HCl) was not expected to affect the protecting group as observed in similar syntheses previously described from 2,3-butanedione[8]. Unfortunately, when the reaction was performed in the aforementioned conditions, the protecting group was completely removed and the deprotected derivative obtained (Scheme 2.4). This was easily confirmed by ^{1}H NMR spectroscopy observing the disappearance of the tert-butyl resonance from the Boc group that is a characteristic singlet at ca. 1.38 ppm integrating for 9 protons.

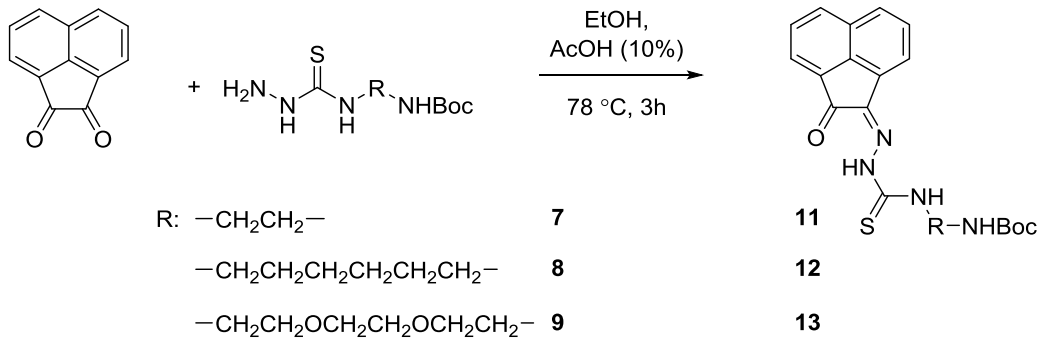

Scheme 2.5: Synthesis of mono(thiosemicarbazone) acenaphthenequinone ligands with a protected amino group.

The deprotection of the Boc group with just a few drops of conc. HCl indicated that the protecting group in the thiosemicarbazone in acenaphthenequinone derivatives was particularly labile in the presence of strong acids even at low concentrations in opposition of what was described in the literature for 2,3-butanedione thiosemicarbazones. Therefore, the use of a weak acid as a catalyst for the reaction to avoid the deprotection of the Boc group was attempted. The reaction was repeated in the same conditions but using acetic acid at a 10% concentration in ethanol instead of conc. HCl. In this case, the desired product was obtained with no deprotection of the amino group (Scheme 2.5, **11**). The compounds containing the hexyl or 2,2′-(ethylenedioxyl) chains (**12** and **13** in Scheme 2.5) were successfully obtained by applying the same reaction conditions.

The presence of the hexyl chain or a PEG unit as a spacer in the last two mono(thiosemicarbazone) examples significantly changed the physical properties of the product. These derivatives (**12** and **13**)

were initially obtained as oils that could be separated from the starting materials by column chromatography in CH_2Cl_2 / MeOH, as opposed to the limited solubility of this class of acenaphthenequinone-based compounds in certain organic solvents. The ligands could, however, be precipitated by stirring in pentane and drying on standing at room temperature.

All NHBoc mono(substituted) thiosemicarbazones were characterised by ^1H and ^{13}C NMR spectroscopy and mass spectrometry. The ^1H NMR spectra of these compounds are comparable with the alkylic or arylic mono(substituted) ligands described in the literature.[6, 10]

The first characteristic hydrazinic proton resonance appears at 12 – 13 ppm while the second characteristic amino proton appears upfield with respect to it at 9 – 10 ppm. This last amino group develops multiplicity due to the coupling with the neighbouring group, appearing as a triplet in contrast to most amino protons that usually appear as broad singlets. The substituent resonances are in the 1 – 4 ppm region with the presence of the characteristic t-butyl resonance for the Boc protecting group at 1.31 ppm. The ^1H NMR spectrum of compound **12** is represented in Figure 2.2. The resonances in the NMR spectrum were assigned by observing the correlations in the 2D ^1H-^1H COSY spectrum (Figure 2.3).

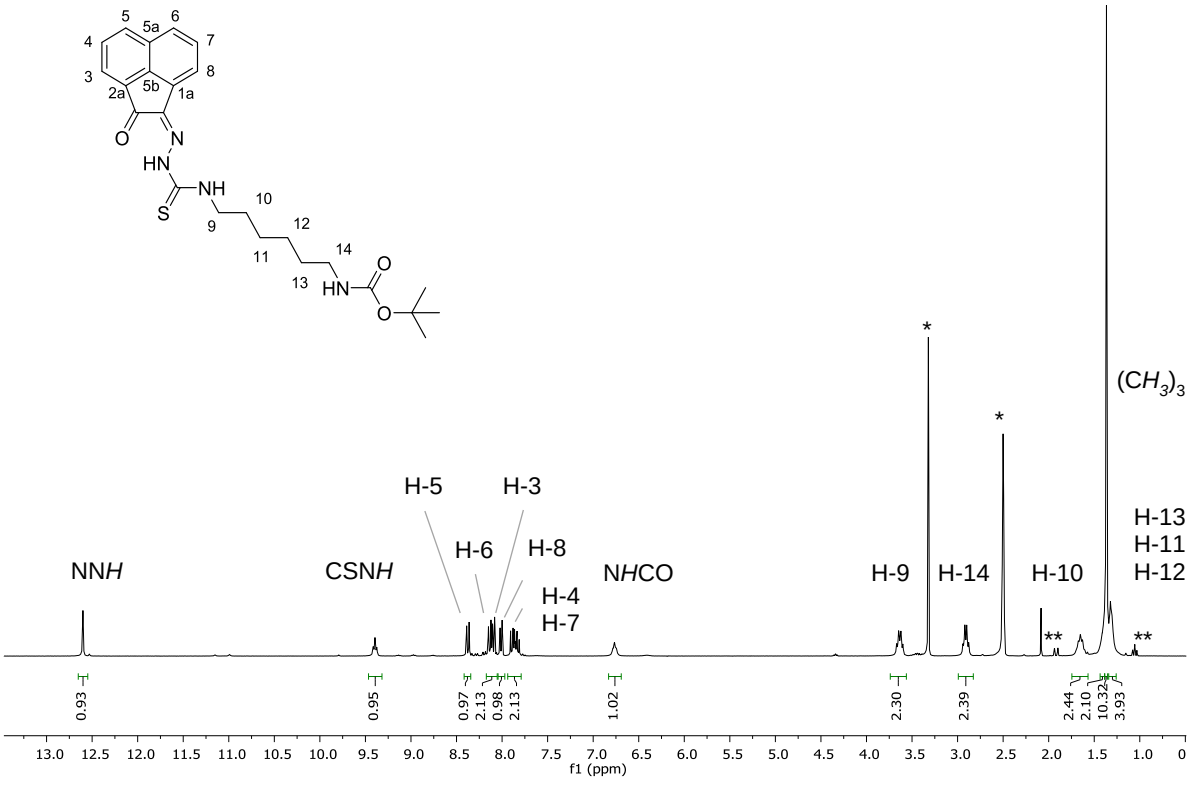

Figure 2.2: ^1H NMR spectrum (d^6-DMSO) of compound **12**. [*Residual deuterated solvent signals and water; **residual solvents and impurities traces].

The NH signals can be differentiated because the amino proton shows a correlation peak with an alkylic proton (H-9). The six aromatic protons can be distinguished and appear as four doublets (H-5, H-6, H-3, H-8) and two doublet of doublets (H-4, H-7). In contrast, only three resonances of the alkylic chain can be observed independently. The more deshielded methylene groups correspond to the ones adjacent to the amino groups (H-9, H-14). The protected amino group presents a correlation peak with H-14 that allows to identify that methylene group. The H-10 methylene group is more deshielded and can be observed as a multiplet at 1.67 ppm while the resonances for H-11, H-12 and H-13 overlap with the singlet for the t-butyl group in the region of 1.2 – 1.5 ppm.

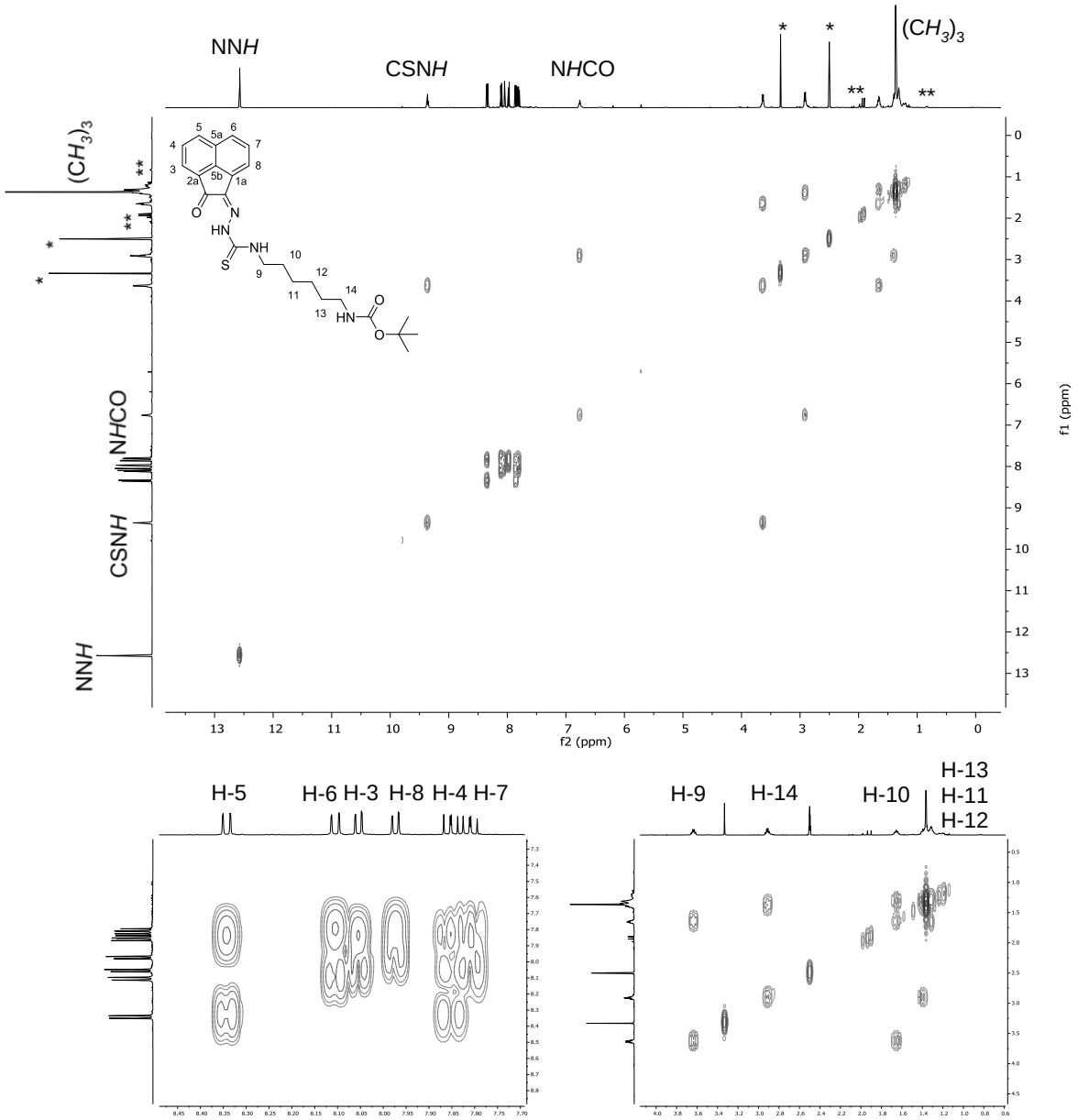

Figure 2.3: ^{1}H-^{1}H COSY NMR spectrum (d^{6}-DMSO) of compound **12**. [*Residual deuterated solvent signals and water; **residual solvents and impurities traces]

In addition, in the case of **11** and **12**, suitable crystals for single-crystal X-ray crystallography were obtained by the vapour diffusion method, dissolving the ligands in THF and using hexane as a co-solvent. The structures were obtained and are displayed in Figure 2.4.

The presence of an intramolecular hydrogen bond between the oxygen and nitrogen (N1) atoms can be observed in **12**. However, this interaction is not present for **11**. The absence of the intramolecular hydrogen bond and the different conformation can be explained due to the presence of a water molecule that presents hydrogen bonding with the oxygen (O) and nitrogen (N1) in **11**.

Table 2.1: Selected bond distances and angles for compounds **11**, **12** and mono(4-ethyl-3-thiosemicarbazone) acenaphthenequinone.

	11	**12**	**R: Et**[10]
O-C1 (Å)	1.233 (4)	1.225 (2)	1.223 (2)
C1-C2 (Å)	1.504 (5)	1.514 (2)	1.515 (2)
N1-C2 (Å)	1.285 (5)	1.296 (2)	1.294 (2)
O-C1-C2 (º)	124.9 (4)	126.24 (17)	125.6 (2)
C1-C2-N1 (º)	115.9 (3)	127.29 (16)	128.2 (2)

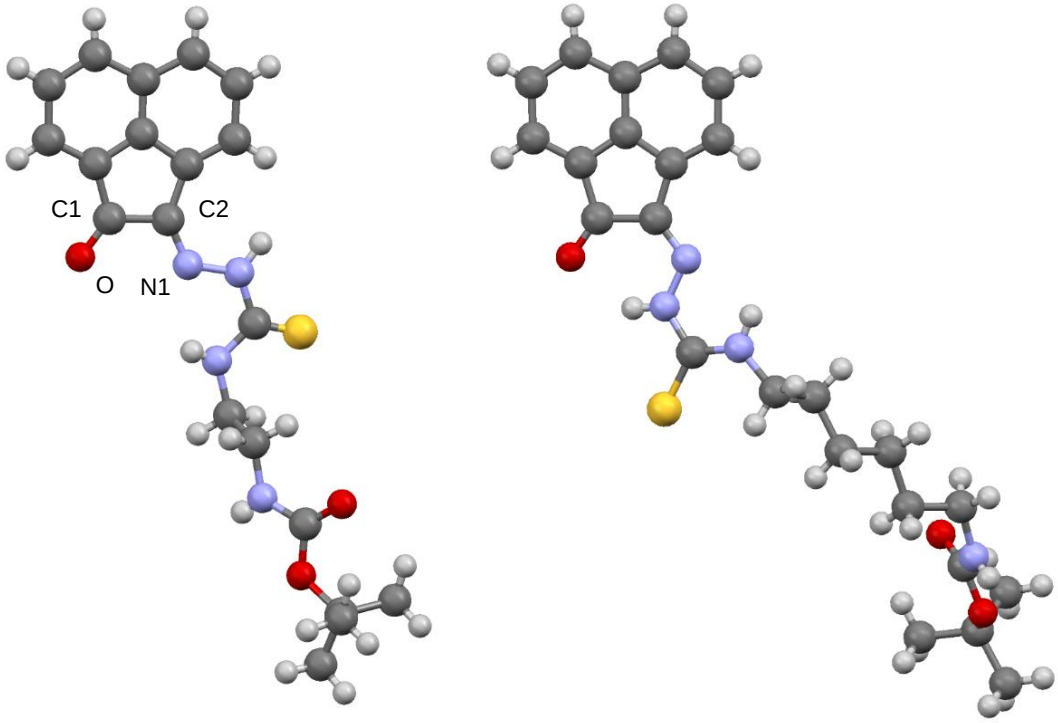

Figure 2.4: Molecular structure for compounds **11** (left) and **12** (right).

A selection of bond distances an angles for **11** and **12** can be seen in Table 2.1. The corresponding parameters for the mono(4-ethyl-3-thiosemicarbazone) acenaphthenequinone derivative have been included for comparison purposes. It can be observed that bond distances are in the same range for the three compounds although the distances are more alike between **12** and mono(4-ethyl-3-thiosemicarbazone) acenaphthenequinone. The same situation is observed for the O-C1-C2 angle being the smaller value the one corresponding to **11** and all of ca. 125º which is in accordance with a sp^2 hybridisation of the carbon atom. In the case of the C1-C2-N1 angle the values are more dispersed with **11** presenting the lower value with just 115.9º while **12** and the ethyl derivative are close to 128 º.

The molecular structure showing the packing of **12** in the unit cell is shown in Figure 2.5. The CO in the acenaphthenequinone units are facing each other in a zig-zag disposition with short contacts between the sulphur and C2. The presence of the intermolecular hydrogen bonds between the CO group of the Boc moiety and the NH of the NHBoc moiety of another molecule are represented with a dashed grey line in Figure 2.5. The intramolecular hydrogen bonding between O and N1 is not visible with the view along the b axis.

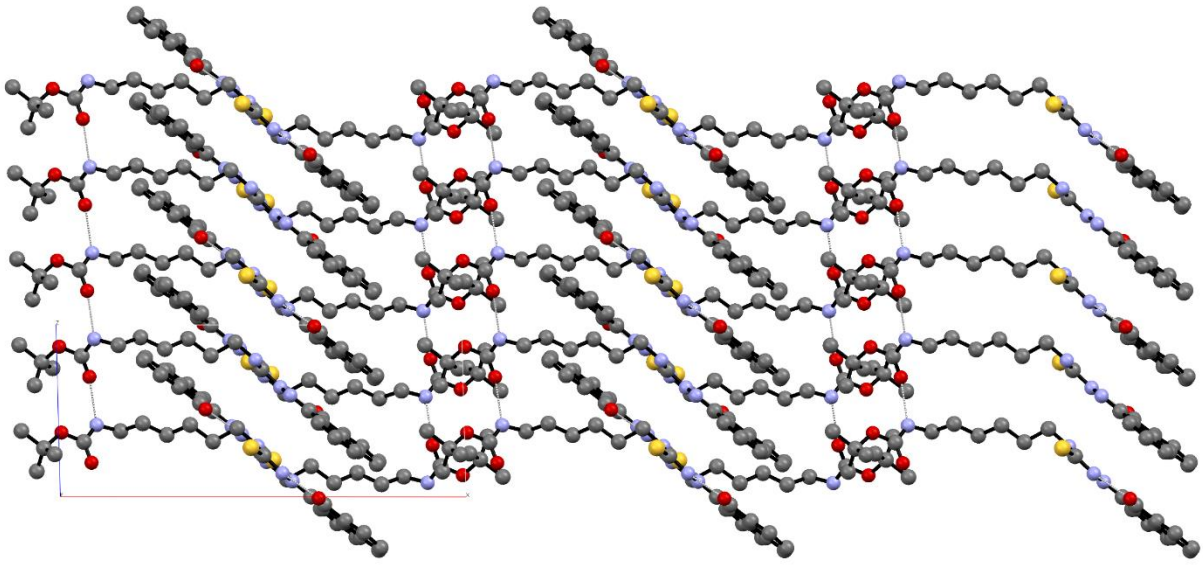

Figure 2.5: Molecular structure of **12** showing the unit cell along the b axis. Hydrogen bonds are showed as dashed grey lines.

Once the functional mono(substituted) ligands were obtained and characterised, the synthesis of unsymmetrical bis(substituted) ligands or complexes was attempted. In the case of the bis(substituted) ligands, the reaction of **10** with thiocarbohydrazide did not provide the desired products when the previously described reaction conditions were applied (i.e. refluxing in EtOH). Either using **10** and thiocarbohydrazide or an alkyl thiosemicarbazide, mainly the starting material was recovered.

The incapability of acetic acid to catalyse the reaction or the need for harsher conditions was hypothesised as the cause of the synthetic difficulties. In this sense, a two-sided approach was adopted, first, the application of microwave-assisted heating that allows to work at higher temperatures and pressures was evaluated and second the effect of the acid catalyst in the reaction was studied.

In order to obtain a model for the reactivity for mono(thiosemicarbazone) acenaphthenequinone ligands and to optimise the reaction conditions, several mono(substituted) ligands were prepared from commercially available thiosemicarbazides with different substituents in position 4-, namely methyl, ethyl, allyl, and phenyl. The derivative including the N,N-dimethyl-3-thiosemicarbazone was obtained with minor impurities as confirmed by ^{1}H NMR. The separation of the impurities proved especially challenging for this species and the use of this specific derivative was not considered hereby.

2.3 Synthesis attempts of unsymmetrical bis(substituted) ligands

The alkylic mono(substituted) ligands can be obtained in good yields by conventional synthesis as described in the literature.[10] The mentioned derivatives can be prepared applying conventional conditions as in the previous section but also by applying microwave heating. There were no examples of the application of microwave-assisted synthesis to the preparation of acenaphthenequinone thiosemicarbazones so the optimisation of the reaction conditions was required (*vide infra*). Once the conditions were optimised, both the mono and bis(substituted) derivatives were obtained just varying the number of equivalents of thiosemicarbazide added. The reaction times were dramatically reduced and comparable yields to the conventional synthesis obtained. The acenaphthenequinone mono methyl (**14**), ethyl (**15**), allyl (**16**) or phenyl (**17**) thiosemicarbazones were prepared and used as a model to evaluate the effects of the acid catalyst and the conditions on the preparation of bis(substituted) ligands.

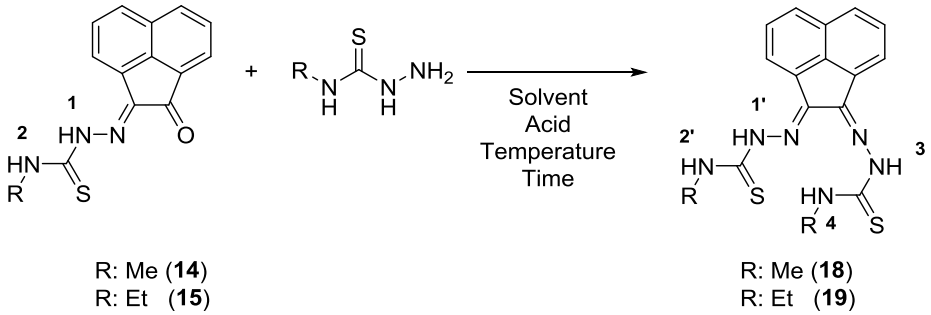

Scheme 2.6: General reaction conditions and parameters evaluated in the synthesis of symmetrical bis(substituted) BTSC ligands. The resonances of the NH protons (1, 2 and 1', 2', 3, 4) were used to follow the reaction evolution and to calculate conversions.

The methyl or ethyl derivatives were indistinctly used in the synthesis of the symmetrical species (Scheme 2.6). The resonances of the hydrazinic and amino NH protons that appear between 8 and 13 ppm were used to monitor the reaction and calculate the proportion of compound obtained in each reaction. The different conditions tested are summarised in Table 2.2. The initial temperature and time conditions for the microwave reaction (21 min, 140 ºC) were extracted from the microwave reactor's manufacturer documents and correspond to 8 h refluxing in ethanol by conventional heating according to an approximation of the Arrhenius equation.[12]

From the information summarised in Table 2.2 different conclusions can be drawn: 1) the effect of the acid catalysis on the reaction is crucial: the addition of just one equivalent of conc. HCl resulted in a 100% conversion (entry 2) while the use of acetic acid yielded a mixture of products and only achieved a 50% conversion with extended reaction times and an excess of thiosemicarbazide (entry 5). 2) The temperature increase did not seem to provide a significant improvement in the reaction output and variations in time had a limited effect. Furthermore, there was a colour change in the product from yellow to light orange when 140 ºC were applied resulting in darker colours in the products. 3) The use of solvents other than ethanol in conventional heating as described in entries 11 and 12 did not seem to vary the reactivity. Furthermore, the substitution of the solvent is not desirable as the work-up, isolation and purification of this class of compounds in ethanol is considerably simpler. 4) The use of an excess of thiosemicarbazide seemed to help to increase the conversion as observed in entry 5.

Table 2.2: Reaction conditions evaluated for the synthesis of symmetrical bis(thiosemicarbazone) ligands.

Entry	R	Eq. TSC	t / min	T / °C, type of heating	Acid	Solvent	Conversion
1	Me	1.1	21	140, µw	HCl, 50 µL	EtOH	100%
2	Et	4	21	140, µw	HCl, 1 eq.	EtOH	100%
3	Me	1.1	21	140, µw	AcOH, 10% (v/v)	EtOH	13%
4	Me	1.1	5+5	160, µw	AcOH, 10% (v/v)	EtOH	4%
5	Me	4	21+21	140, µw	AcOH, 10% (v/v)	EtOH	50%
6	Et	4	60	140, µw	AcOH, 10% (v/v)	EtOH	Decomposition
7	Et	4	21	140, µw	AcOH, 20% (v/v)	EtOH	3%
8	Et	4	30	150, µw	AcOH, 50% (v/v)	EtOH	Decomposition
9	Et	4	21	140, µw	AcOH	AcOH	Decomposition
10	Me	1	240	78, conv.l	AcOH, 10% (v/v)	EtOH	5%
11	Et	1.1	360	65, conv.	AcOH, 10% (v/v)	THF	-
12	Et	4	300	65, conv.	AcOH, 10% (v/v)	MeOH	-

An excerpt of the aromatic and aliphatic regions of the ^{1}H NMR spectrum for the product isolated in entry 5 can be observed in Figure 2.6. In the aromatic region (Figure 2.6, left), the NH protons do not overlap despite the similar chemical shifts and all of them can be identified independently. The hydrazinic protons appear at 12.64 and 12.60 ppm corresponding to 1 and 1' respectively. The additional hydrazinic proton in the bis(substituted product) appears at 11.25 ppm. The three amino protons appear upfield in the 8.7 – 9.5 ppm region as quadruplets. The resonances for the methyl groups appear in the aliphatic region (Figure 2.6, right). In this case, one of the signals overlap and only two doublets are observed for the three methyl groups. The methyl group of the mono(substituted) ligand (**14**) appears at 3.12 ppm along with a methyl group of **18**. The second methyl group of **18** appears at 3.10 ppm. The integration ratio between the two signals is 2:1 which confirms that the **14** and **18** are present in a 1:1 ratio.

The completion of the reaction using a weak acid as catalyst seemed unlikely so the use of conc. HCl was considered. Furthermore, it was observed that the synthesis of the mono(substituted) ligand with thiosemicarbazide **9** and one equivalent of conc. HCl yielded the desired product and maintained intact the protecting group.

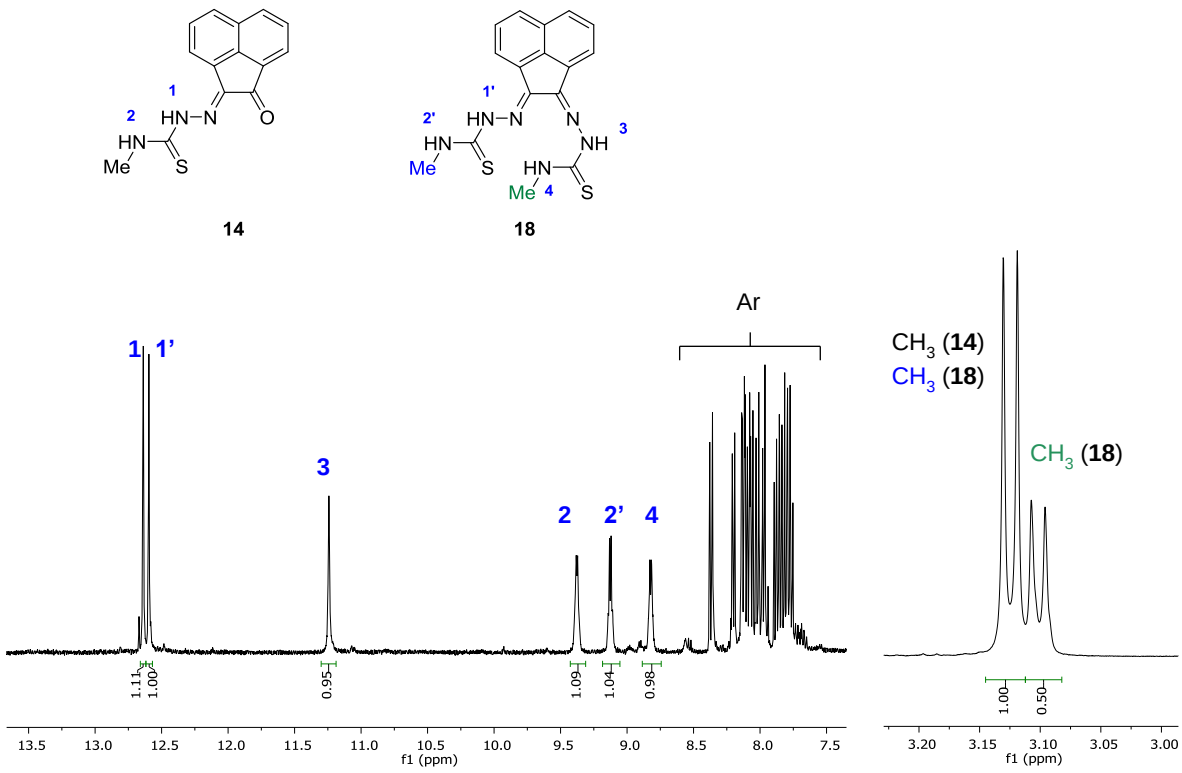

Figure 2.6: ^{1}H NMR spectrum (d^{6}-DMSO) detail of the aromatic (left) and aliphatic (right) regions of the product isolated for entry 5 in Table 2.2.

For this reason, the improvement of the reaction conditions was continued using conc. HCl as a catalyst. The temperature in the microwave conditions applied in the last experiment was reduced when possible due to the observed colour change in the products from bright yellow to dark orange which can point to the presence of decomposition products. Consequently, the preparation of unsymmetrical bis(thiosemicarbazone) ligands was attempted applying the same alkylic model and HCl as an acid catalyst (Scheme 2.7, top).

Surprisingly, the starting material and desired product were accompanied by the thiosemicarbazone exchange or metathesis products (Scheme 2.7, bottom). Therefore, the symmetrical products were also observed in the isolated mixture. Dynamic combinatorial exchange behaviour has been well studied for imines and hydrazones[13] but less for thiosemicarbazones.[14] The presence of this type of thiosemicarbazone exchange in acenaphthenequinone derivatives has never been reported to the best of our knowledge.

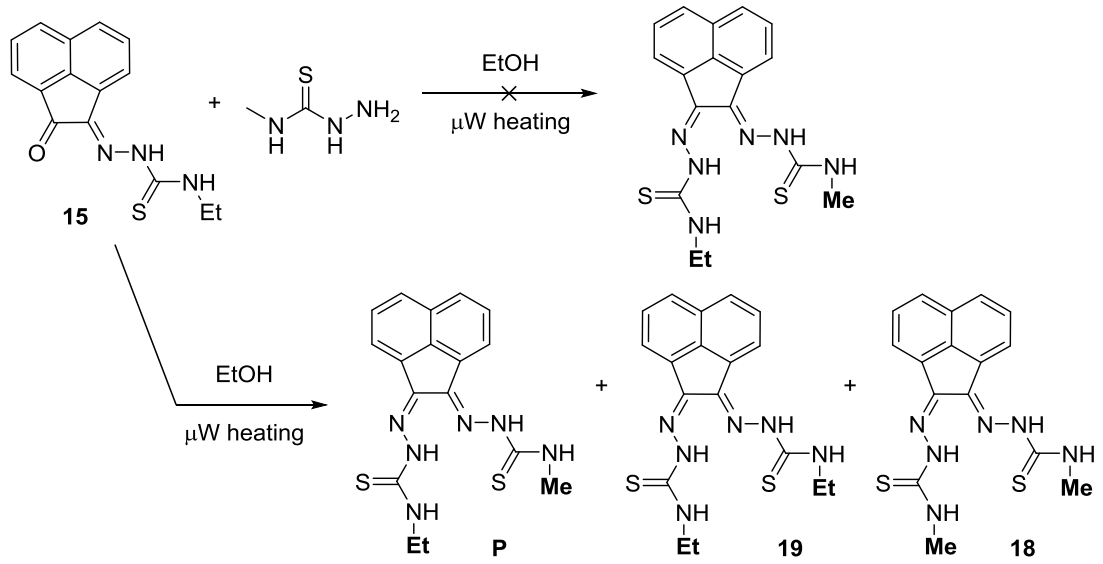

Scheme 2.7: Synthesis attempt of an alkyl unsymmetrical bis(thiosemicarbazone).

The results detailed in Table 2.3 revealed that heating the starting materials with just one equivalent of conc. HCl can lead to the observation of exchange products (entries 1 and 2). The temperature increase seems to have a positive effect for the conversion into the desired product although the proportion of exchange products increases as well (entries 4 and 5). The starting material is not consumed until relatively high temperatures (110 – 130 ºC, entries 4 – 6), which can lead to possible decomposition products. The addition of an excess of thiosemicarbazide along with an increase in the temperature of the reaction does not seem to help to increase the conversion into the desired product. Furthermore, the exchange products, particularly **19**, are more favoured than the desired product in that case.

Table 2.3: Conditions tested in the synthesis attempt of unsymmetrical bis(thiosemicarbazones).

Entry	Eq. TSC	HCl	t / min	T / ºC	Product proportion 15 : P : 19 : 18
1	1	1 eq., 25 µL	2.5	90	0.65 : 0.09 : 0.21 : (*)
2	1	1 eq., 25 µL	5	90	0.60 : 0.10 : 0.24 : 0.06
3	1.2	1.2 eq., 30 µL	10	90	0.35 : 0.12 : 0.36 : 0.16
4	1.2	1.2 eq., 30 µL	10	110	- : 0.26 : 0.50 : 0.24
5	1.2	1.2 eq., 30 µL	10	130	- : 0.28 : 0.45 : 0.27
6	3	1.2 eq., 30 µL	10	120	- : 0.39 : 0.34 : 0.27

(*) Present in the mixture but below 5% according ^{1}H NMR integration

In this case, the product identification and quantification was performed by observing the characteristic NH resonances in ^{1}H NMR spectra as in the previous case but also looking at the resonance of the methyl and ethyl groups.

The ^{1}H NMR spectra of the regions where the methyl groups for the different ligands appear are displayed in Figure 2.7. It can be observed how in the mono(substituted) derivative the methyl group appears as a doublet (top) and the bis(substituted) ligand as a pair of doublets (middle) with a 1:1 integration ratio. Differently, the mixture of products corresponding to entry 5 in Table 2.3 where the ethyl-methyl, bis(methyl) and bis(ethyl) products are represented should give place to three resonances for the three inequivalent methyl groups. However, the methyl resonance from the ethyl-methyl derivative (P) overlaps with the methyl resonances of the bis(methyl) product (**18**) originating a pair of doublets (Figure 2.7, bottom) as occurred in the mixtures of the mono(methyl) and bis(methyl) thiosemicarbazone derivatives (Figure 2.6).

In the case of entry 5, **P** and **18** are present in a 1.04 : 1 ratio as can be observed by the integration of the doublets. Despite the convenience in the use of the NH protons to calculate the proportion of products, the resonances of the methyl group can be employed as well as they can be observed and integrated independently. The proportion of the remaining product (**19**) could be also estimated using the resonances in the alkylic region by observing at the ethyl resonances and subtracting the corresponding contribution of the ethyl-methyl derivative, **P**.

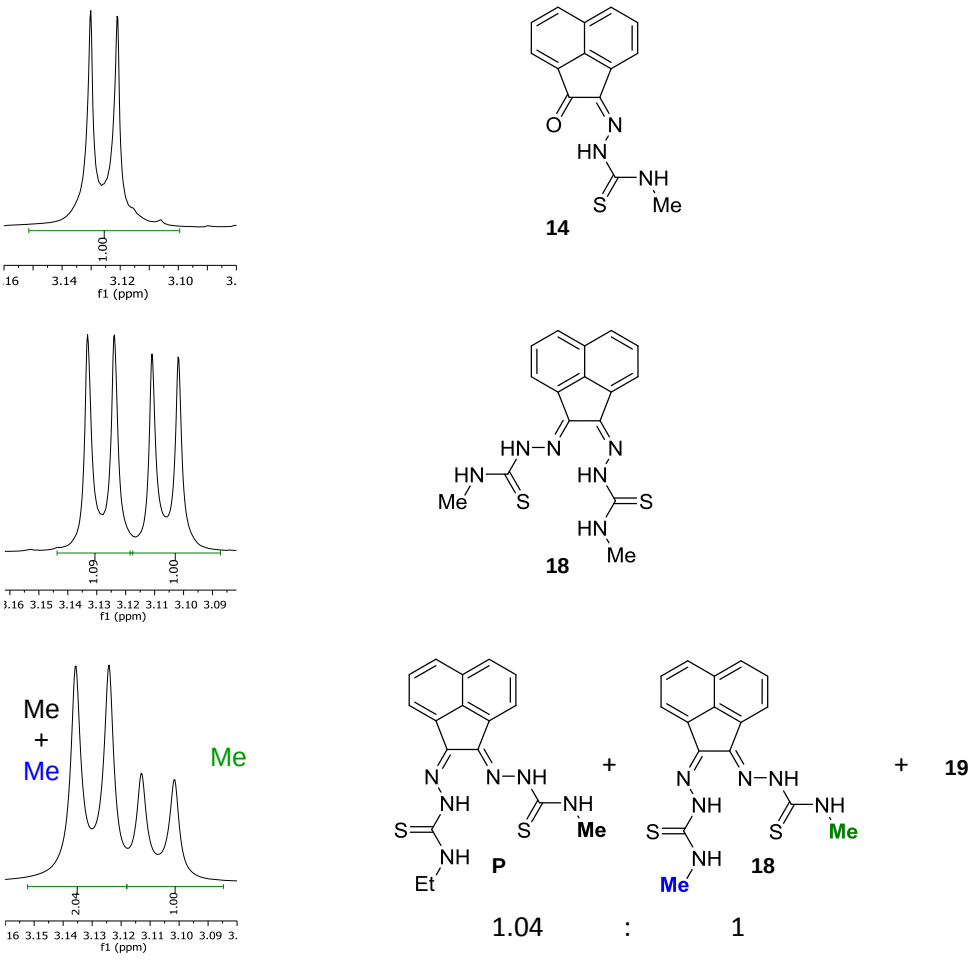

Figure 2.7: ^{1}H NMR spectra of the methyl resonances for mono(4-methyl-3-thiosemicarbazone) (top), bis(4-methyl-3-thiosemicarbazone) (middle) and isolated product of entry 5 in Table 2.3 (bottom).

The same experiment was repeated using 4-phenyl-3-thiosemicarbazide instead of 4-methyl-3-thiosemicarbazide to ascertain if the same reactivity was observed (Scheme 2.8) and to evaluate if the distribution of products was dependant on the thiosemicarbazide species. In this case, the temperature was limited to 90 ºC in order to avoid any possible decomposition. The amount of thiosemicarbazide was also limited to 1 equivalent as the presence of an excess did not have a dramatic effect in the results of previous experiments. The results are summarised in Table 2.4.

The differences are evident in this case, when the thiosemicarbazide is 4-phenyl-3-thiosemicarbazide, it can be observed that the starting material is still present in a high proportion but the exchange products are obtained in a much reduced proportion, being the desired product with one substituent of each class the major component of the mixture (**P'** in Scheme 2.8).

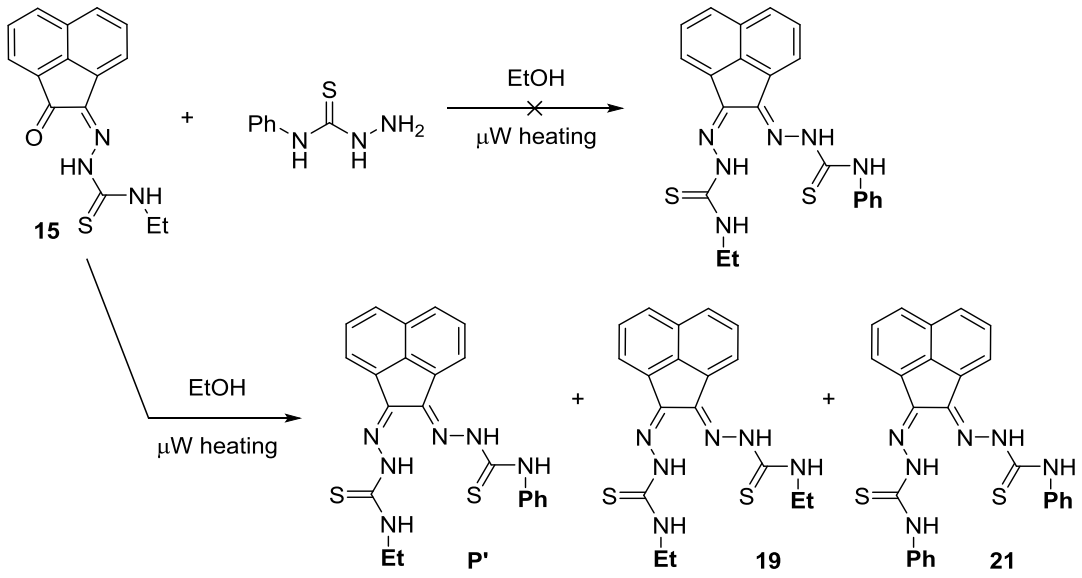

Scheme 2.8: Microwave heating experiment using 4-phenyl-3-thiosemicarbazide and mono(4-ethyl-3-thiosemicarbazone) acenaphthenequinone.

The addition of an excess of HCl catalyst (entry 4) did not produce a significant variation in the distribution of products. The application of a longer reaction time seemed to displace the equilibrium towards the products but unfortunately the proportion of exchange products increased equally (entries 5 – 6). The greater proportion of the starting material followed by the desired product seems to indicate that the process is, in fact, thiosemicarbazide-dependant and bulkier groups as the phenyl group are more difficult to exchange upon heating. In addition, during this experiment the starting material was never consumed.

Table 2.4: Conditions tested in the synthesis of asymmetric Et-Ph BTSC.

Entry	HCl	t / min	Product proportion 15 : P' : 19 : 21
1	1 eq., 16.8 μL	2.5	0.78 : 0.19 : (*) : -
2	1 eq., 16.8 μL	5	0.71 : 0.26 : (*) : -
4	3 eq., 50 μL	5	0.71 : 0.25 : (*) : (*)
5	1 eq., 16.8 μL	10	0.59 : 0.34 : (*) : (*)
6	1 eq., 16.8 μL	15	0.52 : 0.39 : (*) : (*)

(*) Present in the mixture but below 5% according ^{1}H NMR integration

2.4 Synthesis of unsymmetrical bis(thiosemicarbazonato) acenaphthenequinone complexes

The results obtained in the experiments towards the synthesis of unsymmetrical bis(thiosemicarbazone) acenaphthenequinone derivatives indicate that the synthesis of a functional unsymmetrical acenaphthenequinone bis(thiosemicarbazone) ligand would be an incredibly challenging process, considering that the optimisation of the reaction conditions is possible. The problems to purify the resulting mixture add difficulty to the preparation of the product. Consequently, other strategies for the use of thiosemicarbazones needed to be applied to obtain a suitable compound to functionalise the nanoprobe.

The synthesis of unsymmetrical acenaphthenequinone bis(thiosemicarbazonato) complexes including a free NH_2 group has been described by applying a one-pot templating process with a mono(substituted) ligand and thiocarbohydrazide, so this approach was followed (Scheme 2.9).

The Zn(II) complex was obtained in a templated process refluxing mono(4-allyl-3-thiosemicarbazone) acenaphthenequinone (**16**) in acetic acid with thiocarbohydrazide and $Zn(OAc)_2$ for 30 h. The product (**22**) was precipitated with diethyl ether, filtered, washed with more diethyl ether and dried. The corresponding Ga(III) complex was obtained by reaction with $GaCl_3$ heating in methanol by transmetallation of Zn(II) with Ga(III). The incorporation of gallium improves the fluorescence properties of the complex and constitutes a cold complex that could undergo potential radiolabelling with ^{68}Ga. The gallium complex (**23**) was precipitated with dichloromethane, washed with diethyl ether and dried under reduced pressure.

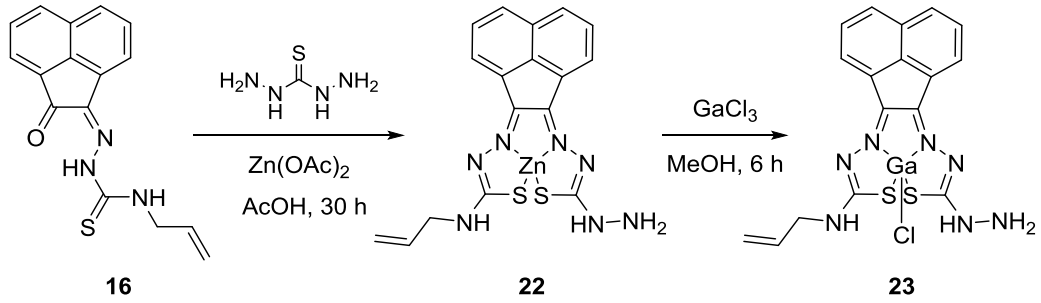

Scheme 2.9: Synthesis of a Ga(III) acenaphthenequinone bis(thiosemicarbazonato) complex with a free amino group.

The presence of a free amino group in this novel Ga(III) complex makes possible its incorporation in the nanoprobe forming an amide bond by simple carboxylic acid activation chemistry.

2.5 Investigations into other aromatic dicarbonyl starting materials

The difficulties encountered in the synthesis of unsymmetrical bis(thiosemicarbazone) ligands and complexes leading to mixtures, decomposition or metathesis-like exchanges can be attributed to the system's inherent rigidity and planarity that makes impossible the free rotation of the C-C bond between the keto groups. All these factors hinder the incorporation of the second thiosemicarbazone to the ligand. In addition, the templated synthesis of metal complexes of acenaphthenequinone mono(thiosemicarbazone) ligands can compete with other processes as the formation of mono(thiosemicarbazonato) metal complexes in a distorted octahedral geometry when the ligand reacts with the metal centre in a 2:1 fashion. This behaviour of a thiosemicarbazone moiety acting as a tridentate ligand has been extensively observed in the literature but never exploited with acenaphthenequinone backbones for imaging.

For these reasons, other aromatic dicarbonylic starting materials were explored in the formation of metal complexes. The synthesis of mono(thiosemicarbazonato) complexes was also explored with 1,2-dicarbonylic compounds while the reactivity of others towards the synthesis of unsymmetrical ligands and complexes was evaluated. Furthermore, it was anticipated that the extended aromaticity of some of the examples may help to enhance the fluorescence yield.

On a first basis, the cleavage of the C-C bond connecting the carbonyl groups of acenaphthenequinone was attempted. The oxidative cleavage of acenaphthene-1,2-diol to give the dialdehyde has been reported in the literature.[15] This reaction would yield an aldehyde, a much more reactive starting material where the rigidity would no longer be a restraint and unsymmetrical ligands could be prepared as long as the condensation with the thiosemicarbazides can be controlled stoichiometrically. Therefore, acenaphthenequinone was reduced to obtain acenaphthene-1,2-diol using sodium borohydride (Scheme 2.10).

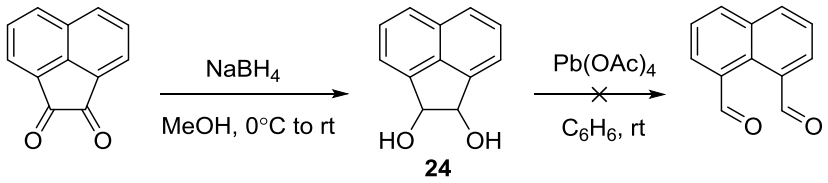

24

Scheme 2.10: Synthesis attempt of naphthalene-1,8-dicarbaldehyde.

The reaction was conducted as described in the literature and the product obtained as a beige solid.[16] The oxidative cleavage, however, did not work as expected. The oxidative procedure, first described by Criegee *et al.*, consisted in the reaction of acenaphthene-1,2-diol with lead acetate in benzene to give the corresponding dialdehyde.[15, 17] The original reaction conditions were tested with the exception of

benzene that was substituted for toluene. However, the isolated solid did not contain the desired product as demonstrated by ^{1}H NMR. The reaction was repeated varying different parameters as solvent (using benzene as in the original reference), a fresh batch of lead acetate and prolonging the reaction time. However, in our hands, the isolated solid contained a mixture of aromatic compounds, none of them being the desired product as the characteristic aldehyde resonance at ca. 10 ppm was not observed by ^{1}H NMR spectroscopy.

The oxidative cleavage of 1,2-diols has also been described with other oxidative agents. One of the most popular is sodium metaperiodate, which can be supported on silica to allow its use in organic solvents.[18, 19] Therefore, the reaction was attempted using $NaIO_4$ supported on silica and the diol in dichloromethane. Despite stirring the reaction mixture for several hours and heating to reflux in CH_2Cl_2, the isolated and purified product was not the expected naphthalene-1,8-dicarbaldehyde. The attempts to obtain the dialdehyde from the oxidative cleavage of acenaphthene-1,2-diol were not pursued any further in light of the synthetic difficulties under usual conditions for this reaction.

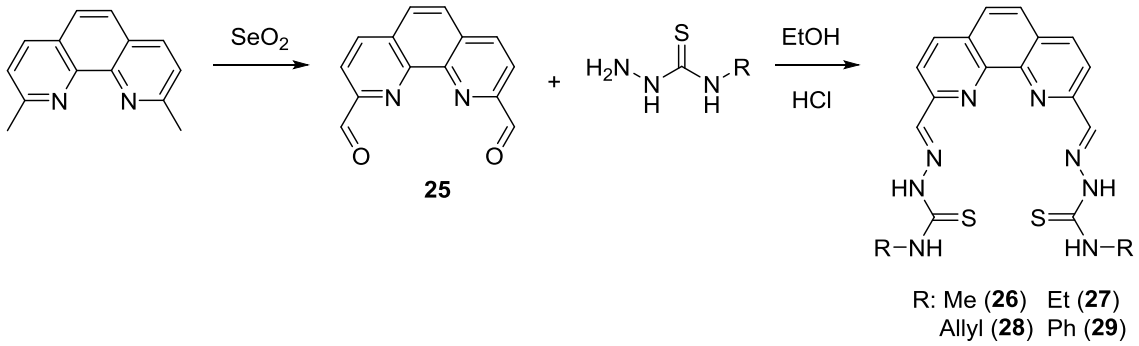

Scheme 2.11: Synthetic protocols for phenanthroline 2,9-bis(thiosemicarbazone) derivatives.

Alternatively, a related aromatic aldehyde derivative was obtained from neocuproine by oxidation with SeO_2 (Scheme 2.11, first step). In this case, the dialdehyde was readily obtained by refluxing neocuproine hydrate in the presence of SeO_2 in dioxane. The residues of SeO_2 were removed by filtration through celite first and dissolving the dry product in DMF to be precipitated with water. The effect was rapidly observed as the pink colour disappeared to obtain the product as an off-white solid.

The use of 1,10-phenanthroline-2,9-dicarbaldehyde for the preparation of unsymmetrical ligands was, however, limited due to the enhanced reactivity of the aldehyde groups compared to the keto groups that yielded the bis(substituted) compounds in all the cases (Scheme 2.11). The attempt to control the substitution stoichiometrically, controlling the equivalents of HCl or by addition at low temperatures failed and the reaction always resulted with the bis(thiosemicarbazone) as the product.

The reaction was extended to all the commercially available thiosemicarbazides mentioned in the previous section that resulted in the bis(thiosemicarbazone) ligands obtained in moderate to high yields. These compounds may present interest as imaging agents in the case that the complexation reaction with different metals like Zn(II), Fe(III) and Ga(III) is possible. Accordingly, the reactivity of this new class of symmetrical bis(thiosemicarbazone) ligands was explored with different metals. The preliminary results with zinc(II) and gallium(III) proved unsuccessful. The reaction with copper(II) acetate in DMF resulted in a colour change from yellow to light brown but the isolated product turned out to be just the starting material. Differently, the addition of $FeCl_3$ caused a colour change and the coordination could be detected by mass spectrometry. However, the geometry of the product could not be confirmed as Fe(III) is paramagnetic and NMR techniques could not be employed. A plausible coordination mode considering the exact mass obtained in mass spectrum, indicating the loss of 4 protons with respect to the ligand, could indicate towards the binding through the hydrazinic nitrogens and the sulphur atoms (after the thione-thiol equilibrium is displaced to the thiol form). Unfortunately, the poor solubility of this class of ligands and the lack of reactivity towards metals in the preliminary experiments were not encouraging to investigate their reactivity in more detail during this project.

In the search for different aromatic dicarbonylic compounds and looking into the possibility of preparing mono(thiosemicarbazonato) metal complexes, two related derivatives to acenaphthenequinone are available commercially, namely, aceanthrenequinone and phenanthrenequinone (Scheme 2.12).

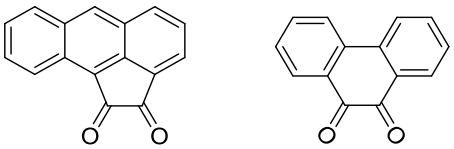

Scheme 2.12: Structures of aceanthrenequinone (left) and phenanthrenequinone (right).

The similarity of these diketones to acenaphthenequinone encouraged us in the search for novel aromatic compounds to form thiosemicarbazones and thiosemicarbazonato metal complexes. Considering the success in the use of microwave-assisted heating for the synthesis of thiosemicarbazones in the previous section, this method in both the synthesis of the ligands and the synthesis of the complexes was explored as it has demonstrated to reduce dramatically the needed reaction time and to improve the yield in some cases. In addition, another aromatic 1,2-diketone was prepared from pyrene. The aromatic starting material was oxidised with $RuCl_2$ to obtain 4,5-pyrenedione (Scheme 2.13). The product was purified by column chromatography and re-crystallised from CH_2Cl_2 / hexane.

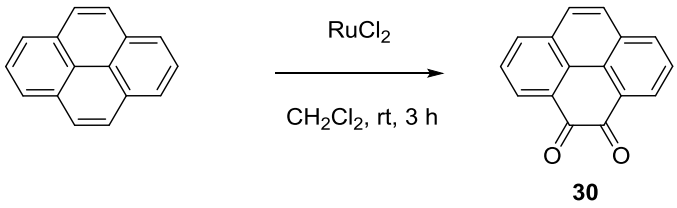

Scheme 2.13: Preparation of pyrene-4,5-dione from pyrene.

The preparation of mono(thiosemicarbazones) with the four different aromatic diketones was conducted applying the optimised reaction conditions for microwave synthesis described in the previous section. The general method involved the addition of the 1,2-diketone and the thiosemicarbazide to a small volume of ethanol (ca. 5 mL), the sonication for 2 – 3 min to homogenise the mixture, the addition of 2 – 3 drops of conc. HCl and heating under microwave irradiation for 10 min at 90 ºC (Scheme 2.14). The suspensions were filtered, washed with methanol or ethanol and diethyl ether to give the pure ligands in most cases. The reactions proceeded with good yields for all derivatives in the range of 70 – 90%.

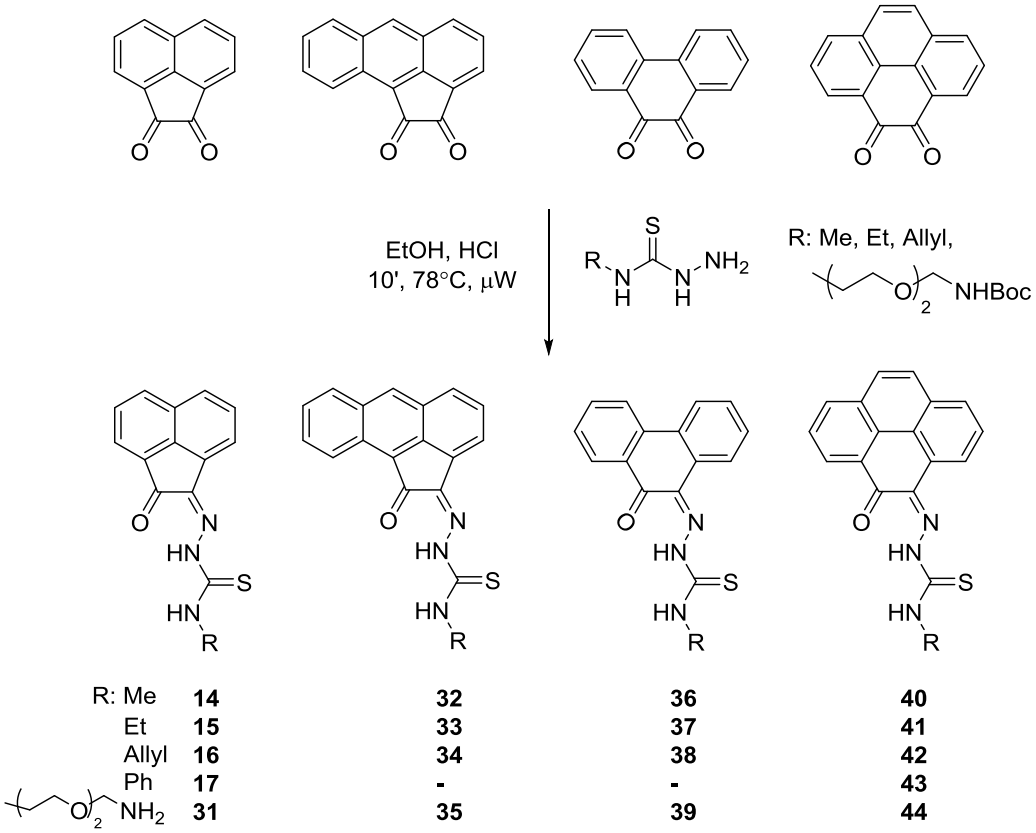

Scheme 2.14: Preparation of mono(thiosemicarbazone) ligands with different aromatic backbones.

The reaction with **9** was also conducted to evaluate the applicability of the method and to obtain a derivative with a free amino group that could be further functionalised. The reaction proceeded with good yields and the desired product was obtained with the deprotection occurring along the formation of the thiosemicarbazone in a one-pot process that did not seem to affect the selectivity in the thiosemicarbazone formation or to produce side-products in an observable proportion. This methodology allows the condensation and deprotection to be performed in a one-pot reaction saving one synthetic step.

The novel ligands were characterised by routine spectroscopic methods. The ^{1}H NMR spectra were comparable to acenaphthenequinone derivatives. The resonances of the aromatic region are characteristic of each backbone and are all present as the symmetry of the starting material is lost with the introduction of the thiosemicarbazone (see resonances in 9.2 – 7.2 ppm region in Figure 2.8).

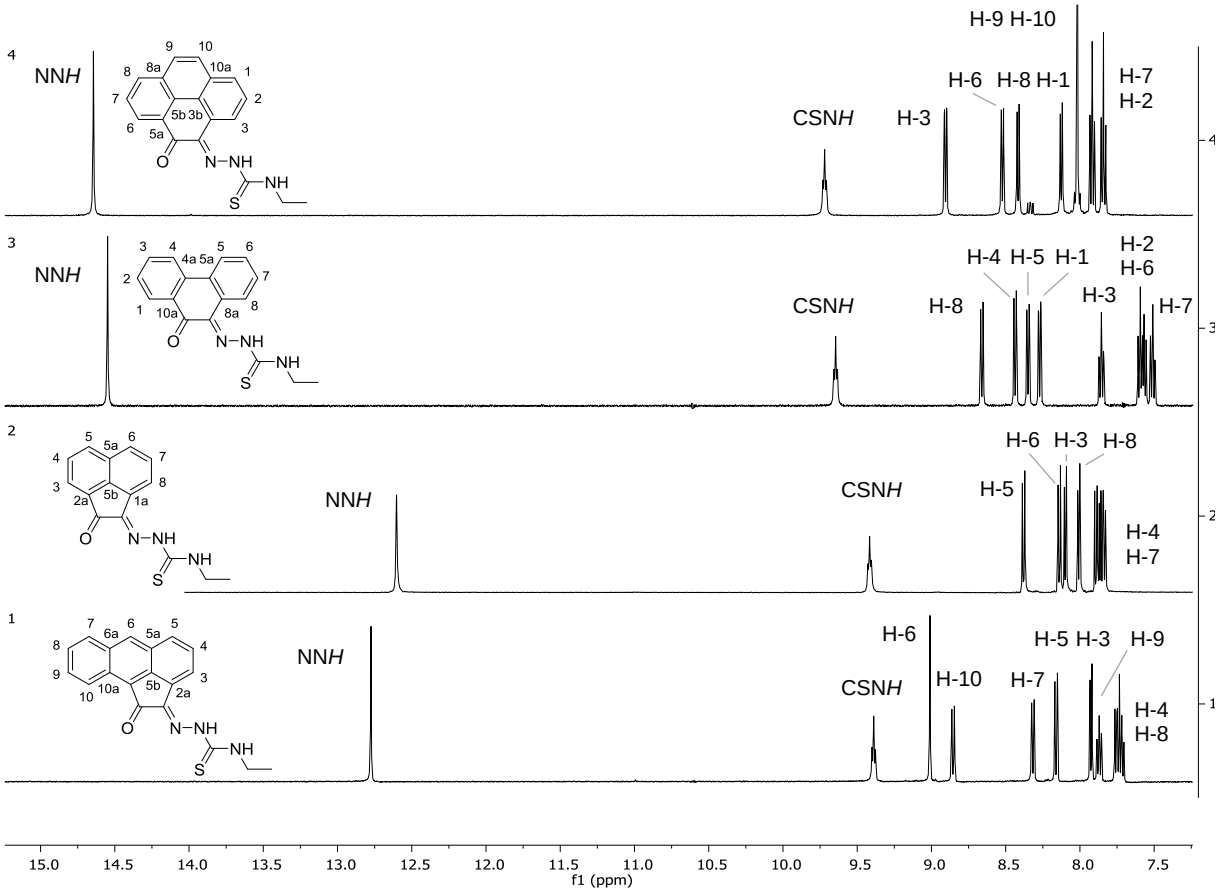

Figure 2.8: Aromatic region of the ^{1}H NMR spectrum (d^{6}-DMSO) of the mono(4-ethyl-3-thiosemicarbazone) ligands. 1) Aceantrenequinone derivative, 2) acenaphthenequinone derivative, 3) phenanthrenequinone derivative and 4) pyrene-4,5-dione derivative.

The resonances that changed in a more significant manner were the corresponding to the NH groups that were considerably deshielded compared to acenaphthenequinone in certain cases. The hydrazinic NH resonances appear as a singlet between 14 – 15 ppm for phenanthrenequinone and pyrene-5,6-dione thiosemicarbazones while acenaphthenequinone and aceanthrenequinone thiosemicarbazones present the corresponding resonances between 12 – 13 ppm (first signal in spectra 1 – 4 in Figure 2.8). The amino NH resonances, in contrast, did not change significantly between species and appear at 9 – 10 ppm presenting the multiplicity that results of the interaction with the neighbouring substituent (second resonance (triplet) in spectra 1 – 4 in Figure 2.8 for ethyl substituted derivatives).

In the case of pyrene-4,5-dione thiosemicarbazones with methyl (**40**), ethyl (**41**), allyl (**42**) and phenyl (**43**) substituents, suitable crystals for X-ray diffraction could be obtained and the structures resolved (Figure 2.9). The crystals were obtained by the vapour diffusion method, dissolving the compound in CH_2Cl_2 and using hexane as co-solvent. It can be observed in Figure 2.9 that all the members in this family of compounds in the solid phase present intramolecular hydrogen bonds between the hydrazinic proton and the oxygen from the ketone group.

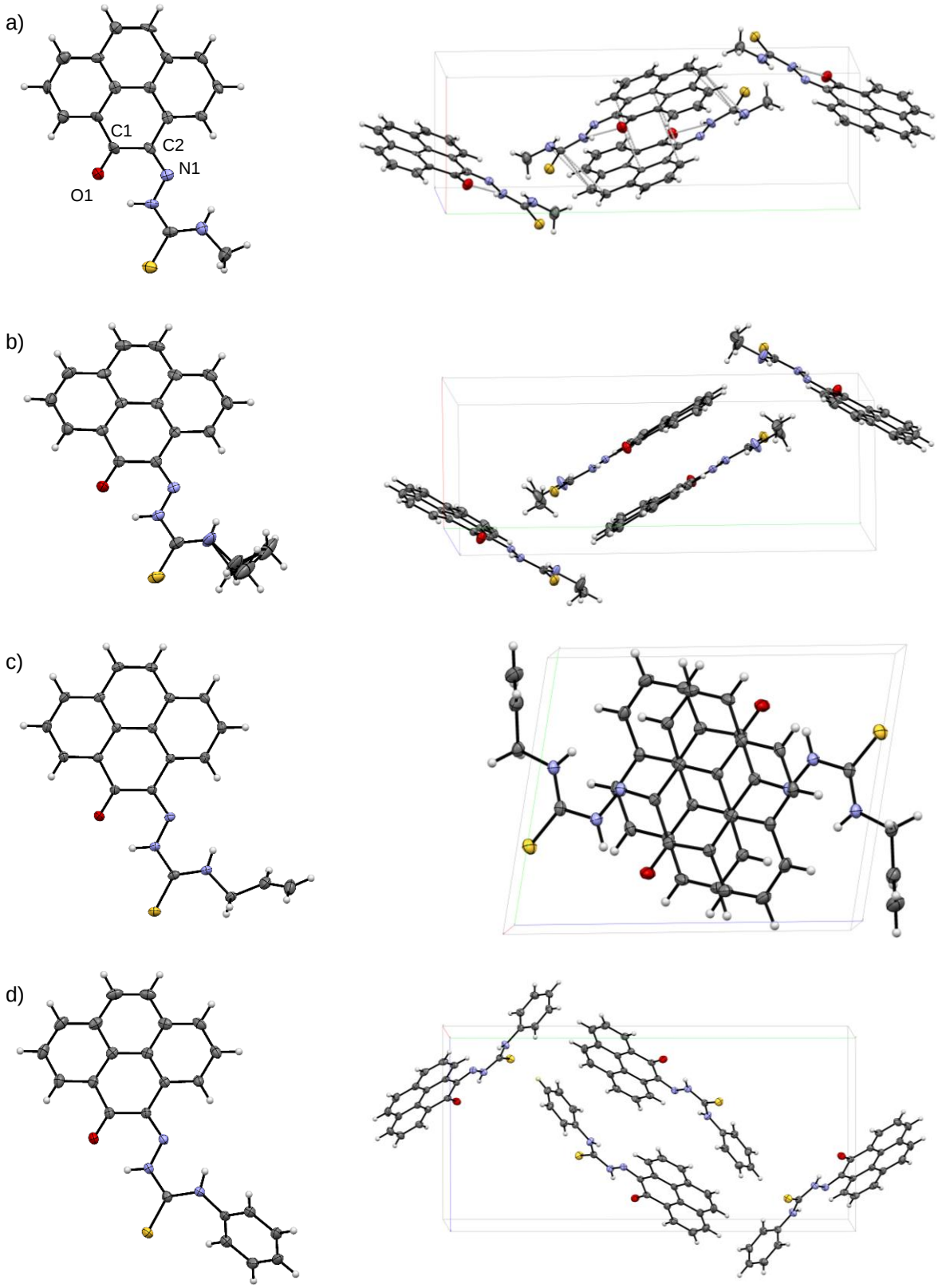

Figure 2.9: ORTEP representations of pyrene-4,5-dione mono(substituted) ligands (left) and molecular structures showing the unit cells (right). a) Methyl derivative, b) ethyl derivative, c) allyl derivative, d) phenyl derivative. a), b) View along c axis; c), d) view along a axis.

A selection of parameters of the mono(substituted) ligands are summarised in Table 2.5. It can be seen how the C1-C2 distance does not vary much among the ligands and has an average value of 1.48 – 1.49 Å. The increase seems to be related to the bulkiness of the substituent in the R group of the thiosemicarbazone. The angles comprised between the O-C1-C2 atoms have a value of 121º for all the compounds in accordance with a sp^2 carbon atom. The tendency observed is opposite to the distance and decreases with the size of the substituent. The complementary angle between the C1-C2-N1 atoms have a value of ca. 124º and a trend to increase as the C1-C2 distance as mentioned above.

The molecules are highly planar with the thiosemicarbazone, the R substituent in the terminal amino group and the backbone in the same plane with small deviations. The exception is the phenyl derivative where the Ph aromatic ring is out of the plane formed by the backbone and the thiosemicarbazone unit by an angle of 56.62º. The distance between planes in the solid packing is close to 3.2 Å except for the Ph derivative where this distance is larger, with a value of 3.556 Å. This difference can be explained by the displacement of the Ph ring out of the plane as already mentioned above.

Table 2.5: Selected bond distances and angles for pyrene-4,5-dione thiosemicarbazones derivatives in Figure 2.9.

	Me (40)	**Et (41)**	**Allyl (42)**	**Ph (43)**
O-C1 (Å)	1.2537 (3)	1.2373 (1)	1.2355 (17)	1.2328 (15)
C1-C2 (Å)	1.4806 (4)	1.487 (2)	1.4899 (18)	1.4968 (16)
N1-C2 (Å)	1.3172 (3)	1.3113 (1)	1.3078(17)	1.3043 (16)
O-C1-C2 (º)	121.0 (6)	120.99 (14)	120.74 (12)	120.63 (11)
C1-C2-N1 (º)	123.1 (6)	123.50 (14)	123.65 (12)	124.04 (11)
Distance between planes (Å)	3.141	3.257	3.175	3.556

The same distances and bond angles have been summarised in Table 2.6 for mono(4-allyl-3-thiosemicarbazones) with different backbones (one aliphatic and four aromatic), specifically butane-2,3-dione, acenaphthenequinone (**16**), phenanthrenequinone (**38**), aceanthrenequinone (**34**) and pyrene-4,5-dione (**42**). The crystallographic data for the mono(4-allyl-3-thiosemicarbazone) butane-2,3-dione were obtained from the literature[20], for **42** was obtained during this project and for **16**, **34** and **38** the crystal structures were provided by Dr S.I. Pascu. The distances in the aliphatic derivatives are similar to the ones found for thiosemicarbazones with aromatic backbone. The O-C1-C2 and C1-C2-N1 angles are, however, smaller than in any of the aromatic analogues. This can be attributed to the E disposition of the keto and imino group along the C1-C2 bond as the free rotation is allowed in the butane-2,3-dione derivative.

Table 2.6: Comparison of selected crystallographic parameters for mono(4-allyl-3-thiosemicarbazones) with different backbones.

	Butanedione derivative	**16**	**34**	**38**	**42**
O-C1 (Å)	1.223 (2)	1.23 (1)	1.227 (2)	1.238 (2)	1.2355 (17)
C1-C2 (Å)	1.494 (3)	1.50 (1)	1.518 (2)	1.491 (2)	1.4899 (18)
N1-C2 (Å)	1.297 (2)	1.30 (1)	1.293 (2)	1.308 (2)	1.3078(17)
O-C1-C2 (º)	119.2 (2)	127.1 (7)	124.6 (1)	121.0 (1)	120.74 (12)
C1-C2-N1 (º)	115.4 (2)	128.8 (7)	128.2 (1)	123.9 (1)	123.65 (12)
Distance between planes (Å)	4.357	-	3.067	2.935	3.175

The different aromatic backbones present equally similar values for bonds and distances. The distance O-C1 increases in the fashion: **34** < **16** < **42** < **38** and so does the N1-C2 distance. The C1-C2 distance follows a different trend decreasing as in **42** < **38** < **16** < **34**. The O-C1-C2 and C1-C2-N1 angles follow a trend as in **42** < **38** < **34** < **16**. Despite the change in order for some of the compounds, an underlying trend can be observed and related to structural characteristics. The derivatives presenting a five-membered ring fused to the aromatic core (acenaphthenequinone and aceanthrenequinone) are grouped and so are the derivatives with a six-membered ring attached to the aromatic core when considering structural parameters. The O-C1 and N1-C2 distances are larger in species presenting the six-membered ring while the C1-C2 distance is shorter compared to the five-membered containing compounds. Furthermore, the O-C1-C2 and C1-C2-N1 angles are larger in derivatives presenting the six-membered cyclic ring fused to the aromatic group.

The packing arrangements can be observed in the right column of Figure 2.9. All the ligands are arranged in the solid state in zig-zags and present interactions with molecules in the planes above and below the aromatic core. The solid packing of these compounds revealed the presence of short contact interactions between the different molecules. The distance between planes and the aromatic character of these compounds point to the presence of $\pi - \pi$ interactions and observing the structures, the character could be attributed to parallel displaced $\pi - \pi$ interactions with the exception of the phenyl derivative (**43**) that also presents perpendicular y-shaped interactions. This fact can be seen as a promising feature as pyrene derivatives have been used to attach groups of interest to carbon nanomaterials and to target specific biological structures like the cell nucleus or intercalators in DNA.[21-23]

2.5 Synthesis of novel mono(thiosemicarbazonato) metal complexes

The formation of unsymmetrical bis(substituted) complexes with acenaphthenequinone has revealed challenging and even the formation of bis(substituted) ligands utilising phenanthrenequinone, aceanthrenequinone or pyrene-4,5-dione proved unsuccessful applying the microwave conditions optimised for acenaphthenequinone.

A possible route to avoid the difficulties observed when trying to obtain the bis(substituted) ligands and/or complexes is to prepare the mono(thiosemicarbazonato) complexes. In this class of compounds, the thiosemicarbazone acts as a tridentate ligand with the oxygen being an additional donor atom. There are numerous examples of tridentate thiosemicarbazones binding to different metals in the literature. Even the preparation of mono(thiosemicarbazonato) acenaphthenequinone complexes has been described. In the work by Rodriguez-Argüelles *et al.*, the ligand mono(thiosemicarbazone) acenaphthenequinone was prepared and the Fe(II), Ni(II), Cu(II) and Zn(II) mono(thiosemicarbazonato) complexes formed.[24]

The preparation of the complexes was carried out refluxing the chlorides or acetates of the metals in ethanol. The reaction time varied between 3 and 7 h depending on the metal. The interest of the authors in these compounds was motivated by the biological properties of similar thiosemicarbazones. However, in this case, the complexes did not show substantial antiproliferative activity although they inhibited DMSO-induced differentiation.

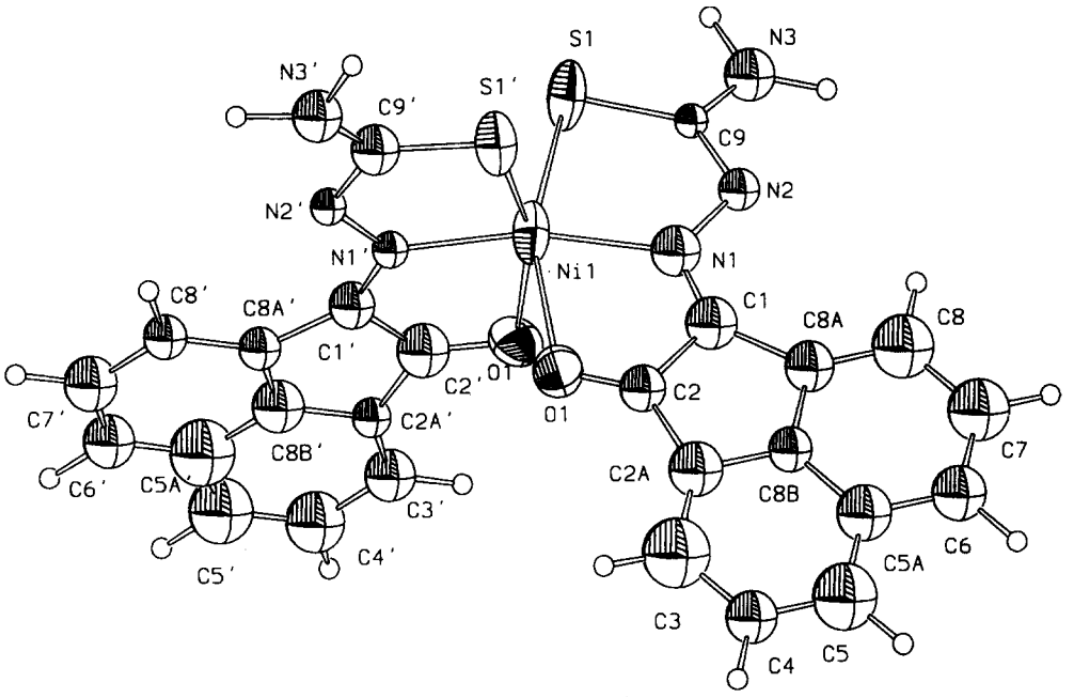

Figure 2.10: Structure of Ni(II) mono(thiosemicarbazonato)$_2$ complex. Figure reproduced from ref. 24 with permission from the publisher.

Initially, the formation of Zn(II) mono(thiosemicarbazonato) complexes with $Zn(OAc)_2$ was attempted. The derivatives containing an allyl substituent of all aromatic backbones were selected as a model. The described synthetic methods consisted in refluxing in ethanol for several hours, as mentioned above, but after the success of microwave-assisted synthesis on the preparation of the ligands, the suitability of microwave heating to the synthesis of the complexes was assessed. The temperature was kept constant at 90 ºC as this temperature has shown to enhance the reaction speed without the products showing signs of decomposition. It was found that the Zn(II) mono(4-allyl-3-thiosemicarbazonato)$_2$ complexes could be successfully obtained in just 1 h applying microwave heating thus avoiding prolonged heating times (Scheme 2.15). The products were isolated by filtration, washed with diethyl ether and dried under vacuum. The complexes were obtained as orange or red solids in good yields.

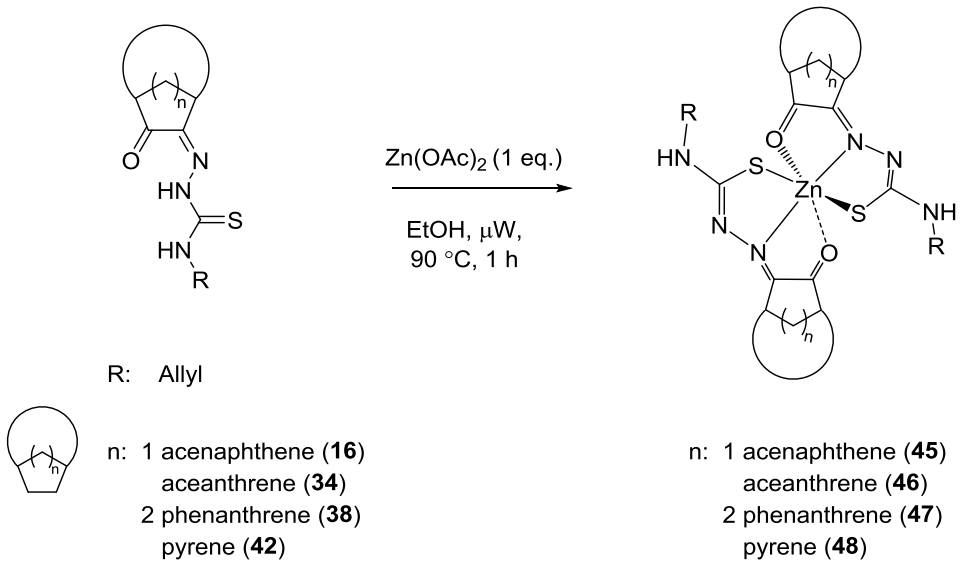

Scheme 2.15: Synthetic conditions for Zn(II) mono(thiosemicarbazonato)$_2$ complexes. The proposed coordination mode to the metal is based on X-ray structures of similar species present in the literature.[24, 25]

The normalised HPLC chromatograms of the Zn(II) complexes can be seen on Figure 2.11. The complexes were obtained in high purity with the presence of minor impurities. The retention times are in the 10 – 13 min range using HPLC method A (see Chapter 7 for details).

The ^{1}H NMR spectra of the complexes were also acquired and the disappearance of the characteristic resonance of the hydrazinic proton was observed when compared to the ligand, supporting the proposed coordination mode showed in Scheme 2.15. The spectra were complex to interpret, probably due to the presence of isomers, the two ligand units being inequivalent and to long-range couplings between protons.

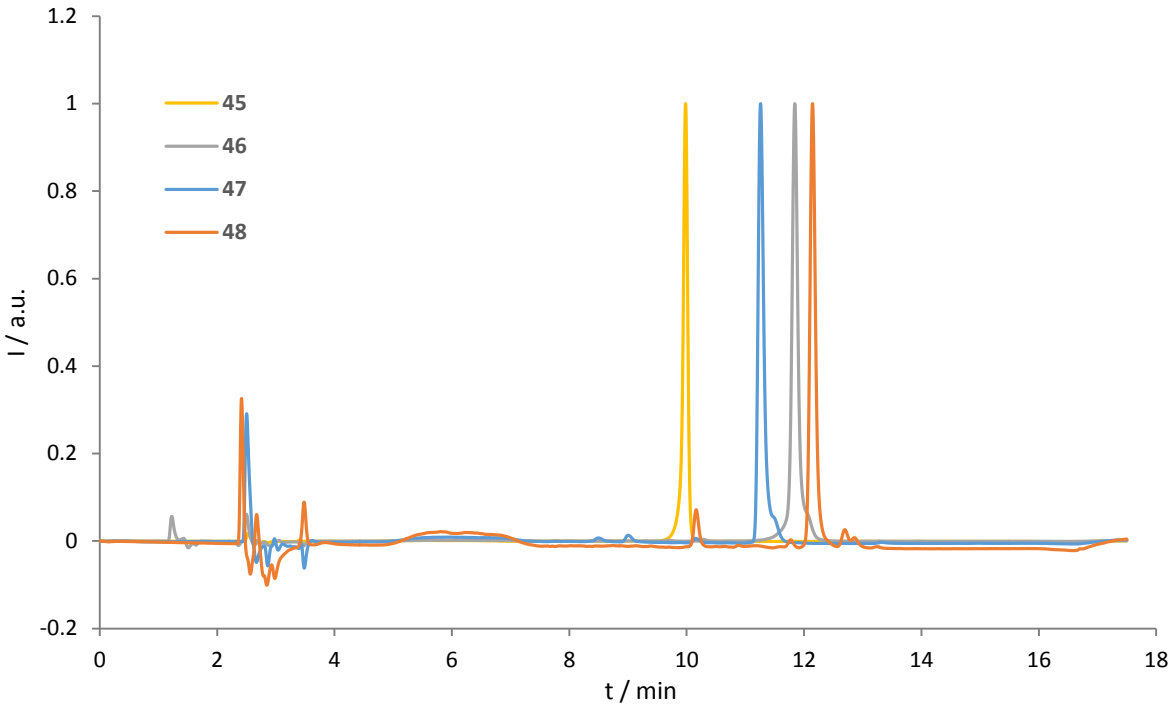

Figure 2.11: Normalised HPLC chromatogram of Zn(II) mono(4-allyl-3-thiosemicarbazonato)$_2$ complexes **45**, **46**, **47** and **48**.

The exact mass could be obtained for most of the complexes using ESI-TOF ionisation in positive mode and the masses corresponded to the protonated molecular ions, which is in accordance with the coordination mode proposed above.

Table 2.7: Spectral properties of BTSC complexes in DMSO solutions.

Compound	$\lambda_{max\text{-}abs}$ (nm)	$\lambda_{max\text{-}em}$ (nm)	$\Delta\lambda$ (nm)	Φ_f
23	482	638	156	0.022
45	360	628	268	$4.48\text{x}10^{-5}$
47	517	610	93	$3.83\text{x}10^{-5}$
48	538	621	83	$6.34\text{x}10^{-5}$
46	427	542	115	$4.81\text{x}10^{-5}$

The UV-vis and fluorescence spectra were studied to evaluate their potential as optical imaging agents. The summary of the UV-vis and fluorescence properties such as maximum absorption wavelength, maximum emission wavelength, Stokes shift ($\Delta\lambda$) and quantum yield (Φ), are summarised in Table 2.7. The properties of Ga(III) complex **23** have also been included for comparison. All the complexes but the one formed by acenaphthenequinone (**45**) have their absorption wavelength maxima in the visible.

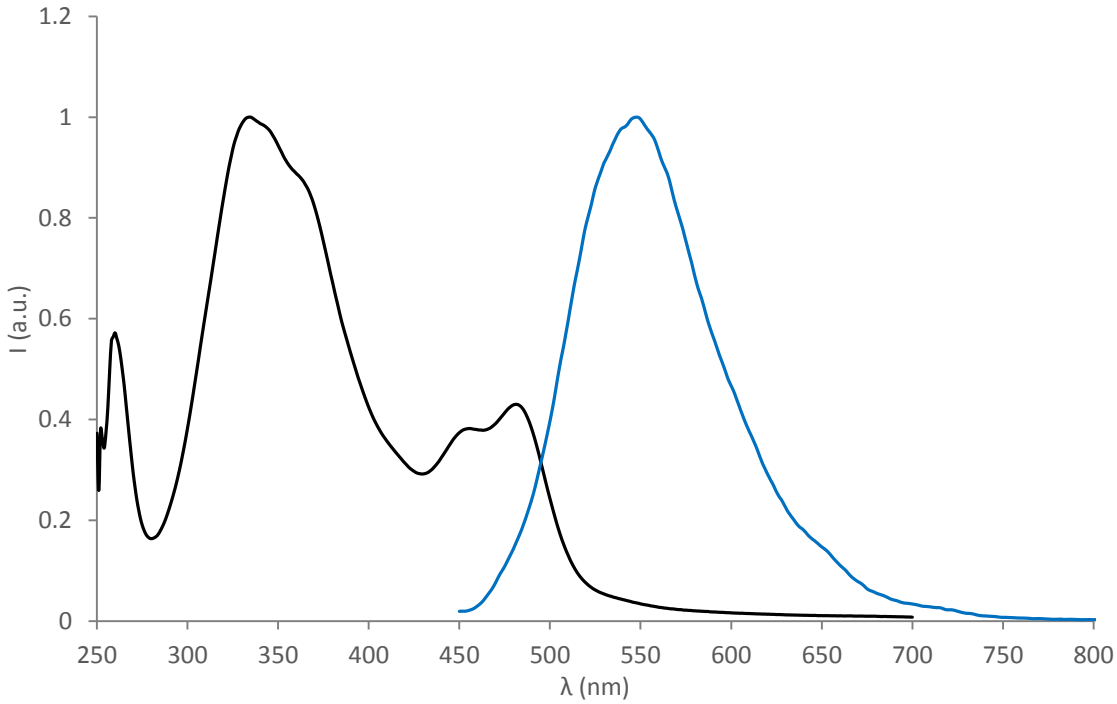

Figure 2.12: Normalised UV-vis spectrum (black line) and fluorescence spectrum (blue line) of **23** in DMSO.

The emission wavelengths are in the visible region at ca. 600 nm except for the complex including the pyrene-4,5-dione backbone (**46**) which is at 542 nm. The Stokes shifts are large for all the complexes. The quantum yields are low for all the mono(thiosemicarbazonato) complexes with respect to other inorganic fluorophores. Despite being a different thiosemicarbazonato species, it can be observed how in the Ga(III) bis(thiosemicarbazonato) complex (**23**) the quantum yield increases in several orders of magnitude compared to the Zn(II) mono(thiosemicarbazonato) complexes.

In an attempt to generalise the synthetic approach to other metals, the same microwave-assisted conditions were applied with $Cu(OAc)_2$. However, the reaction outcome was not as straightforward as with Zn(II). A colour change was observed from the starting materials and the products were observed by mass spectrometry but the reaction mixture contained decomposition products observed as dark residues in the crude reaction mixture and several peaks in the mass spectra. This result indicates that the synthetic method is metal-dependant and would need to be optimised for every metallic species. In the case of gallium, a colour change was initially observed in the reaction when $GaCl_3$ was added to a suspension of the thiosemicarbazone in ethanol but only the starting material was recovered after heating. The preparation of this metal complexes is most certainly possible based on the results shown above and the precedents in the literature. However, the optimisation of the reaction conditions for metals different than zinc needs of further work and are not included in this project.

2.6 Extended mono(thiosemicarbazone) ligands

Due to the nature of many targeting molecules, like peptides, it is common that the coupling with the fluorophore would be made via an amide bond. This fact highlights the need of the presence of a carboxylic acid in the thiosemicarbazonato complex. There are some examples in the literature regarding the introduction of a carboxylic acid moiety into a thiosemicarbazonato complex. Dilworth *et al.* functionalised a 2,3-butanedione molecule to have a benzoic acid in the backbone. This benzoic acid was then employed to couple the complex to a targeting peptide, namely octreotide.[8] Following another strategy, an amino functionalised ligand was reacted with succinic anhydride. The product of the ring-opening reaction after work-up was the corresponding 4-oxobutanoic acid. However, the efficiency of the reaction was not outstanding producing mixtures of difficult separation. In the same work, a more successful alternative was described to introduce the desired carboxyl functionality that consisted in the coupling with a protected glutamine derivative forming an amide bond. This way, the desired group was obtained from an amino-functionalised thiosemicarbazone and additionally, two protected side groups were added obtaining a bipodal linker that could be selectively deprotected. In this project, the last approach was adopted as the functionalisation of the aromatic backbone can produce selectivity problems and a variety of amino-functionalised thiosemicarbazone ligands has already been synthesised.

The coupling of the protected glutamine derivative was evaluated as a proof of principle for thiosemicarbazones based on aromatic backbones. Fmoc-Glu(OtBu)-OH, a commercial derivative, was activated with pyBOP in DMF. The role of pyBOP in carboxylic acid activation is detailed in the following chapter. The deprotected amino-functionalised thiosemicarbazone derivative was added and the reaction mixture stirred at room temperature overnight (Scheme 2.16). The introduction of the amino acid further improves the solubility properties of the thiosemicarbazone ligand in organic solvents and allowed to purify the product by column chromatography.

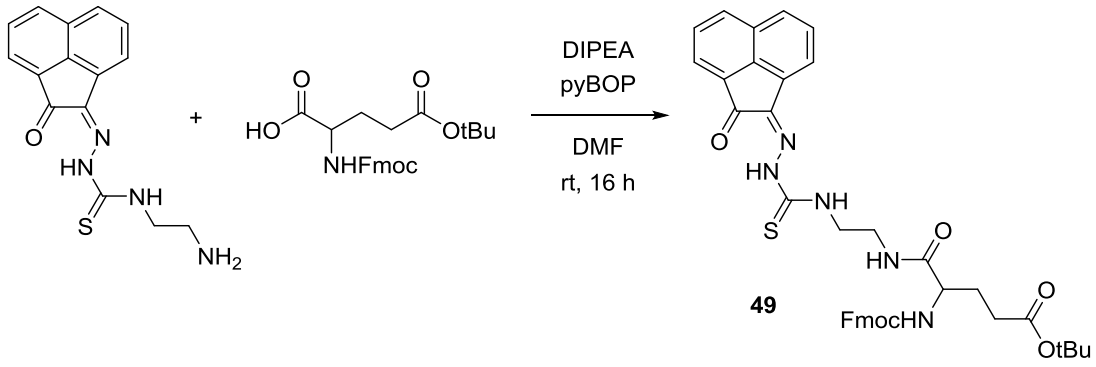

Scheme 2.16: Coupling of amino-functionalised thiosemicarbazone with Fmoc-Glu(OtBu)-OH.

The success of the coupling with the protected amino acid expands the reactivity towards mono(thiosemicarbazonato) complexes and opens the way for the attachment to biomolecules or nanomaterials.

2.7 Evaluation of novel complexes *in vitro*

The complexes prepared in the previous two sections proved to be fluorescent and based on the promising results of acenaphthenequinone thiosemicarbazones in imaging in the past, the complexes were tested *in vitro* in PC-3 prostate cancer cells.

The compounds were added in 100 µM final concentration dissolved in serum free medium (1% DMSO) and incubated in living prostate cancer, PC-3, cells for 15 min at 37 ºC. After washing the excess of compounds from the cells' dish with PBS and restoring the serum-free medium, the single photon confocal microscopy images were acquired immediately.

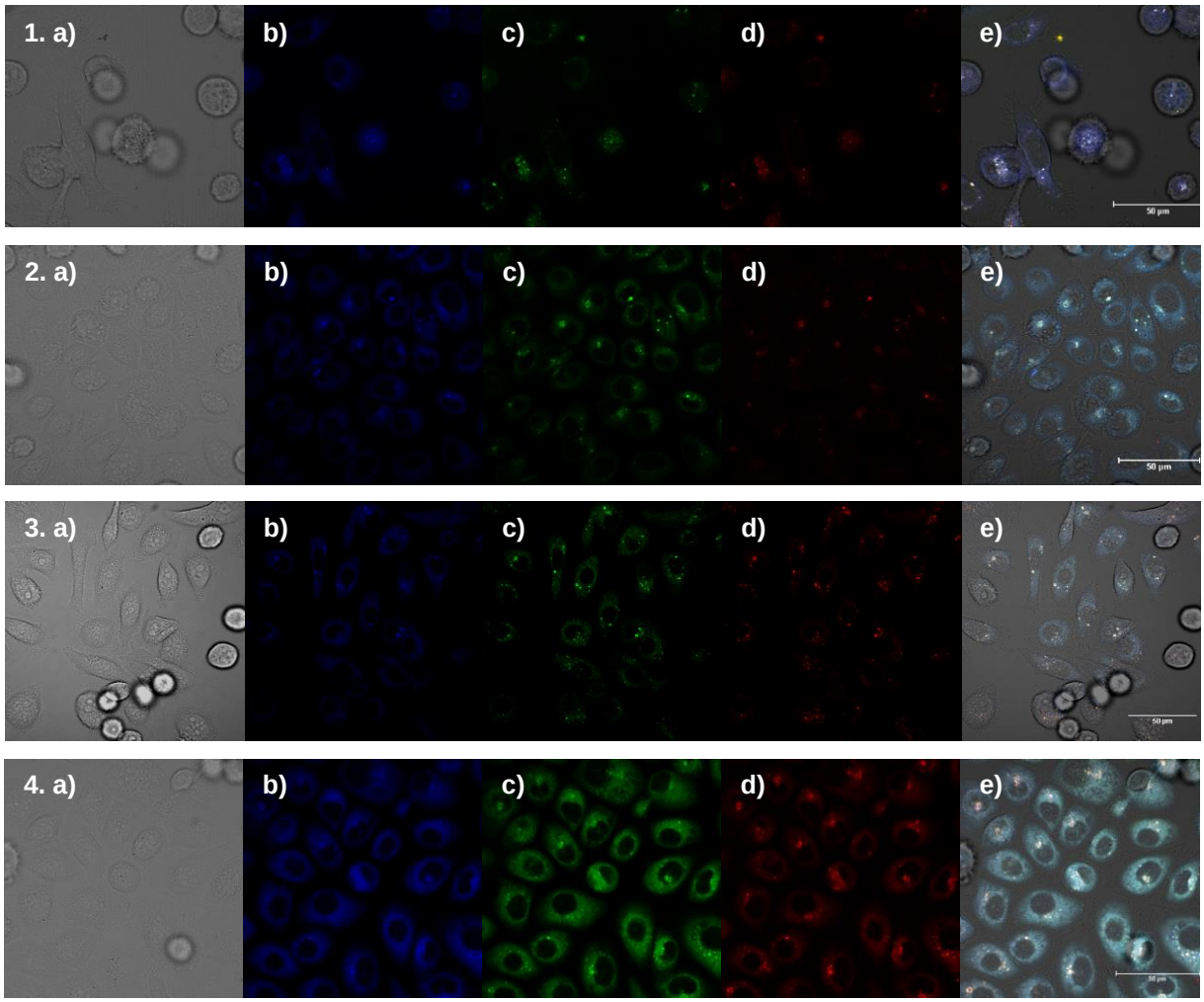

Figure 2.13: Single photon confocal microscopy images of compounds **45** (1), **46** (2), **47** (3) and **48** (4) in PC-3 cells after 15 min incubation at 37 ºC where a) DIC image, b) blue channel, c) green channel, d) red channel and e) overlay of a)-d). Scalebar: 50 µm.

The results can be observed in Figure 2.13 for compounds **45** to **48** and Figure 2.14 for compound **23**. The complexes showed a certain degree of precipitation when the DMSO solutions were added to the serum-free medium, especially **45**. Consequently, in further *in vitro* imaging experiments with this family of compounds the working concentration needs to be under 100 µM.

The uptake of the complexes by the cells was observed and the complexes were concentrated into the cytoplasm with no access to the cell nucleus. Despite no toxicity tests being performed during this initial *in vitro* testing, the acenaphthenequinone based complex **45**, the phenanthrenequinone based complex **47** and the gallium complex **23** seemed to induce cytotoxicity as the shape of the cells varied after incubation with the compound as observed in the confocal images. This can be attributed to cytotoxic effects causing cell death by mitochondrial disruption as it has been reported before for Zn(II) bis(thiosemicarbazonato) acenaphthenequinone complexes.[26] The fluorescence response showed activity in all channels (blue, green and red) due to the broad fluorescence emission profile of the mono(thiosemicarbazonato) complexes, being specially noted in the pyrene-4,5-dione complex **48**.

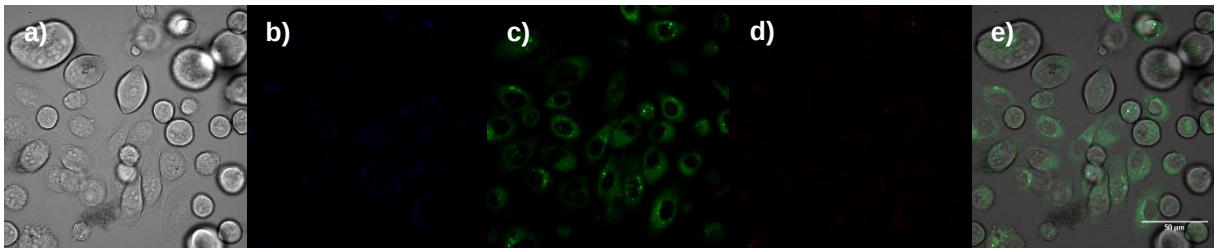

Figure 2.14: Single photon confocal microscopy images of compound **23** in PC-3 cells after 15 min incubation at 37 ºC where a) DIC image, b) blue channel, c) green channel, d) red channel and e) overlay of a)-d). Scalebar: 50 µm.

The fluorescence emission profile of **23**, however, is narrower and there is virtually no fluorescence response in the blue and red channels. The fluorescence intensity of Zn(II) mono(thiosemicarbazonato) compounds *in vitro* seemed to be higher for complex **48**. However, no direct correlations can be made with the photophysical properties of the complex, as the quantum yield, because the comparison between confocal images is not quantitative and other factors as precipitation problems may have a considerable effect in the actual concentration of the complex entering the cells.

The distribution of the complexes in the cells seems to be favoured in small vesicles observed as highly fluorescent points. This could indicate the uptake of the complexes into the lysosomes or mitochondrias as this preference has been described before for other acenaphthenequinone bis(thiosemicarbazonato) complexes in the literature.[6, 26] However, co-localisation experiments are needed to ascertain the distribution of these compounds inside the cell.

2.8 Conclusions

In this chapter, several novel thiosemicarbazides bearing a protected amino group have been synthesised from protected diamines. The corresponding acenaphthenequinone thiosemicarbazones were prepared in an acidic ethanolic solution with acetic acid as it was observed that the protecting group was labile in the presence of small amount of conc. HCl. This constitutes the first example of functional acenaphthenequinone thiosemicarbazone ligands.

The use of conventional heating of the mono(thiosemicarbazone) ligands to obtain the bis(substituted) species in an acidic solution with acetic acid proved unsuccessful so the use of microwave-assisted heating was explored. The results indicated that a strong acid was necessary in the formation of the bis(thiosemicarbazone) ligands. The use of microwave heating enhanced the reaction speed and the deprotection of the product could be controlled by adding an equimolar amount of conc. HCl. Therefore, for the first time in the chemistry of thiosemicarbazones containing aromatic backbones, microwave-assisted heating was applied, demonstrating to be an advantageous technique reducing reaction time from hours to minutes and obtaining improved or comparable yields with reported protocols. The mono(thiosemicarbazone) and symmetrical bis(thiosemicarbazone) ligands were obtained using this method in yields typically above 70%.

However, the synthesis and purification of unsymmetrical bis(substituted) ligands and complexes proved incredibly challenging. The application of microwave-assisted heating to the preparation of the bis(substituted) ligands to overcome the lack of reactivity under conventional conditions led to an unreported metathesis exchange of thiosemicarbazone groups that yielded a statistical mixture of products. The synthesis of the complex in a template process did not produce reproducible results.

Despite these difficulties, unsymmetrical bis(thiosemicarbazonato) complexes of Zn(II) and Ga(III) with a free amino groups were obtained in a one-pot process from the mono(4-allyl-3-thiosemicarbazone) ligand and thiocarbohydrazide.

In addition, a number of novel aromatic dicarbonyl compounds, namely phenanthrenequinone, aceanthrenequinone, pyrene-4,5-dione and 1,10-formyl-2,9-phenanthroline, have been explored as starting materials for the synthesis of novel thiosemicarbazone ligands. All of them produced the desired products in good yields applying microwave conditions optimised during this work. In the case of the phenanthroline group, the bis(substituted) product was obtained due to the enhanced reactivity of the aldehyde groups. The mono(substituted) ligands obtained with novel aromatic groups have been used for the synthesis of mono(thiosemicarbazonato) metal complexes. The derivatives were reacted with Zn(II) and the complexes were obtained in reduced times with respect to the literature under microwave heating conditions. Additional work is needed to expand the chemistry of these ligands to other metals, such as for example, Cu(II) or Ga(III).

The preparation of extended thiosemicarbazone ligands bearing carboxylic acid groups for the coupling with biologically active amines, as peptides, was explored and a promising result was obtained with a protected glutamine derivative.

The fluorescent complexes obtained were tested *in vitro* in prostate cancer PC-3 cancer cells showing good uptake and the stronger emission, generally, in the green channel. The specific localisation of the complexes into the cell and the assessment of cytotoxicity to cancer cells require of further experiments.

2.9 References

1. B. M. Paterson and P. S. Donnelly, *Chem. Soc. Rev.*, 2011, **40**, 3005-3018.
2. J. L. J. Dearling, J. S. Lewis, G. E. D. Mullen, M. T. Rae, J. Zweit and P. J. Blower, *Eur. J. Nucl. Med.*, 1998, **25**, 788-792.
3. N. Takahashi, Y. Fujibayashi, Y. Yonekura, M. Welch, A. Waki, T. Tsuchida, N. Sadato, K. Sugimoto and H. Itoh, *Ann. Nucl. Med.*, 2000, **14**, 323-328.
4. F. Dehdashti, M. Mintun, J. Lewis, J. Bradley, R. Govindan, R. Laforest, M. Welch and B. Siegel, *Eur. J. Nucl. Med. Mol. Imag.*, 2003, **30**, 844-850.
5. D. W. Dietz, F. Dehdashti, P. W. Grigsby, R. S. Malyapa, R. J. Myerson, J. Picus, J. Ritter, J. S. Lewis, M. J. Welch and B. A. Siegel, *Dis. Colon Rectum*, 2008, **51**, 1641-1648.
6. R. L. Arrowsmith, P. A. Waghorn, M. W. Jones, A. Bauman, S. K. Brayshaw, Z. Hu, G. Kociok-Kohn, T. L. Mindt, R. M. Tyrrell, S. W. Botchway, J. R. Dilworth and S. I. Pascu, *Dalton Trans.*, 2011, **40**, 6238-6252.
7. B. M. Paterson, J. A. Karas, D. B. Scanlon, J. M. White and P. S. Donnelly, *Inorg. Chem.*, 2010, **49**, 1884-1893.
8. P. D. Bonnitcha, S. R. Bayly, M. B. M. Theobald, H. M. Betts, J. S. Lewis and J. R. Dilworth, *J. Inorg. Biochem.*, 2010, **104**, 126-135.
9. I. S. Alam, R. L. Arrowsmith, F. Cortezon-Tamarit, F. Twyman, G. Kociok-Kohn, S. W. Botchway, J. R. Dilworth, L. Carroll, E. O. Aboagye and S. I. Pascu, *Dalton Trans.*, 2016, **45**, 144-155.
10. S. I. Pascu, P. A. Waghorn, B. W. C. Kennedy, R. L. Arrowsmith, S. R. Bayly, J. R. Dilworth, M. Christlieb, R. M. Tyrrell, J. Zhong, R. M. Kowalczyk, D. Collison, P. K. Aley, G. C. Churchill and F. I. Aigbirhio, *Chem. Asian J.*, 2010, **5**, 506-519.
11. R. L. Arrowsmith, PhD thesis, University of Bath, 2012.
12. Biotage, Initiator 2.5 - Getting started guide for organic synthesis, http://www.biotage.com/product-group/microwave-knowledge-base, Accessed 25/02/16.
13. B. Rasmussen, A. Sørensen, S. R. Beeren and M. Pittelkow, in *Organic Synthesis and Molecular Engineering*, John Wiley & Sons, Inc., 2013, pp. 393-436.
14. M. Pittelkow, PhD thesis, University of Copenhagen, 2006.
15. R. P. Hopkins, *Biochem. J*, 1968, **108**, 577-582.
16. S. C. Dakdouki, D. Villemin and N. Bar, *Eur. J. Org. Chem.*, 2011, **2011**, 4448-4454.
17. R. Criegee, L. Kraft and B. Rank, *Justus Liebigs Ann. Chem.*, 1933, **507**, 159-197.
18. D. N. Gupta, P. Hodge and J. E. Davies, *J. Chem. Soc., Perkin Trans. 1*, 1981, 2970-2973.
19. Y.-L. Zhong and T. K. M. Shing, *J. Org. Chem.*, 1997, **62**, 2622-2624.
20. J. P. Holland, F. I. Aigbirhio, H. M. Betts, P. D. Bonnitcha, P. Burke, M. Christlieb, G. C. Churchill, A. R. Cowley, J. R. Dilworth, P. S. Donnelly, J. C. Green, J. M. Peach, S. R. Vasudevan and J. E. Warren, *Inorg. Chem.*, 2007, **46**, 465-485.
21. S. Mardanya, S. Karmakar, D. Mondal and S. Baitalik, *Inorg. Chem.*, 2016, **55**, 3475-3489.

22. M. E. Ostergaard, D. C. Guenther, P. Kumar, B. Baral, L. Deobald, A. J. Paszczynski, P. K. Sharma and P. J. Hrdlicka, *Chem. Commun.*, 2010, **46**, 4929-4931.
23. G. Prencipe, S. M. Tabakman, K. Welsher, Z. Liu, A. P. Goodwin, L. Zhang, J. Henry and H. Dai, *J. Am. Chem. Soc.*, 2009, **131**, 4783-4787.
24. M. C. Rodriguez-Argüelles, M. B. Ferrari, G. G. Fava, C. Pelizzi, G. Pelosi, R. Albertini, A. Bonati, P. P. Dall'Aglio, P. Lunghi and S. Pinelli, *J. Inorg. Biochem.*, 1997, **66**, 7-17.
25. T. S. Lobana, R. Sharma, G. Bawa and S. Khanna, *Coord. Chem. Rev.*, 2009, **253**, 977-1055.
26. S. I. Pascu, P. A. Waghorn, T. D. Conry, B. Lin, H. M. Betts, J. R. Dilworth, R. B. Sim, G. C. Churchill, F. I. Aigbirhio and J. E. Warren, *Dalton Trans.*, 2008, 2107-2110.

Chapter 3 : Synthesis of bifunctional BODIPY fluorophores

3.1 Overview

Despite the unique characteristics of bis(thiosemicarbazonato) compounds (e.g. versatile chelators, potential multimodality, possible hypoxia selectivity), the metal complexes present a series of drawbacks, as challenging purification processes, reduced fluorescence intensity, poor solubility in biological media or difficulty in introducing reactive functional groups, when compared to organic dyes. Furthermore, the chemistry to produce functional unsymmetrical derivatives proved to be considerably challenging due to exchange reactions as described in Chapter 2. Therefore, the chemistry of a series of well-known organic dyes was explored to produce a functional fluorophore. BODIPY (4,4-difluoro-4-bora-3a,4a-diaza-s-indacene) dyes have been profusely applied as labelling reagents, chemosensors, laser dyes or switches.[1] A wide range of BODIPY derivatives are commercially available for the labelling of drugs, peptides or nucleotides.[2]

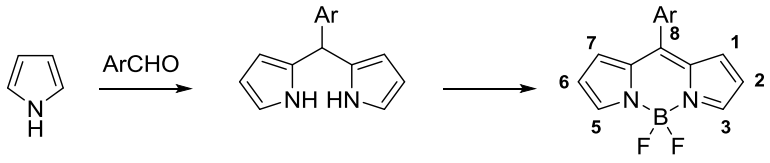

Scheme 3.1: General synthetic route for BODIPY fluorophores with the numbering of the BODIPY core in the final product.

The chemistry of BODIPY derivatives is varied and depending on the substitution, the versatility can be enhanced. These derivatives can undergo electrophilic reactions, substitution reactions or metal-catalysed coupling reactions (e.g. Sonogashira, Heck, Stille, Suzuki) when halogenated atoms are present.[3, 4] The advantageous properties attributed to BODIPY dyes include their photophysical properties. BODIPY dyes are generally strong UV-vis absorbents and emit sharp fluorescence peaks with high quantum yields. Regarding their stability, these species are generally not affected from changes in polarity or pH in the medium and are moderately stable under physiological conditions. Furthermore, the modification of the structure provides enhanced stability, water solubility or tunable fluorescence properties.[5] In addition, BODIPY dyes can also act as multimodal imaging probes. The possibility to construct a multimodal probe by functionalising the BODIPY group with a chelator has been explored and different metals used (examples can be observed in Table 1.2). However, this is not necessary if the BODIPY core is radiolabelled by isotopic substitution of the fluorine atoms connected to the boron by ^{18}F.

The aim of this chapter was to obtain a series of functional BODIPY dyes able to be introduced in the nanoprobe, linking the nanomaterial and the targeting peptide. The possibility of obtaining derivatives emitting at different wavelengths, especially in the near infrared, were also explored.

3.2 Synthesis of a bifunctional BODIPY derivative

Fluorophores based on the 4,4-difluoro-4-bora-3a,4a-diaza-s-indacene (BODIPY) core were investigated taking in consideration all the properties cited above and with the target to obtain a fluorescent nanoprobe. Between the advantages described for BODIPYs probably the most important are the high quantum yields, broad range of substitution that can be obtained by modifying the starting materials, the varied reactivity (electrophilic reactions, coupling reactions, substitution reactions), their reasonable stability in different conditions and the possibility of varying their fluorescence properties by varying the core or substitution.

BODIPY dyes are generally synthesised from the corresponding pyrroles in a condensation with aldehydes, acyl chlorides and acid anhydrides although the use of aromatic aldehydes is considerably more common in the literature. This condensation is followed by the boron complexation by the dipyrromethane intermediate, performed in most cases with $BF_3{\cdot}OEt_2$. The dipyrromethane species is not generally isolated. Tetramethyl substitution in positions 1, 3, 5 and 7 tends to stabilise the BODIPY core, blocking the pyrrole positions from electrophilic attack.

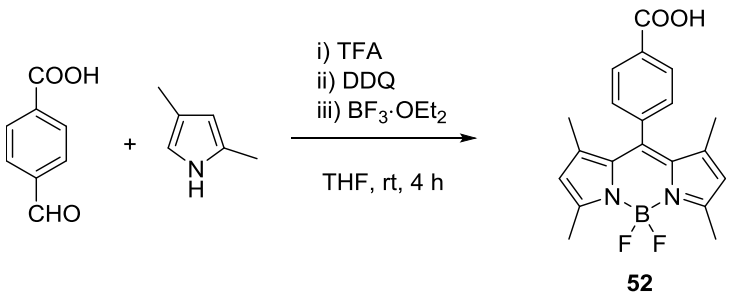

52

Scheme 3.2: Reaction conditions for the synthesis of 8-carboxyphenyl BODIPY (**52**).

In this case, a literature procedure was followed to obtain a 4-carboxyphenyl group in position 8 of the BODIPY core by using 4-formylbenzoic acid and 2,4-dimethylpyrrole (Scheme 3.2).[6] According to the authors of this work, the introduction of methyl groups in the 1, 3, 5, and 7 positions leads to an increase in quantum yield and extinction coefficient. The observed twenty fold increase in quantum yield compared to the species without substitution was related to a 'push-pull' electronic factor of the methyl groups, and steric hindrance that limits the free rotation of the phenyl group hence avoiding the

intramolecular vibrational relaxation. The photostability of the compound was measured by irradiation with a 500 W lamp with 80% of the original absorption remaining after 16 h.[6]

The carboxylic acid group will be the centre of all the following reactivity. The product obtained was purified by flash column chromatography and posterior recrystallisation. The yield could be improved if the crystallisation process was repeated.

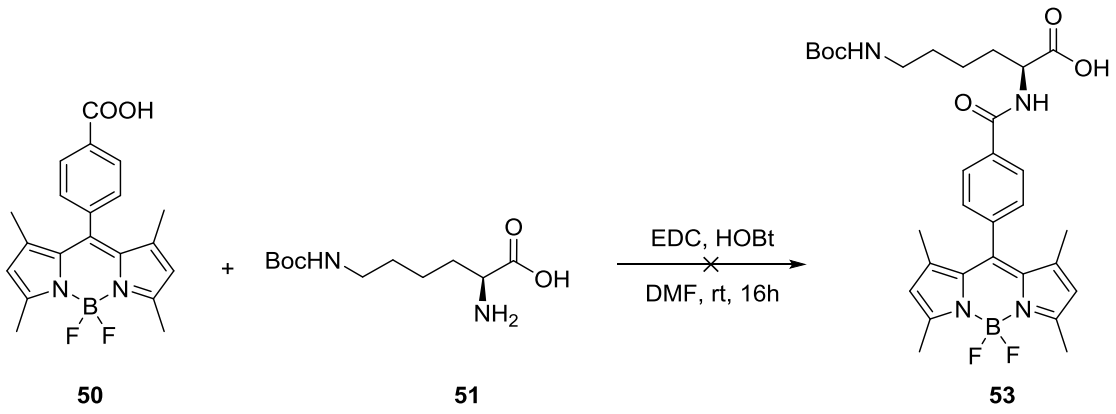

Scheme 3.3: One-pot synthesis attempt for compound **53**.

The following step was to functionalise **50** in a way that acted as a bifunctional dye. In order to achieve this goal, a protected lysine derivative (Fmoc-Lys(Boc)-OH) was employed. One of the protecting groups needed to be removed to use the free amine in the amino acid in the coupling to the fluorophore. Initially, the Fmoc group was removed by treating the amino acid with piperidine in DMF, resulting in the amino acid Lys(Boc)-OH (**51**). The activation of the carboxylic acid using N-(3-dimethylaminopropyl)-N′-ethylcarbodiimide hydrochloride (EDC·HCl) and 1-hydroxybenzotriazole (HOBt) as coupling reagents was attempted to conduct the reaction in a one-pot process (Scheme 3.3).

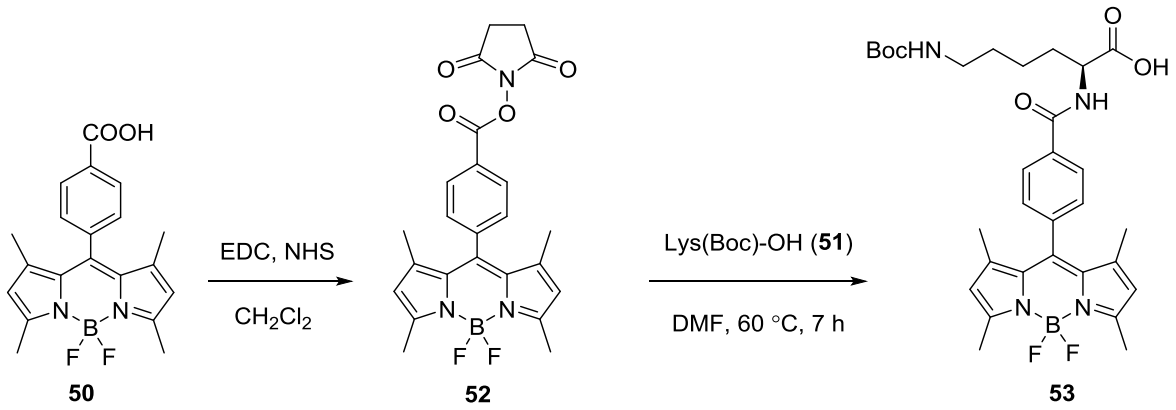

Scheme 3.4: Reaction conditions for the synthesis of **53** through the succinimidyl activated BODIPY.

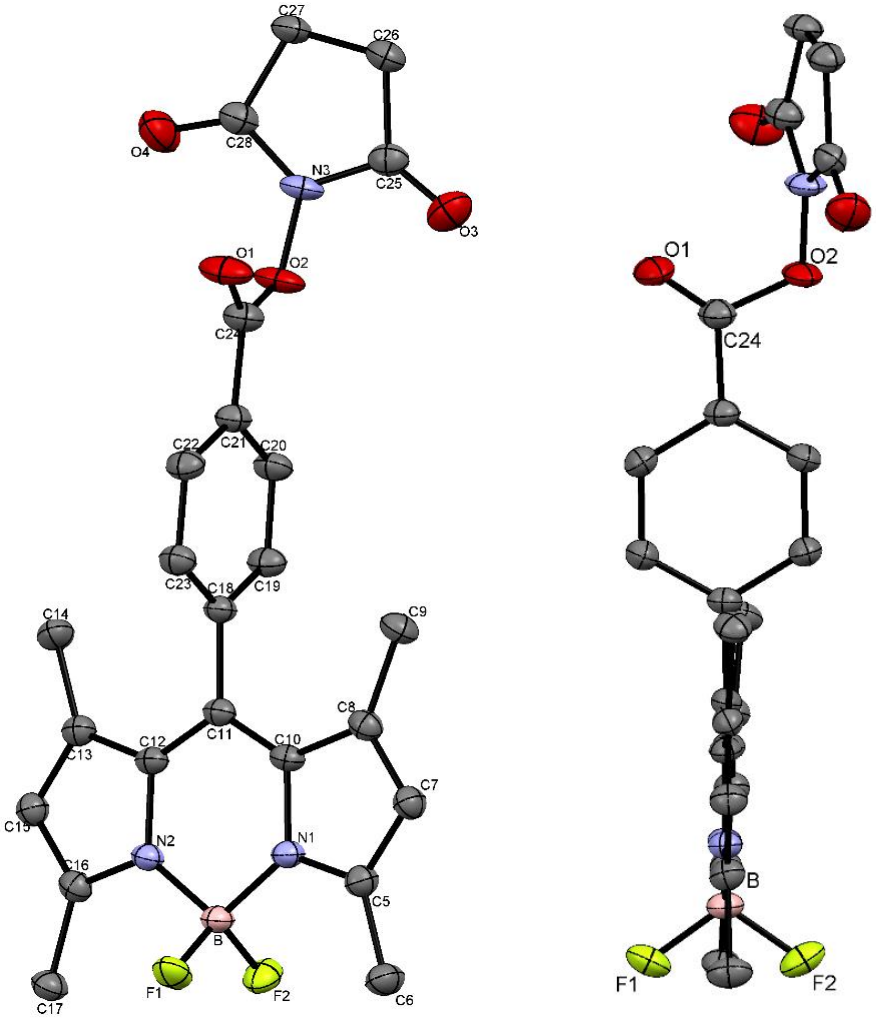

Figure 3.1: Two ORTEP representations of compound **52**. Thermal ellipsoids represented at 50% probability. Hydrogen atoms have been omitted for clarity.

However, the outcome of the reaction did not provide successful results even after increasing the reaction time (Scheme 3.3). Therefore, another activation strategy was followed where the activation of the carboxylic acid and the coupling were performed in a stepwise manner. The carboxylic acid in the BODIPY unit was reacted with EDC·HCl and N-hydroxysuccinimide following similar reaction conditions found in the literature (Scheme 3.4).[7] The activated ester (**52**) was isolated and purified by flash column chromatography.

Crystals suitable for single crystal X-ray crystallographic analysis were obtained for **52**. ORTEP representations of the molecule in two different orientations can be seen in Figure 3.1 and the packing arrangement in Figure 3.2. A selection of bonds and angles are presented in Table 3.1. A selection of bonds and distances for the precursor (**50**) obtained from a crystal structure in a literature reference have been included for comparison.

Table 3.1: Selected bond angles and distances for compound **50** and **52**. Plane 1 is formed by the atoms of the dipyrromethene core excluding the methyl groups and fluorine atoms. Plane 2 is formed by the atoms in the phenyl substituent. Plane 3 is formed by the atoms of the succinimide group.

Distance / angle	**50**[8]	**52**
N1-B (Å)	1.5486 (6)	1.5483 (18)
B-F1 (Å)	1.397 (5)	1.3910 (19)
B-F2 (Å)	1.398 (5)	1.3845 (19)
N1-C5 (Å)	1.342 (5)	1.3465 (19)
N1-C10 (Å)	1.407 (4)	1.3988 (17)
O1-C24 (Å)	1.292 (5)	1.1854 (19)
O2-C24 (Å)	1.253 (5)	1.4000 (19)
O2-N3 (Å)	-	1.3848 (15)
F1-B-F2 (º)	108.1 (3)	109.52 (12)
N2-B-N1 (º)	107.7 (3)	106.82 (11)
N1-B-F1 (º)	109.9 (3)	110.18 (12)
N1-B-F2 (º)	110.0 (3)	109.90 (12)
O1-C24-O2 (º)	121.7 (4)	122.41 (14)
C24-O2-N3 (º)	-	112.50 (11)
Angle planes 1 - 2 (º)	81.15	86.03
Angle planes 1 - 3 (º)	-	17.46
Angle planes 2 - 3 (º)	-	76.52

The planarity of the BODIPY core is evident just by observing the representations of the structure in Figure 3.1. It is also evident that the phenyl substituent is almost perpendicular to the BODIPY core. This fact can be easily observed in Figure 3.1 but also confirmed by measuring the angle between the plane formed by the atoms in the dipyrromethene unit (excluding methyl groups and fluorine atoms, plane 1) and the plane formed by the carbon atoms in the phenyl group (plane 2) that is 86.03º. This angle increases from the carboxyphenyl BODIPY **50**, where this angle has a value of 81.15º, as an effect of the substitution of the COOH group. The plane formed by the atoms in the succinimide substituent forms an angle of 17.46º with the dipyrromethene core and an angle of 76.52º with the phenyl group respectively.

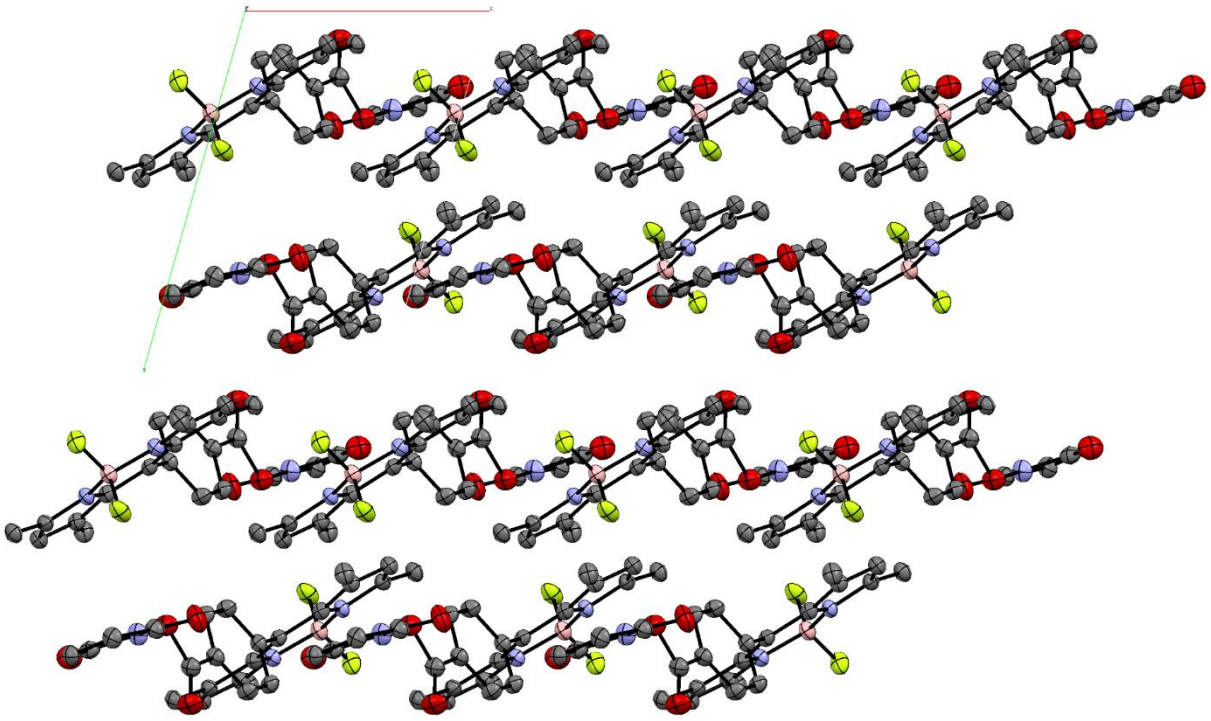

Figure 3.2: Molecular structure of **52** showing the unit cell. View along the c axis. Thermal ellipsoids represented at 50% probability. Hydrogens have been omitted for clarity.

The F1-B-F2 angle has a value of 109.52º for **52** and it increases 1.42º compared to the starting material. The dihedral angle formed by F1-B-N1-C5 has a value of 61.35º respectively. The angles formed by N1 with the boron atom and the two fluorine atoms (F1, F2) are very similar, differing in less than 1º. Similarly, the bond distances in the BF_2 moiety, both are basically identical with a small difference of 0.01 Å. In a different manner, the bond distances of N1 with the carbon atoms in the pyrrole group in **50** and **52** are not equal. The N1-C10 distance in **52** is 1.3988 Å while the N1-C5 distance is considerably shorter, 1.3465 Å. Lastly, it can be observed how the O2-C24 distance increases with the formation of the ester bond from the starting material (1.253 and 1.292 Å) to the activated intermediate (1.4000 Å). The O1-C24-O2 angle, however, is kept relatively unchanged at ca. 122º.

After the activated BODIPY was characterised, some reaction conditions were tested in the synthesis of **53** (Scheme 3.4, second step). Initially, dichloromethane was used as a solvent and different reactions and times were tested but the observed conversion was not optimal. Therefore, the solvent was replaced for DMF and the best conditions resulted from heating compound **52** and the amino acid Lys(Boc)-OH to 60 ºC. The BODIPY-Lys derivative **53** was purified by flash column chromatography and obtained in good yield. Full characterisation was carried out for this compound although no crystals suitable for single crystal X-ray crystallography were obtained using the conditions previously employed for **52** neither changing solvents nor crystallisation method.

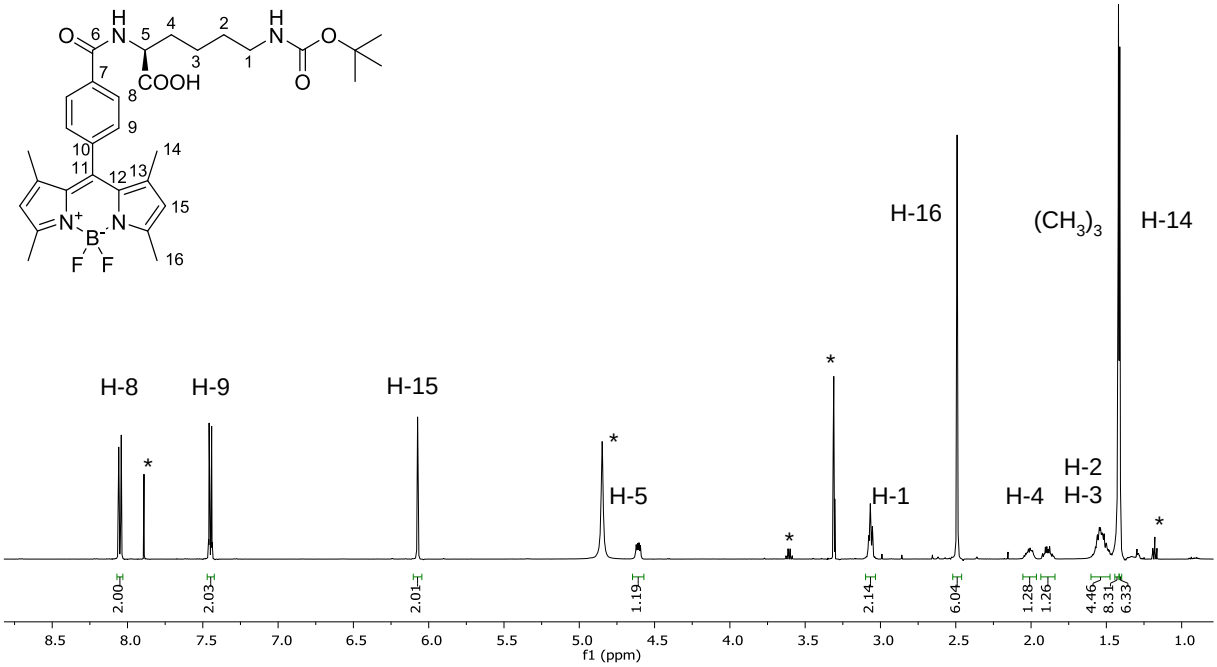

Figure 3.3: ^{1}H NMR spectrum (CD_3OD) of compound **53**. [*Traces of residual solvents].

The ^{1}H NMR spectrum of **53** can be observed in Figure 3.3. The characteristic pattern for the BODIPY group is conserved unchanged with respect to the starting materials including the resonances for the p-substituted aromatic group, the methyl groups and β protons as singlets. The resonances for the lysine group are observed upfield, being H-5 the most deshielded the resonance.

The assignation of the ^{1}H NMR spectrum was carried out using a 2D ^{1}H-^{1}H COSY spectrum (Figure 3.4). In this spectrum, the correlations corresponding to vicinal protons are displayed. However, in some cases, long range correlations can be observed. This is the case of β protons (H-15) and the methyl groups (H-14 and H-16) where a ^{4}J correlation is observed. The resonance of H-5 has correlations with two resonances, corresponding to H-4 (highlighted in red in Figure 3.4). This is explained because the methylene group in H-4 is diastereotopic. The two geminal H-4 protons give separate resonances (multiplets at ca. 1.9 and 1.7 ppm) due to the presence of the adjacent chiral centre in position 5.

H-1 can be identified as a terminal methylene because it has just one correlation with the overlapping resonances of H-2 and H-13. The singlets present in the aliphatic region correspond to the methyl and to the tert-butyl groups respectively. The assignation of H-8, H-9 and H-14, H-16 were realised based on chemical shift values encountered in the literature and in a 2D NOESY spectrum (see Appendix).

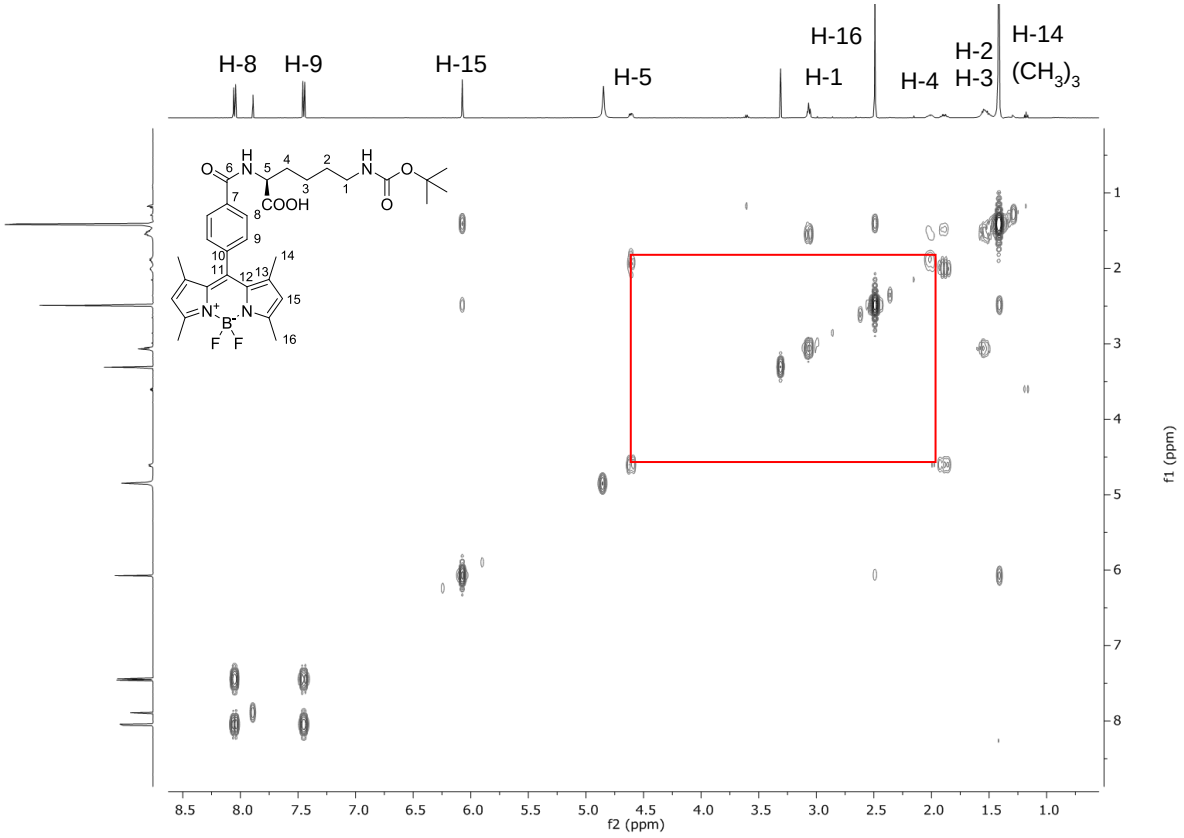

Figure 3.4: ^{1}H-^{1}H COSY (CD_3OD) spectrum of compound **53**.

3.3 Investigations into NIR emitting BODIPY fluorophores

The window of the electromagnetic spectrum going from the near infrared (600 nm) to the far infrared (3 to 100 µm) has a series of advantages that the UV-vis region lacks, as a deep penetration in the tissues or the reduced biological processes/molecules emitting in this region. The absorption of haemoglobin, deoxy-haemoglobin and water has a minimum just above 600 nm. The absorption of water and haemoglobin starts to increase again at 1200 nm (Figure 3.5).[9] Based on these advantages for bioimaging, the preparation of NIR dyes has arisen much interest in recent years.

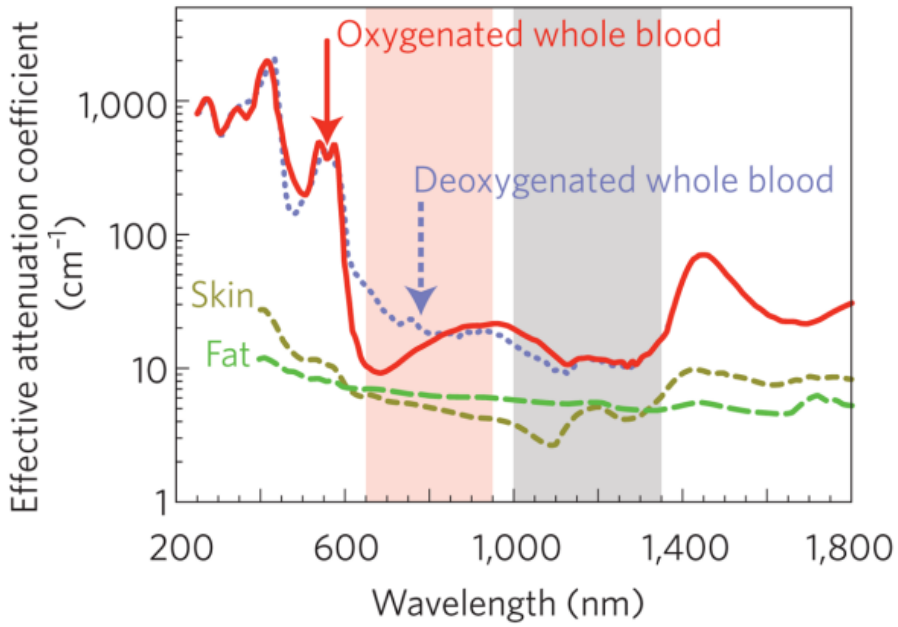

Figure 3.5: Different optical windows in biological tissues against the effective attenuation coefficient. The first NIR window (pink shading) and second NIR window (grey shading) are represented. Figure reproduced from ref. 9 with permission from the publisher.

The shift of the fluorescence emission maximum to the red has been achieved in BODIPY dyes by modifying the structure of the BODIPY core. This shift is also observed in aza-BODIPYS, where the carbon atom in the meso position has been substituted by a nitrogen atom (Figure 3.6, I, II). The preparation of extended aza-BODIPYS have also been explored although, no dramatic change in the maximum emission wavelength was observed. The extension of aromaticity is one example as in di(iso)indomethene dyes (Figure 3.6, III). The strategies mentioned so far imply the modification of the synthetic strategy and structure of the BODIPY to obtain rigid products that imply challenging synthesis and purification processes and limit further reactivity. However, the acidity of the methyl positions in the tetramethylated derivatives can lead to an alternative functionalisation strategy to obtain NIR emitting derivatives. Following a Knoevenagel-type reaction, the methyl groups can be condensed with

an aldehyde, generally a benzaldehyde derivative, to extend the conjugation (Figure 3.6, IV).[10] The introduction of 1, 2, 3 or 4 styryl moieties can be forced by changing the reaction conditions although the purification of reaction mixtures containing more than two derivatives has been described to be challenging. Tetrasubstituted derivatives can be obtained prolonging the reaction time[11] although stepwise condensations has also been described[12]. The degree of red-shift observed in the fluorescence emission maximum is dependent on the number of styryl moieties introduced in the BODIPY core.[12]

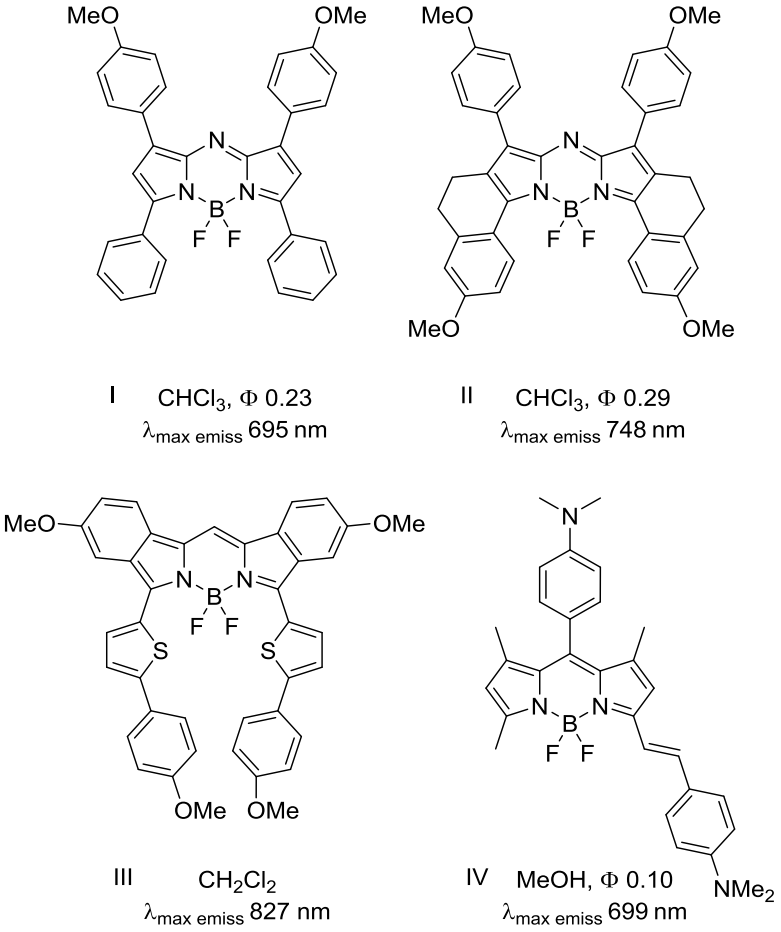

Figure 3.6: Structures of different BODIPY derivatives with NIR fluorescence emission maxima.[1]

In spite of providing a smaller red-shift, the introduction of styryl groups has a number of advantages as conserving the majority of the structure of the BODIPY and other functionalities, being a post-synthetic modification in the BODIPY preparation and not requiring complex starting materials. In addition, a pair of similar fluorophores (before and after modification) with different absorption and emission wavelengths are obtained. Therefore, the acidity of the methyl groups was exploited in a Knoevenagel-type reaction with p-dimethylaminobenzaldehyde. No examples of this reaction in the presence of a carboxylic acid group were found in the literature to the best of our knowledge thus no information about possible synthetic difficulties was available in advance.

The reaction was attempted using the carboxylic acid derivative, **50**, as starting material under Knoevenagel conditions except molecular sieves were used instead of a Dean-Stark apparatus (Scheme 3.5). The purification of the reaction mixture, however, proved difficult as the starting material and products had very similar retention factor and co-eluted under column chromatography conditions. Interestingly, only the mono(substituted) derivative was identified. This fact can be probably explained on the basis of the concentration of the reagents in the reaction mixture.

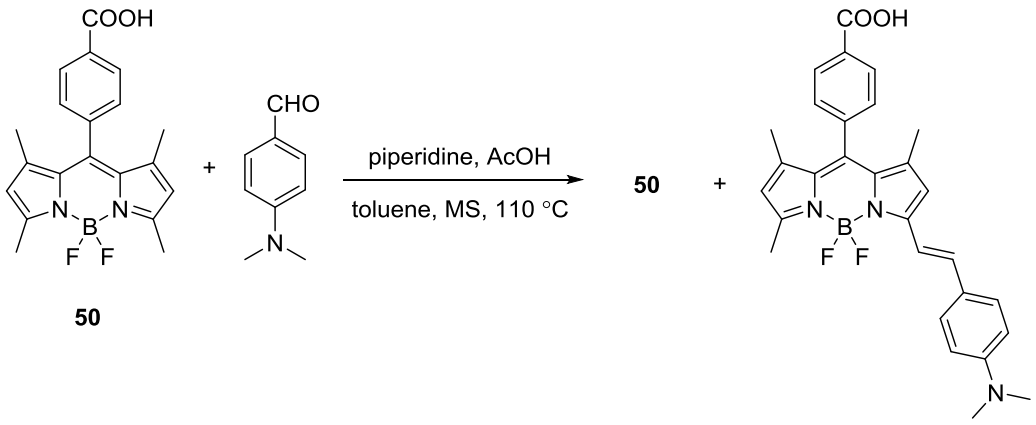

50

Scheme 3.5: Reaction conditions attempted on the synthesis of a styryl-substituted BODIPY.

Consequently, another strategy was attempted to obtain the red-shifted derivative. The final target of this modification was to obtain a bimodal ligand applying an approach of identical characteristics as the one described above. Following this reasoning, the intermediate ester was considered due to the reduced polarity, which may help during the purification, and the presence of examples of carboxyphenyl esters undergoing this reaction in the literature.[13, 14]

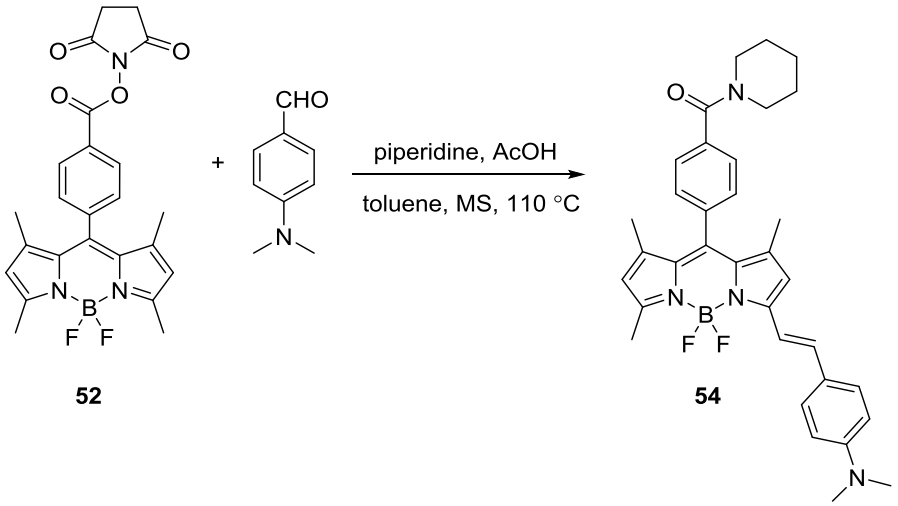

52 **54**

Scheme 3.6: Reaction of activated ester **52** under Knoevenagel conditions.

However, when the previously attempted conditions were applied, BODIPY **52** reacted with the excess of piperidine forming an amide bond (Scheme 3.6). This derivative was nonetheless, isolated by flash column chromatography on silica and characterised.

The possibility of purifying **54** from the reaction mixture was encouraging to further use **52** as a starting material. In order to overcome the undesired reactivity of the activated succinimide group, other non-nucleophilic bases were tested (i.e. DIPEA and Et_3N). Unfortunately, only the starting material was recovered in these reactions. The basicity of all amines is in the same range and although they should subtract the protons of the methyl group, the role of piperidine in the mechanism of the reaction is not trivial. As studied by Thelakkat *et al.*, piperidine plays a principal role in the mechanism of the Knoevenagel-typpe reaction in BODIPYs and is essential in order to obtain the desired product.[15]

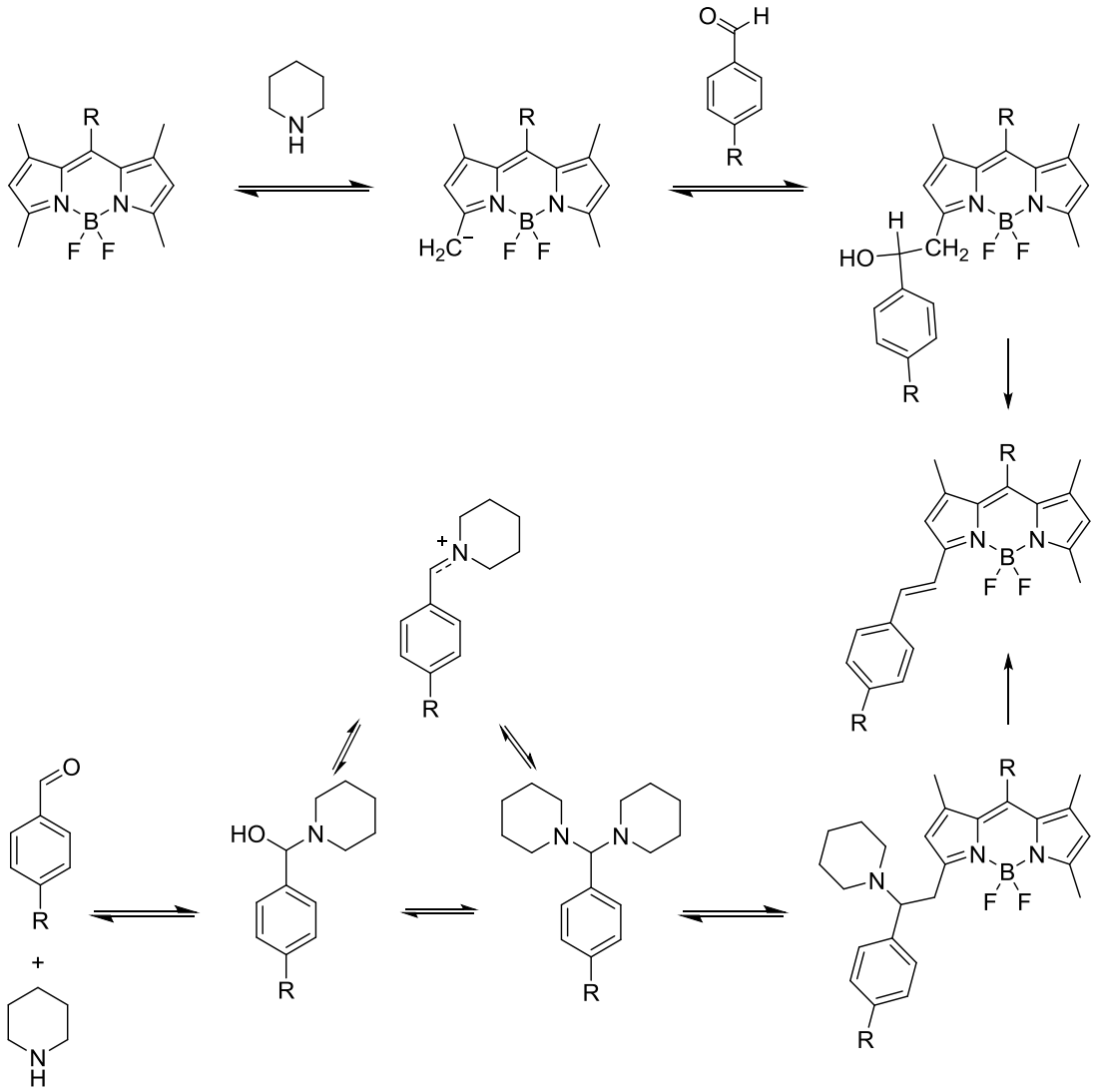

Scheme 3.7: Proposed mechanisms in a Knoevenagel-type condensation for BODIPYs.

Two possible mechanisms have been described for a Knoevenagel reaction, namely the Hann-Lapworth[16] and the organocatalytic (Knoevenagel)[17] mechanisms. In the first one, the base deprotonates the methyl group creating a methylene active intermediate that attacks the aldehyde forming a β-hydroxy intermediate (Scheme 3.7, top). This intermediate generates the vinylidene product by the loss of a water molecule.

However, in the organocatalytic mechanism, piperidine also reacts with the aldehyde to produce a hemiaminal that can further react with another piperidine molecule to generate the aminal or the iminium ion by dehydration (Scheme 3.7, bottom). A β–amino intermediate results of the reaction with the acidic methyl group in the BODIPY that gives the vinylidene product by elimination of piperidine.[15, 17]

The isolation by the corresponding aminal by Thelakkat *et al.* in their work about BODIPYs confirmed the idea that Knoevenagel-type reactions in these species occur through an organocatalytic mechanism. The lack of reactivity of **52** with tertiary amines indicates that this specific derivative obeys the same principle as the examples described in the literature hence piperidine plays a crucial role in the formation mechanism of the vinylidene product. Therefore, the use of the activated ester **52** in Knoevenagel reactions yields the piperidine amide precluding from any further consideration.

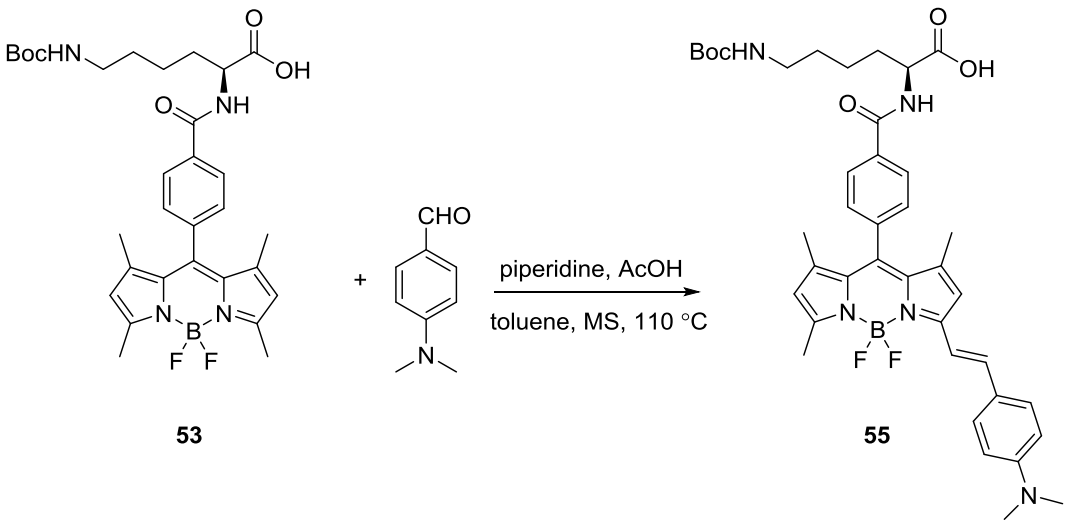

53 **55**

Scheme 3.8: Reaction conditions for the preparation of the styryl-substituted BODIPY from **53**.

In light of these difficulties, the reaction was attempted with the BODIPY species **53**, including the lysine moiety. The reaction was conducted under the same conditions using piperidine as a base in toluene with molecular sieves (Scheme 3.8). The product was isolated and purified by column chromatography followed by recrystallisation. The major observed product was the mono(styryl) derivative (**55**). The trans geometry of the styryl unit can be confirmed by looking at the characteristic coupling constant of the double bond resonances in the ^{1}H NMR spectrum (^{3}J = 16.2 Hz).

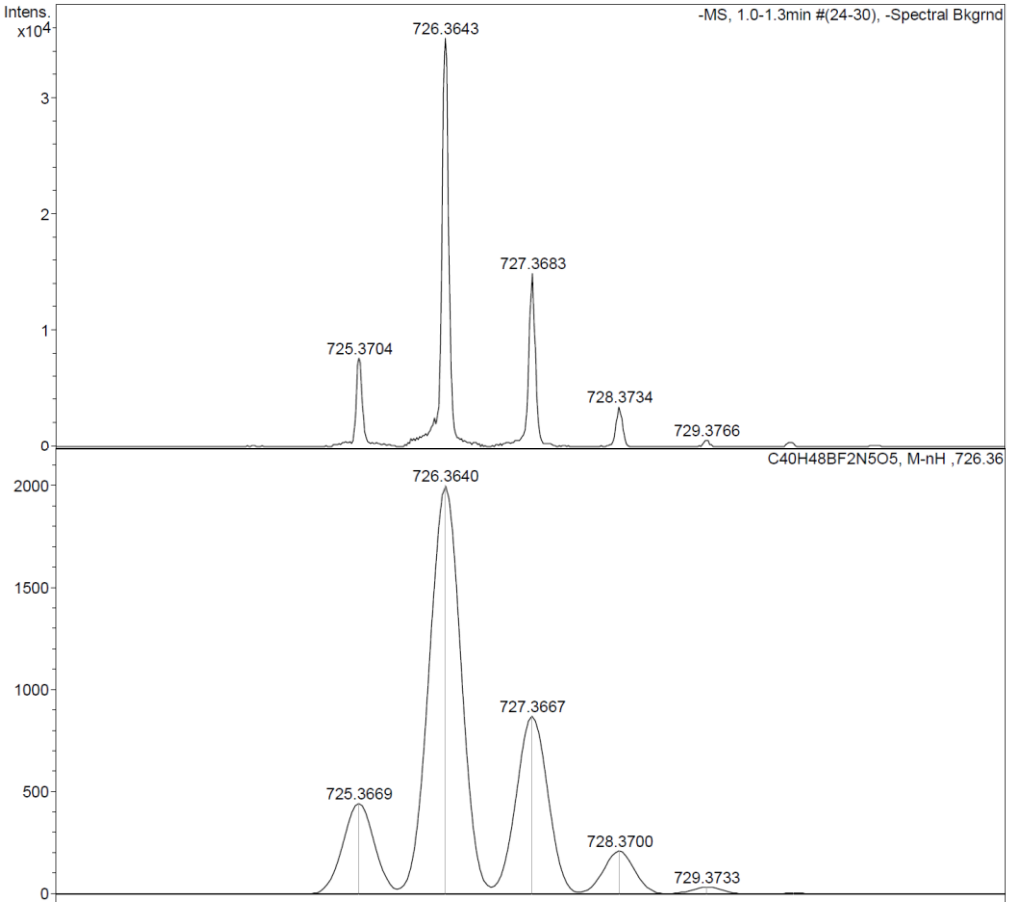

Figure 3.7: Experimental (top) and predicted mass isotopic pattern (bottom) for **55**.

The ESI mass spectrum of the reaction product after column chromatography can be observed in Figure 3.7 along with the representation of the theoretical isotopic pattern. The base peak of the spectrum corresponds to the product $[M–H]^-$. The photophysical properties of **54** and **55**, including fluorescence emission maxima and quantum yields will be commented on in Section 3.6.

3.4 Synthesis attempt of a BODIPY – thiosemicarbazone fluorophore

The coupling of BODIPY **52** with a mono(thiosemicarbazone) ligand derivative was also attempted. The attachment of a BODIPY fluorophore to bis(thiosemicarbazonato) metal complexes has been described before in order to allow for the study of the thiosemicarbazonato aliphatic derivatives *in vitro*. Dilworth *et al.* reported the preparation of Ni(II), Zn(II) and Cu(II) complexes with different alkylic thiosemicarbazone backbones linked to a BODIPY fluorophore to study the stability of the compounds *in vitro* by two-photon fluorescence lifetime imaging measuring the lifetime distribution of the compounds in cells.

In the case of the compounds prepared herein, the attachment of a BODIPY fluorophore to the ligand could help to enhance the fluorescence signal of the ligands or complexes for their use *in vitro*. Furthermore, the synthesis of mono(thiosemicarbazonato) complexes could be attempted following the conditions described in Chapter 2.

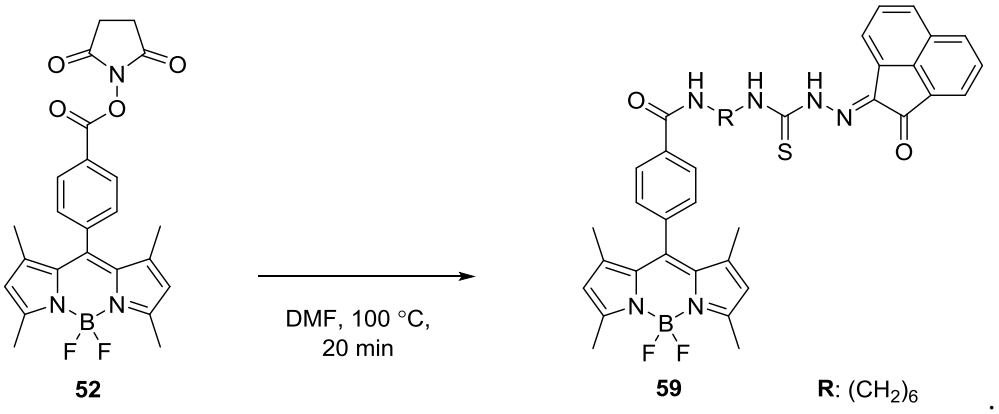

Figure 3.8: Synthesis conditions applied for the synthesis of **59**.

The synthesis attempt of **59** was carried out applying the conditions evaluated in this chapter for the preparation of bifunctional derivatives. However, the starting material was not totally consumed as observed by TLC, even with prolonged reaction times. The application of microwave conditions heating the reaction mixture in DMF at 100 ºC for 20 min yielded the better conversion towards the product.
The product could be detected by mass spectrometry in negative ESI mode as the molecular peak of the spectrum with a chlorine atom $[M+Cl]^-$ and a m/z value of 739.2696 with respect to the theoretical m/z value of 739.2605.

The optimisation of the reaction conditions and evaluation of purification strategies constitutes a fundamental part of the future work needed prior of the potential application of these compounds as potential imaging probes.

3.5 Deprotection attempts for the bifunctional BODIPY derivatives

The next step in the preparation of the targeted nanoprobe involved the coupling of the fluorophore to the bombesin targeting peptide before the final step of supporting both on the functionalised SWNT. The mentioned final step requires the deprotection of the NHBoc group in the bombesin-BODIPY conjugate and the coupling with the terminal carboxylic acid functionalised nanotubes.

In order to explore and optimise the deprotection reaction conditions, some tests were carried out using only the fluorophore. The removal of Boc protecting groups might be challenging in BODIPY species but it has been described to occur successfully using HCl 4 M in dioxane. The presence of minor decomposition was observed but the by-products were easily separated by chromatography.[18] However, depending on the structure of the BODIPY dye, the deprotection was not achieved with protic acids as HCl, TFA or p-toluenesulfonic acid under mild conditions and the application of harsher conditions lead to the decomplexation of the BF_2 moiety.[19] Furthermore, the use of protic acids as HCl or TFA has been described as an efficient method to remove the BF_2 moiety yielding the corresponding dipyrrins in quantitative yields depending on the substituents.[20] The use of Lewis acids is an alternative to the use of Brønsted acids in the deprotection of tertbutoxycarbonyl groups.[21, 22] The same reagent used in the last step of the synthesis of BODIPY dyes, $BF_3{\cdot}OEt_2$, has been applied to the deprotection of Boc groups in substituents of BODIPY dyes in moderate yields.[19]

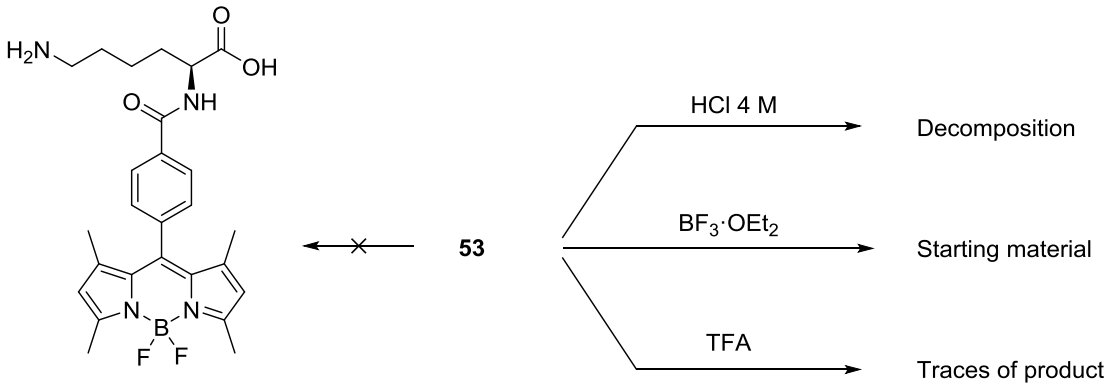

Scheme 3.9: Conditions attempted in the deprotection of the Boc group in BODIPY **53**.

Unfortunately, in the case of **53**, the use of these conditions proved unsuccessful (Scheme 3.9). The use of HCl 4 M in AcOEt lead to the decomposition of the starting material and only a pyrrole by-product was detected by ^{1}H NMR. The use of $BF_3{\cdot}OEt_2$ did not work as described in the literature and only a small conversion was observed by TLC even with large excesses of boron trifluoride and long reaction times.

Furthermore, sodium iodide is another reagent that has been described to deprotect Boc groups in amino acids by the catalytic production of HI. However, in this case only the starting material was recovered. Surprisingly, neat TFA did not produce the removal of the BF_2 group, and deprotected the starting material but the conversion was not complete, the reaction required long reaction times and the presence of decomposition products was also observed.

In light of the difficulties encountered to remove the protecting group from the BODIPY fluorophore **53**, a different modification was pursued for the BODIPY dye. It was necessary that the deprotection of the amino group was conducted under mild conditions in order to avoid decomposition or racemisation of the peptide once the conjugate was obtained. Therefore, the complementary analogue of the amino acid was prepared by deprotecting the Boc group of the protected lysine instead of the Fmoc. The deprotection was achieved by stirring the amino acid in a solution of CH_2Cl_2 / TFA (1:1) for 3 h at room temperature, yielding the Fmoc-Lys-OH species **56**. The subsequent coupling with activated BODIPY **52** was successfully conducted following similar reaction conditions as previously described (Scheme 3.10).

In this case, the deprotection did not present any problems and the reaction proceeded smoothly using piperidine (25% in DMF) as a base and stirring at room temperature for 3 h until the starting material was no longer observed by TLC. The deprotected product **58** was obtained in 83% yield.

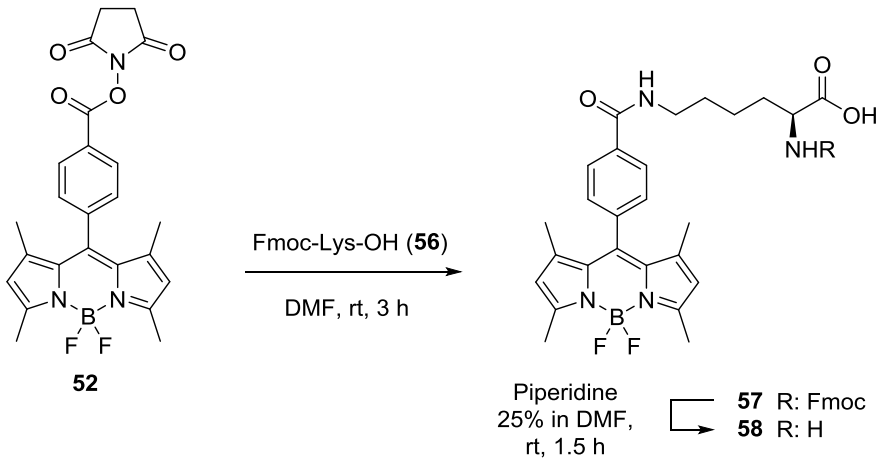

Scheme 3.10: Synthesis and deprotection of a BODIPY dye with a bifunctional linker.

The new BODIPY fluorophores were characterised using routine spectroscopic techniques. The ^{1}H NMR spectrum of **57** presented the characteristic aromatic resonances for the Fmoc protecting group along with the phenyl resonances of the BODIPY core in addition to the aliphatic resonances corresponding to the amino acid.

The ^{1}H NMR spectrum of **58** can be observed in Figure 3.9. The aspect of the spectrum is comparable to the one presented by **53** excluding the Boc group. It can be observed how the two protons attached to C-3 are diastereotopic due to the presence of the adjacent chiral centre. The multiplicity of H-2 is a triplet while all the other aliphatic resonances are present as multiplets.

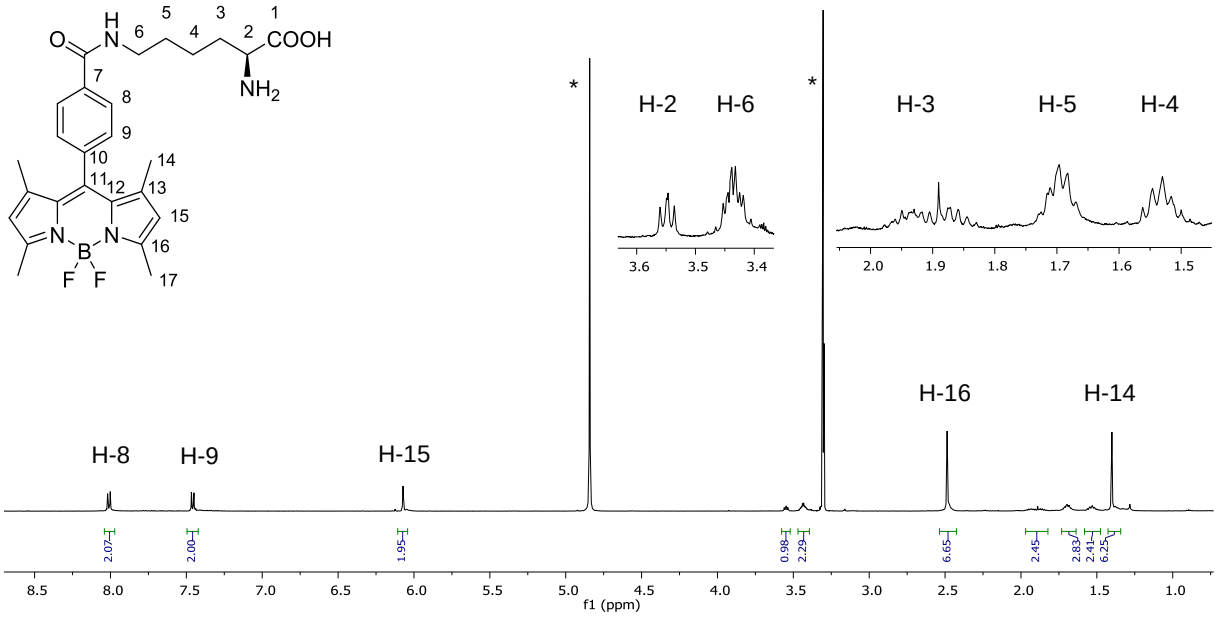

Figure 3.9: ^{1}H NMR spectrum (CD_3OD) of compound **58** [*Traces of non-deuterated/partially deuterated solvents].

The observed deprotection problems for the Boc group, limited the introduction of the near-IR derivative **55** in the targeted nanoprobe. However, a red-emitting targeted fluorescence conjugate can be prepared incorporating the targeting peptide. The details of the conjugation of the fluorophores with the targeting peptide are described in Chapter 5.

3.6 Spectral characterisation of prepared BODIPY fluorophores and preliminary tests *in vitro*

The photophysical characterisation of compounds **53** to **58** was carried out by UV-vis and flurorescence spectroscopies. A summary of the spectral properties for compounds **53** to **58** can be found in Table 3.2. The quantum yields have been calculated according to the Equation 3.1 using $[Ru(bipy)_3]Cl_2$ as a reference. The characteristics of the starting material (**50**) have been included for comparison purposes. It can be observed how the modification of the starting material, **50**, with the protected amino acid, either with the Boc or Fmoc protecting groups (**53** and **57** respectively) does not change considerably the maximum absorption or emission wavelengths. These parameters remain virtually unchanged for the deprotected derivative **58**. The $\lambda_{max\text{-}abs}$ is observed at ca. 500 nm with the $\lambda_{max\text{-}em}$ at ca. 510 nm thus presenting a Stokes shift of only 10 nm. However, the quantum yields present considerable variations from the carboxyphenyl BODIPY to the species incorporating the amino acid, and these differences are more appreciable between the two variants when the amino acid is coupled through the α or ε amino group.

$$\Phi_S = \Phi_R * \frac{A_r}{A_s} * \frac{E_S}{E_r} * \frac{I_r}{I_s} * \frac{n_s{}^2}{n_r{}^2}$$

Equation 3.1: Expression used to calculate quantum yield (where r refers to the reference $[Ru(bipy)_3]Cl_2$ in water, s refers to the compound of interest, A is the absorbance of the solution, E is the corrected emission intensity, I is the relative intensity and n is the refractive index of the solutions).

The quantum yield of the starting material decreases when the Boc-protected lysine is introduced into the fluorophore (from 0.59 to 0.46). Surprisingly, the quantum yield when the Fmoc protected amino acid is introduced increases with respect to the starting material (from 0.59 to 0.85). The rationale behind this increase might be attributed to the bulky aromatic protecting group that makes the molecule more rigid and hinders the non-radiative relaxation from the excited state.

However, this explanation is no longer applicable to the deprotected product **58**, where the quantum yield decreases (0.81 vs. 0.85) but is still considerably higher compared to the starting material. Therefore the increase in quantum yield may be attributed to different factors and to the position of the carboxylic acid in the substituent could be one of them. In the second derivative, the carboxylic acid of the amino acid is separated from the BODIPY by a chain of five carbon atoms which can act in favour of intramolecular hydrogen bonding interactions enhancing the rigidity of the molecule.

Table 3.2: Spectral properties of BODIPY derivatives in DMSO solutions. Data for **50** have been extracted from ref. 6 where the measurements were conducted in EtOH.

Compound	$\lambda_{max\text{-}abs}$ (nm)	$\lambda_{max\text{-}em}$ (nm)	$\Delta\lambda$ (nm)	Φ_f
50[6]	500	509	9	0.59
53	500	510	10	0.46
54	601	694	93	0.03
55	602	752	150	0.009
57	499	510	11	0.85
58	500	510	10	0.81

In the case of the two derivatives incorporating N,N-dimethylstyryl units, it can be observed how the maximum absorption and emission wavelengths are effectively shifted to the NIR region of the spectra. The $\lambda_{max\text{-}abs}$ is pushed 100 nm until the 600 nm and the fluorescence emission maximum is shifted to almost 700 nm for **53** and to a longer wavelength (752 nm) for **55**. It is worth mentioning that the quantum yields of these two species drop dramatically compared to the BODIPYs emitting in the visible range. The derivative presenting the Boc-Lys moiety, **55**, presents the lowest quantum yield. The UV-vis absorption excitation spectra and fluorescence emission spectra for **55** and **58** can be observed in Figure 3.10.

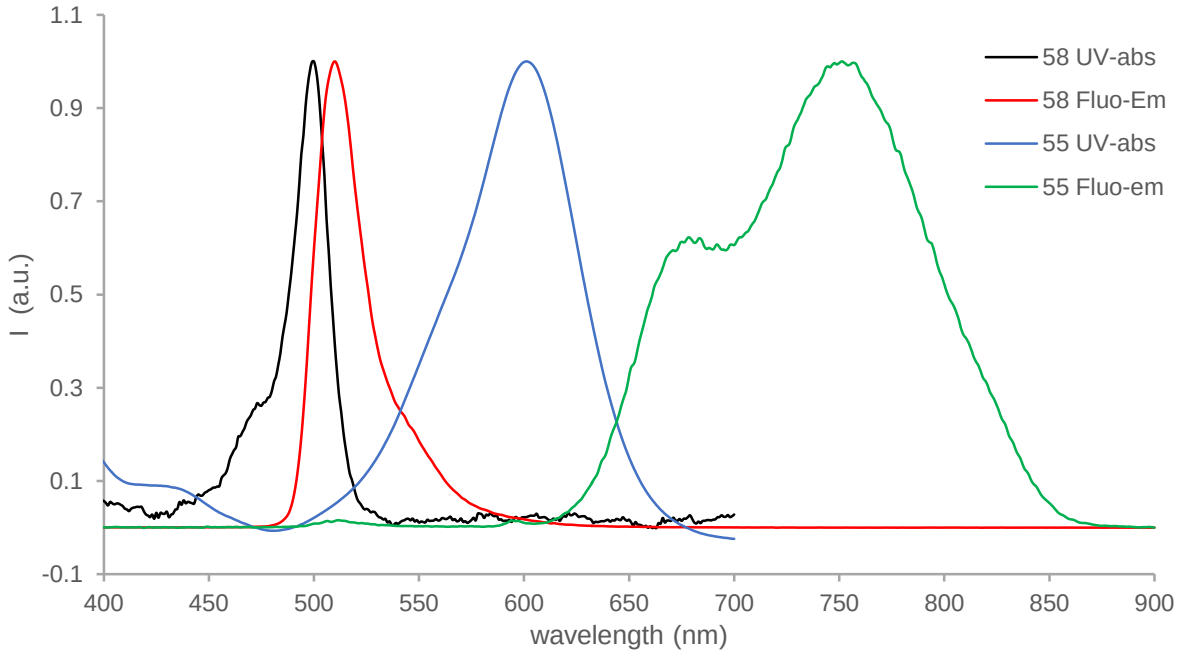

Figure 3.10: Normalised UV-vis absorption spectra for **58** (black line) and **55** (blue line) and normalised fluorescence emission spectra for **58** (red line) and **55** (green line).

It can be clearly observed in Figure 3.10 how the visible emitting derivative, **58**, has a sharp absorption and emission spectra while the Stokes shift is small. In the case of **55**, the absorption and emission spectra are broad and the resulting Stokes shift is larger in the order of hundreds of nm.

After the spectral characterisation of the dyes was conducted, the efficiency of as-prepared BODIPY compounds as imaging agents in PC-3 cells was evaluated. The compounds were added to PC-3 cells in serum free medium (1% DMSO) at a 20 µM final concentration and incubated for 15 min. The images were acquired immediately after in a confocal microscope.

Derivatives **53** and **58** were strongly fluorescent in the green channel with excitation at 488 nm and emission at 518 nm (Figure 3.11). The two derivatives showed similar characteristics despite the differences in the configuration of the lysine linker. The uptake in the cells was concentrated in the cytoplasm and organelles with no apparent preference or uptake in the nucleus. BODIPY dyes are compounds known for targeting the cells endoplasmic reticulum (ER) and mitochondria. In fact, there are commercial dyes for ER staining based on the BODIPY core. However, in this case, the dye seems to be distributed over the cytoplasm although punctuation is observed around the nuclei. Co-localisation experiments would be needed to ascertain the potential preference of the dyes for a specific organelle.

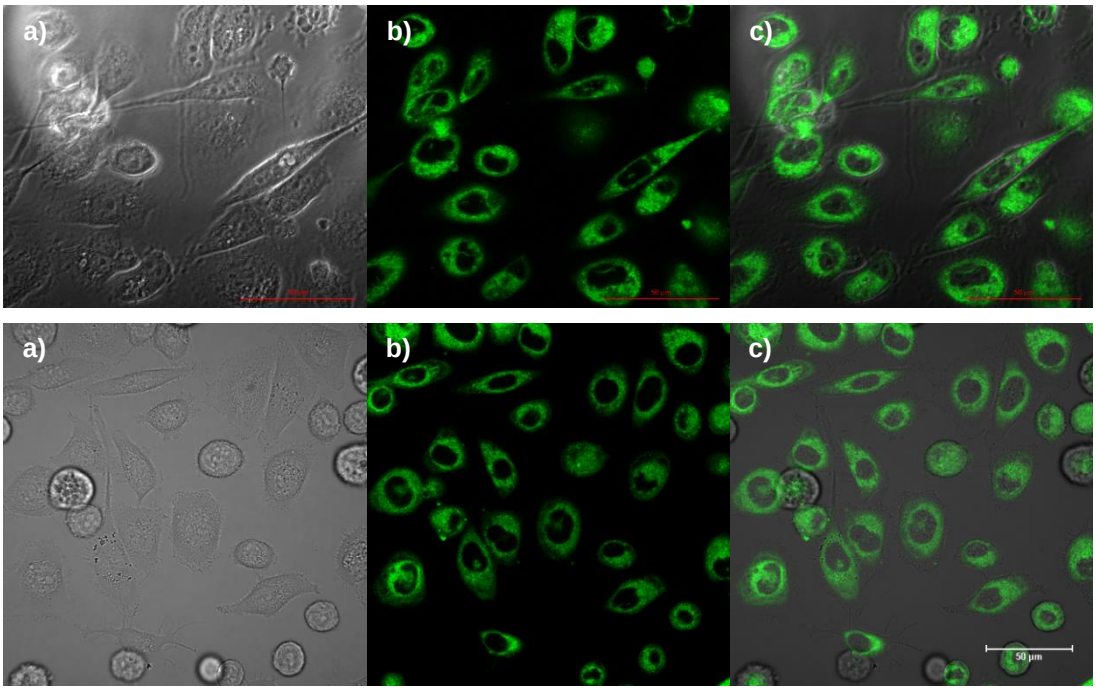

Figure 3.11: Single-photon confocal microscopy images of **53** (top) and **58** (bottom) in PC-3 cells after 15 min incubation, 20 µM 1% DMSO at 37 ºC where a) DIC image, b) green channel, excitation at 488 nm, emission at 518 nm and c) overlay of a) and b). Scalebar: 50 µm.

Derivative **55** showed, however, an intense emission in the green and red channel due to the broader emission profile and the shift of the $\lambda_{max\text{-}em}$ towards the near infrared. In this case, the dye is also distributed in the cytoplasm with no nuclear uptake. However, the higher concentration seems to be displayed in the organelles, probably ER, around the nuclear membrane. Similarly, co-localisation experiments would be needed to ascertain the preference of this species towards a specific organelle in the cell.

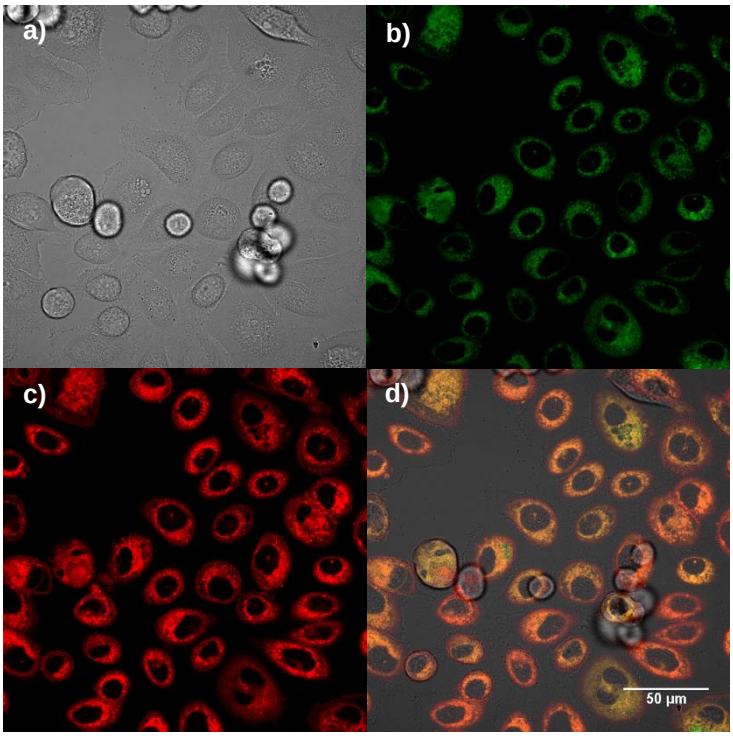

Figure 3.12: Single-photon confocal microscopy images of **55** in PC-3 cells after 10 min incubation, 20 µM 1% DMSO at 37ºC where a) DIC image, b) green channel, excitation at 488 nm, emission at 518 nm and c) red channel, excitation at 561 nm, emission 785 nm d) overlay of a), b) and c). Scalebar: 50 µm.

3.7 Conclusions

BODIPY fluorophores have a number of advantages compared to other organic or inorganic dyes as high quantum yields, narrow fluorescence emission peaks and possibility to tune their characteristics.

In this chapter a BODIPY derivative bearing a carboxyphenyl function was used as a starting material to obtain bifunctional derivatives. The synthesis of a bifunctional derivative was achieved using a protected lysine with orthogonal amino protected groups. The compounds were obtained from the BODIPY N-succinimide ester after exploring other activation strategies for the acid that did not provide satisfactory results.

The shift of the fluorescence emission wavelength from the visible to the NIR was also explored. This can be achieved in BODIPY dyes taking advantage of the acidic methyl groups in a Knoevenagel-type reaction that introduces one or more styryl groups. Under the reaction conditions tested, only the species with one styryl group was observed. The purification of these family of compounds proved especially challenging and the best results were obtained using the BODIPY-Lys(Boc) derivative as starting material.

The removal of the Boc protecting group in the BODIPY-lysine compound was explored in order to optimise the reaction conditions and to avoid problems once the peptide-dye conjugate was prepared. Despite several examples being described in the literature, the deprotection of the Boc group included in the BODIPY resulted problematic. The most promising results were obtained where acids such as TFA were used and it was found that the long reaction times needed could compromise the integrity of the peptide by decomposition or racemisation.

Consequently, the complementary BODIPY derivative with an Fmoc protecting group was prepared. In this case, the removal of the protecting group proceeded successfully in a short time using piperidine (25% in DMF).

The spectral properties of the as-prepared BODIPY dyes were evaluated and the quantum yields measured. The carboxyphenyl starting material and all the compounds incorporating the amino acid showed identical absorption and emission properties and small Stokes shifts. However, the quantum yields varied, being considerably higher in the last derivatives prepared with the Fmoc protecting group. The red-emitting species showed shifted absorption maxima wavelengths in the order of 100 nm compared to the visible derivatives and emission maxima wavelengths shifted more than 200 nm. Unfortunately, in this case, the quantum yields were reduced several orders of magnitude.

Finally, the most promising derivatives were tested in prostate cancer cells (PC-3) by confocal microscopy showing good uptake in the cellular cytoplasm and organelles and promising properties as fluorescence optical dyes. The specific location of the dyes in the cellular organelles requires of additional imaging experiments and co-localisation experiments.

3.8 References

1. A. Loudet and K. Burgess, *Chem. Rev.*, 2007, **107**, 4891-4932.
2. T. Scientific, BODIPY Dye Series - Section 1.4, https://www.thermofisher.com/uk/en/home/references/molecular-probes-the-handbook/fluorophores-and-their-amine-reactive-derivatives/bodipy-dye-series.html#head1, Accessed 17/09/2016.
3. G. Ulrich, R. Ziessel and A. Harriman, *Angew. Chem. Int. Ed.*, 2008, **47**, 1184-1201.
4. V. Lakshmi, M. Rajeswara Rao and M. Ravikanth, *Org. Biomol. Chem.*, 2015, **13**, 2501-2517.
5. S. L. Niu, G. Ulrich, R. Ziessel, A. Kiss, P.-Y. Renard and A. Romieu, *Org. Lett.*, 2009, **11**, 2049-2052.
6. A. Cui, X. Peng, J. Fan, X. Chen, Y. Wu and B. Guo, *J. Photochem. Photobiol. A: Chem.*, 2007, **186**, 85-92.
7. S. Tasan, O. Zava, B. Bertrand, C. Bernhard, C. Goze, M. Picquet, P. Le Gendre, P. Harvey, F. Denat, A. Casini and E. Bodio, *Dalton Trans.*, 2013, **42**, 6102-6109.
8. G.-G. Luo, H. Lu, X.-L. Zhang, J.-C. Dai, J.-H. Wu and J.-J. Wu, *PCCP*, 2015, **17**, 9716-9729.
9. A. M. Smith, M. C. Mancini and S. Nie, *Nat. Nanotech.*, 2009, **4**, 710-711.
10. K. Rurack, M. Kollmannsberger and J. Daub, *Angew. Chem. Int. Ed.*, 2001, **40**, 385-387.
11. O. Buyukcakir, O. A. Bozdemir, S. Kolemen, S. Erbas and E. U. Akkaya, *Org. Lett.*, 2009, **11**, 4644-4647.
12. T. Bura, D. Hablot and R. Ziessel, *Tetrahedron Lett.*, 2011, **52**, 2370-2374.
13. B. Brizet, N. Desbois, A. Bonnot, A. Langlois, A. Dubois, J.-M. Barbe, C. P. Gros, C. Goze, F. Denat and P. D. Harvey, *Inorg. Chem.*, 2014, **53**, 3392-3403.
14. A. Eggenspiller, A. Takai, M. E. El-Khouly, K. Ohkubo, C. P. Gros, C. Bernhard, C. Goze, F. Denat, J.-M. Barbe and S. Fukuzumi, *J. Phys. Chem. A*, 2012, **116**, 3889-3898.
15. K. Graf, T. Korzdorfer, S. Kummel and M. Thelakkat, *New J. Chem.*, 2013, **37**, 1417-1426.
16. A. C. O. Hann and A. Lapworth, *J. Chem. Soc., Trans.*, 1904, **85**, 46-56.
17. S. Bednarz and D. Bogdal, *Int. J. Chem. Kinet.*, 2009, **41**, 589-598.
18. C. Peters, A. Billich, M. Ghobrial, K. Högenauer, T. Ullrich and P. Nussbaumer, *J. Org. Chem.*, 2007, **72**, 1842-1845.
19. Z. Li and R. Bittman, *J. Org. Chem.*, 2007, **72**, 8376-8382.
20. M. Yu, J. K. H. Wong, C. Tang, P. Turner, M. H. Todd and P. J. Rutledge, *Beilstein J. Org. Chem.*, 2015, **11**, 37-41.
21. P. G. M. Wuts and T. W. Greene, in *Greene's Protective Groups in Organic Synthesis*, John Wiley & Sons, Inc., 2006, pp. 696-926.
22. E. F. Evans, N. J. Lewis, I. Kapfer, G. Macdonald and R. J. K. Taylor, *Synth. Commun.*, 1997, **27**, 1819-1825.

Chapter 4 : Functionalisation of Single Walled Carbon Nanotubes

4.1 Overview of functionalisation strategies

Single walled carbon nanotubes (SWNT) have unique properties which make them promising probes for their use in biomedical and sensing fields.[1-3] Their outstanding electrical and mechanical properties make them an excellent scaffold for the building of biosensors.[3] Furthermore, the possibility of performing surface functionalisation, as well as filling functionalisation, has triggered a lot of interest for their application as delivery vectors with drugs or as part of imaging probes.

Much research effort has been devoted to the purification of as-prepared SWNT after synthesis to remove residues of metallic impurities from the catalyst, fullerenes or amorphous carbon. The initial purification methodologies included washing with organic solvents to remove any soluble material such as fullerenes or treatment with acids to remove catalyst particles and amorphous carbon.[4-6] Advanced purification methods were further developed including annealing or steam purification steps in order to remove the oxygen functionalities introduced during purification.[7, 8] The development of these methods allowed for the production of high purity SWNT that are now available from advanced materials companies. Furthermore, the use of SWNT for biomedical applications requires of a functionalisation strategy to allow for the introduction of the molecules of interest, improve stability, and reduce the toxicity of pristine SWNT.[9] In general, this process reduces the SWNT length, reduce their tendency to aggregate and consequently improve their dispersibility in biological media.

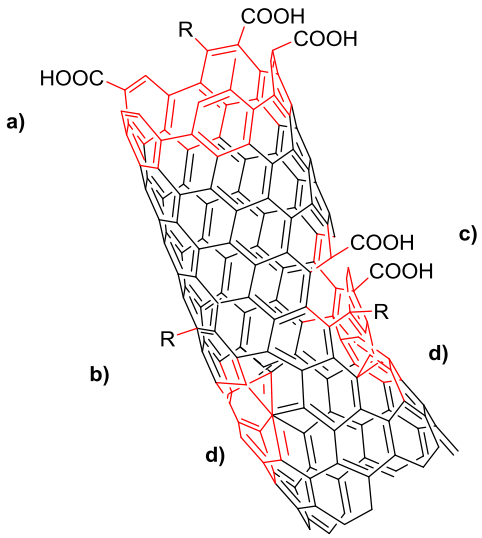

Scheme 4.1: Typical defects found in a SWNT: a) presence of COOH groups in the open end of the nanotube. Other groups as NO_2, OH, H or =O have been reported, b) sp^3 carbon atoms where R: H or OH, c) oxidative damage of the sidewall that generates a hole and the presence of COOH groups, d) presence of five or seven membered rings. Figure adapted from ref. 10.

The chemistry and functionalisation strategies for SWNT have been covered in numerous reviews to date.[11-14] The functionalisation methods for SWNT are generally classified in two categories: covalent and non-covalent modifications.

Non-covalent functionalisation strategies are based on Van der Waals or electrostatic interactions and are normally conducted under mild conditions in standard organic solvents, or even aqueous media. Furthermore, this method presents the advantage of maintaining the integrity of the carbon lattice hence not affecting the intrinsic electrical or mechanical properties of the nanotube. The non-covalent functionalisation of SWNT is generally achieved by polymer wrapping, interaction with biomolecules, as DNA, or adsorption of small molecules, in most cases aromatic molecules where a π-π interaction is possible.[15] However, non-covalently functionalised probes give rise to concerns of potential hazardous effects of the nanomaterial in case the interactions with the functional group are broken or displaced in biological media and the carbon nanomaterial is liberated to the biological medium.[12]

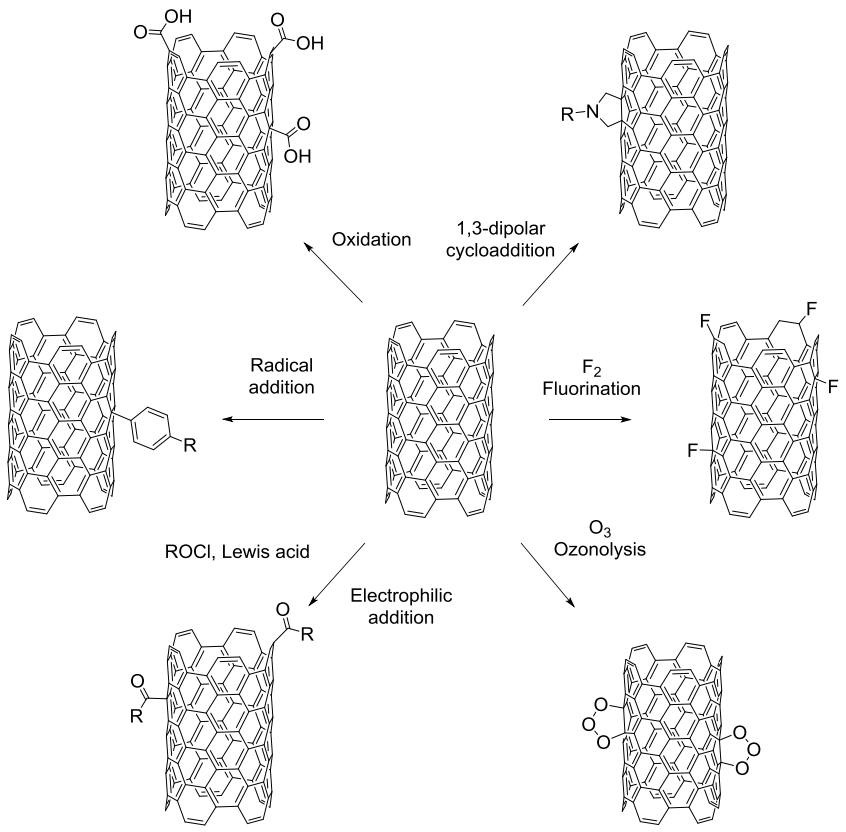

Scheme 4.2: Examples of covalent functionalisation of SWNT.

On the other hand, covalent functionalisation strategies create defects in the graphitic structure to introduce functionalities or to take advantage of the defects already present in the SWNT. A wide range of covalent functionalisation strategies have been described for SWNT.[13, 16] The covalent functionalisation, however, is more robust and offers the advantage of controlling the degree of

functionalisation to a greater extent and facilitating the characterisation of the produced nanomaterial compared to non-covalent methods. The most common strategies reported to covalently functionalise SWNT include oxidation, dipolar cycloadditions, halogenation, ozonolysis, acylation, etc. A selection of these strategies is displayed in Scheme 4.2. The functionalisation via 1,3-dipolar cycloadditions of SWNT has been especially popular for biomedical purposes.[17] One of the disadvantages of 1,3-dipolar cycloadditions is that it requires a multistep synthesis to obtain the required starting material that reacts with the SWNT.[18]

4.2 Initial functionalisation tests for SWNT

All SWNT used were of advanced purity (Ellicarb® provided by Thomas Swan) which have been purified using a rigorous steam purification method, known to remove 98% of all metallic impurities. In this work, covalently modified SWNT were prepared for their integration in the imaging nanoprobe. Two initial functionalisation strategies were selected to obtain the nanoprobe: the oxidation with mineral acids and a modified version of the Tour reaction. These methods were selected as they have been well described in the literature, including their use for biomedical applications, and they are simple and efficient processes.[19, 20] In addition, convenient functional groups as amines or carboxylic acids can be incorporated so the introduction of linkers in the nanomaterial can be conducted via amide chemistry. The two methods can be regarded as complementary since the first method has been described to functionalise preferentially SWNT tips while the second acts on the SWNT walls.

Table 4.1: Selected oxidation strategies for SWNT described in the literature.

Acid / mixture	T (ºC)	Effect on SWNT	Ref.
HNO_3 (2.6 M)	120	Effect on pre-existing defects only	21, 22
HNO_3 (conc.)	120	Introduction of new functional groups, shortening	23
$H2SO_4$ / HNO_3 (conc. v/v 3:1)	100	New defects generated. Shortening observed	21, 24
H_2SO_4 / H_2O_2 (conc. v/v 4:1)	22	Shortening by action on pre-exisiting defects. Minimal carbon loss	25
	70	Shortening proportional to reaction time. Considerable carbon loss	
$KMnO_4$	100	New defects generated but no shortening observed	21

The treatment of SWNT in acidic conditions has been applied to their purification in order to remove catalyst particles and amorphous carbon, and it is known to introduce oxygen-containing groups on the surface.[6, 23] In some cases, the purification processes included an annealing step at high temperatures to remove the oxygen functionalities and close the nanotubes ends produced as a consequence of the treatment with strong acids. On the contrary, the functionalisation of SWNT by oxidation can in itself aim for the introduction of oxygen functionalities, especially carboxylic acids, to modify covalently the nanomaterial in further synthetic steps.

The use of mineral acids as hydrochloric acid, nitric acid, sulphuric acid, a mixture of them or the inclusion of additives as H_2O_2 (in a 3:1 mixture with H_2SO_4 to produce piranha) or $K_2Cr_2O_7$ (to increase the oxidative power) have been reported.[26] A range of conditions for the oxidation of SWNT and their effects on the nanotubes are presented in Table 4.1. It has also been described that depending on the chemical treatment in acidic conditions the length of the nanotube can be reduced. This shortening is produced by an oxidative cutting mechanism that follows different steps: 1) attack on active sites of the SWNT (i.e. CH_2 groups or CH groups on seven membered rings); 2) electrophilic addition that produces new defects with the introduction of –OH groups; 3) collapse of the graphitic structure around the active sites in strong oxidation conditions and cut of the nanotube in two shorter fragments.[11] The disruption of the graphitic network can lead to the loss of the inherent characteristics of the carbon nanotubes so it is vital to consider the final application of the functionalised nanomaterial before applying aggressive conditions (e.g. if the final application of the nanohybrid is in the production of an electronic material a mild oxidation method would be preferred). Dilute concentrations of nitric acid or the use of piranha type mixtures at low temperatures were reported to reduce the length of the SWNT but only by action on pre-existing defects while no new oxygen functionalities were introduced (the oxidative mechanism had mainly the effect described in (1)).[21, 22, 25] The use of a mixture of sulphuric and nitric acid, as well as the use of piranha, at high temperatures resulted in the introduction of new oxygen functionalities and a drastic shortening of the nanotubes, parameter that could be controlled and was proportional to the reaction time. Finally, the use of $KMnO_4$ generated new defects but the oxidative cutting of the SWNT was not observed.[21]

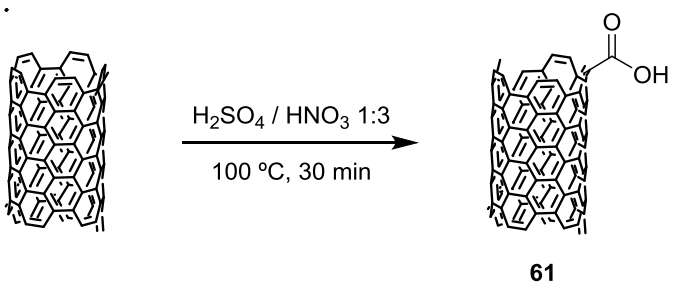

61

Scheme 4.3: Initial functionalisation of pristine SWNT by oxidation.

Therefore, a compromise must be reached between the degree of functionalisation and the shortening of the tubes and distortion of the graphitic network. The use of mild oxidation conditions as 2.6 M HNO_3 seemed insufficient to reduce the length of the tubes and to introduce enough COOH groups in the nanoprobe.[21] On the other hand, the use of a mixture of H_2SO_4 and HNO_3 has been described to cut the entangled groups of nanotubes resulting in nanotubes with open tips and oxygen functionalities.[21, 24]

As stated above, the nanotubes used in this work were high purity Elicarb® single walled nanotubes with low residue obtained from Thomas Swan. The selected oxidation strategy applied herein consisted on heating the nanotubes at 100 ºC for 30 min in a 1:3 mixture of concentrated sulphuric and nitric acids (Scheme 4.3).[27] This treatment produced a shortening of the SWNT while introducing oxygen containing functional groups. The modification of the SWNT could be observed during the course of the reaction as the dispersibility of the nanomaterial increased considerably producing a black dispersion in contrast to the black precipitate observed at the beginning of the reaction. The crude reaction mixture was diluted with water and the nanomaterial was isolated by centrifugation to remove the acidic supernatant. The oxidised nanotubes (**60**) were then filtered through a 0.2 µm hydrophilic membrane and washed with plenty of water and ethanol until the pH of the filtrate was neutral. The product was dried in a 60 ºC oven to yield the oxidised product with a mass loss of 22% with respect to the pristine SWNT, probably due to the excessive shortening of some nanotubes (only initial and final weights compared).

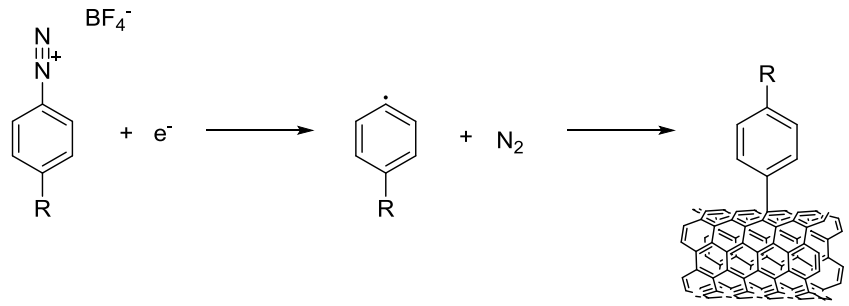

Scheme 4.4: Radical addition reaction of an aryl compound to the SWNT sidewall in a Tour reaction.

The second functionalisation strategy used hereby was based on a modification of the Tour reaction.[28] This process was first described in SWNT as a functionalisation method of the sidewall of the nanotubes by Tour *et al.*[29] The authors functionalised electrochemically SWNT supported on paper using different aryl diazonium salts that were converted into the aryl radical that reacted with the nanotube wall. The functionalisation was demonstrated by using several techniques (Raman, TGA, TEM) and the functionalisation degree proved to be as high as one functionality every 20-30 carbons in the nanotube.[29] The same group demonstrated shortly after that the reaction worked not only electrochemically but also thermally and that the diazonium species could be formed in situ, simplifying greatly the process as

anilines can be easily synthesised and stored.[19] This strategy have been generalised for the functionalisation of SWNT. The reaction conditions evolved and Tour *et al*. successfully conducted this reaction in water by heating a series of aniline derivatives with isopentyl nitrite at 80 ºC, generating the diazonium species in situ.[30] The reactivity in water has advantages as the reduced production of waste, the reduction of reaction times and the increase in the functionalisation degree.

In this work, the reactivity "on water" was applied to SWNT using a procedure described in the literature.[28] The functionalisation procedure was applied using tert-butyl (4-aminobenzyl)carbamate and the reaction time was extended in order to increase the functionalisation degree. The p-SWNT, the protected amine (**61**) and isopentyl nitrite were heated in water at 80 ºC for 48 h (Scheme 4.5, first step). The product was isolated and washed, similarly to **60**, by cycles of centrifugation/re-dispersion and finally by filtration through a 0.2 µm polycarbonate membrane to be washed again with water, ethanol and isopropanol. The product was dried in a 60 ºC oven. Then, the Boc protecting group on the benzylamine moiety was deprotected by stirring **62** in HCl 4M in DMF at room temperature (Scheme 4.5, second step). The product was isolated in a similar manner as in previous steps: centrifuged, filtered and washed with water and ethanol until the pH of the filtrate was neutral. This deprotection method using HCl 4 M in DMF constituted the general procedure to deprotect Boc groups attached to SWNT throughout this work. The dried product **63** presented a weight increase of 22% compared to the pristine SWNT.

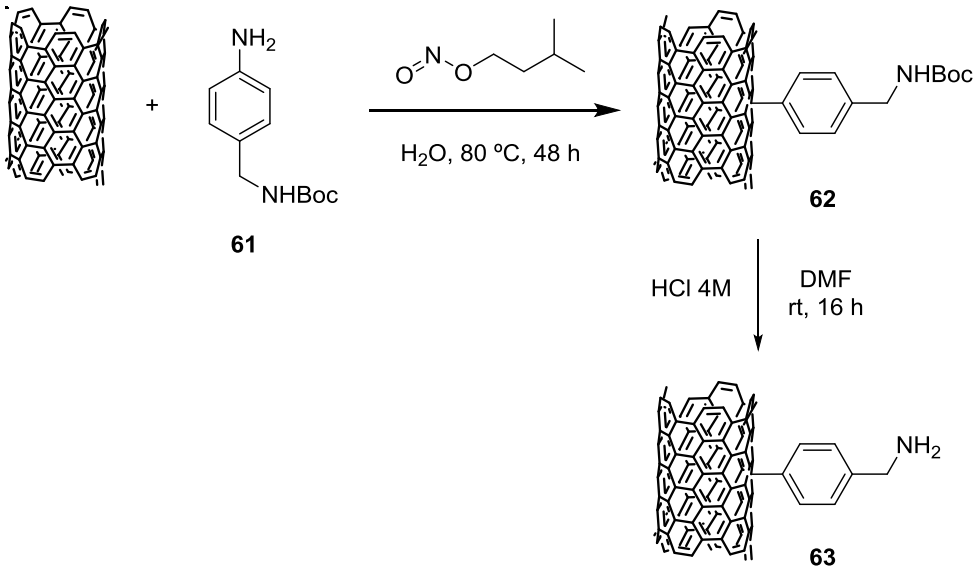

Scheme 4.5: Initial functionalisation of pristine SWNT by a radicalic reaction with tert-butyl (4-aminobenzyl)carbamate (**61**).

The products, **60** and **63**, were characterised using Fourier transform infrared spectroscopy (FTIR), Raman spectroscopy and thermogravimetric analysis (TGA). The acquisition of FTIR spectra in SWNT is challenging due to the small amount of material, and the low functionalisation that renders most of the solid to be composed mainly by carbon. In addition, only a few characteristic functionalities with identifiable IR bands were introduced (e.g. carbonyl groups, amino groups). Nevertheless, the FTIR spectra can be obtained and the presence of indicative bands, identified. In this work, the FTIR spectra were obtained in attenuated total reflectance (ATR) mode. The FTIR spectra for **60** and **63** can be observed in Figure 4.1. The top spectrum corresponds to compound **60** while the spectrum at the bottom corresponds to compound **63**. A baseline correction was applied to the spectra in order to help to identify the most important peaks.

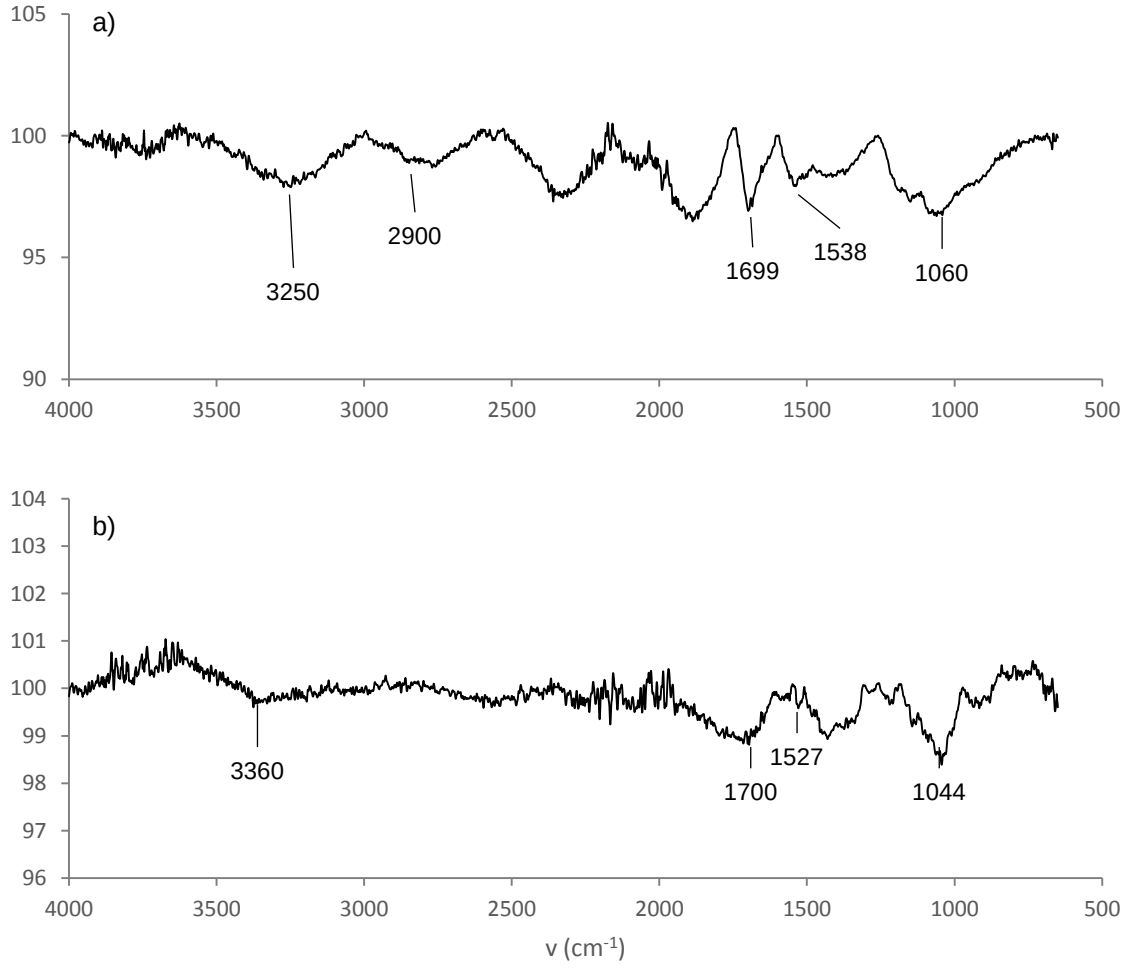

Figure 4.1: FTIR spectra of compounds **60** (a) and **63** (b) with the most significant bands indicated.

The oxidised SWNT (**60**) present the characteristic bands of the carboxylic acid moiety with the COO-H stretching at 3250 cm^{-1} and the C=O stretching at 1699 cm^{-1}. The presence of C-H groups in the open tips of the SWNT can be deduced from the C-H stretching at 2900 cm^{-1}. The bands at ca. 1100 cm^{-1} could be attributed to the =CH rocking out of plane but the assignment is not as clear and bands from other moieties overlap in this area (aromatic rocking out of plane or OH rocking out of plane).

In the case of **63**, the degree of functionalisation seems to be lower than in **60** as the observed intensity of the bands is lower. The presence of the tert-butoxycarbonyl protecting group can be inferred from the presence of the N-H stretching at 3360 cm^{-1}. The CO stretching is present at 1700 cm^{-1} (amide I) while the amide II band can be identified as a weaker band at 1527 cm^{-1}. An intense band is observed at 1044 cm^{-1} that in this case could be attributed to the skeletal vibrations of the CH_3 group although this region is into the fingerprint area and the bands of different groups overlap.

Raman spectroscopy is known to be a powerful technique for the characterisation of bulk carbon nanomaterials. No particular sample preparation is needed, the experiment is quick and non-destructive and the data can reveal essential characteristics of the nanomaterial or its functionalisation. The spectra of SWNT present a series of characteristic bands that help to characterise and elucidate the nature of the carbon nanomaterial, the presence of defects and degree of functionalisation. One of the characteristic bands of a SWNT are the radial breathing modes (RBM) that are present at low wavenumbers in the region of 50 – 300 cm^{-1}. The RBM bands are of great importance in the characterisation of SWNT as they have been used for determining the diameter of the nanotubes and the optical transition energies in isolated tubes.[31] The results of RBM frequencies found in the literature can be described according to Equation 4.1. This equation considers Van der Waals interactions with the environment and further environmental effects. The diameter of the tubes can, therefore, be estimated by Equation 4.2 where $C_e = 0.05786\ nm^{-2}$.[31]

$$\omega_{RBM} = \frac{227}{d_t}(1 + C_e d_t^2)^{1/2}$$

Equation 4.1

$$d_t = \left(\frac{227^2}{\omega_{RBM}^2 - 227^2 C_e}\right)^{1/2}$$

Equation 4.2

Observing the RBM region in the Raman spectra of p-SWNT, **60** and **63** (Figure 4.2), it can be noted that the RBM bands appear at ca. 100 cm^{-1} to ca. 300 cm^{-1}. The intensity of specific bands in the RBM region present maxima at ca. 160, 180 and 270 cm^{-1}. This points to a polydisperse sample where these frequencies can be translated to the diameter of the tubes by applying Equation 4.2. The SWNT samples would contain a distribution of nanotubes with diameters ranging from 0.77 to 2.73 nm with a higher proportion of nanotubes of diameters of 1.51, 1.32 and 0.86 nm by considering the relative intensity of the bands. These results have to be taken with caution as the original equation was calculated only from different pristine SWNT samples reported in the literature.

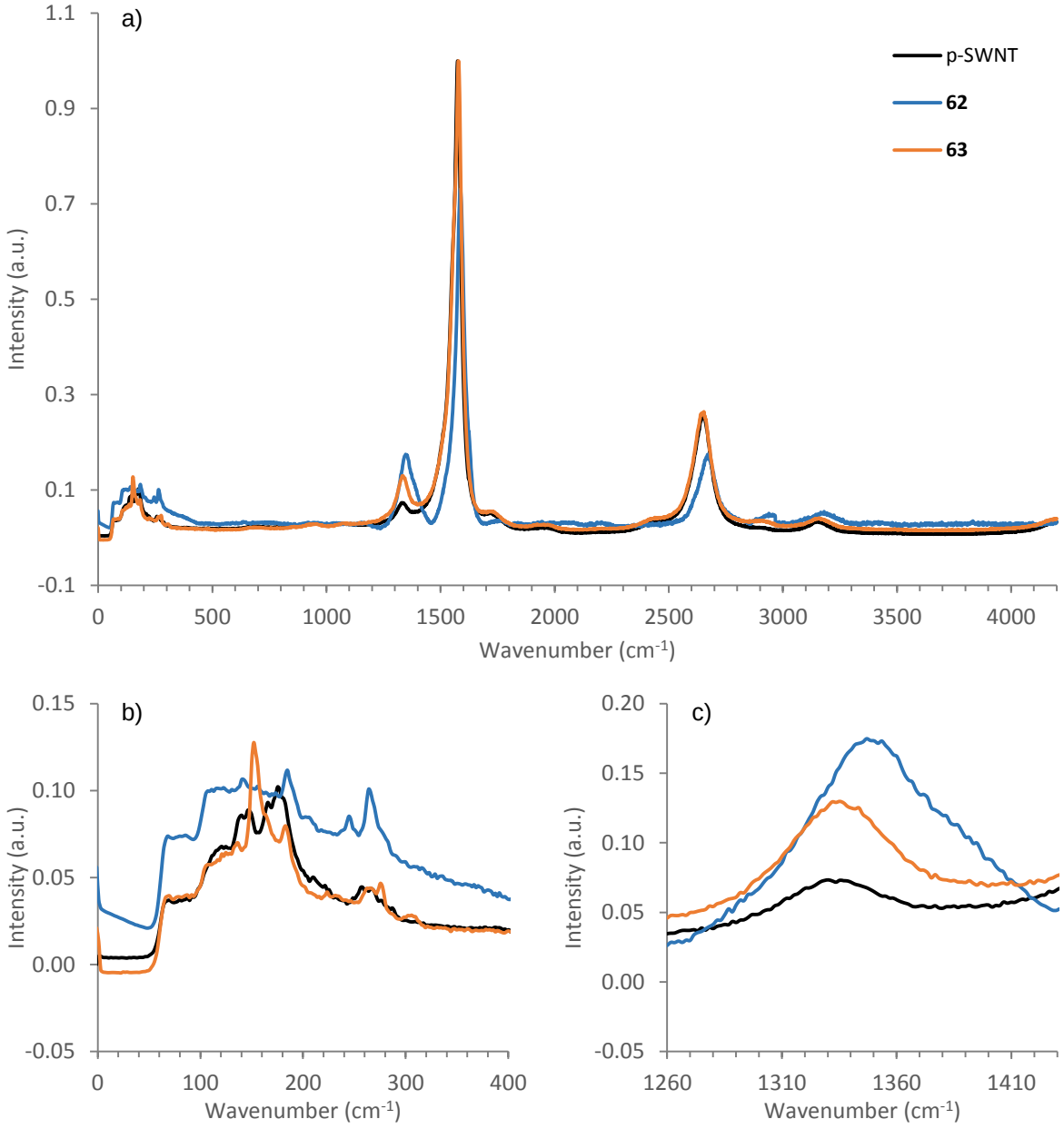

Figure 4.2: Normalised Raman spectra of starting material p-SWNT (black line), **60** (blue line) and **63** (orange line) (a) and expansions for the RBM (b) and D band regions (c).

The G band in SWNT is attributed to the stretching of C-C bonds and is observed at ca. 1580 cm^{-1}. In the case of p-SWNT, **60**, and **63**, the normalised Raman spectra can be observed in Figure 4.2 where the G band is the most intense band in all the spectra. The wavenumbers of characteristic bands for all functionalised SWNT derivatives are summarised in Table 4.2. The wavenumber of the G band for pristine SWNT is 1575 cm^{-1} while it is slightly shifted in the functionalised derivatives (1580 cm^{-1} for **63** and 1584 cm^{-1} for **60**).

The D band is observed at lower wavenumbers than the G band (ca. 1340 cm^{-1}) and is a disorder induced band. The disorder in the rolled graphene sp^2 hybridized layer of a SWNT produces an increase of the D band thus constituting an ideal indicator of the success of a functionalisation strategy.

Table 4.2: Summary of Raman spectroscopy data for p-SWNT, **60** and **63**.

Compound	ν D (cm^{-1})	ν G (cm^{-1})	ν G' (cm^{-1})	I_D/I_G
p-SWNT	1330	1575	2660	0.08
60	1344	1584	2691	0.29
63	1335	1580	2670	0.22

Furthermore, the degree of functionalisation can be measured by comparing the ratio of intensities of the D and G bands. The I_D/I_G ratio constitutes an indicator of the disorder introduced in the nanotube by disruption of the sp^2 graphene network to sp^3 hybridised carbon. The subsequent comparison of the I_D/I_G ratios to the values obtained for pristine SWNT gives a perspective on the degree of functionalisation. The I_D/I_G ratios for p-SWNT, **60**, and **63** were calculated and are summarised in Table 4.2. The values are expressed as an average from the Raman spectra acquired for each sample. In the case of p-SNWT, it can be noted how the I_D/I_G ratio is low, a fact that demonstrates the high purity of the p-SWNT. The functionalised samples present considerably higher I_D/I_G ratios (0.29 for **60** and 0.22 for **63**). According to these values, the functionalisation degree is higher in the oxidised SWNT (**60**) which points to this strategy as the most effective to modify the pristine SWNT as a first step.

Another inherently characteristic band on the SWNT is the G' band. The G' band is the first overtone of the D band and appears at ca. 2650 cm^{-1}. For p-SWNT, **60**, and **63** the G' band is more intense than the D band and the wavenumber varies with the corresponding for the D band. In this way, the G' band for p-SWNT is observed at 2660 cm^{-1} while the G' band for **63** and **60** are observed at 2670 and 2691 cm^{-1} respectively. The G' band wavenumbers follow the same trend as in the D band.

Table 4.3: TGA data showing the mass loss of pristine, and initially functionalised SWNT at 500 ºC.

Compound	Mass loss at 500 ºC (%)
p-SWNT	2
60	21
63	11

In addition, thermogravimetric analysis coupled to mass spectrometry (TGA-MS) was performed to the products. TGA measures the mass loss of the material during the application of a heating ramp under argon that generally ends around 1000 ºC. During this process, all organic functionalities that decorate the SWNT are decomposed and released in the form of different gases as CO_2, N_2, etc. The mass loss at 500 ºC, when all the organic functional groups are decomposed, can be correlated to the functionalisation degree of the material. The MS results can be difficult to interpret as only low molecular weight species are detected and the contribution of moisture or argon from the gas flow can interfere with the results. The TGA curves can be observed in Figure 4.3 and the results of the mass loss at 500 ºC can be observed in Table 4.3. The pristine SWNT lose just 2% of their weight by 500 ºC probably due to adsorbed gases on the surface. The oxidised material, **60**, loses 21% of its weight by 500 ºC and the higher degree of functionalisation compared to **63** demonstrated as the amino-containing SWNT only lose 11% of their original weight.

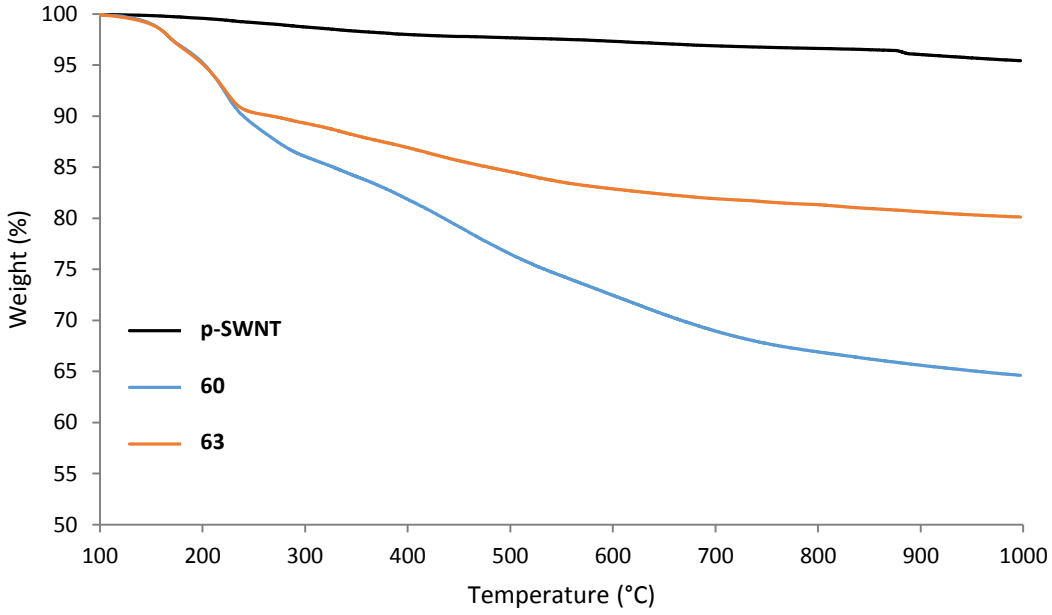

Figure 4.3: TGA curves for starting material, p-SWNT (black line), **60** (blue line) and **63** (orange line).

Another method of determining the loading in compounds containing amino groups is the Kaiser test. The Kaiser test is a colorimetric assay based on the reaction of ninhydrin with primary amines to generate an intense blue dye (Ruhemann's purple). The reaction of amino acids and primary amines with ninhydrin was described in the beginning of the 20th century. The mechanism of formation of the coloured species and the applications of these reactions have been studied.[32] Furthermore, the reaction of ninhydrin with amino acids constitutes an ideal qualitative tool to ascertain the effectiveness of a coupling reaction. This is routinely applied to the solid phase peptide synthesis (SPPS) developed by Merrifield *et al.* by the presence or absence of the blue colour.[33] The reagents were slightly modified and the reaction conditions optimised to avoid common pitfalls as undesired side products or incomplete colour developing previously found in the literature in order to apply the method quantitatively by Sarin *et al*.[34] The best results to estimate the amine loading in routine monitoring were obtained by heating the resin beads with a solution containing phenol, KCN and ninhydrin at 100 ºC. The optimal heating time was found to be 10 min when all the colour had developed but no decomposition was observed. The resulting colour was reported to be stable for more than 2 h.[34]

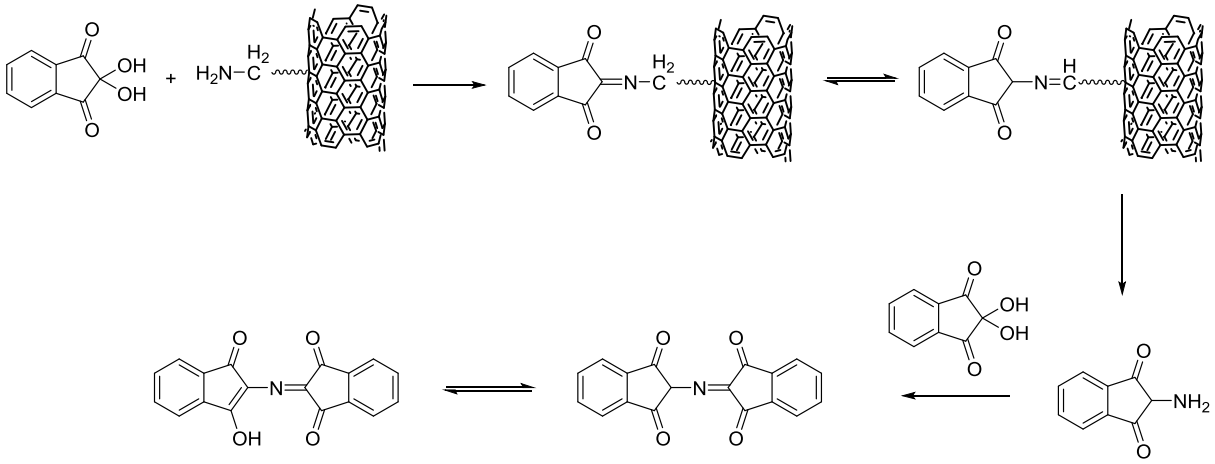

Scheme 4.6: Application of the Kaiser test to probe the occurrence of an amino functionalised SWNT.

The Kaiser test has also been applied to monitor the functionalisation of SWNT when amino groups were present due to the similarities between nanomaterials and resin beads as solid supports.[35] Moreover, the possibility to apply this assay quantitatively in nanotubes has been explored and the loading expressed as mmol of NH_2 per gram of material.[36-38] The production of Ruhemann's blue from an amino functionalised SWNT and ninhydrin is showed in Scheme 4.6.

In this work, Kaiser tests were conducted using 0.5 – 2 mg of SWNT samples that were homogenised with the reagents described by Sarin *et al*.[34] (120 µL of a first solution containing 0.36 g/mL phenol and 0.012 mg/mL KCN in pyridine/ethanol (9:1) and 30 µL of a second solution containing 0.05 g/mL

ninhydrin in ethanol). The SWNT and reagents were heated to 100 ºC for 10 min in capped vials. Then, the solution was filtered and diluted to 25 mL with ethanol/water (6:4). The absorbance of the solutions was measured within the next 30 min to avoid any possible colour fading. The concentration of amino groups was calculated using the Beer-Lambert law applying a molar extinction coefficient of $\varepsilon = 1.3x10^5\ M^{-1}cm^{-1}$, and expressed as mmol($NH_2$) / g of material. In the case of **63** the estimated loading was 0.34 mmol (NH_2) / g. The obtained values account for an approximation that allows comparison between samples when the same procedure is applied. However, to obtain a more accurate value of the concentration of amino groups, Merrifield *et al*. advised to find the specific molar extinction coefficient for each specific peptide/amino species.[34]

4.3 Introduction of linkers used in the current synthetic strategy

The functionalisation of the products obtained in Section 4.2 with organic linkers was performed by amide coupling with different functional molecules. In the case of oxidised nanotubes (**60**), protected diamines of different nature were coupled forming an amide bond via the *in situ* activation of the carboxylic acid in the SWNT using 1-ethyl-3-(3-dimethylaminopropyl)carbodiimide (EDC) / 1-hydroxybenzotriazole (HOBt) followed by the addition of the mono(protected) amine (Scheme 4.8, top, first step). The *in situ* activation of the carboxylic acids in functionalised nanotubes forming an activated ester has been applied in the literature and it resembles the conditions used in molecular chemistry with the exception that the reaction times are generally longer.[39, 40] The addition of HOBt as an additive helps to reduce possible side reactions or epimerisation from the O-acylisourea intermediate formed with EDC (Scheme 4.7). The reaction was carried out dispersing the nanotubes in DMF by sonication and stirring with the coupling reagents and diamines at room temperature for 48 h. The products were processed by centrifugation, washing, filtering through a 0.2 µm membrane and drying.

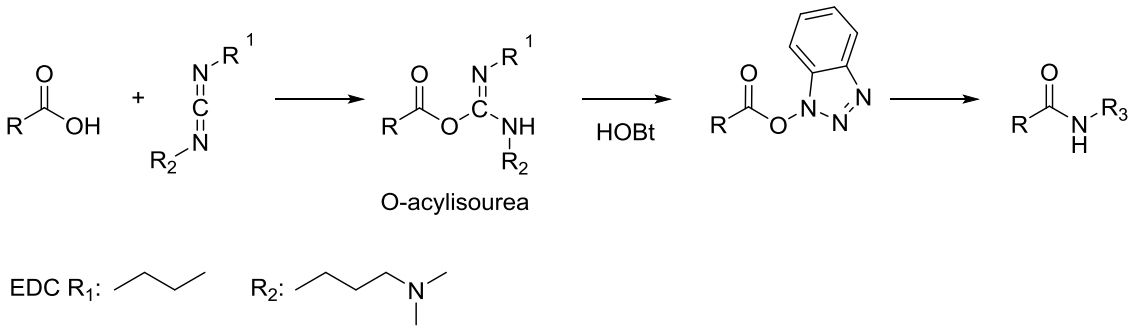

Scheme 4.7: Activation of a carboxylic acid functionality using EDC/HOBt.

In the case of the amino-functionalised nanotubes (**63**) the introduced linkers were protected long chain amino acids, namely 6-((tert-butoxycarbonyl)amino)hexanoic acid (**64**) and 11-((tert-butoxycarbonyl)amino)undecanoic acid (**65**), where the amino group had been Boc protected. The reaction proceeded by the activation of the carboxylic acids in the protected amino acid with EDC/HOBt. The activated intermediate was added to a dispersion of amino-functionalised nanotubes in DMF and the reaction mixture stirred for 48 h (Scheme 4.8, bottom, first step).

The introduction of protected diamines in CNT has been previously described in the literature. In particular, this group of diamines (tert-butyl 2-aminoethyl carbamate[39], tert-butyl 6-aminohexyl carbamate[41, 42] and tert-butyl-2-(2-(2-aminoethoxy)ethoxy)ethylcarbamate[43, 44, 45]) have been previously applied to the functionalisation of SWNT and MWNT for biomedical applications. The couplings were performed through the acid halide or using activating agents as EDC or N-hydroxysuccinimide (NHS).

The preparation of acid halides involves the use of oxalyl chloride or thionyl chloride that are comparatively much more toxic than diimide-based activating agents. Therefore, the conditions using EDC/HOBt for the coupling were preferred. The interest in these derivatives for biomedical applications was encouraging to apply similar reaction conditions to reproduce the results in the batch of high purity SWNT used herein. The use of 6-aminohexanoic acid and 11-aminoundecanoic acids as linkers for the decoration of SWNT and MWNT has been reported. However, the amino-functionalised SWNT were obtained from the fluorinated SWNT instead of the oxidised derivatives.[46, 47]

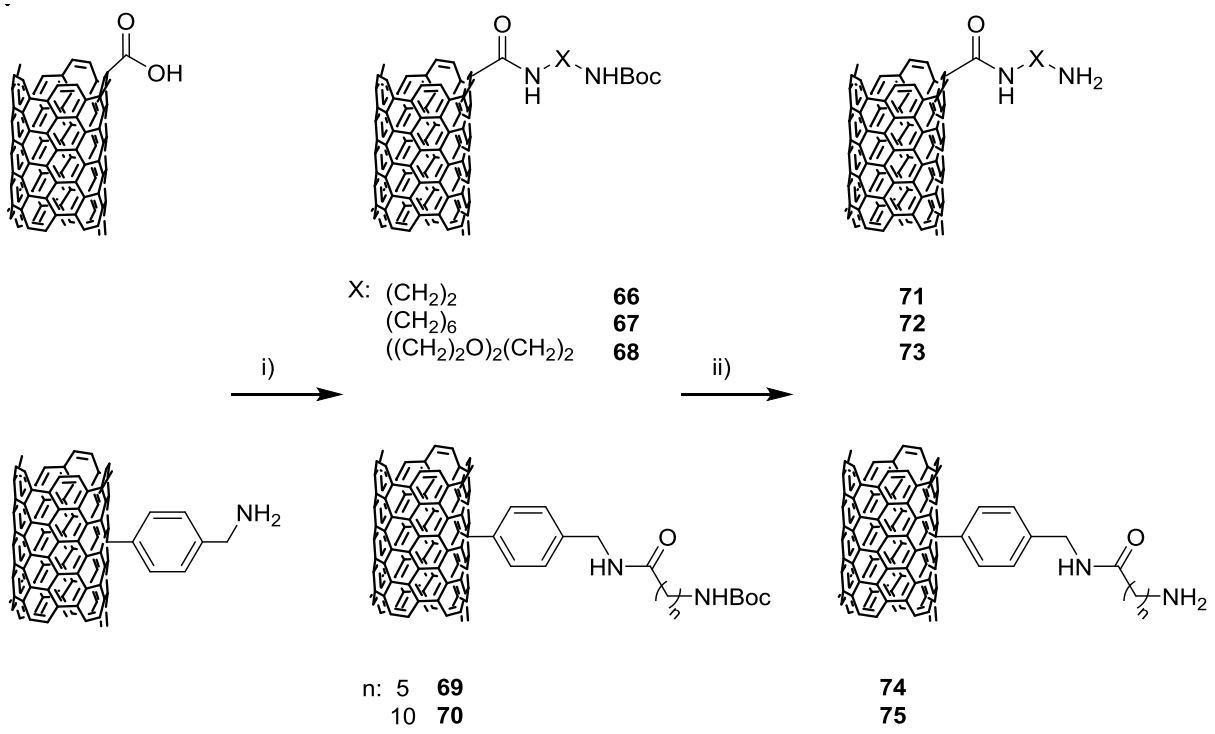

Scheme 4.8: Reaction conditions for the modification with linkers of oxidised nanotubes, **60** (top) and amino-functionalised nanotubes **63** (bottom); i) EDC/HOBt, DMF, rt, 48 h, ii) HCl 4M, DMF, rt, 16 h.

In both cases, the SWNT derivatives contained a Boc protected amino group as a terminal moiety. The next step consisted in the deprotection of the Boc group with HCl 4M in DMF (Scheme 4.8, second step). This way, the amino-terminated SWNT products **71**, **72**, **73**, **74** and **75** were obtained.

The novel amino-functionalised SWNT denoted **71** – **75** were characterised by applying the methods described in section 4.2 (i.e. FTIR and Raman spectroscopies). In addition, the Kaiser test was applied to the identification and quantification of amino groups as described above. The summary of the characterisation data containing results from the Kaiser test and Raman spectroscopy are given in Table 4.4 where the data obtained for compounds **60** and **63** have been included for comparison purposes.

Table 4.4: Characterisation data for functionalised SWNT derivatives **71 – 75**.

Compound	mmol NH_2 / g	ν D (cm^{-1})	ν G (cm^{-1})	I_D/I_G
60	-	1344	1584	0.29
63	0.34	1335	1580	0.22
71	0.19	1343	1582	0.15
72	0.23	1344	1585	0.15
73	0.17	1345	1587	0.22
74	0.25	1334	1580	0.11
75	0.24	1336	1580	0.16

The wavenumbers corresponding to the D and G bands present in the Raman spectra do not appear to change appreciably with the introduction of the amino-terminated linkers. The D band of the functionalised SWNT derived from the oxidised nanomaterial (**71**, **72** and **73**) is observed at ca. 1344 cm^{-1} similarly to the starting material while the same situation is encountered with the G band that appears at ca. 1584 nm. The scenario with the functionalised derivatives derived from **63** is repeated with the D and G bands (ca. 1335 and 1580 cm^{-1} respectively) appearing at very similar wavenumbers compared to **63**.

Interestingly, the I_D/I_G ratios were reduced in the compounds with the amino-terminated linkers when compared to the initially functionalised SWNT. This may be attributed to the loss of highly functionalised SWNT that might have suffered a dramatic shortening during the initial functionalisation treatment. This way, the disappearance of these SWNT, that contributed to increase notably the I_D/I_G ratio, results in an overall decrease of the I_D/I_G ratio for the new material.

The results obtained from the quantitative Kaiser test showed a loading of ca. 0.20 mmol NH_2 / g in the functionalised materials derived from the oxidised SWNT with the highest loading obtained for the probe including the hexyl linker (**72**). The functionalisation of **74** and **75** was slightly higher than in the previous derivatives and the loading reaches ca. 0.25 mmol NH_2 / g. The existence of data from the starting material allowed to estimate the coupling efficiency in the introduction of the linker by comparing the two values and assuming the latest result is originated from the amino groups in the linkers. The coupling step of the benzylamine residue proved to be slightly more efficient with 6-aminohexanoic acid (74%) than with 11-aminoundecanoic acid (70%).

Due to the targeting nature of the peptide and the preferred coupling strategy to the fluorophore, a carboxylic acid group was necessary to support the conjugate on the nanotubes. Therefore, the amino-terminated linkers were expanded by reaction with succinic anhydride. The opening of the succinic

anhydride by the amine yields a 4-oxobutanoic acid at the end of the linker. This reaction has been reported to produce satisfactory results for MWNT.[44] This reaction was performed using a general method for nanomaterials **71**, **72**, **73**, **74** and **75**. The procedure consisted in dispersing the nanomaterial by sonication in dry THF followed by the addition of succinic anhydride and stirring the reaction mixture overnight at room temperature (Scheme 4.9).

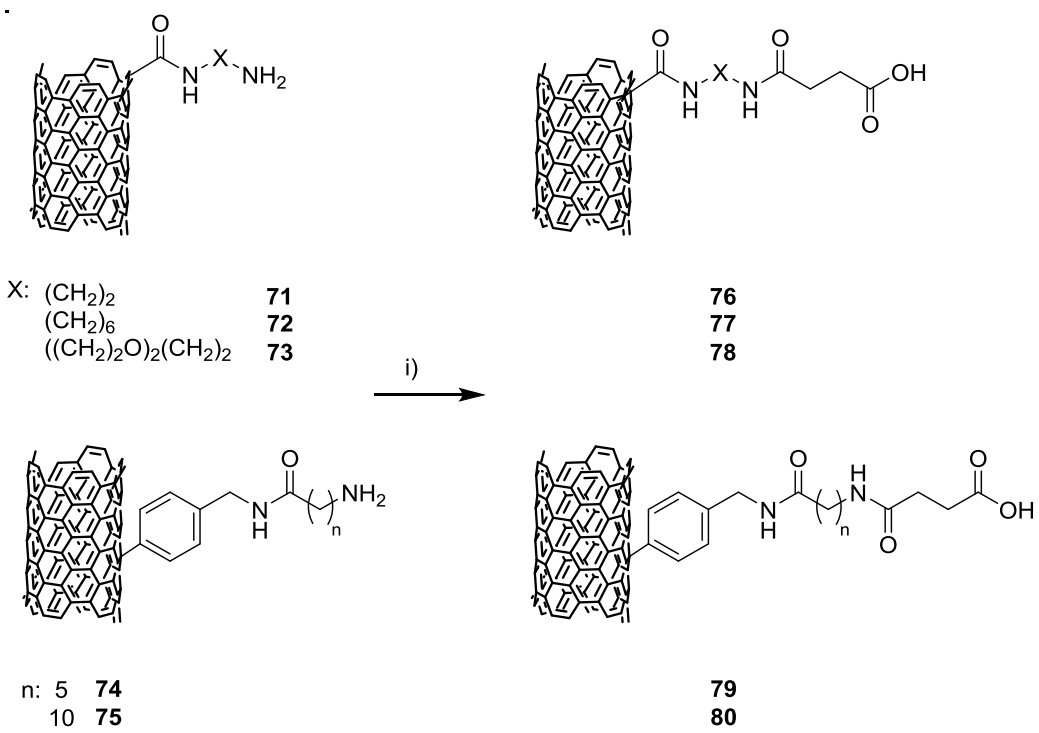

Scheme 4.9: Introduction of a succinic acid moiety into the functionalised SWNT. Conditions: i) succinic anhydride, THF, rt, 16 h.

The product was isolated by centrifugation, washed, filtered through a 0.2 µm polycarbonate membrane and dried in a similar manner as described for the initial functionalised products. The introduction of the carboxylic acid group was evident during the work-up. The improvement on the dispersibility of the samples can be observed in Figure 4.4, the image at the top corresponds to compounds **71**, **72**, **73**, **74** and **75** (from left to right) after a 20 min sonication period and 30 min standing at room temperature. The introduction of a polyethylene glycol (PEG) group in the linker chain improves dramatically the stability of the dispersion of functionalised nanotubes (**73**). The dispersibility improvement is generalised for all nanomaterials after the addition of N,N-diisopropylethylamine (DIPEA) as a base. The exception of **75** which offers a similar appearance can be attributed to the length of the alkylic chain that does not favour the suspension in a polar solvent as ethanol. The deprotonation of the terminal carboxylic acid proton by DIPEA improves significantly the dispersibility and serves as a confirmation of the success of the functionalisation reaction.

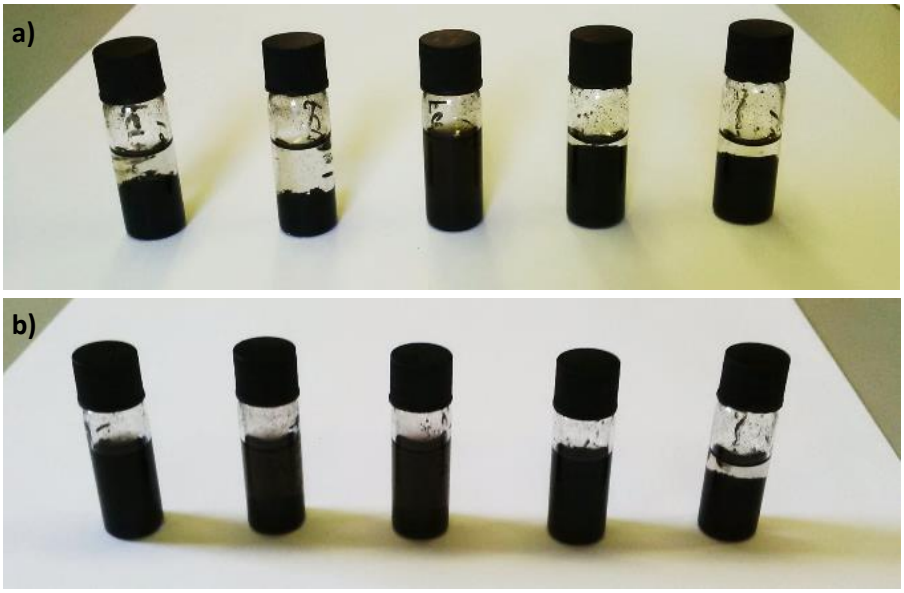

Figure 4.4: Images of the dispersions emerging from sonication of 1 mg/mL functionalised SWNT dispersions in ethanol (left to right) of: **76**, **77**, **78**, **79** and **80**. a) Conditions: 20 min sonication and 30 min standing at room temperature; b) the same dispersions after the addition of 50 μL of DIPEA.

The final functionalised SWNT samples were characterised using techniques previously described in this chapter. Additionally, TGA was conducted in the samples as well as TEM for the derivatives terminated in the carboxylic acid (**76** – **80**) and the pristine SWNT in order to observe the morphology changes in the products after the functionalisation. A summary of the characterisation data can be observed in Table 4.5

The variation in the D band wavenumber is greater in the functionalised SWNT derived from **60**. The observed values go from 1333 to 1352 cm^{-1}. The G band wavenumber is more constant through the different samples and in the same range of the starting materials within a 10 cm^{-1} difference.

Table 4.5: Summary of characterisation data for functionalised SWNT **76** – **80**.

Compound	Mass loss (500 ºC)	D wavenumber	G wavenumber	I_D/I_G
76	22	1352	1570	0.15
77	22	1339	1574	0.15
78	28	1333	1571	0.12
79	17	1331	1573	0.10
80	20	1337	1578	0.16

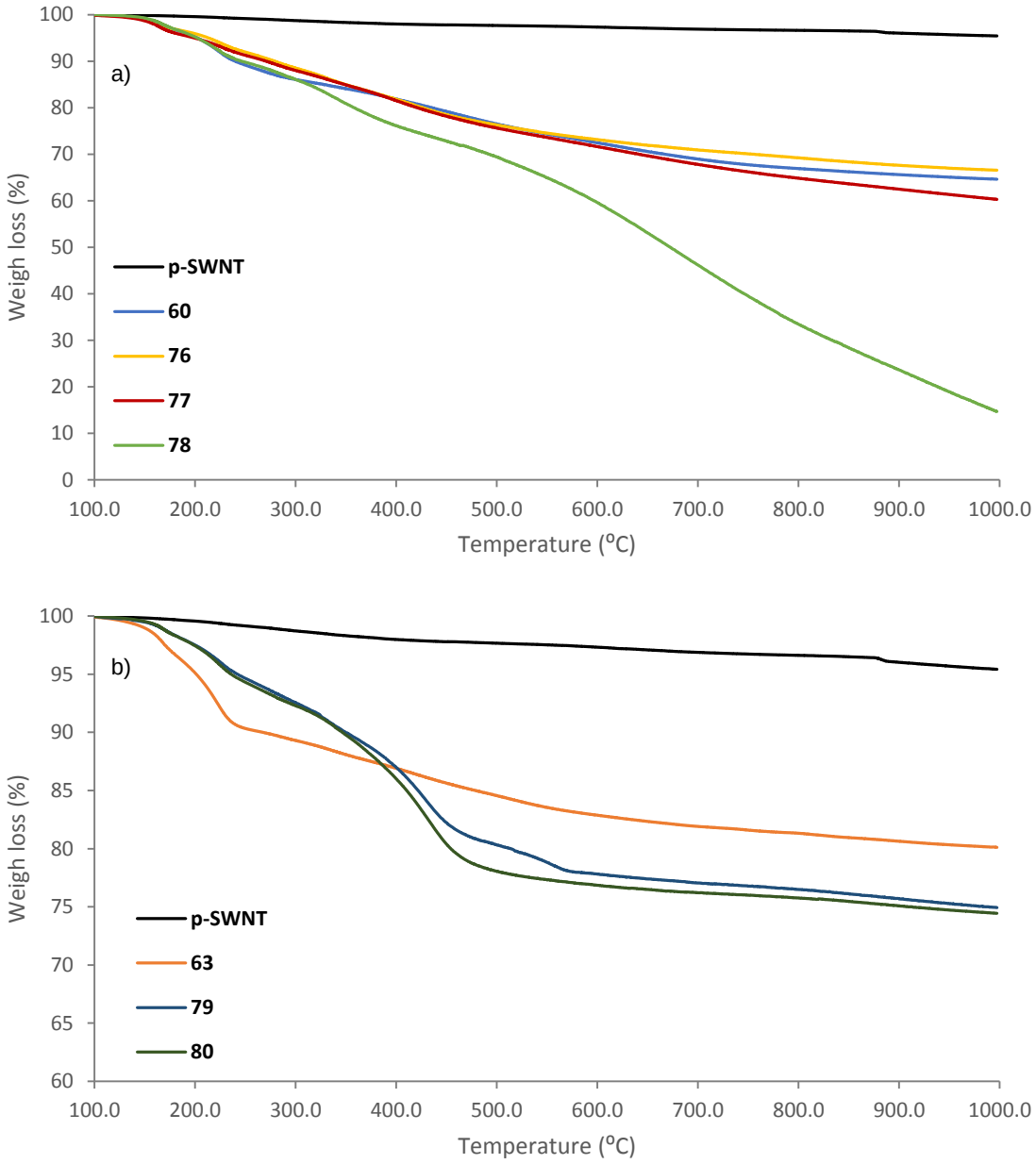

Figure 4.5: TGA curves for functionalised SWNT **76** – **80**. a) Functionalised SWNT prepared from **60** (**76**, **77** and **78**) and b) functionalised SWNT prepared from **63** (**79** and **80**). The curves for the pristine SWNT used as a starting material have been included for comparison.

In the case of **79** and **80**, the values of D and G bands wavenumbers are similar for both nanomaterials and in accordance with the values obtained for the starting materials.

The I_D/I_G ratios are kept in the same range of values when compared to the amino-functionalised SWNT for all samples (**76** – **80**) which indicates that the introduction of the succinic acid moiety did not affect the structure of the nanotube.

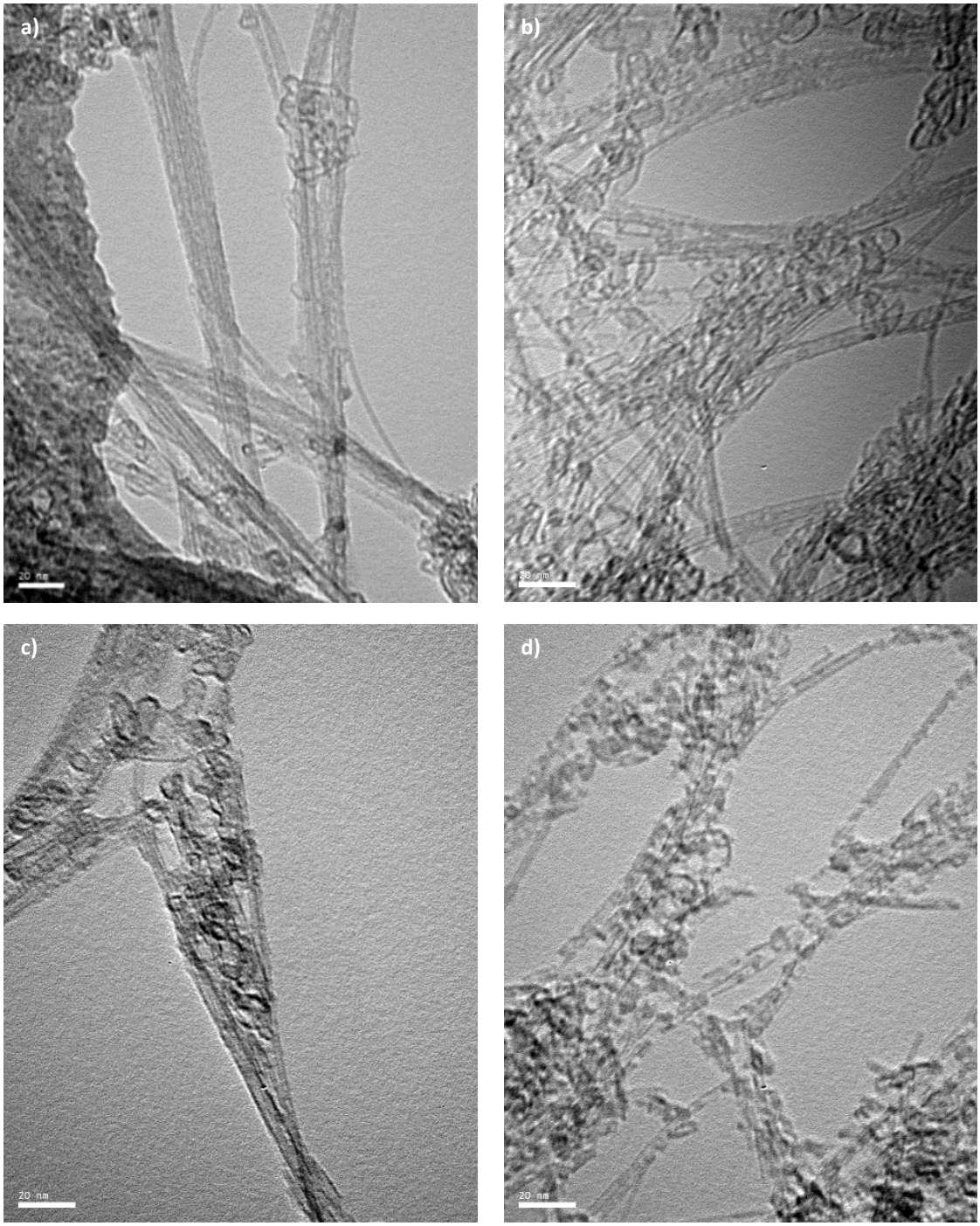

Figure 4.6: TEM images of SWNT samples where a) pristine SWNT, b) **76**, c) **77** and d) **78**. Scalebar: 20 nm.

The TGA curves for functionalised SWNT **76** – **78** present small steps in mass loss at low temperatures (100 – 300 ºC) and the mass loss is constant until 500 ºC. In the case of compounds **63**, **79** and **80**, the mass loss presents a big step before 350 ºC. In the case of **63**, this step is more evident and the mass loss is constant at higher temperatures. Differently, **79** and **80** present a second step at ca. 500 ºC with the mass loss being constant at higher temperatures.

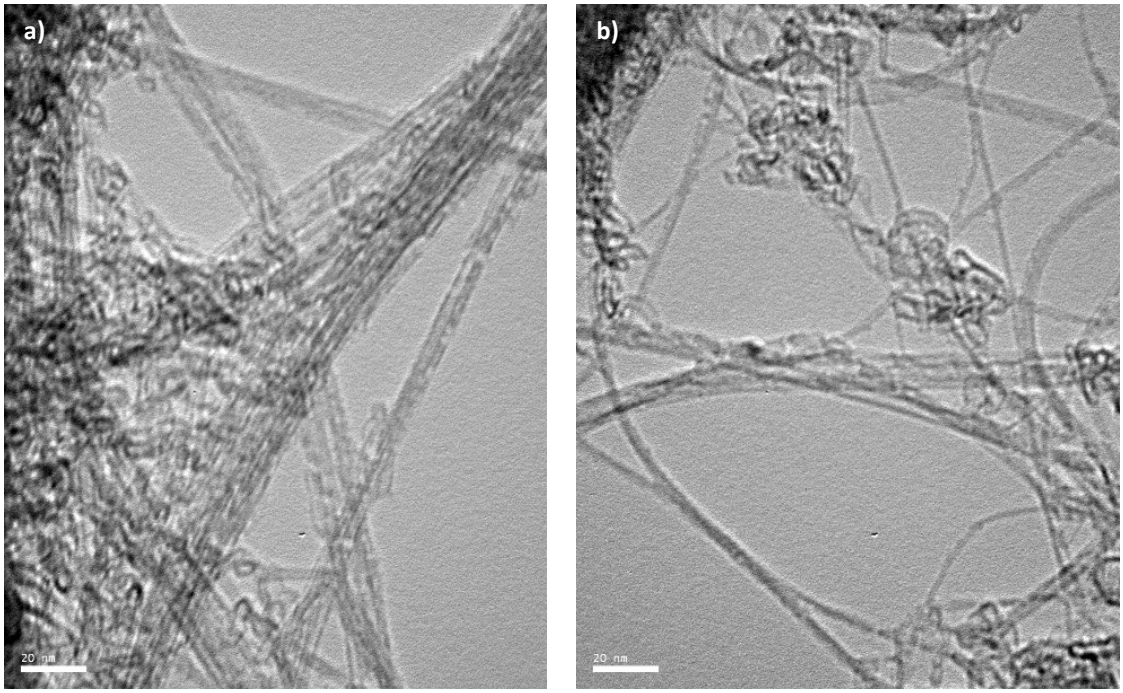

Figure 4.7: TEM images of functionalised SWNT a) **79** and b) **80**. Scalebar: 20 nm.

The mass loss results obtained from TGA (Figure 4.5 and Table 4.5) indicate that, in general, the oxidative strategy proved more successful to introduce functional groups as it was demonstrated with the initial functionalisation of the SWNT. However, the overall increase from the initially functionalised SWNT is higher for the nanomaterial obtained in the radicalic reaction **63** with the mass loss starting at 11% and the final products **79** and **80** presenting a value of 17 and 20% respectively. In comparison, in samples **76** – **78**, obtained from oxidised nanotubes (**60**), the margin of mass loss increase is much narrower with a 1% increase for **76** and **77** and the bigger difference for **78** that presents a final 28% mass loss at 500 ºC.

Transmission electron microscopy (TEM) is a powerful technique employed to characterise SWNT. TEM is especially useful as it allows to observe the surface functionalisation of the nanotubes, their morphological changes (shortening, bending) and other characteristics. The TEM samples were prepared by drop casting a suspension of the corresponding SWNT sample in ethanol on to a 400 mesh copper grid.

The TEM image for pristine SWNT at 500k magnification can be observed in Figure 4.6, a). It can be seen that the pristine material is aggregated in ropes of several tubes as well as bundles that are distributed randomly. The surface of walls of the p-SWNT are generally smooth which confirms the absence of functional groups.

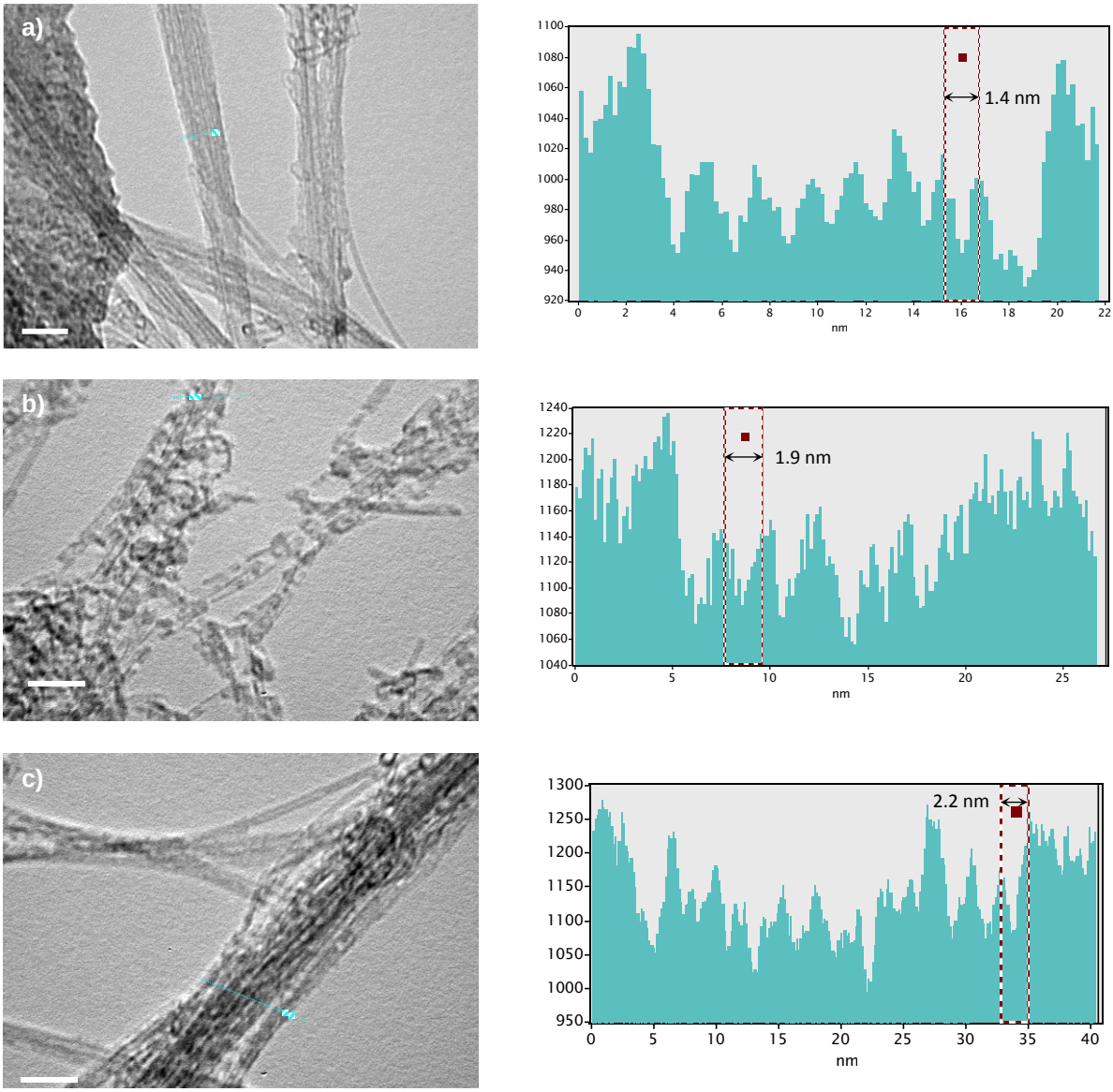

Figure 4.8: TEM images and corresponding profiles (indicated by the dashed blue line in the images) for starting material p-SWNT (a), **78** (b) and **79** (c).

The TEM images for **76**, **77**, and **78** are displayed in Figure 4.6, b), c) and d) respectively. The effect of the functionalisation is apparent as bumps on the surface of the SWNT with a darker contrast in the image. The tubes are still aggregated in ropes and bundles but the observation of individualised tubes or tubes in smaller groups is more frequent. The higher functionalisation degree is observed for the functionalised SWNT sample **78** where the tubes are dispersed to a greater extent, the irregular features on the sidewalls are more evident and occurrence of much shorter tubes can also be observed.

The TEM images for **79** and **80** are displayed in Figure 4.7. In this case, the tubes are observed with a better dispersion than the pristine material and invidualised tubes can be observed although there is

aggregation in form of ropes and bundles. The introduction of the phenyl and linker groups is observed as darkened areas on the nanotube surface and bumps on the sidewalls (more evident for **80**).

The initial functionalisation via the Tour reaction seems to produce a lower degree of shortening of the tube as well as less opening of the nanotubes ends. This is in accordance with the preferred sidewall functionalisation of the nanotubes. The SWNT in the images obtained for **76**, **77**, and **78** seemed to present a better dispersion on the grid as well.

The height profiles obtained from selected TEM images for the starting material p-SWNT, **78** and **79** are shown in Figure 4.8. The profile of the pristine SWNT shows the aggregation of the nanotubes in ropes with diameters going from 1.4 to 1.8 nm. In the case of the functionalised SWNT derivatives **78** the length of the nanotubes was considerably reduced while the diameter is in the same range as for the p-SWNT although in the profile showed in the picture, examples of SWNT with wider diameters are observed with values going from 1.7 to 2.4 nm (Figure 4.8, b). A similar situation is observed for **79**, where the functionalisation does not indicate a considerable increase in the coating around the nanotube. The diameters of the SWNT for **79** are kept in the range of 1.4 to 2.6 nm (Figure 4.8, c). The observed increase in the diameters in functionalised samples demonstrates the success of the functionalisation strategies applied to the starting pristine SWNT.

4.4 Translation of the functionalisation strategy to graphene oxide

Much research effort had been applied to obtain graphene but it was not until 2004 that individual graphene sheets could be isolated from graphite and characterised. The new material was described as stable and highly conductive, even at room temperature.[48] The structure of graphene is that of a fused benzene-ring honeycomb lattice, but with only one atom thickness. One of the most common routes to the preparation of graphene derivatives is through the exfoliation of graphite oxide that produces graphene oxide (GO) (Figure 4.9). Graphene oxide presents many defects in the honeycomb structure, mainly oxygenated functions, that alter the unique properties of graphene as the high electrical conductivity. The preparation of graphene needs the final reduction of the GO structure. On the other hand, the presence of functional groups can be advantageous as it allows the introduction of groups of interest in the structure and at the same time it enhances the dispersibility in aqueous and organic solvents.

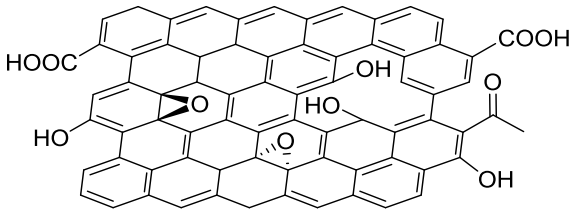

Figure 4.9: Structure of graphene oxide including its most common defects.

Since the discovery of graphene, increasing attention has been dedicated to the application of this innovative carbon nanomaterial to the biomedical field with special attention to the fabrication of biosensors.[49] Nevertheless, graphene and its derivatives have also been employed in biomedical imaging.[2] The functionalisation strategies of graphene are similar to the ones typically applied to SWNT and can be categorised as covalent and non-covalent.

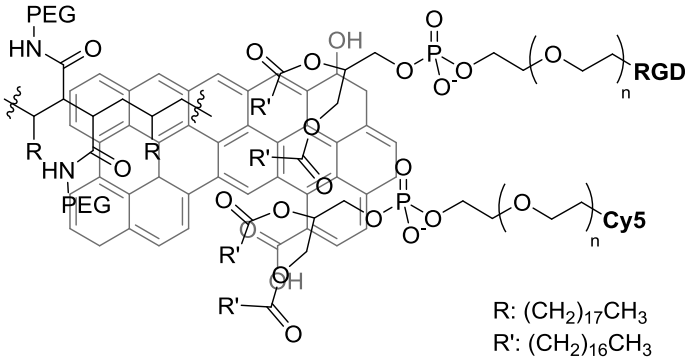

Figure 4.10: Representation of an imaging probe based on PEGylated rGO flakes where a Cy5 dye and the RGD targeting peptide have been introduced. Structure adapted from ref. 50.

One example of non-covalent functionalisation of reduced graphene oxide to prepare a targeted imaging probe for integrin receptors can be observed in Figure 4.10. In this example, the authors used long PEG chains to functionalise reduced graphene oxide and introduce Cy5 dyes and the peptide RGD as targeting molecule. The imaging nanoprobe was biocompatible and could be detected *in vitro* thanks to the Cy5 dye and *in vivo* thanks to the enhanced NIR absorbance of reduced GO compared to GO.[50]

In this work, a PEG linker was introduced to graphene oxide via amidation, similarly to the strategy developed for **72**, taking advantage of the presence of carboxylic acid groups in the structure. In this work, graphene oxide was synthesised in bulk in the group under the supervision of Dr Boyang Mao and used as received. The graphene oxide (GO) was obtained from graphite by a modification of the Hummers method following a described procedure.[51] Shortly, graphite oxide was obtained from graphite powder by treatment with sodium nitrate and concentrated sulphuric acid. The dispersion was cooled to 0 ºC and potassium permanganate added. When the suspension reached room temperature and had been stirring for another 30 min, hydrogen peroxide was added. The work-up of the reaction included dilution with water, filtration and washing of the precipitate and a final dialysis step to remove any remaining salts. Graphene oxide was obtained from the dried product by sonication periods.
A TEM image for the same batch is showed in Figure 4.11 a). The crystallographic structure was obtained by selected area electron diffraction (SAED) and the resulting hexagonal diffraction pattern[52] is showed in Figure 4.11 b). The results of FTIR and Raman spectroscopies will be described later in this section.

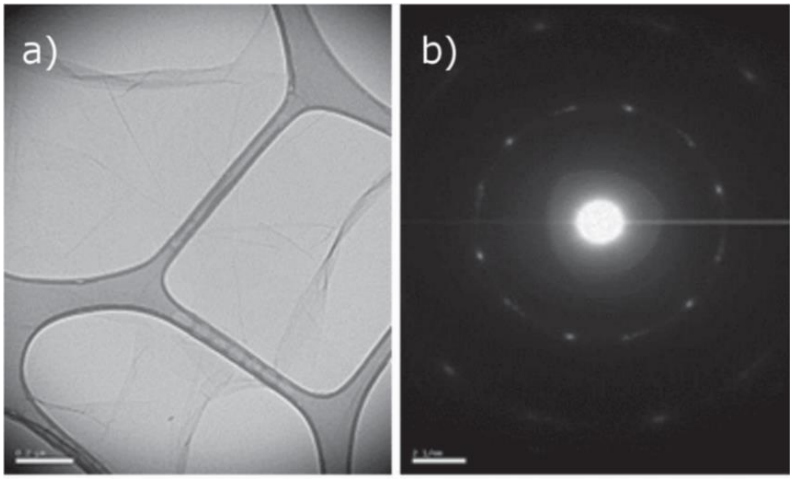

Figure 4.11: a) TEM image of graphene oxide. Scalebar: 200 nm. b) SAED of graphene oxide. Scalebar: 2 nm. Figure reproduced from ref. 51.

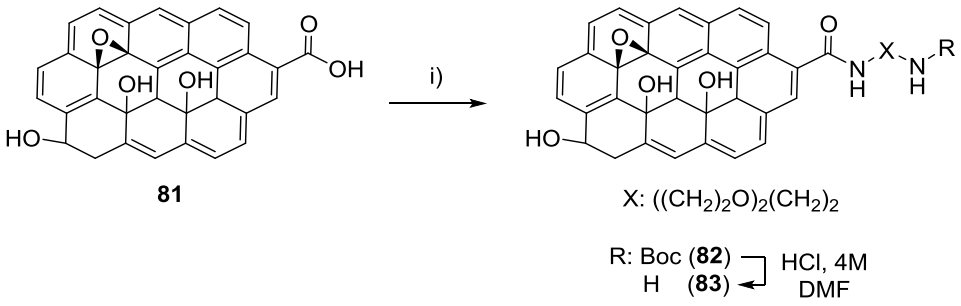

Scheme 4.10: Functionalisation route of GO to introduce an amino-terminated linker. i) EDC, HOBt, tert-butyl-2-(2-(2-aminoethoxy)ethoxy)ethylcarbamate (**6**), DMF, rt, 48 h.

The amidation of GO was conducted using EDC/HOBt as activating agents and tert-butyl-2-(2-(2-aminoethoxy)ethoxy)ethylcarbamate (**6**) as a linker (Scheme 4.10, first step). The deprotection of the t-butoxycarbonyl group was achieved by treatment with HCl 4M in DMF to obtain **83**. In a similar way as for the strategy followed in the preparation of SWNT probes, the presence of terminal carboxylic acid was necessary to build the imaging nanoprobe. For this reason, the amino-terminated GO species **83** was reacted with succinic anhydride in THF to produce **84**. The product was isolated by centrifugation, the supernatant removed and the residue re-suspended and washed again. The final step included filtration through a 0.2 µm membrane, washing and drying under air.

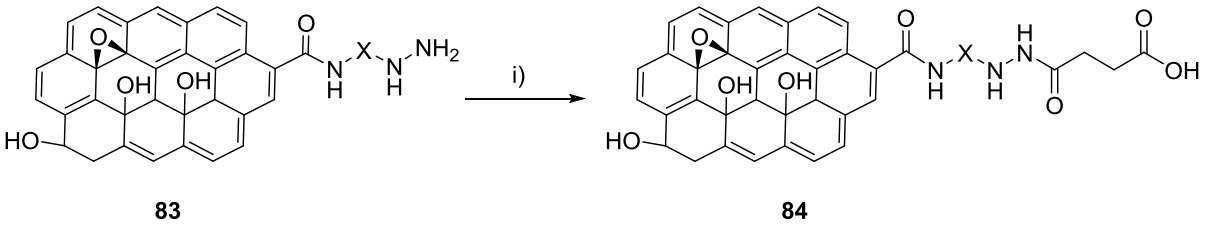

Scheme 4.11: Reaction conditions for the preparation of carboxylic acid terminated GO. i) Succinic anhydride, THF, rt, 16 h.

The nanohybrids were obtained as a brown powder that could be more easily dispersed in water or polar organic solvents compared to SWNT derivatives. The nanohybrids based on graphene oxide were characterised by FTIR and Raman spectroscopy as well as TGA. The characterisation data are summarised in Table 4.6. The initial characterisation data suggest that the introduction of functional groups in GO is comparatively low with respect to SWNT based derivatives. The performance of the

Kaiser test in the amino functionalised derivative **83** offered an estimated loading of 0.02 mmol NH_2/g which represents a reduced loading compared to the functionalised SWNT counterparts.

The FTIR spectra of **81**, **83** and **84** can be observed in Figure 4.12. The IR spectrum of the graphene oxide starting material (Figure 4.12, a)) shows characteristic bands of oxygenated functionalities introduced as defects in the honeycomb aromatic structure of graphene. The OH stretching is observed at 3300 cm^{-1} as a broad band. This band includes individual hydroxyl groups as well as COO-H groups. The band at 1043 cm^{-1} can be assigned to the corresponding C-O stretching bands of hydroxyl groups. The CO stretching can be observed at 1718 cm^{-1} next to the C=C stretching at 1620 cm^{-1}. The bands observed at ca. 1200 cm^{-1} could be attributed to the C-O stretching in epoxide groups.

The spectrum of **83** presents some essential differences to that of GO. The presence of a NH stretching can be inferred as a shoulder at 3370 cm^{-1} although the band is dominated by the OH stretching.

Table 4.6: Summary of characterisation data for functionalised graphene oxide derivatives.

Compound	mmol NH_2 / g	Mass loss (%) at 500 °C	ν D (cm^{-1})	ν G (cm^{-1})	I_D/I_G
81 (GO)	-	42	1351	1600	0.97
83	0.02	-	1379	1580	1.14
84	-	37	1344	1580	0.98

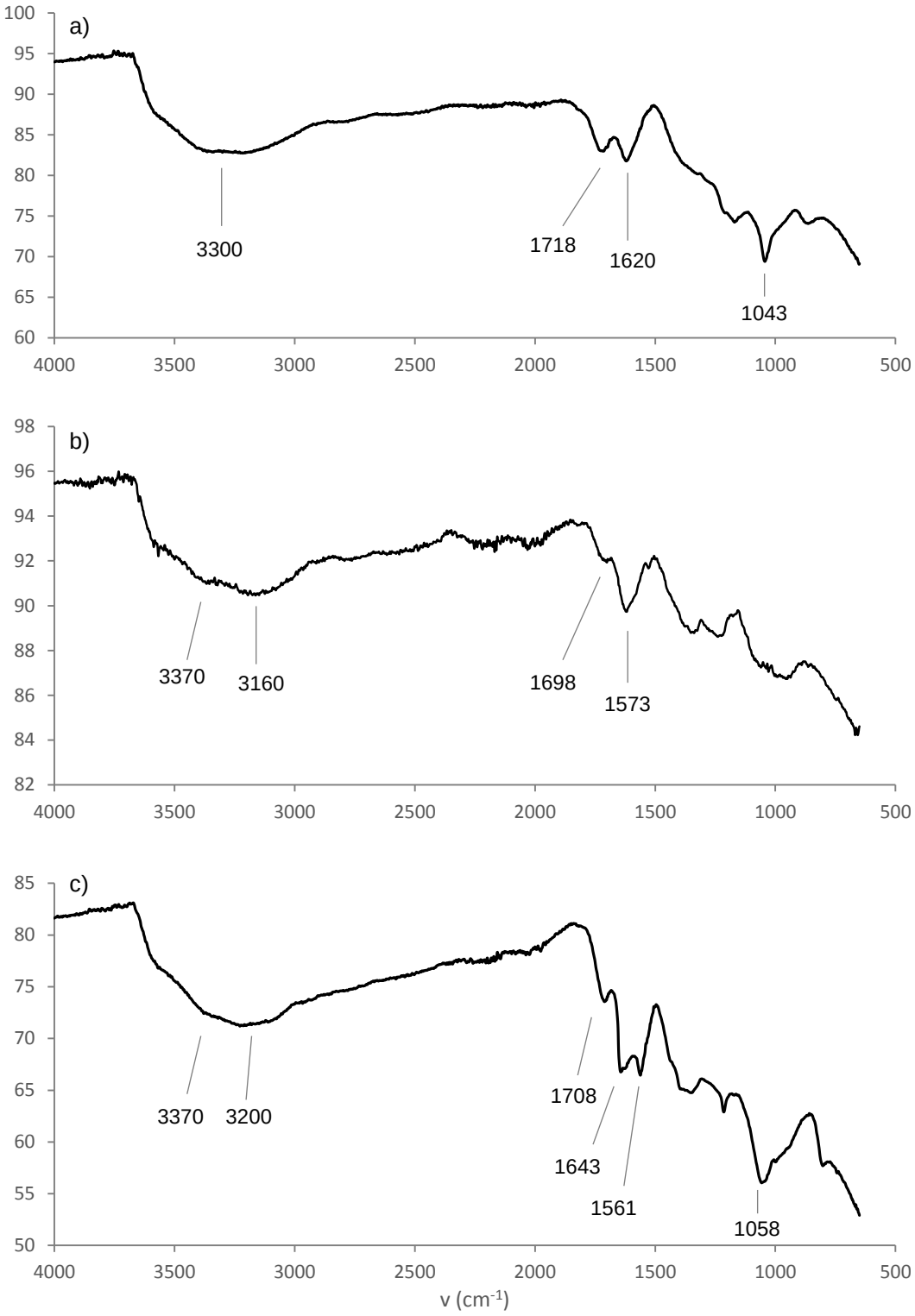

Figure 4.12: FTIR spectra of **81** (a), **83** (b) and **84** (c).

The CO stretching is shifted to 1698 cm^{-1} for **83** that confirms the modification of the carboxylic acid to the amide. In the band at 1573 cm^{-1} the amide II band and the C=C stretching can overlap producing an intense band. The C-O stretching is present as a broad band at ca. 1000 cm^{-1}.

The spectrum of **84** is similar to the one for **83**. The zone of 3200 – 3300 cm^{-1} has the same profile and contains the bands corresponding to the stretching of OH and NH groups. The C-O stretching is observed as a sharp peak in this spectrum at 1058 cm^{-1}. The band at 1561 cm^{-1} corresponds to the overlap of the amide II band at the C=C stretching. Interestingly, the introduction of the carboxylic acid terminated linker produces the appearance of a second CO stretching. The stretching corresponding to the amide, as observed in the previous spectrum, is slightly shifted herein and appears as 1708 cm^{-1} while the corresponding CO stretching for the carboxylic acid is present at 1643 cm^{-1}. This splitting of the CO stretching serves as a confirmation of the success of the functionalisation strategy.

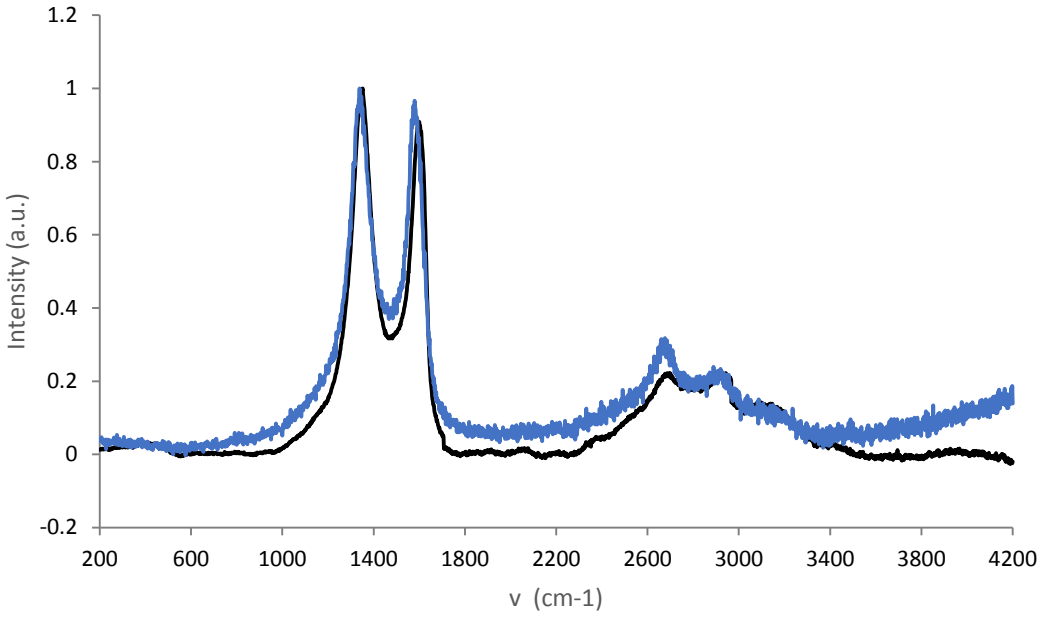

Figure 4.13: Normalised Raman spectra of starting material GO (black line) and **84** (blue line).

The Raman spectrum for GO and **84** can be observed in Figure 4.13. The spectra of graphene oxide, **81**, **83** and **84** present the same appearance. The Raman spectra for GO derivatives are markedly different to the spectra for SWNT derivatives. Graphene oxide presents a much higher D band that equals in intensity the G band and can even have a higher intensity. The I_D/I_G ratios (Table 4.6) did not present much variation with the functionalisation. The ratio increased with the synthesis of **83** but remained practically the same of GO in the final product, **84**. The wavenumbers of the D band change over the functionalisation of the GO with a trend that is not clear. The wavenumber of the G band remains more stable in the functionalised derivatives although it suffers a shift from the original graphene oxide. The blue shift of the G band in graphitic structures has been attributed to the merging with the D' band as caused by defects which would be in accordance with the data observed for **83** and **84**.[53] The 2D band for **84** appears at ca. 2684 cm^{-1}.

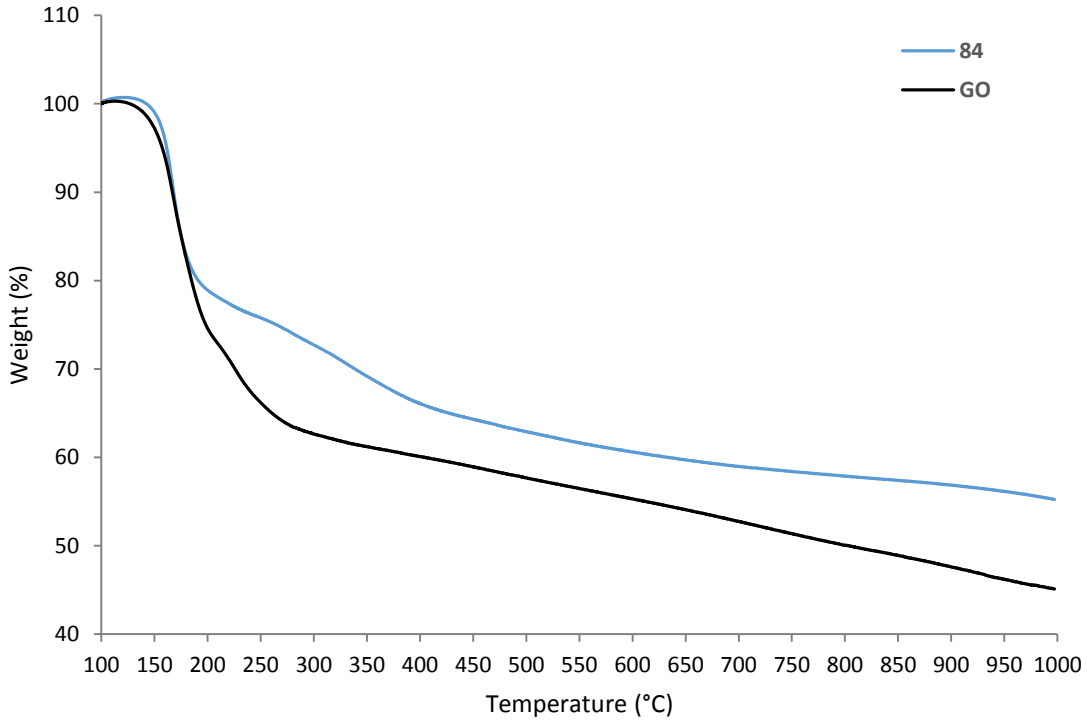

Figure 4.14: TGA curves for graphene oxide starting material (black line) and **84** (blue line).

The TGA curves for graphene oxide and **84** are shown on Figure 4.14. Both nanomaterials were dry as no mass loss due to dehydration was observed in the TGA experiment. The mass loss starts at approximately 130 ºC with a steep change that continues until 280 ºC for graphene oxide and to 180 ºC for **84**. This dramatic mass loss is attributed to the pyrolysis of oxygenated functional groups that are released as CO, CO_2 or steam.[54] The change of slope and reduction of the dramatic mass change in **84** demonstrates that the formation of the amide bonds confers thermal stability to the carbon lattice structure. This is proved by the overall mass loss by 500 ºC for GO that constitutes a 42% compared to the functionalised nanohybrid (**84**) where the mass loss is reduced to 37%.

4.5 Conclusions

In this chapter, the functionalisation of SWNT to produce novel biocompatible materials, able to be conjugated with fluorophores and targeting peptides, has been explored. The translation of the SWNT functionalisation strategy to graphene oxide was also evaluated and it was demonstrated that the methodologies are compatible.

Initially, the SWNT were functionalised following two complementary strategies. One consisted in the oxidation of the SWNT with a mixture of concentrated acids to introduce oxygen functionalities (hydroxyl groups, carboxylic acids) and improve the dispersibility in solution. The oxidative strategy produced the functionalised SWNT (**60**). This strategy demonstrated to shorten the SWNT and open the ends as expected due to the increased reactivity of the carbon nanotube tips in acid mixtures. The second strategy was based on the Tour reaction where an aryl radical species, generated *in situ* from the diazo compound, reacts with the sidewall of the SWNT. This method allowed us to prepare SWNT with a benzylamine group in the sidewall, after deprotection (**63**). The nanoprobes were characterised by FTIR and Raman spectroscopies. FTIR provided the most representative bands for the introduced functional groups (as the CO stretching, the CH stretching or the COOH stretching) while Raman provided an indication of the degree of functionalisation by comparing the intensity of D and G bands (I_D/I_G ratio). The values of this relation in both cases demonstrated the success of the functionalisation reactions.

The introduction of organic linkers/spacers in the SWNT was performed via amide formation chemistry. Oxidised SWNT were modified with diamines (**71**, **72**, **73**) while long chain amino acids were used for the amino-functionalised SWNT (**74**, **75**). The couplings were performed using EDC and HOBt as activating agents and the protecting groups present in all linkers removed by treatment with HCl. The presence of free amines allowed us to perform the Kaiser test, a colorimetric assay, which provides a value for the loading of NH_2 functional groups in the nanomaterial. The loading was slightly higher on derivatives containing amino acid linkers but was around 0.2 mmol NH_2 / g for all samples. The Raman spectroscopy results for the SWNT functionalised with the linkers showed a decrease of the I_D/I_G ratio in the products. This can be attributed to the removal of highly functionalised SWNT during the reaction and work-up in the introduction of linkers.

The amino terminated SWNT were reacted with succinic anhydride in order to obtain a terminal carboxylic acid group, necessary to build the imaging nanoprobe. The dispersibility of the COOH terminated SWNT was considerably enhanced compared to previous derivatives, especially in a basic medium, which confirmed the presence of the desired functional groups. The final products (**76**, **77**, **78**, **79**, **80**) were characterised by TGA and TEM. TGA results proved the functionalisation and showed a higher amount of functional groups for initially oxidised SWNT probes but the greater variation in mass

loss was for the SWNT derivatives containing amino acid linkers. The comparison of the TEM results for the pristine and functionalised SWNT demonstrated the successful functionalisation. The as functionalised tubes showed better dispersion, shorter lengths and open ends. The morphology of their sidewalls indicated that they were no longer smooth as indicated by TEM. The initially oxidised nanoprobes in ethanol showed better dispersion and shorter lengths although aggregation in bundles was still observed. The initially amino functionalised SWNT were aggregated in ropes, presented longer tubes and the functionalisation was evident in the sidewalls.

The most promising SWNT functionalisation strategy in terms of stability in solution (amidation with PEG linker) was translated to the functionalisation of graphene oxide. The linkers introduced in GO allowed us to prepare a novel nanomaterial containing spacers and adequate functional groups to build a new nanohybrid that may be suitable for imaging applications. The characterisation of GO and GO nanohybrids was performed by FTIR and Raman spectroscopies and TGA. The functionalisation of the GO derivatives (**81**, **83**, **84**) was demonstrated by changes in FTIR bands, especially the splitting of the CO stretching bands in the final product. In addition, the introduction of the linker improved the thermal stability of the nanohybrid as observed by TGA.

In summary, a range of novel functionalised carbon nanomaterials with promising properties for the building of the targeted imaging nanoprobe have been prepared and fully characterised. The most promising of these functional nanomaterials were taken forward to the assembly of fluorescent nanomaterials too, as described in Chapter 5.

4.6 References

1. F. Cortezon-Tamarit, H. Ge, V. Mirabello, M.B.M. Theobald, D.G. Calatayud and S. I. Pascu, in *Inorganic and Organometallic Transition Metal Complexes with Biological Molecules and Living Cells*, Academic Press, 2017, pp. 245-327.
2. G. Hong, S. Diao, A. L. Antaris and H. Dai, *Chem. Rev.*, 2015, **115**, 10816-10906.
3. S. Liu, Q. Shen, Y. Cao, L. Gan, Z. Wang, M. L. Steigerwald and X. Guo, *Coord. Chem. Rev.*, 2010, **254**, 1101-1116.
4. A. G. Rinzler, J. Liu, H. Dai, P. Nikolaev, C. B. Huffman, F. J. Rodríguez-Macías, P. J. Boul, A. H. Lu, D. Heymann, D. T. Colbert, R. S. Lee, J. E. Fischer, A. M. Rao, P. C. Eklund and R. E. Smalley, *Appl. Phys. A*, 1998, **67**, 29-37.
5. A. C. Dillon, T. Gennett, K. M. Jones, J. L. Alleman, P. A. Parilla and M. J. Heben, *Adv. Mater.*, 1999, **11**, 1354-1358.
6. I. W. Chiang, B. E. Brinson, A. Y. Huang, P. A. Willis, M. J. Bronikowski, J. L. Margrave, R. E. Smalley and R. H. Hauge, *J. Phys. Chem. B*, 2001, **105**, 8297-8301.
7. G. Tobias, L. Shao, C. G. Salzmann, Y. Huh and M. L. H. Green, *J. Phys. Chem. B*, 2006, **110**, 22318-22322.
8. B. Ballesteros, G. Tobias, L. Shao, E. Pellicer, J. Nogués, E. Mendoza and M. L. H. Green, *Small*, 2008, **4**, 1501-1506.
9. J. Wen, Y. Xu, H. Li, A. Lu and S. Sun, *Chem. Commun.*, 2015, **51**, 11346-11358.
10. A. Hirsch, *Angew. Chem. Int. Ed.*, 2002, **41**, 1853-1859.
11. D. Tasis, N. Tagmatarchis, A. Bianco and M. Prato, *Chem. Rev.*, 2006, **106**, 1105-1136.
12. H.-C. Wu, X. Chang, L. Liu, F. Zhao and Y. Zhao, *J. Mater. Chem.*, 2010, **20**, 1036-1052.
13. P. Singh, S. Campidelli, S. Giordani, D. Bonifazi, A. Bianco and M. Prato, *Chem. Soc. Rev.*, 2009, **38**, 2214-2230.
14. N. Karousis, N. Tagmatarchis and D. Tasis, *Chem. Rev.*, 2010, **110**, 5366-5397.
15. M. A. Herranz and N. Martín, in *Carbon Nanotubes and Related Structures*, Wiley-VCH Verlag GmbH & Co. KGaA, 2010, pp. 103-134.
16. F. Hauke and A. Hirsch, in *Carbon Nanotubes and Related Structures*, Wiley-VCH Verlag GmbH & Co. KGaA, 2010, pp. 135-198.
17. A. Battigelli, C. Ménard-Moyon, T. Da Ros, M. Prato and A. Bianco, *Adv. Drug Del. Rev.*, 2013, **65**, 1899-1920.
18. K. Kordatos, T. Da Ros, S. Bosi, E. Vázquez, M. Bergamin, C. Cusan, F. Pellarini, V. Tomberli, B. Baiti, D. Pantarotto, V. Georgakilas, G. Spalluto and M. Prato, *J. Org. Chem.*, 2001, **66**, 4915-4920.
19. J. L. Bahr and J. M. Tour, *Chem. Mater.*, 2001, **13**, 3823-3824.
20. V. Datsyuk, M. Kalyva, K. Papagelis, J. Parthenios, D. Tasis, A. Siokou, I. Kallitsis and C. Galiotis, *Carbon*, 2008, **46**, 833-840.

21. J. Zhang, H. Zou, Q. Qing, Y. Yang, Q. Li, Z. Liu, X. Guo and Z. Du, *J. Phys. Chem. B*, 2003, **107**, 3712-3718.
22. M. N. Tchoul, W. T. Ford, G. Lolli, D. E. Resasco and S. Arepalli, *Chem. Mater.*, 2007, **19**, 5765-5772.
23. H. Hu, B. Zhao, M. E. Itkis and R. C. Haddon, *J. Phys. Chem. B*, 2003, **107**, 13838-13842.
24. J. Liu, A. G. Rinzler, H. Dai, J. H. Hafner, R. K. Bradley, P. J. Boul, A. Lu, T. Iverson, K. Shelimov, C. B. Huffman, F. Rodriguez-Macias, Y.-S. Shon, T. R. Lee, D. T. Colbert and R. E. Smalley, *Science*, 1998, **280**, 1253-1256.
25. K. J. Ziegler, Z. Gu, H. Peng, E. L. Flor, R. H. Hauge and R. E. Smalley, *J. Am. Chem. Soc.*, 2005, **127**, 1541-1547.
26. K. Esumi, M. Ishigami, A. Nakajima, K. Sawada and H. Honda, *Carbon*, 1996, **34**, 279-281.
27. M. S. P. Shaffer, X. Fan and A. H. Windle, *Carbon*, 1998, **36**, 1603-1612.
28. L. Maggini, F. M. Toma, L. Feruglio, J. M. Malicka, T. Da Ros, N. Armaroli, M. Prato and D. Bonifazi, *Chem. Eur. J.*, 2012, **18**, 5889-5897.
29. J. L. Bahr, J. Yang, D. V. Kosynkin, M. J. Bronikowski, R. E. Smalley and J. M. Tour, *J. Am. Chem. Soc.*, 2001, **123**, 6536-6542.
30. B. K. Price and J. M. Tour, *J. Am. Chem. Soc.*, 2006, **128**, 12899-12904.
31. P. T. Araujo, I. O. Maciel, P. B. C. Pesce, M. A. Pimenta, S. K. Doorn, H. Qian, A. Hartschuh, M. Steiner, L. Grigorian, K. Hata and A. Jorio, *Phys. Rev. B*, 2008, **77**, 241403.
32. D. J. McCaldin, *Chem. Rev.*, 1960, **60**, 39-51.
33. E. Kaiser, R. L. Colescott, C. D. Bossinger and P. I. Cook, *Anal. Biochem.*, 1970, **34**, 595-598.
34. V. K. Sarin, S. B. H. Kent, J. P. Tam and R. B. Merrifield, *Anal. Biochem.*, 1981, **117**, 147-157.
35. J. L. Stevens, A. Y. Huang, H. Peng, I. W. Chiang, V. N. Khabashesku and J. L. Margrave, *Nano Lett.*, 2003, **3**, 331-336.
36. M. Quintana and M. Prato, *Chem. Commun.*, 2009, 6005-6007.
37. C. H. Villa, M. R. McDevitt, F. E. Escorcia, D. A. Rey, M. Bergkvist, C. A. Batt and D. A. Scheinberg, *Nano Lett.*, 2008, **8**, 4221-4228.
38. V. Georgakilas, N. Tagmatarchis, D. Pantarotto, A. Bianco, J.-P. Briand and M. Prato, *Chem. Commun.*, 2002, 3050-3051.
39. D. He, Y. Peng, H. Yang, D. Ma, Y. Wang, K. Chen, P. Chen and J. Shi, *Dyes and Pigments*, 2013, **99**, 395-401.
40. M. Á. Herranz, N. Martín, S. Campidelli, M. Prato, G. Brehm and D. M. Guldi, *Angew. Chem.*, 2006, **118**, 4590-4594.
41. X. Yang, Z. Zhang, Z. Liu, Y. Ma, R. Yang and Y. Chen, *J. Nanopart. Res.*, 2008, **10**, 815-822.
42. Z. Zhang, X. Yang, Y. Zhang, B. Zeng, S. Wang, T. Zhu, R. B. S. Roden, Y. Chen and R. Yang, *Clin. Cancer. Res.*, 2006, **12**, 4933-4939.
43. R. Marega, V. Aroulmoji, F. Dinon, L. Vaccari, S. Giordani, A. Bianco, E. Murano and M. Prato, *J. Am. Chem. Soc.*, 2009, **131**, 9086-9093.

44. D. Iannazzo, A. Pistone, S. Galvagno, S. Ferro, L. De Luca, A. M. Monforte, T. Da Ros, C. Hadad, M. Prato and C. Pannecouque, *Carbon*, 2015, **82**, 548-561.
45. D. Iannazzo, A. Piperno, A. Ferlazzo, A. Pistone, C. Milone, M. Lanza, F. Cimino, A. Speciale, D. Trombetta, A. Saija and S. Galvagno, *Org. Biomol. Chem.*, 2012, **10**, 1025-1031.
46. L. Zeng, L. B. Alemany, C. L. Edwards and A. R. Barron, *Nano Research*, 2008, **1**, 72-88.
47. L. Zeng, L. Zhang and A. R. Barron, *Nano Lett.*, 2005, **5**, 2001-2004.
48. K. S. Novoselov, A. K. Geim, S. V. Morozov, D. Jiang, Y. Zhang, S. V. Dubonos, I. V. Grigorieva and A. A. Firsov, *Science*, 2004, **306**, 666-669.
49. W. Yang, K. R. Ratinac, S. P. Ringer, P. Thordarson, J. J. Gooding and F. Braet, *Angew. Chem. Int. Ed.*, 2010, **49**, 2114-2138.
50. J. T. Robinson, S. M. Tabakman, Y. Liang, H. Wang, H. Sanchez Casalongue, D. Vinh and H. Dai, *J. Am. Chem. Soc.*, 2011, **133**, 6825-6831.
51. B. Mao, D. G. Calatayud, V. Mirabello, B. J. Hodges, J. A. R. Martins, S. W. Botchway, J. M. Mitchels and S. I. Pascu, *Adv. Funct. Mater.*, 2016, **26**, 687-697.
52. N. R. Wilson, P. A. Pandey, R. Beanland, R. J. Young, I. A. Kinloch, L. Gong, Z. Liu, K. Suenaga, J. P. Rourke, S. J. York and J. Sloan, *ACS Nano*, 2009, **3**, 2547-2556.
53. A. Alazmi, S. Rasul, S. P. Patole and P. M. F. J. Costa, *Polyhedron*, 2016, **116**, 153-161.
54. S. Stankovich, D. A. Dikin, R. D. Piner, K. A. Kohlhaas, A. Kleinhammes, Y. Jia, Y. Wu, S. T. Nguyen and R. S. Ruoff, *Carbon*, 2007, **45**, 1558-1565.

Chapter 5 : Synthesis and evaluation of novel targeted nanoprobes

5.1 Overview

To date, the state-of-the-art has generally focused on targeting aspects involving three main types of membrane receptors used by cells to detect environmental changes and to communicate with the extracellular environment: receptor tyrosine kinases (RTK), ion channel receptors and G protein-coupled receptors (GPCR). The study of ion channels and RTK in the progression of cancer has been extensively reported, being the best example the epidermal growth factor receptor (EGFR).[1]

The targeting and study of GPCR receptors is now receiving increasing attention as these receptors have demonstrated to play an essential role in tumorigenesis, tumour progression, invasion and metastasis.[1] The gastrin releasing peptide receptor (GRPR) is a type of GPCR that has been found to be overexpressed in several types of cancers as non-small cell lung carcinoma[2] and head and neck carcinoma[3]. Furthermore, the GRPR has been extensively applied for the detection of prostate adenocarcinoma, as the receptors are overexpressed in a large proportion of prostate cancer cases compared to the low expression found in healthy tissues or tissues affected by other prostatic affections such as BPH or prostatitis.[4] The main type of agonists to target the GRP family of receptors is composed by small peptides like bombesin (14 amino acids).

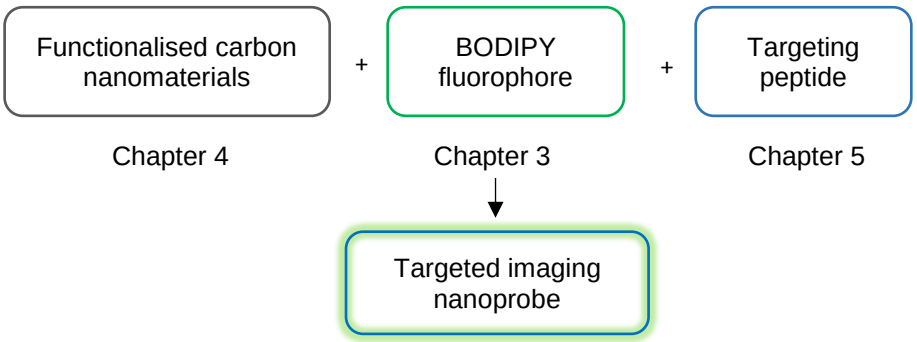

Figure 5.1: Schematic representation of the components of the imaging nanoprobe.

Despite the fact that bombesin is a tetradecapeptide, it is currently believed that only 7 amino acids from the C-terminal are essential for its targeting role and the use of the [7-14] or [7-13] fragments have been widely applied in molecular imaging so far.[5] In this work, the simpler [7-13] fragment was prepared via an adapted synthetic protocol, then coupled to a novel BODIPY fluorophore and further applied in the synthesis of diverse imaging probes, including optical imaging agents supported on the functionalised carbon nanomaterials (described in Chapter 4, Figure 5.1). Furthermore, the synthesis and characterisation of other nanohybrids including Ga(III) thiosemicarbazonato species were explored hereby.

5.2 Synthesis of a bombesin [7-13] fragment

As stated above, the selected targeting peptide sequence was a fragment of the bombesin peptide, specifically the [7-13] fragment. The complete amino acid sequence of bombesin is shown in Figure 5.2, with the [7-13] fragment highlighted in blue. This fragment has been successfully applied in imaging and drug design so far, and several studies by others have shown that the targeting nature for overexpressed gastrin releasing peptide receptors of the original peptide can be maintained.[6, 7]

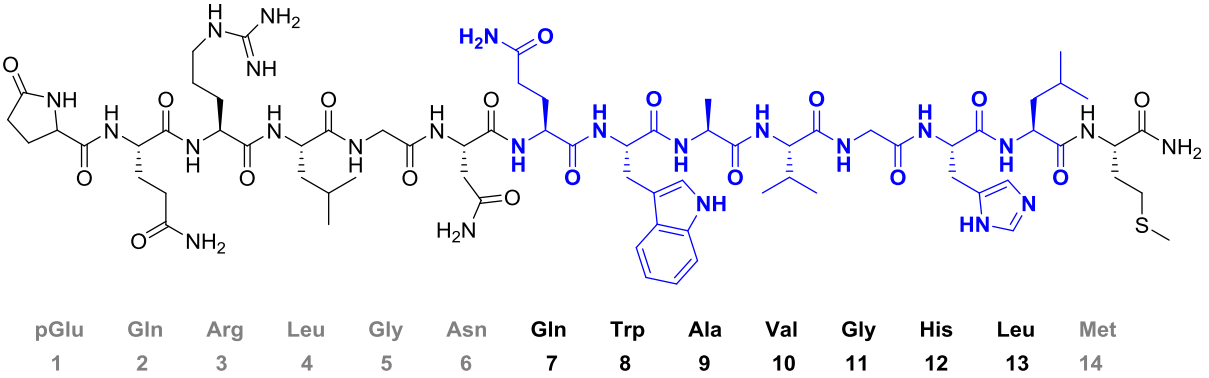

Figure 5.2: Structure of bombesin with the [7-13] fragment of bombesin (synthesised in this work) highlighted in blue.

The peptide sequence was prepared by the widely used strategy of solid-phase peptide synthesis (SPPS). The use of microwave reactors in peptide synthesis is now a routine methodology with some fully automated systems.[8]

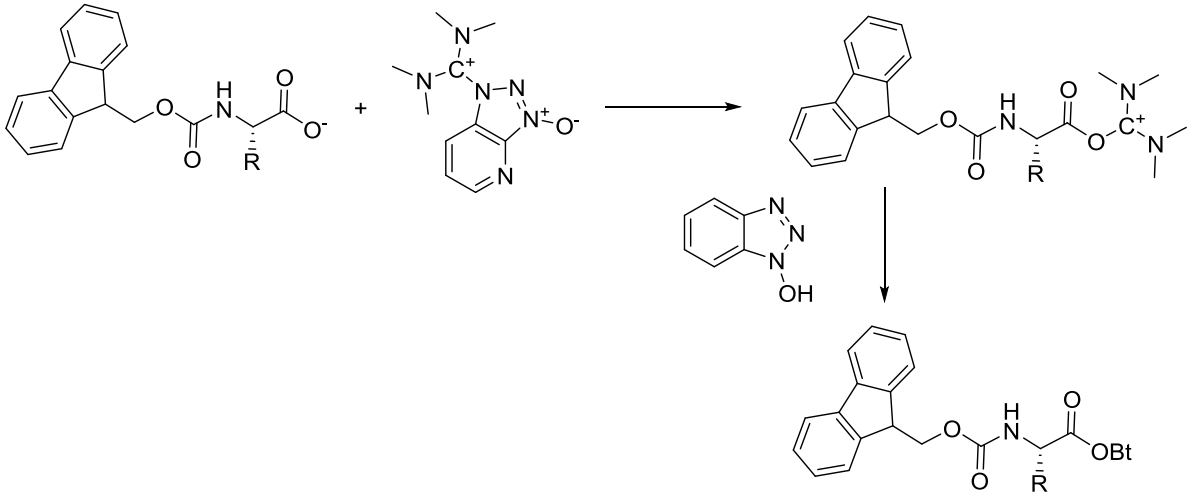

Scheme 5.1: Role of 1-hydroxybenzotriazole (HOBt) in the activation mechanism of amino acids using N-[(dimethylamino)-1H-1,2,3-triazolo-[4,5-b]pyridin-1-ylmethylene]-N-methylmethanaminium hexafluorophosphate N-oxide (HATU).[9]

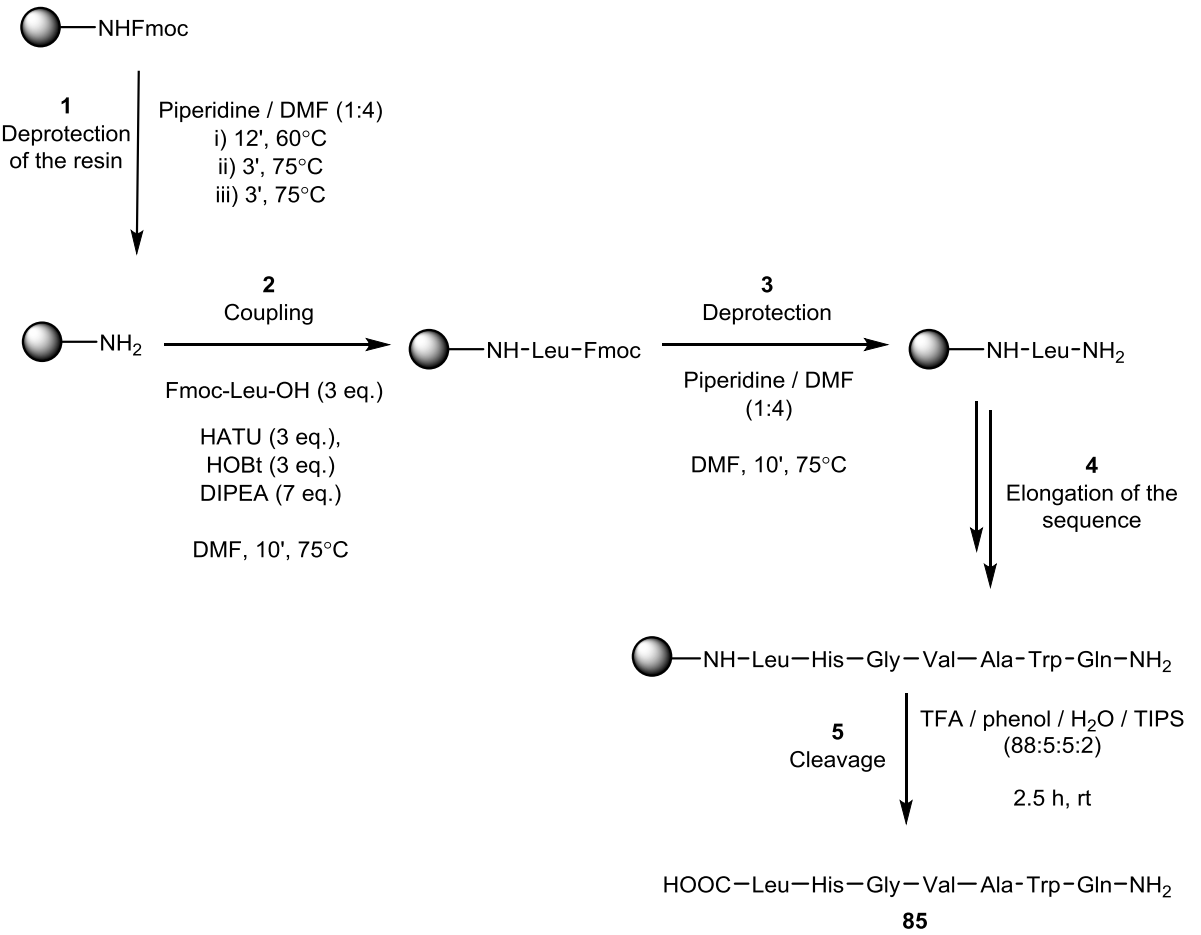

Scheme 5.2: Steps involved in the synthesis of the fragment [7-13] of bombesin applied hereby.

The use of microwave radiation can increase the efficiency of the couplings and reduce substantially reaction times even if the systems are operated manually.[9] In this case, a Rink amide resin (with a 0.59 mmol/g substitution) was used as solid support and the couplings conducted using N-[(dimethylamino)-1H-1,2,3-triazolo-[4,5-b]pyridin-1-ylmethylene]-N-methylmethanaminium hexafluorophosphate N-oxide (HATU) as activating reagent. The risk of undesired side reactions can be reduced and the optical integrity of the final product protected by the addition of 1-hydroxybenzotriazole (HOBt) to the reaction mixture (Scheme 5.1).[9, 10] A combination of HATU and HOBt were employed hereby as coupling reagents in a 1:1:1 stoichiometry with the amino acid.[11] N,N-diisopropylethylamine (DIPEA) was used as a base and the couplings carried out in DMF heating 10 min at 75 ºC under microwave irradiation. The full synthetic methodology is depicted in Scheme 5.2 and it involved five stages. The first was the deprotection of the resin after it had been swelled. This was achieved by heating the resin during three cycles in piperidine/DMF (1:4 v/v) at 60 ºC and 75 ºC. The resin was thoroughly washed with DMF and CH_2Cl_2 after each cycle. The deprotection was confirmed qualitatively in some resin beads by the reaction of the free amino groups with ninhydrin, yielding a deep blue solution (Kaiser test). The first coupling (step 2 in Scheme 5.2) was conducted with the first amino acid and the coupling reagents added in a three-fold excess with respect to the loading of the

resin. The deprotection of the supported amino acid on the resin followed (step 3 in Scheme 5.2) and was performed by heating the resin with piperidine/DMF (1:4 v/v) for 10 min at 75 ºC. The success of the coupling and deprotection reactions were equally demonstrated with a qualitative Kaiser test. In case the result of the test was opposite to that expected, the coupling or deprotection step was repeated under the same conditions.

The amino acid sequence was consequently elongated (step 4 in Scheme 5.2) by repeating steps 2 and 3 with the remaining amino acids. Histidine was an exception as the coupling needed to be performed at room temperature to avoid racemisation reactions.[12]

The final step in the synthetic process was the cleavage of the peptide from the resin (step 5 in Scheme 5.2), that was achieved by stirring the resin 2.5 h at room temperature with a cleavage cocktail containing trifluoroacetic acid, phenol, water and triisopropylsilane (88:5:5:2). The reaction was performed protected from light and the time was limited in order to avoid the potential oxidation or alkylation of the side chains of labile amino acids as His or Trp.[13] The peptide was isolated as a white solid by precipitation in cold ether and posterior centrifugation. The crude peptide was purified by automated flash column chromatography in a C18 cartridge using water and acetonitrile as solvent system.

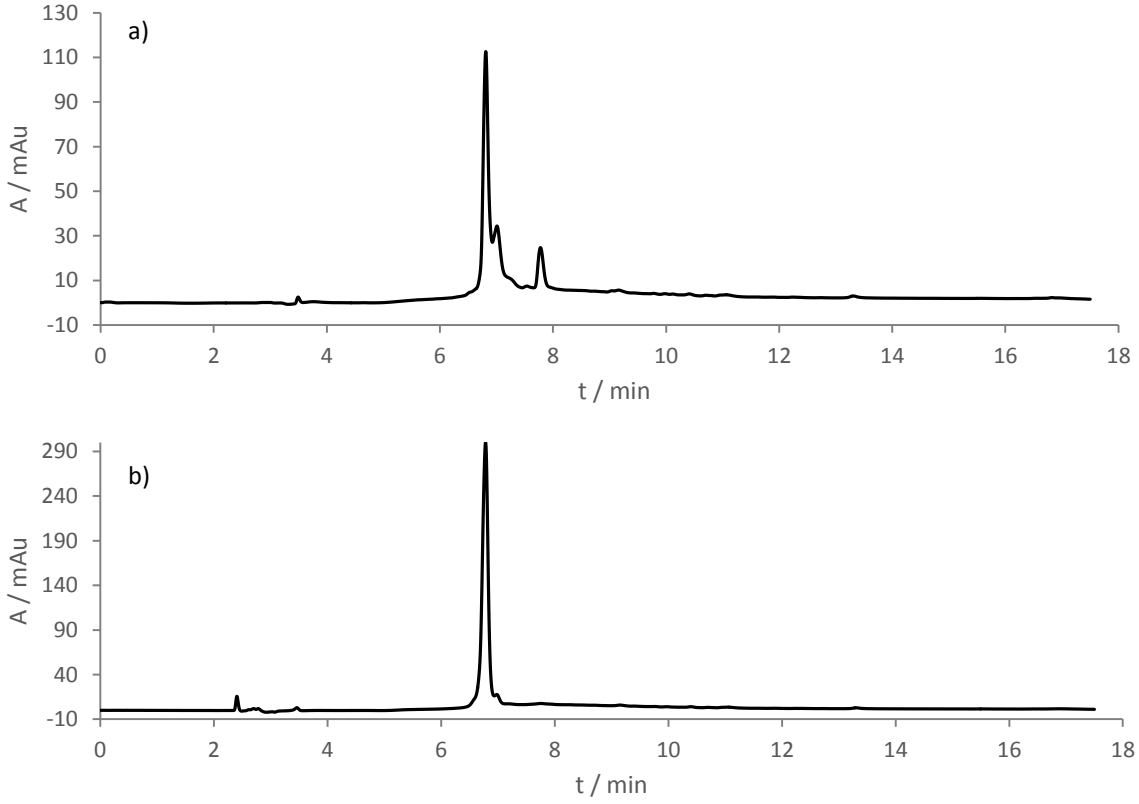

Figure 5.3: HPLC traces of the crude peptide after cleavage (a) and after purification by automated flash chromatography (b) (HPLC method A).

The purified product was analysed by HPLC (Figure 5.3) demonstrating the efficacy of the purification process. The nature of the product was confirmed by mass spectrometry. The ESI-TOF technique in positive mode showed the radical cation $[M]^{+\cdot}$ of the peptide as the molecular peak of the spectrum but the sodium salt $[M\text{-}Na]^{+}$ was also observed. The mass spectrum and experimental isotopic patterns and theoretical isotopic patterns proposed for the product can be observed in Figure 5.4.

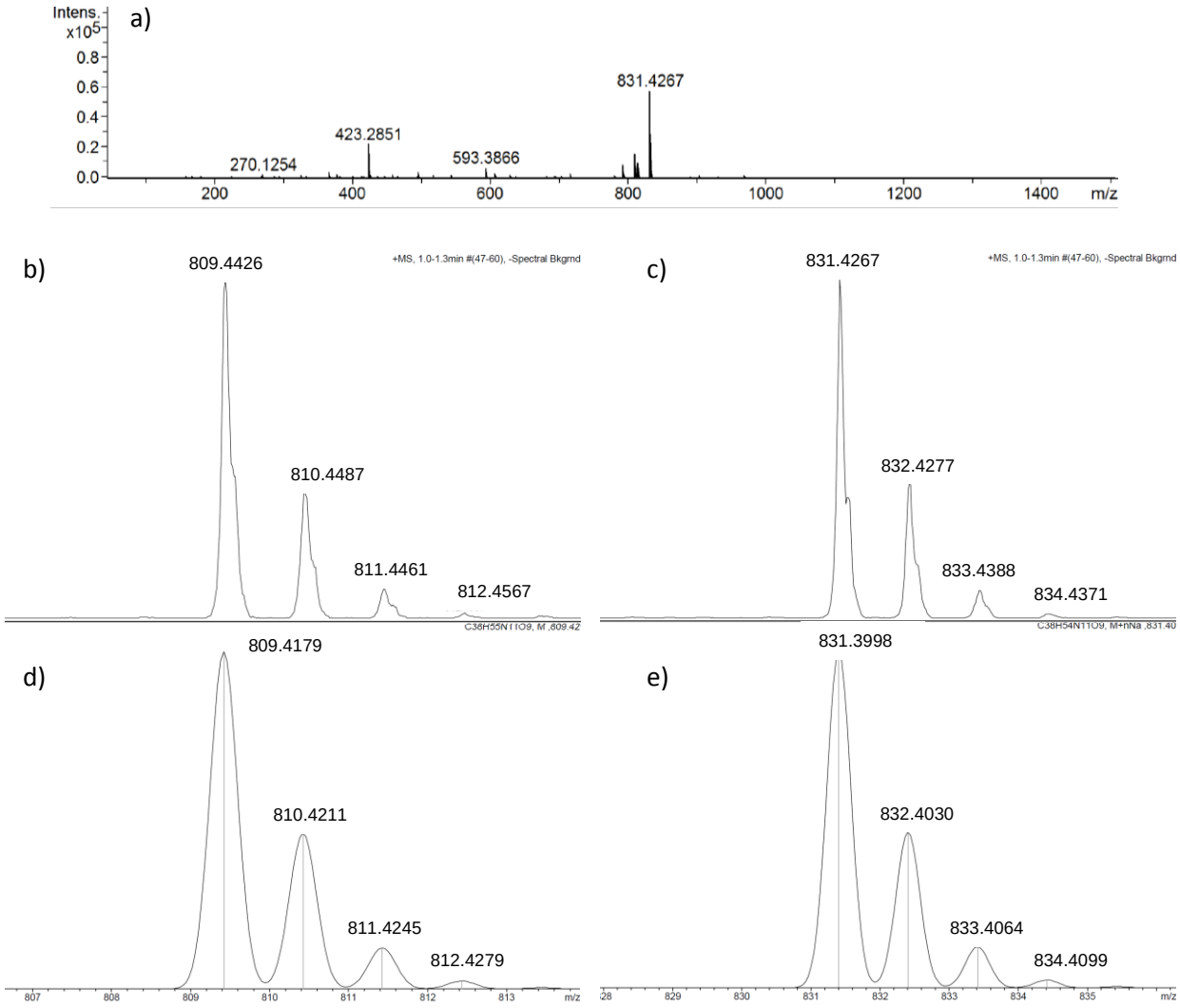

Figure 5.4: ESI-TOF mass spectrum of **85** (a). Experimental isotopic patterns of $[M]^{+\cdot}$ (b) and sodium salt (c). Theoretical isotopic patterns of $[M]^{+\cdot}$ (d) and sodium salt (e).

The ^{1}H NMR spectrum of the peptide **85** was acquired in deuterium oxide and the resonances assigned thanks to the bidimensional ^{1}H-^{1}H COSY spectrum (see Appendix A). The chemical shifts of the resonances were in accordance with the values found in the literature.[14]

The ^{1}H resonances for amino acid residues incorporating aromatic groups (Trp and His) occur between 7.0 – 8.5 ppm. The assignment of this region was straightforward as the His protons are present as broad

singlets with only one correlation peak in the ^{1}H-^{1}H COSY spectrum. In contrast, the tryptophan residue presents a singlet for H-2 and the pattern of a 1,2-disubstituted benzene ring. These resonances can be identified as two deshielded doublets, one triplet (H-6) and one multiplet (H-5). The resonance of the protons adjacent to the NH groups in the peptide backbone ($^{\alpha}CH$) are observed between 3.8 – 4.7 ppm, downfield in the aliphatic zone. The $^{\alpha}CH$ resonances for His and Trp are the most deshielded (ca. 4.7 ppm) appearing as triplets although the resonances of $^{\alpha}CH$ His and D_2O overlap hence not showing a defined multiplicity. The only remaining $^{\alpha}CH$ resonance with a clear multiplicity is that of Gln that appears as a triplet. The two protons of Gly also appear in this region as a multiplet overlapping with the $^{\alpha}CH$ of Val.

The resonances of the side groups of the amino acids appear in the 0.5 – 3.3 ppm region. The most deshielded resonances are the methylene groups of His and Trp ($^{\beta}CH_2$) that overlap in a multiplet.

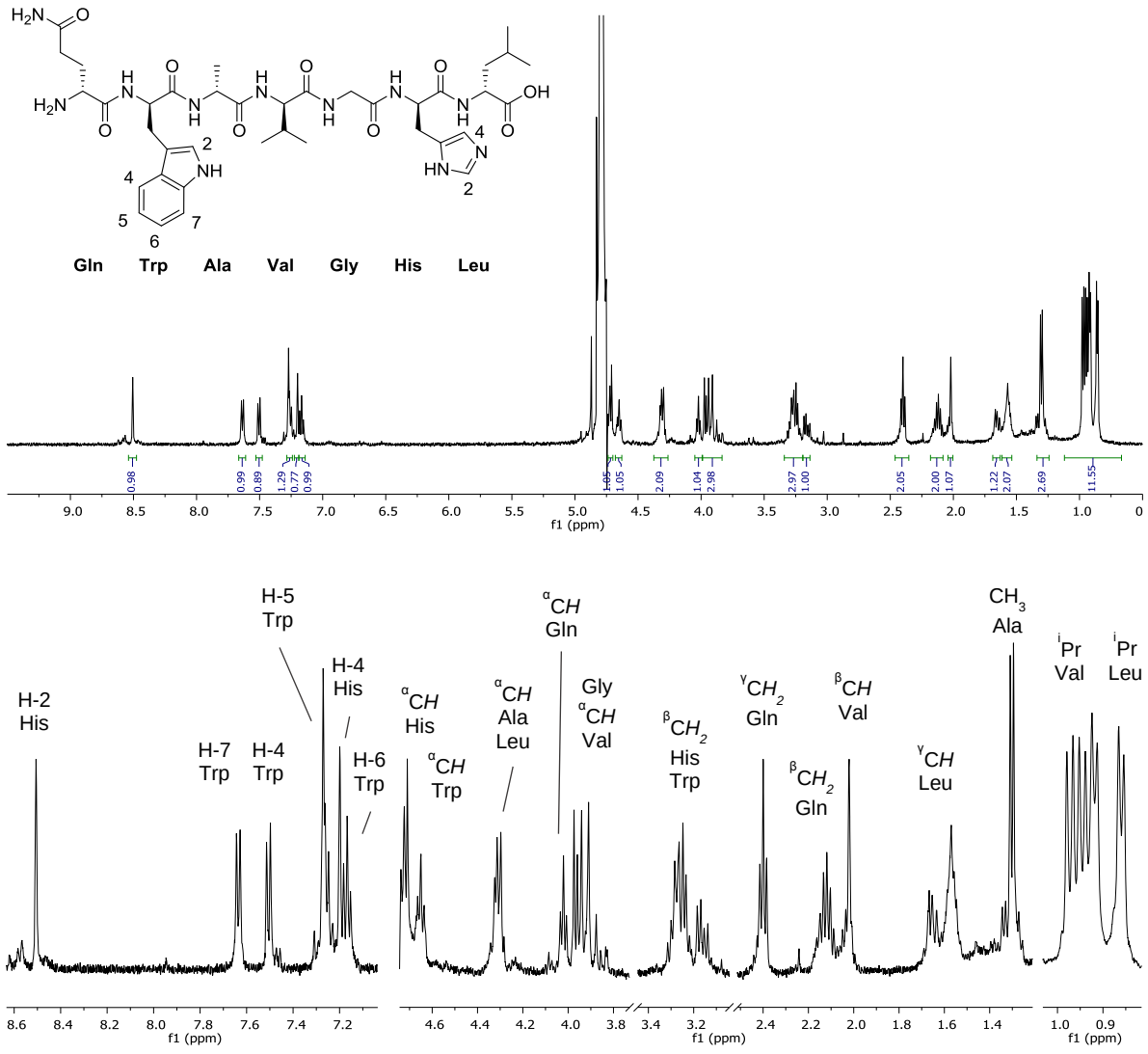

Figure 5.5: ^{1}H NMR (D_2O) spectrum of bombesin [7-13] (**85**).

The ^{1}H resonance assignable to the $^{\gamma}CH_2$ group of Gln follows, in a descending order of chemical shift, and appears as a triplet. The most characteristic and identifiable resonances are the methyl groups of Ala and isopropyl groups of Val and Leu that are helpful to assign the corresponding resonances. The methyl group of Ala appears as a doublet integrating for three protons while the isopropyl groups of Val and Leu are observed as four doublets. The resonances for the isopropyl group in Val are more deshielded and the doublets closer. The pair of doublets for Leu appear more separated and downfield.

5.3 Preparation of a novel BODIPY-bombesin conjugate

After the [7-13] fragment of bombesin was prepared and purified, the targeted fluorophore was prepared by coupling with BODIPY **57**. Several conditions were evaluated following the reaction by TLC and HPLC and the best conversion was obtained by stirring the reaction mixture for 20 h at 60 ºC in DMF. The coupling proceeded by activation of the carboxylic acid in the side chain of the BODIPY linker with (benzotriazol-1-yloxy)tripyrrolidinophosphonium hexafluorophosphate (pyBOP) for three hours when the peptide was added and the reaction mixture stirred overnight (Scheme 5.3).

The solvent was concentrated under vacuum and the crude reaction mixture purified by automated flash column chromatography in a C18 cartridge. The product was subsequently deprotected using the same procedure as in the peptide synthesis (piperidine/DMF, 1:4 v/v) in just 1.5 h as followed by TLC. The product was purified by semi-preparative HPLC and lyophilised to yield the desired product as a red powder.

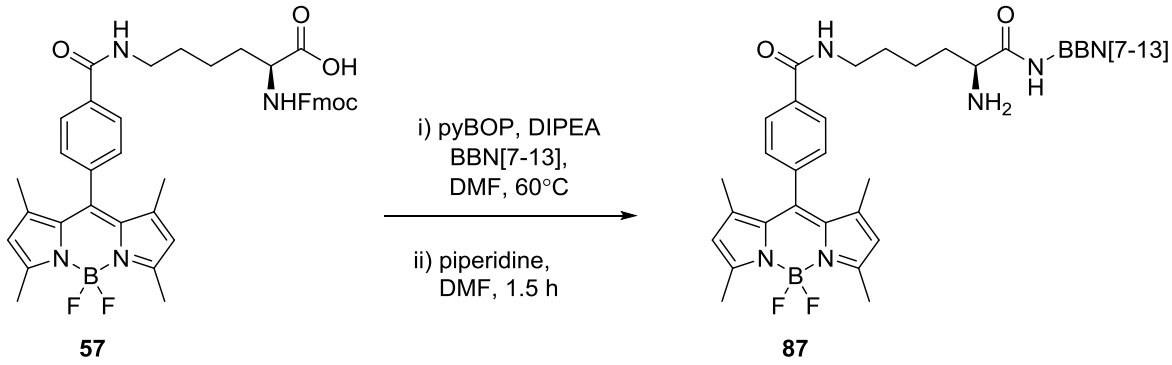

57 **87**

Scheme 5.3: Reaction conditions for the coupling of BBN[7-13] and BODIPY **57** applied hereby.

The product was fully characterised using spectroscopic techniques such as NMR or mass spectrometry. The mass spectrum of compound **87** is shown in Figure 5.6 (top). The radical cation of the product is observed as the molecular ion with a m/z value of 1287.6445 with the sodium salt also identified. The compared theoretical and experimental isotopic patterns for the two species can be observed under the spectrum in Figure 5.6 for the cation radical species (left) and the sodium salt (right). The experimental and isotopic patterns matched with a high level of accuracy demonstrating the nature of the product.

The characterisation of **87** was also carried out with different NMR spectroscopies and all the resonances in the ^{1}H NMR spectrum assigned. The ^{1}H NMR spectrum can be observed in Figure 5.7 with expansions in Figure 5.8 for the aromatic (a) and aliphatic (b and c) regions. The assignment of the resonances for every group in the conjugate was possible thanks to the application of bidimensional techniques as ^{1}H-^{1}H COSY, that shows vicinal correlation between H nuclei, TOCSY, that reveals long distance correlation between ^{1}H nuclei or ^{1}H-^{13}C HSQC that shows ^{1}J correlations between ^{1}H and ^{13}C nuclei.

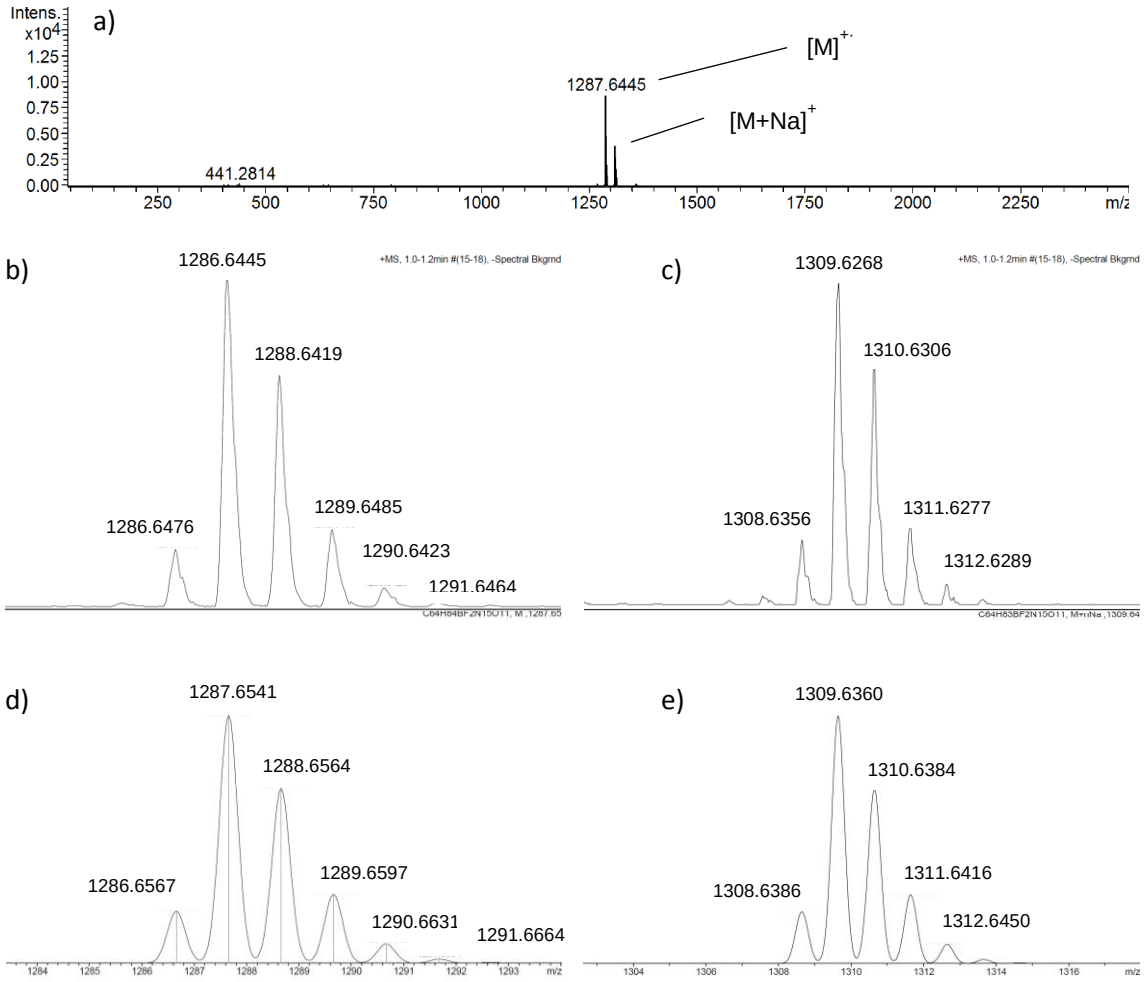

Figure 5.6: ESI-TOF mass spectrum of compound **87** (a). Experimental isotopic patterns of $[M]^{\cdot+}$ (b) and the sodium salt (c). Theoretical isotopic patterns for $[M]^{\cdot+}$ (d) and the sodium salt (e).

The identification of the resonances for the BODIPY fluorophore in the ^{1}H NMR spectrum of the conjugate was straightforward as they are similar to the starting material. The protons of the phenyl group appear as a doublet (H-3) and a multiplet (H-4) in the aromatic region. The methyl groups corresponding to H-8 and H-10 appear as singlets in the aliphatic region although a long distance correlation with H-9 is present. The fact that H-4 appears as a multiplet rather than a doublet and that H-9 is displayed as pair of singlets reveals that under the NMR experiment conditions, the rotation of the BODIPY group might not be totally free around the C-C bond linking the phenyl group to the boron dipyrromethene core which causes these protons to no longer be equivalent. The resonances of the Lys linker largely overlap with the rest of the amino acid residues in the peptide.

The aromatic region of the spectrum also includes the resonances of the residues with aromatic groups (His and Trp) as in the original peptide, although the chemical shift was more deshielded (ca. 0.2 ppm) for both amino acids. The His resonances appear as two singlets presenting a long distance correlation.

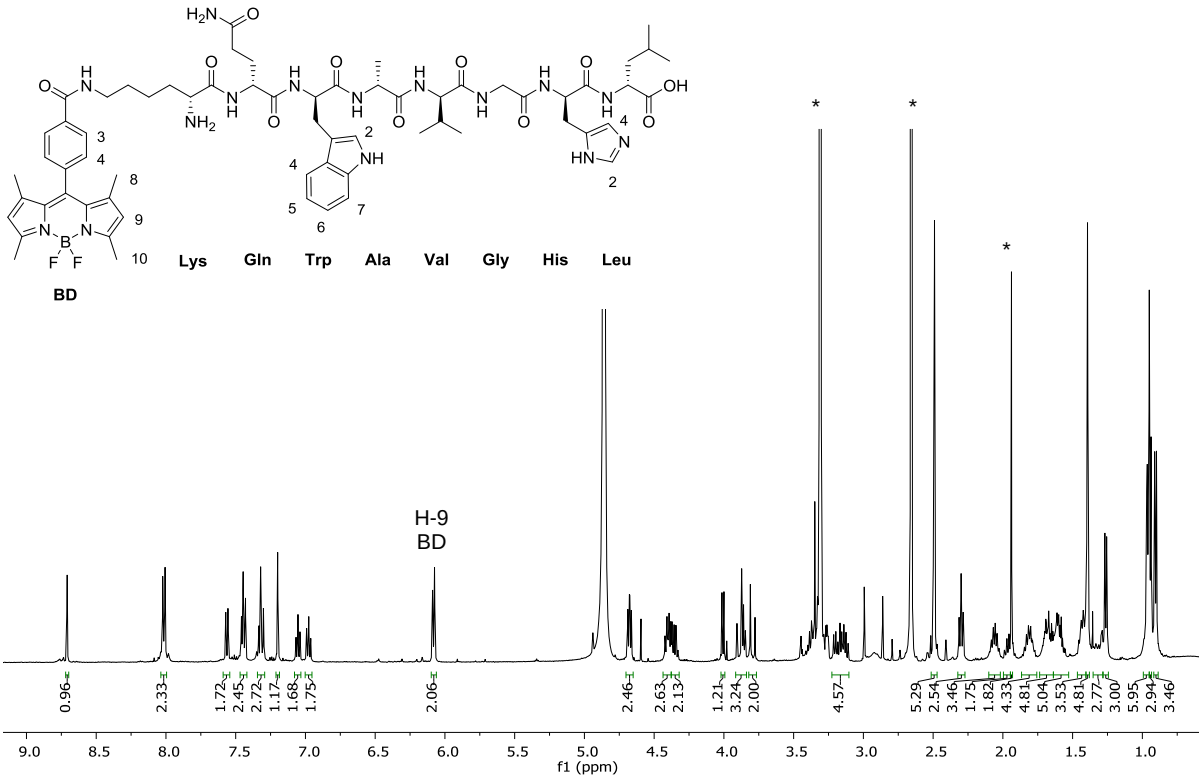

Figure 5.7: ^{1}H NMR spectrum (CD_3OD) of BODIPY-bombesin conjugate **87**. [*Traces of deuterated and non-deuterated solvents].

The Trp resonances appear as one doublet for H-7, a multiplet for H-4 (due to the overlap with His resonances), two triplets for H-5 and H-6 and a singlet for H-2.

As in the starting material, the $^{\alpha}$CH resonances appear downfield between 3.8 and 4.7 ppm (Figure 5.8, b). The $^{\alpha}$CH resonances for His and Trp are the more deshielded and overlap in a pseudo doublet of doublets. The only $^{\alpha}$CH resonance that can be observed independently is the one for Val that appears as a doublet. The $^{\alpha}$CH resonances for Gln, Ala and Leu overlap in a multiplet and the one for the Lys residue overlaps with the Gly resonances. In this case, the two protons for Gly are observed as an AB system (^{2}J = 16.7 Hz) with centre at 3.84 ppm.

The ^{1}H resonances assignable to the aliphatic side chains of the amino acids residues are observed upfield in the spectrum between 0.8 and 2.4 ppm (Figure 5.8, c). There are characteristic resonances that can be independently observed and develop a clear multiplicity and are helpful indicators in order to identify the amino acid residues. The $^{\gamma}CH_2$ resonances for Gln, for example, appear as triplet with two correlation peaks in the ^{1}H-^{1}H COSY spectrum. Thanks to the correlation to the same carbon in the ^{1}H-^{13}C HSQC spectrum for those two resonances, they are assignable to the adjacent $^{\beta}CH_2$ of Gln that appear as two different resonances because they are diastereotopic.

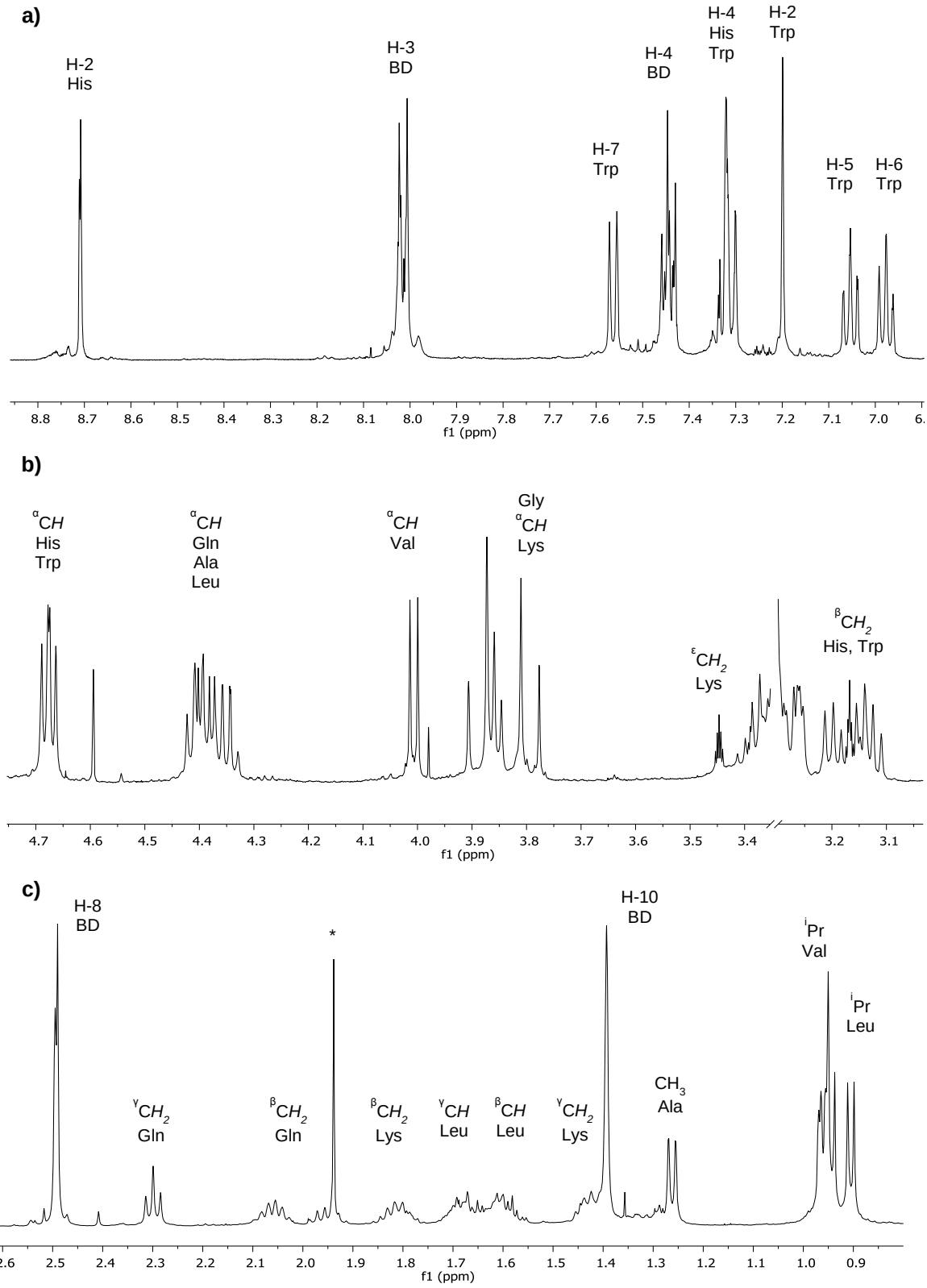

Figure 5.8: Expansions of the aromatic (a) and aliphatic regions (b) and (c) of the ^{1}H NMR spectrum (CD_3OD) of **87**.

Another characteristic resonance is the CH_3 group of Ala that appears as a doublet due to the coupling with the $^{\alpha}CH$ group. The isopropyl groups of Val and Leu appear as a pair of doublets as in the starting material. The vicinal correlations in the ^1H-^1H COSY spectrum reveal that the resonances of the $^{\beta}CH_2$ group of Leu are also diastereotopic giving two different multiplets.

The assignment of the methylene groups in the Lys linker were conducted finally as the majority of the resonances overlap with other groups. The use of the TOCSY spectroscopy (Appendix A) was helpful as it revealed long distance ^1H-^1H correlations and allowed the identification of the groups of resonances in the same spin system.

Furthermore, UV-vis and fluorescence spectroscopic investigations were carried out, and the photophysical properties of the conjugate **87** will be discussed in Section 5.6.

5.4 Preparation of functional SWNT nanoprobes for optical imaging

In order to obtain SWNT nanoprobes, the functionalised derivatives presenting the most promising properties in terms of functionalisation and dispersion stability containing the terminal carboxyl linkers were selected to be functionalised with the fluorophore and fluorophore-peptide conjugate. The coupling to the different COOH-functionalised SWNT was performed similarly to the amide couplings described in previous sections. The carboxylic acid groups on the nanotubes were activated with pyBOP for 3 h in DMF. The excess activating reagent was removed in order to prevent any possible auto coupling reactions of the fluorophore by centrifuging the reaction mixture, removing the supernatant and re-suspending the carbon nanomaterial in fresh DMF. The fluorophore, **58**, was coupled to the oxidised derivative **78** (Scheme 5.4) in order to compare the behaviour with the targeted derivative.

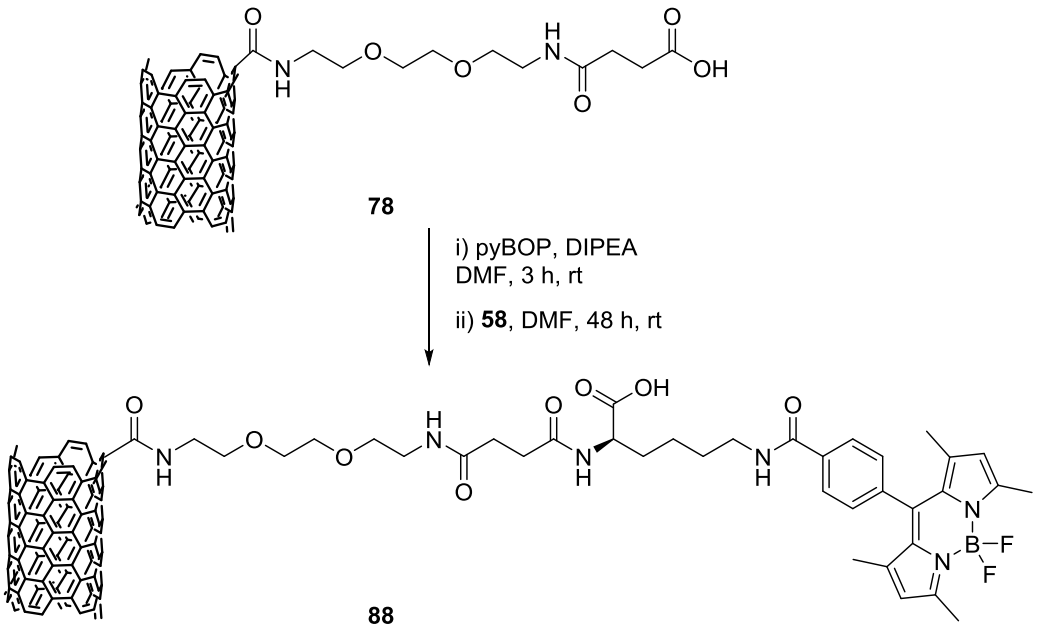

Scheme 5.4: Coupling procedure followed in order to incorporate the fluorophore **58** covalently onto the functionalised SWNT **78**.

The reaction mixture was stirred at room temperature for 48 h. Then, the nanohybrid was isolated by centrifugation of the reaction mixture, removing the supernatant and dispersing in fresh solvent. This process was repeated several times followed by a filtration step. The nanomaterial was filtered, washed with DMF, re-suspended in DMF by sonication and filtered again. This process was repeated several times, even if the filtrate was no longer coloured or fluorescent to ensure that all the fluorophore in excess had been discarded. The residue was dried under vacuum and lyophilised.

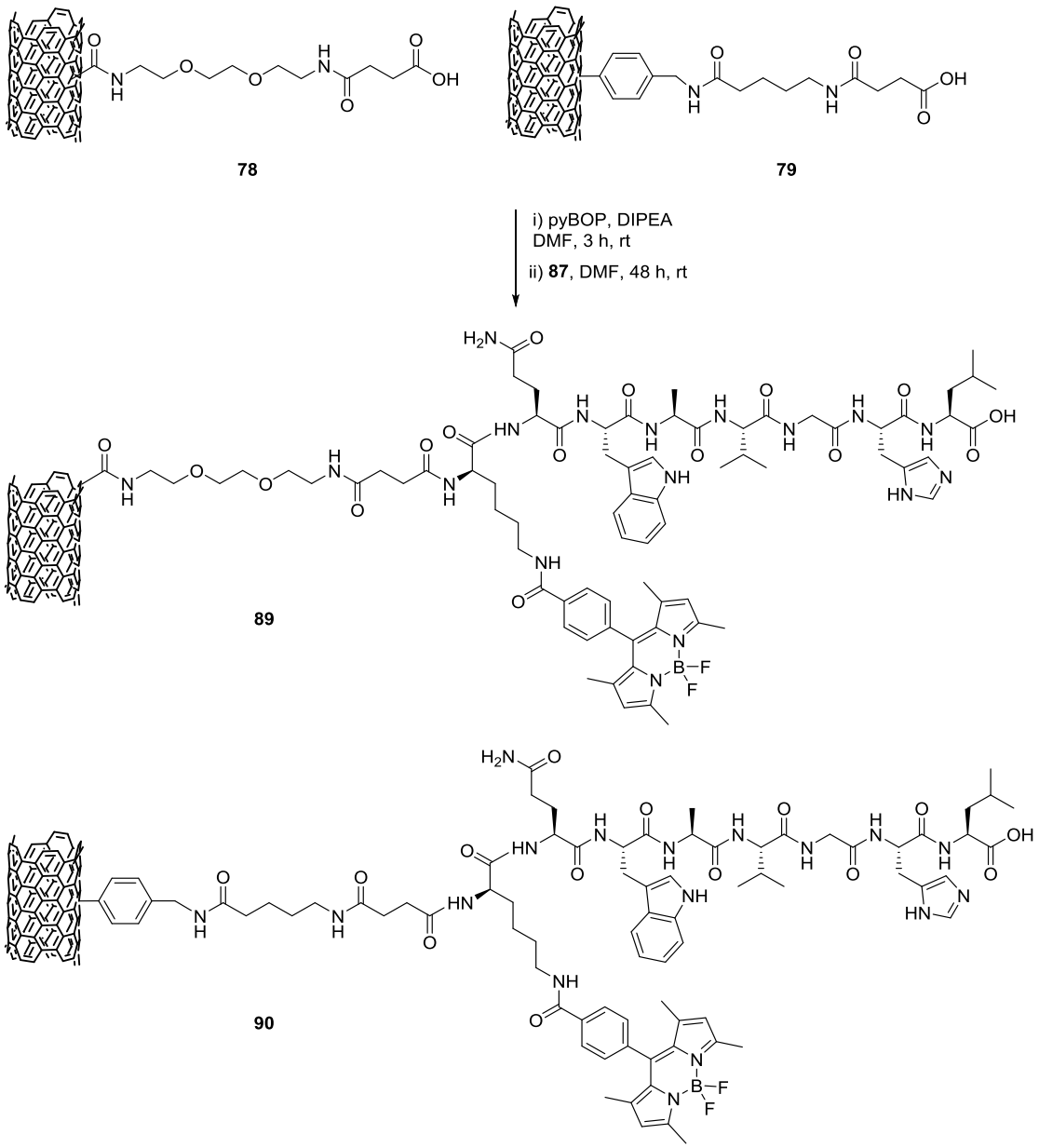

Scheme 5.5: Reaction conditions applied hereby for the synthesis of targeted nanoprobes **89** and **90**.

Following the same principle, the BODIPY-bombesin conjugate, **87**, was coupled to two functionalised SWNT derivatives, **78** and **79** yielding the targeted nanoprobes **89** and **90** as depicted in Scheme 5.5.

In both cases, the dispersions containing the desired nanohybrid samples were centrifuged and washed with DMF and methanol until a clear supernatant was obtained before being filtered and washed with more DMF and methanol until no fluorescence response was observed in the filtrate. The nanoprobes were dried and stored at low temperature to prevent any possible decomposition of the peptide.

In addition, an imaging probe based on a nanohybrid containing the gallium complex **23** was prepared (Scheme 5.6). The coupling was conducted in the same manner as the examples described in Scheme 5.4 and Scheme 5.5. The carboxylic acid groups in the functionalised SWNT were activated with pyBOP and an amide bond formed taking advantage of the free amino groups in the Ga(III) complex. The resulting product was isolated by centrifugation, washed, filtered and washed again.

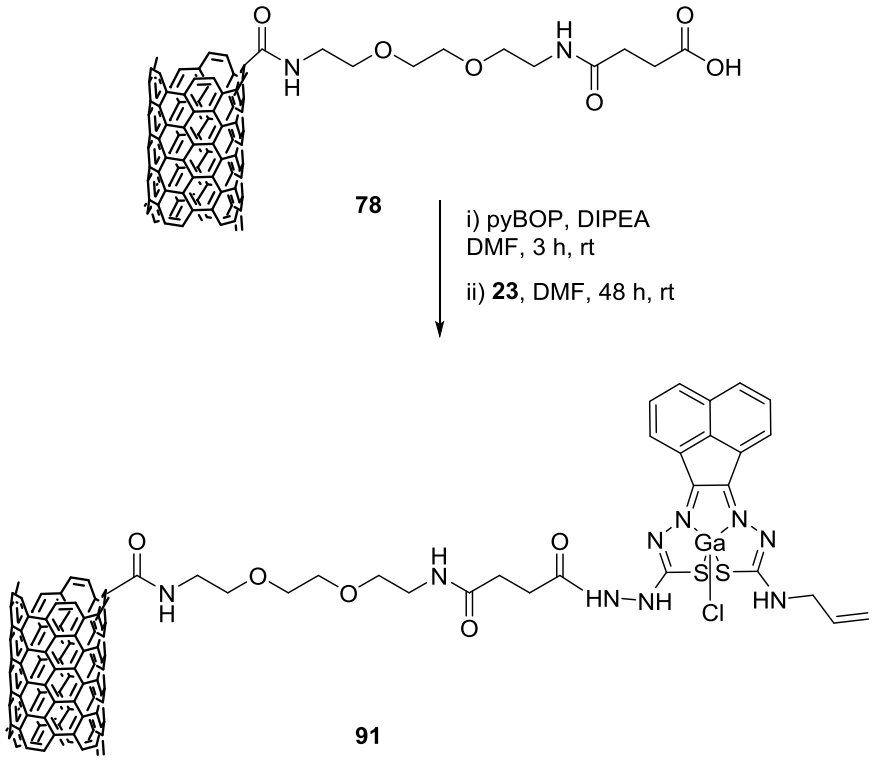

Scheme 5.6: Reaction conditions in the preparation of desired imaging probe **91**.

The prepared nanohybrids were characterised by using the techniques already described in Chapter 4 (e.g. FTIR and Raman spectroscopies and imaged by TEM).

Table 5.1: Characterisation data for nanohybrids **87** – **90** obtained by solid state Raman spectroscopy.

Compound	ν D (cm^{-1})	ν G (cm^{-1})	I_D/I_G
87	1336	1574	0.12
88	1338	1579	0.11
89	1334	1575	0.10
90	1338	1576	0.13

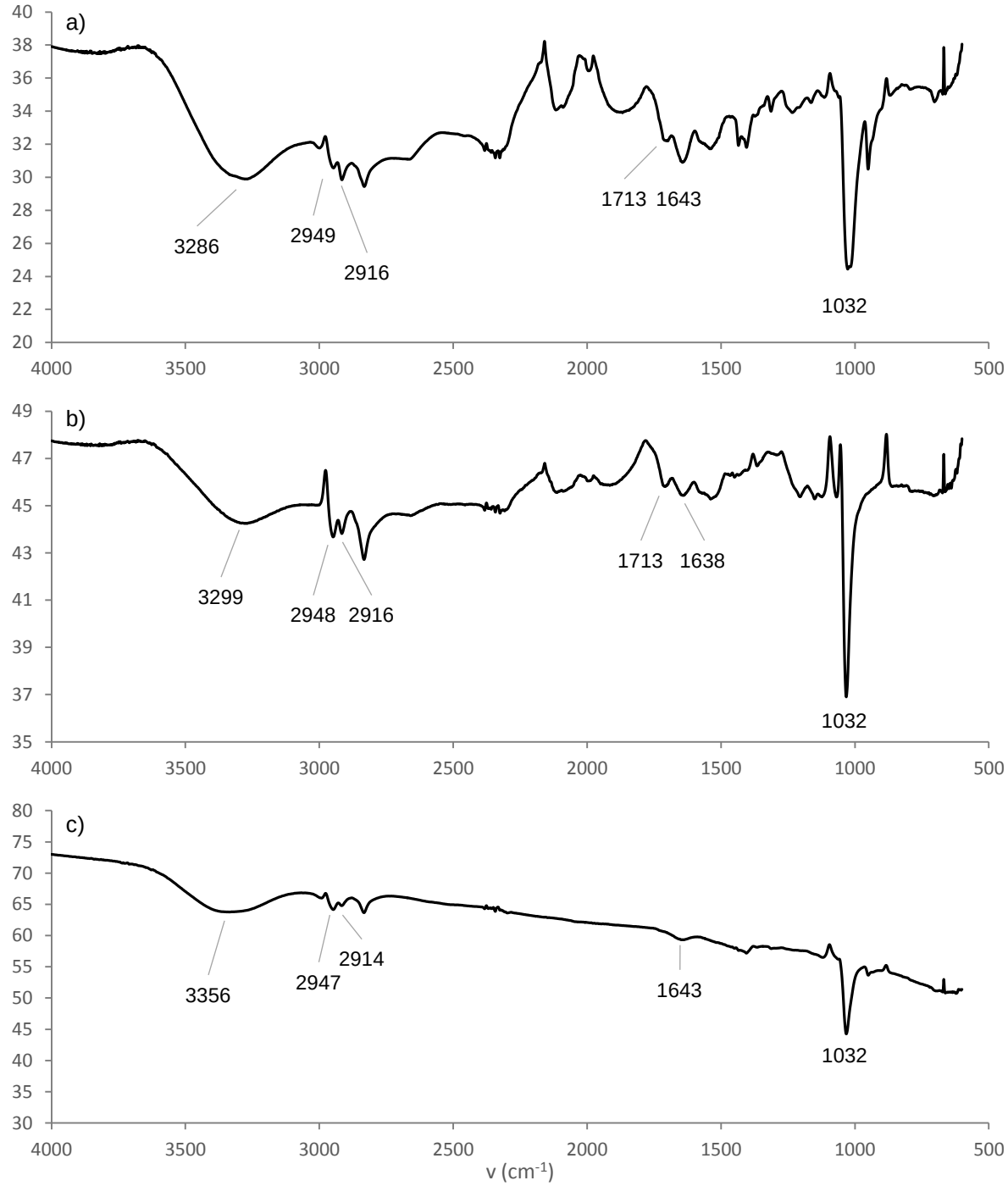

Figure 5.9: Solid state FTIR spectra of nanohybrids **88** (a), **89** (b) and **90** (c).

A summary of the characterisation data obtained by Raman spectroscopy including the wavenumbers of the D and G bands and the I_D/I_G ratio are showed in Table 5.1. It can be observed how the wavenumber of the D and G bands only suffer slight changes with respect to the starting materials and between nanohybrids. The I_D/I_G ratios are maintained in the same scale as the values obtained for the functionalised SWNTimplying that the coupling steps with the fluorophores or conjugate do not affect to the nanotube carbon lattice.

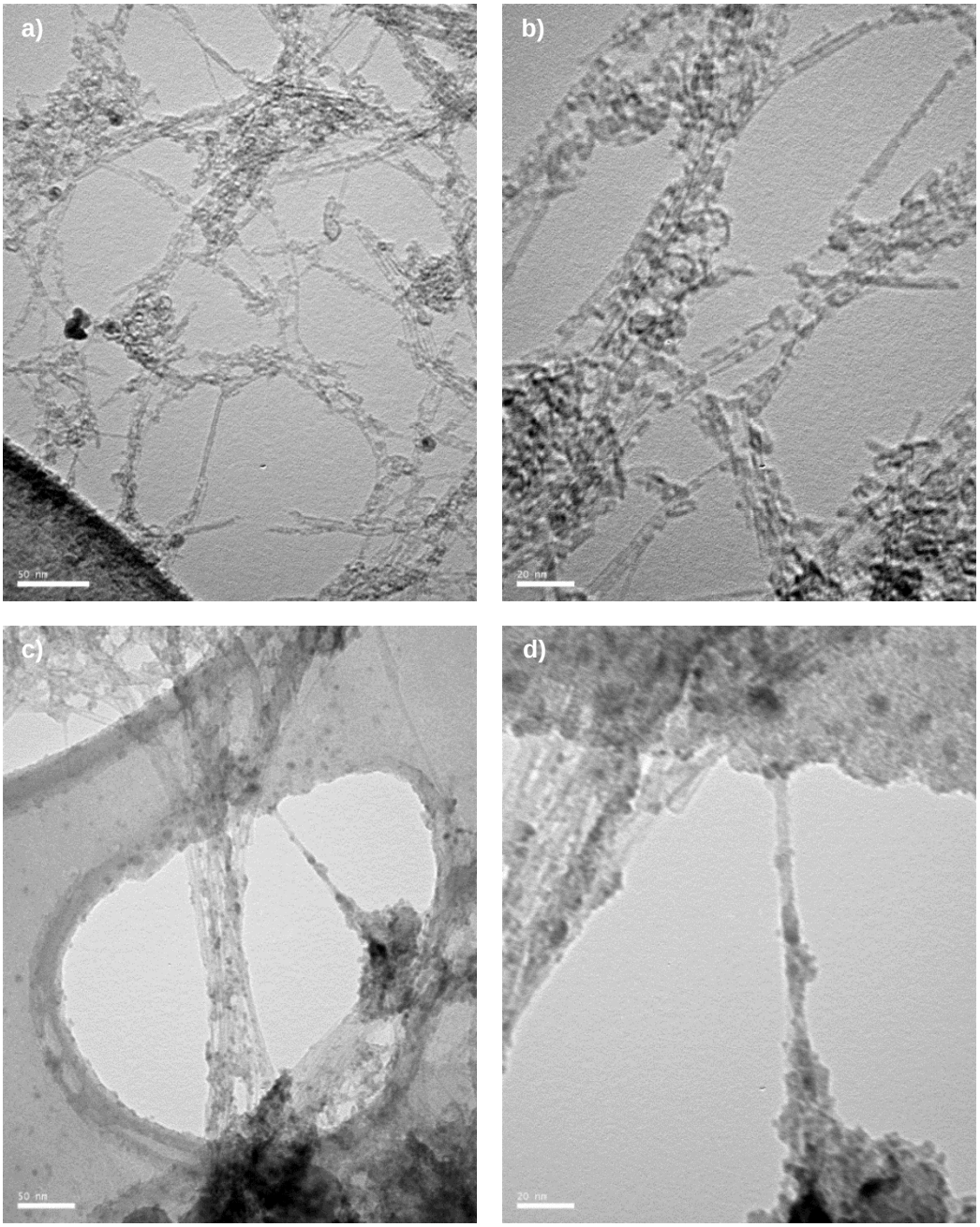

Figure 5.10: TEM images of functionalised SWNT **78** (a and b) and nanohybrid **88** (c and d). Scalebar for images on the left: 50 nm. Scalebar for images on the right: 20 nm.

The corresponding FTIR spectra for nanoprobes **88** – **90** can be observed in Figure 5.9. The FTIR spectra are similar among them with characteristic bands appearing in all three examples, probably due to the similarity of the functional groups introduced. A broad band at ca. 3300 cm^{-1} is visible in all of them and can be assigned to the NH stretching and OH stretching of the carboxylic acids. Another feature visible in all three spectra are the bands corresponding to the aliphatic CH stretching at ca. 2950 cm^{-1}. At least two different C=O stretching bands (ca. 1710 and 1640 cm^{-1}) are observed for **88** and **89** while only the

most intense (1643 cm^{-1}) is observable for **90**. Other intense and sharp band observable in the three spectra is the corresponding to the C-O stretching at ca. 1030 cm^{-1}.

Transmission electron microscopy was performed for a selection of SWNT probes. The TEM images for nanoprobes **88** – **90** can be observed in Figure 5.10 and Figure 5.11.

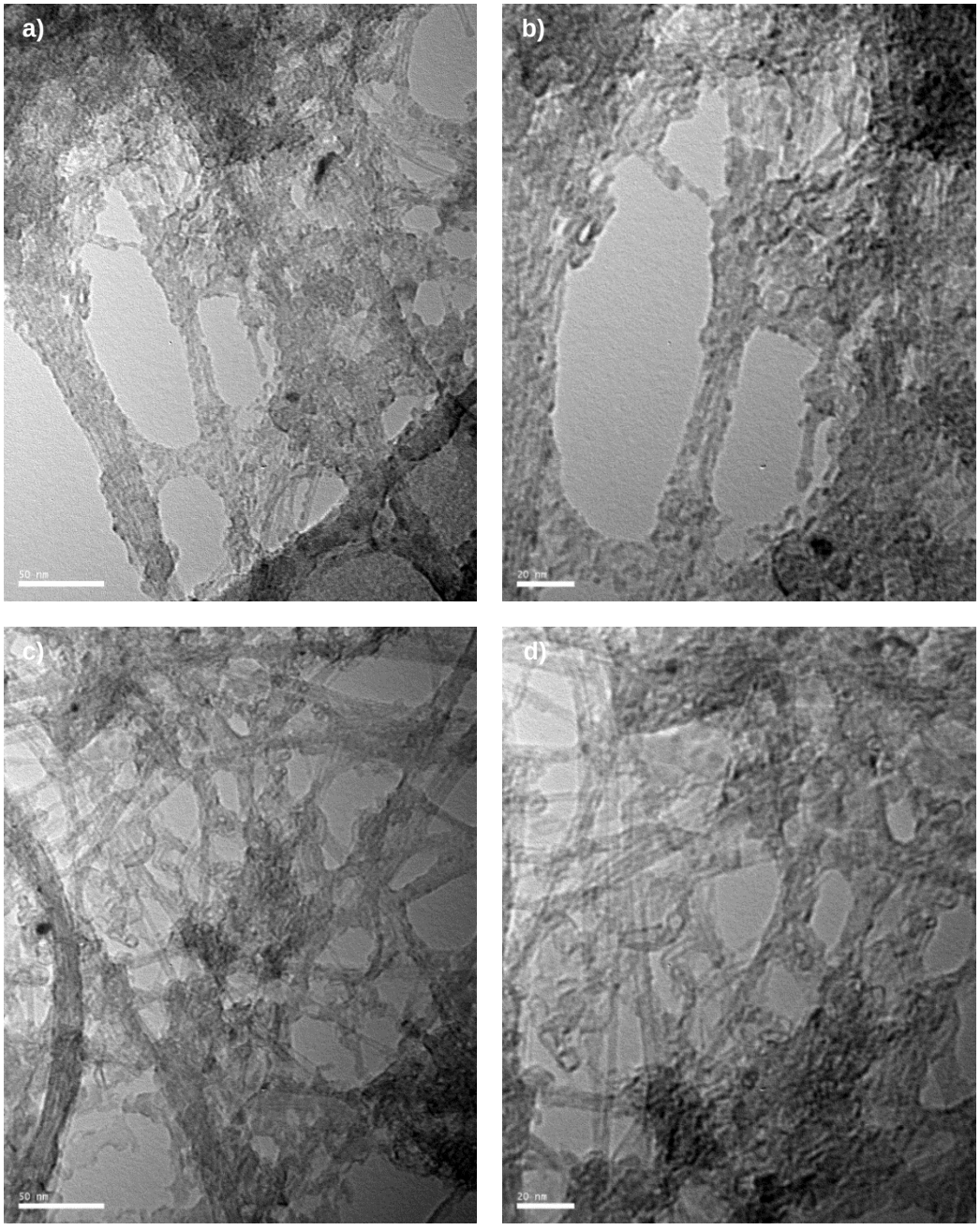

Figure 5.11: TEM images of targeted functional nanohybrids **89** (a and b) and **90** (c and d). Scalebar for images on the left: 50 nm. Scalebar for images on the right: 20 nm.

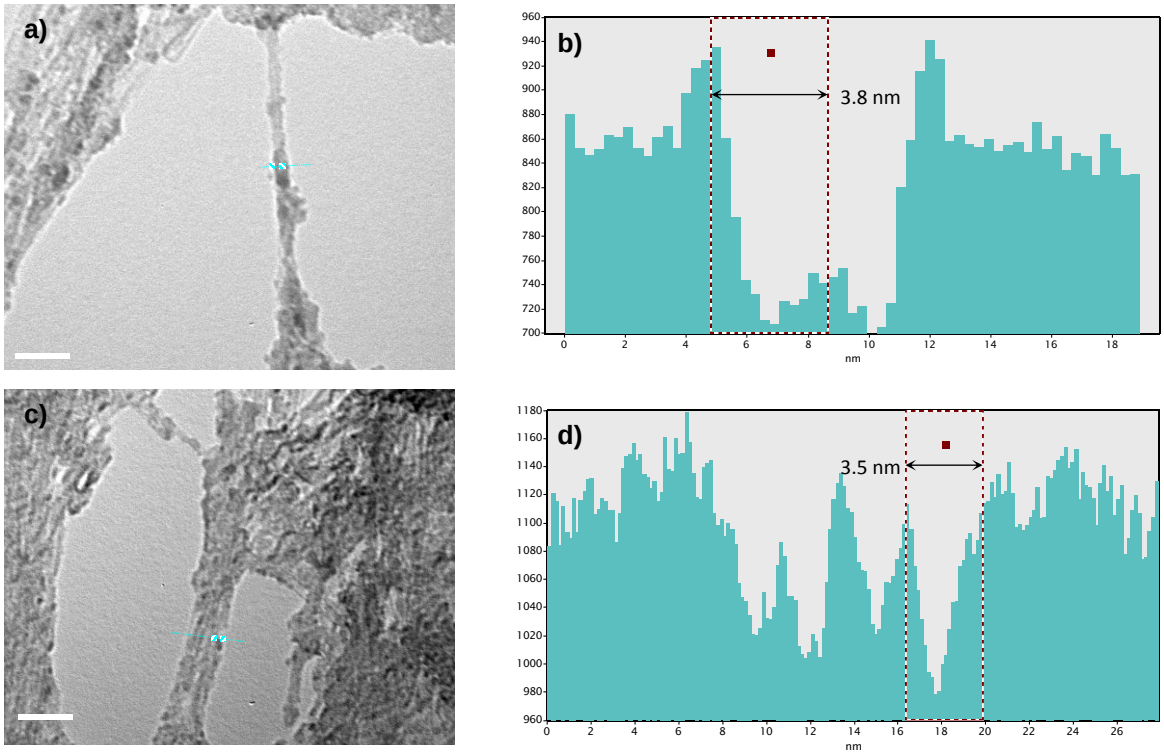

Figure 5.12: TEM images and height profiles (over the dashed blue lines) for **88** (a and b) and **89** (c and d).

The TEM images of the oxidised SWNT with the carboxyl terminated linker (**78**) have been included in Figure 5.10 for comparison as **78** served as starting material for **88** and **89**. In Figure 5.10 (left) the images of **78** and **88** at a lower magnification (300k and 250k respectively) can be observed. On the right column, a detailed picture at a higher magnification (500k) is showed. It can be observed how **78** shows an even distribution of SWNT individual tubes or groups of a few tubes can be observed. The SWNT present functionalised walls and tips that appear as imperfections and areas of darker contrast on walls and tips. However no extensive coating is observed. This is in accordance with the functionalisation nature as **78** only contains an aliphatic linker terminating in a carboxylic acid. In the case of **88** it appears that the SWNT strands are more aggregated in fibres or ropes of several SWNT. Nevertheless it is still possible to observe individual tubes in regions of the sample. The observed functionalisation seems higher in this case displayed as a thick coating around the tube with some dotted areas of darker contrast. This is in accordance with the introduction of the fluorophore containing the amino acid linker. The superior aggregation with respect to **78** can be caused by further aromatic or electrostatic interactions facilitated by the BODIPY group. An image at a greater magnification can be observed in the right column of Figure 5.10, which in the case of **88** shows aggregation of tubes but also an individual tube where the exterior coating is particularly evident.

In order to evaluate the increase in the thickness of the resulting nanohybrids, TEM profiles were measured and the examples for **88** and **89** are showed in Figure 5.12. For **88**, the profile measured over two aggregated SWNT (Figure 5.12, top) shows an overall thickness of 7 nm and the measured distance in Figure 5.12 reveals a tube with a thickness of ca. 3.8 nm while the second one would have a thickness of around 3.2 nm.

In the case of **89** and **90** (Figure 5.11) the situation is analogous although the coating around the SWNT is observed in a higher degree. The SWNT nanohybrid **89** can also be compared to **78**, and in this case the variation is much more appreciable from the linker-containing tubes where the functionalisation is apparent in the presence of shorter tubes, imperfections and areas of darker contrast but the nanotube walls are still relatively smooth. This changes dramatically for **89** where the SWNT are aggregated in ropes and tangles and is difficult to observe individual tubes. The coating around the nanotubes' wall is much thicker in this case and it covers the nanotube homogenously over the nanotube length with respect to **88**. A detailed section at a higher magnification where the aggregation of the tubes in tangles, ropes as well as some individual tubes can be observed in Figure 5.11, top right. The TEM profile measured for **89** (Figure 5.12, bottom) also shows an increase in the SWNT thickness as a result of the functionalisation with the conjugate. The measured thickness is comparable to that of **88** (3.2 nm). The measured profile shows a range of values for SWNT thickness that goes from 2.4 to 3.5 nm.

The case of nanohybrid **90** is similar to that of **89**: the morphology of the SWNT observed suggests the presence of a coating around the walls, which are no longer "smooth". However, in this particular case, the tubes seemed to be aggregated preferably in ropes that cross the grid in all directions. This is in accordance with the functionalisation strategy as the initially functionalised SWNT with benzylamine moieties presented a less damaged structure and aggregation into ropes with respect to the oxidised materials.

The TEM microscopy results seem to suggest that the introduction of the fluorophore and conjugate has been successful by the increase in the functionalisation around the SWNT tubes. This is more apparent where the BODIPY-peptide compound was used.

5.5 Preparation of GO nanoprobes

The functionalisation strategy to introduce the BODIPY fluorophore, BTSC gallium complex or BODIPY-bombesin conjugate was translated to graphene oxide similarly to the strategy described in Chapter 4 for the introduction of linkers to GO.

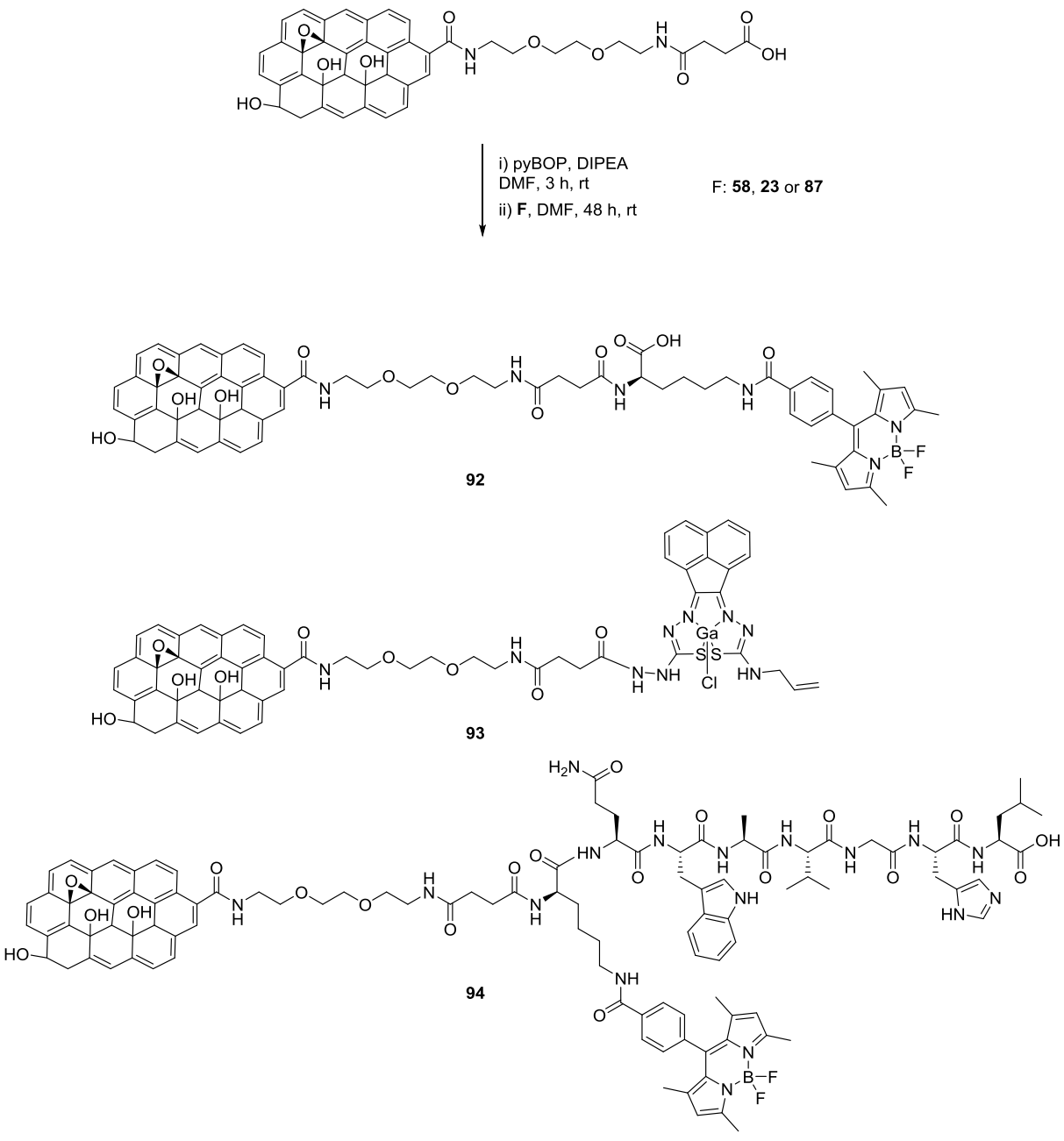

Scheme 5.7: Reaction conditions for the preparation of nanohybrids of GO (**92**, **93** and **94**) (products shown schematically).

In this case, the carboxylic acid groups in the functionalised GO were activated using pyBOP and the reaction mixtures stirred for 48 h. The nanohybrids were then isolated by centrifugation, the supernatant removed and the solid residue re-dispersed again in fresh solvent. These cycles of centrifugation and washing were repeated several times. The suspensions were finally filtered through a 0.2 μm membrane and further washed until no colouration or fluorescence was observed in the filtrate. The brown solid residue was dried under vacuum.

The nanohybrids were characterised by applying the techniques described in the previous section (FTIR and Raman spectroscopies). A summary of data obtained by Raman spectroscopy including D and G wavenumbers and I_D/I_G ratios can be observed in Table 5.2. The D and G wavenumbers are comparable between nanohybrids and in the same range to the ones obtained for the functionalised GO derivative including the linker (**84**). In contrast, the I_D/I_G ratios are slightly lower than the ones observed for the starting material. This can be an indicative (as it also occurred in the case of functionalised SWNT) that a fraction of highly functionalised GO has been lost during the reaction and subsequent processing of the reaction mixtures.

Table 5.2: Summary of Raman data for GO nanohybrids **92** – **94**.

Compound	ν D (cm^{-1})	ν G (cm^{-1})	I_D/I_G
92	1354	1589	0.92
93	1347	1585	0.94
94	1352	1587	0.87

The FTIR spectra for the GO nanohybrids **93** and **94** are shown in Figure 5.13. The FTIR spectra present bands observed in the starting material. The broad band at ca. 3200 corresponds to the OH and NH stretching. Therefore, in this region overlap the hydroxyl groups of graphene oxide, the NH groups in the linker and fluorophore groups (amide bonds) and the hydroxyl groups in carboxylic acids. This can explain why this band is broader with respect to similar SWNT nanohybrids (Figure 5.9). The band for the CH stretching was observed as a shoulder of the aforementioned band at ca. 2930 cm^{-1}. This band is indicative of saturation in the graphene oxide lattice and of methine, methylene and methyl groups in the linker and fluorophore moieties. There are at least two different C=O stretching bands with wavenumbers at ca. 1710 and 1630 cm^{-1} although the presence of a shoulder at slightly lower wavenumbers can be deduced by observing the spectra. The bands in this region correspond to the different C=O groups in the linker and fluorophore. The C-O stretching is also observed at lower wavenumber (ca. 1060 cm^{-1}).

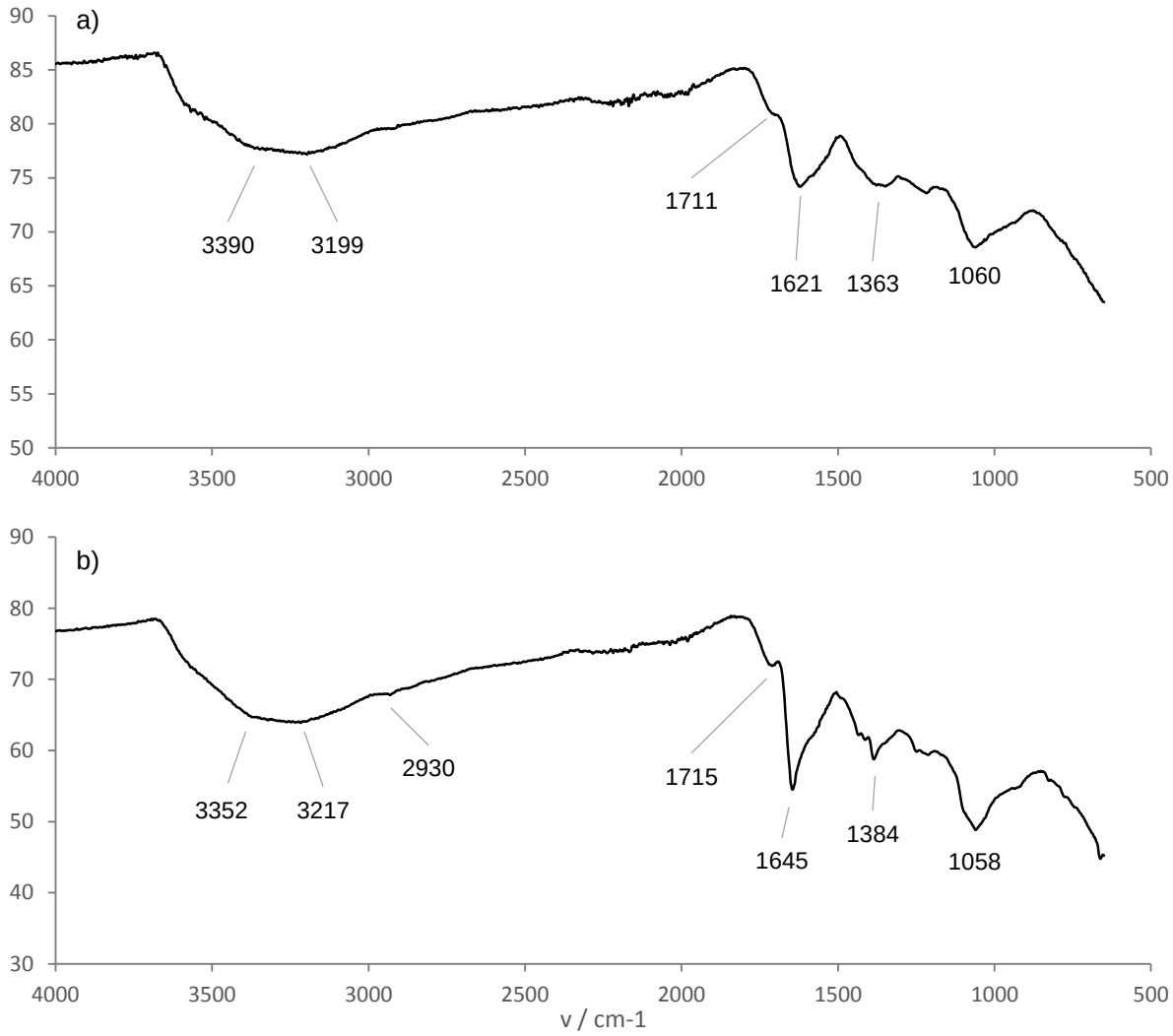

Figure 5.13: FTIR spectra for nanohybrids **93** (a) and **94** (b).

5.6 Photophysical characterisation of novel probes and nanoprobes

The photophysical characterisation of the conjugate and all nanohybrids synthesised hereby was carried out by UV-vis and fluorescence spectroscopies. The maximum absorption and emission wavelengths and quantum yield in the derivatives presenting a strong enough fluorescence signal was calculated.

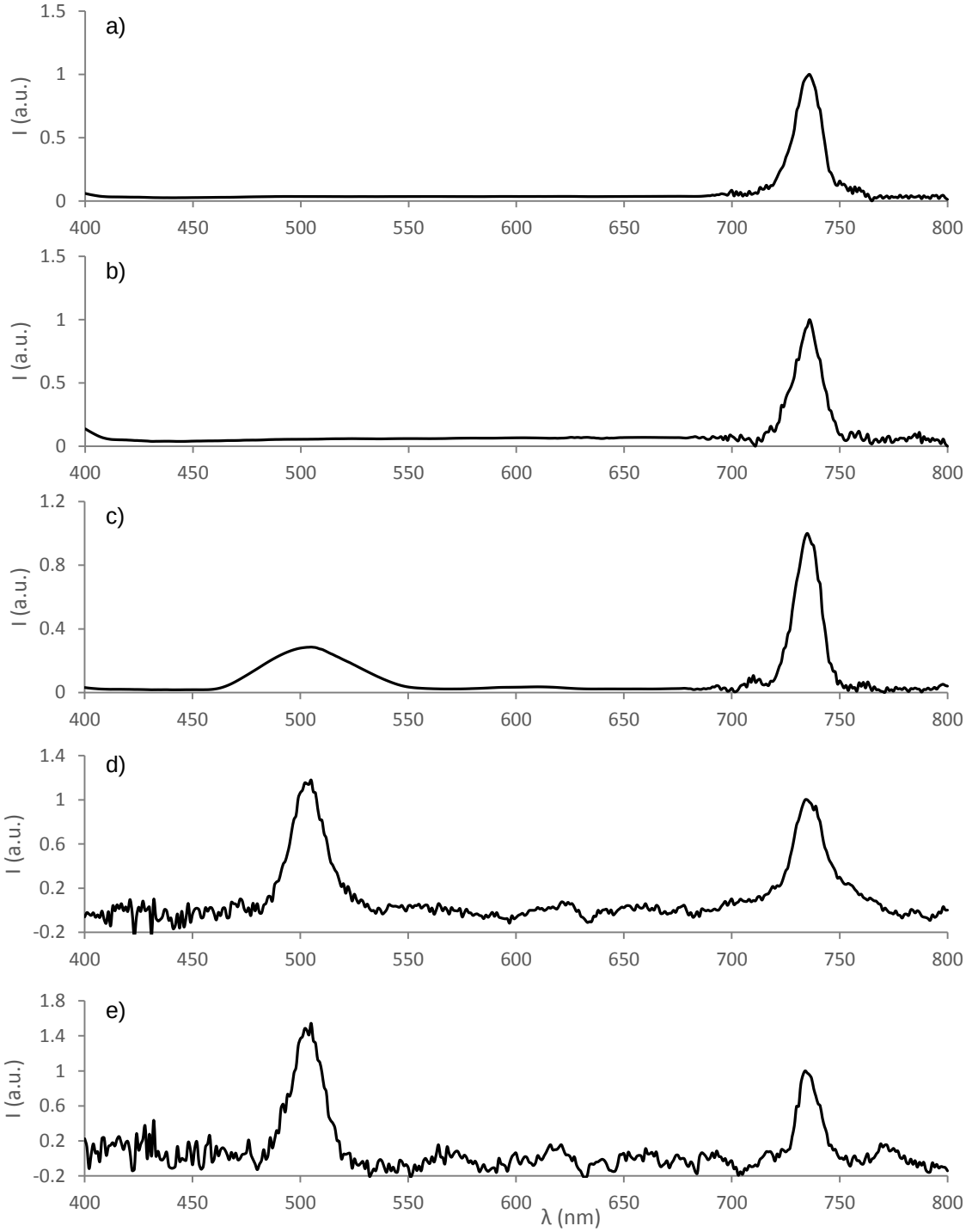

Figure 5.14: Normalised UV-vis spectra of SWNT dispersions (ca. 0.05 mg/mL in DMSO). a) p-SWNT, b) **78** c) **88**, d) **89** and e) **90**.

The UV-vis spectra for nanohybrids **88** – **90** are displayed in Figure 5.14. The spectra had been normalised and a baseline correction applied for clarity. In addition, the UV-vis spectra of the p-SWNT and the functionalised SWNT including the carboxyl terminated linkers were included for comparison. It can be observed how the pristine SWNT and linker functionalised SWNT present a single peak at 736 nm that can be attributed to the first Van Hove transition due to metallic SWNT.[15]
In contrast, the nanoprobes not only present the aforementioned peak but also others with the maximum absorption at ca. 500 nm although the specific wavelength depends on the compound. This peak can be attributed to the absorption of the BODIPY fluorophore in the case of **88** or the absorption of the BODIPY-bombesin conjugate in the case of **89** and **90**.

The spectral properties of the BODIPY-bombesin conjugate were evaluated, the excitation and emission spectra were acquired and can be observed in Figure 5.15. It is apparent how the excitation and emission profiles are identical to the BODIPY fluorophore. Therefore, in the case of **87** the conjugation to the peptide did not cause a variation in the properties of the fluorescent profile of the product.

A summary of the spectral properties of **87** and different nanohybrids is presented in Table 5.3.
Despite the conjugation to the peptide not causing a change in the excitation and emission profile of **87**, it had a quenching effect. The quantum yield is affected in the product and decreases to 0.69 with respect to the BODIPY starting material. The Stokes shift of 10 nm is identical to the value found for the BODIPY starting materials described in Chapter 3.

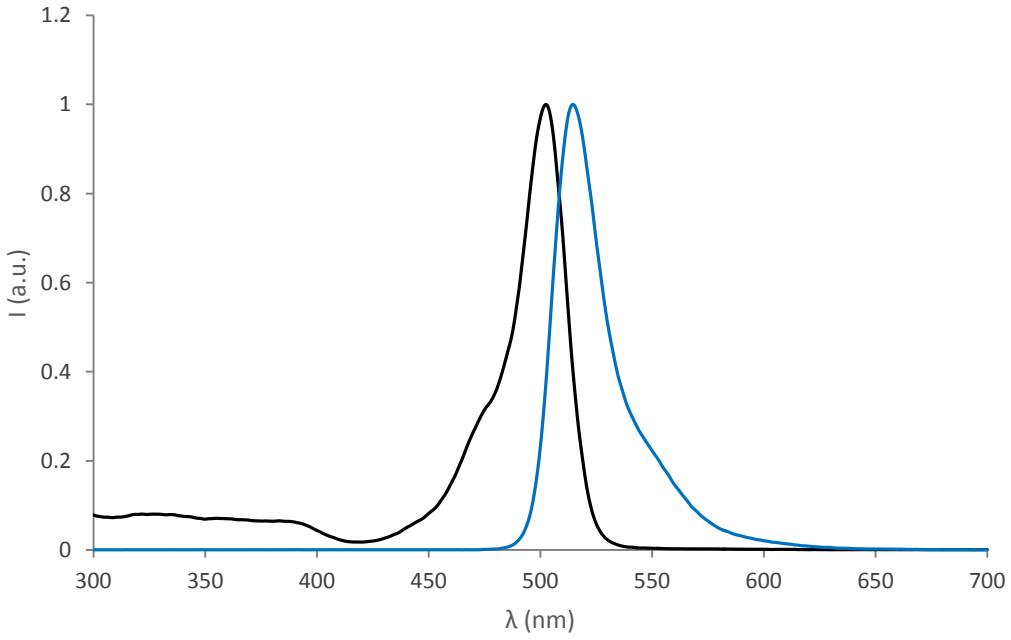

Figure 5.15: Fluorescence spectra of BODIPY-bombesin conjugate **87**. Excitation spectrum (black line) and emission spectrum (blue line).

Table 5.3: Spectral properties of **87** and nanohybrids **88**, **89** and **90** in DMSO dispersions.

Compound	$\lambda_{max\text{-}abs}$ (nm)	$\lambda_{max\text{-}em}$ (nm)	$\Delta\lambda$ (nm)	Φ_f
87	500	510	10	0.69
88	504	505	1	0.03
89	502	505	3	0.05
90	502	504	2	0.02
92	504	505	1	0.04
93	502	504	2	0.04

The coupling of the BODIPY fluorophore to the functionalised SWNT or GO respectively had a strong quenching effect in the resulting nanohybrids (**88** and **92**). The quantum yields are reduced to 0.03 and 0.04 respectively. Interestingly, the Stokes shift is also reduced and the nanohybrids only present a 1 nm difference between the excitation and emission spectra. In the case of the coupling with conjugate **87** the situation is similar, a strong quenching is observed as a decrease in the quantum yields of the resulting SWNT and GO nanohybrids (**89**, **90** and **93**). The quantum yields are in the same range (0.02 to 0.05) and the Stokes shifts are also reduced to 2 – 3 nm.

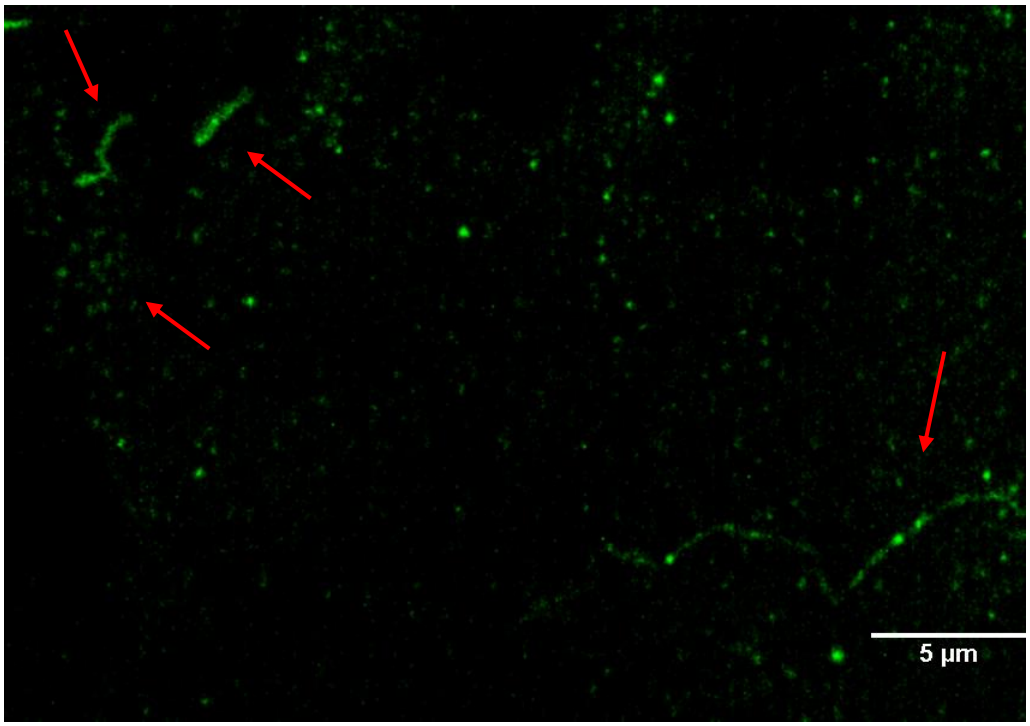

Figure 5.16: iSIM super-resolution confocal image of **89** in the green channel (λ_{ex} 488 nm, λ_{em} 525 nm). The nanoprobe was deposited on a petri dish. Scalebar: 5 µm. Images recorded and processed by Colin Wright, Nikon Bioimaging UK, Ltd.[16]

The instant structured illumination microscopy (iSIM) super-resolution confocal images of nanoprobe **89** on the solid state are shown in Figure 5.16. The nanoprobe was deposited on a Petri dish with glass bottom (MatTek) from a 1 mg/mL DMSO solution and the solvent removed under vacuum. The fluorescence signals can be observed in isolated spots corresponding to aggregate particulate SWNT. However, it can also be observed how the SWNT nanoprobes seemed to undergo certain supramolecular interactions when the solvent was removed resulting in aggregation as micrometre long fibres. This is more apparent in long fibre-like aggregates in the corners of Figure 5.16 (pointed with red arrows). This interesting behaviour needs to be further explored using other derivatives, exploiting the available offer of fluorescence super-resolution microscopy techniques with nanometre spatial resolution as well as employing other techniques such as AFM and SEM.

In addition to the UV-vis and fluorescence spectra, the fluorescence lifetime decays were acquired by 2-photon time-correlated single photon counting (TCSPC) and the corresponding lifetimes calculated from the mathematical fitting of the decay. Fluorescence lifetime experiments were conducted in the Central Laser Facility at the Research complex at Harwell under the supervision of Prof Stan Botchway. The specific conditions used during fluorescence lifetime experiments are detailed in Chapter 7.

The fluorescence lifetime (τ) is a measurement of the time that the fluorophore remains in the excited state. The fluorescence lifetime provides information about the environment of the fluorophore and it has the advantage of being independent of the fluorophore concentration.[17, 18] The goodness of the fitting can be estimated with parameters such as χ^2. The better the fitting, the closer χ^2 is to unity. The fluorescence decay measured for a homogenous group of molecules can be expressed as a mono exponential function.[19] A large difference of χ^2 with the ideal value for a mono exponential fitting ($\chi^2 >$ 1.5) indicates to a multi-exponential decay process originated from various fluorescent components.[17]

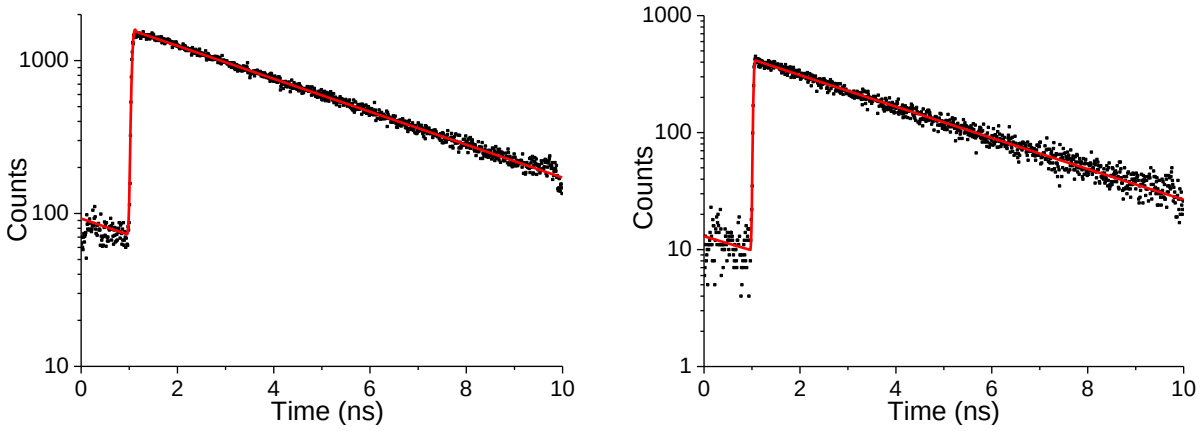

Figure 5.17: 2P-TCSPC fluorescence decay curves for **87** (left) and **89** (right) and corresponding fitting curves (red lines).

The fluorescence decays curves and corresponding fittings for **87** and **89** are shown in Figure 5.17. The fluorescence lifetimes were calculated in different solvents (DMSO, phosphate-buffered saline, PBS, and serum-free medium, SFM) in order to ascertain the effect of the solvent in the lifetime of the fluorophore (Table 5.4).

In the case of **58**, **87** – **90**, one component or mono exponential fittings were valid and worked well for the compounds tested in all the solvents as χ^2 was close to unity with slight variations. The exception was compound **58** in DMSO and SFM where the χ^2 value was slightly higher but within the range of values allowed for a one-component fitting.

The lifetime results indicate a trend for **58** and **87** where the longest lifetime is obtained in DMSO, followed by PBS and SFM. The use of DMSO has been reported to increase the lifetime of organic dyes with respect to aqueous solvents due to the decrease of hydrogen bonding and hence the reduction of non-radiative decay.[20, 21] The lifetimes of **58** are ca. 3.5 ns and the lifetime differences are ca. 0.5 ns depending on the solvent. Differently, for **87** there is a larger difference (> 1 ns) between the lifetime in DMSO and in PBS or SFM. The lifetimes in PBS and SFM decreased with respect to **58** and increased in DMSO.

Table 5.4: 2P-TCSPC fluorescence lifetime decay data for **58**, **87** – **90** in DMSO, PBS and SFM. One component fitting.

Compound	Solvent	P (mW)	χ^2	a_1 (%)	t_1 (ns)
58	DMSO	0.64	1.26	100	4.00
	PBS	0.5	1.08	100	3.37
	SFM	2.2	1.35	100	3.35
87	DMSO	0.98	1.18	100	4.03
	PBS	0.5	0.98	100	2.88
	SFM	2.2	0.99	100	2.67
88	DMSO	13.7	1.04	100	2.93
	PBS	8.1	1.11	100	2.57
	SFM	5.8	1.11	100	3.23
89	DMSO	7.1	1.11	100	3.21
	PBS	7.8	1.16	100	2.39
	SFM	5.8	1.17	100	3.02
90	DMSO	8.2	1.10	100	3.04
	PBS	7.9	1.19	100	3.00
	SFM	7.9	1.15	100	3.49

This could be explained by the extended presence of hydrogen bonding generated by the presence of the peptide residue in polar protic solvents. The lifetime of **87** was 4.03 ns in DMSO while is reduced to 2.88 ns and 2.68 ns in PBS and SFM respectively.

The lifetimes values observed herein for the BODIPY derivatives are in accordance with previously observed values for similar BODIPY species functionalised with small molecules. Dilworth *et al.* reported values in the range of 2 – 3 ns for BODIPYs functionalised with bis(thiosemicarbazone) ligands and the corresponding copper complexes.[22]

In the case of the nanohybrids, the situation was analogous when the solvent was DMSO. The nanoprobe functionalised with the BODIPY fluorophore (**88**) showed a lifetime of 2.93 ns and was in a similar range for the corresponding nanohybrids containing the fluorophore-peptide conjugate: 3.21 ns and 3.04 ns for **89** and **90** respectively. When the solvent was PBS or SFM the situation was more complex. In general, the lifetimes increased with respect to the conjugate **87**. The trend observed for the molecular species was maintained for **89** where the lifetimes were shorter with respect to the derivative containing just the fluorophore, a fact that can be attributed to the higher degree of hydrogen bonding interactions in aqueous solvents that favour non-radiative decay processes and shorten the fluorescent lifetime in the excited state. However, in the case of **90** an increase of the lifetime in PBS and SFM was observed with respect to **88**. Furthermore, the nanohybrids presented longer lifetimes in SFM and PBS with respect to **87** which can be indicative that the SWNT are hindering the hydrogen bonding in aqueous solvents and allowing the nanoprobe to remain a longer period of time in the excited state.

5.7 Cell viability assays

The use of tetrazolium salts have become a widely employed technique in cell biology to measure metabolic activity. In particular, the use of 2-(4,5-dimethyl-2-thiazolyl)-3,5-diphenyl-2H-tetrazolium bromide (MTT) is now an accepted method to measure cell viability.[23, 24] The accepted mechanism for the action of MTT implies the cellular uptake of the MTT dye and its reduction by nicotinamide species (i.e. NAD(P)H) in the cytoplasm and mitochondria of the cells to form the formazan species (Scheme 5.8). The coloured formazan species is non-soluble in cellular media so it needs to be solubilised in order to measure the absorbance. The concentration can be calculated from the absorbance and the number of viable cells in the presence of a compound of interest calculated.[25]

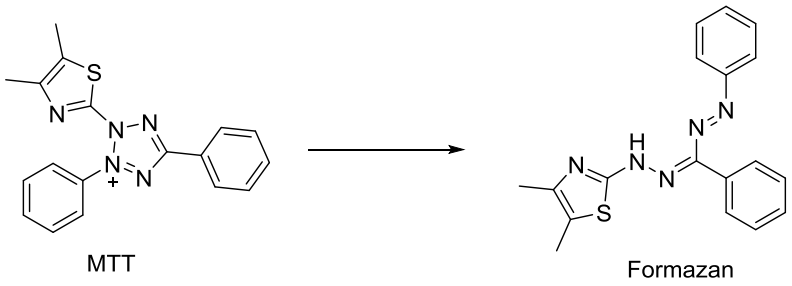

Scheme 5.8: Formation of the dye detected in MTT assays by biological reduction.

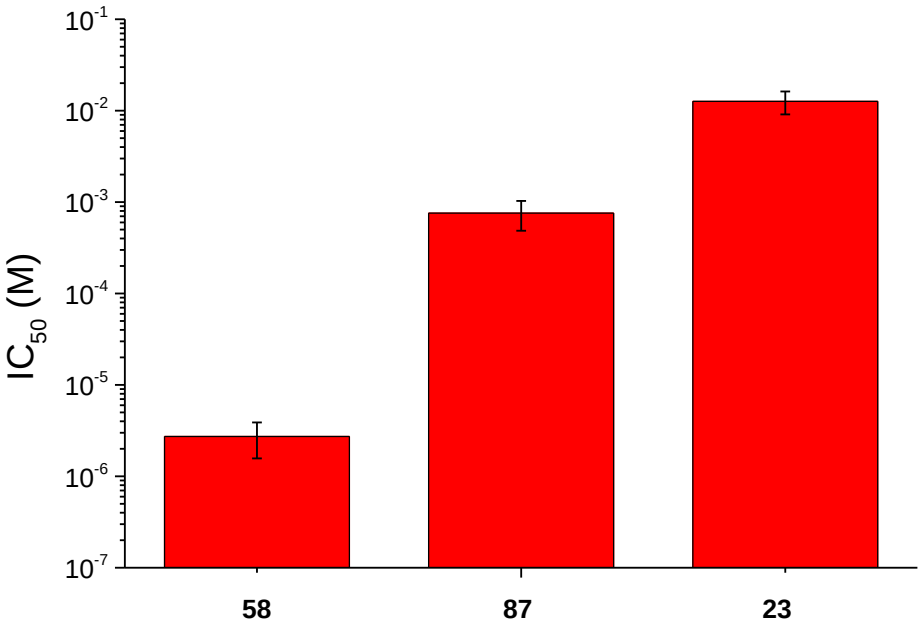

Figure 5.18: Cell viability studies for compounds **58**, **87** and **23**.

In this work, MTT assays were performed in a range of concentrations to calculate the IC_{50} values of a selection of fluorophores and nanohybrids. The viability assays were carried out in PC-3 cells in 96 well plates incubated with the selected compounds in serum medium (1% DMSO) at different concentrations for 48 h at 37 ºC. Then, MTT was added and incubated for 2 h. The insoluble formazan species was solubilised with 100 µL DMSO and the corresponding absorbance measured using a plate reader. The MTT assays showed herein were carried out by Dr Haobo Ge at the University of Bath following previously validated protocols.[26, 27] The detailed conditions can be found in Chapter 7.

The IC_{50} values for a group of fluorophores can be observed in Figure 5.18 (IC_{50} values here refer to the concentration at which the number of viable cells is reduced 50%). It can be seen how the BODIPY fluorophore **58** presents a remarkable cytotoxicity in PC-3 cells in the µM range. The conjugation of the fluorophore with the bombesin peptide to form **87** results in a considerable reduction of the cytotoxicity with the conjugate's IC_{50} in the mM range. Surprisingly, the IC_{50} value for the Ga(III) complex **23** is higher than for **58** being in the ten of mM range. Similar symmetrical Ga(III) complexes described in the literature proved to be considerably more toxic for HeLa cells with IC_{50} values in the micromolar range.[28] In this case, the response of **23** can be strongly cell-dependent, showing a reduced cytotoxic effect in PC-3 cells or the introduction of a free amino group in the thiosemicarbazonato structure might have a considerable effect in the uptake and viability of this cell line. This result requires of further investigation into the properties of this compound to understand its effect in living PC-3 cells.

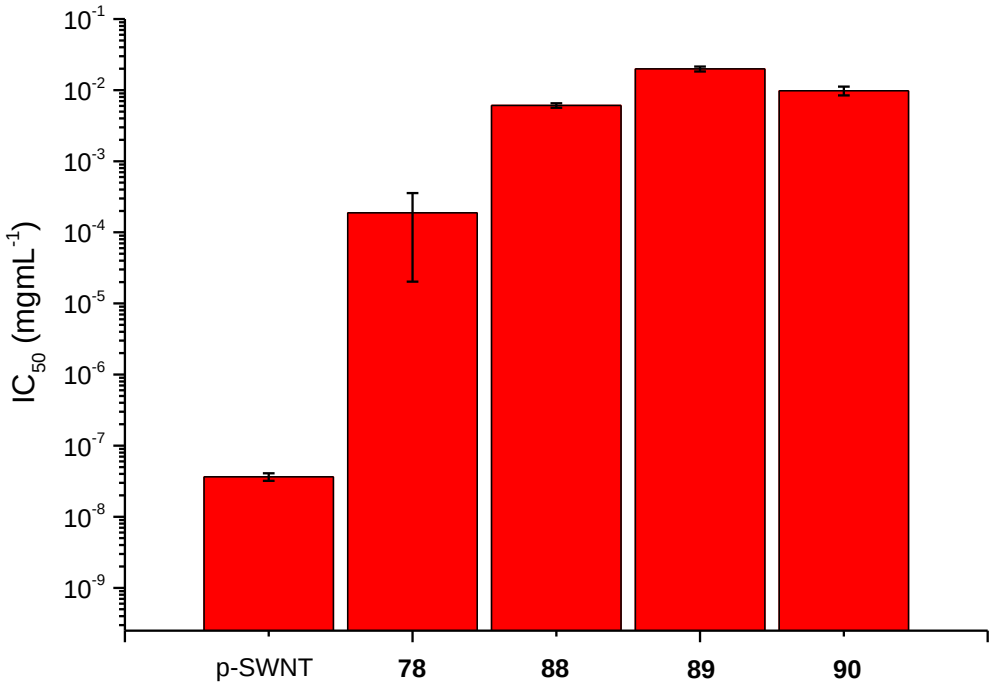

Figure 5.19: Cell viability studies for p-SWNT, functionalised SWNT and SWNT based nanohybrids.

The cell viability results for a selection of functionalised SWNT can be observed in Figure 5.19. A clear trend can be observed where the functionalisation of the SWNT clearly reduces the cytotoxicity of the nanomaterial. The pristine SWNT show a high cytotoxicity with an IC_{50} value on the sub $ngmL^{-1}$ scale. A drastic change is observed when the linkers are introduced in the SWNT and the cytotoxicity of the functionalised material with terminal carboxylic acids presents a reduction of four orders of magnitude being in the μgmL^{-1} scale. The functionalisation with the BODIPY or BODIPY-bombesin peptide in nanohybrids **88**, **89** and **90** yields the lowest cytotoxicity in the functionalised SWNT family. This increase might be motivated for the action of the fluorophore and its linker in **88** and due to the enhanced biocompatibility generated because of the introduction of the peptide in **89** and **90**.

The cell viability results for graphene oxide and graphene oxide nanohybrids can be observed in Figure 5.20. The trend observed for SWNT derivatives is not observed herein. Graphene oxide has the lowest cytotoxicity with an IC_{50} value in the μgmL^{-1} scale, comparable to the linker functionalised SWNT (**78**). This can be rationalised on the basis that GO already contains numerous oxygenated functionalities and their number is reduced during the synthetic process. Surprisingly, the cytotoxicity increases for the GO derivatives containing the linker (**84**) with respect to the original GO. The highest cytotoxicity was observed for the nanohybrid containing the BODIPY-bombesin conjugate which is surprising and contradicts the trend observed in the SWNT case. In this case, the increase in cytotoxicity might be attributed to potential aggregation effects when the GO is functionalised with the conjugates.

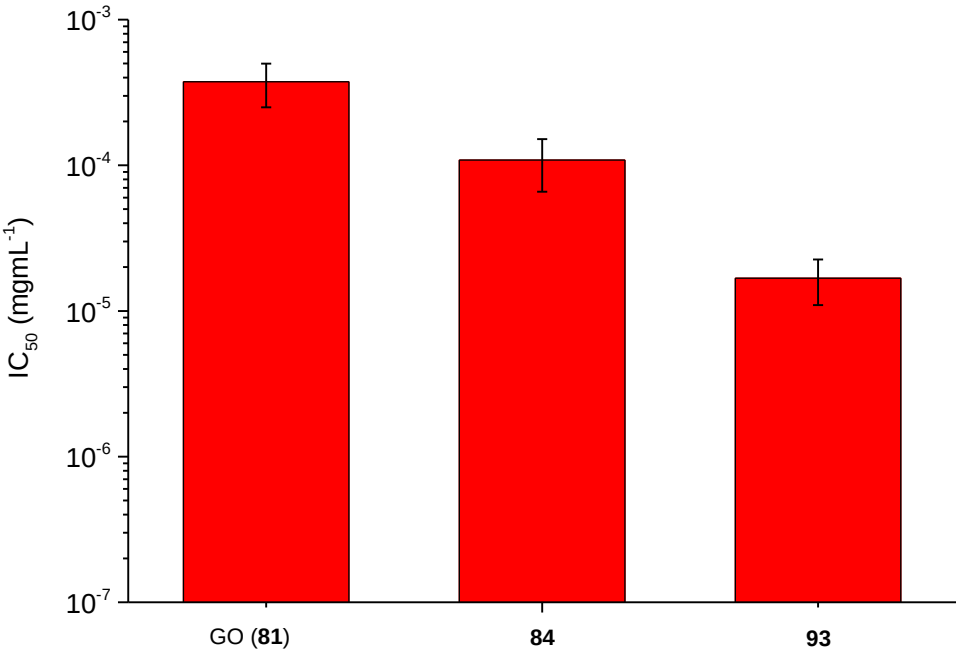

Figure 5.20: Cell viability studies for GO and GO based nanohybrids.

A summary of the IC_{50} values for the fluorophores and nanomaterials described above can be observed in Table 5.5.

Table 5.5: Summary of estimated IC_{50} values for a selection of fluorophores and SWNT and GO nanomaterials. The mean of at least six determinations is indicated with the corresponding SEM.

Compound	**IC_{50} (mM) ± SEM**
58	0.0027 ± 0.0011
87	0.75 ± 0.27
23	13 ± 3
Compound	**IC_{50} (μgmL^{-1}) ± SEM**
p-SWNT	0.000036 ± 0.000004
[**78**	0.18 ± 0.17]
88	6.1 ± 0.4
89	20 ± 2
90	98 ± 1
81	0.37 ± 0.12
84	0.011 ± 0.004
93	0.017 ± 0.006

The cytotoxicity results for SWNT should be interpreted with caution. The cytotoxicity effects of single walled carbon nanotubes have revealed to be controversial as they are affected by a considerable number of factors as the presence of metallic or carbonaceous impurities, the type of functionalisation, the use of dispersants, the agglomeration or the cell line evaluated.[29-33] Even the use of the MTT reagent has been questioned for the estimation cell viability with SWNT due to the insolubility of the formazan species and the authors advised to use at least two different techniques.[34]

However, there seems to be an agreement about the effect of the functionalisation of SWNT on cell viability. The cytotoxicity of highly pure SWNT where no additives or dispersants were employed was reported to be higher with respect to other comparable functionalised samples.[29] Furthermore, the increase in the degree of functionalisation could be related to the decrease in cytotoxicity.[32, 35, 36]

The results observed in this work are in accordance with the mentioned behaviour and showed a clear tendency in the direction of the reduction of the cytotoxicity with each step of the functionalisation.

5.8 *In vitro* imaging with new compounds synthesised and corresponding nanoprobes

The imaging probes and nanoprobes synthesised hereby were proposed as optical imaging agents in living PC-3 cells and the cellular uptake observed by single-photon confocal microscopy. The cells were cultured by standard techniques and grown until ca. 70% confluency. In general, the compounds were incubated for periods of 15-20 min to verify the hypothesis that these systems presented a rapid uptake in cells. The imaging conditions are detailed in Chapter 7 and Figures 5.21 – 5.24.

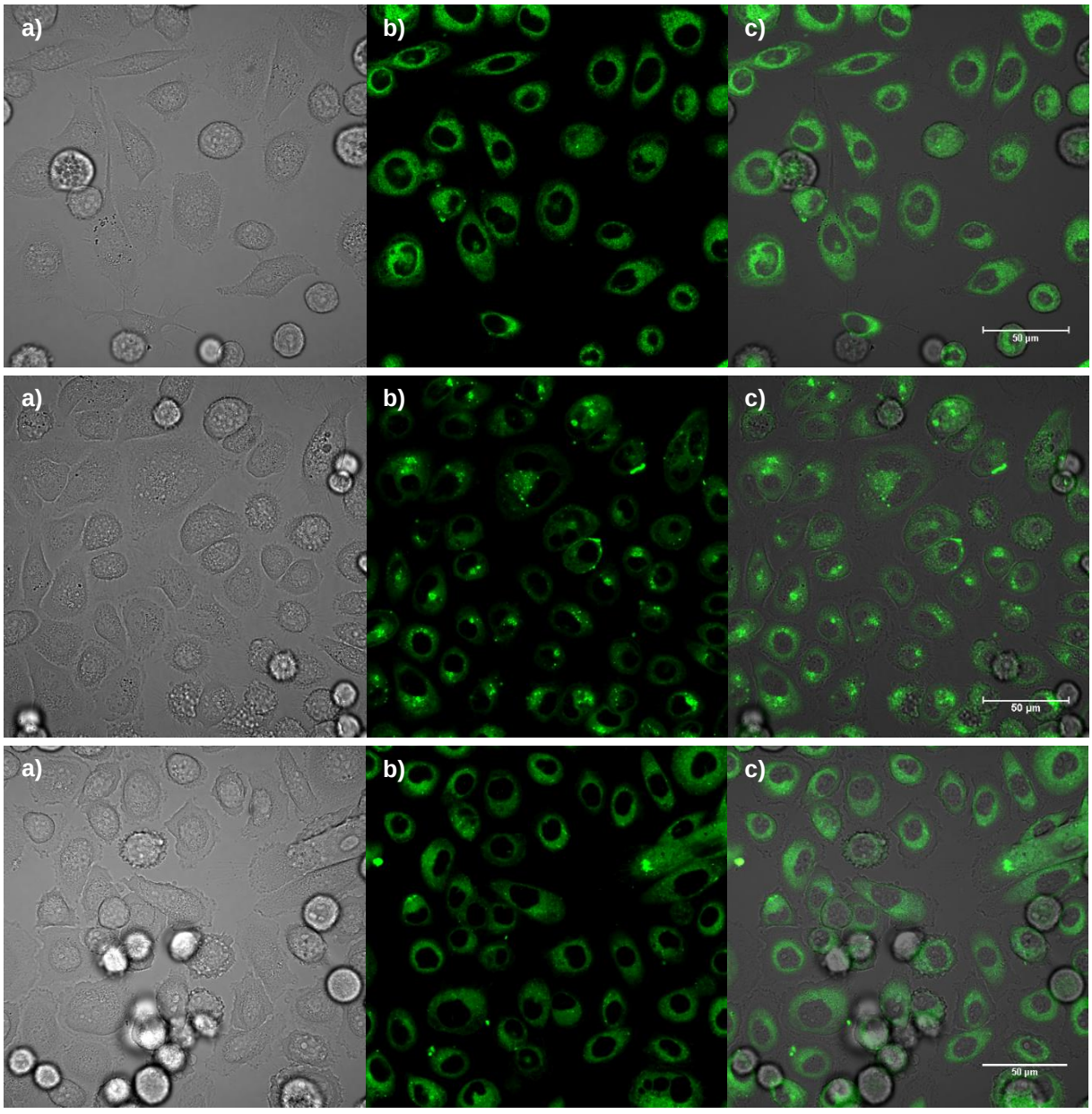

Figure 5.21: Single-photon confocal microscopy images of **58** (top) **87** (middle) and blocking experiment with **87** in PC-3 cells after 15 min incubation, 20 µM 1% DMSO at 37 ºC where a) DIC image, b) green channel, λ_{ex} 488 nm, λ_{em} 518 nm and c) overlay of a) and b). Scalebar: 50 µm.

The BODIPY **58** and BODIPY-bombesin conjugate **87** were tested in PC-3 cells. The compounds were added in a 20 μM concentration in serum-free medium (1% DMSO). The images obtained by single photon confocal microscopy are shown in Figure 5.21. The fluorophore **58** is displayed in the top row and it can be observed that the fluorescence signal is intense in the green channel and the compound is distributed in the cytoplasm with occasional location in organelles/micelles observed as punctuation. Interestingly, the conjugate **87** (Figure 5.21, middle) presents a very different distribution in the cell. It can be observed how for the conjugate, a fraction of the compound is present dispersed in the cytoplasm showing some fluorescent response.

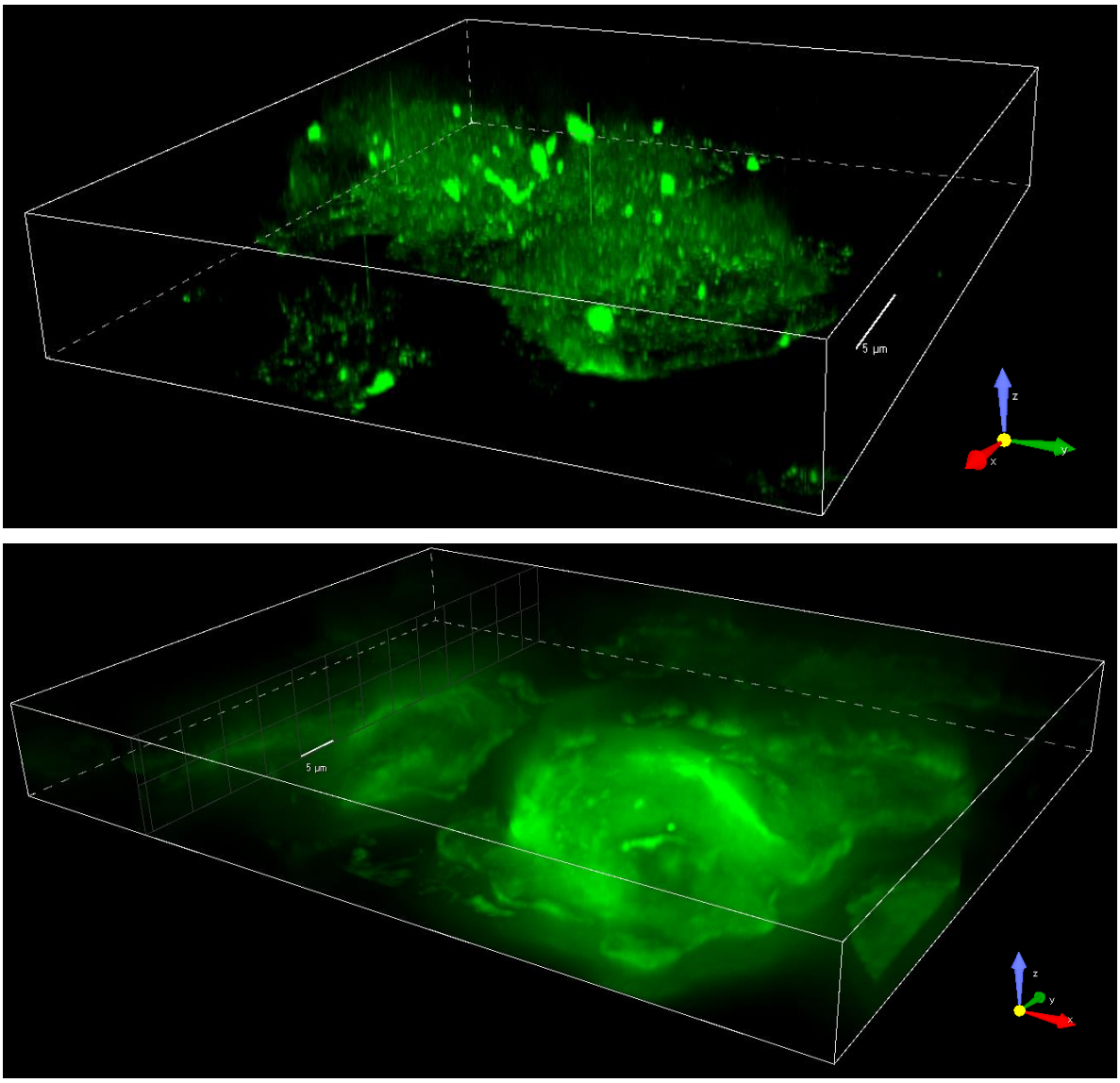

Figure 5.22: 3D representation of the iSIM confocal images of **58** (top) and **87** (bottom) in fixed PC-3 cells. Both images show the green channel (λ_{ex} 488 nm, λ_{em} 525 nm). Scalebar: 5 µm. Images recorded and processed by Colin Wright, Nikon Bioimaging UK, Ltd.[16]

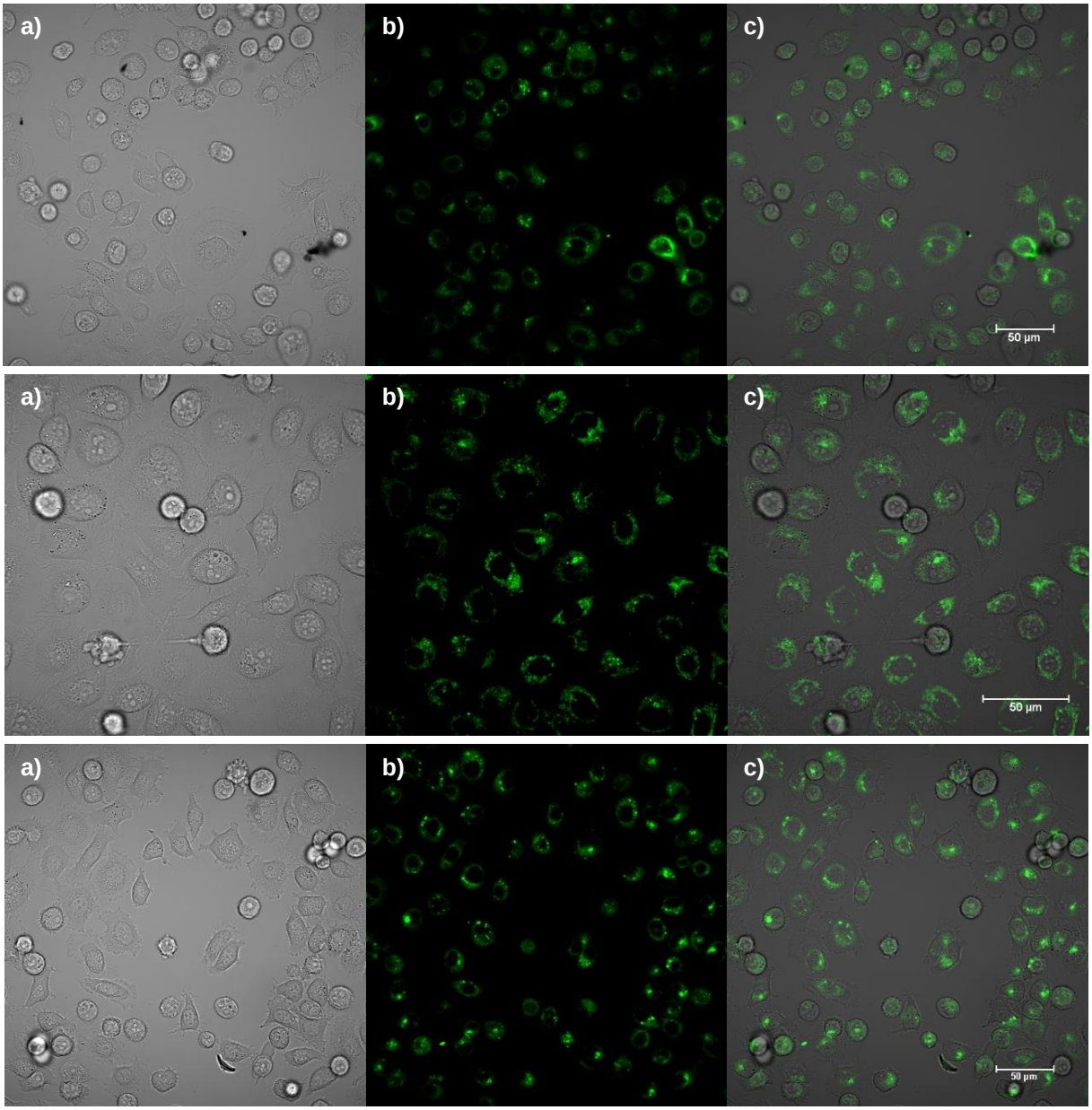

Figure 5.23: Single photon confocal microscopy images of SWNT nanoprobes **88** (top), **89** (middle) and **90** (bottom) in PC-3 cells after 15 min incubation, 10 µg/mL 1% DMSO at 37 ºC where a) DIC image, b) green channel, λ_{ex} 488 nm, λ_{em} 518 nm and c) overlay of a) and b). Scalebar: 50 µm.

However, the most intense fluorescence signal was observed around the cell membranes as well as localised in a dotted pattern inside the cytoplasm. This is in accordance with a targeted uptake directed by the GRP receptors in PC-3 cells. To further prove this observation, a blocking imaging experiment was conducted (Figure 5.21, bottom). In this experiment, the cells were first incubated in the presence of a high concentration of bombesin [7-13] (10 mM) for 30 min. After this time, the cells were washed with PBS, the serum free medium replaced and the cells incubated with conjugate **87**. After washing the excess of compound, the images acquired showed a dispersed distribution of **87** in the cytoplasm with

occasional concentration with a punctuated distribution but remarkably different to the uptake observed for **87**. This result would point at a non-specific behaviour where the uptake under the evaluated conditions is governed not only by the targeting peptide, showing a preference for the GRP receptors and a targeted behaviour, but also by the BODIPY fluorophore that shows a distribution in the cytoplasm known to be typically in the ER. This has been observed before for BODIPYs or porphyrin derivatives.[22] This was further explored by the acquisition of 3D super-resolution confocal microscopy images (iSIM) for **58** and **87** in fixed PC-3 cells (Figure 5.22). In the case of the BODIPY fluorophore it can be observed how the maximum fluorescence intensity locations are observed in a punctuated pattern inside the cellular cytoplasm. On the contrary, the cells incubated with **87** showed a completely different aspect. In this case, the observed maximum fluorescence intensity is distributed over the exterior of the cell with points of aggregation around the membrane. This result would further confirm the observations made by single photon confocal microscopy in living cells.

The response for the nanoprobe **88** and targeted nanoprobes **89** and **90** can be observed in Figure 5.23.

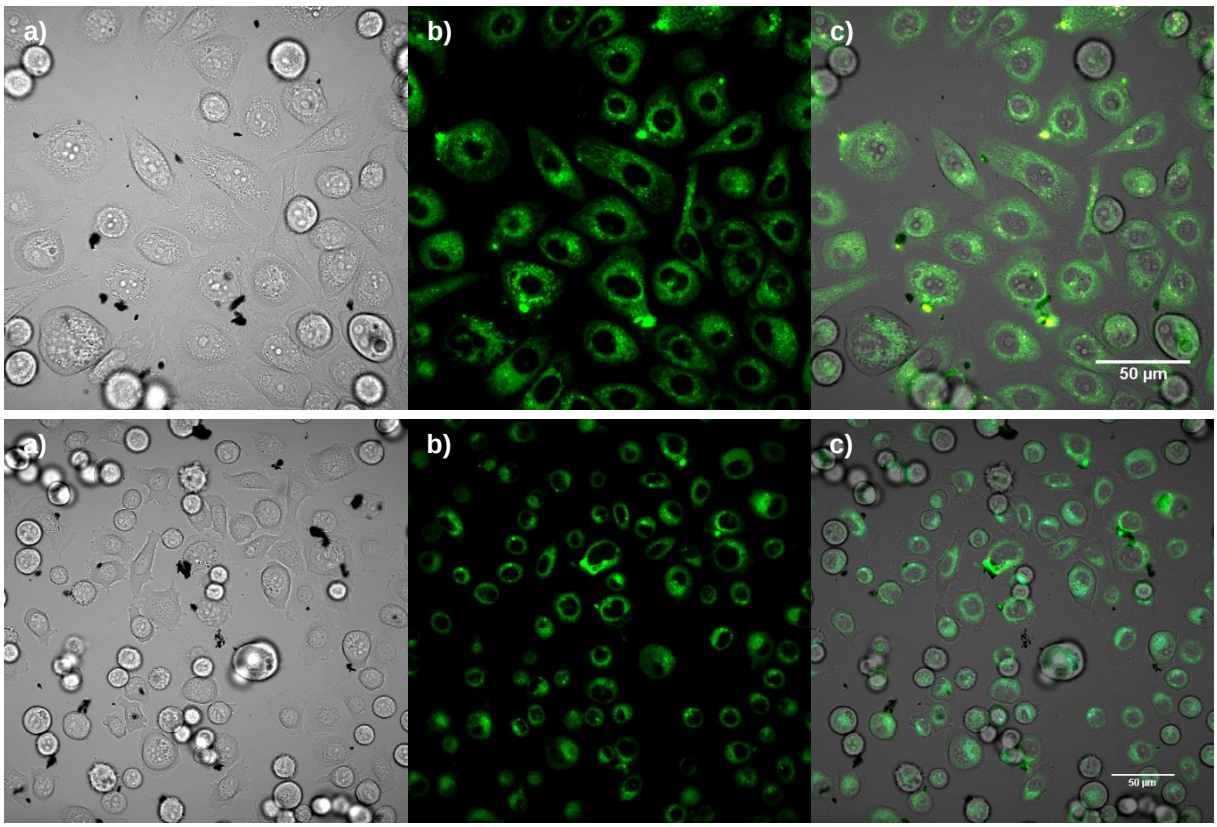

Figure 5.24: Single photon confocal microscopy images of GO nanoprobes **92** (top) and **93** (bottom) in PC-3 cells after 15 min incubation, 10 µg/mL 1% DMSO at 37 ºC where a) DIC image, b) green channel, λ_{ex} 488 nm, λ_{em} 518 nm, and c) overlay of a) and b). Scalebar: 50 µm.

In the case of the nanohybrids based on SWNT, it can be observed how **88**, that contains only the BODIPY fluorophore, shows a more homogeneous distribution in the cytoplasm than **89** and **90**. The targeted nanoprobes present a punctuated distribution, similar to **87**, and a more intense fluorescence response inside the cellular cytoplasm in organelles or vesicles. This behaviour was especially noted for **90**. However, this effect compared to **88** could be attributed due to the enhanced dispersibility in DMSO thanks to the functionalisation with the peptide that can favour cell uptake, and further work on cellular co-localisation with dyes is needed in detailed *in vitro* studies beyond the scope of this thesis.

Similarly, the imaging experiments conducted with GO nanoprobes can be observed in Figure 5.24. In this case, the response for the material containing the fluorophore alone (**92**) or the targeted derivative (**93**) present a similar response. The fluorescence response is widely distributed around the cell cytoplasm and the uptake seems to result in the nanohybrids located in small vesicles that are observed as a fluorescent punctuation.

The imaging experiments performed for the nanohybrids containing the Ga(III) BTSC complex (Figure **5.25**) showed a completely different behaviour. In this case, the fluorescence response in the green channel was equivalent in the blue and red channels due to the broader emission spectrum of the thiosemicarbazonato complex. The distribution of the nanohybrids can be related to the original gallium complex, with the fluorescence signal mainly concentrated in a dotted pattern inside the cytoplasm mostly around the nuclei that can be attributed to localisation in the endoplasmic reticulum due to the preference of thiosemicarbazonato complexes for this type of organelles.

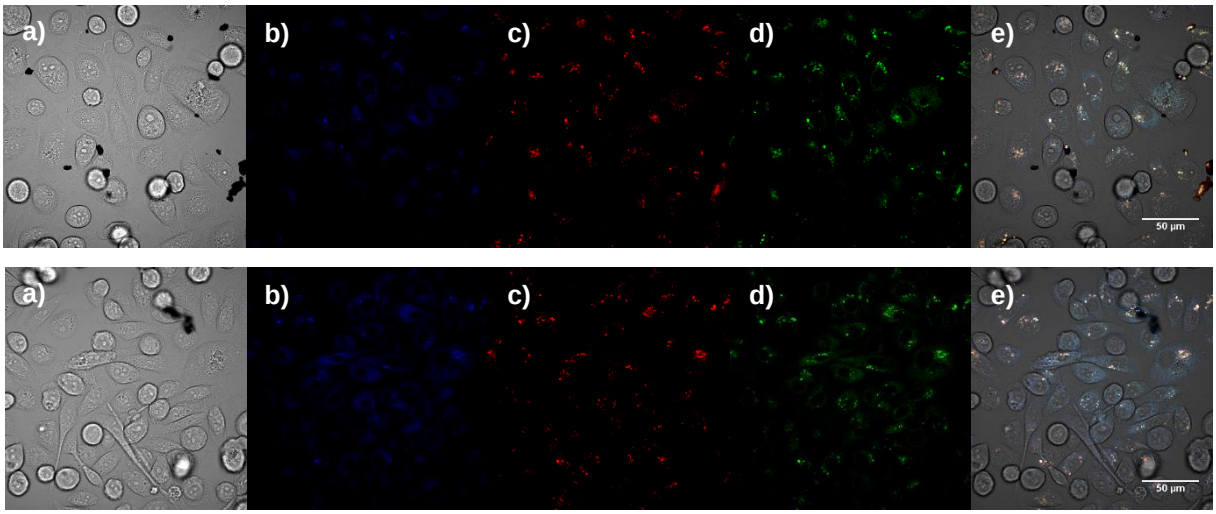

Figure 5.25: Single photon confocal microscopy images of compounds **91** (top) and **94** (bottom) in PC-3 cells after 15 min incubation at 37 ºC where a) DIC image, b) blue channel, c) green channel, d) red channel and e) overlay of a)-d). Scalebar: 50 µm.

5.9 Fluorescence lifetime imaging evolution of new BODIPY-functionalised probes

The development of multi-photon and TCSPC systems opened the way for the development of fluorescence lifetime imaging that can be carried out using a confocal microscopy setup thus allowing study of living cells and biological interactions. Two-photon excitation consists of the process where a fluorophore absorbs two photons simultaneously at approximately double the wavelength of the one-photon absorption wavelengths. The emission, however, occurs at the same wavelength of the one-photon emission allowing to perform the imaging experiments in the visible range. This allows to use excitation wavelengths in the NIR region of the spectrum that benefits of a number of advantages as higher tissue penetration, reduced photobleaching or reduction of autofluorescence in biological systems.[17, 37]

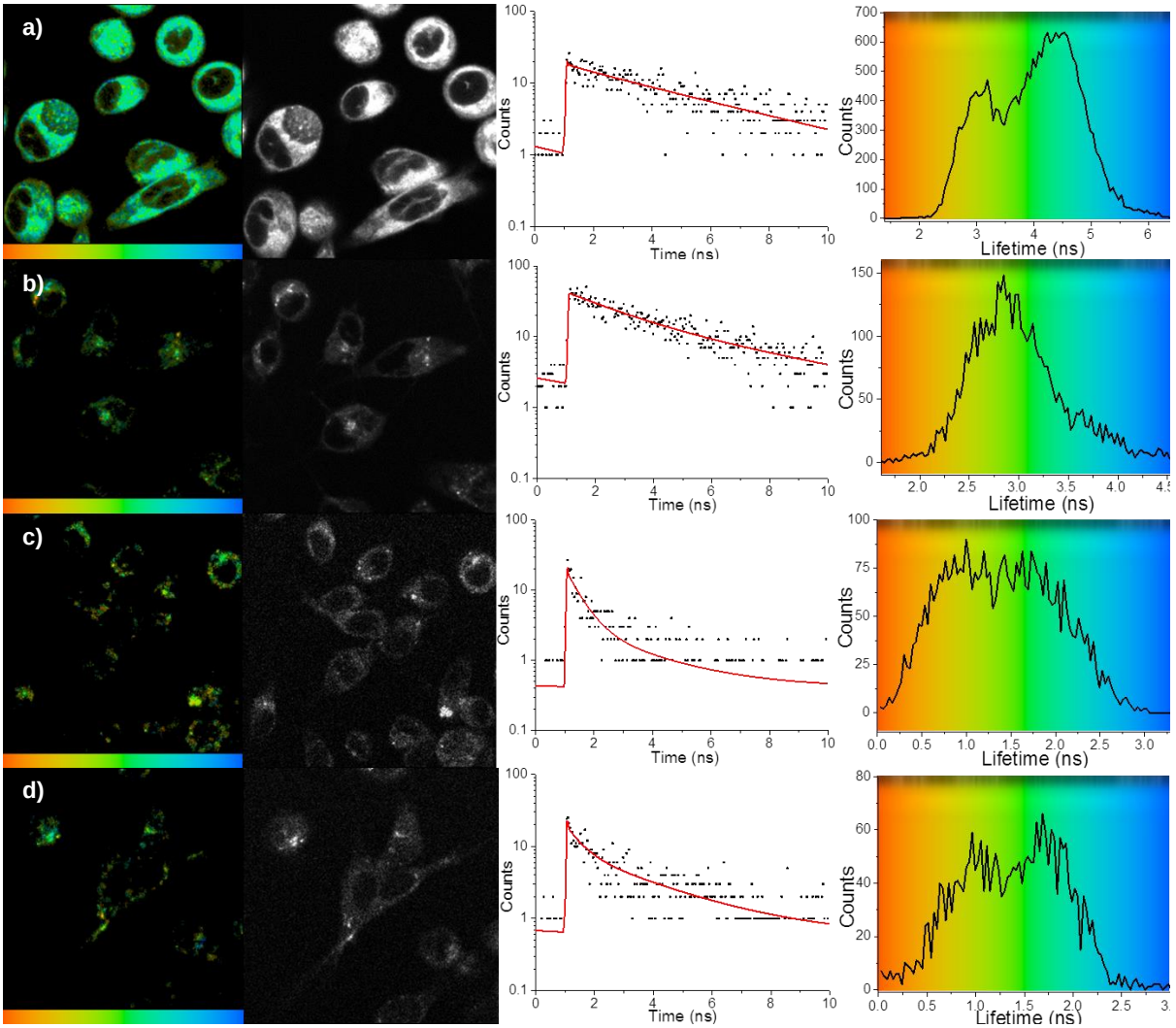

Figure 5.26: FLIM maps in PC-3 cells with lifetime distribution plots and profiles for a) **58**, b) **87**, c) **88** and d) **89**.

The use of FLIM techniques allows us to represent lifetime maps of the compounds of interest in living cells which give an insight in the interaction of the fluorophore with cellular environment and the effect that this environment produces in the fluorophore's lifetime.[38] The application of FLIM to study protein-protein interactions in cells has been profusely reported.[39] However, FLIM has not only been applied to the study of proteins but also to small molecules including organic fluorophores or coordination complexes such as thiosemicarbazonato species.[22] Furthermore, this technique has revealed as a powerful tool to evaluate the interactions of fluorescent nanomaterials such as quantum dots, nanoparticles or carbon nanotubes in living cells.[26]

In this work, FLIM experiments were conducted for a selection of probes and nanoprobes in PC-3 cells. The conditions applied were analogous to those used in the acquisition of lifetime decays and single-photon confocal imaging experiments. The FLIM maps, lifetime distribution plots and lifetime profiles for **58**, **87**, **88** and **89** can be observed in Figure 5.26 while a summary of the calculated parameters is showed in Table 5.6.

In this case, the lifetime decays were fitted to an exponential decay with two components. Therefore the fluorescence lifetime decays are fitted to a model where the intensity is presumed to decay as the sum of two individual single exponential decays. In the case of a sample containing only one fluorophore as in this case, assuming that no decomposition of the probes is being produced *in vitro* on the imaging timescale, the different decays can be attributed to the presence of different environments or to conformational changes.[18]

Table 5.6: Two-photon Time Correlated Single Photon Counting data of compounds **58**, **87**, **88**, **89** and **90** incubated in PC-3 cells for 15 min, in SFM (1% DMSO), λ_{ex} = 910 nm.

Compound	P (mW)	χ^2	a_1 (%)	t_1 (ps)	a_2 (%)	t_2 (ns)
58	2.1	1.00	11.4	1403	88.6	4.50
87	2.3	0.99	60.7	1057	39.3	4.42
88	7.7	1.25	84.1	480	15.9	2.27
89	7.3	1.26	73.9	327	26.1	2.11
90	7.9	0.99	82.3	281	7.7	2.20

The fluorophore **58** and the conjugate **87** presented two lifetime components that were in the nanosecond range. The first component presented the shortest lifetime (ca. 1 ns). However, the weighting varied from the fluorophore, where the second and longest component is the principal (88.6%), to the conjugate where the situation was reversed and the first and shortest component is now dominant (60.7%). The second components present longer lifetimes with respect to the lifetimes of the free compounds in SFM but both are in the same range. In the case of the fluorophore **58** the lifetime of the major component is in the same range of the observed in the free species. However, the conjugate presents a major component with a much shorter lifetime to the observed for the free compound in SFM. This might be attributed to interactions in the cellular environment that quench the fluorescence decay in favour of alternative non-radiative process to dissipate the energy of the excited state.

The situation for the nanohybrids is different to that described for the fluorophore and conjugate although the results are similar among the three nanohybrids (**88**, **89** and **90**). The nanohybrids present a major component (ca. 80%) with the shortest estimated lifetime, in the picosecond scale and a second minor component with a lifetime in the nanosecond scale (ca. 2 ns). In this case, the second component is similar to the lifetimes observed for the nanoprobes in dispersion in PBS or SFM. However, the interactions in the cell environment produce a strong quenching effect for the nanoprobes that shortens considerably the time that the imaging nanohybrids based on SWNT spend in the excited state.

The distribution for nanohybrids **88** and **89** in PC-3 cells can be observed in the lifetime maps depicted in Figure 5.26.

5.10 Conclusions

In this chapter, the [7-13] fragment of the bombesin peptide was synthesised via a modified route. The preparation of the peptide was conducted by solid-phase peptide synthesis using microwave-assisted heating. This peptide has been known to act as a targeting molecule for GRP receptors that are overexpressed in prostate cancer. The use of microwave radiation in peptide synthesis has a number of advantages such as the dramatic reduction of reaction times or providing access to sequences that are not accessible by conventional synthesis. The peptide was purified by automated flash column chromatography and the purity assessed by HPLC. The characterisation was carried out by common spectroscopic techniques such as ^{1}H NMR or mass spectrometry.

The peptide fragment was successfully coupled to a selected BODIPY fluorophore (**58**) described in Chapter 3. The purification in this case was performed by RP-HPLC. The conjugate was studied by mono and bidimensional ^{1}H NMR and mass spectrometry. Furthermore, the photophysical properties were evaluated and the conjugate showed identical behaviour to the initial fluorophore in terms of fluorescence profiles and maximum excitation and emission wavelength. However, the incorporation of the peptide to the structure provoked a quenching of the fluorescence and the quantum yield was reduced with respect to the starting material.

Different nanohybrids were prepared by coupling selected fluorophores described in Chapter 2 and Chapter 3, as well as the BODIPY-bombesin conjugated, with functionalised SWNT. The nanoprobes were prepared by amide chemistry activating the carboxylic acids present in the functionalised SWNT. Nanoprobes containing the BODIPY fluorophore and others containing a new aromatic Ga(BTSC) complex were obtained. In addition, targeted nanohybrids were prepared using the same procedure by coupling to the BODIPY-bombesin conjugate. All SWNT nanohybrids were thoroughly washed with different organic solvents to maximise the chances that all of the unbound excess reagents present being removed. The novel materials were characterised by FTIR and Raman spectroscopies and TEM was carried out for a subset of compounds. In this family, the photophysical properties were evaluated by UV-vis and fluorescence spectroscopy and the spectra revealed that a fluorescence response was still appreciable although the fluorescence was quenched due to the coupling to the nanomaterial as demonstrated by the reduction of the quantum yields.

Furthermore, the procedures developed for the assembly of new SWNT probes were translated to functionalised graphene oxide species, as described in Chapter 4. This way, the GO derivative including the linker was coupled to the BODIPY fluorophore, the BTSC complex and the BODIPY-bombesin conjugate. The GO nanohybrids were equally characterised by FTIR and Raman spectroscopies and the photophysical properties evaluated. The GO nanoprobes emerging showed an appreciable fluorescent response which was encouraging towards their use for optical imaging purposes.

The fluorescence of the nanohybrids containing BODIPY fluorophores showed similarities in their optical properties, i.e. in a similar excitation and emission profiles with respect to the starting materials although the emission profiles were slightly blue shifted and the Stokes shifts were smaller (in the order of 2 – 5 nm). The quenching of the fluorescence emission was evident by the coupling to the nanomaterials, as it was demonstrated by the reduction in the quantum yields and the fluorescence lifetimes.

Cell viability experiments were performed to assess the cytotoxicity of these novel compounds. The experiments were carried out in PC-3 cells and the IC_{50} estimated. The values for the fluorophores showed how the formation of the BODIPY-peptide conjugate produced a reduction of the cytotoxicity of the BODIPY starting material. In the same way the Ga(III) thiosemicarbazonato complex showed a surprisingly low cytotoxicity compared with similar derivatives reported in the literature. For the SWNT series, a clear trend was observed in the direction of the reduction of cytotoxicity with subsequent functionalisation as expected. Pristine SWNT proved to be the most cytotoxic nanomaterial for cells, which is in accordance with literature data by this group and others, the initial functionalisation and introduction of linkers produced a dramatic reduction in cytotoxicity while the coupling with the fluorophore or the conjugate produced further reduction in the cytotoxicity.

This trend was not observed for the GO and GO nanohybrids. In the case of GO, the lower cytotoxicity was observed for the starting material (GO) while the linker functionalised derivative was more toxic and the nanohybrid incorporating the fluorophore-peptide conjugate proved to be the more cytotoxic of the derivatives under the evaluated conditions. However, the IC_{50} values did not change as dramatically as in the case of the functionalisation of SWNT.

The prepared fluorophores and nanohybrids were evaluated as optical imaging probes in living PC-3 cells by confocal microscopy. When the behaviour of the BODIPY fluorophore was compared to the conjugate, it could be observed that the targeted conjugate showed a preference for the cell membranes and it entered the cell in the form of vesicles. This is in accordance with the targeted behaviour reported in the literature for similar bombesin derivatives. A blocking experiment was carried out to demonstrate this fact and it could be seen how the cellular distribution after the GRP receptors were blocked with an excess of bombesin was highly similar to the fluorophore alone. This suggests that a split uptake mechanism is taking place that is directed jointly by the peptide and also by the fluorophore.
The SWNT nanohybrids were evaluated and demonstrated their applicability as imaging probes. A difference was also observed between the uptake and distribution of the derivatives containing only the fluorophore or the conjugate but more experiments are needed to demonstrate the targeted uptake of the SWNT nanohybrids.

The GO nanohybrids proved useful as imaging agents although the difference between the derivatives containing just the BODIPY fluorophore or the targeted species was not as evident as in the last case. The cytotoxicity of these nanohybrids seemed higher in the imaging experiment timescale, which is in accordance with the results obtained in cell viability experiments.

The SWNT and GO nanohybrids containing the Ga(III) thiosemicarbazonato complex were also tested in PC-3 cells. In this case, the fluorescence emission observed was broader and the fluorescence intensity reduced compared to the case of the probes containing BODIPY fluorophores in samples of comparable concentration. The uptake and localisation in the cells was comparable to that described for the fluorophore alone that might reveal a strong effect of the metal complex in the uptake mechanism of the nanoprobe.

Furthermore, fluorescence lifetime imaging experiments were carried out for a selection of compounds. The FLIM experiments were conducted in living PC-3 cells and allowed to obtain the lifetime of the fluorophores and nanohybrids *in vitro*. In this case, the fluorescence lifetime decays were fitted to an exponential function with two fluorescent components.
The fluorophore **58** presented a major component with a long lifetime, comparable to the observed for the species in solution. The second minor component presented a shorter lifetime in the picosecond scale. This situation was reversed for the conjugate **87** where the major component was the one that presented a shorter lifetime value in the picosecond scale. The minor component presented a lifetime comparable to the observed in solution. From these observations, it can be inferred that the conjugate undergoes interactions *in vitro* that result in a quenching process that shortens its lifetime.

In the case of the nanohybrids, the major component is the first with a shorter lifetime in the picosecond scale. The second minor component, presents comparable lifetime values as the ones observed for suspensions in PBS or SFM. Therefore, the nanohybrids similarly to **87** present certain interactions *in vitro* that result in the quenching of the fluorescence through other non-radiative process as the lifetime in the excited state is shortened.

5.11 References

1. Y. Liu, S. An, R. Ward, Y. Yang, X.-X. Guo, W. Li and T.-R. Xu, *Cancer Lett.*, 2016, **376**, 226-239.
2. J. Mattei, R. D. Achcar, C. H. Cano, B. R. Macedo, L. Meurer, B. S. Batlle, S. D. Groshong, J. M. Kulczynski, R. Roesler, L. D. Lago, A. T. Brunetto and G. Schwartsmann, *Arch. Pathol. Lab. Med.*, 2014, **138**, 98-104.
3. Q. Zhang, N. E. Bhola, V. W. Y. Lui, D. R. Siwak, S. M. Thomas, C. T. Gubish, J. M. Siegfried, G. B. Mills, D. Shin and J. R. Grandis, *Mol. Cancer Ther.*, 2007, **6**, 1414-1424.
4. J. Santos, D. Mesquita, J. D. Barros-Silva, C. Jeronimo, R. Henrique, A. Morais, P. Paulo and M. R. Teixeira, *Oncoscience*, 2015, **2**, 497-507.
5. H. Zhang, *PLoS One*, 2012, **7**.
6. B. E. Rogers, M. E. Rosenfeld, M. B. Khazaeli, G. Mikheeva, M. A. Stackhouse, T. Liu, D. T. Curiel and D. J. Buchsbaum, *J. Nucl. Med.*, 1997, **38**, 1221-1229.
7. A. Safavy, K. P. Raisch, M. B. Khazaeli, D. J. Buchsbaum and J. A. Bonner, *J. Med. Chem.*, 1999, **42**, 4919-4924.
8. S. L. Pedersen, K. K. Sørensen and K. J. Jensen, *Biopolymers*, 2010, **94**, 206-212.
9. S. L. Pedersen, A. P. Tofteng, L. Malik and K. J. Jensen, *Chem. Soc. Rev.*, 2012, **41**, 1826-1844.
10. E. Valeur and M. Bradley, *Chem. Soc. Rev.*, 2009, **38**, 606-631.
11. L. Ju and J. W. Bode, *Org. Biomol. Chem.*, 2009, **7**, 2259-2264.
12. S. A. Palasek, Z. J. Cox and J. M. Collins, *J. Pept. Sci.*, 2007, **13**, 143-148.
13. A. Biosystems, Cleavage, Deprotection, and Isolation of Peptides after Fmoc Synthesis: Technical Bulletin: Rev 2, http://tools.thermofisher.com/content/sfs/brochures/cms_040654.pdf, Accessed 27/10/2016.
14. E. Gourni, P. Bouziotis, D. Benaki, G. Loudos, S. Xanthopoulos, M. Paravatou-Petsotas, M. Mavri-Vavagianni, M. Pelecanou, S. C. Archimandritis and A. D. Varvarigou, *J. Med. Chem.*, 2009, **52**, 4234-4246.
15. I. W. Chiang, B. E. Brinson, R. E. Smalley, J. L. Margrave and R. H. Hauge, *J. Phys. Chem. B*, 2001, **105**, 1157-1161.
16. V. International, www.visitech.co.uk/vt-isim.html, Accessed 16/11/2016.
17. M. Y. Berezin and S. Achilefu, *Chem. Rev.*, 2010, **110**, 2641-2684.
18. J. R. Lakowicz, *Principles of fluorescence spectroscopy*, 4th Printing edn., Springer, 2006.
19. W. Becker, *J. Microsc.*, 2012, **247**, 119-136.
20. H. S. Muddana, T. T. Morgan, J. H. Adair and P. J. Butler, *Nano Lett.*, 2009, **9**, 1559-1566.
21. T. Rohand, J. Lycoops, S. Smout, E. Braeken, M. Sliwa, M. Van der Auweraer, W. Dehaen, W. M. De Borggraeve and N. Boens, *Photochem. Photobiol. Sci.*, 2007, **6**, 1061-1066.
22. P. A. Waghorn, M. W. Jones, M. B. M. Theobald, R. L. Arrowsmith, S. I. Pascu, S. W. Botchway, S. Faulkner and J. R. Dilworth, *Chem. Sci.*, 2013, **4**, 1430-1441.
23. M. V. Berridge and A. S. Tan, *Arch. Biochem. Biophys.*, 1993, **303**, 474-482.

24. T. Mosmann, *J. Immunol. Methods*, 1983, **65**, 55-63.
25. M. V. Berridge, P. M. Herst and A. S. Tan, *Biotechnol. Ann. Rev.*, 2005, **11**, 127-152.
26. Z. Hu, G. D. Pantoş, N. Kuganathan, R. L. Arrowsmith, R. M. J. Jacobs, G. Kociok-Köhn, J. O'Byrne, K. Jurkschat, P. Burgos, R. M. Tyrrell, S. W. Botchway, J. K. M. Sanders and S. I. Pascu, *Adv. Funct. Mater.*, 2012, **22**, 503-518.
27. S. I. Pascu, P. A. Waghorn, B. W. C. Kennedy, R. L. Arrowsmith, S. R. Bayly, J. R. Dilworth, M. Christlieb, R. M. Tyrrell, J. Zhong, R. M. Kowalczyk, D. Collison, P. K. Aley, G. C. Churchill and F. I. Aigbirhio, *Chem. Asian J.*, 2010, **5**, 506-519.
28. I. S. Alam, R. L. Arrowsmith, F. Cortezon-Tamarit, F. Twyman, G. Kociok-Kohn, S. W. Botchway, J. R. Dilworth, L. Carroll, E. O. Aboagye and S. I. Pascu, *Dalton Trans.*, 2016, **45**, 144-155.
29. J. Kolosnjaj, H. Szwarc and F. Moussa, in *Bio-Applications of Nanoparticles*, ed. W. C. W. Chan, Springer New York, New York, NY, 2007, pp. 181-204.
30. V. E. Kagan, Y. Y. Tyurina, V. A. Tyurin, N. V. Konduru, A. I. Potapovich, A. N. Osipov, E. R. Kisin, D. Schwegler-Berry, R. Mercer, V. Castranova and A. A. Shvedova, *Toxicol. Lett.*, 2006, **165**, 88-100.
31. P. Wick, P. Manser, L. K. Limbach, U. Dettlaff-Weglikowska, F. Krumeich, S. Roth, W. J. Stark and A. Bruinink, *Toxicol. Lett.*, 2007, **168**, 121-131.
32. L.-C. Ong, F. F.-L. Chung, Y.-F. Tan and C.-O. Leong, *Arch. Toxicol.*, 2016, **90**, 103-118.
33. R. Alshehri, A. M. Ilyas, A. Hasan, A. Arnaout, F. Ahmed and A. Memic, *J. Med. Chem.*, 2016, **59**, 8149-8167.
34. J. M. Wörle-Knirsch, K. Pulskamp and H. F. Krug, *Nano Lett.*, 2006, **6**, 1261-1268.
35. C. M. Sayes, F. Liang, J. L. Hudson, J. Mendez, W. Guo, J. M. Beach, V. C. Moore, C. D. Doyle, J. L. West, W. E. Billups, K. D. Ausman and V. L. Colvin, *Toxicol. Lett.*, 2006, **161**, 135-142.
36. A. Nimmagadda, K. Thurston, M. U. Nollert and P. S. McFetridge, *J. Biomed. Mater. Res. A*, 2006, **76A**, 614-625.
37. Y. Chen and A. Periasamy, *Microsc. Res. Tech.*, 2004, **63**, 72-80.
38. S. W. Botchway, M. Charnley, J. W. Haycock, A. W. Parker, D. L. Rochester, J. A. Weinstein and J. A. G. Williams, *Proc. Natl. Acad. Sci. U.S.A.*, 2008, **105**, 16071-16076.
39. D. W. Piston and G.-J. Kremers, *Trends Biochem. Sci*, 2007, **32**, 407-414.

Chapter 6 : Summary and outlook

The synthesis and characterisation of fluorescent nanohybrids based on carbon nanomaterials (i.e. functionalised SWNT and functionalised GO) for their application in optical imaging were described in this thesis. New nanohybrids incorporating a thiosemicarbazonato complex, a BODIPY fluorophore and/or a BODIPY-bombesin conjugate were evaluated *in vitro* in living prostate cancer PC-3 cells using different optical imaging techniques and it appears that they show promising prospects as imaging agents. The novel nanohybrids demonstrated their capability to enter into the cancer cells, reduced cytotoxicity with respects to the starting materials and possibilities of further functionalisation using non covalent or filling strategies to expand their applications.

The chemistry of thiosemicarbazones and the formation of the zinc and gallium complexes for several different novel derivatives was described in Chapter 2. New synthetic routes for known, and novel functional thiosemicarbazides were explored, as necessary steps in order to apply them further to the synthesis of new unsymmetrical bis(thiosemicarbazonato) complexes. The preparation of unsymmetrical derivatives using the standard methods described in the literature proved challenging, so a novel set of conditions was explored by using microwave-assisted heating. The application of the microwave conditions to the synthesis of mono(thiosemicarbazone) and symmetrical bis(thiosemicarbazone) ligands proved successful leading to considerably reduced reaction times and enhanced yields. This emerged as a new desirable method to obtain this type of compound in the future. However, the synthesis of unsymmetrical ligands proved to be further complicated by the occurrence of a metathesis exchange between the thiosemicarbazone moieties, which was observed upon heating. This exchange yielded a statistical mixture of the starting material and all derivatives originated by exchange of the thiosemicarbazone groups. Although such synthetic difficulties were encountered, a zinc complex was successfully prepared by a one-pot templated method from the mono(substituted) ligand with thiocarbohydrazide and the desired free amino group was present in the final product as demonstrated by spectroscopic techniques. The corresponding gallium complex was obtained by transmetallation with gallium chloride and the final product proved to be a promising bis(thiosemicarbazonato) fluorophore. This was demonstrated and fluorescence spectroscopy data suggested its usefulness for further imaging applications.

Furthermore, other aromatic dicarbonylic compounds were explored for the preparation of intrinsically fluorescent thiosemicarbazones. Four different starting materials were used in the preparation of thiosemicarbazones that had never been reported before. The structural investigations into these compounds were carried out by ^{1}H and ^{13}C NMR spectroscopies, mass spectrometry and, in the case of pyrene-4,5-dione mono(thiosemicarbazones), by single crystal X-ray crystallography. The mono(allyl)

thiosemicarbazones ligands with acenaphthenequinone, aceanthrenequinone, phenanthtrenequinone and pyrene-4,5-dione backbones were evaluated as synthetic scaffolds for the preparation of the zinc thiosemicarbazonato species. The complexes were successfully obtained by microwave-assisted heating which considerably reduced the reaction time with respect of similar acenaphthenequinone examples already reported in the literature.

A selection of compounds was tested in PC-3 cells showing cellular uptake and concentration in organelles but further work is needed to discern a preferred cellular localisation.

The preparation of functional derivatives incorporating protected amino acids opens the way of coupling the thiosemicarbazone ligands or complexes to targeting molecules. The coupling to bombesin would be a logical next step as bombesin has been used as a targeting peptide for prostate cancer cells throughout this project. These targeted derivatives will be tested *in vitro* in PC-3 cells and other prostate cancer cell lines to evaluate their selectivity towards GRP receptors. Furthermore, the biological evaluation will be extended to explore the hypoxia selectivity of the novel thiosemicarbazonato complexes as it has been already described for certain compounds in this family. Imaging experiments of the prepared compounds at variable oxygen levels can provide valuable information about the potential hypoxia selectivity prior to further biological experiments.

In addition, the radiolabelling of the distinct thiosemicarbazonato compounds by transmetallation of Zn or Ga with ^{68}Ga would make their use possible in PET imaging. Preliminary results in the radiolabelling of mono(thiosemicarbazonato) compounds showing high incorporation and radiochemical yield are encouraging to study the possibilities of the radiolabelled compounds as *in vivo* imaging agents.

The study of BODIPY fluorophores was described in Chapter 3. BODIPY fluorophores were selected due to their advantageous photophysical properties and stability under a wide range of conditions. A bifunctional derivative was prepared including a protected lysine residue. The preparation of derivatives emitting in the IR was also explored taking advantage of the possibility of the methyl groups in the BODIPY core to undergo a Knoevenagel-type reaction. This way, a styryl residue was introduced, extending the conjugation and shifting the fluorescence emission maximum towards the NIR region of the spectrum ($\lambda_{em\text{-}max}$ 752 nm).

The deprotection of the Boc group in the lysine residue was explored prior to the coupling of the fluorophore with the peptide, and some difficulties were found when treating the bifunctional BODIPY under acidic conditions. Several reaction conditions were tested but an efficient synthetic method, compatible with the presence of a peptide group, was not established. In order to overcome the deprotection difficulties, the equivalent bifunctional derivative was prepared by coupling the BODIPY with the Fmoc amino protecting group. This way, an equivalent bifunctional BODIPY derivative was obtained but in this case the deprotection could be achieved using piperidine in mild conditions and reduced reaction times. The characterisation of the BODIPY derivatives was carried out by ^{1}H- and ^{13}C NMR spectroscopies, single X-ray crystallography for one of the intermediate compounds and UV-vis

and fluorescence spectroscopies to evaluate the photophysical properties. The absorption and emission of this family of compounds occurs in the visible region of the spectrum (λ_{max} 500 nm) presenting high quantum yields (with the exception of the styryl BODIPY derivatives that had their emission in the NIR region of the spectrum and the quantum yield significantly reduced with respect to other BODIPY species).
The novel BODIPY derivatives prepared hereby were tested in PC-3 cells proving as promising optical imaging dyes showing cell uptake and localisation in the cytoplasm. The understanding of the fate of these compounds *in vitro* is essential for their applicability and potential modification to target specific organelles inside the cell. Co-localisation experiments with specific dyes to ascertain the specific localisation in the cell (membranes, nuclei, endoplasmic reticulum, mitochondria, etc.) are being designed for this family of compounds.

The preparation of carbon nanomaterials based on single walled carbon nanotubes for their use in biological systems was described in Chapter 4. Two initial functionalisation strategies were used herein: oxidation and a Tour reaction. The oxidation yielded carboxylic acid groups in the tips and sidewalls of the SWNT, while the Tour reaction provided a free amino group by functionalising the sidewalls of the SWNT. The introduction of linkers followed to improve the dispersibility and stability of the dispersions of the nanotubes. Different diamines or long chain amino acids were applied that resulted in terminal amino groups for the different nanoprobes. The introduction of terminal carboxylic acids was achieved by reaction with succinic anhydride that improved the dispersions' stability and yielded a convenient functional group for the introduction of the fluorophores or fluorophore-peptide conjugate.
The different functional SWNT prepared hereby were characterised by FTIR and Raman spectroscopies, the Kaiser test and by TGA and TEM for selected derivatives. The functionalisation could be demonstrated using these techniques and the functionalisation degree estimated by TGA and the Kaiser test.

In addition, the functionalisation strategy applied hereby to SWNT was translated to graphene oxide (GO). In this case, one selected diamine compound was used as a linker taking advantage of the carboxylic acid groups in the graphene oxide structure. The GO nanohybrids were characterised using the techniques described above for SWNT (FTIR, Raman, Kaiser test, TGA) that demonstrated the functionalisation of the material. However, the functionalisation degree found for the GO derivatives proved to be lower than the observed for equivalent SWNT compounds, probably due to the lower concentration of functional groups in the starting material.

The preparation and characterisation of bombesin, a targeting peptide towards prostate cancer cells was described in Chapter 5. The peptide was prepared by solid phase peptide synthesis (SPPS) using microwave heating. The crude peptide was purified by automated flash column chromatography and

characterised by HPLC, mass spectrometry and ^{1}H NMR spectroscopy. The resonances of the different amino acids could be assigned by applying different bidimensional NMR techniques revealing the correlation between coupled ^{1}H-^{1}H nuclei. Furthermore, the coupling of bombesin to the bifunctional BODIPY fluorophore was described hereby. The conjugate was purified by RP-HPLC and characterised by ^{1}H NMR, mass spectrometry and UV-vis and fluorescence spectroscopies. The photophysical properties revealed that the conjugate presented identical fluorescence excitation and emission profiles with respect to the starting materials although the quantum yield was reduced. The fluorescence lifetime, acquired by time-correlated single photon counting, was also measured in solution and proved to be shorter than that found in the BODIPY starting material, revealing that the peptide changed the environment of the fluorophore and induced a process of quenching of the fluorescence.

Different targeted nanohybrids, based on functionalised SWNT and functionalised GO, were prepared incorporating the conjugate. In addition, nanohybrids were also prepared incorporating the gallium thiosemicarbazonato complex and the BODIPY fluorophore.

The evaluation of the conjugate and nanohybrids *in vitro* was carried out in PC-3 cells by confocal imaging microscopy. The different uptake presented by the fluorophore and the fluorophore-bombesin conjugate proved the targeting behaviour of the conjugate. This was further explored by performing a blocking experiment and acquiring super-resolution microscopy images. The nanohybrids showed good uptake and maintained the fluorescence probing as promising imaging probes. The fluorescence lifetime imaging (FLIM) of a selection of compounds was carried out and the existence of a quenching mechanism was demonstrated in the cellular environment whilst the environment of the fluorophores was clearly influenced by the interaction with cellular biomolecules. Cell viability studies (MTT assays) suggested that the reduction of toxicity of the SWNT nanohybrids with respect to the starting materials, that further points towards their advantageous properties as potential cellular imaging probes.

The evaluation of the nanohybrids *in vitro* showed promising results that are encouraging to continue the study of their behaviour in other cancer cell lines especially the ones rich in GRP receptors. The preference of the nanohybrid for the overexpressed GRP receptors can be demonstrated by the performance of blocking experiments, similar to the experiments performed for the BODIPY fluorophore and the conjugate that revealed a preference of the conjugate for the cellular membranes.

Co-localisation experiments are being designed as well to help understand the fate of the carbon nanomaterials *in vitro* and their presence in the cellular membrane, in vacuoles or near the endoplasmic reticulum.

Furthermore, the excellent conducting properties of SWNT make them ideal candidates to form part of electrical sensing devices. The use of gold electrodes on a glass substrate opens the possibility of dual electrical and optical detection. Preliminary experiments for the deposition of pristine nanotubes between gold electrodes by dielectrophoresis showed promising results. Therefore, the building of a

sensor towards the GRP receptor, overexpressed in different cancer cell lines, could be developed by depositing the obtained nanohybrids between gold electrodes.

The application of functionalised GO towards the development of a sensor is also encouraging. However, an alternative functionalisation strategy will need to be applied in order to increase the functionalisation degree and a final reduction step introduced to obtain the reduced derivative in order to improve the conducting properties of the nanomaterial.

Chapter 7 : Experimental section

7.1 General information

Reagents were obtained from commercial sources (Sigma Aldrich, Alfa Aesar, Acros Organics, Merck Chemicals, Fluorochem) and used as received unless otherwise specified. Solvents were reagent or HPLC grade obtained from Sigma Aldrich or VWR. Water was obtained from a Millipore milli-Q purification system and anhydrous solvents from a PS-400-7 Innovative technologies SPS system.

Microwave reactions were conducted in 5 or 20 mL capped vessels in a Biotage Initiator 2.5 microwave reactor pre-stirring for 30 s and heating to the desired temperature by applying a maximum power of 400 W that was reduced and kept constant once the target temperature was reached.
Automated flash chromatography purification was performed in a Biotage Isolera Four system using 10, 25 or 50 g Biotage SNAP silica cartridges.

NMR spectra were acquired in a 300 MHz BRUKER Avance, 400 MHz Bruker Avance, 500 MHz Bruker Avance II+ or a 500 MHz Agilent automated system. Spectra were processed using MestReNova 10.0.2 and referenced to the residual solvent peaks. Splitting patterns are identified as singlet (s), doublet (d), triplet (t), quartet (q) and multiplet (m).

Mass spectra were acquired in a Bruker MicroTOF equipment. The mass spectra of **23** and **46** were acquired in a nano-ESI LTQ Orbitrap XL instrument. The mass spectra of **52** and **54** were acquired in an APCI Xevo-G2S equipment. The mass spectra for **23**, **46**, **52** and **54** were acquired at the EPSRC UK National Mass Spectrometry Facility at Swansea University.

HPLC was performed in a Dionex Ultimate 3000 HPLC instrument with a UV-vis diode array detector measuring at eight wavelengths between 200 and 800 nm. Analytical HPLC chromatograms were acquired in RP mode using a Dionex C18 Acclaim column (5 µm, 4.6 x 150 mm). In this case, a 20 min gradient method (method A) was applied using MeCN / H_2O containing 0.1% TFA as mobile phases with the following conditions: 0 min 5% MeCN; 1 min 5% MeCN; 6 min 95% MeCN, 13 min 95% MeCN, 16 min 5% MeCN; 20 min 5% MeCN. Alternatively, an 18 min gradient method (method B) was employed with the following conditions: 0 min 5% MeCN; 7.5 min 95% MeCN; 15 min 95% MeCN, 18 min 95% MeCN. Flow rate = 0.8 mL / min. Semi-preparative HPLC was performed using a C18 Nucleodur HTEC column (5 µm, 10 x 250 mm). The gradient method was extended to 37 min (method C) using the same mobile phases and the following conditions: 0 min 5% MeCN; 1 min 5% MeCN; 11 min 95% MeCN, 26 min 95% MeCN, 31 min 5% MeCN; 36 min 5% MeCN. Flow rate = 1.8 mL / min.

X-ray crystallography data were acquired by Dr Gabrielle Kociok-Kohn at the University of Bath. Intensity data for **12**, **43** and **52** were collected at 150(2) K on an Agilent SuperNova Dual diffractometer, Cu at zero, EosS2 and using monochromated Cu-Kα radiation λ = 1.54184 Å. Intensity data for **40**, **41** and **42** were collected at 150(2) K on a Rigaku New Xcalibur diffractmometer, EosS2 using graphite monochromated Mo-Kα radiation λ = 0.71073 Å. All structures were solved with SHELXT and refined by a full-matrix least-squares procedure based on F^2 (Shelxl-2014/7).[1] All non-hydrogen atoms were refined anisotropically. Hydrogen atoms were placed onto calculated positions and refined using a riding model except for the OH hydrogen atoms which have been located in the difference fourier map and were refined with bond lengths restraints. Additional programmes used for analysing data and their graphical manipulation included: SHELXle[2] and ORTEP 3 for windows.[3]

IR spectra were acquired in a Perkin Elmer Frontier FTIR machine in ATR mode.

UV-vis spectra were acquired in 1 cm quartz cuvettes in a Perkin Elmer Lambda 35 UV-vis spectrometer controlled by UV-Winlab software.

Fluorescence spectra were acquired in 1 cm quartz cuvettes in a Perkin Elmer LS55 luminescence spectrometer controlled by FL-Winlab 4.0 software.

Quantum yields were calculated according to equation 7.1 using $Ru(bpy)_3$ as standard.

$$\Phi_S = \Phi_R * \frac{A_r}{A_s} * \frac{E_S}{E_r} * \frac{I_r}{I_s} * \frac{n_s{}^2}{n_r{}^2}$$

Equation 7.1

Raman spectra were acquired in a Renishaw inVia microscope equipped with a 532 nm excitation laser.

TEM experiments were performed in a JEOL JEM1200EXII instrument with a maximum voltage of 120 kV at the Microscopy and Analysis Suite at the University of Bath with the assistance of Dr David Gonzalez Calatayud. Samples were prepared by evaporation of a drop of a dispersion of the nanomaterial in ethanol onto a carbon-coated 200 Mesh copper grid (Aggar scientific).

TGA experiments were performed in a Setaram Setsys Evolution TGA 16/18 instrument with an Omnistar GSD 320 MS detector equipped with a quadrupole mass analyser and a SEM detector. TG curves were acquired heating the sample between 100 and 1000 ºC under an argon atmosphere at a

10 ºC / min rate. TGA data were collected by Dr Remi Castaing in the Chemical Characterisation and Analysis Facility at the University of Bath.

Cells were cultured at 37 ºC in RPMI medium containing foetal calf serum (10%), penicillin/streptomycin (10,000 IU mL^{-1}) and L-glutamine (200 mM). All steps were performed in the absence of phenol red. Cell culturing was carried out with the assistance of Dr Haobo Ge.

Cell viability assays (MTT) were performed culturing cells as above in 96 well plates (ca. $5x10^4$ cells mL^{-1}). The cells were incubated for 48 h to adhere and then the compounds of interest added in different concentrations in RPMI medium (1% DMSO). The concentrations used were 1, 0.1, 0.05, 0.01, $1x10^{-3}$, $1x10^{-4}$, $1x10^{-5}$, $1x10^{-6}$ mM for compounds **23**, **58** and **87**. The concentrations used for p-SWNT, **78**, **88**, **89**, **90**, **81**, **84** and **93** were 1, 0.25, 0.1, 0.01, $1x10^{-3}$, $1x10^{-4}$, $1x10^{-5}$, $1x10^{-6}$ $mgmL^{-1}$. The compounds were incubated for 48 h at 37 ºC to be subsequently washed with PBS and MTT reagent added. The tetrazolium reagent was incubated for 2 h, the cell media removed by aspiration and DMSO added. The absorbance of the generated colour was measured using a Molecular Devices Versa Max ELISA plate reader. Data were calculated from at least six consistent results and IC_{50} values calculated from the fitting obtained with Origin 9.0. The error reported corresponds to the error of the mean. Cell viability studies were carried out by Dr Haobo Ge.

Confocal microscopy images were acquired in a Nikon Eclipse Ti instrument equipped with 405 / 488 / 561 excitation lasers. The images obtained were processed using the Nikon NIS elements-AR Analysis 4.30.02 software.

Fluorescence lifetimes and FLIM measurements were conducted at the Rutherford Appleton Laboratory (Central Lasers Facility, Research Complex at Harwell) with the assistance of Dr Vincenzo Mirabello and Dr Haobo Ge. A detailed description of the characteristics of FLIM measurements acquisition can be found in ref. 18. Lifetime calculations were processed using SPCImage software.

Elemental analyses were carried out by Stephen Boyer at the Science Centre (London Metropolitan University) using a Thermo Scientific CE Flash 2000 Elemental Analyser configured for %CHN.

7.2 Experimental procedures

1. Tert-butyl (2-aminoethyl)carbamate (adapted from a literature procedure[4])

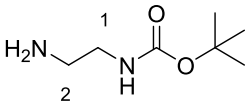

Di-tert-butyl dicarbonate (3.000 g, 13.7 mmol) in $CHCl_3$ (100 mL) was added dropwise to a stirring solution of ethylenediamine (4.960 g, 82.5 mmol) dissolved in $CHCl_3$ (100 mL) at 0 ºC over a period of 2 h. The reaction mixture was allowed to reach room temperature and stirred for 16 h. The solvent was removed under vacuum, the white residue re-suspended in $CHCl_3$ (150 mL) and washed with sat. aqueous sodium carbonate (150 mL) and brine (100 mL). The organic phase was dried over $MgSO_4$ and concentrated under vacuum. The product was obtained as a yellowish oil (2.150 g, 98%).

^{1}H NMR (400 MHz, $CDCl_3$, 25 ºC): δ 4.99 (brs, 1H, NH), 3.21 – 3.07 (m, 2H, H-1), 2.76 (t, ^3J = 5.9 Hz, 3H, H-2), 1.42 (s, 9H, *(CH₃)₃*), 1.23 (s, 2H, *NH₂*).
^{13}C NMR (125 MHz, $CDCl_3$, 25 ºC): δ 156.5 (*CO)*, 79.4 (*C*$(CH_3)_3$), 43.2 (C-1), 41.7 (C-2), 28.4 (*C*$H_3)_3$).
Mass spectrum: ESI-MS calc. for $C_7H_{16}N_2NaO_2$ $[M+Na]^+$: 183.1109; found: 183.1110.
IR (solid): ν (cm^{-1}) 3359, 2986, 1684, 1528, 1268, 1165.

2. Tert-butyl (6-aminohexyl)carbamate (adapted from a literature procedure[5])

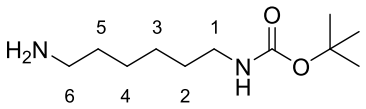

Hexamethylenediamine (39.930 g, 0.343 mol) was dissolved in CH_2Cl_2 (150 mL), triethylamine added (10 mL) and the reaction mixture cooled to 0 ºC. Di-tert-butyl dicarbonate (15.000 g, 68.7 mmol) dissolved in CH_2Cl_2 (150 mL) was then added dropwise over a 2 h period and the reaction mixture was allowed to warm-up to room temperature and stirred for another 16 h. The solvent was removed under vacuum to yield a white slurry that was re-dissolved in CH_2Cl_2 (150 mL) and washed with sat. sodium carbonate. The aqueous phase was extracted with CH_2Cl_2 (3x 100 mL), the organic layers collected, washed with brine, dried over $MgSO_4$ and concentrated under vacuum. The resulting residue was dissolved in CH_2Cl_2 and purified by flash column chromatography using CH_2Cl_2 / MeOH (0 - 10%) as eluent. The product was obtained as a yellowish oil that solidified over time (14.289 g, 96%).

^{1}H NMR (500 MHz, $CDCl_3$, 25 ºC): δ 4.52 (brs, 1H, *NH*), 3.12 – 2.96 (m, 2H, H-1), 2.68 (t, ^3J = 7.0 Hz, 2H, H-6), 1.49 – 1.37 (m, 13H, H-3, H-5, $(CH_3)_3$), 1.38 – 1.28 (m, 4H, H-3, H-4).
^{13}C NMR (125 MHz, $CDCl_3$, 25 ºC): δ 156.1 (CO), 79.2 (*C*$(CH_3)_3$), 42.2 (C-6), 40.6 (C-1), 33.6 (C-5), 30.2 (C-3), 28.6 ((*C*$H_3)_3$), 26.8 (C-4), 26.6 (C-3).
Mass spectrum: ESI-MS calc. for $C_{11}H_{24}N_2NaO_2$ $[M+Na]^+$: 239.1735; found: 239.1731.
IR (solid): ν (cm^{-1}) 3367, 2930, 1683, 1520, 1167.

3. Tert-butyl (2-(2-(2-aminoethoxy)ethoxy)ethyl)carbamate (adapted from a literature procedure[6])

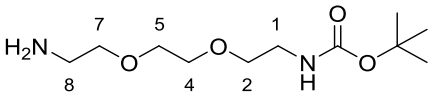

2,2'-(ethylenedioxy)bis(ethylamine) (20.507 g, 0.138 mol) was dissolved in 1,4-dioxane (40 mL) and cooled to 0 ºC. Di-tert-butyl dicarbonate (5.033 g, 0.023 mol) dissolved in 40 mL of 1,4-dioxane was added dropwise over a period of 2 h. The reaction mixture was allowed to warm to room temperature and left stirring for 16 h. The solvent was removed under vacuum to yield a white slurry that was re-dissolved in CH_2Cl_2 (500 mL) and washed with water (3x 300 mL) and brine (3x 150 mL). The organic phase was dried over $MgSO_4$ and concentrated under vacuum. The oil obtained was purified by flash column chromatography using CH_2Cl_2 / MeOH (0 – 10%) as eluent. The product was obtained as a yellowish oil (4.620 g, 81%).

^{1}H NMR (500 MHz, $CDCl_3$, 25 ºC): δ 5.23 (s, 1H, N*H*), 3.60 (s, 4H, H-4, H-5), 3.55 – 3.49 (m, 4H, H-2, H-7), 3.29 (brs, 2H, H-1), 2.87 (t, ^3J = 5.2 Hz, 2H, H-8), 1.42 (s, 9H, (CH_3)$_3$).
^{13}C NMR (125 MHz, $CDCl_3$, 25 ºC): δ 156.2 (*C*O), 79.3 (*C*(CH_3)$_3$), 72.6, 70.3 (C-2, C-7), 70.3, 70.2 (C-4, C-5), 41.5 (C-8), 40.4 (C-1), 28.5 (CH_3)$_3$).
Mass spectrum: ESI-MS calc. for $C_{11}H_{24}N_2NaO_4$ $[M+Na]^+$: 271.1634; found: 271.1614.
IR (solid): ν (cm^{-1}) 3351, 2974, 1695, 1516, 1365, 1103.

4. Tert-butyl (2-(((methylthio)carbonothioyl)amino)ethyl)carbamate (adapted from a literature procedure[7])

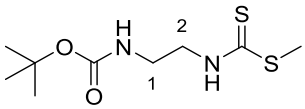

To a stirring solution of Boc-protected ethylenediamine (**1**) (0.869 g, 5.42 mmol) and triethylamine (0.83 mL, 5.96 mmol) in ethanol (20 mL) at 25 ºC in a water bath, carbon disulphide (0.36 mL, 5.96 mmol) was added dropwise. The reaction was stirred for 1.5 h and iodomethane (0.37 mL, 5.96 mmol) was added dropwise and the reaction mixture stirred for 2 h. The solvent was removed under vacuum and the resulting residue re-suspended in ethyl acetate (100 mL) and washed with, 1 M HCl (100 mL), aq. sat. $NaHCO_3$ solution (100 mL) and water (100 mL). The organic fraction was dried over $MgSO_4$ and the solvent removed under vacuum. The product was obtained as a yellowish solid (1.101 g, 81%).

^{1}H NMR (500 MHz, $CDCl_3$, 25 ºC): δ 8.43 (s, 1H, N*H*CS), 5.16 (s, 1H, CON*H*), 3.76 (d, ^3J = 5.0 Hz, 2H, H-2), 3.39 (d, ^3J = 5.0 Hz, 2H, H-1), 2.55 (s, 3H, SCH_3), 1.41 (s, 9H, (CH_3)$_3$).
^{13}C NMR (125 MHz, $CDCl_3$, 25 ºC): δ 199.2 (*C*S), 157.8 (*C*O), 80.4 (*C*(CH_3)$_3$), 49.4 (C-2), 39.1 (C-1), 28.4 ((*C*H_3)$_3$), 18.0 (S*C*H_3).
Mass spectrum: ESI-MS calc. for $C_9H_{19}N_2O_2S_2$ $[M+H]^+$: 251.0888; found: 251.0875.

5. Tert-butyl (6-(((methylthio)carbonothioyl)amino)hexyl)carbamate

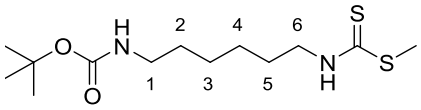

Carbon disulphide (1.73 mL, 28.8 mmol) was added dropwise to a stirring solution of tert-butyl (6-aminohexyl)carbamate (**2**) (4.150 g, 19.2 mmol) and triethylamine (5.3 mL, 38.3 mmol) in ethanol at 25 ºC. The reaction mixture was stirred for 1.5 h when iodomethane (1.8 mL, 28.8 mmol) was added dropwise. After the addition finished, the stirring continued for another 2.5 h. The solvent was removed under vacuum and the residue re-suspended in ethyl acetate (50 mL) and washed with 1M HCl (50 mL), aq. sat. $NaHCO_3$ (50 mL) and water (50 mL). The organic fraction was dried over $MgSO_4$ and the solvent removed under vacuum. The product was obtained as a yellowish oil that solidified on standing (4.414 g, 75%).

^{1}H NMR (400 MHz, $CDCl_3$, 25 ºC): δ 7.72 (s, 1H, N*H*CS), 4.64 (s, 1H, CON*H*), 3.67 (q, ^3J = 6.7 Hz, 2H, H-6), 3.05 (q, ^3J = 6.7 Hz, 2H, H-1), 2.56 (s, 3H, SCH_3), 1.67 – 1.57 (m, 2H, H-5), 1.48 – 1.36 (m, 11H, H-2, (CH_3)$_3$), 1.34 – 1.28 (m, 4H, H-3, H-4).
^{13}C NMR (125 MHz, $CDCl_3$, 25 ºC): δ 198.8 (*C*S), 156.2 (*C*O), 79.1 (*C*(CH_3)$_3$), 46.9 (C-6), 46.2, 40.1 (C-1), 30.0 (C-2), 28.5 ((*C*H$_3$)$_3$), 28.4 (C-5), 26.3, 26.2 (C-3, C-4), 18.1 (S*C*H$_3$).
Mass spectrum: ESI-MS calc. for $C_{13}H_{26}N_2NaO_2S_2$ $[M+Na]^+$: 329.1333; found: 329.1313.

6. Tert-butyl (3-thioxo-7,10-dioxa-2-thia-4-azadodecan-12-yl)carbamate

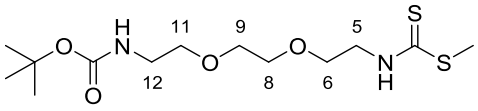

Tert-butyl (2-(2-(2-aminoethoxy)ethoxy)ethyl)carbamate (**3**) (2.500 g, 10.1 mmol) and triethylamine (1.41 mL, 10.1 mmol) were dissolved in ethanol (50 mL) and warmed to 25 ºC. Carbon disulphide (0.606 mL, 10.1 mmol) was added dropwise and the reaction mixture stirred at 25 ºC for 2 h. Methyl iodide (0.63 mL, 10.1 mmol) was added to the reaction mixture further stirred for 2 h. The solvent was concentrated under vacuum, the residue dissolved in 50 mL AcOEt and washed with HCl 1M, sat. $NaHCO_3$ and water. The organic phase was dried over $MgSO_4$ and the solvent removed under vacuum. The resulting oil was passed through a silica plug using CH_2Cl_2 first and then a mixture 8:2 of CH_2Cl_2 / MeOH. The second fraction was concentrated and dried under vacuum. The product was obtained as an off-white solid (2.971 g, 87%).

^{1}H NMR (500 MHz, $CDCl_3$, 25 ºC): δ 8.02 (s, 1H, N*H*CS), 5.10 (s, 1H, CON*H*), 3.78 (brs, 2H, H-5), 3.60 – 3.52 (m, 2H, H-6), 3.48 (s, 4H, H-8, H-9), 3.41 – 3.39 (m, 2H, H-11), 3.16 (brs, 2H, H-12), 2.45 (s, 3H, SCH_3), 1.28 (s, 9H).

^{13}C NMR (125 MHz, $CDCl_3$, 25 ºC): δ 198.8 (*C*S), 170.8, 155.7 (*C*O), 78.9 (*C*(C*H*$_3$)$_3$), 69.9 (C-8, C-9), 69.9 (C-11), 68.1 (C-6), 46.5 (C-5), 40.0 (C-12), 28.1 ((*C*H$_3$)$_3$), 17.8 (S*C*H$_3$).

Mass spectrum: ESI-MS calc. for $C_{13}H_{26}N_2NaO_4S_2$ $[M+Na]^+$: 361.1232; found: 361.1218.

7. Tert-butyl (2-(hydrazinecarbothioamido)ethyl)carbamate

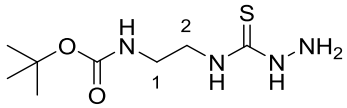

A stirring solution of methyl-N-(2-t-butoxycarbonylaminoethyl)dithiocarbamate (**4**) (0.272 g, 1.10 mmol) and hydrazine hydrate (73 µL, 1.5 mmol) in ethanol was heated under reflux for 2.5 h. The solvent was removed under vacuum and the residue re-dissolved in $CHCl_3$. The product was passed through a silica plug, washed with $CHCl_3$ and eluted with MeOH. The solvent was removed from the methanolic fraction and the product obtained as a yellowish oil that solidified over time (0.260 g, 95%).

^{1}H NMR (500 MHz, $CDCl_3$, 25 ºC): δ 8.33 (s, 1H, N*H*NH$_2$), 7.89 (s, 1H, N*H*CS), 4.94 (s, 1H, CON*H*), 3.86 – 3.71 (m, 2H, H-2), 3.47 – 3.27 (m, 2H, H-1), 1.43 (s, 9H, (C*H*$_3$)$_3$).

^{13}C NMR (125 MHz, $CDCl_3$, 25 ºC): δ 178.6 (*C*S), 159.3 (*C*O), 83.0 (*C*(C*H*$_3$)$_3$), 45.0 (*C*-2), 40.2 (*C*-1), 28.5 (*C*H$_3$)$_3$.

Mass spectrum: ESI-MS calc. for $C_8H_{18}N_4NaO_2S$ $[M+Na]^+$: 257.1048; found: 257.1042.

IR (solid): ν (cm^{-1}) 3358, 3315, 3245, 2976, 2942, 1670, 1519, 1140.

HPLC (Method A): Rt (min) 8.12.

8. Tert-butyl (6-(hydrazinecarbothioamido)hexyl)carbamate

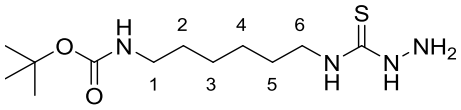

Methyl-N-(2-t-butoxycarbonylaminohexyl)dithiocarbamate (**5**) (4.414 g, 14.4 mmol) and hydrazine hydrate (1.0 mL, 21.6 mmol) were heated under reflux in ethanol for 2.5 h. The solvent was removed under vacuum and the residue redissolved in CH_2Cl_2 (20 mL) and passed through a silica plug that was washed with CH_2Cl_2 and the product eluted with MeOH. The product was obtained as a yellowish oil that solidified on standing (3.756 g, 90%).

^{1}H NMR (500 MHz, $CDCl_3$, 25 ºC): δ 8.32 (brs, 1H, N*H*NH$_2$), 7.43 (brs, 1H, N*H*CS), 4.53 (brs, 1H, CON*H*), 3.77 (brs, 2H, NHN*H*$_2$), 3.62 (td, $^{3,3}J$ = 7.2, 5.8 Hz, 1H, H-6), 3.13 – 3.06 (m, 2H, H-1), 1.70 – 1.57 (m, 1H, H-5), 1.52 – 1.43 (m, 2H, H-2), 1.43 (s, 9H, (C*H*$_3$)$_3$), 1.41 – 1.32 (m, 4H, H-3, H-4).

^{13}C NMR (125 MHz, $CDCl_3$, 25 ºC): δ 177.9 (*C*S), 156.0 (*C*S), 79.2 (*C*(C*H*$_3$)$_3$), 44.0 (C-6), 40.3 (C-1), 30.1 (C-2), 29.3 (C-5), 28.3 (*C*H$_3$)$_3$), 26.6, 26.5 (C-3, C-4).

Mass spectrum: ESI-MS calc. for $C_{12}H_{27}N_4O_2S$ $[M+H]^+$: 291.1855; found: 291.1852.

IR (solid): ν (cm^{-1}) 3336, 3196, 2930, 2861, 1682, 1520, 1248, 1166.

HPLC (Method A): Rt (min) 8.10.

9. Tert-butyl (2-(2-(2-(hydrazinecarbothioamido)ethoxy)ethoxy)ethyl)carbamate

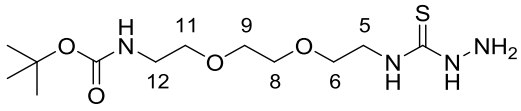

Tert-butyl (3-thioxo-7,10-dioxa-2-thia-4-azadodecan-12-yl)carbamate (**6**) (2.776 g, 8.80 mmol) was dissolved in ethanol (60 mL), hydrazine hydrate (0.9 mL, 12.1 mmol) added and the reaction mixture heated under reflux for 3 h. The solution was left to cool and the solvent removed under vacuum. The residue was dissolved in $CHCl_3$ and passed through a silica plug, washing with $CHCl_3$ before eluting the product with MeOH. The methanolic fraction was concentrated under vacuum to yield the product as a grey solid (1.928 g, 68%).

^{1}H NMR (500 MHz, $CDCl_3$, 25 ºC): δ 7.98 (s, 1H, N*H*NH_2), 7.69 (s, 1H, N*H*CS), 5.13 (s, 1H, CON*H*), 3.92 (brs, 2H, NH_2), 3.75 (appq, ^3J = 5.3 Hz, 2H, H-5), 3.57 (t, ^3J = 5.1 Hz, 2H, H6), 3.54 (s, 4H, H-8, H-9), 3.45 (t, ^3J = 5.2, 1H, H-11), 3.21 (appq, ^3J = 5.7 Hz, 2H, H-12), 1.35 (s, 9H).

^{13}C NMR (125 MHz, $CDCl_3$, 25 ºC): δ 181.8 (*C*S), 156.0 (*C*O), 79.2 (*C*(CH_3)$_3$), 70.1 (C-8, C-9), 70.1 (C-11), 69.5 (C-6), 43.6 (C-5), 40.3 (C-12), 28.4 (*C*H_3)$_3$).

Mass spectrum: ESI-MS calc. for $C_{12}H_{27}N_4O_4S$ $[M+H]^+$: 323.1753; found: 323.1734.

IR (solid): ν (cm^{-1}) 3333, 3193, 3126, 2980, 2869, 1692, 1679, 1530, 1278, 1120.

HPLC (Method A): Rt (min) 7.74.

10. Mono(4-(2-aminoethyl)-3-thiosemicarbazone) acenaphthenequinone

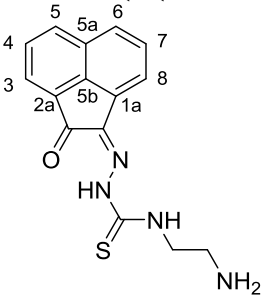

Compound **10** was synthesised under conventional mode (refluxing acenaphthenequinone (0.148 g, 0.81 mmol) and the protected thiosemicarbazide (**7**) (0.200 g, 0.85 mmol) in ethanol with 2 – 3 drops conc. HCl for 3 h) or microwave mode (heating acenaphthenequinone (0.265 g, 1.45 mmol) and the protected thiosemicarbazide (0.340 g, 1.45 mmol) in ethanol with 2 – 3 drops conc. HCl under microwave irradiation for 10 min at 90 ºC). In both cases, the work-up included filtering the reaction

mixture whilst hot and washing with methanol and diethyl ether. The product was obtained as a yellow solid (0.150 g, 62% by conventional synthesis; 0.258 g, 60% by MW synthesis).

^{1}H NMR (500 MHz, d^{6}-DMSO, 25 ºC): δ 12.72 (s, 1H, NN*H*), 9.68 (t, ^{3}J = 5.8 Hz, 1H, N*H*CH$_2$), 8.39 (dd, $^{3,4}J$ = 8.2, 0.7 Hz, 1H, H-5), 8.29 – 8.19 (brs, 2H, N*H*$_2$), 8.16 (dd, $^{3,4}J$ = 8.5, 0.7 Hz, 1H, H-6), 8.11 (dd, $^{3,4}J$ = 7.0, 0.7 Hz, 1H, H-3), 8.10 (dd, $^{3,4}J$ = 7.0, 0.7 Hz, 1H, H-8), 7.89 (dd, $^{3,3}J$ = 8.2, 7.1 Hz, 1H, H-4), 7.85 (dd, $^{3,3}J$ = 8.4, 7.0 Hz, 1H, H-7), 3.95 (q, ^{3}J = 6.3 Hz, 2H, NHC*H*$_2$), 3.11 (s, 2H, C*H*$_2$NH$_2$).
^{13}C NMR (125 MHz, d^{6}-DMSO, 25 ºC): δ 188.6 (*C*O), 178.0 (*C*S), 139.3 (C-5b), 137.6 (*C*N), 132.9 (C-5), 130.4, 129.9 (C-5a, C-1a, C-2a), 129.9 (C-4), 128.9 (C-8), 128.6 (C-3), 127.2 (C-6), 122.5 (C-7), 118.6 (C-4), 41.8 (NH*C*H$_2$), 37.7 (*C*H$_2$NH$_2$).
Mass spectrum: ESI-MS calc. for $C_{15}H_{15}N_4OS$ [M+H]$^+$: 299.0967; found: 299.0959.
IR (solid): ν (cm^{-1}) 3280, 3204, 2836, 1693, 1523, 1467, 1452, 1050.
HPLC (Method A): Rt (min) 7.42.

11. Mono (4-(tertbutyl-(2-aminoethyl)carbamate)-3-thiosemicarbazone) acenaphthenequinone

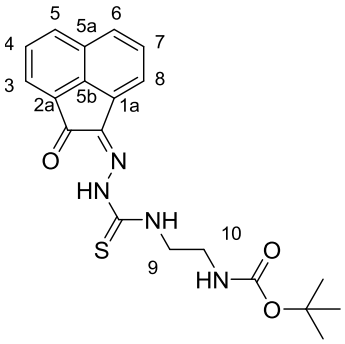

Acenaphthenequinone (0.125 g, 0.69 mmol) and tert-butyl (2-(hydrazinecarbothioamido)ethyl) carbamate (**7**) (0.160 g, 0.69 mmol) were heated to 78 ºC for 6 h in EtOH (10% acetic acid). The reaction mixture was filtered whilst hot and washed with methanol, diethyl ether and dried under vacuum. The product was obtained as a bright yellow solid (0.139 g, 51%).

^{1}H NMR (500 MHz, d^{6}-DMSO, 25 ºC): δ 12.61 (s, 1H, NN*H*), 9.41 (t, ^{3}J = 5.6 Hz, 1H, N*H*CH$_2$), 8.37 (dd, $^{3,4}J$ = 8.2, 0.7 Hz, 1H, H-5), 8.13 (dd, $^{3,4}J$ = 8.4, 0.7 Hz, 1H, H-6), 8.09 (dd, $^{3,4}J$ = 7.1, 0.7 Hz, 1H, H-3), 8.01 (d, ^{3}J = 7.0 Hz, 1H, H-8), 7.87 (dd, $^{3,3}J$ = 8.2, 7.0 Hz, 1H, H-4), 7.83 (dd, $^{3,3}J$ = 8.3, 7.0 Hz, 1H, H-7), 7.06 (t, ^{3}J = 5.7 Hz, 1H, N*H*CO), 3.65 (q, ^{3}J = 5.9 Hz, 2H, H-9), 3.25 (q, ^{3}J = 6.2 Hz, 2H, H-10), 1.38 (s, 9H, (C*H*$_3$)$_3$).
^{13}C NMR (125 MHz, d^{6}-DMSO, 25 ºC): δ 188.5 (*C*O), 177.6 (*C*S), 156.2 (NH*C*O), 139.5 (C-5b), 137.2 (*C*N), 132.8 (C-5), 130.5, 130.0, 129.9 (C-1a, C-2a, C-5a), 128.9 (C-7), 128.4 (C-4), 127.1 (C-6), 122.5 (C-3), 118.2 (C-8), 78.0 (*C*(*C*H$_3$)$_3$), 44.9 (C-9), 39.2 (C-10), 28.2 ((*C*H$_3$)$_3$).
Mass spectrum: ESI-MS calc. for $C_{20}H_{22}N_4NaO_3S$ [M+Na]$^+$: 421.1310; found: 421.1329.
IR (solid): ν (cm^{-1}) 3384, 3326, 3260, 2980, 1719, 1685, 1670, 1512, 1480.
HPLC (Method A): Rt (min) 10.04.

12. Mono(4-(tertbutyl-(6-aminohexyl)carbamate)-3-thiosemicarbazone acenaphthenequinone

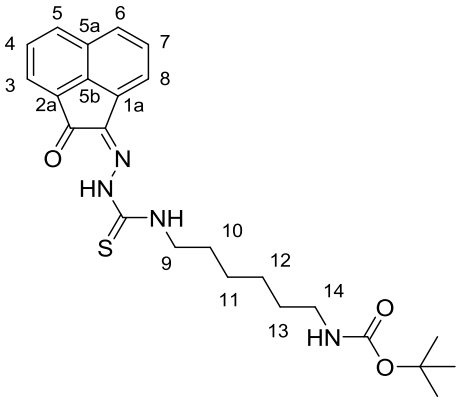

Compound **12** was synthesised following the same synthetic procedure as in **11**. Alternatively, it could be prepared from acenaphthenequinone (0.050 g, 0.27 mmol), tert-butyl (6-(hydrazinecarbothioamido)hexyl)carbamate (**8**) (0.318 g, 1.10 mmol) and hydrochloric acid (0.010 g, 0.27 mmol) heating in ethanol (5 mL) for 10 min at 90 ºC under microwave irradiation. The work-up followed the same experimental procedure of **11**. The product was obtained as a bright yellow solid (0.112 g, 93%).

^{1}H NMR (300 MHz, d^{6}-DMSO, 25 ºC): δ 12.60 (s, 1H, NN*H*), 9.39 (t, ^{3}J = 5.9 Hz, 1H, *NH*CH$_2$), 8.38 (d, ^{3}J = 8.2 Hz, 1H, H-5), 8.14 (d, ^{3}J = 8.3 Hz, 1H, H-6), 8.09 (d, ^{3}J = 7.0 Hz, 1H, H-3), 8.01 (d, ^{3}J = 6.9 Hz, 1H, H-8), 7.91 – 7.86 (m, 1H, H-4), 7.86 – 7.79 (m, 1H, H-7), 6.77 (t, ^{3}J = 5.1 Hz, 2H, N*H*CO), 3.63 (q, ^{3}J = 6.8 Hz, 2H, H-9), 2.91 (q, ^{3}J = 6.4 Hz, 2H, H-14), 1.70 – 1.63 (m, 2H, H-10), 1.45 – 1.34 (m, 11H, H-13, (C*H*$_3$)$_3$), 1.34 – 1.27 (m, 4H, H-11, H-12).

^{13}C NMR (75 MHz, d^{6}-DMSO, 25 ºC): δ 188.4 (*C*O), 177.1 (*C*S), 155.6 (NH*C*O), 139.0 (C-5b), 137.0 (*C*N), 132.8 (C-5), 130.4, 130.0, 129.8 (C-5a, C-2a, C-1a), 128.8 (C-7), 128.6 (C-4), 127.0 (C-8), 122.4 (C-6), 118.4 (C-3), 77.25 (*C*(CH$_3$)$_3$), 44.2 (C-9), 39.0 (C-14), 28.4 (C-10), 28.2 ((*C*H$_3$)$_3$), 26.0, 25.9 (C-11, C-12), 25.6 (C-13).

Mass spectrum: ESI-MS calc. for $C_{24}H_{29}N_4O_3S$ [M-H]$^-$: 453.1960; found: 453.1976.

HPLC (Method A): Rt (min) 7.72.

13. Mono(4-(tertbutyl (2-(2-(2-aminoethoxy)ethoxy)ethylcarbamate)-3-thiosemicarbazone acenaphthenequinone

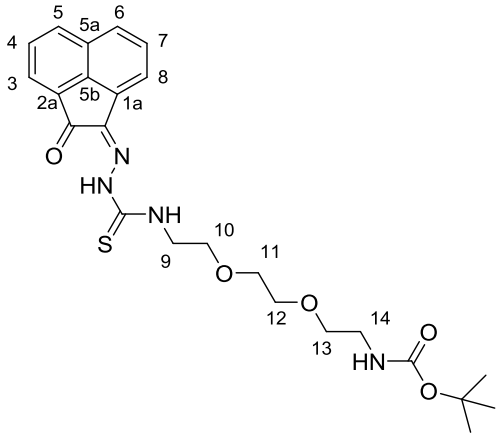

Acenaphthenequinone (0.042 g, 0.22 mmol) and tert-butyl (2-(2-(2-(hydrazinecarbothioamido)ethoxy)ethoxy)ethyl)carbamate (**9**) (0.071 g, 0.22 mmol) were heated to 78 ºC for 3 h in ethanol (60 mL, 10% acetic acid). The work-up procedure followed the described for compound **11**. The product was purified by column chromatography using CH_2Cl_2 / MeOH (0 – 20%) as eluent. The product was obtained as a dark yellow oil that solidified over time (0.856 g, 88%).

^{1}H NMR (500 MHz, d^6-DMSO, 25 ºC): δ 12.62 (s, 1H, NN*H*), 9.29 (t, J = 5.7 Hz, 1H, N*H*CH_2), 8.36 (dd, $^{3,4}J$ = 8.3, 0.7 Hz, 1H, H-5), 8.12 (dd, $^{3,4}J$ = 8.4, 0.7 Hz, 1H, H-6), 8.07 (dd, $^{3,4}J$ = 7.1, 0.7 Hz, 1H, H-3), 7.95 (dd, $^{3,4}J$ = 7.0, 0.7 Hz, 1H, H-8), 7.86 (dd, $^{3,3}J$ = 8.2, 7.0 Hz, 1H, H-4), 7.82 (dd, $^{3,3}J$ = 8.3, 7.0 Hz, 1H, H-7), 6.74 (t, ^3J = 5.7 Hz, 1H, N*H*CO), 3.82 (q, ^3J = 5.9 Hz, 2H, H-9), 3.69 (t, ^3J = 5.9 Hz, 2H, H-10), 3.63 – 3.52 (m, 4H, H-11, H-12), 3.40 (t, ^3J = 6.1 Hz, 2H, H-13), 3.07 (q, ^3J = 6.0 Hz, 2H, H-14), 1.34 (s, 9H, (CH_3)$_3$).

^{13}C NMR (125 MHz, d^6-DMSO, 25 ºC): δ 188.8 (*C*O), 178.6 (*C*S), 155.4, 140.2 (C-5b), 137.5 (*C*N), 132.7 (C-5), 130.8, 130.5, 130.2 (C-1a, C-2a, C-5a) 128.9 (C-7), 128.5 (C-4), 127.4 (C-6), 122.8 (C-3), 118.2 (C-8), 70.5, 70.5, 70.4 (C-11, C-12, C13), 69.4 (C-10), 44.6 (C-9), 40.5 (C-14), 28.6 ((CH_3)$_3$).

Mass spectrum: ESI-MS calc. for $C_{24}H_{31}N_4O_5S$ $[M+H]^+$: 487.2015; found: 487.2041.

Elem. Anal. (%). Found (calc.) for $C_{24}H_{30}N_4O_5S$: C, 59.24 (57.94); H, 5.75 (6.21); N, 11.14 (11.51).

IR (solid): ν (cm^{-1}) 3358, 3270, 2974, 2868, 1687, 1524, 1476, 1171.

HPLC (Method A): Rt (min) 9.99.

14. Mono(4-methyl-3-thiosemicarbazone) acenaphthenequinone

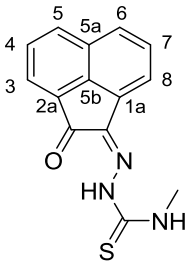

Acenaphthenequinone (0.200 g, 1.10 mmol), 4-methyl-3-thiosemicarbazide (0.108 g, 1.00 mmol) and ethanol (10 mL) were added to a 20 mL microwave vial. The mixture was sonicated for 3 min to generate a homogeneous dispersion and then 3 drops of concentrated hydrochloric acid were added. A colour change to a brighter yellow colour was observed upon addition of the acid. The vial was capped and heated under microwave irradiation at 90 ºC for 10 min. The reaction mixture was filtered whilst hot, re-suspended in hot methanol (ca. 15 mL) and stirred for 15 min before filtering again, washing with methanol and diethyl ether and drying under vacuum. The product was obtained as a yellow solid (0.215 g, 70%).

^{1}H NMR (500 MHz, d^{6}-DMSO, 25 ºC): δ 12.64 (s, 1H, NN*H*), 9.38 (q, ^{3}J = 4.5 Hz, 1H, N*H*CH$_3$), 8.37 (d, ^{3}J = 8.1 Hz, 1H, H-5), 8.13 (d, ^{3}J = 8.3 Hz, 1H, H-6), 8.09 (d, ^{3}J = 7.0 Hz, 1H, H-3), 7.97 (d, ^{3}J = 7.0 Hz, 1H, H-8), 7.88 (dd, $^{3,3}J$ = 8.1, 7.0 Hz, 1H, H-4), 7.84 (dd, $^{3,3}J$ = 8.3, 7.0 Hz, 1H, H-7), 3.11 (d, ^{3}J = 4.5 Hz, 3H, C*H$_3$*).

^{13}C NMR (125 MHz, d^{6}-DMSO, 25 ºC): δ 188.5 (*C*O), 177.9 (*C*S), 139.0 (C-5b), 137.1 (*C*N), 132.8 (C-5), 130.4, 130.1, 129.9 (C-1a C-2a C-5a), 128.9 (C-7), 128.6 (C-4), 127.0 (C-6), 122.4 (C-3), 118.1 (C-8), 31.4 (*C*H$_3$).

Mass spectrum: ESI-MS calc. for $C_{14}H_{11}N_3OS$ $[M+H]^+$: 270.0701; found 270.0700.

IR (solid): ν (cm^{-1}) 3219, 1689, 1540, 1475, 1055, 1027.

HPLC (Method A): Rt (min) 9.53.

15. Mono(4-ethyl-3-thiosemicarbazone) acenaphthenequinone

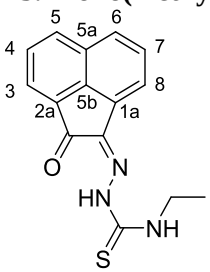

Compound **15** was prepared following the experimental procedure for **14**. Acenaphthenequinone (0.200 g, 1.10 mmol), 4-ethyl-3-thiosemicarbazide (0.124 g, 1.00 mmol) and 3 drops of concentrated

hydrochloric acid were heated in ethanol at 90 ºC 10 min by microwave irradiation. The product was obtained as a yellow solid (0.215 g, 70%).

^{1}H NMR (500 MHz, d^{6}-DMSO, 25 ºC): δ 12.60 (s, 1H, NN*H*), 9.42 (t, ^{3}J = 5.7 Hz, 1H, N*H*CH$_2$), 8.38 (d, ^{3}J = 8.2 Hz, 1H, H-5), 8.14 (d, ^{3}J = 8.3 Hz, 1H, H-6), 8.10 (d, ^{3}J = 7.0 Hz, 1H, H-3), 8.01 (d, ^{3}J = 7.0 Hz, 1H, H-8), 7.89 (dd, $^{3,3}J$ = 8.2, 7.0 Hz, 1H, H-4), 7.84 (dd, $^{3,3}J$ = 8.3, 7.0 Hz, 1H, H-7), 3.75 – 3.63 (m, 2H, C*H*$_2$), 1.23 (t, ^{3}J = 7.2 Hz, 3H, C*H*$_3$).
^{13}C NMR (125 MHz, d^{6}-DMSO, 25 ºC): δ 188.5 (*C*O), 176.9 (*C*S), 139.1 (C-5b), 137.1 (*C*N), 132.8 (C-5), 130.4, 130.1, 129.9 (C-1a, C-2a, C-5a), 128.9 (C-7), 128.6 (C-4), 127.0 (C-6), 122.4 (C-3), 118.2 (C-8), 39.5 (*C*H$_2$), 14.0 (*C*H$_3$).
Mass spectrum: ESI-MS calc. for $C_{15}H_{14}N_3OS$ $[M+H]^+$: 284.0857; found 284.0860.
IR (solid): ν (cm^{-1}) 3302, 3280, 2977, 1685, 1538, 1475, 1056, 1027.
HPLC (Method A): Rt (min) 9.90.

16. Mono(4-allyl-3-thiosemicarbazone) acenaphthenequinone

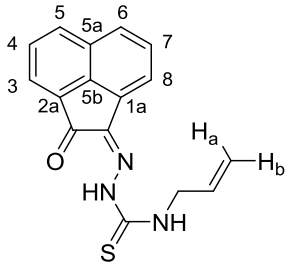

Compound **16** was prepared following the experimental procedure for **14**. Acenaphthenequinone (0.200 g, 1.10 mmol), 4-allyl-3-thiosemicarbazide (0.137 g, 1.00 mmol) and 3 drops of concentrated hydrochloric acid were heated in ethanol at 90 ºC 10 min by microwave irradiation. The product was obtained as a yellow solid (0.225 g, 76%).

^{1}H NMR (500 MHz, d^{6}-DMSO, 25 ºC): δ 12.65 (s, 1H, NN*H*), 9.57 (t, ^{3}J = 5.8 Hz, 1H, N*H*CH$_2$), 8.38 (d, ^{3}J = 8.1 Hz, 1H, H-5), 8.14 (d, ^{3}J = 8.2 Hz, 1H, H-6), 8.10 (d, ^{3}J = 6.9 Hz, 1H, H-3), 8.01 (d, ^{3}J = 6.8 Hz, 1H, H-8), 7.88 (dd, $^{3,3}J$ = 8.2, 7.1 Hz, 1H, H-4), 7.84 (dd, $^{3,3}J$ = 8.3, 7.0 Hz, 1H, H-7), 6.04 – 5.89 (m, 1H, C*H*), 5.24 (ddd, $^{3,2,4}J_{trans,\ gem}$ = 17.2, 3.1, 1.5 Hz, 1H, Ha), 5.17 (ddd, $^{3,2,4}J_{cis,gem}$ = 10.3, 3.1, 1.5 Hz, 1H, Hb), 4.35 – 4.26 (m, 2H, NHC*H*$_2$).
^{13}C NMR (125 MHz, d^{6}-DMSO, 25 ºC): δ 188.5 (*C*O), 177.6 (*C*S), 139.1 (C-5b), 137.3 (*C*N), 134.0 (*C*H), 132.8 (C-5), 130.4, 130.0, 129.9 (C-1a C-2a C-5a), 128.9 (C-7), 128.6 (C-4), 127.1 (C-6), 122.4 (C-3), 118.3 (C-8), 116.3 (*C*H$_2$), 46.4 (NH*C*H$_2$).
Mass spectrum: ESI-MS calc. for $C_{16}H_{13}N_3NaOS$ $[M+Na]^+$: 318.0677; found: 318.0666.
IR (solid): ν (cm^{-1}) 3318, 3049, 1688, 1523, 1478, 1178, 773.
HPLC (Method A): Rt (min) 11.38.

17. Mono(4-phenyl-3-thiosemicarbazone) acenaphthenequinone

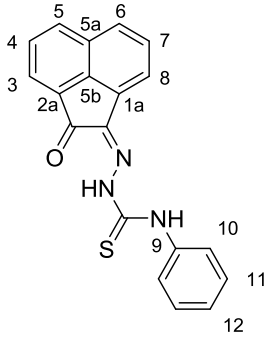

Compound **17** was prepared following the experimental procedure for **14**. Acenaphthenequinone (0.102 g, 0.53 mmol), 4-phenyl-3-thiosemicarbazide (0.089 g, 0.53 mmol) and 3 drops of concentrated hydrochloric acid were heated in ethanol at 90 ºC 10 min by microwave irradiation. The product was obtained as an orange solid (0.137 g, 78%).

^{1}H NMR (500 MHz, d^{6}-DMSO, 25 ºC): δ 12.83 (s, 1H, NN*H*), 10.95 (s, 1H, CSN*H*), 8.40 (dd, $^{3,4}J$ = 8.3, 0.7 Hz, 1H, H-5), 8.16 (dd, $^{3,4}J$ = 8.4, 0.7 Hz, 1H, H-6), 8.14 (d, ^{3}J = 6.8 Hz, 1H, H-3), 8.12 (d, ^{3}J = 7.0 Hz, 1H, H-8), 7.90 (dd, $^{3,3}J$ = 8.2, 7.0 Hz, 1H, H-4), 7.86 (dd, $^{3,3}J$ = 8.3, 7.0 Hz, 1H, H-7), 7.65 (dd, $^{3,4}J$ = 8.5, 1.2 Hz, 2H, H-10), 7.45 (dd, $^{3,3}J$ = 8.4, 7.4 Hz, 2H, H-11), 7.32 – 7.28 (m, 1H, H-12).
^{13}C NMR (125 MHz, d^{6}-DMSO, 25 ºC): δ 188.6 (*C*O), 176.6 (*C*S), 139.4 (C-5b), 138.5 (C-9), 137.7 (*C*N), 132.8 (C-5), 130.4, 129.9, 129.9 (C-1a, C-2a, C-5a), 128.9 (C-7), 128.6 (C-4), 128.4 (C-11), 127.2 (C-6), 126.1 (C-12), 125.7 (C-10), 122.5 (C-3), 118.8 (C-8).
Mass spectrum: ESI-MS calc. for $C_{19}H_{14}N_3OS$ $[M+H]^+$: 332.0856; found: 332.0841.
IR (solid): ν (cm^{-1}) 3336, 3269, 3059, 1688, 1671, 1596, 1523, 1475.
HPLC (Method A): Rt (min) 10.23.

18. Bis(4-methyl-3-thiosemicarbazone) acenaphthenequinone

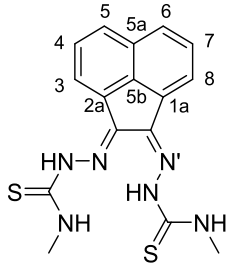

Compound **18** was prepared following the experimental procedure for **14**. Acenaphthenequinone (0.200 g, 1.00 mmol), 4-methyl-3-thiosemicarbazide (0.339 g, 3.10 mmol) and 3 drops of concentrated hydrochloric acid were heated in ethanol at 90 ºC 10 min by microwave irradiation. The product was obtained as a dark yellow solid (0.384 g, 95%).

^{1}H NMR (500 MHz, d^{6}-DMSO, 25 ºC): δ 12.60 (s, 1H, NN*H'*), 11.23 (s, 1H, NN*H*), 9.12 (q, ^{3}J = 4.5 Hz, 1H, N*H*CH$_3$'), 8.81 (q, ^{3}J = 4.6 Hz, 1H, N*H*CH$_3$), 8.20 (d, ^{3}J = 7.1 Hz, 1H, H-3), 8.12 (d, ^{3}J = 8.3 Hz, 1H, H-5), 8.06 (dd, $^{3,4}J$ = 7.1, 0.7 Hz, 1H, H-8), 8.02 (dd, $^{3,4}J$ = 8.3, 0.7 Hz, 1H, H-6), 7.80 (dd, ^{3}J = 8.3, 7.2 Hz, 1H, H-4), 7.77 (dd, ^{3}J = 8.3, 7.0 Hz, 1H, H-7), 3.13 (d, ^{3}J = 4.6 Hz, 3H, C*H*$_3$'), 3.11 (d, ^{3}J = 4.5 Hz, 3H, C*H*$_3$).

^{13}C NMR (125 MHz, d^{6}-DMSO, 25 ºC): δ 180.6 (*C*S), 178.1, (*C*S') 146.5 (*C*N), 137.6 (*C*N'), 136.0 (C-5b), 132.8 (C-5a), 129.9 (C-1a, C-2a), 128.8 (C-5), 128.5 (C-7), 128.2 (C-4), 127.8 (C-1a, C-2a), 126.6 (C-6), 124.6 (C-3), 118.3 (C-8), 31.4 (*C*H$_3$), 31.2 (*C*H$_3$').

Mass spectrum: ESI-MS calc. for $C_{16}H_{15}N_6S_2$ [M-H]$^-$: 355.0800; found: 355.0811.

IR (solid): ν (cm^{-1}) 3368, 3225, 1641, 1523, 1474.

HPLC (Method A): Rt (min) 9.69.

19. Bis(4-ethyl-3-thiosemicarbazone) acenaphthenequinone

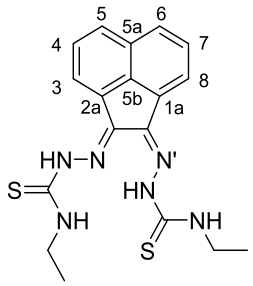

Compound **19** was prepared following the experimental procedure for **14**. Acenaphthenequinone (0.200 g, 1.00 mmol), 4-ethyl-3-thiosemicarbazide (0.384 g, 3.10 mmol) and 3 drops of concentrated hydrochloric acid were heated in ethanol at 90 ºC 10 min by microwave irradiation. The product was obtained as a yellow solid (0.359 g, 90%).

^{1}H NMR (500 MHz, d^{6}-DMSO, 25 ºC): δ 12.56 (s, 1H, NN*H*'), 11.18 (s, 1H, NN*H*), 9.17 (t, ^{3}J = 5.9 Hz, 1H, N*H*CH$_2$'), 8.78 (t, ^{3}J = 5.5 Hz, 1H, N*H*CH$_2$), 8.20 (d, ^{3}J = 7.2 Hz, 1H, H-3), 8.13 (d, ^{3}J = 8.3 Hz, 1H, H-5), 8.09 (dd, $^{3,4}J$ = 7.1, 0.7 Hz, 1H, H-8), 8.03 (dd, $^{3,4}J$ = 8.2, 0.8 Hz, 1H, H-6), 7.80 (dd, $^{3,3}J$ = 8.3, 7.2 Hz, 1H, H-4), 7.78 (dd, $^{3,3}J$ = 8.3, 7.0 Hz, 1H, H-7), 3.72 – 3.67 (m, 2H, C*H*$_2$), 3.67 – 3.61 (m, 2H, C*H*$_2$'), 1.26 (t, ^{3}J = 7.2 Hz, 3H, C*H*$_3$'), 1.22 (t, ^{3}J = 7.1 Hz, 3H, C*H*$_3$).

^{13}C NMR (125 MHz, d^{6}-DMSO, 25 ºC): δ 179.9 (CS), 177.5 (CS'), 146.9 (*C*N), 138.1 (*C*N'), 136.5 (C-5b), 133.3 (C-5a), 130.4 (C-1a, C-2a), 128.9 (C-5), 128.6 (C-7), 128.3 (C-4), 127.5 (C-1a, C-2a), 127.1 (C-6), 125.1 (C-3), 118.9 (C-8), 39.5 (*C*H$_2$), 39.2 (*C*H$_2$'), 14.8 (*C*H$_3$), 14.6 (*C*H$_3$').

Mass spectrum: ESI-MS calc. for $C_{18}H_{20}N_6NaS_2$ [M+Na]$^+$: 407.1089; found: 407.1127.

IR (solid): ν (cm^{-1}) 3366, 3303, 2971, 1685, 1533, 1473.

HPLC (Method A): Rt (min) 10.51.

20. Bis(4-allyl-3-thiosemicarbazone) acenaphthenequinone

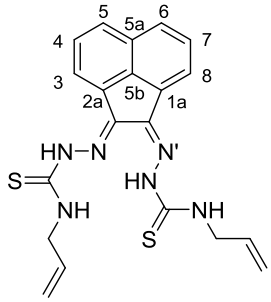

Compound **20** was prepared following the experimental procedure for **14**. Acenaphthenequinone (0.200 g, 1.00 mmol), 4-allyl-3-thiosemicarbazide (0.410 g, 3.10 mmol) and 3 drops of concentrated hydrochloric acid were heated in ethanol at 90 ºC 10 min by microwave irradiation. The product was obtained as a yellow solid (0.402 g, 94%).

^{1}H NMR (500 MHz, d^{6}-DMSO, 25 ºC): δ 12.61 (s, 1H, NN*H*'), 11.24 (s, 1H, NN*H*), 9.29 (t, ^{3}J = 5.8 Hz, 1H, N*H*CH$_2$'), 9.00 (t, ^{3}J = 5.3 Hz, 1H, N*H*CH$_2$), 8.21 (d, ^{3}J = 7.2 Hz, 1H, H-3), 8.14 (d, ^{3}J = 8.6 Hz, 1H, H-5), 8.12 (d, ^{3}J = 7.4 Hz, 1H, H-8). 8.01 (d, ^{3}J = 8.2 Hz, 1H, H-6), 7.81 – 7.73 (m, 2H, H-7, H-4), 6.05 – 5.91 (m, 1H, C*H*, C*H'*), 5.32 (dd, $^{3,4}J_{trans}$ = 17.2, 1.7 Hz, 1H, Ha, Ha'), 5.23 (dd, $^{3,4}J_{trans}$ = 17.2, 1.8 Hz, 1H, Ha, Ha'), 5.20 – 5.12 (m, 2H, Hb, Hb'), 4.35 – 4.21 (m, 4H, CH_2, CH_2').

^{13}C NMR (125 MHz, d^{6}-DMSO, 25 ºC): δ 180.1 (*C*S), 177.8 (*C*S'), 137.8 (*C*N), 136.1 (*C*N'), 134.5 (C-5b), 134.0 (*C*H, *C*H'), 132.8 (C-5a), 129.9 (C-5a), 128.9 (C-1a, C-2a), 128.5 (C-5), 128.2 (C-1a, C-2a), 127.8 (C-4, C-7), 126.7 (C-6), 124.5 (C-3), 118.5 (C-8), 116.4, 115.9 (*C*HaHb, *C*HaHb'), 46.7, 46.1 (CH_2, CH_2').

Mass spectrum: ESI-MS calc. for $C_{20}H_{20}N_6NaS_2$ [M+Na]$^{+}$: 431.1089; found: 431.1067.

IR (solid): ν (cm^{-1}) 3365, 3220, 1641, 1521, 1473.

HPLC (Method A): Rt (min) 10.75.

21. Bis(4-phenyl-3-thiosemicarbazone) acenaphthenequinone

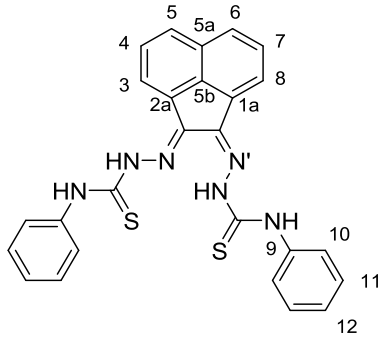

Compound **21** was prepared following the experimental procedure for **14**. Acenaphthenequinone (0.103 g, 0.53 mmol), 4-phenyl-3-thiosemicarbazide (0.269 g, 1.61 mmol) and 3 drops of concentrated

hydrochloric acid were heated in ethanol at 90 ºC 10 min by microwave irradiation. The product was obtained as an orange solid (0.216 g, 85%).

^{1}H NMR (500 MHz, d^{6}-DMSO, 25 ºC): δ 12.95 (s, 1H, NN*H'*), 11.55 (s, 1H, NN*H*), 10.74 (s, 1H, N*H*Ph'), 10.68 (s, 1H, N*H*Ph), 8.32 (d, ^{3}J = 7.2 Hz, 1H, H-3), 8.29 (dd, $^{3,4}J$ = 7.1, 0.7 Hz, 1H, H-8), 8.18 (d, ^{3}J = 8.3 Hz, 1H, H-5), 8.08 (dd, $^{3,4}J$ = 8.3, 0.7 Hz, 1H, H-6), 7.89 – 7.84 (m, 1H, H-4), 7.84 (d, ^{3}J = 7.5 Hz, 2H, H-10), 7.83 – 7.78 (m, 1H, H-7), 7.67 (dd, $^{3,4}J$ = 8.6, 1.2 Hz, 2H, H-10'), 7.46 – 7.39 (m, 4H, H-11. H-11'), 7.30 – 7.25 (m, 2H, H-12, H-12').

^{13}C NMR (125 MHz, d^{6}-DMSO, 25 ºC): δ 178.4 (*C*S), 176.5 (*C*S'), 138.9 (*C*N), 138.4 (*C*N'), 136.3 (C-5b), 132.7 (C-5a), 130.0 (C-1a, C-2a), 129.1 (C-5), 128.6 (C-9, C-9'), 128.3 (C-1a, C-2a), 128.3 (C-11, C-11'), 128.2 (C-7), 127.7 (C-4), 126.9 (C-6), 125.8 (C-12'), 125.6 (C-10), 125.4 (C-12), 124.7 (C-3), 124.2 (C-10), 119.2 (C-8).

Mass spectrum: ESI-MS calc. for $C_{26}H_{20}N_6NaS_2$ $[M+Na]^+$: 503.1089; found: 503.1105.

IR (solid): ν (cm^{-1}) 3377, 3346, 3280, 3049, 1596, 1530, 1474.

HPLC (Method A): Rt (min) 11.38.

22. Zinc(II) 4-allyl-4'-hydrazino-3,3'-bis(thiosemicarbazonato) acenaphthenequinone

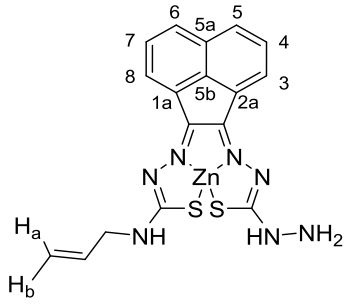

Mono(4-allyl-3-thiosemicarbazone) acenaphthenequinone (0.400 g, 1.40 mmol) and zinc acetate (0.990 g, 5.40 mmol) were suspended in acetic acid (30 mL) and homogenised by sonication for 3 min. The mixture was heated to 60 ºC and thiocarbohydrazide (0.575 g, 5.40 mmol) added. The suspension was heated to 120 ºC for 24 h. The reaction mixture was filtered whilst hot, washed with THF (20 mL) and diethyl ether (100 mL) and dried under vacuum. The product was obtained as a brown solid (0.528 g, 87%).

^{1}H NMR (500 MHz, d^{6}-DMSO, 25 ºC): δ 9.59 (brs, 1H, *NH*NH_2), 8.58 (brs, 1H, H-3), 8.20 (s, 1H, *NH*CH_2), 8.09 (brs, 1H, H-3), 7.95 (d, ^{3}J = 8.2 Hz, 1H, H-5), 7.90 (d, ^{3}J = 7.2 Hz, 1H, H-6), 7.66 (t, ^{3}J = 7.3 Hz, 1H, H-4), 7.63 (t, ^{3}J = 7.1 Hz, 1H, H-7), 6.43 (brs, 2H, *NH_2*), 6.03 (s, 1H, *CH*), 5.29 (d, $^{3}J_{trans}$ = 17.9 Hz, 1H, Ha), 5.14 (d, $^{3}J_{cis}$ = 10.8 Hz, 1H, Hb), 4.18 (brs, 2H, C*H_2*).

^{13}C NMR (125 MHz, d^{6}-DMSO, 25 ºC): δ 134.7 (*C*H), 127.8 (C-4), 127.5 (C-7), 126.8 (C-5), 125.9 (C-6), 125.5 (C-3), 115.4 (*C*HaHb), 45.0 (*C*H_2).

Mass spectrum: ESI-MS calc. for $C_{17}H_{14}N_7S_2Zn$ $[M+H]^+$: 444.0044; found: 444.0102.

Elem. Anal. (%). Found (calc.) for $C_{17}H_{15}N_7S_2Zn{\cdot}CH_2Cl_2$: C, 41.09 (40.66); H, 3.45 (3.22); N, 17.40 (18.44).

IR (solid): ν (cm^{-1}) 3305, 3254, 3136, 2935, 1627, 1578, 1392, 1242, 1137.

HPLC (Method B): Rt (min): 8.74.

23. Gallium(III) 4-allyl-4'-hydrazino-3,3'-bis(thiosemicarbazonato) acenaphthenequinone

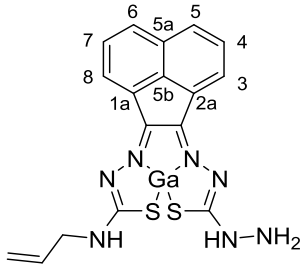

A suspension of zinc(II) 4-allyl-4'-hydrazino-3,3'-bis(thiosemicarbazonato) acenaphthenequinone (**22**) (0.250 g, 0.56 mmol) in dry methanol (30 mL) was added dropwise to gallium(III) chloride (1.480 g, 8.40 mmol) and the reaction mixture heated to 65 ºC for 6 h. The majority of the solvent was removed under vacuum and diethyl ether added dropwise to the residue until a precipitate appeared. The precipitate was filtered and the filtrate was concentrated under vacuum and the process repeated adding CH_2Cl_2. The product was obtained as a red-orange solid (0.239, 94%).

^{1}H NMR (500 MHz, d^6-DMSO, 25 ºC): δ 10.23 (s, 1H, *NH*NH_2), 8.75 (s, 1H, *NH*CH_2), 8.62 (d, ^3J = 7.1 Hz, 1H, H-5), 8.15 (d, ^3J = 8.3 Hz, 1H, H-3), 7.99 (d, ^3J = 8.2 Hz, 1H, H-8), 7.86 (d, ^3J = 6.9 Hz, 1H, H-6), 7.82 (t, ^3J = 7.8 Hz, 1H, H-4), 7.76 (t, ^3J = 7.6 Hz, 1H, H-7), 7.59 (s, 2H, *NH_2*), 6.09 – 5.93 (m, 1H, *CH*), 5.33 (d, $^3J_{trans}$ = 17.3 Hz, 1H, Ha), 5.19 (d, $^3J_{cis}$ = 10.4 Hz, 1H, Hb), 4.22 (s, 2H, C*H_2*).

^{13}C NMR (125 MHz, d^6-DMSO, 25 ºC): δ 185.2, 170.7, 147.0, 135.3 (CN, *C*N', *C*S, *C*S'), 134. 6 (*C*H), 134.2, 130.4 (C-5b, C-5a), 129.8 (C-5), 129.4, 129.0 (C-4, C-7), 129.0, 128.6 (C-2a, C-1a), 127.1 (C-3), 125.7 (C-8), 117.8 (C-6), 116.2 (*C*HaHb), 45.2 (*CH_2*).

Mass spectrum: nanoESI-MS calc. for $C_{17}H_{15}GaN_7NaS_2$ $[M+Na]^+$: 450.0086; found: 450.0074.

IR (solid): ν (cm^{-1}) 3202, 2997, 1607, 1508, 1412, 1140, 1107.

HPLC (Method B): Rt (min) 7.15.

24. 1,2-Dihydroacenaphthylene-1,2-diol (adapted from a literature procedure[8])

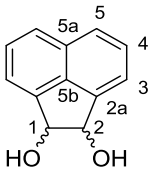

To a stirred suspension of acenaphthenequinone (3.000 g, 16.0 mmol) in methanol (50 mL) sodium borohydride (1.250 g, 33.0 mmol) was added portion wise over 15 min at 0 ºC. Once the addition

finished, the brown reaction mixture was stirred at room temperature for 1.5 h. The solvent was removed under vacuum, the solid washed with water and filtered. The product was obtained as a light brown solid (1.287 g, 42%).

^{1}H NMR (500 MHz, d^{6}-DMSO, 25 ºC): δ 7.76 (d, ^{3}J = 8.2 Hz, 2H, H-3), 7.57 (dd, $^{3,3}J$ = 8.2, 6.8 Hz, 2H, H-4), 7.44 (d, ^{3}J = 6.8 Hz, 2H, H-5), 5.81 (brs, 2H, O*H*), 5.19 (brs, 2H, H-2).

^{13}C NMR (125 MHz, d^{6}-DMSO, 25 ºC): δ 143.8 (C-5b), 135.4 (C-5a), 130.2 (C-2a), 128.2 (C-4), 123.8 (C-3), 119.9 (C-5), 82.5 (C-2).

Mass spectrum: ESI-MS calc. for $C_{12}H_{10}NaO_2$ $[M+Na]^+$: 209.0578; found: 209.0577.

IR (solid): ν (cm^{-1}) 3229, 3049, 1336, 803, 771.

HPLC (Method A): Rt (min) 7.17.

25. 1,10-phenanthroline-2,9-dicarbaldehyde (adapted from a literature procedure [9])

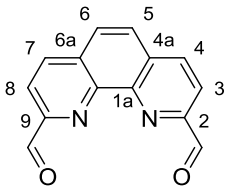

2,9-dimethyl-1,10-phenanthroline (3.530 g, 16.9 mmol) was dissolved in hot dioxane (100 mL), selenium dioxide (4.681 g, 42.4 mmol) added portion wise and the reaction mixture heated under reflux for 2 h. The heating was stopped and activated charcoal was added to the reaction mixture that was stirred for 5 – 10 min. The resulting suspension was filtered through celite and washed with hot dioxane. The solvent was removed under vacuum and the resulting pink solid dissolved in DMF, the solution was cooled to 0 ºC and filtered. Water was added dropwise to the filtrate yielding a white precipitate that was isolated by filtration. The product was obtained as an off-white solid (1.248 g, 31%).

^{1}H NMR (300 MHz, d^{6}-DMSO, 25 ºC): δ 10.34 (s, 2H, C*H*O), 8.78 (d, ^{3}J = 8.2 Hz, 2H, H-3), 8.30 (d, ^{3}J = 8.2 Hz, 2H, H-4), 8.27 (s, 2H, H-5).

^{13}C NMR (125 MHz, d^{6}-DMSO, 25 ºC): δ 193.7 (*C*O), 152.2 (C-2), 145. 2 (C-1a), 138.4 (C-3), 131.4 (C-4a), 129.2 (C-5), 120.1 (C-4).

Mass spectrum: ESI-MS calc. for $C_{14}H_8N_2NaO_2$ $[M+Na]^+$: 259.0483; found: 259.0460.

IR (solid): ν (cm^{-1}) 3064, 2860, 1699, 1596, 1555, 1279, 1237.

HPLC (Method A): Rt (min) 6.60.

26. Bis(4-methyl-3-thiosemicarbazone) 1,10-phenanthroline-2,9-dicarbaldehyde

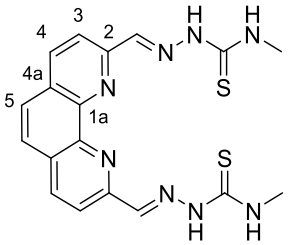

Compound **26** was prepared following the experimental procedure for **14**. 1,10-Phenanthroline-2,9-dicarbaldehyde (0.050 g, 0.21 mmol), 4-methyl-3-thiosemicarbazide (0.056 g, 0.53 mmol) and 3 drops of concentrated hydrochloric acid were heated in ethanol at 90 ºC 10 min by microwave irradiation. The product was obtained as a bright yellow solid (0.087 g, 99%).

^{1}H NMR (500 MHz, d^{6}-DMSO, 25 ºC): δ 12.15 (s, 2H, NN*H*), 8.95 (q, ^{3}J = 4.4 Hz, 2H, N*H*CH$_3$), 8.79 (d, ^{3}J = 8.6 Hz, 2H, H-3), 8.65 (d, ^{3}J = 8.6 Hz, 2H, H-4), 8.50 (s, 2H, H-5), 8.09 (s, 2H, C*H*N), 3.08 (d, ^{3}J = 4.5 Hz, 6H, C*H*$_3$).

^{13}C NMR (125 MHz, d^{6}-DMSO, 25 ºC): δ 178.0 (*C*S), 153.4 (C-2), 141.0 (*C*HN), 138.8 (C-4), 128.8 (C-1a), 127.0 (C-4a), 120.1 (C-3), 31.0 (*C*H$_3$).

Mass spectrum: ESI-MS calc. for $C_{20}H_{22}N_8NaS_2$ [M+Na]$^{+}$: 461.1307; found: 461.1290.

IR (solid): ν (cm^{-1}) 3355, 2934, 1744, 1544, 1511, 1494, 1214.

HPLC (Method A): Rt (min) 7.68.

27 Bis(4-ethyl-3-thiosemicarbazone) 1,10-phenanthroline-2,9-dicarbaldehyde

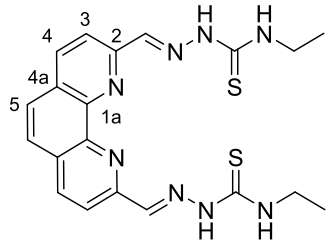

Compound **27** was prepared following the experimental procedure for **14**. 1,10-Phenanthroline-2,9-dicarbaldehyde (0.200 g, 0.85 mmol), 4-ethyl-3-thiosemicarbazide (0.260 g, 2.12 mmol) and 3 drops of concentrated hydrochloric acid were heated in ethanol at 90 ºC 10 min by microwave irradiation. The product was obtained as a bright yellow solid (0.322, 88%).

^{1}H NMR (300 MHz, d^{6}-DMSO, 25 ºC): δ 12.08 (s, 2H, NN*H*), 9.00 (t, ^{3}J = 5.9 Hz, 2H, N*H*CH$_2$), 8.79 (d, ^{3}J = 8.5 Hz, 2H, H-3), 8.64 (d, ^{3}J = 8.5 Hz, 2H, H-4), 8.49 (s, 2H, H-5), 8.09 (s, 2H, C*H*N), 3.78 – 3.55 (m, 4H, C*H*$_2$), 1.20 (t, ^{3}J = 7.1 Hz, 6H, C*H*$_3$).

^{13}C NMR (125 MHz, d^{6}-DMSO, 25 ºC): δ 177.0 (*C*S), 153.3 (C-2), 142.9 (C-1a), 140.7 (C-5), 137.6 (C-4), 128.9 (C-4a), 127.0 (*C*HN), 120.4 (C-3), 38.5 (*C*H$_2$), 14.5 (*C*H$_3$).

Mass spectrum: ESI-MS calc. for $C_{20}H_{22}N_8NaS_2$ $[M+Na]^+$: 461.1307; found: 461.1290.

IR (solid): ν (cm^{-1}) 3354, 2972, 1623, 1537, 1488, 1132.

HPLC (Method A): Rt (min) 8.18.

28. Bis(4-allyl-3-thiosemicarbazone) 1,10-phenanthroline-2,9-dicarbaldehyde

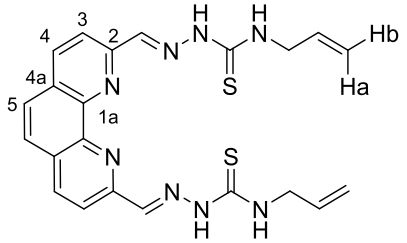

Compound **28** was prepared following the experimental procedure for **14**. 1,10-Phenanthroline-2,9-dicarbaldehyde (0.200 g, 0.84 mmol), 4-allyl-3-thiosemicarbazide (0.280 g, 2.13 mmol) and 3 drops of concentrated hydrochloric acid were heated in ethanol at 90 ºC 10 min by microwave irradiation. The product was obtained as a bright yellow solid (0.290 g, 75%).

^{1}H NMR (500 MHz, d^6-DMSO, 25 ºC): δ 12.15 (s, 2H, NN*H*), 9.14 (t, ^3J = 5.9 Hz, 2H, N*H*CH_2), 8.81 (d, ^3J = 8.5 Hz, 1H, H-3), 8.63 (d, ^3J = 8.5 Hz, 1H, H-4), 8.52 (s, 1H, H-5), 8.09 (s, 1H, C*H*N), 6.02 – 5.90 (m, 1H, C*H*), 5.21 (dq, $^{3,4}J_{trans}$ = 17.2, 1.6 Hz, 1H, Ha), 5.14 (dq, $^{3,4}J_{cis}$ = 10.2, 1.4 Hz, 1H, Hb), 4.32 – 4.26 (m, 2H, NHCH_2).

^{13}C NMR (125 MHz, d^6-DMSO, 25 ºC): δ 177.5 (*C*S), 153.5 (C-2), 142.2 (C-5), 141.7 (C-1a), 137.0 (C-4), 134.8 (*C*H), 128.8 (C-4a), 127.0 (*C*HN), 120.1 (C-3), 115.7 (*C*HaHb), 45.9 (NH*C*H_2).

Mass spectrum: ESI-MS calc. for $C_{22}H_{21}N_8S_2$ $[M-H]^-$: 461.1331; found: 461.1393.

IR (solid): ν (cm^{-1}) 3357, 3315, 3191, 1489, 1272, 1185.

HPLC (Method A): Rt (min) 8.37.

29 Bis(4-phenyl-3-thiosemicarbazone) 1,10-phenanthroline-2,9-dicarbaldehyde

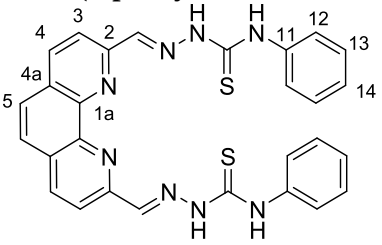

Compound **29** was prepared following the experimental procedure of **14**. 1,10-Phenanthroline-2,9-dicarbaldehyde (0.114 g, 0.48 mmol), 4-phenyl-3-thiosemicarbazide (0.201 g, 1.20 mmol) and 3 drops of conc. HCl were heated in ethanol at 90 ºC 10 min by microwave irradiation. The product was obtained as a yellow solid (0.238 g, 92%).

^{1}H NMR (500 MHz, d^{6}-DMSO, 25 ºC): δ 12.41 (s, 2H, NN*H*), 10.47 (s, 2H, CSN*H*), 8.93 (d, ^{3}J = 8.6 Hz, 2H, H-3), 8.61 (d, ^{3}J = 8.6 Hz, 2H, H-4), 8.59 (s, 2H, H-5), 8.08 (s, 2H, C*H*N), 7.57 (d, ^{3}J = 7.2Hz, 2H, H-12), 7.45 – 7.38 (m, 2H, H-13), 7.27 – 7.23 (m, 2H, H-14).

^{13}C NMR (125 MHz, d^{6}-DMSO, 25 ºC): δ 176.6 (*C*S), 149.0 (C-2), 146.5 (C-1a), 142.2 (*C*HN), 137.1 (C-4), 128.8 (C-4a), 128.1 (C-13), 127.2 (C-2), 126.4 (C-12), 125.9 (C-14), 120.2 (C-3).

Mass spectrum: ESI-MS calc. for $C_{28}H_{22}N_8NaS_2$ $[M+Na]^+$: 557.1307; found: 557.1427.

IR (solid): ν (cm^{-1}) 3657, 3344, 3256, 2968, 1633,97, 1542, 1509, 1187, 1176.

HPLC (Method A): Rt (min) 8.95.

30. 4,5-Pyrenedione (adapted from a literature procedure[10])

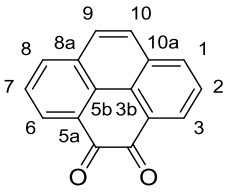

Sodium metaperiodate (22.050 g, 0.10 mol) and $RuCl_3 \cdot xH_2O$ (0.480 g, 2.32 mmol) were added to pyrene (4.780 g, 23.2 mmol) in CH_2Cl_2 (150 mL), THF (150 mL) and H_2O (200 mL). The reaction mixture was stirred at room temperature for 3 h. The reaction mixture was poured in 1 L of water and the phases separated. The aqueous phase was extracted with CH_2Cl_2 (3x 150 mL). The collected organic phases were washed with water (3x 150 mL), dried over $MgSO_4$ and the solvent removed under vacuum. The product was purified by flash column chromatography using CH_2Cl_2 as eluent. The product was obtained as an orange solid after re-crystallisation from CH_2Cl_2 / hexane (1.538 g, 29%).

^{1}H NMR (300 MHz, $CDCl_3$, 25 ºC): δ 8.45 (dd, $^{3,4}J$ = 7.4, 1.1 Hz, 2H, H-3), 8.15 (dd, $^{3,4}J$ = 8.0, 1.1 Hz, 2H, H-1), 7.82 (s, 2H, H-9), 7.73 (appt, ^{3}J = 7.5 Hz, 2H, H-2).

^{13}C NMR (75 MHz, $CDCl_3$, 25 ºC): δ 180.6 (*C*O), 135.9 (C-1), 132.1 (C-8a), 130.3 (C-3), 130.2 (C-3b), 128.5 (C-2), 128.1 (C-3a)), 127.4 (C-9).

Mass spectrum: ESI-MS calc. for $C_{16}H_9O_2$ $[M+H]^+$: 233.0602; found: 233.0601.

IR (solid): ν (cm^{-1}) 3048, 2892, 1667, 1614, 1336, 1089.

HPLC (Method A): Rt (min) 9.18.

31. Mono(4-(N-(2-(2-(2-aminoethoxy)ethoxy)ethyl))-3-thiosemicarbazone) acenaphthenequinone

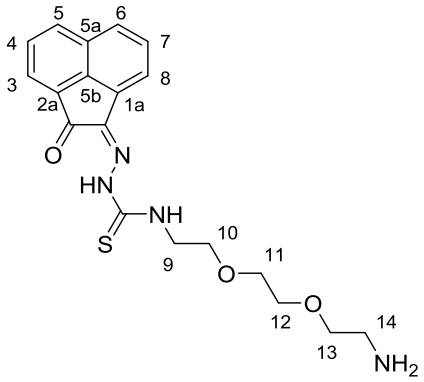

Acenaphthenequinone (14 mg, 71 µmol) and 4-(N-(2-(2-(2-aminoethoxy)ethoxy)ethyl))-3-thiosemicarbazide (**9**) (23 mg, 71 µmol) were suspended in ethanol and homogenised by sonication for 3 min. Concentrated HCl (3 drops) was added and the reaction mixture heated to 90 ºC for 10 min. The solvent was removed under vacuum, the residue re-suspended in CH_2Cl_2 and passed through a silica plug. The product was eluted with CH_2Cl_2 / MeOH (9:1). The solvent was removed under vacuum and the product obtained as a yellow solid (10 mg, 37%).

^{1}H NMR (500 MHz, d^6-DMSO, 25 ºC): δ 12.66 (s, 1H, NN*H*), 9.42 (t, ^3J = 5.8 Hz, 1H, N*H*CH_2), 8.39 (d, ^3J = 8.1 Hz, 1H, H-5), 8.15 (d, ^3J = 8.3 Hz, 1H, H-6), 8.10 (d, ^3J = 7.0 Hz, 1H, H-3), 8.05 (s, 2H, NH_2), 8.04 (d, ^3J = 6.9 Hz, 2H, H-8), 7.93 – 7.86 (m, 1H, H-4), 7.85 (dd, $^{3,3}J$ = 8.3, 7.0 Hz, 1H, H-7), 3.83 (q, ^3J = 6.0 Hz, 2H, H-9), 3.70 (t, ^3J = 6.1 Hz, 2H, H-10), 3.66 – 3.58 (m, 6H, H-11, H-12, H-13), 2.94 (q, ^3J = 5.5 Hz, 2H, H-14).

^{13}C NMR (125 MHz, d^6-DMSO, 25 ºC): δ 188.5 (*C*O), 177.5 (*C*S), 139.2 (C-5b), 137.5 (*C*N), 132.8 (C-5), 130.4, 130.0, 129.9 (C-1a, C-2a, C-5a), 128.9 (C-7), 128.6 (C-4), 127.1 (C-6), 122.5 (C-3), 118.4 (C-8), 69.7, 69.5 (C-11, C-12), 68.0 (C-10), 66.6 (C-13), 43.8 (C-9), 38.5 (C-14).

Mass spectrum: ESI-MS calc. for $C_{19}H_{23}N_4O_3S$ $[M+H]^+$: 387.1491; found: 387.1561.

IR (solid): ν (cm^{-1}) 3300, 1659, 1496, 1388, 1097, 1066.

HPLC (Method A): Rt (min) 11.84.

32. Mono(4-methyl-3-thiosemicarbazone) aceanthrenequinone

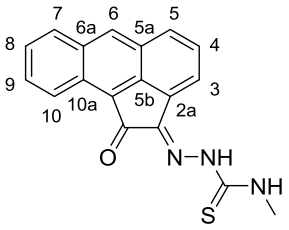

Compound **32** was prepared following the experimental procedure for **14**. Aceanthrenequinone (0.208 g, 0.86 mmol), 4-methyl-3-thiosemicarbazide (0.086 g, 0.82 mmol) and 3 drops of concentrated

hydrochloric acid were heated in ethanol at 90 ºC 10 min by microwave irradiation. The product was obtained as a red-brown solid (0.207 g, 79%).

^{1}H NMR (500 MHz, d^{6}-DMSO, 25 ºC): δ 12.89 (s, 1H, NN*H*), 9.41 (q, ^{3}J = 4.0 Hz, 1H, N*H*CH$_3$), 9.11 (s, 1H, H-6), 8.95 (d, ^{3}J = 8.5 Hz, 1H, H-10), 8.38 (d, ^{3}J = 8.4 Hz, 1H, H-7), 8.23 (d, ^{3}J = 8.6 Hz, 1H, H 5), 7.97 (d, ^{3}J = 6.6 Hz, 1H, H-3), 7.95 – 7.89 (m, 1H, H-9), 7.81 (dd, $^{3,3}J$ = 8.6, 6.6 Hz, 1H, H-4), 7.78 – 7.72 (m, 1H, H-8), 3.15 (d, ^{3}J = 4.6 Hz, 3H, C*H*$_3$).

^{13}C NMR (125 MHz, d^{6}-DMSO, 25 ºC): δ 188.5 (*C*O), 178.0 (*C*S), 140.9 (C-5b), 137.1 (*C*N), 134.7 (C-6), 132.8 (C-6a), 130.5 (C-9), 130.2 (C-7), 129.5 (C-2a), 128.0 (C-4), 127.5 (C-10a), 127.4 (C-5a), 127.2 (C-5), 126.9 (C-8), 123.6 (C-10b),123.3 (C-10), 118.1 (C-3), 31.4 (*C*H$_3$).

Mass spectrum: ESI-MS calc. for $C_{18}H_{13}N_3NaOS$ [M+Na]$^+$: 342.0677, found: 342.0658.

Elem. Anal. (%). Found (calc.) for $C_{18}H_{13}N_3OS$: C, 66.81 (67.69); H, 4.25 (4.10); N, 12.96 (13.16).

IR (solid): ν (cm^{-1}) 3373, 3250, 1661, 1542, 1479, 1048.

HPLC (Method A): Rt (min) 11.08.

33. Mono(4-ethyl-3-thiosemicarbazone) aceanthrenequinone

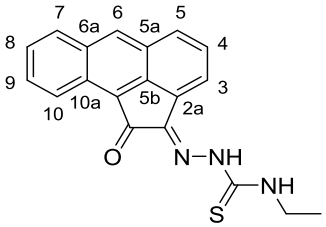

Compound **33** was prepared following the experimental procedure for **14**. Aceanthrenequinone (0.208 g, 0.86 mmol), 4-ethyl-3-thiosemicarbazide (0.098 g, 0.82 mmol) and 3 drops of concentrated hydrochloric acid were heated in ethanol at 90 ºC 10 min by microwave irradiation. The product was obtained as an orange solid (0.243 g, 89%).

^{1}H NMR (500 MHz, d^{6}-DMSO, 25 ºC): δ 12.81 (s, 1H, NN*H*), 9.41 (t, ^{3}J = 5.6 Hz, 1HN*H*CH$_2$), 9.06 (s, 1H, H-6), 8.90 (d, ^{3}J = 8.6 Hz, 1H, H-10), 8.35 (d, ^{3}J = 8.5 Hz, 1H, H-7), 8.20 (d, ^{3}J = 8.6 Hz, 1H, H-5), 7.96 (d, ^{3}J = 6.7 Hz, 1H, H-3), 7.93 – 7.86 (m, 1H, H-9), 7.78 (dd, $^{3,3}J$ = 8.6, 6.7 Hz, 1H, H-4), 7.76 – 7.70 (m, 1H, H-8), 3.80 – 3.63 (m, 2H, C*H*$_2$), 1.25 (t, ^{3}J = 7.1 Hz, 3H, C*H*$_3$).

^{13}C NMR (125 MHz, d^{6}-DMSO, 25 ºC): δ 188.4 (*C*O), 177.0 (*C*S), 140.8 (C-5b), 137.0 (*C*N), 134.6 (C-6), 132.7 (C-6a), 130.5 (C-9), 130.1 (C-7), 129.4 (C-2a), 127.9 (C-4), 127.5 (C-10a), 127.3 (C-5a), 127.1 (C-5), 126.9 (C-8), 123.5 (C-10b), 123.3 (C-10), 118.2 (C-3), 39.0 (*C*H$_2$), 14.1 (*C*H$_3$).

Mass spectrum: ESI-MS calc. for $C_{19}H_{15}N_3NaOS$ [M+Na]$^+$: 356.0833; found: 356.0801.

Elem. Anal. (%). Found (calc.) for $C_{19}H_{15}N_3OS$: C, 68.51 (68.45); H, 4.47 (4.53); N, 12.48 (12.60).

IR (solid): ν (cm^{-1}) 3373, 3220, 2967, 1665, 1527, 1482, 1193, 1147, 1072.

HPLC (Method A): Rt (min) 11.57.

34. Mono(4-allyl-3-thiosemicarbazone) aceanthrenequinone

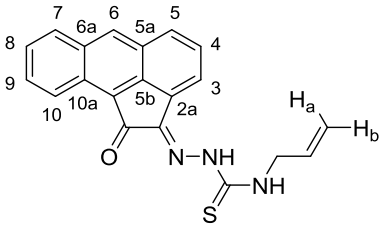

Compound **34** was prepared following the experimental procedure of **14**. Aceanthrenequinone (0.208 g, 0.86 mmol), 4-allyl-3-thiosemicarbazide (0.107 g, 0.82 mmol) and 3 drops of concentrated hydrochloric acid were heated in ethanol at 90 ºC 10 min by microwave irradiation. The product was obtained as an orange solid (0.229 g, 81%).

^{1}H NMR (500 MHz, d^{6}-DMSO, 25 ºC): δ 12.89 (s, 1H, NN*H*), 9.59 (t, ^{3}J = 5.9 Hz, 1H, N*H*CH$_2$), 9.09 (s, 1H, H-6), 8.93 (d, ^{3}J = 8.8 Hz, 1H, H-10), 8.37 (d, ^{3}J = 8.5 Hz, 1H, H-7), 8.22 (d, ^{3}J = 8.7 Hz, 1H, H-5), 8.00 (d, ^{3}J = 6.4 Hz, 1H, H-3), 7.91 (ddd, $^{3,3,4}J$ = 8.4, 6.7, 1.3 Hz, 1H, H-9), 7.79 (dd, $^{3,3}J$ = 8.1, 6.7 Hz, 1H, H-4), 7.75 (ddd, $^{3,3,4}J$ = 8.3, 6.7, 1.3 Hz, 1H, H-8), 6.07 – 5.84 (m, 1H, 1H, C*H*), 5.26 (d, $^{3}J_{trans}$ = 17.1 Hz, 1H, Ha), 5.19 (d, $^{3}J_{cis}$ = 10.2 Hz, 1H, Hb), 4.33 (brs, 2H, NHCH_2).

^{13}C NMR (125 MHz, d^{6}-DMSO, 25 ºC): δ 188.4 (*C*O), 177.6 (*C*S), 140.9 (C-5b), 137.3 (*C*N), 134.7 (C-6), 134.0 (*C*H), 132.8 (C-6a), 130.5 (C-9), 130.2 (C-7), 129.4 (C-2a), 127.9 (C-4), 127.5 (C-10a), 127.3 (C-5a), 127.2 (C-5), 126.9 (C-8), 123.6 (C-10b), 123.3 (C-10), 118.3 (C-3), 116.3 (*C*HaHb), 46.4 (NH*C*H$_2$).

Mass spectrum: ESI-MS calc. for $C_{20}H_{15}N_3NaOS$ [M+Na]$^{+}$: 368.0833; found: 368.0824.

Elem. Anal. (%). Found (calc.) for $C_{20}H_{15}N_3OS$: C, 69.64 (69.54); H, 4.21 (4.38); N, 12.09 (12.17).

IR (solid): ν (cm^{-1}) 3360, 3217, 3066, 1664, 1526, 1485, 1190, 1149, 1075.

HPLC (Method A): Rt (min) 11.59.

35. Mono(4-(N-(2-(2-(2-aminoethoxy)ethoxy)ethyl))-3-thiosemicarbazone) aceanthrenequinone

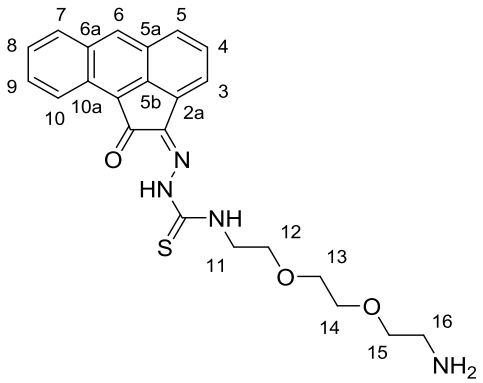

Aceanthrenequinone (0.104 g, 0.86 mmol) and thiosemicarbazide **9** (0.132 g, 0.41 mmol) were suspended in ethanol (5 mL) and homogenised by sonication for 3 min. Concentrated HCl (3 drops) was

added and the reaction mixture heated to 90 ºC for 10 min by microwave irradiation. The solvent was removed under vacuum and the product re-suspended in CH_2Cl_2 and passed through a silica plug. After washing with CH_2Cl_2, the product was eluted with CH_2Cl_2 / MeOH (9:1). The solvent was removed under vacuum and the product obtained as an orange solid (0.094 g, 53%).

^{1}H NMR (500 MHz, d^6-DMSO, 25 ºC): δ 12.86 (s, 1H, NN*H*), 9.40 (t, ^3J = 5.8 Hz, 1H, N*H*CH$_2$), 9.06 (s, 1H, H-6), 8.88 (dt, $^{3,4}J$ = 8.5, 1.0 Hz, 1H, H-10), 8.35 (dd, $^{3,4}J$ = 8.3, 1.0 Hz, 1H, H-7), 8.20 (d, ^3J = 8.6 Hz, 1H, H-5), 8.00 (brs, 2H, N*H*$_2$), 7.96 (dd, $^{3,4}J$ = 6.7, 0.7 Hz, 1H, H-3), 7.89 (ddd, $^{3,3,4}J$ = 8.4, 6.7, 1.2 Hz, 1H, H-9), 7.78 (dd, $^{3,3}J$ = 8.6, 6.7 Hz, 1H, H-4), 7.74 (ddd, $^{3,3,4}J$ = 8.1, 6.6, 1.2 Hz, 1H, H-8), 3.86 (q, ^3J = 6.0 Hz, 2H, H-11), 3.73 (t, ^3J = 6.0 Hz, 2H, H-12), 3.68 – 3.61 (m, 6H, H-13, H-14, H-15), 2.96 (q, ^3J = 5.4 Hz, 2H, H-16).

Mass spectrum: ESI-MS calc. for $C_{23}H_{23}N_4O_3S$ $[M+H]^+$: 435.1491; found: 435.1453.

Elem. Anal. (%). Found (calc.) for $C_{23}H_{24}N_4O_3S{\cdot}HCl{\cdot}C_3H_7NO$: C, 58.05 (57.19); H, 6.34 (5.91); N, 12.69 (12.82).

IR (solid): ν (cm^{-1}): 3367, 3324, 2870, 1630, 1598, 1538, 1485, 1446.

HPLC (Method A): Rt (min) 11.84.

36. Mono(4-methyl-3-thiosemicarbazone) phenanthrenequinone

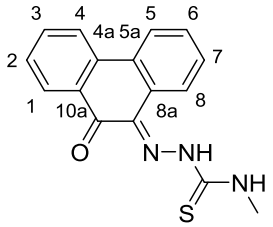

Compound **36** was prepared following the experimental procedure of **14**. Phenanthrenequinone (0.210 g, 0.96 mmol), 4-methyl-3-thiosemicarbazide (0.096 g, 0.91 mmol) and 3 drops of concentrated hydrochloric acid were heated in ethanol at 90 ºC 10 min by microwave irradiation. The product was obtained as a yellow solid (0.249 g, 92%).

^{1}H NMR (500 MHz, d^6-DMSO, 25 ºC): δ 14.59 (s, 1H, NN*H*) 9.56 (q, ^3J = 4.5 Hz, 1H, N*H*CH$_3$), 8.66 (dd, $^{3,4}J$ = 8.0, 1.3 Hz, 1H, H-8), 8.43 (d, ^3J = 8.0 Hz, 1H, H-4), 8.34 (dd, $^{3,4}J$ = 7.9, 0.5 Hz, 1H, H-5), 8.26 (dd, $^{3,4}J$ = 7.9, 1.4 Hz, 1H, H-1), 7.85 (ddd, $^{3,3,4}J$ = 8.0, 7.2, 1.4 Hz, 1H, H-3), 7.60 – 7.57 (m, 1H, H-2), 7.57 – 7.54 (m, 1H, H-6), 7.49 (ddd, $^{3,3,4}J$ = 8.0, 7.1, 1.2 Hz, 1H, H-7), 3.16 (d, ^3J = 4.5 Hz, 3H, C*H*$_3$).

^{13}C NMR (125 MHz, d^6-DMSO, 25 ºC): δ 181.2 (*C*O), 178.1 (*C*S), 136.0 (C-4a), 135.3 (C-3), 130.5 (C-2a), 129.8, 129.7 (*C*N, C-1a), 129.4 (C-6), 128.8 (C-5a), 128.8 (C-7), 128.4 (C-2), 128.2 (C-1), 125.0 (C-8), 123.8, 123.7 (C-4, C-5), 31.8 (*C*H$_3$).

Mass spectrum: ESI-MS calc. for $C_{16}H_{13}N_3NaOS$ $[M+Na]^+$: 318.0677; found: 318.0718.

Elem. Anal. (%). Found (calc.) for $C_{16}H_{13}N_3OS$: C, 65.17 (65.07); H, 4.28 (4.44); N, 14.13 (14.23).
IR (solid): ν (cm^{-1}) 3324, 2976, 1638, 1595, 1552, 1448, 1040.
HPLC (Method A): Rt (min) 8.83.

37. Mono(4-ethyl-3-thiosemicarbazone) phenanthrenequinone

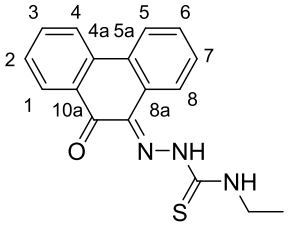

Compound **37** was prepared following the experimental procedure of **14**. Phenanthrenequinone (0.210 g, 0.96 mmol), 4-ethyl-3-thiosemicarbazide (0.109 g, 0.91 mmol) and 3 drops of concentrated hydrochloric acid were heated in ethanol at 90 ºC 10 min by microwave irradiation. The product was obtained as a red solid (0.214 g, 76%).

^{1}H NMR (500 MHz, d^6-DMSO, 25 ºC): δ 14.55 (s, 1H, NN*H*), 9.65 (t, ^3J = 5.8 Hz, 1H, N*H*CH_2), 8.66 (dd, $^{3,4}J$ = 8.0, 1.3 Hz, 1H, H-8), 8.44 (d, ^3J = 8.1 Hz, 1H, H-4), 8.35 (d, ^3J = 7.3 Hz, 1H, H-5), 8.27 (dd, $^{3,4}J$ = 7.9, 1.4 Hz, 1H, H-1), 7.86 (ddd, $^{3,3,4}J$ = 8.1, 7.3, 1.5 Hz, 1H, H-3), 7.61 – 7.58 (m, 1H, H-2), 7.58 – 7.55 (m, 1H, H-6), 7.51 (ddd, $^{3,3,4}J$ = 8.0, 7.1, 1.3 Hz, 1H, H-7), 3.77 – 3.67 (m, 2H, CH_2), 1.24 (t, ^3J = 7.1 Hz, 3H, CH_3).
^{13}C NMR (125 MHz, d^6-DMSO, 25 ºC): δ 181.2 (*C*O), 177.2 (*C*S), 136.0 (C-4a), 135.3 (C-3), 130.5 (C-2a), 129.8 (*C*N, C-1a), 129.4 (C-6), 128.9 (C-5a), 128.8 (C-7), 128.4 (C-2), 128.3 (C-1), 125.1 (C-8), 123.8, 123.7 (C-4, C-5), 39.0 (*C*H_2), 13.8 (*C*H_3).
Mass spectrum: ESI-MS calc. for $C_{17}H_{15}N_3NaOS$ $[M+Na]^+$: 332.0833; found: 332.0822.
Elem. Anal. (%). Found (calc.) for $C_{17}H_{15}N_3OS$: C, 65.94 (66.00); H, 4.78 (4.89); N, 13.44 (13.58).
IR (solid): ν (cm^{-1}) 3339, 2977, 1682, 1600, 1595, 1482.
HPLC (Method A): Rt (min) 8.46.

38. Mono(4-allyl-3-thiosemicarbazone) phenanthrenequinone

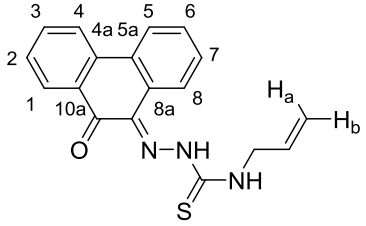

Compound **38** was prepared following the experimental procedure of **14**. Phenanthrenequinone (0.210 g, 0.96 mmol), 4-allyl-3-thiosemicarbazide (0.120 g, 0.91 mmol) and 3 drops of concentrated hydrochloric

acid were heated in ethanol at 90 ºC 10 min by microwave irradiation. The product was obtained as a yellow solid (0.253 g, 86%).

^{1}H NMR (500 MHz, d^{6}-DMSO, 25 ºC): δ 14.59 (s, 1H, NN*H*), 9.79 (t, ^{3}J = 5.8 Hz, 1H, NN*H*), 8.67 (dd, $^{3,4}J$ = 8.0, 1.4 Hz, 1H, H-8), 8.42 (d, ^{3}J = 8.1 Hz, 1H, H-4), 8.33 (d, ^{3}J = 8.0 Hz, 1H, H-5), 8.26 (dd, $^{3,4}J$ = 7.9, 1.3 Hz, 1H, H-1), 7.87 – 7.82 (m, 1H, H-3), 7.61 – 7.57 (m, 1H, H-2), 7.57 – 7.54 (m, 1H, H-6), 7.52 – 7.47 (m, 1H, H-7), 6.02 – 5.92 (m, 1H, CH_2CH), 5.24 (dd, $^{3,4}J_{trans}$ = 17.2, 1.2 Hz, 1H, H-a), 5.17 (dd, $^{3,4}J_{cis}$ = 10.3, 1.1 Hz, 1H, H-b), 4.33 (t, ^{3}J = 5.6 Hz, 2H, CH_2).

^{13}C NMR (125 MHz, d^{6}-DMSO, 25 ºC): δ 181.3 (*C*O), 177.9 (*C*S), 136.0 (C-4a), 135.3 (C-3), 133.7 (CH_2*C*H), 130.4 (C-2a), 130.0, 129.8 (*C*N, C-1a), 129.4 (C-2), 128.9 (C-5a), 128.8 (C-7), 128.4 (C-2), 128.3 (C-1), 125.2 (C-8), 123.8, 123.7 (C-4, C-5), 116.3 (*C*HaHb), 46.6 (CH_2).

Mass spectrum: ESI-MS calc. for $C_{18}H_{15}N_3NaOS$ $[M+Na]^+$: 344.0833; found: 344.0815.

Elem. Anal. (%). Found (calc.) for $C_{18}H_{15}N_3OS$: C, 67.22 (67.27); H, 4.61 (4.70); N, 12.98 (13.07).

IR (solid): ν (cm^{-1}) 3311, 2977, 1645, 1599, 1588, 1449.

HPLC (Method A): Rt (min) 11.02.

39. Mono(4-(N-(2-(2-(2-aminoethoxy)ethoxy)ethyl))-3-thiosemicarbazone) phenanthrenequinone

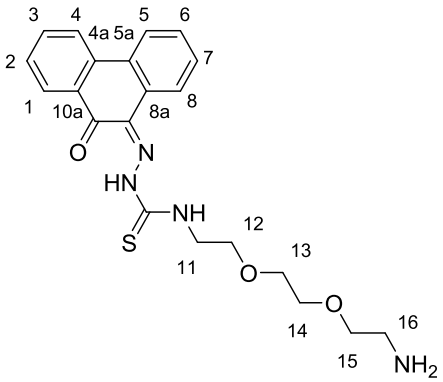

Phenanthrenequinone (0.105 g, 0.48 mmol) and thiosemicarbazide **9** (0.147 g, 0.46 mmol) were suspended in ethanol (5 mL) and homogenised by sonication for 3 min. Concentrated HCl (3 drops) was added and the reaction mixture heated to 90 ºC for 10 min by microwave irradiation. The solvent was removed under vacuum and the product re-suspended in CH_2Cl_2 and passed through a silica plug. After washing with CH_2Cl_2, the product was eluted with CH_2Cl_2 / MeOH (9:1). The solvent was removed under vacuum and the product obtained as an orange solid (0.109 g, 58%).

^{1}H NMR (500 MHz, d^{6}-DMSO, 25 ºC): δ 14.57 (s, 1H, NN*H*), 9.60 (t, ^{3}J = 5.9 Hz, 1H, N*H*CH_2), 8.64 (dd, $^{3,4}J$ = 8.1, 1.4 Hz, 1H, H-8), 8.43 (d, ^{3}J = 7.8 Hz, 1H, H-4), 8.34 (dd, $^{3,4}J$ = 8.2, 1.2 Hz, 1H, H-5), 8.26 (dd, $^{3,4}J$ = 7.9, 1.5 Hz, 1H, H-1), 7.97 (brs, 2H, NH_2), 7.85 (ddd, $^{3,3,4}J$ = 8.4, 7.2, 1.5 Hz, 1H, H-3), 7.60 – 7.54 (m, 2H, H-3, H-2, H-6), 7.50 (ddd, $^{3,3,4}J$ = 8.2, 7.1, 1.2 Hz, 1H, H-7), 3.86 (q, ^{3}J = 6.1 Hz,

2H, H-11), 3.70 (t, ^{3}J = 6.2 Hz, 2H, H-12), 3.64 – 3.56 (m, 6H, H-13, H-14, H-15), 2.92 (q, ^{3}J = 5.4 Hz, 2H, H-16).

^{13}C NMR (125 MHz, d^{6}-DMSO, 25 ºC): δ 181.4 (*C*O), 177.9 (*C*S), 136.0 (C-4a), 135.4 (C-3), 130.4 (C-2a), 130.1, 129.8 (*C*N, C-1a), 129.5 (C-6), 129.0 (C-7), 128.5 (C-2, C-5a), 128.3 (C-1), 125.1 (C-8), 123.8 (C-4, C-5), 69.7, 69.5 (C-13, C-14), 67.8 (C-12), 66.7 (C-15), 44.0 (C-11), 38.5 (C-16).

Mass spectrum: ESI-MS calc. for $C_{21}H_{25}N_4NaO_3S$ $[M+Na]^+$: 435.1467; found: 435.1542.

IR (solid): ν (cm^{-1}) 3300, 1659, 1496, 1388, 1097, 1066.

HPLC (Method A): Rt (min) 11.84.

40. Mono(4-methyl-3-thiosemicarbazone)-4,5-pyrenedione

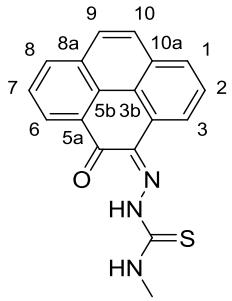

Compound **40** was prepared following the experimental procedure for **14**. 4,5-Pyrenedione (0.200 g, 0.86 mmol), 4-methyl-3-thiosemicarbazide (0.086 g, 0.82 mmol) and 3 drops of concentrated hydrochloric acid were heated in ethanol at 90 ºC 10 min by microwave irradiation. The product was obtained as a red solid (0.217 g, 83%).

^{1}H NMR (500 MHz, d^{6}-DMSO, 25 ºC): δ 14.70 (s, 1H, N*NH*), 9.65 (q, ^{3}J = 4.4 Hz, 1H, *NH*CH$_3$), 8.93 (dd, $^{3,4}J$ = 7.7, 1.2 Hz, 1H, H-3), 8.54 (dd, $^{3,4}J$ = 7.5, 1.3 Hz, 1H, H-6), 8.42 (dd, $^{3,4}J$ = 7.8, 1.3 Hz, 1H, H-8), 8.13 (dd, $^{3,4}J$ = 7.8, 1.1 Hz, 1H, H-1), 8.02 (d, ^{4}J = 1.2 Hz, 2H, H-9, H-10), 7.92 (t, ^{3}J = 7.7 Hz, 1H, H-7), 7.84 (t, ^{3}J = 7.8 Hz, 1H, H-2), 3.19 (d, ^{3}J = 4.6 Hz, 3H, *CH$_3$*).

^{13}C NMR (125 MHz, d^{6}-DMSO, 25 ºC): δ 181.9 (*C*O), 178.1 (*C*S), 134.9 (C-8), 134.4 (*C*N), 131.2, 131.0 (C-5a, C-3a), 129.8 (C-10a), 129.0 (C-8a), 128.6 (C-5b), 128.5 (C-5a), 128.1 (C-1), 127.9 (C-7), 127.6 (C-10, C-2), 127.3 (C-6), 127.1 (C-7), 126.4 (C-9), 123.1 (C-3), 31.8 (*C*H$_3$).

Mass spectrum: ESI-MS calc. for $C_{18}H_{13}N_3NaOS$ $[M+Na]^+$: 3042.0677; found: 342.0658.

IR (solid): ν (cm^{-1}) 3299, 3053, 2932, 1667, 1616, 1543, 1481, 1174.

HPLC (Method A): Rt (min) 11.15.

41. Mono(4-ethyl-3-thiosemicarbazone)-4,5-pyrenedione

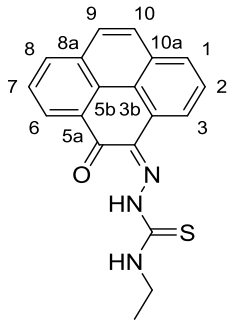

Compound **41** was prepared following the experimental procedure for **14**. 4,5-Pyrenedione (0.200 g, 0.86 mmol), 4-ethyl-3-thiosemicarbazide (0.098 g, 0.82 mmol) and 3 drops of concentrated hydrochloric acid were heated in ethanol at 90 ºC 10 min by microwave irradiation. The product was obtained as a red solid (0.236 g, 86%).

^{1}H NMR (500 MHz, d^{6}-DMSO, 25 ºC): δ 14.64 (s, 1H, N*NH*), 9.72 (t, ^{3}J = 5.8 Hz, 1H, *NH*CH$_2$), 8.90 (dd, $^{3,4}J$ = 7.7, 1.1 Hz, 1H, H-3), 8.52 (dd, $^{3,4}J$ = 7.5, 1.2 Hz, 1H, H-6), 8.42 (dd, $^{3,4}J$ = 7.8, 1.2 Hz, 1H, H-8), 8.13 (dd, $^{3,4}J$ = 7.8, 1.1 Hz, 1H, H-1), 8.01 (s, 2H, H-9, H-10), 7.92 (t, ^{3}J = 7.7 Hz, 1H, H-7), 7.84 (t, ^{3}J = 7.8 Hz, 1H, H-2), 3.86 – 3.67 (m, 2H, C*H$_2$*), 1.27 (t, ^{3}J = 7.1 Hz, 3H, C*H$_3$*).
^{13}C NMR (125 MHz, d^{6}-DMSO, 25 ºC): δ 181.82 (*C*O), 177.22 (*C*S), 134.42 (C-8), 131.2, 131.1 (C-5a, C-3a, C-3b), 130.5 (*C*N), 129.7 (C-10a), 129.0 (C-8a), 128.6 (C-1), 128.1 (C-5b), 127.7 (C-10, C-2), 127.3 (C-6), 127.1 (C-7), 126.4 (C-9), 123.1 (C-3), 39.02 (*C*H$_2$), 13.93 (*C*H$_3$).
Mass spectrum: ESI-MS calc. for $C_{19}H_{15}N_3NaOS$ $[M+Na]^+$: 356.0834; found: 356.0833.
IR (solid): ν (cm^{-1}) 3338, 2976, 1670, 1619, 1485, 1416, 1037.
HPLC (Method A): Rt (min) 12.00.

42. Mono(4-allyl-3-thiosemicarbazone)-4,5-pyrenedione

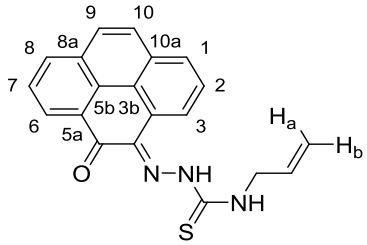

Compound **42** was prepared following the experimental procedure for **14**. 4,5-Pyrenedione (0.200 g, 0.86 mmol), 4-allyl-3-thiosemicarbazide (0.107 g, 0.82 mmol) and 3 drops of concentrated hydrochloric acid were heated in ethanol at 90 ºC 10 min by microwave irradiation. The product was obtained as a red solid (0.233 g, 82%).

^{1}H NMR (500 MHz, d^{6}-DMSO, 25 ºC): δ 14.72 (s, 1H, NN*H*), 9.89 (t, ^{3}J = 6.0 Hz, 1H, NHC*H$_2$*), 8.95 (dd, $^{3,4}J$ = 7.8, 1.1 Hz, 1H, H-3), 8.55 (dd, $^{3,4}J$ = 7.5, 1.3 Hz, 1H, H-6), 8.43 (dd, $^{3,4}J$ = 7.8, 1.3 Hz, 1H,

H-8), 8.14 (dd, $^{3,4}J$ = 7.8, 1.1 Hz, 1H, H-1), 8.03 (d, ^{4}J = 1.1 Hz, 2H, H-9, H-10), 7.93 (t, ^{3}J = 7.7 Hz, 1H, H-7), 7.85 (t, ^{3}J = 7.8 Hz, 1H, H-2), 6.04 – 5.93 (m, 1H, C*H*), 5.27 (dd, $^{3,4}J_{trans}$ = 17.2, 1.7 Hz, 1H, Ha), 5.19 (dd, $^{3,4}J_{cis}$ = 10.3, 1.7 Hz, 1H, Hb), 4.41 – 4.33 (m, 2H, CH_2).

^{13}C NMR (125 MHz, d^6-DMSO, 25 ºC): δ 181.5 (*C*O), 177.8 (*C*S), 134.2 (C-8), 133.8 (*C*H), 131.0, 130.9 (C-3a, C-3b, C-5a), 130.3 (*C*N), 129.5 (C-10a), 128.7 (C-8a), 128.4 (C-1), 127.8, 127.5 (C-10, C-2), 127.4 (C-6), 127.1 (C-7), 126.2 (C-9), 123.0 (C-3), 116.3 (*C*HaHb), 46.7 (*C*H_2).

Mass spectrum: ESI-MS calc. for $C_{20}H_{15}N_3NaOS$ $[M+Na]^+$: 368.0834; found: 368.0829.

Elem. Anal. (%). Found (calc.) for $C_{20}H_{15}N_3OS$: C, 69.37 (69.54); H, 4.51 (4.38); N, 12.01 (12.17).

IR (solid): ν (cm^{-1}) 3354, 1618, 1532, 1484, 1035.

HPLC (Method A): Rt (min) 11.31.

43. Mono(4-phenyl-3-thiosemicarbazone)-4,5-pyrenedione

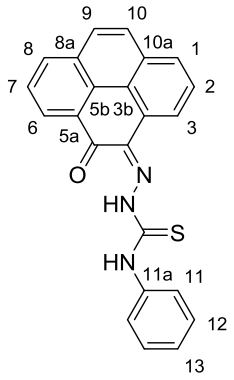

Mono(4-phenyl-3-thiosemicarbazone)-4,5-pyrenedione was prepared following the experimental procedure for compound **14**. Pyrene-4,5-dione (0.200 g, 0.86 mmol) and 4-phenyl-3-thiosemicarbazide (0.432 g, 2.58 mmol) were heated 10 min at 90 ºC in a microwave reactor. The product was obtained as a red solid (0.274 g, 83%).

^{1}H NMR (500 MHz, d^6-DMSO, 25 ºC): δ 14.82 (s, 1H, NN*H*) 11.12 (s, 1H, CSN*H*), 8.97 (d, ^{3}J = 7.8 Hz, 1H, H-3), 8.48 (dd, $^{3,4}J$ = 7.5, 1.3 Hz, 1H, H-6), 8.38 (dd, $^{3,4}J$ = 7.8, 1.3 Hz, 1H, H-8), 8.08 (dd, $^{3,4}J$ = 7.8, 1.2 Hz, 1H, H-1), 7.98 (s, 2H, H-9, H-10), 7.89 (t, ^{3}J = 7.7 Hz, 1H, H-7), 7.77 (t, ^{3}J = 7.7 Hz, 1H, H-2), 7.65 (dd, $^{3,4}J$ = 8.5, 1.3 Hz, 2H, H-11), 7.52 – 7.46 (m, 2H, H-12), 7.37 – 7.32 (m, 1H, H-13).

^{13}C NMR (125 MHz, d^6-DMSO, 25 ºC): δ 181.9 (*C*O), 177.2 (*C*S), 138.6 (C-11a), 134.5 (C-8), 131.2, 131.0 (C-2a, C-3b, C-5a), 130.9 (*C*N), 129.5 (C-10a), 128.8 (C-8a), 128.7 (C-1), 128.5 (C-5b), 127.6 (C-10, C-2), 127.3 (C-6), 127.0 (C-7), 126.5 (C-13), 126.3 (C-11), 126.2 (C-9), 123.7 (C-3).

Mass spectrum: ESI-MS calc. for $C_{23}H_{15}N_3NaOS$ $[M+Na]^+$: 404.0833; found: 404.0830.

IR (solid): ν (cm^{-1}) 3295, 3053, 1638, 1619, 1499, 1130.

HPLC (Method A): Rt (min) 12.61.

44. Mono(4-N(2-(2-(2-aminoethoxy)ethoxy)ethyl))-3-thiosemicarbazone pyrene-4,5-dione

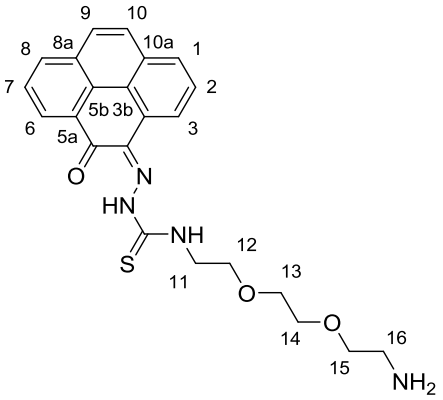

Pyrene-4,5-dione (0.100 g, 0.43 mmol) and thiosemicarbazide **9** (0.132 g, 0.41 mmol) were suspended in ethanol (5 mL), homogenised by sonication for 3 min and heated 10 min at 90 ºC in the microwave reactor. The solvent was removed under vacuum and the residue re-suspended in CH_2Cl_2 and passed through a silica plug washing with CH_2Cl_2 and eluting with CH_2Cl_2 / MeOH (9:1). The solvent was removed under vacuum and the product was obtained as a red solid (0.121 g, 68 %).

^{1}H NMR (400 MHz, $CDCl_3$, 25 ºC): δ 14.67 (s, 1H, NN*H*), 9.68 (t, ^3J = 5.9 Hz, 1H, N*H*CH_2), 8.92 (dd, $^{3,4}J$ = 7.7, 1.1 Hz, 1H, H-3), 8.54 (dd, $^{3,4}J$ = 7.5, 1.3 Hz, 1H, H-6), 8.44 (dd, $^{3,4}J$ = 7.9, 1.3 Hz, 1H, H-8), 8.15 (dd, $^{3,4}J$ = 7.9, 1.1 Hz, 1H, H-1), 8.04 (d, ^4J = 0.8 Hz, 2H, H-9, H-10), 7.93 (t, ^3J = 7.7 Hz, 1H, H-7), 7.89 (brs, 2H, NH_2), 7.85 (t, ^3J = 7.8 Hz, 1H, H-2), 3.91 (q, ^3J = 6.1 Hz, 2H, H-11), 3.75 (t, ^3J = 6.2 Hz, 2H, H-12), 3.68 – 3.60 (m, 6H, H-13, H-14, H-15), 2.98 – 2.91 (m, 2H, H-16).

^{13}C NMR (125 MHz, $CDCl_3$, 25 ºC): δ 182.0 (*C*O), 178.0 (*C*S), 134.6 (C-8), 131.3, 131.1, 131.0 (C-3a, C-3b, C-5a), 129.7 (*C*N), 129.0 (C-10a), 128.7 (C-1), 128.1 (C-5b), 127.7 (C-10, C-2), 127.4 (C-6), 127.2 (C-7), 126.4 (C-9), 123.2 (C-3), 69.7, 69.6 (C-13, C-14), 67.9 (C-12), 66.7 (C-15), 44.1 (C-11), 38.6 (C-16).

Mass spectrum: ESI-MS calc. for $C_{23}H_{25}N_4O_3S$ $[M+H]^+$: 437.1647; found: 437.1656.

IR (solid): ν (cm^{-1}) 3300, 1659, 1496, 1388, 1097, 1066.

HPLC (Method A): Rt (min) 11.84.

45. Zn(II)[mono(allyl-thiosemicarbazonato) acenaphthenequinone]$_2$

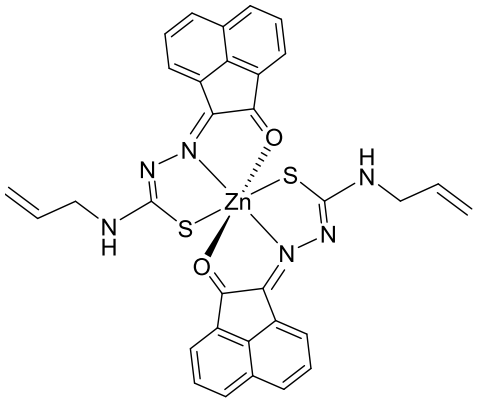

Mono(4-allyl-3-thiosemicarbazone) acenaphthenequinone (0.286 g, 0.97 mmol) and anhydrous zinc acetate (0.177 g, 0.97 mmol) were suspended in ethanol (5 mL) and homogenised by ultrasonication. The reaction mixture was heated 1 h at 90 ºC under microwave irradiation. The reaction mixture was filtered whilst hot, washed with ethanol and dried under vacuum. The solid was dissolved in CH_2Cl_2 and purified using a silica plug, washing with CH_2Cl_2 and eluting with CH_2Cl_2 / MeOH (8:2). The solvent was concentrated under vacuum. The product was obtained as an orange solid (0.288 g, 91%).

Mass spectrum: ESI-MS calc. for $C_{32}H_{25}N_6O_2S_2Zn$ $[M+H]^+$: 653.0772; found: 653.0804.

Elem. Anal. (%). Found (calc.) for $C_{32}H_{24}N_6O_2S_2Zn{\cdot}CHCl_3$: C, 50.53 (51.25); H, 3.15 (3.26); N, 10.90 (10.87).

IR (solid): ν (cm^{-1}) 3321, 3059, 1675, 1484, 1247, 1090, 1026.

HPLC (Method A): Rt (min) 9.98.

46. Zn(II) [mono(allyl-thiosemicarbazonato) aceanthrenequinone]$_2$

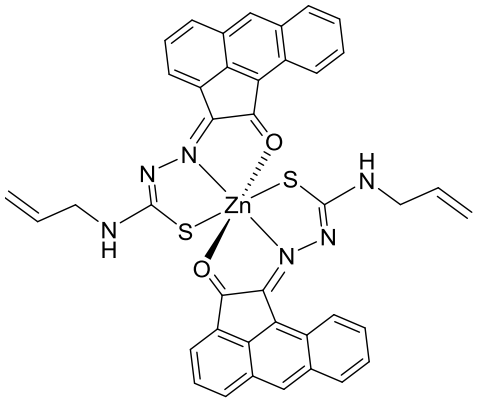

Compound **46** was synthesised following the experimental procedure of **45**. Mono(4-allyl-3-thiosemicarbazone) aceanthrenequinone (0.060 g, 0.14 mmol) and anhydrous zinc acetate (0.027 g, 0.14 mmol) were heated in ethanol for 1 h at 90 ºC under microwave irradiation. The product was obtained as a red solid (0.059 g, 91%).

Mass spectrum: nanoESI-MS calc. for $C_{40}H_{29}N_6O_2Zn$ $[M+H]^+$: 753.1085; found: 753.1079.

IR (solid): ν (cm^{-1}) 3300, 1659, 1496, 1388, 1097, 1066.

HPLC (Method A): Rt (min) 11.84.

47. Zn(II) [mono(allyl-thiosemicarbazonato) phenanthrenequinone]$_2$

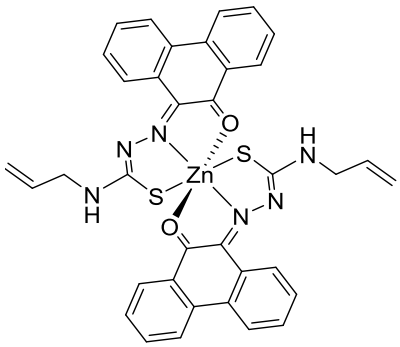

Compound **47** was synthesised following the experimental procedure of **45**. Mono(4-allyl-3-thiosemicarbazone) phenanthrenequinone (0.050 g, 0.16 mmol) and anhydrous zinc acetate (0.028 g, 0.16 mmol) were heated in ethanol for 1 h at 90 ºC under microwave irradiation. The product was obtained as a red solid (0.046 g, 84%).

Mass spectrum: ESI-MS calc. for $C_{36}H_{29}N_6O_2S_2Zn$ $[M+H]^+$: 705.1085; found: 705.1200.

Elem. Anal. (%). Found (calc.) for $C_{36}H_{28}N_6O_2S_2Zn \cdot C_6H_{14}$: C, 64.11 (63.67); H, 5.27 (5.34); N, 9.18 (10.61).

IR (solid): ν (cm^{-1}) 3313, 2961, 2925, 1486, 1078, 1014.

HPLC (Method A): Rt (min) 11.26.

48. Zn(II) [mono(allyl-thiosemicarbazonato) pyrene-4,5-dione]$_2$

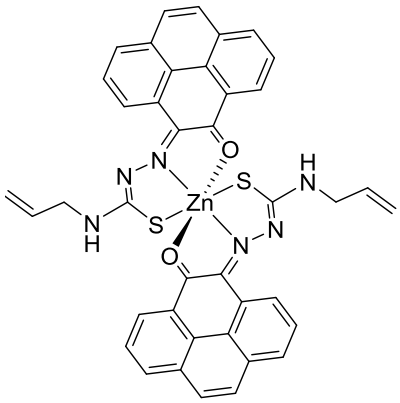

Compound **48** was synthesised following the experimental procedure of **45**. Mono(4-allyl-3-thiosemicarbazonato) pyrene-4,5-dione (0.050 g, 0.14 mmol) and anhydrous zinc acetate (0.026 g,

0.14 mmol) were heated in ethanol for 1 h at 90 ºC under microwave irradiation. The product was obtained as a dark red solid (0.057 g, 99%).

Mass spectrum: ESI-MS calc. for $C_{40}H_{29}N_6O_2S_2Zn$ $[M+H]^+$: 753.1085; found: 753.1186.

IR (solid): ν (cm^{-1}) 3355, 2918, 1679, 1484, 1075, 1026.

HPLC (Method A): Rt (min) 12.15.

49. Mono(4-tert-butyl-4-((((9H-fluoren-9-yl)methoxy)carbonyl)amino)-5-oxo-5-(propylamino)pentanoyl)-3-thiosemicarbazone) acenaphthenequinone

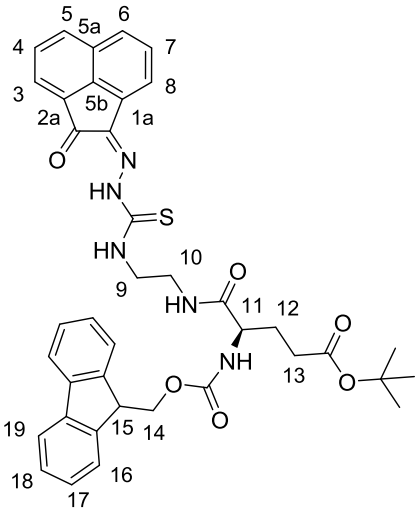

A solution of Fmoc-Glu(O^{t}Bu)-OH (0.214 g, 0.50 mmol), pyBOP (0.262 g, 0.50 mmol) and DIPEA (0.11 ml, 0.63 mmol) were stirred for 2 h at room temperature in DMF (5 mL). Mono(thiosemicarbazone) **10** (0.125 g, 0.42 mmol) was added to the reaction mixture dissolved in DMF (5 mL) and the reaction mixture stirred at room temperature for 20 h. The solvent was removed under vacuum, the crude re-dissolved in CH_2Cl_2 and purified by column chromatography using CH_2Cl_2 / MeOH (0-10%) as solvent system. The solvent was concentrated under vacuum to yield a yellow solid (0.147 g, 49%).

^{1}H NMR (500 MHz, d^6-DMSO, 25 ºC): δ 12.61 (s, 1H, NN*H*), 9.36 (t, ^3J = 5.4 Hz, 1H, CSN*H*), 8.35 (d, ^3J = 8.2 Hz, 1H, H-5), 8.20 (t, ^3J = 6.0 Hz, 1H, C-10-N*H*), 8.10 (d, ^3J = 8.5 Hz, 1H, H-6), 8.07 (d, ^3J = 7.1 Hz, 2H, H-3), 8.02 (d, ^3J = 7.0 Hz, 1H, H-8), 7.90 – 7.86 (m, 1H, H-4), 7.86 – 7.81 (m, 2H, H-19, H-19'), 7.78 (dd, $^{3,3}J$ = 8.9, 7.0, 2H, H-7), 7.70 (d, ^3J = 7.5 Hz, 2H, H-16, H-16'), 7.66 (d, ^3J = 7.7 Hz, 1H, H-17, H-17'), 7.54 (d, ^3J = 7.4 Hz, 1H, C-11-N*H*), 7.38 (t, ^3J = 7.5 Hz, 2H, H-18, H-18'), 7.29 (t, ^3J = 7.5 Hz, 2H, H-17, H-17'), 4.36 – 4.11 (m, 3H, H-14, H-16), 4.09 – 3.94 (m, 2H, H-11), 3.77 – 3.64 (m, 2H, H-9), 3.51 – 3.38 (m, 2H, H-10), 2.23 (t, ^3J = 7.7 Hz, 3H, H-13), 2.05 – 1.87 (m, 1H, H-12), 1.87 – 1.70 (m, 2H, H-12).

^{13}C NMR (125 MHz, d^6-DMSO, 25 ºC): δ 188.9 (C-2a*C*O), 178.1 (*C*S), 172.6 (*C*OC11), 172.0 (*C*OOtBu), 156.4 (*C*OOFmoc), 144.3, 144.1, 141.1, 139.6 (Cq Fmoc), 137.6 (*C*N), 133.3 (C-5), 130.8

(C-5a), 130.4, 130.3, 129.3 (C-1a, C-2a, C-5a), 129.1 (C-7), 129.0 (C-4), 128.0 (C-18, C-18'), 127.5, 127.4 (C-4, C-17, C-17'), 125.7 (C-16, C-16'), 122.9 (C-3), 120.5 (C-19, C-19'), 118.8 (C-8), 66.1 (C-14), 54.5 (C-11), 47.1 (H-15), 44.9 (C-9), 38.1 (C-10), 31.8 (C-13), 28.1 ((CH_3)$_3$), 27.7 (C-12).

Mass spectrum: ESI-MS calc. for $C_{39}H_{39}N_5NaO_6S$ $[M+Na]^+$: 728.2518; found: 728.2580.

HPLC (Method A): Rt (min) 10.96.

50. 4,4-Difluoro-8-(4'-carboxyphenyl)-1,3,5,7-tetramethyl-4-bora-3a,4a-diaza-s-indacene (adapted from a literature procedure [11])

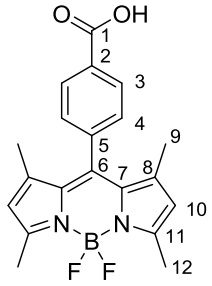

2,4-dimethylpyrrole (5.000 g, 52.6 mmol) and 4-formylbenzoic acid (3.718 g, 22.5 mmol) were dissolved in CH_2Cl_2 (2 L) and 10 drops of TFA added. The reaction mixture was allowed to stir at room temperature for 1.5 h. 2,3-Dichloro-5,6-dicyano-1,4-benzoquinone (DDQ) (5.098 g, 22.5 mmol) was added portion wise followed by triethylamine (50 mL) and $BF_3 \cdot OEt_2$ (50 mL) added dropwise. The reaction was quenched by the addition of water (1 L). The aqueous phase was extracted with CH_2Cl_2 (3x 600 mL). The organic fractions were collected, dried over $MgSO_4$ and the solvent removed under vacuum. The crude was purified by flash column chromatography using CH_2Cl_2 / MeOH (0 – 20%) as eluent. After recrystallisation from THF/hexane, the product was obtained as a red solid (3.147 g, 38%).

^{1}H NMR (500 MHz, d^8-THF, 25 ºC): δ 8.19 (d, ^3J = 8.2 Hz, 2H, H-3), 7.48 (d, ^3J = 8.2 Hz, 2H, H-4), 6.03 (s, 2H, H-2, H-10), 2.49 (s, 6H, H-12), 1.38 (s, 6H, H-9).
^{13}C NMR (125 MHz, d^8-THF, 25 ºC): δ 167.2 (*C*OOH), 156.7 (C-11), 143.6 (C-5), 142.1 (C-8), 140.6 (C-6), 132.9 (C-7), 132.0 (C-2), 131.5 (C-3), 129.5 (C-4), 122.1 (C-10), 14.8, 14.7 (C-9, C-12).
Mass spectrum: ESI-MS calc. for $C_{20}H_{18}BF_2N_2O_2$ [M-H]$^-$: 367.1429; found: 367.1435.
Elem. Anal. (%). Found (calc.) for $C_{20}H_{19}BF_2N_2O_2$: C, 64.05 (65.24); H, 5.18 (5.20); N, 7.21 (7.61).
IR (solid) ν (cm^{-1}): 2974, 1678, 1544, 1076, 1043, 972, 738.
HPLC (Method A): Rt (min) 10.22.

51. N6-(tert-butoxycarbonyl)lysine (adapted from a literature procedure [12])

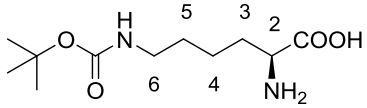

Piperidine (2.5 mL) was added to a stirring solution of N2-(((9H-fluoren-9-yl)methoxy)carbonyl)-N6-(tert-butoxycarbonyl)lysine (1.000 g, 2.13 mmol) in DMF (10 mL) at 25 ºC. The reaction mixture was allowed to stir at room temperature for 2 h. The solvent was removed under vacuum and the residue re-suspended in water (20 mL) and washed with petroleum ether (3x 25 mL). The aqueous phase was concentrated under vacuum and freeze dried. The product was obtained as a white solid (0.499 g, 95%).

^{1}H NMR (500 MHz, D_2O, 25 ºC): δ 3.66 (t, ^{3}J = 6.1 Hz, 1H, H-2), 3.01 (t, ^{3}J = 6.7 Hz, 2H, H-6), 1.89 – 1.73 (m, 2H, H-3), 1.52 – 1.41 (m, 2H, H-5), 1.36 (s, 9H, (CH_3)$_3$), 1.34 – 1.20 (m, 2H, H-4).

^{13}C NMR (125 MHz, D_2O, 25 ºC): δ 174.7 (*C*OOH), 158.3 (*C*O), 54.7 (C-2), 39.56 (C-6), 30.1 (C-3), 28.6 (C-5), 27.6 (CH_3)$_3$, 21.6 (C-4).

Mass spectrum: ESI-MS calc. for $C_{11}H_{22}N_2NaO_4$ $[M+Na]^+$: 269.1477; found: 269.1476.

IR (solid): ν (cm^{-1}): 3364, 2985, 2945, 2872, 1684, 1516, 1164.

52. 2,5-dioxopyrrolidin-1-yl 4-(5,5-difluoro-1,3,7,9-tetramethyl-5H-4l4,5l4-dipyrrolo[1,2-c:2',1'-f][1,3,2]diazaborinin-10-yl)benzoate

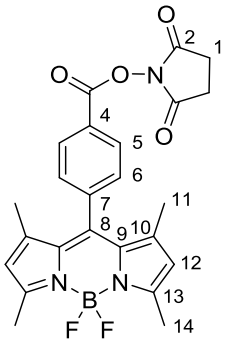

8-carboxyphenyl BODIPY (**50**) (0.100 g, 0.27 mmol), N-hydroxysuccinimide (0.065 g, 0.27 mmol) and EDC·HCl (0.107 g, 0.56 mmol) were dissolved in CH_2Cl_2 (60 mL). The reaction mixture was stirred at room temperature for 3 h. The solvent was removed under vacuum and the residue purified by flash column chromatography using hexane / ethyl acetate (1:1) as eluent. The product was obtained as a crystalline orange solid (0.135 g, 99%).

^{1}H NMR (500 MHz, $CDCl_3$, 25 ºC): δ 8.27 (d, ^{3}J = 8.4 Hz, 2H, H-4), 7.50 (d, ^{3}J = 8.4 Hz, 2H, H-6), 6.01 (s, 2H, H-12), 2.94 (s, 4H, H-1), 2.56 (s, 6H, H-14), 1.38 (s, 6H, H-11).

^{13}C NMR (125 MHz, $CDCl_3$, 25 ºC): δ 169.3 (C-2), 161.4 (C-3), 156.5 (C-13), 143.0 (C-10), 142.2 (C-8), 139.4 (C-7), 131.4 (C-5), 130.8 (C-4), 129.2 (C-6), 125.9 (C-9), 121.8 (C-12), 25.8 (C-1), 14.9 (C-14), 14.8 (C-11).

Mass spectrum: ESI-MS calc. for $C_{25}H_{25}BF_2N_3O_5$ $[M-H]^-$: 496.1855; found: 496.1867.

Elem. Anal. (%). Found (calc.) for $C_{24}H_{22}BF_2N_3O_4$: C, 61.78 (61.96); H, 4.88 (4.77); N, 8.89 (9.03).

IR (solid): ν (cm^{-1}) 2921, 2852, 1802, 1778, 1737, 1542, 1065, 721.

HPLC (Method B): Rt (min) 10.64.

53. N6-(tert-butoxycarbonyl)-N2-(4-(5,5-difluoro-1,3,7,9-tetramethyl-5H-4l4,5l4-dipyrrolo[1,2-c:2',1'-f][1,3,2]diazaborinin-10-yl)benzoyl)lysine

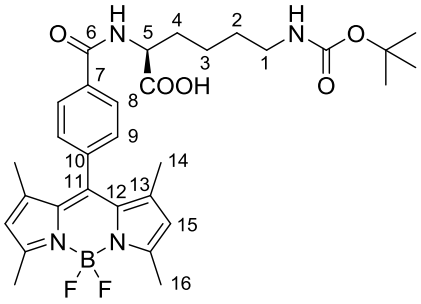

To a solution of NHS-activated BODIPY (**52**) (0.600 g, 1.29 mmol) and N,N-DIPEA (2.5 mL, 12.9 mmol) in DMF (50 mL) at 60 ºC, N-6-(tert-butoxycarbonyl)lysine (0.950 g, 3.86 mmol) was added portion wise and the reaction mixture stirred at 60 ºC for 7 h. The solvent was removed under vacuum and the residue dissolved in CH_2Cl_2 and washed with water (3x50 mL). The organic layer was dried over $MgSO_4$ and the solvent removed under vacuum. The purification was performed by automated flash column chromatography using CH_2Cl_2 / MeOH (0 – 10%) as eluent. The product was obtained as a red solid (0.699 g, 91%).

^{1}H NMR (500 MHz, $CDCl_3$, 25 ºC): δ 7.95 (d, ^3J = 8.2 Hz, 2H, H-8), 7.31 (d, ^3J = 8.2 Hz, 2H, H-9), 5.93 (s, 2H, H-15), 4.83 (s, 1H, H-5), 4.76 (s, 1H, N*H*CO), 3.07 (brs, 2H, H-4), 2.48 (s, 6H, H-17), 2.05 – 1.93 (m, 1H, H-3), 1.90 – 1.79 (m, 1H, H-3), 1.56 – 1.41 (m, 4H, H-1, H-2), 1.36 (s, 9H, (C*H*$_3$)$_3$), 1.29 (s, 6H, H-14).

^{13}C NMR (125 MHz, $CDCl_3$, 25 ºC): δ 156.1 (NH*C*O), 143.0, 128.7 (C-9), 128.3 (C-8), 121.6 (C-15), 66.0, 53.0 (C-5), 36.8, 31.7 (C-3), 30.0 (C-1, C-2), 28.6 (*C*H$_3$)$_3$, 22.8 (C-1, C-2), 14.8 (C-14, C-17).

Mass spectrum: ESI-MS calc. for $C_{31}H_{39}BF_2NaN_4O_5$ $[M+Na]^+$: 619.2879; found 619.2908.

IR (solid): ν (cm^{-1}) 3327, 2929, 1646, 1542, 1508, 1154, 974.

HPLC (Method A): Rt (min) 9.25.

54. (E)-(4-(3-(4-(dimethylamino)styryl)-5,5-difluoro-1,7,9-trimethyl-5H-5l4,6l4-dipyrrolo[1,2-c:2',1'-f][1,3,2]diazaborinin-10-yl)phenyl)(piperidin-1-yl)methanone

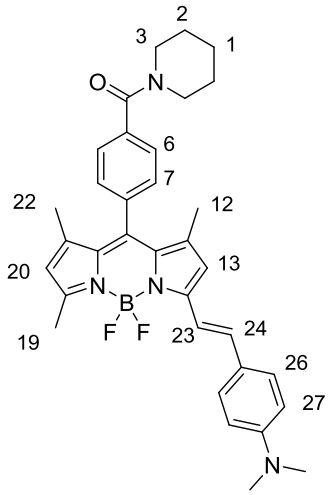

NHS-activated BODIPY (**52**) (0.108 g, 0.23 mmol) and 4-(N,N-dimethylamino)benzaldehyde (0.138 g, 0.93 mmol) were dissolved in toluene and piperidine (206 µL, 2.08 mmol) and acetic acid (158 µL, 2.77 mmol) added. The reaction mixture was heated at 110 ºC for 6 h. The solvent was removed under vacuum, the residue re-dissolved in CH_2Cl_2 and washed with water. The organic layer was dried over $MgSO_4$ and the solvent removed under vacuum. The purification was carried out by automated flash column chromatography using an increasing concentration of THF / MeOH (20 – 40%) as eluent. The product was obtained as a blue solid (0.030 g, 22%).

^{1}H NMR (500 MHz, 500 MHz, $CDCl_3$) δ 7.55 (d, ^3J = 7.8 Hz, 2H, H-6), 7.52 (d, ^3J = 8.6 Hz, 2H, H-26), 7.49 (d, $^3J_{trans}$ = 15.7 Hz, 1H, H-23), 7.39 (d, ^3J = 7.9 Hz, 2H, H-7), 7.23 (d, $^3J_{trans}$ = 15.7 Hz, 1H, H-24), 6.69 (d, ^3J = 8.6 Hz, 2H, H-27), 6.61 (s, 1H, H-13), 5.97 (s, 1H, H-20), 3.75 (s, 4H, H-3), 3.36 (s, 4H, H-2), 3.03 (s, 6H, $N(CH_3)_2$), 2.59 (s, 3H, H-19), 2.05 (s, 2H, H-1), 1.45 (s, 3H, H-12), 1.40 (s, 3H, H-22).

Mass spectrum: APCI-MS calc. for $C_{34}H_{37}BF_2N_4O$ $[M+H]^+$: 567.3113; found: 567.3102.

IR (solid): ν (cm^{-1}) 2962, 1615, 1596, 1258, 1012.

HPLC (Method A): Rt (min) 10.92.

55. (E)-N6-(tert-butoxycarbonyl)-N2-(4-(3-(4-(dimethylamino)styryl)-5,5-difluoro-1,7,9-trimethyl-5H-5l4,6l4-dipyrrolo[1,2-c:2',1'-f][1,3,2]diazaborinin-10-yl)benzoyl)lysine

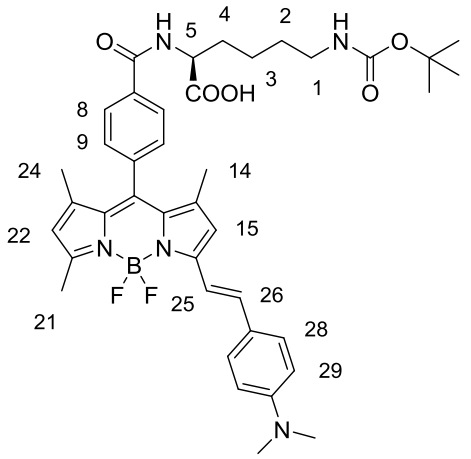

BODIPY **53** (56 mg, 94 µmol) and 4-(N,N-dimethylamino)benzaldehyde (56 mg, 0.37 mmol) were dissolved in toluene. Piperidine (93 µL, 0.94 mmol) and acetic acid (32 µL, 0.56 mmol) were added and the reaction mixture heated to 110 ºC for 7 h. The solvent was removed under vacuum, the resulting residue re-suspended in CH_2Cl_2 and washed with water. The organic layer was dried over $MgSO_4$ and the solvent removed under vacuum. The purification was carried out by automated flash column chromatography using CH_2Cl_2 / MeOH (0 – 10%) as eluent. The product was obtained as a dark blue solid.

^{1}H NMR (500 MHz, CD_3OD) δ 8.06 (d, ^3J = 8.2 Hz, 2H, H-8), 7.50 (d, ^3J = 8.3 Hz, 2H, H-9), 7.49 (d, ^3J = 8.9 Hz, 2H, H-28), 7.42 (d, $^3J_{trans}$ = 16.2 Hz, 1H, H-25), 7.35 (d, $^3J_{trans}$ = 16.2 Hz, 1H, H-26), 6.78 (d, ^3J = 8.9 Hz, 2H, H-29), 6.08 (s, 1H, H-15, H-22), 6.04 (s, 1H, H-15, H-22), 4.60 (s, 1H, H-5), 3.09 – 3.05 (m, 2H, H-1), 3.03 (s, 6H, N(CH_3)$_2$), 2.52 (s, 3H, H-24), 2.10 – 1.97 (m, 2H, H-3), 1.96 – 1.83 (m, 2H, H-4), 1.61 – 1.50 (m, 5H, H-2, H-21), 1.48 (s, 3H, H-14), 1.42 (s, 9H, (CH_3)$_3$).
Mass spectrum: ESI-MS calc. for $C_{40}H_{47}BF_2N_5O_5$ $[M+H]^+$: 726.3638; found: 726.3643.
IR (solid): ν (cm^{-1}) 3352, 2920, 1703, 1663, 1524, 1479, 1072.
HPLC (Method A): Rt (min) 9.11.

56. (((9H-fluoren-9-yl)methoxy)carbonyl)lysine

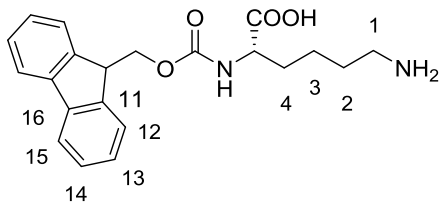

Fmoc-Lys(Boc) (1.058 g, 2.15 mmol) was dissolved in a 1:1 mixture of TFA and CH_2Cl_2 (20 mL) and the reaction mixture was stirred at room temperature for 3 h. The solvent was removed under vacuum

and the remaining TFA removed by adding diethyl ether and concentrated under vacuum repeatedly. The product was obtained as a white solid (0.638 g, 80%).

^{1}H NMR (500 MHz, $CDCl_3$, 25 ºC): δ 12.63 (s, 1H, COO*H*), 7.89 (dd, $^{3,4}J$ = 7.6, 1.0 Hz, 2H, H-15), 7.71 (ddd, $^{3,4,5}J$ = 7.5, 4.9, 1.0 Hz, 2H, H-12), 7.60 (d, ^{3}J = 8.3 Hz, 1H, CONH), 7.42 (t, ^{3}J = 7.5 Hz, 2H, H-13), 7.33 (td, $^{3,4}J$ = 7.5, 1.1 Hz, 2H, H-14), 4.34 – 4.28 (m, 1H, CHCH2O), 4.27 – 4.18 (m, 2H, CH2O), 3.99 – 3.86 (m, 1H, CHCOOH), 2.82 – 2.71 (m, 2H, H-1), 1.76 – 1.67 (m, 1H, H-4), 1.66 – 1.54 (m, 1H, H-4), 1.57 – 1.45 (m, 1H, H-2), 1.42 – 1.30 (m, 2H, H-3).

^{13}C NMR (125 MHz, $CDCl_3$, 25 ºC): δ 175.6 (*C*OOH), 158.7 (*C*ONH), 145.3 (C-11), 145.1 (C-16), 128.8 (C-13), 128.2 (C-14), 126.2 (C-12), 120.9 (C-15), 67.9 (*C*H_2O), 54.9 (*C*HCOOH), 48.5 (*C*HCH_2O), 40.5 (C-1), 40.4, 32.2 (C-4), 28.0 (C-2), 23.8 (C-3).

Mass spectrum: ESI-MS calc. for $C_{21}H_{24}N_2NaO_4$ $[M+Na]^+$: 391.1634; found: 391.1631.

IR (solid): ν (cm^{-1}) 3077, 2946, 1670, 1634, 1516, 1180.

HPLC (Method A): Rt (min) 7.30.

57. N2-(((9H-fluoren-9-yl)methoxy)carbonyl)-N6-(4-(5,5-difluoro-1,3,7,9-tetramethyl-5H-4l4,5l4-dipyrrolo[1,2-c:2',1'-f][1,3,2]diazaborinin-10-yl)benzoyl)lysine

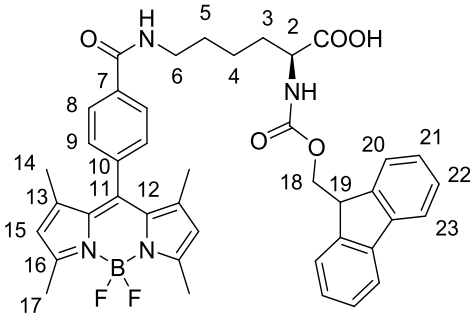

To a solution of NHS-activated BODIPY (**52**) (0.210 g, 0.45 mmol) and N,N-DIPEA (0.78 mL, 4.50 mmol) in DMF (15 mL), (((9H-fluoren-9-yl)methoxy)carbonyl)lysine (0.652 g, 1.35 mmol) was added portion wise. The reaction mixture was stirred at room temperature for 2 h until the starting material was consumed as confirmed by TLC. The solvent was removed under vacuum, the residue re-dissolved in CH_2Cl_2 and washed with water. The organic layer was collected, dried over $MgSO_4$ and the solvent removed under vacuum. The purification was performed by automated flash column chromatography using CH_2Cl_2 / MeOH (0 – 15%) as eluent. The product was obtained as an orange solid (0.024 g, 75%).

^{1}H NMR (500 MHz, CD_3OD, 25 ºC): δ 7.93 (d, ^{3}J = 8.3 Hz, 2H, H-8), 7.74 (d, ^{3}J = 7.8 Hz, 2H, H-23, H-23'), 7.70 (d, ^{3}J = 7.4 Hz, 1H, H-20), 7.65 (d, ^{3}J = 7.3 Hz, 1H, H-20'), 7.39 – 7.29 (m, 4H, H-22, H-22', H-23, H-23'), 7.28 (d, ^{3}J = 8.3 Hz, 2H, H-9), 6.04 (s, 2H, H-15), 4.43 – 4.25 (m, 2H, H-18), 4.24 – 4.16 (m, 2H, H-2, H-19), 3.47 – 3.37 (m, 2H, H-6), 1.99 – 1.88 (m, 1H, H-3), 1.83 – 1.72 (m, 1H, H-3), 1.73 – 1.62 (m, 2H, H-5), 1.60 – 1.47 (m, 2H, H-4).

^{13}C NMR (125 MHz, CD_3OD, 25 ºC): δ 175.9 (*C*OOH), 169.5 (C-7), 158.8 (O*C*ONH), 157.0 (C-16), 145.4 (C-13), 145.0, 144.4, 142.5, 142.3 (Cq Fmoc), 139.4 (C-11), 136.8 (C-10), 132.3 (C-7), 129.6 (C-9), 129.3 (C-8), 128.8, 128.2, 128.1 (C-21, C-21', C-22, C-22'), 126.4, 126.2 (C-20, C-20'), 122.4 (C-15), 121.0 (C-23, C-23'), 68.1 (C-18), 55.2 (C-2), 48.2 (C-19), 40.8 (C-6), 32.5 (C-3), 29.9 (C-5), 24.4 (C-4), 14.7, 14.6 (C-14, C-17).

Mass spectrum: ESI-MS calc. for $C_{41}H_{40}BF_2N_4O_5$ $[M-H]^-$: 717.3060; found: 717.3103.

Elem. Anal. (%). Found (calc.) for $C_{41}H_{41}BF_2N_4O_5 \cdot C_3H_7NO$: C, 65.94 (66.75); H, 5.68 (6.11); N, 7.63 (8.85).

IR (solid): ν (cm^{-1}) 3268, 2931, 1713, 1655, 1541, 1507, 1189.

HPLC (Method A): Rt (min) 10.83.

58. N6-(4-(5,5-difluoro-1,3,7,9-tetramethyl-5H-4l4,5l4-dipyrrolo [1,2-c:2',1'-f][1,3,2]diazaborinin-10-yl)benzoyl)lysine

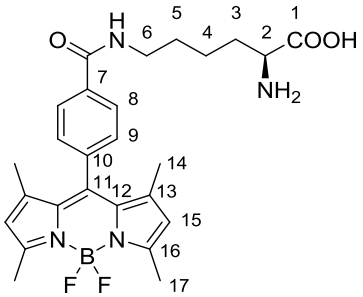

Compound **57** (36 mg, 46 µmol) was dissolved in a solution of CH_2Cl_2 / piperidine (1:4) (7.5 mL) and the reaction mixture stirred at room temperature until consumption of the starting material (1 h). Water was added to the reaction mixture, the organic phase washed with HCl (1M), brine, dried over $MgSO_4$ and concentrated under vacuum. The residue was purified by flash column chromatography using CH_2Cl_2 / MeOH (0 – 15%) as an eluent. The product was obtained as a red solid (19 mg, 82%).

^{1}H NMR (500 MHz, CD_3OD, 25 ºC): δ 8.02 (d, ^3J = 8.5 Hz, 2H, H-8), 7.46 (d, ^3J = 8.5 Hz, 2H, H-9), 6.08 (s, 2H, H-15), 3.55 (dd, $^{3,3}J$ = 6.9, 5.2 Hz, 1H, H-2), 3.49 – 3.39 (m, 2H, H-6), 2.49 (s, 6H, H-16), 1.99 – 1.82 (m, 2H, H-3), 1.75 – 1.65 (m, 2H, H-5), 1.58 – 1.49 (m, 2H, H-4), 1.41 (s, 6H, H-14).

^{13}C NMR (125 MHz, CD_3OD, 25 ºC): δ 174.2 (*C*OOH), 169.4 (*C*ONH), 157.1 (C-16), 144.4 (C-13), 139.5 (C-11), 136.7 (C-10), 132.3 (C-7), 129.7 (C-9), 129.4 (C-8), 122.4 (C-15), 56.1 (C-2), 40.7 (C-6), 32.0 (C-3), 30.2 (C-5), 23.8 (C-4), 14.7 (C-16), 14.6 (C-14).

Mass spectrum: ESI-MS calc. for $C_{26}H_{31}BF_2N_4NaO_3$ $[M+Na]^+$: 519.2355; found: 519.2383.

IR (solid): ν (cm^{-1}) 3296, 2968, 1707, 1640, 1543, 1508, 1191, 1156.

HPLC (Method A): Rt (min) 7.71.

59. 4-(5,5-difluoro-1,3,7,9-tetramethyl-5H-4l4,5l4-dipyrrolo[1,2-c:2',1'-f][1,3,2]diazaborinin-10-yl)-N-(6-(2-(2-oxoacenaphthylen-1(2H)-ylidene)hydrazine-1-carbothioamido)hexyl)benzamide

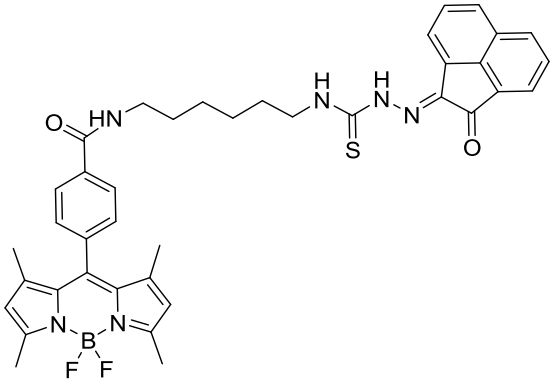

Activated BODIPY **52** (6 mg, 13 µmol), mono(4-(6-aminohexyl)-3-thiosemicarbazone) acenaphthenequinone (24 mg, 67 µmol) and DIPEA (12 µL, 67 µmol) were charged in a microwave vial and dissolved in DMF (1 mL). The reaction mixture was heated to 100 ºC for 20 min. The solvent was removed under vacuum to yield the crude as a red solid.

Mass spectrum: ESI-MS calc. for $C_{39}H_{39}BF_2N_6O_2SCl$ $[M+Cl]^-$: 739.2605; found: 739.2696.

60. Oxidised single-walled carbon nanotubes (adapted from a literature procedure[13])

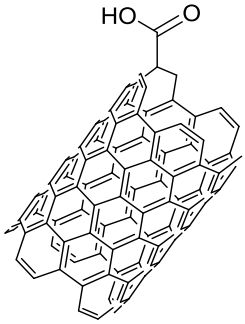

Elicarb® pristine SWNT (0.300 g) were added to a Schlenk flask under inert atmosphere. Sulphuric acid (15 mL) and nitric acid (5 mL) were added to the solid. The reaction mixture was heated to 100 ºC for 30 minutes and cooled down to be diluted with water. The dark suspension was transferred to centrifuge tubes and centrifuged 30 min at 4000 rcf. The yellow supernatant was removed, the solid pellet re-suspended in water and the suspension filtered through a 0.2 µm polycarbonate membrane. The oxidised nanotubes were washed with plenty of water and ethanol until the filtrate's pH was neutral. The nanotubes were dried in the oven at 60 ºC overnight to yield 0.234 g of material.

IR (solid): ν (cm^{-1}) 3250, 1699, 1060.

Raman: ν (cm^{-1}) 198, 277, 1344, 1583, 2656, 2684.

TGA, mass loss at 500 ºC: 21%.

61. Tert-butyl (4-aminoben zyl)carbamate

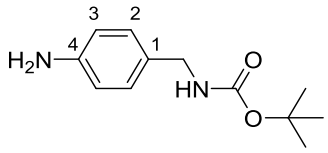

To a solution of 4-aminobenzylamine (1.016 g, 8.32 mmol) in dry THF (30 mL) at room temperature, di-tert-butyl dicarbonate (1.994 g, 9.14 mmol) was added dropwise dissolved in 20 mL THF over 15 min. The reaction mixture was stirred for 2.5 h. The solvent was removed under vacuum and the product was purified by flash column chromatography using hexane / ethyl acetate 3:2 as eluent. The product was isolated as a yellow solid (1.593 g, 86%).

^{1}H NMR (500 MHz, d^{6}-DMSO, 25 ºC): δ 7.03 (d, ^{3}J = 8.2 Hz, 2H, H-2), 6.59 (d, ^{3}J = 8.2 Hz, 2H, H-3), 4.87 (brs, 1H, N*H*), 4.15 (d, ^{3}J = 4.9 Hz, 2H, CH_2), 3.68 (brs, 2H, NH_2), 1.43 (s, 9H, (CH_3)$_3$).

^{13}C NMR (125 MHz, d^{6}-DMSO, 25 ºC): δ 156.0 (*C*O), 145.8 (C-4), 129.0 (C-2), 128.8 (C-1), 115.3 (C-3), 79.3 (*C*(CH_3)$_3$), 44.4 CH_2, 28.5 ((*C*H_3)$_3$).

Mass spectrum: ESI-MS calc. for $C_{12}H_{18}N_2NaO_2$ $[M+Na]^+$: 245.1266; found: 245.1270.

IR (solid): ν (cm^{-1}) 3452, 3365, 2973, 1688, 1514, 1245, 1156.

62. Boc-benzylamine modified SWNT (adapted from a literature procedure[14])

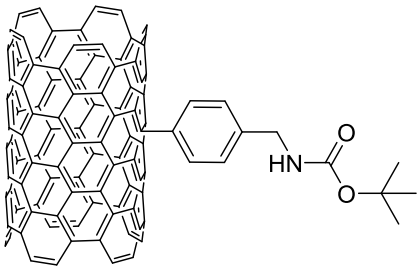

Elicarb® pristine SWNT (0.300 g) were added to a Schlenk flask under inert atmosphere. Tert-butyl (4-aminobenzyl)carbamate (**61**) (1.140 g, 5.1 mmol) was added and the mixture sonicated in milliQ water (25 mL) for 15 min. Isopentyl nitrite (0.901 g, 7.7 mmol) was added and the mixture heated to 80 ºC for 48 h. The reaction mixture was transferred to a centrifuge tube, centrifuged 15 min. at 4000 rcf, the supernatant removed and the residue re-suspended in water. The process was repeated three more times and finally the nanotubes were re-dispersed in water, filtered through a 0.2 µm polycarbonate membrane, washed with water, methanol and isopropanol until the filtrate was clear. The SWNT were dried in the oven at 60 ºC overnight to yield 0.423 g of material.

IR (solid): ν (cm^{-1}) 3200, 2901, 1870, 996.

Raman: ν (cm^{-1}) 179, 258, 1337, 1577, 2668.

63. Benzylamine modified SWNT

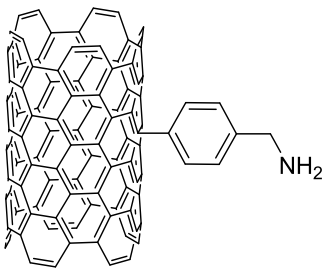

Compound **62** was dispersed in DMF by sonication (15 min) before adding concentrated HCl to a final concentration of 4 M (25 mL). The reaction mixture was stirred overnight. The nanotubes were centrifuged 15 min at 4000 rcf, the supernatant removed, the residue re-dispersed in water and the process repeated three times. Finally, the residue was re-dispersed in water, filtered through a 0.2 µm membrane and washed with water and methanol until the pH of the filtrate was neutral. The SWNT were dried in the oven at 60 ºC overnight to yield 0.368 g of material.

IR (solid): ν (cm^{-1}) 3360, 1527, 1434, 1044.

Raman: ν (cm^{-1}) 169, 261, 1336, 1580, 2668.

TGA, mass loss at 500 ºC: 11%.

Kaiser test: 0.34 mmol/g.

64. 6-((Tert-butoxycarbonyl)amino)hexanoic acid (adapted from a literature procedure[15])

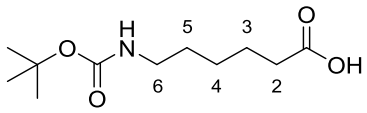

6-Aminohexanoic acid (1.312 g, 10 mmol) and sodium hydroxide (0.400 g, 10 mmol) were dissolved in a 2:1 solution of dioxane and water. The reaction mixture was cooled to 0 ºC. Di-tert-butyl dicarbonate (2.400 g, 11 mmol) was added portion wise and the reaction mixture stirred for 4 h. The solvent was removed under vacuum and the residue re-dissolved in water (30 mL) and extracted with ethyl acetate (2x 25 mL). The aqueous phase was acidified until pH 1-2 with 1M aq. HCl and extracted again with ethyl acetate (3x 25 mL). The combined organic layers were dried over $MgSO_4$ and concentrated under vacuum. The product was obtained as a white solid (1.742 g, 75%).

^{1}H NMR (500 MHz, $CDCl_3$, 25 ºC): δ 9.59 (brs, 1H, COO*H*), 4.61 (brs, 1H, N*H*), 3.08 (brs, 2H, H-6), 2.32 (t, ^3J = 7.4 Hz, 2H, H-2), 1.62 (m, 2H, H-3), 1.51 – 1.44 (m, 2H, H-5), 1.42 (s, 9H, (CH_3)$_3$), 1.38 – 1.31 (m, 2H, H-4).
^{13}C NMR (125 MHz, $CDCl_3$, 25 ºC): δ 178.9 (*C*OOH), 156.2 (*C*O), 79.4 (*C*(CH_3)$_3$), 40.5 (C-6), 34.0 (C-2), 29.8 (C-5), 28.5 ((CH_3)$_3$), 26.3 (C-4), 24.5 (C-3).
Mass spectrum: ESI-MS calc. for $C_{11}H_{21}NNaO_4$ $[M+Na]^+$: 254.1368; found: 254.1339.
IR (solid): ν (cm^{-1}) 3364, 2945, 2872, 1684, 1516, 1248, 1164.

65. 11-((Tert-butoxycarbonyl)amino)undecanoic acid

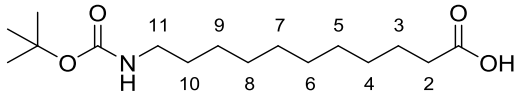

Compound **65** was prepared following the experimental procedure of **64**. 11-Aminoundecanoic acid (1.000 g, 4.97 mmol) and sodium hydroxide (0.199 g, 4.97 mmol) were dissolved in dioxane / water (2:1), cooled to 0 ºC and di-tertbutyl dicarboante (1.193 g, 5.47 mmol) added portion wise. The product was obtained as a white solid (1.123 g, 75%).

^{1}H NMR (500 MHz, $CDCl_3$, 25 ºC): δ 10.57 (brs, 1H, COO*H*), 4.55 (s, 1H, N*H*), 3.08 (m, 2H, H-11), 2.32 (t, ^3J = 7.5 Hz, 2H, H-2), 1.65 – 1.56 (m, 2H, H-3), 1.43 (m, 11H, H-10, (CH_3)$_3$), 1.36 – 1.20 (m, 12H, H-4, H-5, H-6, H-7, H-8, H-9).
^{13}C NMR (125 MHz, $CDCl_3$, 25 ºC): δ 179.4 (*C*OOH), 156.2 (*C*O), 79.2 (*C*(CH_3)$_3$), 40.8 (C-11), 34.2 (C-2), 30.1 (C-10), 29.5 (C-3), 29.4, 29.3, 29.3, 29.2 (C-4, C-5, C-8, C-9), 28.6 ((CH_3)$_3$), 26.9, 24.8 (C-6, C-7).
Mass spectrum: ESI-MS calc. for $C_{16}H_{32}NO_4$ $[M+H]^+$: 302.2331; found: 302.2314.
IR (solid): ν (cm^{-1}) 3365, 2918, 1684, 1520, 1169.

66. Ox-Boc-ethylenediamine SWNT (adapted from a literature procedure[16])

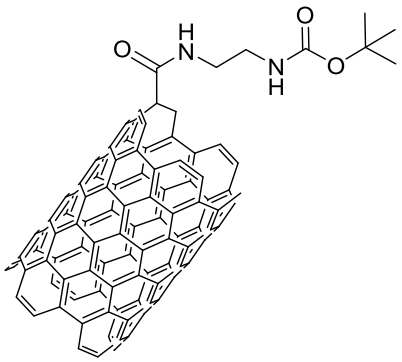

Oxidised nanotubes (**60**) (40 mg) were suspended in 10 mL dry DMF by sonicating for 20 min until a homogenous dispersion was observed. EDC·HCl (40 mg, 0.26 mmol) and HOBt (40 mg, 0.30 mmol) were added and the reaction mixture was stirred for 30 min when tert-butyl (2-aminoethyl)carbamate (**1**) (60 mg, 0.37 mmol) was added dissolved in 5 mL DMF. The reaction mixture was stirred at room temperature for 48 h. The suspension was transferred to centrifuge tubes and centrifuged at 3000 rcf for 20 min, the supernatant discarded and the residue re-suspended in ethanol. The suspension was filtered through a 0.2 µm polycarbonate membrane, the solid washed with methanol and dried under vacuum. The SWNT were further dried in the oven at 60 ºC, yielding 34 mg of material.

IR (solid): ν (cm^{-1}) 3270, 1705, 1689.
Raman: ν (cm^{-1}) 206, 1345, 1585, 2690.

67. Ox-Boc-hexylenediamine SWNT

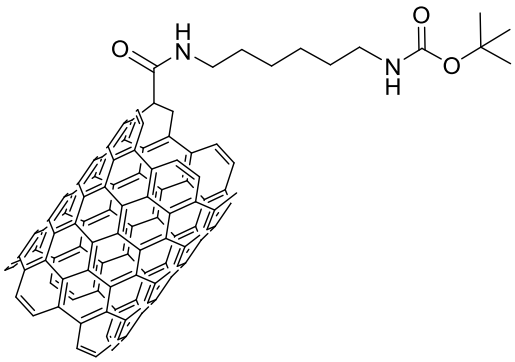

The experimental procedure followed was the same as in **66**. Oxidised nanotubes (40 mg) suspended in DMF, EDC·HCl (40 mg, 0.26 mmol) and HOBt (40 mg, 0.30 mmol) added and the reaction mixture was stirred for 30 min before the addition of tert-butyl (6-aminohexyl)carbamate (**2**) (80 mg, 0.37 mmol). The product was isolated and dried to yield 41 mg of material.

IR (solid): ν (cm^{-1}) 3300, 1636, 1506.
Raman: ν (cm^{-1}) 165, 1344, 1580, 2658.

68. Ox-Boc-pegdiamine SWNT

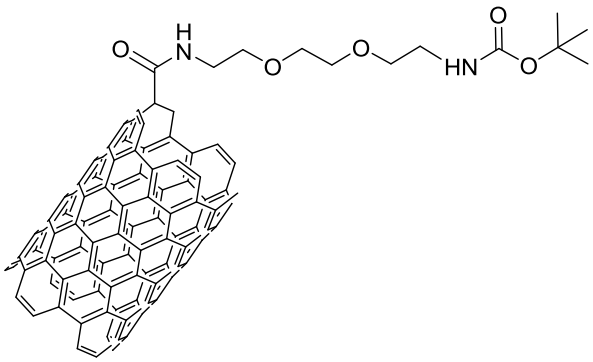

The experimental procedure followed was the same as in **66**. Oxidised nanotubes (41 mg) suspended in DMF, EDC·HCl (40 mg, 0.26 mmol) and HOBt (40 mg, 0.30 mmol) added and the reaction mixture stirred for 30 min before the addition of tert-butyl (2-(2-(2-aminoethoxy)ethoxy)ethyl)carbamate (**3**) (90 mg, 0.37 mmol). The product was isolated and dried to yield 43 mg of material.

IR (solid): ν (cm^{-1}) 3226, 1680, 1078.
Raman: ν (cm^{-1}) 160, 1344, 1582, 2665.

69. Bz-Boc-hexylaa SWNT

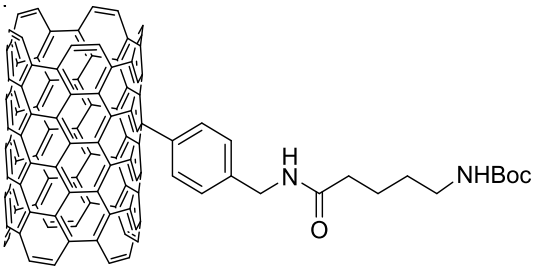

6-((Tert-butoxycarbonyl)amino)hexanoic acid (**64**) (0.050 g, 0.22 mmol) was dissolved in DMF (10 mL), EDC·HCl (0.034 g, 0.22 mmol) and HOBt (0.035 g, 0.26 mmol) added. The reaction mixture was stirred for 30 min at room temperature. In parallel, functionalised SWNT **63** were suspended in DMF (10 mL) by sonicating 10 min. The activated amino acid solution was added to the SWNT solution and the resulting suspension was stirred at room temperature for 48 h. The reaction mixture was centrifuged at 3000 rcf for 20 min, the supernatant removed, the resulting residue resuspended in ethanol and the process repeated three times. The solid was resuspended one more time in ethanol and filtered through a 0.2 μm membrane, washed with ethanol and dried under vacuum. The isolated product yielded 54 mg of material.

IR (solid): ν (cm^{-1}) 3478, 2910, 1633, 1340.
Raman: ν (cm^{-1}) 183, 1335, 1577, 2653.

70. Bz-undecaa SWNT

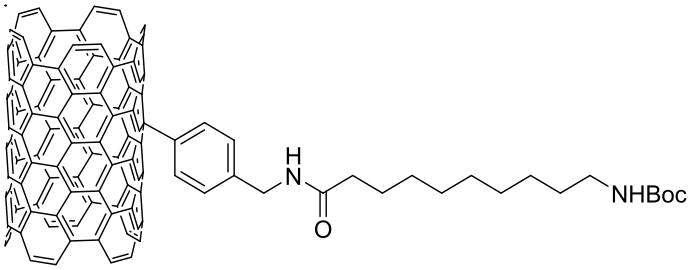

The same experimental procedure as in **69** was followed. 11-((Tert-butoxycarbonyl)amino)undecanoic acid (**65**) (0.050 g, 0.17 mmol), EDC·HCl (0.026 g, 0.17 mmol) and HOBt (0.027 g, 0.20 mmol) were used in the activation of the amino acid. The amino acid solution was added to functionalised SWNT **63** (0.050 g) and the reaction mixture stirred for 48 h. The isolated product yielded 53 mg of material.

IR (solid): ν (cm^{-1}) 3500, 2911, 1699, 1647, 1151.
Raman: ν (cm^{-1}) 177, 1333, 1582, 2658.

71. Ox- ethylenediamine SWNT

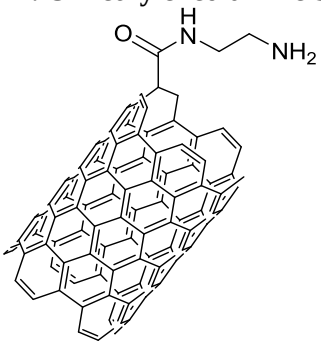

The deprotection of product **71** was conducted in the same way as in **63**. Shortly, product **66** was dispersed in DMF before the addition of conc. HCl (3.28 mL) to a 4 M final concentration. The dispersion was stirred at room temperature overnight. The suspension of SWNT was centrifuged for 30 min at 3000 rcf, the supernatant removed, the solid re-suspended and filtered through a 0.2 μm membrane. The residue was washed with DMF and methanol. After drying in the oven overnight 32 mg of material were obtained.

IR (solid): ν (cm^{-1}) 3264, 1705, 1519.
Raman: ν (cm^{-1}) 277, 1343, 1583, 2660.
Kaiser test: 0.19 mmol/g.

72. Ox-hexylenediamine SWNT

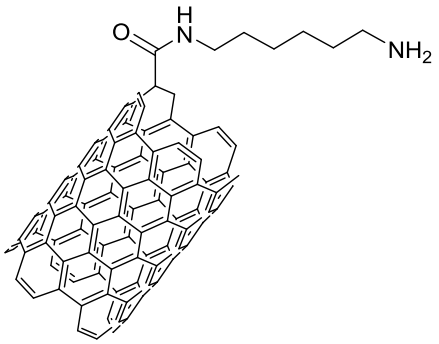

The experimental procedure followed was the same as in **71**. Functionalised nanotubes **67** were stirred at room temperature overnight in a solution of 4 M HCl in DMF. The dried product yielded 40 mg of material.

IR (solid): ν (cm^{-1}) 3220, 1711, 1067.
Raman: ν (cm^{-1}) 181, 1344, 1585, 2670.
Kaiser test: 0.23 mmol/g.

73. Ox- pegdiamine SWNT

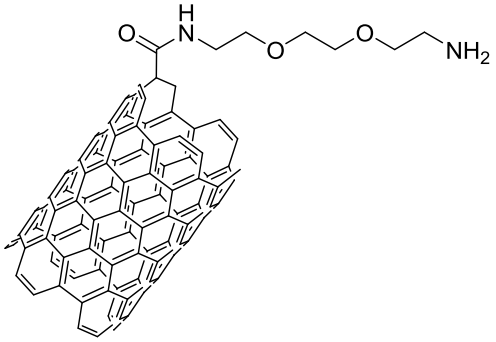

The experimental procedure followed was the same as in **71**. Functionalised nanotubes **68** were stirred at room temperature overnight in a solution of 4 M HCl in DMF. The dried product yielded 34 mg of material.

IR (solid): ν (cm^{-1}) 3106, 1863, 1699, 1586, 1006.
Raman: ν (cm^{-1}) 198, 1345, 1587, 2674.
Kaiser test: 0.17 mmol/g.

74. Bz-hexylaa SWNT

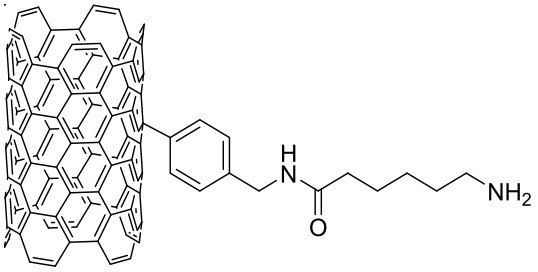

The same experimental procedure as in **71** was followed. Functionalised nanotubes **69** were dispersed in HCl 4 M in DMF (10 mL) and stirred overnight at room temperature. The isolated product yielded 42 mg of material.

IR (solid): ν (cm^{-1}) 3300, 1696, 1041.

Raman: ν (cm^{-1}) 166, 1334, 1580, 2653.

Kaiser test: 0.25 mmol/g.

75. Bz-undecaa SWNT

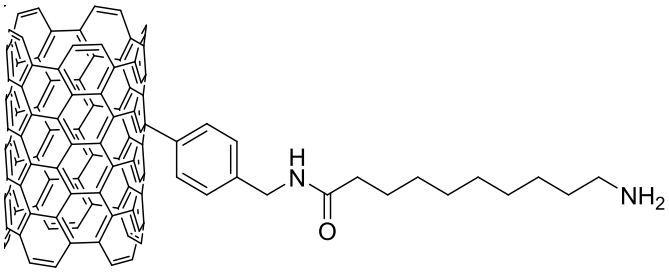

The same experimental procedure as in **71** was followed. Isolated material 52 mg.

IR (solid): ν (cm^{-1}) 3367, 2889, 1672, 1062.

Raman: ν (cm^{-1}) 166, 1336, 1580, 2653.

Kaiser test: 0.24 mmol/g.

76. Ox-ethylenediamine-COOH SWNT[17]

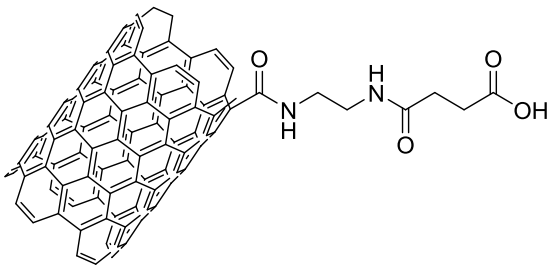

Ethylenediamine-functionalised SWNT (**71**) (20 mg) were dispersed in 15 mL dry THF by 30 min. sonication. Succinic anhydride (40 mg, 0.40 mmol), DMAP (0.049 g, 0.40 mmol) and triethylamine

(0.040 g, 0.04 mmol) were added to the mixture and the solution stirred at room temperature for 24 h. The dispersion was centrifuged at 3000 rcf for 20 min., the supernatant discarded and the residue re-suspended in water and filtered through a 0.2 μm membrane. The solid was washed with water, 1 M HCl aq. and methanol. The product was dried in the oven yielding 18 mg of material.

IR (solid): ν (cm^{-1}) 3257, 2900, 1695, 1624, 1042.
Raman: ν (cm^{-1}) 188, 1352, 1570, 2670, 3139.
TGA, mass loss at 500 ºC: 21.7%.

77. Ox-hexylenediamine-COOH SWNT

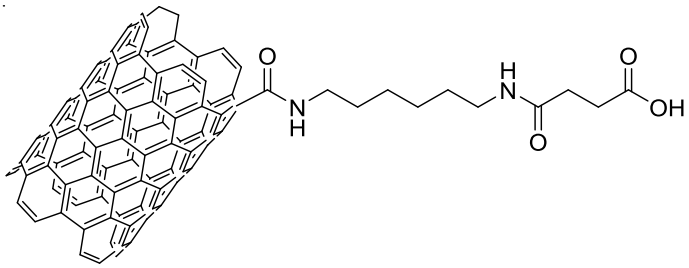

The same experimental procedure as in **76** was followed. Hexamethylenediamine-functionalised SWNT (**72**) (20 mg) were dispersed in dry THF (15 mL) and succinic anhydride (40 mg, 0.40 mmol), DMAP (0.049 g, 0.40 mmol) and triethylamine (0.040 g, 0.04 mmol) added. The dried product yielded 16 mg of material.

IR (solid): ν (cm^{-1}) 3200, 1705, 1702, 1050.
Raman: ν (cm^{-1}) 171, 1339, 1574, 2680, 3146.
TGA, mass loss at 500 ºC: 22.0%.

78. Ox- pegdiamine-COOH SWNT

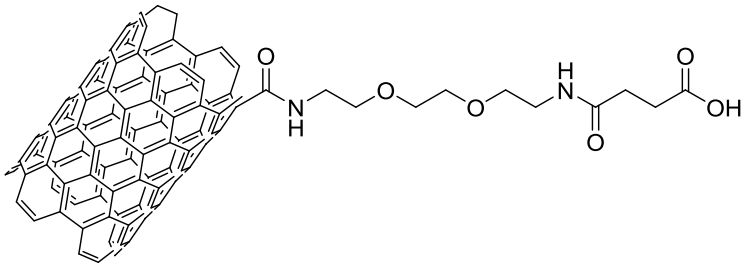

The same experimental procedure as in **76** was followed. 2,2′-(Ethylenedioxy)bis(ethylamine)-functionalised SWNT (**73**) (20 mg) were dispersed in dry THF (15 mL) and succinic anhydride (40 mg, 0.40 mmol), DMAP (0.048 g, 0.40 mmol) and triethylamine (0.040 g, 0.04 mmol) added. The dried product yielded 16 mg of material.

IR (solid): ν (cm^{-1}) 1705, 1634, 1521.

Raman: ν (cm^{-1}) 167, 1334, 1571, 2641, 3145.

TGA, mass loss at 500 ºC: 28.2%.

79. Bz-hexylaa-COOH SWNT

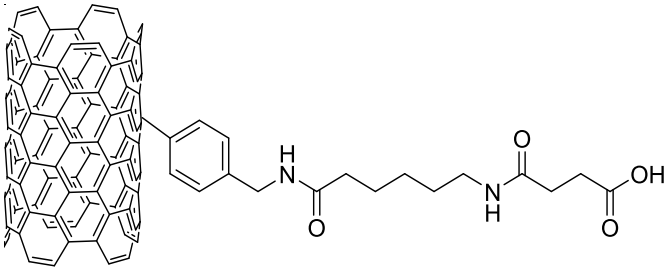

The same experimental procedure as in **76** was followed. Functionalised SWNT **74** (20 mg) were dispersed in dry THF (15 mL) and succinic anhydride (40 mg, 0.40 mmol), DMAP (0.048 g, 0.40 mmol) and triethylamine (0.040 g, 0.040 mmol) added. The dried product yielded 15.4 mg of material.

IR (solid): ν (cm^{-1}) 3254, 1700, 1001.

Raman: ν (cm^{-1}) 183, 1331, 1573, 2656, 3167.

TGA, mass loss at 500 ºC: 17.3%.

80. Bz-Boc-undecaa SWNT

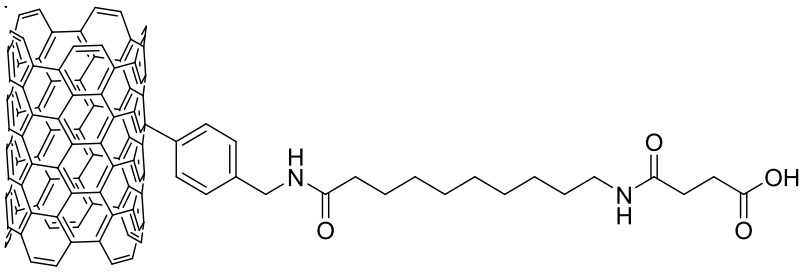

The same experimental procedure as in **76** was followed. Functionalised SWNT **75** (20 mg) were dispersed in dry THF (15 mL) and succinic anhydride (40 mg, 0.40 mmol), DMAP (0.048 g, 0.40 mmol) and triethylamine (0.040 g, 0.04 mmol) added. The dried product yielded 19 mg of material.

IR (solid): ν (cm^{-1}) 3200, 1685, 1644, 1050.

Raman: ν (cm^{-1}) 165, 1337, 1578, 2663, 3164.

TGA, mass loss at 500 ºC: 19.6%.

81. Graphene oxide (GO)

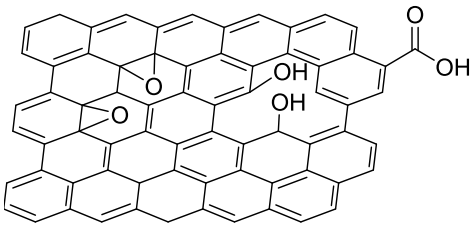

Graphene oxide was prepared by Dr Boyang Mao following a procedure reported in the literature from graphite powder converted in graphite oxide following a modified Hummers method.[18] Shortly, graphite powder and sodium nitrate were stirred in sulphuric acid. The mixture was cooled to 0 ºC, potassium permanganate added and the temperature allowed to rise to room temperature to be diluted with water. Hydrogen peroxide was added to the dispersion and the suspension was filtered through a 0.2 µm polycarbonate membrane. A dialysis process was used to remove any remaining salts before further filtering, washing and drying the resulting graphite oxide. Graphene oxide was subsequently prepared by sonication cycles. The non-dispersed material was removed by centrifugation.

IR (solid): ν (cm^{-1}) 3200, 1718, 1620, 1177, 1043.

Raman: ν (cm^{-1}) 1350, 1604.

82. GO-PEG-NHBoc

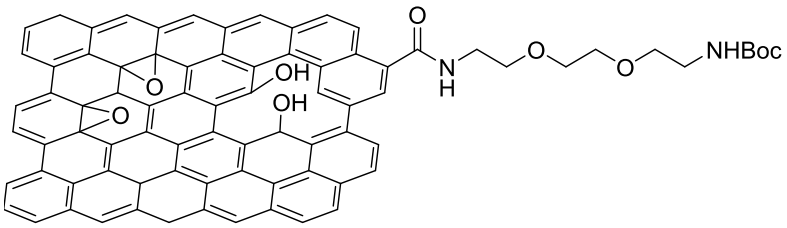

Graphene oxide (56 mg) was dispersed in DMF by 5 min sonication. EDC·HCl (0.100 g, 0.60 mmol), HOBt (0.104 g, 0.77 mmol) followed by protected amine **3** (0.191 g, 0.77 mmol). The reaction mixture was stirred at room temperature for 48 h. The resulting suspension was filtered through a 0.2 µm polycarbonate membrane and washed with DMF and MeOH. The solid was dried at 60 ºC. The product was obtained as a black solid (60 mg).

IR (solid): ν (cm^{-1}) 3544, 3130, 1698, 1573, 1002.

Raman: ν (cm^{-1}) 1345, 1580.

83. GO-PEG-NH_2

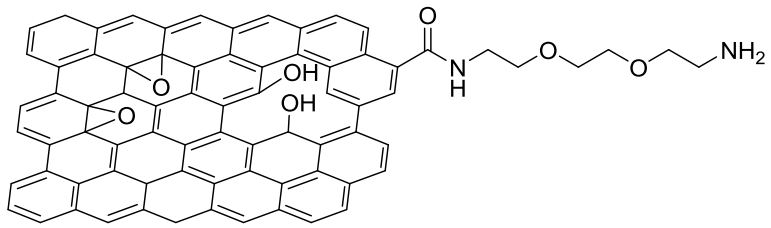

Product **82** was dispersed in a solution of HCl 4 M in DMF and stirred at room temperature during 16 h. The resulting suspension was filtered through a 0.2 µm membrane and washed with DMF. The solid was re-suspended by sonication, filtered and washed with a large amount of water until the pH of the filtrate was neutral. The solid was further washed with methanol and dried under vacuum and at 60 ºC. The product was obtained as a black solid (46 mg).

IR (solid): ν (cm^{-1}) 3200, 1708, 1618 1350, 1235.

Raman: ν (cm^{-1}) 1379, 1580.

Kaiser test: 0.03 mmol/g.

84. GO-PEG-COOH

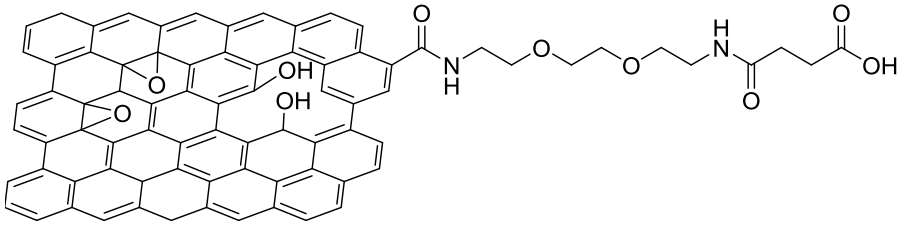

Product **83** (30 mg) was dispersed in a 5:1 mixture of dry DMF and dry THF. Succinic anhydride (0.060 g, 0.60 mmol), triethylamine (83 µL, 0.60 mmol) and DMAP (0.073 g, 0.60 mmol) were added and the reaction mixture was stirred for 24 h at room temperature. The reaction mixture was filtered through a 0.2 µm membrane and washed with THF, DMF and methanol. The product was dried under vacuum and in the oven at 60 ºC. The product was isolated as a black solid (27 mg).

IR (solid): ν (cm^{-1}) 3230, 1708, 1643, 1561, 1348, 1214.

Raman: ν (cm^{-1}) 1349, 1582.

85. Bombesin [7-13] (L-glutaminyl-L-tryptophyl-L-alanyl-L-valylglycyl-L-histidyl-L-leucine)

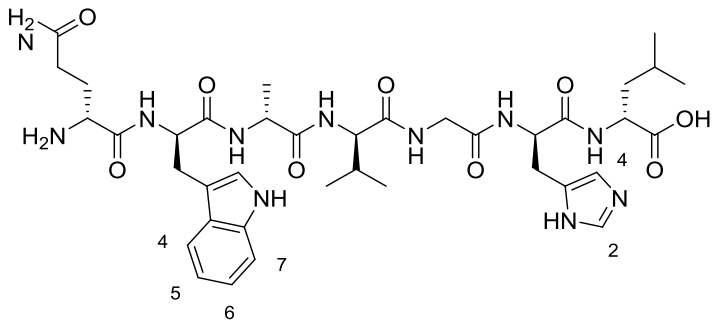

The [7-13] fragment of bombesin was synthesised by SPPS using a Biotage Initiator 2.5 microwave reactor and a rink amide resin as a solid support (1.011 g, 0.60 mmol). First, the resin was swelled in dichloromethane and DMF. The deprotection of the resin was carried out in piperidine/DMF 1:4 in three cycles heating at 75 ºC for 10 minutes, 3 minutes and 3 minutes. The resin was washed between steps with dichloromethane and DMF. The coupling steps were carried out with an excess of the amino acid (1.79 mmol, 3 eq.), HATU (1.79 mmol, 3 eq.), HOBt (1.79 mmol, 3 eq.) in DIPEA (4.18 mmol, 7 eq.) and DMF (5 mL). The reaction mixture, once homogenised, was heated at 75 ºC for 10 minutes except in the case of His that was coupled at room temperature for 2 h. The deprotection after each coupling step was carried out in piperidine/DMF heating at 75 ºC for 10 minutes. The resin was washed with dichloromethane and DMF after each coupling and deprotection step and the efficiency of the coupling assessed by the Kaiser test using some resin beads. Finally, the cleavage of the peptide from the resin was performed using a cleavage cocktail containing TFA/phenol/H_2O/TIPS (88:5:5:2). The reaction mixture was stirred for 2.5 h at room temperature and the peptide precipitated in cold diethyl ether and dried. The crude was purified by automated flash column chromatography using a C18 cartridge (method C) and lyophilised from acetic acid to yield a white solid.

^{1}H NMR (500 MHz, D_2O, 25 ºC): δ 8.51 (brs, 1H, H-2, His), 7.64 (d, ^3J = 7.9 Hz, 1H, H-7, Trp), 7.51 (d, ^3J = 8.2 Hz, 1H, H-4, Trp), 7.29 – 7.24 (m, 1H, H-5, Trp), 7.20 (brs, 1H, H-4, His), 7.17 (t, ^3J = 7.6 Hz, 1H, H-6, Trp), 4.72 (t, ^3J = 7.1 Hz, 1H, αC*H*, His), 4.65 (t, ^3J = 7.2 Hz, 1H, αC*H*, Trp), 4.35 – 4.25 (m, 2H, αC*H*, Ala, Leu), 4.02 (t, ^3J = 6.7 Hz, 1H, αC*H*, Gln), 3.99 – 3.89 (m, 3H, CH_2 Gly, αC*H* Val), 3.36 – 3.20 (m, 2H, βCH_2, His), 3.20 – 3.11 (m, 2H, βCH_2, Trp), 2.40 (t, ^3J = 7.5 Hz, 2H, γCH_2, Gln), 2.18 – 2.07 (m, 2H, βCH_2, Gln), 2.05 – 1.98 (m, 1H, βC*H*, Val), 1.70 – 1.61 (m, 1H, βCH_2, γC*H*, Leu), 1.62 – 1.53 (m, 2H, βCH_2, γC*H*, Leu), 1.30 (d, ^3J = 7.2 Hz, 3H, CH_3,Ala), 0.97 (d, ^3J = 6.7 Hz, 3H, CH_3,Val), 0.95 (d, ^3J = 6.7 Hz, 3H, CH_3', Val), 0.92 (d, ^3J = 5.7 Hz, 3H, CH_3, Leu), 0.86 (d, ^3J = 5.7 Hz, 3H, CH_3', Leu).

HPLC (Method B): Rt (min) 6.80.

Mass spectrum: ESI-MS calc. for $C_{38}H_{55}N_{11}NaO_9$ $[M+Na]^+$: 831.4004; found: 831.4242.

86. (2-((((9H-fluoren-9-yl)methoxy)carbonyl)amino)-5-(4-(5,5-difluoro-1,3,7,9-tetramethyl-5H-4l4,5l4-dipyrrolo[1,2-c:2',1'-f][1,3,2]diazaborinin-10-yl)benzamido)pentanoyl)-L-glutaminyl-L-tryptophyl-L-alanyl-L-valylglycyl-L-histidyl-L-leucine

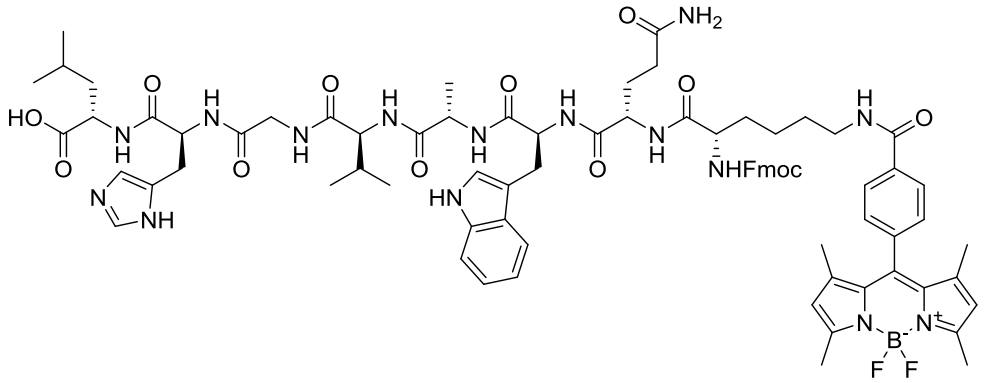

BODIPY **57** (46 mg, 65 µmol) was dissolved in DMF (0.5 mL) and DIPEA (15 µL, 86 µmol) added followed by pyBOP (39 mg, 75 µmol). The reaction mixture was stirred at room temperature for 2 h and [7-13]-bombesin (17 mg, 22 µmol) dissolved in 0.5 mL DMF, added. The temperature was raised to 60 ºC and the reaction stirred for 20 h. The crude was purified by semi-preparative HPLC using method C. The product was obtained as a red solid (14 mg, 44%).

HPLC (Method B): Rt (min) 8.76.

Mass spectrum: ESI-MS calc. for $C_{79}H_{93}BF_2N_{15}O_{13}$ $[M+H]^+$: 1509.7217; found: 1509.7361.

87. N6-(4-(5,5-difluoro-1,3,7,9-tetramethyl-5H-4l4,5l4-dipyrrolo[1,2-c:2',1'-f][1,3,2]diazaborinin-10-yl)benzoyl)-L-lysyl-L-glutaminyl-L-tryptophyl-L-alanyl-L-valylglycyl-L-histidyl-L-leucine.

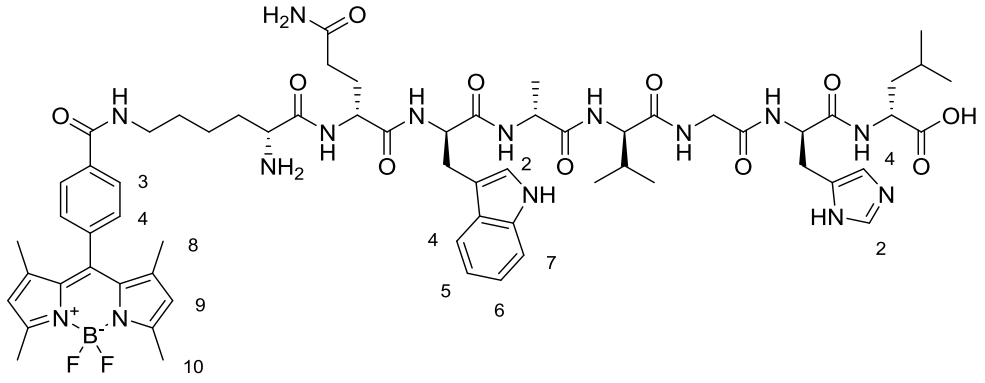

Compound **86** (19 mg, 12 µmol) was dissolved in piperidine/DMF 1:4 (total volume: 2 mL) and the reaction mixture stirred at room temperature for 1 h until the reaction was completed as confirmed by HPLC. The reaction mixture was washed with hexane and the DMF crude purified by semi-preparative HPLC (method C). The product was obtained as a red powder (16 mg, quant.).

^{1}H NMR (500 MHz, CD_3OD, 25 ºC): δ 8.73 (d, ^4J = 1.4 Hz, 1H, H-2 His), 8.02 (d, ^3J = 8.4 Hz, 2H, H-3 BD), 7.56 (dt, $^{3,4}J$ = 7.9, 1.0 Hz, 1H, H-7 Trp), 7.46 – 7.43 (m, 2H, H-4 BD), 7.34 – 7.32 (m, 1H, H-4

His), 7.30 (dt, $^{3,4}J$ = 8.1, 0.9 Hz, 1H, H-4 Trp), 7.21 (s, 1H, H-2 Trp), 7.05 (ddd, $^{3,3,4}J$ = 8.1, 7.0, 1.2 Hz, 1H, H-5 Trp), 6.97 (ddd, $^{3,3,4}J$ = 8.1, 7.0, 1.1 Hz, 1H, H-6 Trp), 6.09 (s, 2H, H-9), 4.68 (dd, $^{3,3}J$ = 7.4, 5.5 Hz, 2H, $^{\alpha}$CH His, Trp), 4.43 – 4.33 (m, 3H, $^{\alpha}$CH Gln, Ala, Leu), 4.00 (d, ^{3}J = 7.3 Hz, 1H, $^{\alpha}$CH Val), 3.90 (d, ^{2}J = 16.8 Hz, 1H, Gly), 3.85 (t, ^{3}J = 6.6 Hz, 1H, $^{\alpha}$CH Lys), 3.79 (d, ^{2}J = 16.8 Hz, 1H, Gly), 3.41 – 3.35 (m, 2H, $^{\varepsilon}$CH$_2$ Lys), 3.22 – 3.09 (m, 2H, $^{\beta}$CH, His, Trp), 2.49 (s, 6H, H-8 BD), 2.30 (t, ^{3}J = 7.6 Hz, 2H, $^{\gamma}$CH$_2$ Gln), 2.09 – 1.95 (m, 2H, $^{\beta}$CH$_2$ Gln), 1.86 – 1.76 (m, 2H, $^{\beta}$CH$_2$ Lys), 1.73 – 1.65 (m, 1H, $^{\gamma}$CH Leu), 1.64 – 1.55 (m, 3H, $^{\delta}$CH$_2$ Lys, $^{\beta}$CH Leu), 1.49 – 1.38 (m, 2H, $^{\gamma}$CH$_2$ Lys), 1.39 (s, 6H, H-10 BD), 1.26 (d, ^{3}J = 7.1 Hz, 3H, CH_3 Ala), 0.98 – 0.95 (m, 6H, iPr Val). 0.94 (d, ^{3}J = 6.5 Hz, 3H, CH_3 Leu), 0.91 (d, ^{3}J = 6.4 Hz, 3H, CH_3' Leu).

Mass spectrum: ESI-MS calc. for $C_{64}H_{84}BF_2N_{15}O_{11}$ $[M+H]^+$: 1287.6536; found: 1287.6445.

HPLC (Method A): Rt (min) 7.33.

88. BOD-SWNT

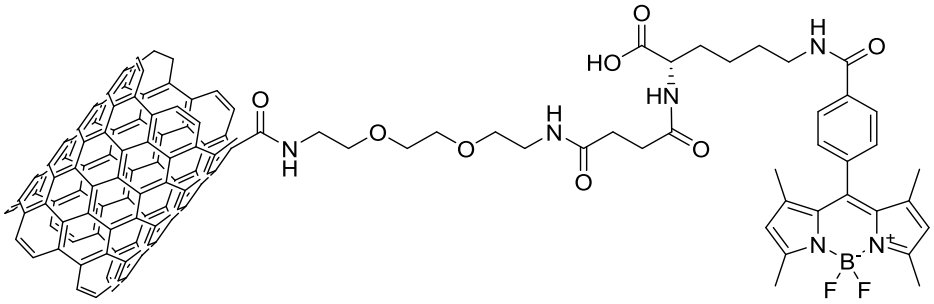

Functionalised SWNT **78** (3 mg) were dispersed in DMF (1.5 mL) and DIPEA (25 µL) by sonication for 15 min. PyBOP (21 mg, 40 µmol) was added and the reaction mixture stirred at room temperature for 4 h. The dispersion was filtered through a 0.2 µm polycarbonate membrane to remove excess of pyBOP and re-suspended in DMF (1.5 mL). BODIPY **58** (4 mg, 8 µmol) was added to the dispersion dissolved in DMF (0.5 mL) and the reaction mixture stirred at room tempereature for 48 h. The suspension was centrifuged for 10 min at 14,000 rpm, the supernatant removed, the solid residue re-suspended in MeOH, sonicated for 3 min and the process repeated several times. The dispersion was filtered through a 0.2 µm membrane, washed with DMF, MeOH, re-suspended in MeOH, sonicated for 3 min and filtered again. This process was repeated at least 4 times. In the last step, the solid was left drying under vacuum. The product was obtained as a black solid (4 mg).

IR (solid): ν (cm^{-1}) 3286, 2949, 1713, 1643, 1022.

Raman: ν (cm^{-1}) 137, 1336, 1574, 2652.

89. BOD-BBN-SWNT

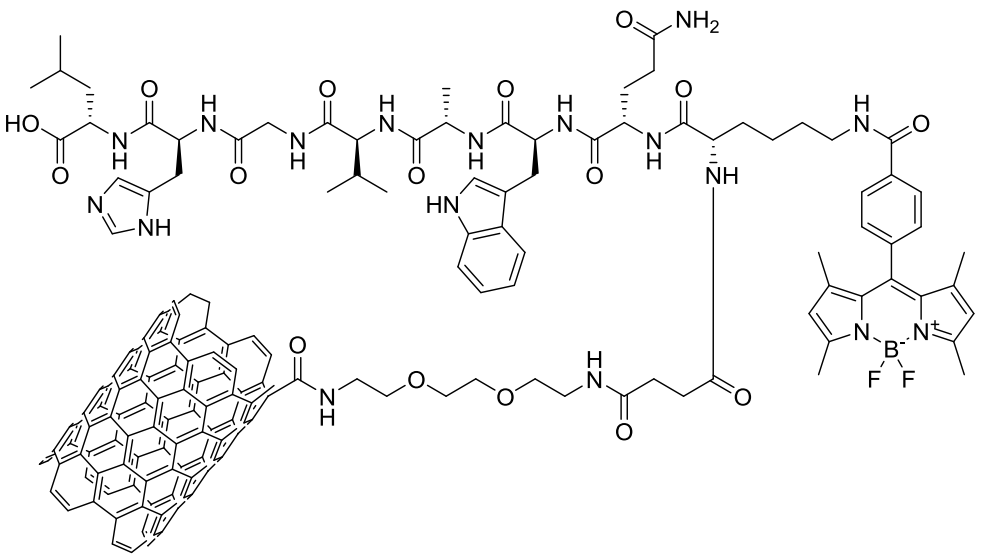

Nanoprobe **89** was prepared following the experimental procedure of **88**. Functionalised SWNT **78** (3 mg) were dispersed in DMF (1.5 mL) and DIPEA (25 µL). PyBOP (6 mg, 12 µmol) was added and the reaction mixture stirred at room temperature for 4 h. After removing the excess of pyBOP, conjugate **87** (3 mg, 2 µmol) was added. The product was obtained as black solid (5 mg).

IR (solid): ν (cm^{-1}) 3299, 2948, 1713, 1638, 1032.

Raman: ν (cm^{-1}) 149, 1339, 1579, 2660.

90. BOD-BBN-SWNT 2

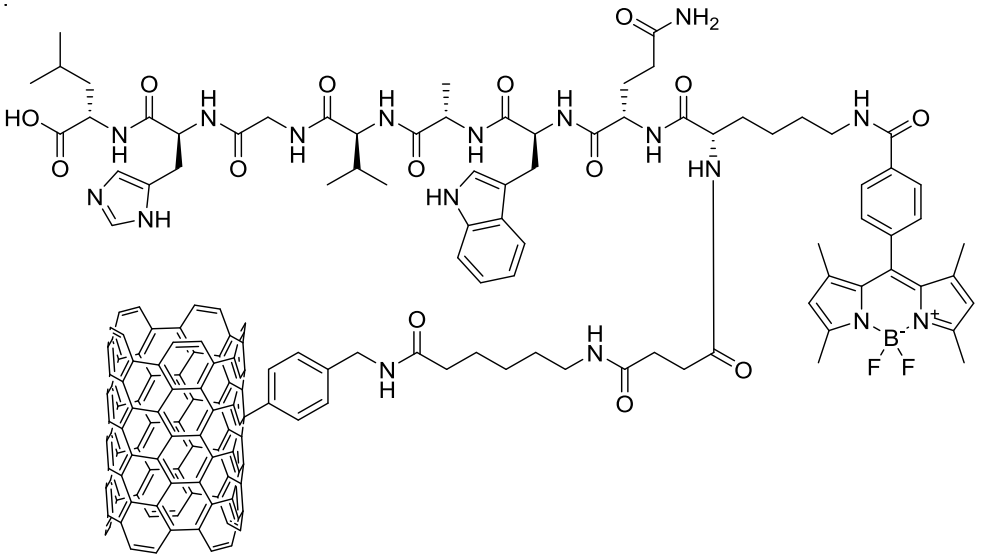

Nanoprobe **90** was prepared following the experimental procedure of **88**. Functionalised SWNT **79** (4 mg) were dispersed in DMF and DIPEA (25 µL) by sonication. PyBOP (6 mg, 12 µmol) added and

the reaction mixture stirred for 4 h. The excess of pyBOP was removed by filtration and conjugate **87** (3 mg, 2 µmol) was added. The product was obtained as a black solid (4 mg).

IR (solid): ν (cm^{-1}) 3356, 2947, 1643, 1032.

Raman: ν (cm^{-1}) 183, 1333, 1575, 2651.

91. SWNT Ga(III)BTSC

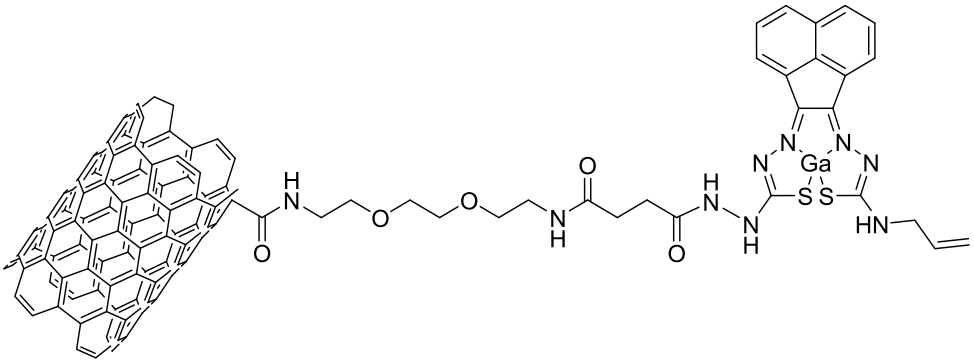

Nanoprobe **91** was prepared in a similar way as **88**. Functionalised SWNT **78** (5 mg) and DIPEA (25 µL) were dispersed in DMF (1 mL) by sonication. PyBOP (37.4 mg, 72 µmol) was added and the reaction mixture stirred at room temperature for 2 h. Gallium complex **23** (7 mg, 14 µmol) was added to the reaction mixture dissolved in DMF (1 mL) and the reaction mixture stirred at room temperature for 48 h. The product was obtained as a black solid (3 mg).

Raman: ν (cm^{-1}) 167, 1340, 1573, 2660.

92. GO-PEG-BOD

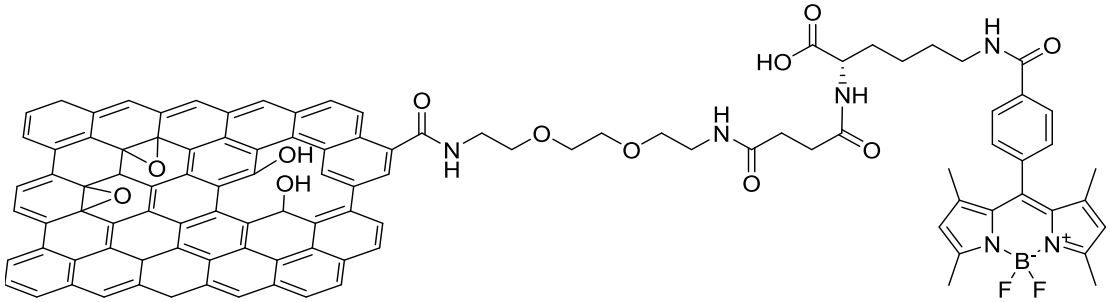

Graphene oxide derivative **84** (4 mg) and DIPEA (25 µL) were suspended in DMF and the mixture homogenised by sonication for 3 min. PyBOP (0.026 g, 50 µmol) was added and the reaction mixture stirred at room temperature for 4 h. BODIPY **58** (5 mg, 10 µmol) was added and the resulting suspension was stirred at room temperature for 48 h. The excess of fluorophore was removed by various cycles of centrifugation at 10,000 rpm for 15 min and washing with DMF. The solid was then re-suspended in DMF and filtered through a 0.2 µm membrane to be washed with DMF and MeOH before being dried

under vacuum. The product was obtained as a black solid (1 mg).

IR (solid): ν (cm^{-1}) 3200, 1721, 1619, 1353, 1062.
Raman: ν (cm^{-1}) 1354, 1589.

93. GO-PEG-BOD-BBN

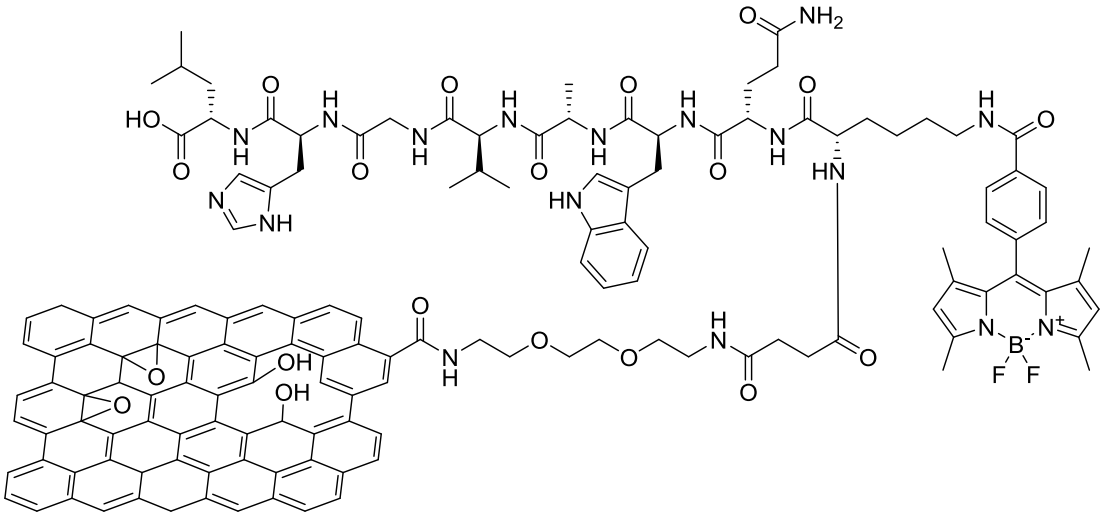

Graphene oxide derivative **84** (3 mg) and DIPEA (25 µL) were suspended in DMF and the mixture homogenised by sonication for 3 min. PyBOP (0.010 g, 19 µmol) was added and the reaction mixture stirred at room temperature for 4 h. Conjugate **87** (3 mg, 2 µmol) was added and the resulting suspension was stirred at room temperature for 48 h. The excess of conjugate was removed by various cycles of centrifugation at 10,000 rpm for 15 min and washing with DMF. The solid was then re-suspended in DMF and filtered through a 0.2 µm membrane to be washed with DMF and MeOH before being dried under vacuum. The product was obtained as a black solid (1 mg).

IR (solid): ν (cm^{-1}) 3200, 1618, 1354, 1218, 1062.
Raman: ν (cm^{-1}) 1347, 1586.

94. GO-PEG-Ga(III)BTSC

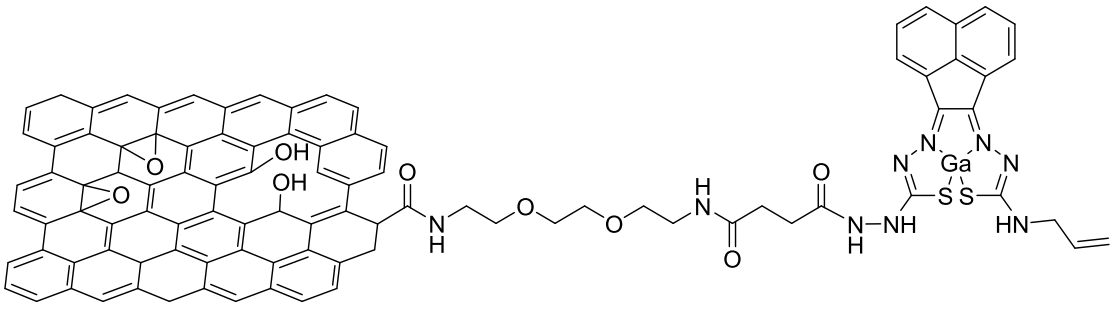

Graphene oxide derivative **84** (4 mg) and DIPEA (25 µL) were suspended in DMF and the mixture

homogenised by sonication for 3 min. PyBOP (0.026 g, 51 μmol) was added and the reaction mixture stirred at room temperature for 4 h. Ga(III) bis(thiosemicarbazonato) complex **23** (5 mg, 10 μmol) was added and the resulting suspension was stirred at room temperature for 48 h. The excess of complex was removed by various cycles of centrifugation at 10,000 rpm for 15 min and washing with DMF. The solid was then re-suspended in DMF and filtered through a 0.2 μm membrane to be washed with DMF and MeOH before being dried under vacuum. The product was obtained as a black solid (4 mg).

IR (solid): ν (cm^{-1}) 3200, 1711, 1646, 1386, 1060.
Raman: ν (cm^{-1}) 1352, 1586.

7.3 References

1. G. Sheldrick, *Acta Crystallographica Section C*, 2015, **71**, 3-8.
2. C. B. Hubschle, G. M. Sheldrick and B. Dittrich, *J. Appl. Crystallogr.*, 2011, **44**, 1281-1284.
3. L. Farrugia, *J. Appl. Crystallogr.*, 1997, **30**, 565.
4. M. A. Cinelli, B. Cordero, T. S. Dexheimer, Y. Pommier and M. Cushman, *Biorg. Med. Chem.*, 2009, **17**, 7145-7155.
5. L. A. Howell, R. Gulam, A. Mueller, M. A. O'Connell and M. Searcey, *Bioorg. Med. Chem. Lett.*, 2010, **20**, 6956-6959.
6. R. N. Zuckermann, E. J. Martin, D. C. Spellmeyer, G. B. Stauber, K. R. Shoemaker, J. M. Kerr, G. M. Figliozzi, D. A. Goff and M. A. Siani, *J. Med. Chem.*, 1994, **37**, 2678-2685.
7. P. D. Bonnitcha, S. R. Bayly, M. B. M. Theobald, H. M. Betts, J. S. Lewis and J. R. Dilworth, *J. Inorg. Biochem.*, 2010, **104**, 126-135.
8. S. C. Dakdouki, D. Villemin and N. Bar, *Eur. J. Org. Chem.*, 2011, **2011**, 4448-4454.
9. J. C. Garcia-Ramos, Y. Toledano-Magana, L. G. Talavera-Contreras, M. Flores-Alamo, V. Ramirez-Delgado, E. Morales-Leon, L. Ortiz-Frade, A. G. Gutierrez, A. Vazquez-Aguirre, C. Mejia, J. C. Carrero, J. P. Laclette, R. Moreno-Esparza and L. Ruiz-Azuara, *Dalton Trans.*, 2012, **41**, 10164-10174.
10. G. Venkataramana, P. Dongare, L. N. Dawe, D. W. Thompson, Y. Zhao and G. J. Bodwell, *Org. Lett.*, 2011, **13**, 2240-2243.
11. A. Cui, X. Peng, J. Fan, X. Chen, Y. Wu and B. Guo, *J. Photochem. Photobiol. A: Chem.*, 2007, **186**, 85-92.
12. Y. Cen, J. N. Falco, P. Xu, D. Y. Youn and A. A. Sauve, *Org. Biomol. Chem.*, 2011, **9**, 987-993.
13. M. S. P. Shaffer, X. Fan and A. H. Windle, *Carbon*, 1998, **36**, 1603-1612.
14. L. Maggini, F. M. Toma, L. Feruglio, J. M. Malicka, T. Da Ros, N. Armaroli, M. Prato and D. Bonifazi, *Chem. Eur. J.*, 2012, **18**, 5889-5897.
15. N. Gavande, H.-L. Kim, M. R. Doddareddy, G. A. R. Johnston, M. Chebib and J. R. Hanrahan, *ACS Medicinal Chemistry Letters*, 2013, **4**, 402-407.
16. D. He, Y. Peng, H. Yang, D. Ma, Y. Wang, K. Chen, P. Chen and J. Shi, *Dyes and Pigments*, 2013, **99**, 395-401.
17. D. Iannazzo, A. Pistone, S. Galvagno, S. Ferro, L. De Luca, A. M. Monforte, T. Da Ros, C. Hadad, M. Prato and C. Pannecouque, *Carbon*, 2015, **82**, 548-561.
18. B. Mao, D. G. Calatayud, V. Mirabello, B. J. Hodges, J. A. R. Martins, S. W. Botchway, J. M. Mitchels and S. I. Pascu, *Adv. Funct. Mater.*, 2016, **26**, 687-697.

Appendices

Appendix A. NMR spectra for selected compounds

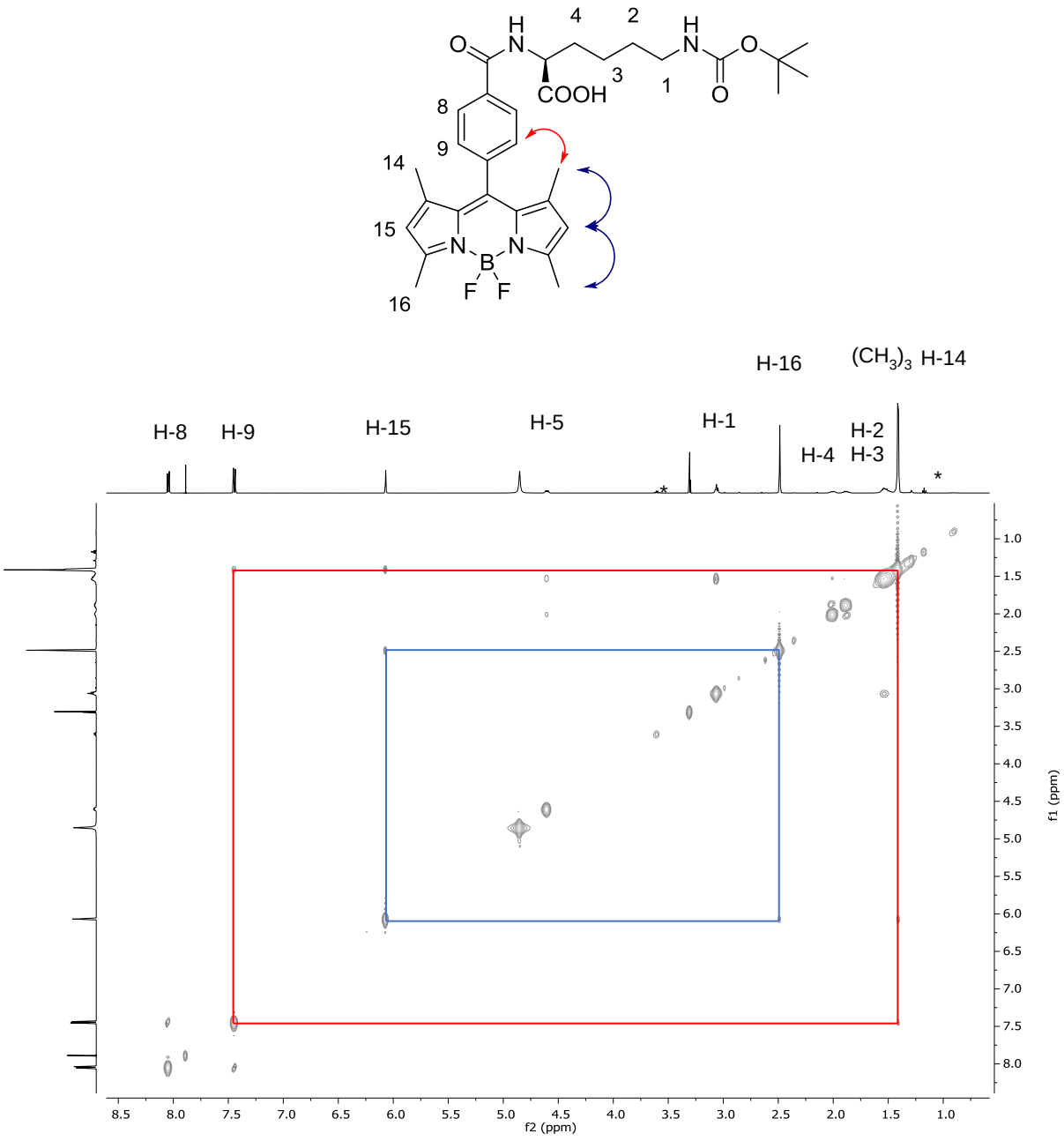

Figure 27: NOESY (CD_3OD) spectrum of **53**.

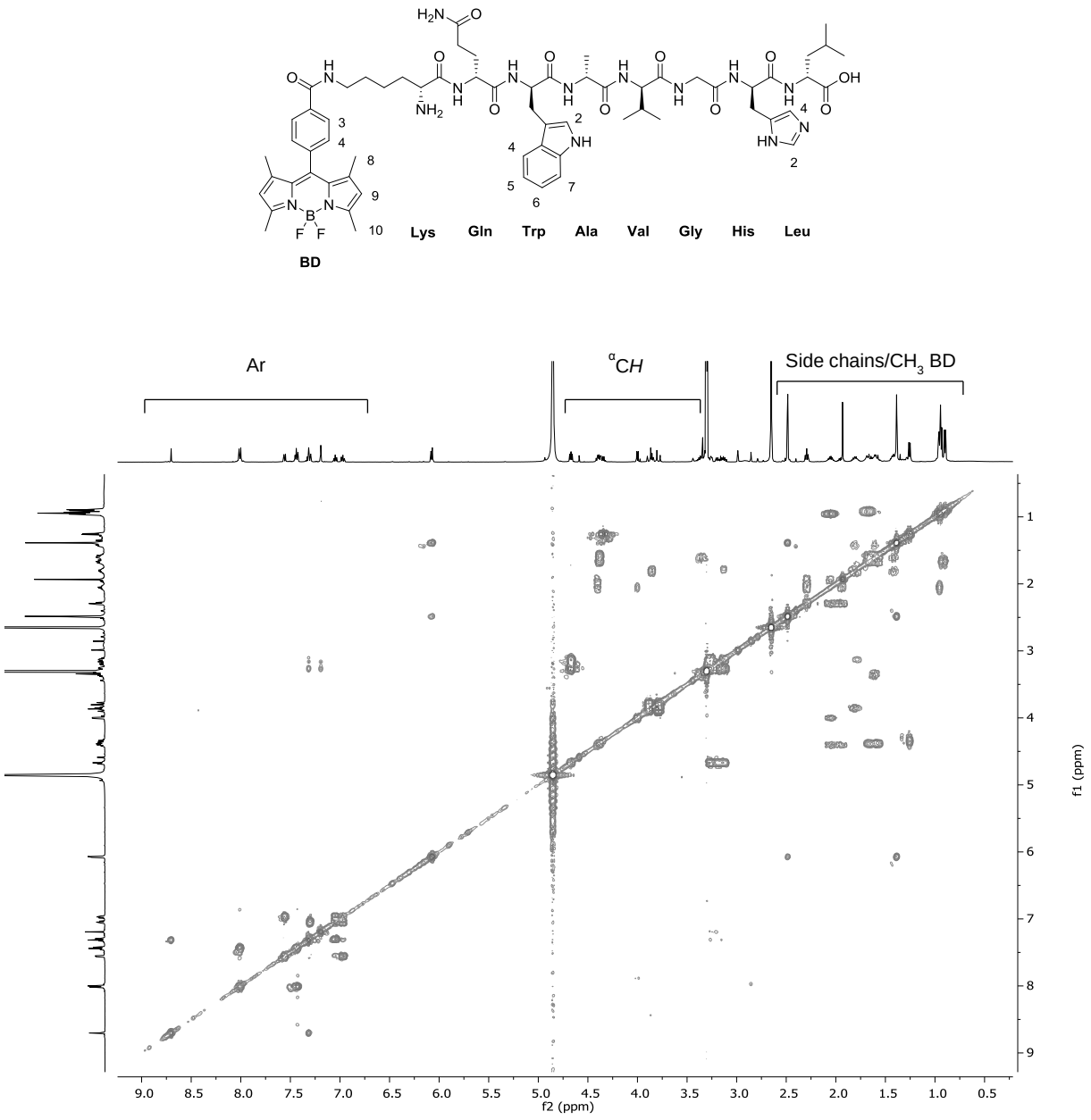

Figure 28: ^{1}H ^{1}H COSY spectrum (CD_3OD) of 87.

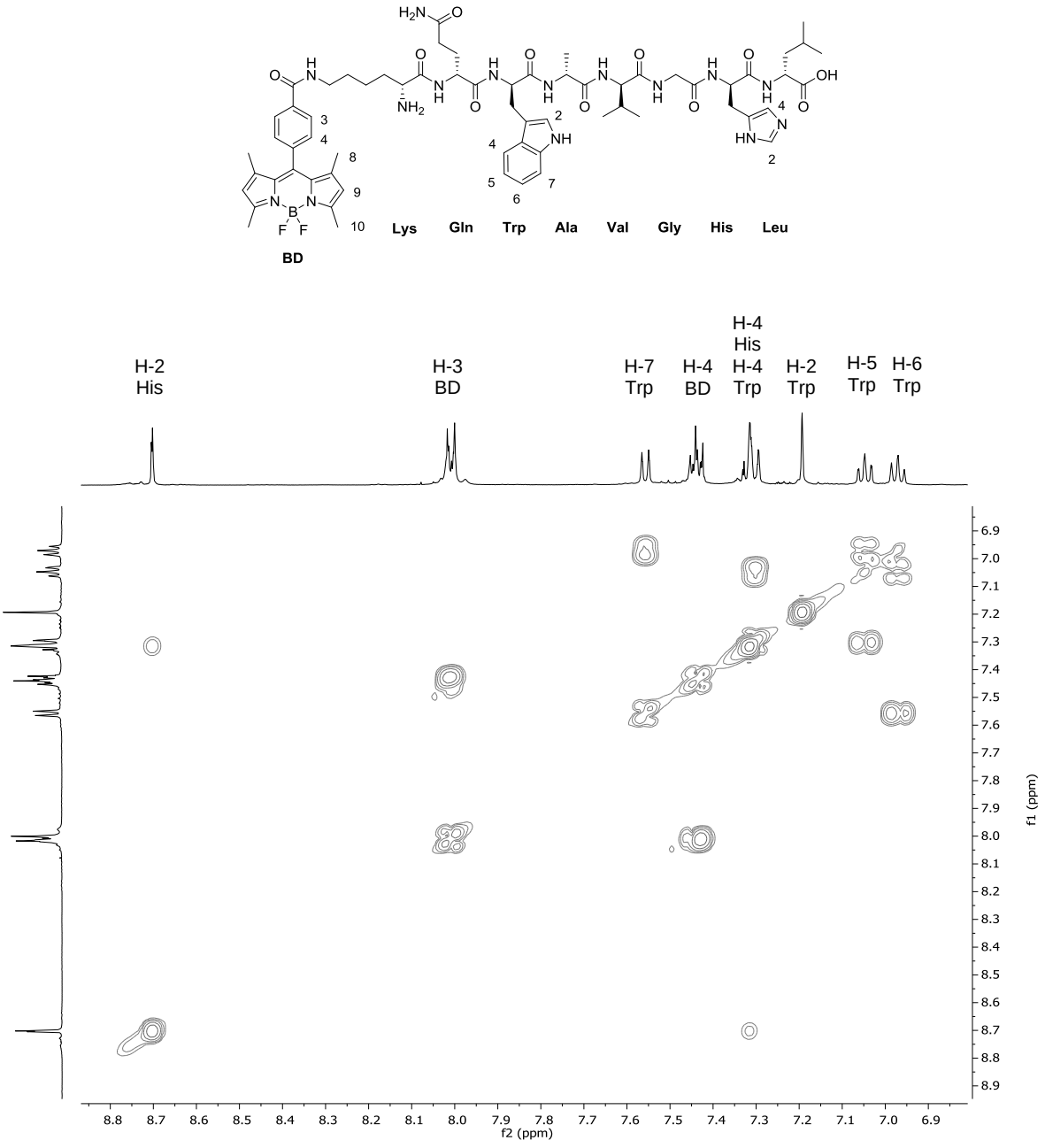

Figure 29: Aromatic region in the ^{1}H ^{1}H COSY spectrum (CD_3OD) of 87.

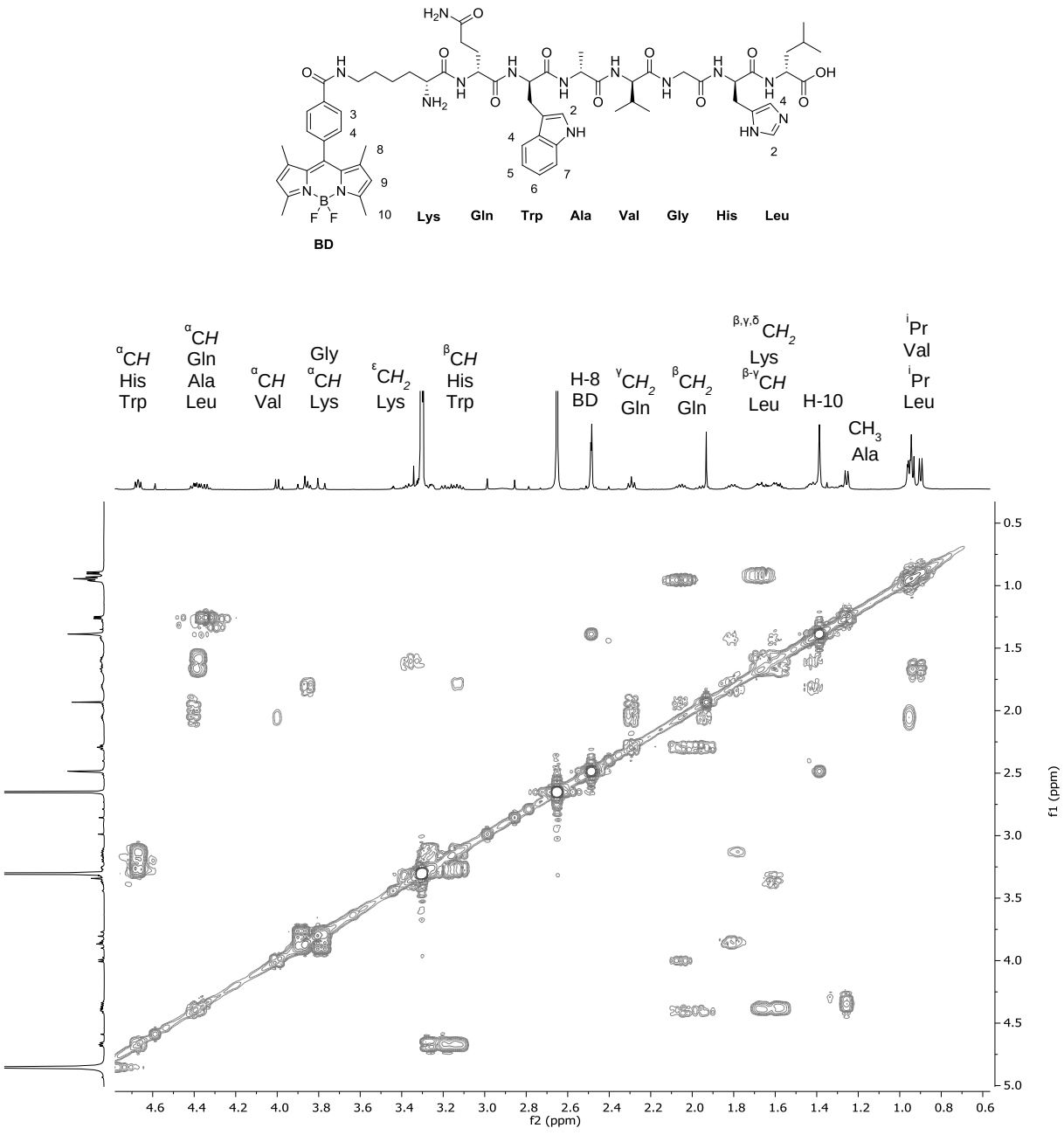

Figure 30: Aliphatic region in the ^{1}H ^{1}H COSY spectrum (CD_3OD) of 87.

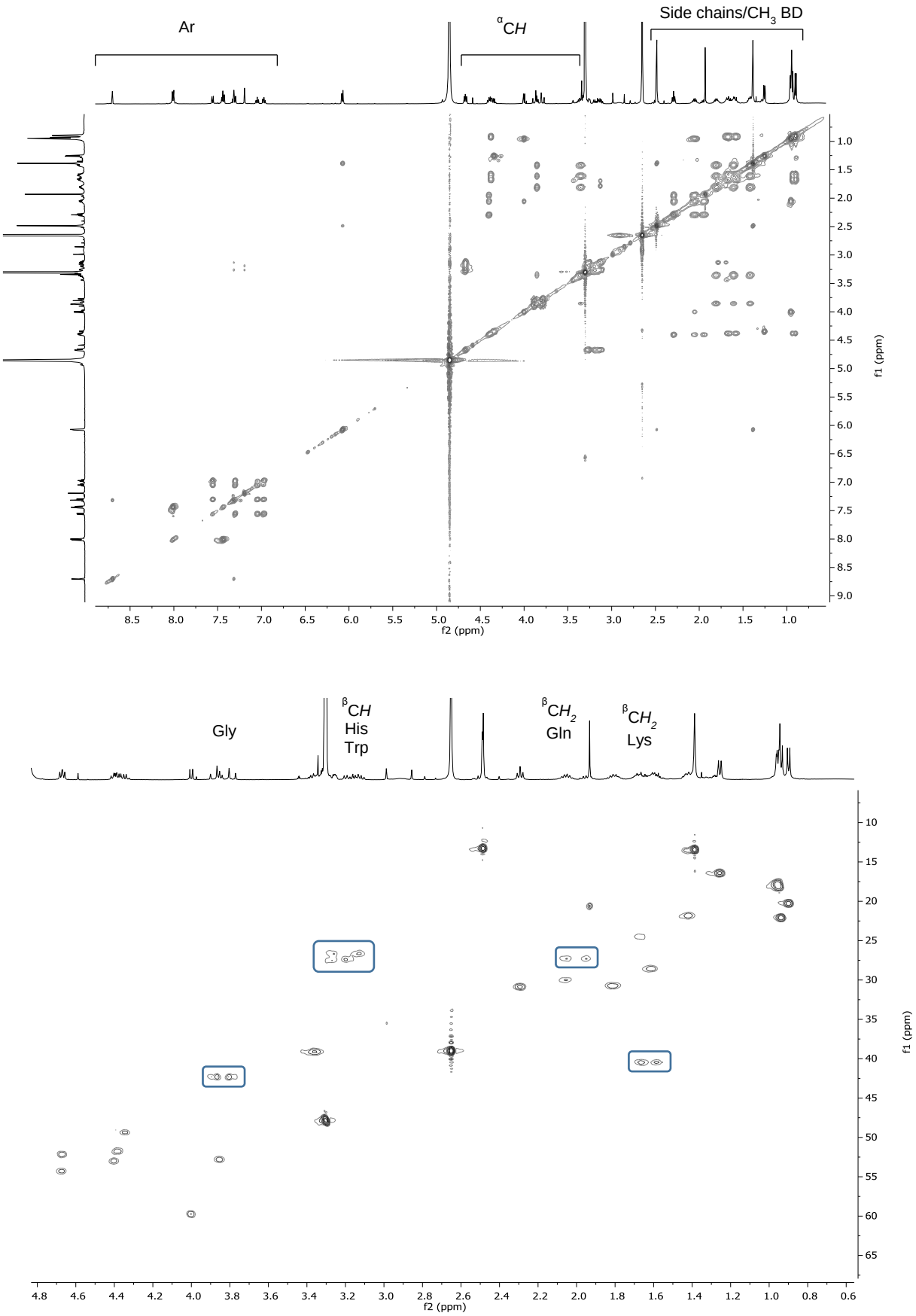

Figure 31: ^{1}H ^{1}H TOCSY spectrum (top) and ^{1}H ^{13}C HSQC spectrum (bottom) (CD_3OD) of **87**.

Appendix B. X-ray crystallography data

Intensity data for **12**, **43** and **52** were collected at 150(2) K on an Agilent SuperNova Dual, Cu at zero, EosS2 diffractometer and using monochromated Cu-Kα radiation λ = 1.54184 Å.
Intensity data for **40**, **41** and **42** were collected at 150(2) K on a Rigaku New Xcalibur, EosS2 diffractometer using graphite monochromated Mo-Kα radiation λ = 0.71073 Å.

Intensity data for **11** were collected at the National Crystallography Service (University of Southampton) at 293(2) K on a AFC-12 diffractometer equipped with a Rigaku Saturn 724 CCD detector using monochromated Mo-Kα radiation α = 0.71073 Å.

All structures were solved with SHELXT and refined by a full-matrix least-squares procedure based on F^2 (Shelxl-2014/7).[1] All non-hydrogen atoms were refined anisotropically.

Hydrogen atoms were placed onto calculated positions and refined using a riding model except for the OH hydrogen atoms which have been located in the difference Fourier map and were refined with bond lengths restraints.

Additional programmes used for analysing data and their graphical manipulation included: SHELXle[2] and ORTEP 3 for windows[3].

[1] Sheldrick, *Acta Crystallographica Section C*, 2015, **71**, 3-8.

[2] C. B. Hubschle, G. M. Sheldrick and B. Dittrich, *J. Appl. Crystallogr.*, 2011, **44**, 1281-1284.

[3] Farrugia, *J. Appl. Crystallogr.*, 1997, **30**, 565

Crystal Data and structure refinement for **11**

Identification code	FCT090	
Empirical formula	C20 H23 N4 O3.5 S	
Formula weight	407.48	
Temperature	293(2) K	
Wavelength	0.71073 Å	
Crystal system	Monoclinic	
Space group	P2/n	
Unit cell dimensions	a = 17.9444(13) Å	α = 90°
	b = 5.6177(4) Å	β = 104.650(3)°
	c = 20.2368(14) Å	γ = 90°
Volume	1973.7(2) $Å^3$	
Z	4	
Density (calculated)	1.371 Mg/m^3	
Absorption coefficient	0.196 mm^{-1}	
F(000)	860.0	
Crystal size	0.350 x 0.060 x 0.010 mm^3	
Theta range for data collection	4.16 to 55.1°	
Index ranges	-23<=h<=23, -7<=k<=6, -26<=l<=26	
Reflections collected	22629	
Independent reflections	4542 [R(int) = 0.0845]	
Completeness to theta = 25.242°	99.9 %	
Absorption correction	Multi-scan	
Max. and min. transmission	1.000 and 0.456	
Refinement method	Full-matrix least-squares on F^2	
Data / restraints / parameters	4542 / 0 / 274	
Goodness-of-fit on F^2	1.369	
Final R indices [I>2sigma(I)]	R1 = 0.1044, wR2 = 0.3248	
R indices (all data)	R1 = 0.1433, wR2 = 0.3647	
Extinction coefficient	n/a	
Largest diff. peak and hole	0.59 and 1.69 e.$Å^{-3}$	

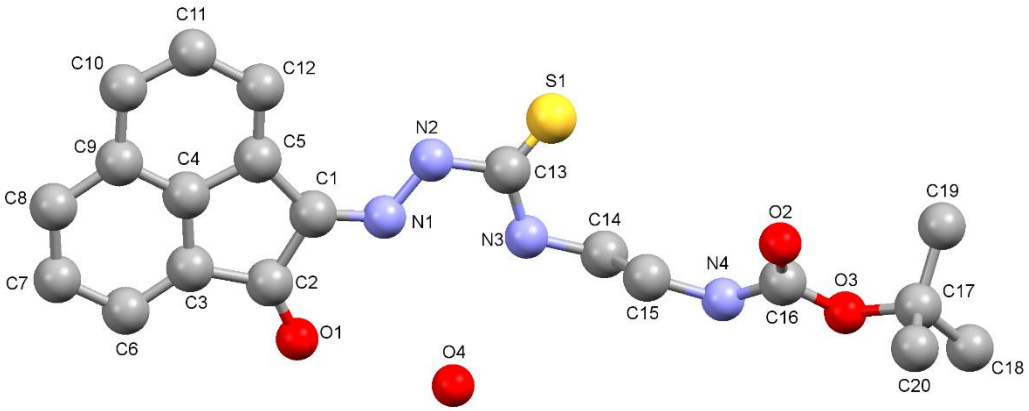

Crystal Data and structure refinement for **12**

Identification code	s15sip1	
Empirical formula	C24 H30 N4 O3 S	
Formula weight	454.58	
Temperature	150(2) K	
Wavelength	1.54184 Å	
Crystal system	Monoclinic	
Space group	$P2_1/c$	
Unit cell dimensions	a = 21.7348(4) Å	α = 90°
	b = 11.8244(2) Å	β = 91.497(2)°
	c = 9.1991(2) Å	γ = 90°
Volume	2363.37(8) $Å^3$	
Z	4	
Density (calculated)	1.278 Mg/m^3	
Absorption coefficient	1.481 mm^{-1}	
F(000)	968	
Crystal size	0.250 x 0.200 x 0.010 mm^3	
Theta range for data collection	4.257 to 72.189°.	
Index ranges	-26<=h<=26, -13<=k<=14, -11<=l<=7	
Reflections collected	17176	
Independent reflections	4588 [R(int) = 0.0451]	
Completeness to theta = 67.684°	99.9 %	
Absorption correction	Semi-empirical from equivalents	
Max. and min. transmission	1.00000 and 0.61870	
Refinement method	Full-matrix least-squares on F^2	
Data / restraints / parameters	4588 / 0 / 304	
Goodness-of-fit on F^2	1.030	
Final R indices [I>2sigma(I)]	R1 = 0.0512, wR2 = 0.1354	
R indices (all data)	R1 = 0.0584, wR2 = 0.1426	
Extinction coefficient	n/a	
Largest diff. peak and hole	0.290 and -0.273 $e.Å^{-3}$	

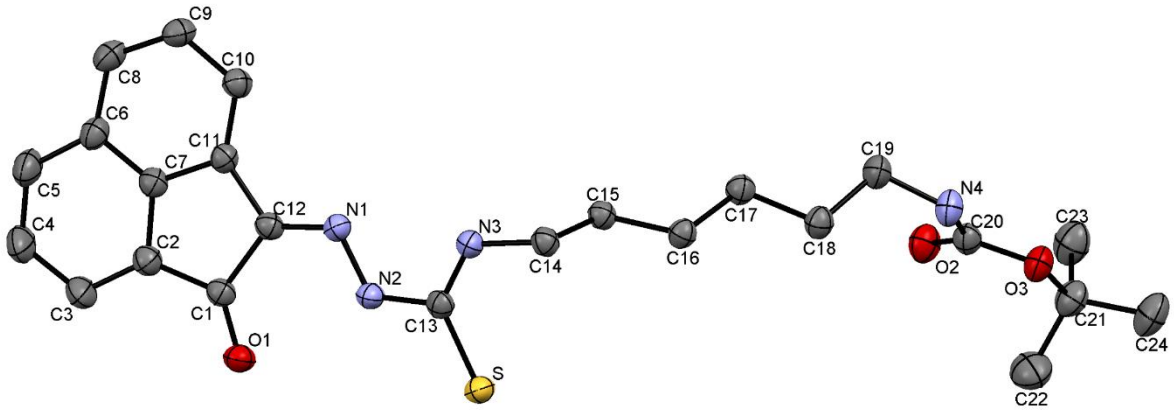

Crystal Data and structure refinement for **40**

Identification code	e15sip4	
Empirical formula	C36 H26 N6 O2 S2	
Formula weight	638.75	
Temperature	150.00(10) K	
Wavelength	0.71073 Å	
Crystal system	Monoclinic	
Space group	$P2_1/n$	
Unit cell dimensions	a = 7.378(2) Å	α = 90°
	b = 21.882(7) Å	β = 94.82(3)°
	c = 9.166(3) Å	γ = 90°
Volume	1474.6(8) $Å^3$	
Z	2	
Density (calculated)	1.439 Mg/m^3	
Absorption coefficient	0.227 mm^{-1}	
F(000)	664	
Crystal size	0.200 x 0.100 x 0.050 mm^3	
Theta range for data collection	3.339 to 25.385°.	
Index ranges	-8<=h<=8, -26<=k<=24, -11<=l<=5	
Reflections collected	5780	
Independent reflections	2692 [R(int) = 0.1250]	
Completeness to theta = 25.242°	99.8 %	
Absorption correction	Semi-empirical from equivalents	
Max. and min. transmission	1.00000 and 0.98133	
Refinement method	Full-matrix least-squares on F^2	
Data / restraints / parameters	2692 / 2 / 218	
Goodness-of-fit on F^2	0.978	
Final R indices [I>2sigma(I)]	R1 = 0.0906, wR2 = 0.1092	
R indices (all data)	R1 = 0.2388, wR2 = 0.1613	
Extinction coefficient	n/a	
Largest diff. peak and hole	0.361 and -0.383 $e.Å^{-3}$	

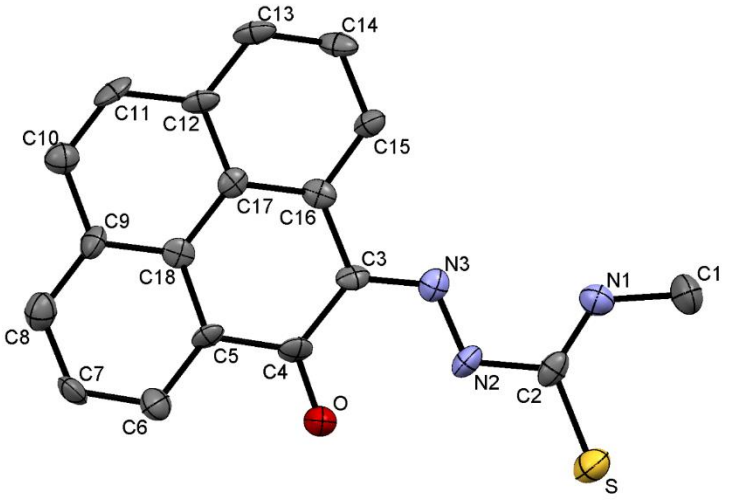

Crystal Data and structure refinement for **41**

Identification code	e15sip3	
Empirical formula	C19 H15 N3 O S	
Formula weight	333.40	
Temperature	150(2) K	
Wavelength	0.71073 Å	
Crystal system	Monoclinic	
Space group	$P2_1/n$	
Unit cell dimensions	a = 7.8711(4) Å	α = 90°
	b = 21.9365(13) Å	β = 99.273(5)°
	c = 9.3107(6) Å	γ = 90°
Volume	1586.62(16) Å	
Z	4	
Density (calculated)	1.396 Mg/m^3	
Absorption coefficient	0.215 mm^{-1}	
F(000)	696	
Crystal size	0.400 x 0.220 x 0.180 mm^3	
Theta range for data collection	3.561 to 29.378°.	
Index ranges	-10<=h<=10, -28<=k<=29, -12<=l<=12	
Reflections collected	14236	
Independent reflections	3839 [R(int) = 0.0309]	
Completeness to theta = 25.242°	99.7 %	
Absorption correction	Semi-empirical from equivalents	
Max. and min. transmission	1.00000 and 0.90874	
Refinement method	Full-matrix least-squares on F^2	
Data / restraints / parameters	3839 / 12 / 244	
Goodness-of-fit on F^2	1.069	
Final R indices [I>2sigma(I)]	R1 = 0.0494, wR2 = 0.1126	
R indices (all data)	R1 = 0.0664, wR2 = 0.1210	
Extinction coefficient	n/a	
Largest diff. peak and hole	0.280 and -0.303 $e.Å^{-3}$	

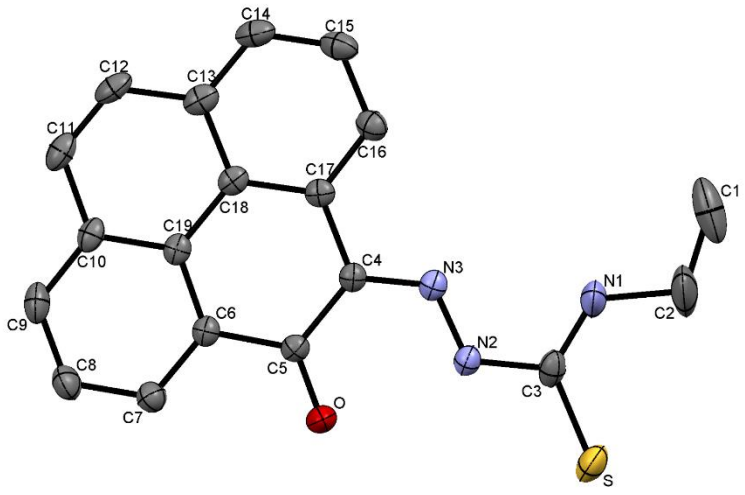

Crystal Data and structure refinement for **42**

Identification code	e15sip2	
Empirical formula	C20 H15 N3 O S	
Formula weight	345.41	
Temperature	150(2) K	
Wavelength	0.71073 Å	
Crystal system	Triclinic	
Space group	P-1	
Unit cell dimensions	a = 8.1032(3) Å	α = 79.553(3)°
	b = 9.0297(3) Å	β = 87.125(3)°
	c = 11.1963(4) Å	γ = 85.009(3)°
Volume	802.10(5) $Å^3$	
Z	2	
Density (calculated)	1.430 Mg/m^3	
Absorption coefficient	0.215 mm^{-1}	
F(000)	360	
Crystal size	0.300 x 0.300 x 0.200 mm^3	
Theta range for data collection	3.512 to 29.244°.	
Index ranges	-10<=h<=10, -12<=k<=12, -14<=l<=15	
Reflections collected	20946	
Independent reflections	4026 [R(int) = 0.0291]	
Completeness to theta = 25.242°	99.7 %	
Absorption correction	Semi-empirical from equivalents	
Max. and min. transmission	1.00000 and 0.97450	
Refinement method	Full-matrix least-squares on F^2	
Data / restraints / parameters	4026 / 0 / 234	
Goodness-of-fit on F^2	1.102	
Final R indices [I>2sigma(I)]	R1 = 0.0437, wR2 = 0.1141	
R indices (all data)	R1 = 0.0508, wR2 = 0.1180	
Extinction coefficient	n/a	
Largest diff. peak and hole	0.407 and -0.248 e.$Å^{-3}$	

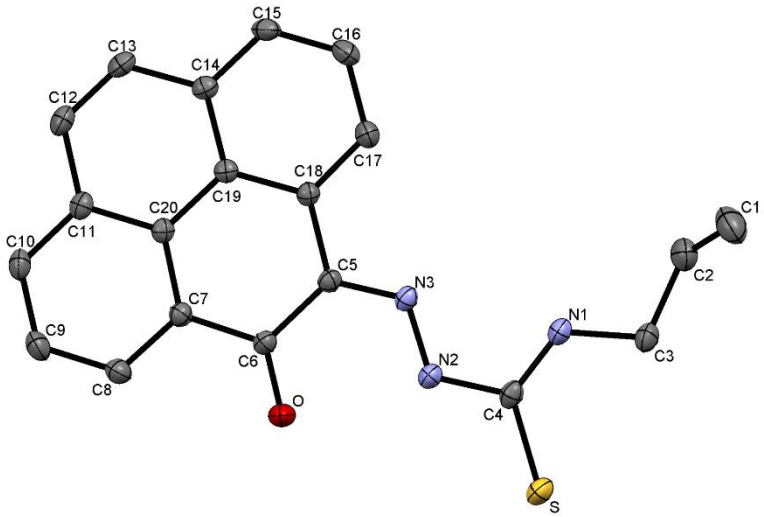

Crystal Data and structure refinement for **43**

Identification code	s15sip8
Empirical formula	C23 H15 N3 O S
Formula weight	381.44
Temperature	150(2) K
Wavelength	1.54184 Å
Crystal system	Monoclinic
Space group	$P2_1/c$
Unit cell dimensions	a = 5.84390(10) Å α = 90°
	b = 25.4324(3) Å β = 98.9650(10)°
	c = 12.07750(10) Å γ = 90°
Volume	1773.08(4) $Å^3$
Z	4
Density (calculated)	1.429 Mg/m^3
Absorption coefficient	1.776 mm^{-1}
F(000)	792
Crystal size	0.300 x 0.150 x 0.080 mm^3
Theta range for data collection	3.476 to 72.591°.
Index ranges	-7<=h<=7, -31<=k<=30, -12<=l<=14
Reflections collected	19536
Independent reflections	3525 [R(int) = 0.0325]
Completeness to theta = 67.684°	100.0 %
Absorption correction	Semi-empirical from equivalents
Max. and min. transmission	1.00000 and 0.72375
Refinement method	Full-matrix least-squares on F^2
Data / restraints / parameters	3525 / 0 / 261
Goodness-of-fit on F^2	1.064
Final R indices [I>2sigma(I)]	R1 = 0.0314, wR2 = 0.0813
R indices (all data)	R1 = 0.0334, wR2 = 0.0827
Extinction coefficient	n/a
Largest diff. peak and hole	0.254 and -0.220 $e.Å^{-3}$

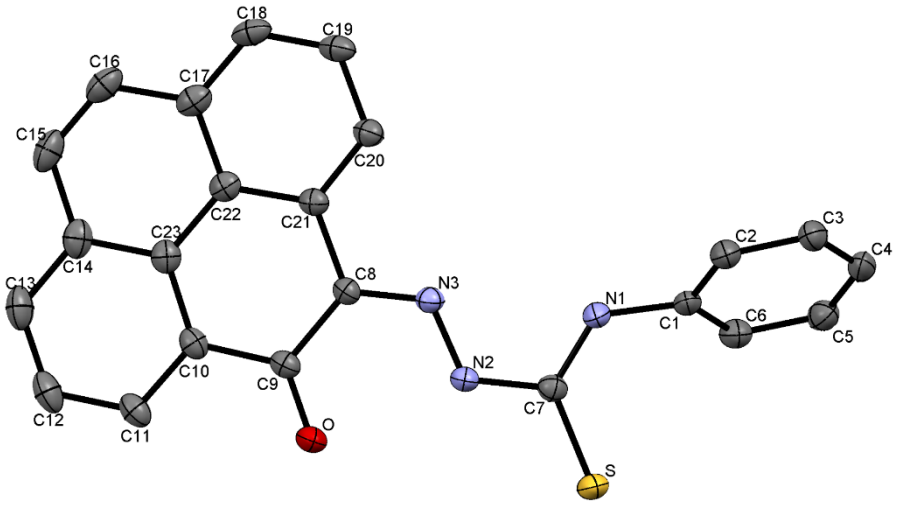

Crystal Data and structure refinement for **52**

Identification code	s16sip6	
Empirical formula	C24 H22 B F2 N3 O4	
Formula weight	465.25	
Temperature	150.00(10) K	
Wavelength	1.54184 Å	
Crystal system	Triclinic	
Space group	P-1	
Unit cell dimensions	a = 6.7311(2) Å	α = 98.686(3)°
	b = 10.4072(3) Å	β = 96.430(3)°
	c = 16.3244(6) Å	γ = 104.497(3)°
Volume	1080.96(6) $Å^3$	
Z	2	
Density (calculated)	1.429 Mg/m^3	
Absorption coefficient	0.915 mm^{-1}	
F(000)	484	
Crystal size	0.150 x 0.150 x 0.040 mm^3	
Theta range for data collection	2.772 to 73.489°.	
Index ranges	-5<=h<=8, -12<=k<=12, -20<=l<=20	
Reflections collected	12844	
Independent reflections	4336 [R(int) = 0.0256]	
Completeness to theta = 67.684°	100.0 %	
Absorption correction	Semi-empirical from equivalents	
Max. and min. transmission	1.00000 and 0.73067	
Refinement method	Full-matrix least-squares on F^2	
Data / restraints / parameters	4336 / 0 / 311	
Goodness-of-fit on F^2	1.040	
Final R indices [I>2sigma(I)]	R1 = 0.0386, wR2 = 0.0974	
R indices (all data)	R1 = 0.0466, wR2 = 0.1027	
Extinction coefficient	n/a	
Largest diff. peak and hole	0.288 and -0.222 $e.Å^{-3}$